ISSN 0288-4534
CODEN: KPPJAD

KONA Powder and Particle Journal

No.31 (2014)

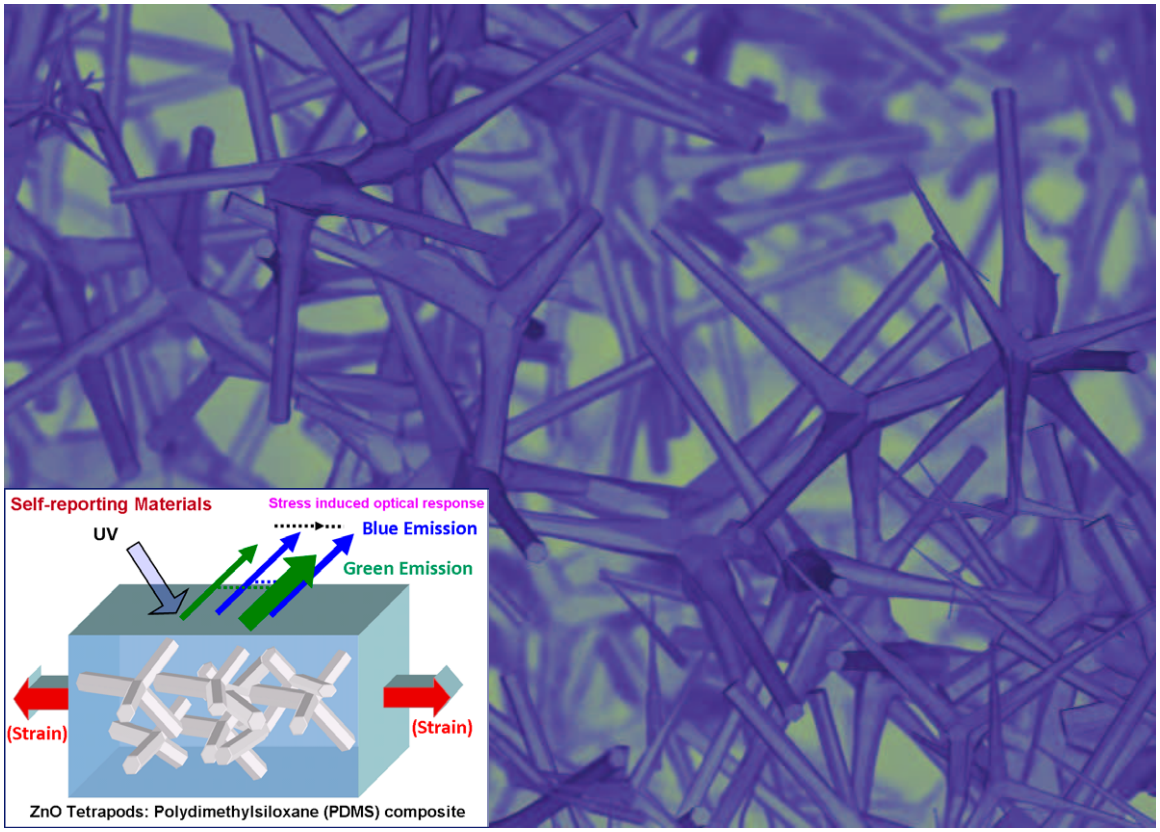

Hosokawa Powder Technology Foundation

available online-www.kona.or.jp

About this Journal

KONA Powder and Particle Journal is a refereed scientific journal that publishes articles on powder and particle science and technology. This journal has been published annually since 1983 and is distributed free of charge to researchers, members of the scientific communities, universities and research libraries throughout the world, by Hosokawa Powder Technology Foundation (http://www.kona.or.jp/) established by Mr. Masuo Hosokawa in 1991.

The Chinese character "粉" in the cover is pronounced "KONA" in Japanese, and means "Powder". The hand written "粉" is after the late Mr. Eiichi Hosokawa, founder of the Hosokawa Micron Corporation (http://www.hosokawa-micron.co.jp).

About the Cover:

Self-reporting materials belong to a subclass of intelligent materials which exhibit the capability to provide the authentic signal of structural damage propagating inside. The cover picture demonstrates a novel concept of self-reporting composite materials built from multifunctional ZnO tetrapods (SEM image) and a polymer matrix. The blue and green luminescent emissions from ZnO tetrapods embedded in the polymer matrix are altered under stress and by monitoring the relative change in their intensities the internal damage can be identified. Please read the full article on pp. 91–109.

Headquarters of Hosokawa Micron Corporation

Editorial Board

■ Publication Office

Hosokawa Powder Technology Foundation (http://www.kona.or.jp)
(in the headquarters building of Hosokawa Micron Corporation)
Shodai- Tajika 1-9, Hirakata, Osaka, 573-1132 Japan
e-mail : info@kona.or.jp

Contents

<Information Articles>

Editor's Preface

Jusuke Hidaka, Editor-in-Chief

Doshisha University, JAPAN

I am pleased to announce the issue of KONA Powder and Particle Journal No. 31. The issue contains outstanding review papers pertaining to a wide range of fields in powder technology—extending from very useful particle production technologies that provide excellent control of particle characteristics including shape and important subjects encountered in actual powder industrial processes such as dust explosion and powder sampling method for quality control, to nanoparticle toxicity and risk assessment—topics that have attracted a great deal of interest in recent years. These review papers will provide the readers with detailed knowledge on the continuing rapid progress of powder technology involving powder processing technologies and the development of advanced functional materials related to powders.

KONA Powder and Particle Journal aims to publish comprehensive review papers authored by researchers who have made remarkable achievements on powder technology. It should make significant contribution to the advancement of powder technology.

This year sees the start of this journal's publication through the Japan Science and Technology Information Aggregator, Electronic (J-STAGE), the online publication platform provided by Japan Science and Technology Agency (JST), a Japanese government agency. J-STAGE is a system for international distribution of journals that are published in Japan. Through its publication via this system, KONA can now be accessed easily, promptly, and free of charge by researchers worldwide. Moreover, although KONA is an annually printed journal, J-STAGE allows for its early publication. The papers reviewed by the Editorial Boards in Europe, America, and Asia will be distributed globally at an earliest possible time in the form of an online journal.

In the publication of a journal on J-STAGE, its article format must be standardized, and writing guidelines need to be more strictly adhered to than was previously done. Therefore, I ask you to make use of the template prepared by the Editorial Boards to meet this requirement.

The development of advanced particles and powder materials is of increasing importance in solving difficult problems faced by the modern society. This journal will provide powder technology researchers worldwide with prompt and detailed information on research trends pertaining to new powder materials and process development. By publishing review papers on the different aspects of powder technology, they inform us not only on advances in each special field but also educate us in other areas where we may find keys to solving future engineering problems on powder technology.

I sincerely hope that this journal will be a platform for lively discussion by powder technology researchers. I would like to thank you for your cooperation.

J. Hidaka

Jusuke Hidaka
Editor-in-Chief
November 22, 2013

KONA Powder and Particle Journal No. 31 (2014) 2–9/Doi:10.14356/kona.2014001 Review Paper

A $PM_{1.0/2.5/10}$ Trichotomous Virtual Impactor Based Sampler: Design and Applied to Arid Southwest Aerosols Part II: Application to Arid Southwest Aerosols †

Virgil Marple [1]*, Dale Lundgren [2] and Bernard Olson [1]

[1] *Particle Calibration Laboratory, University of Minnesota, USA*
[2] *University of Florida, USA*

Abstract

A $PM_{1.0/2.5/10}$ Trichotomous sampler has been developed to determine if the particles in the saddle point between the coarse and fine particle modes (specifically the 1.0 μm to 2.5 μm size range) are primarily coarse or fine mode particles. The sampler consists of a standard high volume sampler with two high volume virtual impactors (one with a cut size of 2.5 μm and the other with a cut size of 1.0 μm) inserted between the PM_{10} inlet and the 8 × 10 inch after filter. Filters in this sampler were analyzed with ion chromatography (IC) to determine SO_4^{-2} concentrations, representing a specie primarily found in the fine mode aerosol and proton-induced X-ray emission (PIXE) for determining concentrations of Si, S, Ca and Fe, representing species normally found in coarse mode aerosols. Application of this sampler to Phoenix, AZ, representing an arid region, showed that particles in the saddle point consisted of about 75% of particles from the coarse mode and about 25% from the fine mode.

Keywords: atmospheric aerosols, virtual impactors, PM_{10}, $PM_{2.5}$, PM_1

Introduction

In the mid-1990s the United States Environmental Protection Agency (EPA) was reviewing the National Ambient Air Quality Standards (NAAQS) for particulate matter (PM). The agency was devising a new Federal Reference Method (FRM) and set a new fine particle standard at either PM_1 or $PM_{2.5}$ to replace the then current 24-hour PM_{10} standard of 150 micrograms per cubic meter ($\mu g/m^3$). When the fine particle standard was being established, there was much discussion amongst experts as to whether the standard should be set at 1.0 μm or 2.5 μm. The problem arose from the nature of the particle size distributions in atmospheric aerosols. Whitby (1978) discovered that atmospheric particle size distributions were trimodal in nature, with fresh combustion particles in the smallest mode, aged combustion particles in the intermediate mode (fine particle mode) and mechanically generated particles in the largest mode (coarse particle mode). These fine and coarse particles have different chemical and physical characteristics and come from different sources (John, 2011). Dr. J.P. Lodge stated in 1995 in the Journal of the AWMA in a "Critical Review Discussion: Measurement Methods to Determine Compliance with Ambient Air Quality Standards for Suspended Particles" (Watson et. al., 1995) that:

> "I had a lengthy discussion with the late K.T. Whitby over the optimum upper boundary for fine particles, which he held to be "... 1.8 μm, or, if you want a purer sample of fine particles, 1 μm." If fine particles are the cause of health effects, and if routine monitoring data are used in epidemiological studies, as Dr. Chow anticipates, we must advocate the use of $PM_{1.0}$ to clarify the composition of the population of the fine particle modes."

This statement would indicate that an ideal particle cut size would be one below which almost all the fine particles are contained, but very few coarse particles are present. Particles in this size range consist of particles from the lower tail of the coarse particle mode and particles from the upper tail of the fine particle mode (see **Fig. 1**).

Of specific interest in this study was the atmospheric particulate matter of the arid southwest USA. The city chosen to study was Phoenix, Arizona from May to October,

† Accepted: January 23, 2013
1 111 Church Street S. E Minnneapolis, MN 55455, USA
* Corresponding author:
E-mail: marple@me.umn.edu
TEL: +1-612-625-3441 FAX: +1-612-625-6069

1995. In this area of the country the coarse particle mode can be much larger than the fine particle mode and, thus, may dominate the particulate matter in the saddle region between the fine and coarse particle modes.

The concern was that the large particle mode lower tail, consisting of fugitive and windblown dust, could dominate the particles in the 1 to 2.5 µm size range, a test program was initiated to collect particulate matter in this size range and determine the fraction of the particulate matter that may be coarse mode aerosol.

In part I of this paper, published in the 2012 issue of KONA (Marple et.al., 2012), a $PM_{1.0/2.5/10}$ trichotomous sampler (see **Fig. 2**) was developed to specifically answer the question of what fraction of particles in the 1.0 µm to 2.5 µm size range are part of the fine particle mode and what fraction are from the coarse particle mode, is described.

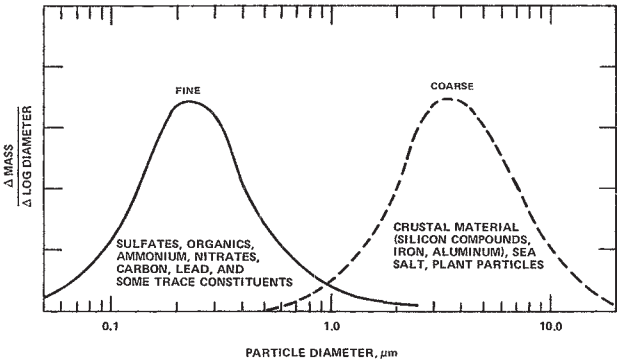

Fig. 1 Fine and Coarse Particle Modes. From U.S. Environmental Protection Agency (1982)

Review of the $PM_{1.0/2.5/10}$ trichotomous sampler

In the $PM_{1.0/2.5/10}$ trichotomous sampler two High Volume Virtual Impactors (HVVIs), with cutsizes of 2.5 µm and 1.0 µm were inserted between the PM10 size selective inlet and the 8×10 inch (20×25 cm) filter of a standard high volume 40 cfm (1.13 m^3/min) flowrate PM10 sampler (Marple and Olson, 1995). **Fig. 2a** shows the assembled trichotomous sampler, while **Figs. 2b** and **2c** shows the sampler opened to provide access to the 2.5 µm and the 1.0 µm HVVIs, respectively.

By using nine 47 mm filters at various locations in the trichotomous sampler, concentration and composition of particles could be obtained for particulate matter in the ranges of PM_{10}, $PM_{2.5–10}$, $PM_{2.5}$, $PM_{1–2.5}$, and PM_1. From data analysis of these filters, the fraction of the particulate matter in the 1.0 µm to 2.5 µm size range that are fine and coarse mode particles can be determined. See Part I for further details of this sampler.

Mass and specie analysis techniques

The net mass gains on the filters were determined gravimetrically by weighing them before and after sampling. The weighings were conducted in a controlled environment where the temperature was maintained at 24 ± 3°C and the relative humidity at 30 ± 10% to minimize loss of soluble and volatile compounds. As a quality control measure, approximately one out of ten filters was later reweighed.

Several methods were available to determine elemental compositions of the PM collected on the filters. For this study, proton-induced X-ray emission (PIXE)

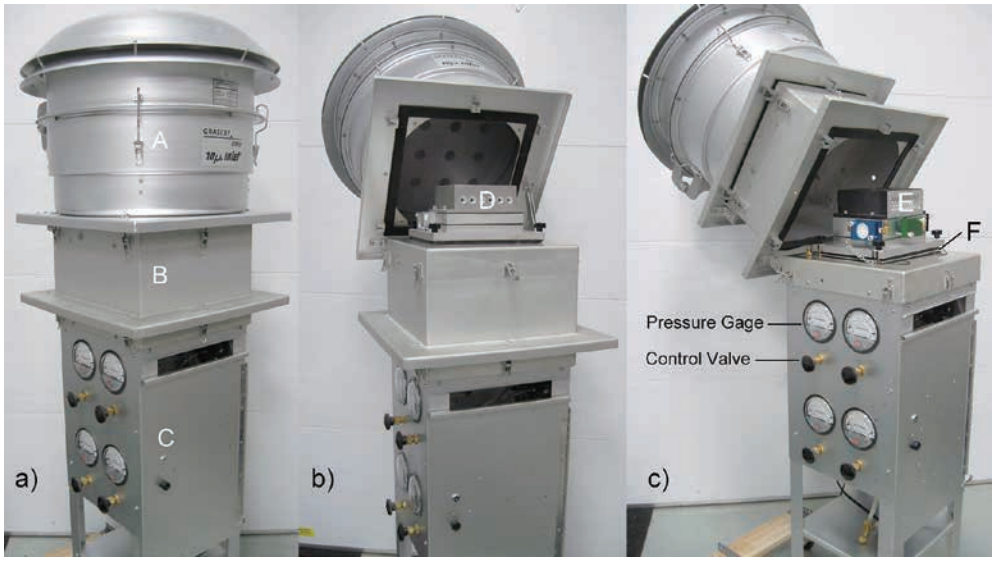

Fig. 2 Photos of $PM_{1.0/2.5/10}$ Trichotomous Sampler. a) Assembled sampler; b) 2.5 µm HVVI; c) 1.0 µm HVVI
A-PM10 inlet; B-Intermediate chamber; C-Base; D-2.5 µm HVVI; E-1.0 µm HVVI; F-After filter

and photon-induced x-ray fluorescence (XRF) methods were used. Both of these methods are commonly used due to their nondestructive multi-element capabilities and relatively good sensitivities.

Aerosol ions (i.e., the water-soluble portion of the suspended particles in the atmosphere) were quantified using ion chromatography (IC). Using the IC method, the extracted sample passes through an ion-exchange column and the separated ions are individually analyzed by an electroconductivity detector.

Volatile aerosol materials such as organics and nitrates were not included in this study. Although a large portion of the fine aerosol often consists of volatile organics or nitrates, little of the remaining (weighable) PM collected on the filters was expected to be volatile, since the filters were exposed to the high summer temperatures of Phoenix (often exceeding 40°C during the day).

Mass concentrations

PM mass concentrations (μg/m^3) were determined by dividing the net weight gain (μg) on a filter by the total air volume (m^3) that passed through it during the 24-hour sampling period. Although a small decrease in flowrate can be expected at the end of sampling period due to a slightly higher pressure drop caused by particle loading on the filters, no flowrate correction was deemed necessary for the purposes of this study. Mass concentrations were, however, divided by an appropriate "flow factor" to account for the fact that the samplers did not run for exactly 24 hours in most cases. The general equation used for mass calculations is as follows:

$$PM_X = \frac{\Delta m}{V \times f} \tag{1}$$

Where PM_X = PM mass concentration for size fraction × (μg/m^3), Δm = mass gain on filter (μg), V = flow volume through filter in 24 hours (m^3) and f = flow factor (fraction of 24-hour day that sampler was operated). Thus, the following equations were then used to calculate mass concentrations for various PM size fractions:

$$PM_{10} = \frac{\Delta m\ (\mathrm{PM_{10}})}{81.6 \times f} \tag{2}$$

$$PM_{2.5} = \frac{\Delta m\ (\mathrm{PM_{2.5}})}{81.6 \times f} \tag{3}$$

$$PM_1 = \frac{\sum \Delta m\ (\mathrm{PM_1})}{81.6 \times f} \tag{4}$$

$$PM_{2.5\text{–}10} = \frac{\Delta m(\mathrm{PM_{2.5\text{–}10}}) - \dfrac{\Delta m\ (\mathrm{PM_{2.5}})}{10}}{163 \times f} \tag{5}$$

$$PM_{1\text{–}2.5} = \frac{\sum \Delta m(\mathrm{PM_{1\text{–}2.5}}) - \sum \Delta m\ (\mathrm{PM_1})}{1469 \times f} \tag{6}$$

In equations (5) and (6), the terms $\{\Delta m(\mathrm{PM_{2.5\text{–}10}})\}$ and $\{\Sigma\Delta m(\mathrm{PM_{1\text{–}2.5}})\}$ are the masses collected on the minor flow filters of the 2.5 μm and 1.0 μm HVVIs, respectively. The Σ sign in equation (6) indicates summing the mass collected on both filters being used to collect minor flow particles in the 1.0 μm HVVI. As described in Part I of this paper, particles collected in the minor flow of the HVVIs contain background particles (particles of a size less than the cutsize of the HVVI) and the mass of these background particles must be subtracted from the mass of the particles in the minor flow to determine the true mass of particles in the minor flow that are larger than the cutsize of the HVVI. In equations (5) and (6), this background mass is represented by the terms $\{\Delta m(\mathrm{PM_{2.5}})/10\}$ and $\{\Sigma\Delta m(\mathrm{PM_1})\}$ in the 2.5 μm and 1.0 μm HVVIs, respectively. The factor of 10 in the denominator of equation (5) is due to the flowrate of the filter collecting the major flow particulate matter of the 2.5 μm HVVI is 2 cfm and the flowrate of the filter collecting particulate matter in the minor flow is 0.2 cfm.

Using equations (2) to (6), results of the 6-month sampling program in Phoenix are summarized as mass concentrations in **Table 1** and as percent of PM_{10} in **Table 2**. Average PM_1, $PM_{2.5}$ and PM_{10} concentrations for the Phoenix area are 5.9, 8.6, and 32.8 μg/m^3, respectively. In terms of percentages, PM_{10} was made of 69% $PM_{2.5\text{–}10}$, 26% $PM_{2.5}$ (< 2.5 μm), 8% $PM_{1\text{–}2.5}$, and 18% PM_1 (< 1 μm). It is also interesting to note that average % $PM_{1\text{–}2.5}$ appears to be nearly constant (at about 8%) for all six months. A comparison of measured PM_{10} and summed PM_{10} ($PM_{2.5\text{–}10}$ + $PM_{1\text{–}2.5}$ + PM_1) can also be seen in **Tables 1** and **2**. In general, summed PM_{10} is slightly less than measured PM_{10}, most likely due to particle loss in the HVVIs.

Intermodal size range ($PM_{1\text{–}2.5}$) calculations

Atmospheric aerosol is formed by two basic processes: the dispersion process, which is the breakup of solid and liquid particles; and the condensation/reaction process, which represents particle formation by coming together of gases and smaller particles (including surface reactions). Aerosol formed by the dispersion mechanism is generally of larger size (normally > 1 μm in diameter) and will be referred to as "coarse" mode aerosol (and the particles as coarse particles) (ref). On the other hand, aerosol formed by the condensation/reaction mechanism is usually of

Table 1 Summary of PM concentrations (μg/m^3), Phoenix, AZ

Month (1995)	PM_{10}	$PM_{2.5}$	PM_1	$PM_{2.5-10}$	$PM_{1-2.5}$	PM_{10} ($PM_{2.5-10}$+$PM_{1-2.5}$+PM_1)
May	25.8	6.6	4.4	18.4	2.2	25.0
June	34.0	8.8	5.7	26.8	3.3	35.7
July	35.0	8.6	5.8	26.3	2.9	35.0
August	25.9	7.9	5.7	15.3	2.0	23.0
September	26.9	7.8	5.8	16.1	2.0	23.9
October	57.8	14.2	9.9	35.7	4.2	49.8
Average	32.8	8.6	5.9	22.6	2.7	31.3

Table 2 Phoenix PM data expressed as percentages of PM_{10}

Month (1995)	PM_{10}	$PM_{2.5}$	PM_1	$PM_{2.5-10}$	$PM_{1-2.5}$	PM_{10} ($PM_{2.5-10}$+$PM_{1-2.5}$+PM_1)
May	100%	26%	17%	72%	8%	97%
June	100%	26%	17%	79%	10%	105%
July	100%	25%	17%	75%	8%	100%
August	100%	30%	22%	59%	8%	89%
September	100%	29%	21%	60%	8%	89%
October	100%	25%	17%	62%	7%	86%
Average	100%	26%	18%	69%	8%	95%

smaller size (normally < 2.5 μm in diameter) and will be referred to as "fine" mode aerosol (and the particles as fine particles). All diameters are of aerodynamic particle size (i.e., a unit density spherical particle with equivalent aerodynamic properties).

Intermodal size range ($PM_{1-2.5}$) calculations in this study were made using chemical composition data obtained from the PM_1, $PM_{1-2.5}$, and $PM_{2.5-10}$ filter samples. The following assumptions were made for the calculations: 1) Intermodal aerosol is composed of coarse and fine mode aerosol with the two modes overlapping in the intermodal size range; 2) Both coarse and fine modes are chemically homogeneous over their respective particle size ranges; 3) Coarse mode aerosol is contained within the 1 to > 10 μm size range, and the chemical composition of the coarse mode aerosol is fairly represented by that of $PM_{2.5-10}$; and 4) Fine mode aerosol is contained within the 0 to 2.5 μm size range, and the chemical composition of fine mode aerosol in fairly represented by that of PM_1 (i.e., < 1 μm).

Based upon these assumptions, it is possible to calculate how much of the intermodal particle mass was contributed by the coarse mode PM (wind-blown dust) and how much by the fine mode PM (gas reaction or condensation products). The following algorithms were developed:

$$X + Y = I \tag{7}$$

$$(X\%S_C) + (Y\%S_F) = I\%S_I \tag{8}$$

where X = mass contribution from coarse mode (μg/m^3), Y = mass contribution from fine mode (μg/m^3), I = $PM_{1\text{-}2.5}$ mass (μg/m^3), $\%S_C$ = percent of species in $PM_{2.5-10}$ (used to represent the coarse mode), $\%S_F$ = percent of species in PM_1 (used to represent the fine mode), $\%S_I$ = percent of species in $PM_{1-2.5}$ (considered as the intermediate range).

Equations (7) and (8) can easily be solved for X and Y, since X and Y are the only two unknowns. The percent of any specie "$_i$" in the intermediate range that is contributed by the coarse, $(\%X)_i$, and fine, $(\%Y)_i$, modes can then be calculated. For the coarse mode contribution:

$$(\%X)_i = \frac{(\%S_I)_i - (\%S_F)_i}{(\%S_C)_i - (\%S_F)_i} \times 100 \tag{9}$$

And for the fine mode contribution:

$$(\%Y)_i = \frac{(\%S_I)_i - (\%S_F)_i}{(\%S_C)_i - (\%S_F)_i} \times 100 \tag{10}$$

Sample Calculation

Example calculations are based on data from two Trichotomous samplers for July 19.1995:

	Mass Conc. (μg/m^3)			SO_4^{-2} Data	
	Unit 1	Unit 2	Average	(μg/m3)	%
$PM_{2.5-10}$ (coarse)	14.06	12.23	13.15	0.27	2.1
$PM_{1-2.5}$ (intermediate)	1.75	1.62	1.68	0.13	7.7
PM_1 (fine)	5.53	4.07	4.80	1.71	35.6

Using equations (9) and (10),

$\%X = (7.7 - 35.6)/(2.1 - 35.6)$
$= 83\%$ contribution from coarse mode

and

$\%Y = (7.7 - 2.1)/(35.6 - 2.1)$
$= 17\%$ contribution from fine mode

Thus, this example indicates that 83% of the SO_4^{-2} particles in the intermediate region (sizes from 1.0 to 2.5 μm) are from the lower tail of the coarse mode and 17% are from the upper tail of the fine mode.

The data gathered from the trichotomous samplers from May to October, 1995, was analyzed using the method laid out in the above sample calculation. Two sets of data were chosen for analysis; 1) data from six days in July, 1995, was analyzed by ion chromatography (IC) and 2) data from five days in May, 1995, was analyzed by proton-induced X-ray emission (PIXE).

IC analyses were used to determine concentrations for the anions SO_4^{-2}, NO_3^-, and Cl^-. **Table 3** presents the calculated percent contributions of coarse and fine mode PM to the intermediate size PM ($PM_{1-2.5}$), based upon SO_4^{-2} concentration data for six July days of high, medium, and low mass concentrations. The results indicate that the coarse mode contribution to the intermodal size varies from 75% to 91% (with an average of 83%), and therefore, the fine mode contributions ranges from 9% to 25% (with an average of 17%). Due to their instability and associated analytical problems, the contribution analysis of NO_3^- and Cl^- were found to be inconclusive, and are not shown.

The PIXE results indicated that Si, S, Ca, Fe, K, and Al were among the most abundant species in the samples analyzed. Therefore, they were chosen for the elemental contribution analysis in this study. The K and Al contribution results were questionable and thus excluded. Elemental concentrations for the five days in May are shown in **Table 4**. **Table 5** shows the contribution results from analysis of the data in **Table 4**.

The results in **Table 5** clearly indicate that most of the PM in the intermediate region is associated with coarse mode particulate.

Data quality assessment

As with any field project, some sampling and analytical problems were encountered in this study. To ascertain that the data presented here is statistically valid, certain data reduction procedures were carefully followed in addition to the standard laboratory quality control measures. For example, no apparently-out-of-line data (i.e., does not fall within the 95% confidence limits) was invalidated, unless the cause was known or obvious (e.g., power failure). When two samplers were run, mass concentrations were averaged between both samplers as well as between two filters of the same particle size, so that the data are statis-

Table 3 Sulfate and mass data for six July days (μg/m^3)

Day	$PM_{2.5-10}$ (Coarse)		$PM_{1-2.5}$ (Intermediate)		PM_1 (Fine)		%X*
	Mass	Sulfates	Mass	Sulfates	Mass	Sulfates	
7/15/95	12.94	0.19 (1.5%)	1.40	0.09 (6.4%)	5.70	1.20 (21.1%)	75%
7/19/95	13.15	0.27 (2.1%)	1.68	0.13 (7.7%)	4.80	1.71 (35.7%)	83%
7/23/95	20.92	0.30 (1.4%)	2.79	0.10 (3.6%)	5.87	0.78 (13.3%)	82%
7/26/95	29.98	0.36 (1.2%)	3.15	0.13 (4.1%)	3.54	1.12 (31.6%)	90%
7/28/95	62.39	0.26 (0.4%)	5.38	0.16 (3.0%)	11.26	1.41 (12.5%)	79%
7/30/95	74.02	0.64 (0.9%)	7.68	0.20 (2.6%)	6.86	1.34 (19.5%)	91%
Average	35.57	0.34 (1.0%)	3.21	0.14 (4.4%)	6.34	1.26 (19.9%)	83%

X* is the calculated coarse mode contribution to $PM_{1-2.5}$ (See text).

Table 4 Elemental data for five May days (μg/m^3)

		Total Mass	Si	S	Ca	Fe	K	Al
5/2/95	$PM_{2.5–10}$	15.67	1.82	0.06	0.69	0.64	0.27	0.61
	$PM_{1–2.5}$	2.03	0.20	0.03	0.03	0.07	0.03	0.08
	PM_1	3.04	0.05	0.18	0.01	0.03	0.02	0.03
5/6/95	$PM_{2.5–10}$	11.77	1.37	0.05	0.42	0.48	0.20	0.48
	$PM_{1–2.5}$	1.66	0.21	0.03	0.05	0.06	0.03	0.08
	PM_1	3.88	0.04	0.21	0.01	0.01	0.02	0.02
5/18/95	$PM_{2.5–10}$	32.38	3.93	0.11	1.34	1.50	0.58	1.29
	$PM_{1–2.5}$	2.70	0.20	0.03	0.07	0.11	0.03	0.07
	PM_1	8.84	0.03	0.20	0.01	0.03	0.02	0.01
5/19/95	$PM_{2.5–10}$	20.55	1.95	0.07	0.68	0.69	0.29	0.65
	$PM_{1–2.5}$	2.08	0.16	0.03	0.06	0.07	0.03	0.06
	PM_1	5.76	0.03	0.15	0.01	0.02	0.03	0.01
5/26/95	$PM_{2.5–10}$	24.73	2.25	0.08	0.80	0.89	0.34	0.76
	$PM_{1–2.5}$	2.18	0.19	0.03	0.06	0.08	0.03	0.07
	PM_1	5.54	0.03	0.23	0.01	0.02	0.03	0.02
Average	$PM_{2.5–10}$	21.02	2.26	0.07	0.79	0.84	0.34	0.76
	$PM_{1–2.5}$	2.03	0.19	0.03	0.06	0.08	0.03	0.07
	PM_1	5.41	0.03	0.19	0.01	0.02	0.02	0.02

Si = Silicon, S = Sulfur, Ca = Calcium, Fe = Iron, K = Potassium, Al = Aluminum

Table 5 Contribution to the intermodal ($PM_{1–2.5}$) aerosol from coarse and fine particle modes

	Average for the five days in May, 1995	
Specie	%*X*	%*Y*
Si	79	21
S	67	33
Ca	76	24
Fe	85	15
Average	78	22

tically more representative.

Table 6 shows precision data for the two co-located trichotomous samplers. The EPA performance specifications call for precision in the range of ± 5 μg/m^3 for PM_{10} concentrations less than 80 μg/m^3 and ± 7% for concentrations over 80 μg/m^3.

Conclusions

Results of the Phoenix $PM_{10}/PM_{2.5}/PM_1$ study using the trichotomous sampler technique can be summarized as follows: First, it can be shown that most of the PM_{10} in this area is made up of coarse mode aerosol ($PM_{2.5–10}$). Secondly, most of the intermediate size aerosol ($PM_{1–2.5}$) was due to the coarse mode (dispersion) aerosol. Therefore, crustal materials from sources such as windblown dust are the most significant contributor to the PM concentration in this area, far more so than the combustion related sources. Based up on the calculations presented, it appears that PM measurement using a cutpoint of 1 μm would capture about 90% as much fine mode mass as those made using a cutpoint of 2.5 μm, and would minimize any interference from natural sources (e.g., windblown dust). The reader should bear in mind that these results and conclusions are only valid for conditions similar to those at the Phoenix site, namely the dry, arid Southwest.

Acknowledgements

Development and calibration of the $PM_{1.0/2.5/10}$ Trichotomous sampler has been supported by the National Mining Association.

Table 6 Precision data for the two trichotomous samplers

	May	June	July	August	Average
PM_{10}					
Unit 1	26.9	34.4	34.9	25.8	30.5
Unit 2	24.7	33.5	35.1	25.9	29.8
S.D. (μg/m^3)	5.5	2.6	2.6	1.8	3.1
S.D. (%)	20.3	7.0	7.9	6.8	10.5
$PM_{2.5}$					
Unit 1	6.6	9.5	8.9	7.9	8.2
Unit 2	6.6	8.1	8.3	7.9	7.7
S.D. (μg/m^3)	1.0	1.0	2.9	0.9	1.5
S.D. (%)	16.7	11.3	27.6	11.5	16.8
PM_1					
Unit 1	4.4	5.9	6.0	5.9	5.6
Unit 2	4.4	5.5	5.6	5.6	5.3
S.D. (μg/m^3)	0.9	2.3	2.9	1.8	2.0
S.D. (%)	22.1	54.5	45.4	32.9	38.7
$PM_{2.5–10}$					
Unit 1	17.8	25.3	26.1	15.3	21.1
Unit 2	19.0	28.3	26.5	15.3	22.3
S.D. (μg/m^3)	1.4	6.3	2.9	1.4	3.0
S.D. (%)	7.0	28.1	11.3	13.6	15.0
$PM_{1–2.5}$					
Unit 1	2.2	3.6	3.0	2.0	2.7
Unit 2	2.2	2.9	2.9	1.9	2.5
S.D. (μg/m^3)	0.1	0.3	0.5	0.2	0.3
S.D. (%)	5.5	7.5	29.6	13.4	14.0
PM_{10} (sum)					
Unit 1	24.4	34.8	35.0	23.1	29.3
Unit 2	25.6	36.7	35.0	22.8	30.0
S.D. (μg/m^3)	1.7	5.9	3.7	2.1	3.4
S.D. (%)	5.9	18.3	10.0	9.1	10.8

S.D.= Standard Deviation of the differences between Unit 1 and Unit 2.
For PM_{10} samplers, EPA specifies precision of 5 μg/m^3 for conc. less than 80 μg/m^3, and 7% for conc. greater than 80 μg/m^3.

References

John W., Size distribution characteristics of aerosols, in: Kulkarni P., Baron P.A., Willeke K. (Eds.), Aerosol Measurement: Principles, Techniques, and Applications, 3rd Edition, Wiley, New Jersey, 2011, pp. 41–54.

Marple V.A., Lundgren D.A., Olson B.A., A $PM_{1.0/2.5/10}$ trichotomous virtual impactor based sampler: Design and applied to arid southwest aerosols—Part I: Design, KONA Powder and Particle Journal, 30 (2012) 15–21.

Marple V.A., Olson B.A., A high volume $PM_{10/2.5/1.0}$ trichotomous sampler, in: Particulate Matter: Health and Regulatory Issues, VIP-49, Air and Waste Management Assoc. International Specialty Conference, Pittsburg, PA, 1995, pp. 237–261.

U.S. Environmental Protection Agency, Air quality criteria for particulate matter and sulfur, EPA-600/882-029b, December, 1982.

Watson J.G., Thurston G., Frank N., Lodge J.P., Wiener R.W., McElroy F.F., Kleinman M.T., Mueller P.K., Schmidt A.C., Lipfert F.W., Thompson R.J., Dasgupta P.K., Marrack D., Michaels R.A., Moore T., Penkala S., Tombach I., Vestman L., Hauser T., Chow J.C., Measurement Methods to Determine Compliance with Ambient Air Quality Standards for Suspended Particles, Journal of the air & Waste Management Association, 45 (1995) 666–684.

Whitby K.T., The physical characteristics of sulfur aerosols, Atmospheric Environment, 12 (1978) 135–159.

Author's short biography

Virgil A. Marple

Virgil A. Marple is a Professor in the Mechanical Engineering Department at the University of Minnesota. He received his Ph.D. from the University of Minnesota in 1970. He is Director of the Particle Calibration Laboratory, and his research interest includes development of inertial classifiers, measurement of mining related aerosol in both the coal and taconite industries and measurement of pharmaceutical aerosols.

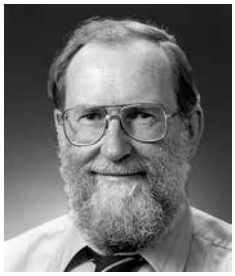

Dale A. Lundgren

Dale A. Lundgren is Professor Emeritus—Environmental Engineering Department, University of Florida. He received his Ph.D. from the University of Minnesota in 1973. His recent research interest has been as a consultant to the National Resource Research Institute (University of Minnesota Duluth campus) studying particulate concentrations in cities and taconite mines on the Minnesota Iron range.

Bernard A. Olson

Bernard A. Olson is a Research Associate and Manager of the Particle Calibration Laboratory in the Mechanical Engineering Department at the University of Minnesota. He received his BSME, MSME, and Ph.D. from the University of Minnesota. For the past 22 years his research has been in the design, testing and numerical modeling of aerosol sampling instruments, characterization of mining aerosols related to the coal mine and taconite industries and effluents generated by cooking appliances in the commercial kitchen industry.

KONA Powder and Particle Journal No. 31 (2014) 10–21/Doi:10.14356/kona.2014002 Review Paper

The Relationships among Structure, Activity, and Toxicity of Engineered Nanoparticles†

Christie M. Sayes

[1] *Center for Aerosol and Nanomaterials Engineering, RTI International, USA*

Abstract

Particles within the nanometer size regime (1–100 nm) exhibit properties across quantum and classical mechanics. An example of the quantum mechanical nature of some particles includes their ability to bend light and change color appearance in suspension. An example of the classical mechanical nature of some particles includes their tendency to agglomerate in suspension. Both of these phenomenons are extensively studied in the literature and are the subject of many research projects that examine the utility of nanoparticles in biomedical and environmental applications. However, these unique properties have also been shown to induce unintentional toxicological effects in various biological and ecological systems. In this paper, the applications and implications of engineered nanoparticles in aqueous suspensions will be reviewed and discussed relevant to the particle's structure on the nanometer size scale and its subsequent biological activity at the cellular level.

Keywords: nanoparticles, nanotoxicology, physicochemical, SARs, safety

1. Introduction

Engineered nanostructures are ubiquitous in the world around us. Personal interactions with these materials are inevitable, most notably through worker exposure in the chemical industry or consumer exposure through biomedical products. Therefore, assessments of potential risks associated with contact, including toxicological evaluations, are of paramount importance in the safe development of engineered nanostructures. One important factor within the regulatory discussion is the need for accurate and relevant nanomaterial characterization of the physicochemical properties for toxicological evaluations. The toxicity of nanomaterials can be ranked according induced toxicities and inflammation at different concentrations over different time points. Chemical composition and surface coating of the nanomaterial can be related to toxicological responses. Data suggest that users of certain nanomaterials may rely on ex vivo measures of concentration, composition, agglomeration, leached metal ions, and reactive species production, as well as other features such as crystallite phase, surface chemistry, and particle surface charge as indicators for safety assessment.

† Accepted: May 31, 2013

[1] 3040 Cornwallis Road, Durham, NC 27709, USA
E-mail: csayes@rti.org
TEL: +1-919-541-6414 FAX: +1-919-541-6936

2. Structure-activity relationships and their relevance to particle science

The model engineered-nanoparticle has three distinct structural features that strongly contribute to its potential biological activity. These common features of a nanoparticle include highly crystalline, monodisperse, and large surface area materials. These features are exploited to gain a unique material-type for a particular application; however, this exploitation comes at a cost in that highly crystalline particles often produce reactive oxygen species when suspended in aqueous solutions, small monodisperse particles distribute within an *in vivo* model rapidly and distally, and particles with large surface area interact with native biomolecules which in turn disrupt normal biological processes.

Traditionally, structure-activity relationships (SARs) relate the chemical structure of a compound to qualitative biological activity. Toxicologists worldwide face a daunting task in screening hundreds of chemicals suspended in different media for innumerable toxicological endpoints. While *in vivo* (animal) and *in vitro* (cell culture) testing are still considered the backbones of obtaining a comprehensive toxicological and risk assessment framework, these traditional methods are both time consuming and expensive. A systematic and organized approach such as computer-based modeling methods that relates experimental data to measurable biological responses is the need of the hour. These resulting "models" will hence be a quick and effective tool in predicting and characterizing

a chemical's toxicity mechanism and consequently integrating physicochemical and biological properties into a strong risk assessment framework for regulatory considerations. Thus, SARs is a multidisciplinary concept and is a powerful link that ties three major fields, namely chemistry, biology and statistics together.

The application of SARs to the field of nanotoxicology in particular seems promising. A host of engineered-nanomaterials is already being incorporated in several consumer products, resulting in large-scale production of these new, innovative classes of materials. Given the complex life cycle of these nano-enabled products, it is essential to predict toxicological effects in a fast and inexpensive manner in order to reduce the risk and improve the benefits of this new technology. Mathematical models can, therefore, be employed to rank, relate, and predict toxicities based on physicochemical nanomaterial properties. This approach has the potential to reduce the need for, or extent of animal testing. Furthermore, these models generate a common conceptual framework for all stakeholders affected by toxicological regulations. Consequently, scientifically rational and informed decisions can be made which leads to a better environmental health protection.

3. Structure, activity, and toxicity of engineered nanoparticles

When designing a nanotoxicology study, a three-step process must be utilized to determine the interaction of an engineered-nanoparticle with tissue or cell. First, the structure of nanoparticle must be determined. Second, the chemical reactivity of the nanoparticle must be understood. Third, the particles' route of exposure, reaction with the biological target, and resultant cellular dysfunction must be reported. These experiments should be conducted over a range of increasing concentrations as well over a well-defined time period. **Table 1** summarizes some of the most common techniques to measure this three-step process.

3.1 Structure

3.1.1 Surface area

Brunauer, Emmett, and Teller (BET)—the original authors of the 1938 article describing this technique-physisorption is a method of measuring surface area and porosity of a material by physically adsorbing molecules of nitrogen gas (N_2) onto the surface of a solid. BET is one of the most widely used methods of determining surface area. It is accomplished by designating particular points at which relative pressure measurements are to be taken—pressure of a tube containing sample measured against saturation pressure tube. BET Surface Area measurements are used in the pharmaceutical, ceramics, carbon black, fuel, and electronics industry, as well as being a key physical characterization method for nanoparticles. The BET Surface Area of various building materials were measured by passing Nitrogen gas over a "degassed" solid at the boiling temperature of liquid nitrogen. The building materials were kept as close to their native state as possible however "coupons" had to be made in order to fit them through a 1/4 inch diameter opening on the sample tube. The instrument should be installed on a stable tabletop and gas tanks should be secured. Also do not kink the gas lines or damage the integrity of the lines lead to the machine. The operator is responsible for proper cleaning of the sample tubes for each use. The operator should report mass values to a level as precise as possible. The operator is responsible for identifying a degas procedure. The operator should ensure that no test sample is sucked up into the degas or analysis ports when removing sample tubes after degassing and analysis. Unused gas ports should be covered or plugged when not in use. Liquid Nitrogen can cause cryoburns, wear proper PPE when filling up liquid nitrogen Dewar for use in analysis. Allow sample tubes to warm to room temp after completion of the analysis run. Degas temperature can get quit high (upwards of 350°C), allow sample tubes to cool down before touching and removal of the heating jackets.

There are thermodynamic consequences of high surface areas. Difference in free energy between bulk material and nanoparticle contribute to the difficulty in predicting unknown effects of a nanoparticle based on known effects of larger micrometer sized materials. Specific to nanocrystals, reduced melting points, large surface areas, and increased lattice contraction give nanoparticles the heightened ability to produce reactive oxygen and nitrogen species on the particle's surface. While crystals on the larger size scale are also known to produce reactive species, some nanocrystals have different crystallographic structures when compared to their bulk phase counterparts.

3.1.2 Dynamic light scattering

Dynamic light scattering (DLS) is also referred to as Photon Correlation Spectroscopy (PCS). The technique is used for measuring particle size and size distribution when in liquid suspension. DLS measures the Brownian motion of the particles. Brownian motion is the random movement of suspended particles due to bombardment between the particle and the solvent molecules. As the solvent molecules collide with the particles, they exert a force, which is capable of moving the particles in a random direction. This random movement is more exaggerated in a small particle than for a large particle of the same composition in the same time period. This movement is known as the translational diffusion and is captured in the Einstein-Stokes equation as D along with the hydrodynamic

Table 1 Commonly Studied Physicochemical Properties of Engineered Nanomaterials

Nanomaterial Property	Description	Common Instrument or Measurement Technique
Particle structure	• Size and size distribution • Surface area • Topology • Aggregation/agglomeration state • Shape • Crystal structure and allotropy	• Brunauer, Emmett, and Teller (BET) physisorption for surface area analyses • Nanoparticle Tracking Analysis (NTA) for size and size distribution • Dynamic light scattering (DLS) for agglomeration and aggregation analyses • Transmission and scanning electron microscopy (TEM & SEM) for primary particle size determination • High resolution transmission and scanning electron microscopy (HR-TEM & HR-SEM) for nano clusters • Atomic force microscopy (AFM) for topology • X-ray diffraction (XRD) and electron diffraction (ED) for crystallinity information
Chemical activity	• Stability • Sample purity • Surface characterization • Chemical composition (includes both composition of the particle's core and its surface) • Therapeutic • Imaging • Functionality • Photo luminescence • Surface charge • Solubility	• UV-Visible spectroscopy (UV-Vis) • Ion selective electrodes (ISE) to measure leaked ions • X-ray photoemission spectroscopy (XPS) to measure electronic state of the elements that exist within a material • Inductively coupled plasma mass spectroscopy (ICP-MS) for trace metal analysis • Fourier-transform infrared spectroscopy (FTIR) to analyze chemical bonding • Differential thermal analysis (DTA) • Energy Dispersive X-Ray spectroscopy (EDS) for elemental analysis and chemical characterization • Zeta potential and isoelectric point for surface charge and stability measurements • Electron spin resonance (ESR) for studying materials with unpaired electrons • Spectrofluorometer for photoluminiscence and quantum yield measurements for fluorescent particles
Cytotoxicity	• Decrease in viability • Alterations in metabolism • Oxidative stress due to reactive species • Trigger apoptosis • Membrane damage (nuclear, cytoplasmic, other)	• Glutathione and oxidation detection • Colorimetric indicators for decrease in metabolism (XTT, MTT) • Live and dead cell counts via fluorescent dyes • Leaky membrane LDH release • Protein, cytokine, and chemokine expressions (ELISAs, western blotting) • Damage and repair to DNA (TUNEL)

radius of the particle.

$$d(H) = kT/3\pi nD \quad (1)$$

where D is the translational diffusion coefficient, k is Boltzmann's constant, T is temperature, and n is the viscosity of the solvent. The Stokes equation is only applicable for spherical or spheroidal particle-types.

Measuring the size of particles when suspended in aqueous solvent is an important characterization metric for nanotoxicology studies. It provides the researcher with a rapid means of generating a size profile (or hydrodynamic radius) of nanoparticles. DLS is also used to measure proteins in a biological buffer. The technique does have some limitations. For example, in a polydisperse sample, the larger particles will scatter more light, thus skewing the intensity of the size profile. The intensity of scattered light is proportional to the diameter of the particle to the 6th power. This phenomenon is called Rayleigh Scattering. It is difficult to determine the size of individual particles using light scattering when aggregates or agglomerates are present in the suspension—a polydisperse sample mixture may read as if it were void of the smaller fraction of nanoparticles. It is important to use control samples without the nanoparticle to determine the sizing profile of components in the suspension medium.

3.1.3 Transmission electron microscopy and energy dispersive spectroscopy

The use of transmission electron microscopy (TEM) is a necessary characterization tool in nanotoxicology. TEM takes advantage of the extremely small wavelength of electrons (0.2 nm) to increase the resolution and magnification of nanometer sized particles as well as cellular organelles. In transmission electron microscopy, the sample, generally referred to as the specimen, is exposed to an electron beam. The transmitted electrons are viewed on a phosphorescent screen, camera, or film. Depending on the specimen characteristics, the TEM can provide information such as size, shape, aggregation, and crystalline structure. This technique may be used post-exposure for both *in vitro* and *in vivo* tissue samples to determine

Table 2 Comparison of Microscopy Methods used in Nanotoxicology

	Molecular structure	Sizing limits	Aggregation State (in liquids)	Composition determination	Generation of artifacts	Special features
Optical	No	> 250 nm	No	Staining	Low	Real time imaging
SEM	No	> 30 nm	No	EDX	High	Topography of complex shapes
TEM, dried	Yes	> 0.5 nm	No	EELS	High	Cross-sectional details
TEM, cryo	No	1.5 nm	Yes	None	Medium	Preserves the native state of the sample

the intracellular localization of particles and cell structure changes (Reynolds, 1963). **Table 2** summarises the comparisons of microscopy methods used in nanotoxicology.

TEM provides information about a nanomaterial in its native state or in a complex mixture. However, there are some limitations to this technique. Biological specimens are immediately damaged upon exposure due to the high energy of the electron beam. Proper biological specimen preparation determines the quality of the specimen. Preparation is a multiple step process consisting of fixation, dehydration, embedding, and sectioning. Post-staining the specimen with a combination of uranyl acetate and lead citrate will enhance contrast and allow better visualization of cell structure. The combination of TEM with composition determination is an even more powerful technique. Complementary methodologies such as energy dispersive spectroscopy (EDS), electron diffraction (ED), and high resolution transmission electron microscopy (HRTEM) are useful. Energy dispersive spectroscopy as a micro-analytical tool can yield both quantitative and qualitative results. When emitted electrons strike the atoms of interest in the sample, inelastic reactions generate emitted electrons and X-rays that are then detected via spectroscopy. The technique is very sensitive and, therefore, special attention must be placed on sterility during specimen preparation as to not add artifacts to the sample.

3.1.4 Crystallinity

X-ray diffraction (XRD) is one of the most commonly used methods for confirming crystalline product. Limitations of the technique include large sample amount needed (100 mg powder sample). While small grain sizes can be determined, the technique requires long collection times. The chemical composition influences the crystalline structure, as does synthesis (and sometimes storage) method.

Two equations are used in this technique: Bragg's law and Scherrer equation. Bragg's law is used to determine the angles for coherent and incoherent scattering from a crystal lattice.

$$n\lambda = 2d \sin \theta \tag{2}$$

where n is an integer, λ is the wavelength of incident wave, d is the spacing between the planes in the atomic lattice, and θ is the angle between the incident ray and the scattering planes.

Scherrer equation is used to determine the size and shape of the nanocrystalline material, also known as crystallite.

$$D(\text{Å}) = 0.89\lambda/\beta \cos \theta_B \tag{3}$$

where D is the crystallite size, λ is the X-ray wavelength (1.54 Å for Cu Ka radiation), θ_B is the Bragg angle, and $\beta = (B^2 - b^2)^{1/2}$ where B and b are taken as the FWHM (full width at half max peak) of standard and sample.

Electron diffraction (ED) is the phenomenon that results in an interference pattern when a beam of electrons bombard a sample. It is a commonly used technique to study the crystal structure of solids, especially in material characterization techniques such as transmission and scanning electron microscopy. Based on the diffraction patterns, the crystallinity of the sample under investigation can be determined. Once this pattern has been attained, it is compared with that of a standard material. This technique may come into play when a particle has multiple crystalline states (Sayes et al., 2006a). HRTEM is also used to study the crystallographic structure at the atomic scale.

Recent studies have related the crystal structure of a material to its photocatalytic and cytotoxicological activities (Sayes et al., 2006b). Different crystalline phases of nanoscale titania (TiO_2) particles contribute to their differential cytotoxic responses in cultured cells. The most inactive catalytic material (TiO_2 in the rutile crystal phase) is less cytotoxic than similarly sized TiO_2 particles in the anatase crystal phase. Anatase TiO_2 also exhibits high photoactivity. This correlation is a manifestation of a fundamental structure-activity relationship in nanoscale titania—nanoparticle structures optimized to produce reactive species under UV illumination also are more effective at disrupting cellular functioning. Simple ex vivo tests of nanoscale titania photoactivity could prove useful as a comparative screen for cytotoxicity in this important class of materials.

3.2 Activity

3.2.1 Zeta potential

The zeta potential of a particle is used as a measure of the particle's surface charge. In actuality, the zeta potential is a measure of the electric double layer and is generated from oriented solute molecules and ions surrounding the nanoparticle surface. The electric double layer is dependent on it environment and will change intensity if pH or ionic strength is altered. For example, all nanoparticles have an isoelectric point. The particle's isoelectric point is the pH of the suspension when the particle's zeta potential is zero net charge (Berg et al., 2009).

Zeta potential is also used as a measurement of colloidal stability (Harush-Frenkel et al., 2007; Zhang, 2009). Values above ±30 mV are considered a stable system while values below ±30 mV are deemed unstable suspensions and aggregate readily. The benchmark time scale for this assessment is generally 30 days. This aggregation is due to the lack of charge-charge repulsion between individual nanoparticles.

3.2.2 Photocatalytic degradation

The surface of a nanoparticle has been identified as a source of leached ions, molecules, and reactive species. There are a variety of techniques and an array of colorimetric probes that are used to measure the reactivity of the surface of a nanoparticle that yields these species into the surrounding particle matrix. Vitamin C and Congo Red are probes used to measure the photocatalytic degradation of the particle's surface. When identifying and quantifying the reactivity of a particle's surface, it is important to recognize that no single technique can be used for all types of nanoparticles. Results in the literature indicate that the mechanism for color change in these tests is a result of charge transfer complexes between the probe and the "active sites" on the particle surface (Warheit et al., 2007a).

3.2.3 Spectroscopy

One of the most common analytical techniques in nanoscience is spectroscopy. Spectroscopy is defined as the measurement and interpretation of changes in the electromagnetic spectra arising from either absorption or emission of radiant energy by a sample. Spectroscopic techniques are especially useful for particle analyses. Information about the chemical composition, structure, surface functionality, and optical/electronic properties of the sample can be obtained. For example, mass spectroscopy is used to determine the masses of small electrically charged particles and can be utilized to measure properties proteins absorbed onto the particle surface. Raman spectroscopy is used to study vibrational, rotational, and other low-frequency modes in a system and can determine the type and degree of functionalization on the particle surface. Absorption spectroscopy is used to quantify the amount of photons a substance absorbs and can be utilized to measure the size of nanoparticles. Fluorescence spectroscopy is used to analyze the different frequencies of light emitted by a substance which is then used to determine the structure of the vibrational levels of that substance.

3.3 Toxicity

3.3.1 Concentration

Of all the physicochemical properties associated with nanomaterials, the feature that is most easily correlated to toxicity is concentration or dose. However, to measure the concentration of a sample is non-trivial. Three techniques are usually employed to determine concentration of a nanoparticle in a suspension. Gravimetric tests can be used, but must assume particle composition. Methods based on chemical reactant reactions can be utilized, but can produce erroneous results. Transmission electron microscopy of cryogenically frozen samples in suspension is the best measure of particle concentration. There are a variety of factors that influence the accuracy of measurements of concentration, such as the purity of sample and quantity of material available for analyses. Special considerations must be taken when a nanoparticle is surface functionalized with an organic coating. For example, surfactant coatings are not stable, and much like a protein absorbed onto the particle's surface, the surfactant will dissociate and be replaced with other molecules present in the suspension.

3.3.2 Exposure to nanomaterial samples

Real-world exposure to engineered nanomaterials is very likely to be a mixture of multiple substances, such as airborne particulate matter. Epidemiological data had suggested that airborne particulate matter (a mixture of many different substances) was more toxic than the sum of its parts. This was attributed to the "synergistic" effect due to the mixture of critical components within airborne particulate matter. In the nanotoxicology environment, human exposure to mixed nanomaterials is likely because multiple types of nanomaterials are often used simultaneously. For example, both metal oxide nanoparticles (e.g., Fe2O3) and graphitic carbon nanoparticles (e.g., carbon black) are likely to be used in various industrial applications. Therefore, it is imperative to understand the toxicological effect of exposure to mixed nanomaterials as well as the effects of the individual components alone. Recent publications have highlighted the importance of studying multiple nanoparticle exposure scenarios (Berg et al., 2010).

3.3.3 Hemolytic potential

The hemolytic potential of a nanoparticle sample gives

vital information on the effects of the particle on a biological membrane. The assay has been used in the past century with a variety of particulates including silicate powders, asbestos, and more recently a multitude of nanoparticles. Hemolysis (i.e. rupturing of erythrocytes or red blood cells) is an ex vivo characterization method that is complementary to assessing cell death. The ability of nanoparticles to react with a biological membrane is an important indicator especially for particles incorporated into medicinal devices for therapy or diagnosis (Warheit et al., 2007a) (Harington et al., 1971; Nolan et al., 1981; Warheit et al., 2007b).

Particulates, such as nanomaterials, interact with the erythrocyte and exert their cytotoxic effect via a multitude of hypothesized mechanisms depending on the characteristics of the particle such as size, composition, surface functionalization, and zeta potential. The mechanical interaction between the particle and the membrane can cause rupture releasing the intracellular hemoglobin into the ambient solution thus turning the solution pink to red in color. In addition to mechanical interactions, nanoparticles may react with the membrane of the erythrocyte indirectly via actively oxidizing the membrane molecular structure thereby increasing the membrane permeability. The particles may alter the ionic composition of the suspension medium through particle surface degradation, which could then increase the amount of hemoglobin in surrounding medium, as well.

3.3.4 Oxidative stress indicators

The presence of excessive reactive oxygen species (ROS) can cause cellular oxidative stress, which may lead to sub-cellular damage such as DNA, RNA, protein, mitochondrial, and membrane or other lipid degradation (Sayes et al., 2004; Fortner et al., 2005; Lyon et al., 2005; Sayes et al., 2005; Sayes et al., 2006). Exposure to nanoparticles has been shown to produce excess ROS. Consequently, oxidative stress damage has become a critical assessment tool in characterization the physical, chemical, and toxicological properties of engineered nanostructures.

In nanotoxicology, DNA oxidative stress is used as an indicator for potential cytotoxicity (Cattley and Glover, 1993; Hwang and Kim, 2007). Research has shown that different types of DNA damage and repair after oxidative damage can provide insights into mechanisms of action (Cooke et al., 2003). DNA damage is a result of a break or change in the chemical sequence of DNA in the nucleus of a cell. Each type of DNA lesion has different affects on the cells. For example, some DNA lesions result in mutations and can affect DNA replication and transcription; other types of DNA damage are repairable (Cooke et al., 2003). There are numerous biomarkers that measure oxidative stress endpoints in cells, urine, blood, and other tissues. The assays capable of determining DNA oxidative stress, damage, or repair after damage usually measure levels of 8-hydroxyguanosine (8-OHG) and 8-hydroxydeoxyguanosine (8-OHdG) nucleosides (Cattley and Glover, 1993; Hwang and Kim, 2007). The Comet assay measures general DNA damage via gel electrophoresis of cell lysate, followed by fluorescence signal quantification.

Protein oxidation is the process of oxidative damage to polypeptides and amino acids present in cells. Examples of assays that measure oxidative protein damage are protein carbonyl content (PCC) and 3-nitrotyrosine. Techniques used to evaluate the oxidant-antioxidant biomarkers are enzyme-linked immunosorbent assays (ELISA), ion exchange chromatography, immunoblotting, and electron paramagnetic resonance imaging. Several mechanisms are known that describe how electophiles and pro-oxidants cause protein damage. Alterations in protein function can occur following formation of covalent bonds between electrophiles and nucleophilic amino acids, oxidation of nucleophilic amino acids, or production of reactive nucleophiles.

Oxidative stress can also be caused by the accumulation of nanoparticles within the mitochondria (Nicholls and Budd, 2000) (Oberdorster et al., 2005; Li et al., 2008) (Sayes et al., 2004). It has been demonstrated that nanoparticles of various size and chemical composition are preferentially transferred to and accumulate in the mitochondria (Li et al., 2008) . ROS from the nanoparticle surface at the site of the mitochondria or ROS produced by the mitochondria because of nanoparticle exposure leads to cell damage or death. In structurally intact mitochondria, the production of ROS is balanced by an extensive antioxidant defense system that works to detoxify the oxygen radical generation (Nicholls and Budd, 2000). This protection is generally provided via glutathione and superoxide dismutase. Heightened cellular production of ROS occurs after damage to the mitochondria; thus, oxidative stress is often detected by measuring mitochondrial function.

Lipid peroxidation and membrane damage are used as indicators of oxidative stress and cellular damage. The major concern in this type of oxidative damage is disruption the ion channel flow. Lipid peroxides are unstable and degrade to molecules such as reactive carbonyl compounds. Polyunsaturated fatty acid peroxides generate malondialdehyde (MDA) and 4-hydroxyalkenals (HAE). MDA and HAE are colorimetric/flourometric indicators for this type of oxidation. Cytoplasmic and other cellular component membranes are easily targeted due to the amount of lipids found within the membrane.

Fluorescent dyes are very good indicators to detect oxidative stress in cells and tissues (Wang and Joseph, 1999; Lin et al., 2006). These ROS-sepcific dyes are categorized according to which type of ROS being probed. In general, there are multiple fluorescence probes for the detection of superoxide radical ($O_2^{\bullet-}$), hydrogen peroxide (H_2O_2), singlet oxygen ($1O_2$), hydroxyl radical ($HO^{\bullet}$), or peroxy

Table 3 Examples of fluorescent ROS dyes

Fluorescent probe	Excitation/emission wavelengths (nm)	ROS species detected
DCFDA (2,7-dichlorodihydrofluorescein)	498/522	H_2O_2 $ROO^{\bullet}$ $HO^{\bullet}$
DHE (Dihydroethidium)	520/610	$O_2^{\bullet -}$
B-TOH (BOPIDY-α-tocopherol)	514/565	$ROO^{\bullet}$ $RO^{\bullet}$ $HO^{\bullet}$
HPF (Hydroxyphenyl fluorescein)	485/535	$HO^{\bullet}$
CM-H2DCFDA (chloro methyl dihydro derivative of fluorescein)	485/538	H_2O_2 $ROO^{\bullet}$ $HO^{\bullet}$

radical ($ROO^{\bullet}$), as well as others (see **Table 3**). As with any colorimetric or fluorescent indictors, however, special attention must be placed on whether or not the nanoparticle auto fluoresces at the same wavelength or interferes with dye to avoid false positives or false negatives in results. There is a wide range of applications for these dyes within the realm of detecting ROS. For example, some probes are mainly used in an indirect approach to probe for antioxidant capacity, while others probe for oxidation in particular sub-cellular compartments and membranes (Gomes and Fernandes, 2005).

In addition to fluorescence spectroscopy, confocal microscopy can be used as a tool to probe stress (Uggeri, 2004). Oxidative stress can induce a dose-related increase or decrease in the level of fluorescence depending on the fluorescent probe of choice. In confocal microscopy, fluorescent probes are used to stain cell structures. The fluorescent probes dihydrorhodamine 123, dihydroethidium, 2',7' dihydro-dichlorofluorescein (H2DCF), and dichlorodihydrofluorescein diacetate (H2DCFDA) are some of the most commonly used detectors of reactive oxygen species (ROS) in spectroscopy and microscopy (Uggeri, 2004).

3.3.5 *In vitro* toxicology

The successful development of *in vitro* assays as predictive screens for assessing particle toxicity is an important goal during early product development. Ideally, the screen would be utilized prior to more substantive *in vivo* toxicity testing. If properly validated, the advantages of these early screening tests would be evident. *In vitro* testing is simpler, faster, and less expensive than *in vivo* assays. Successful development of *in vitro* toxicity models should reduce the use of animals for hazard identification of potential toxicants as well as to improve the ability to evaluate new materials in small quantities. Although implementation of *in vitro* toxicity screens would be beneficial, the accuracy and predictability of these tests with particulates have shown high correlative evidence when compared to results obtained *in vivo* models.

An interne national panel of scientists recommended five grand challenges associated with the safe handling of nanotechnology. The panel has recommended strategic research strategies to support sustainable nanotechnologies by maximizing benefits and minimizing environmental and health risks (Maynard et al., 2006). One of the five key grand challenges cited was to develop and validate alternatives to *in vivo* toxicity testing of engineered nanomaterials, recognizing that there would be several limitations inherent to *in vitro* assays and cell culture systems when simulating complex biological effects after exposure to nanoparticles. These limitations include particle dose, selection of cell-type for simulating the organ system of choice, characterization of exposure, effects over time, and appropriateness of endpoints for hazard evaluation (Sayes et al., 2007).

In recent study, a number of variables which strongly impact the ability of *in vitro* screens to accurately reflect *in vivo* pulmonary toxicity of several particle types in rats were systematically evaluated (Sayes et al., 2007). The variables tested included particle dose, time course, duration of treatment exposure, and pulmonary cell types. *In vivo* effects in the lungs of rats were utilized as the barometer for comparison. Under the conditions of this study, the results of *in vivo* and *in vitro* cytotoxicity and inflammatory cell measurements demonstrated little correlation when single cell cultures were used, but resulted in a higher level of correlation when co-cultures of epithelial cells and macrophages were used together. There is a need for better culture systems and for more research to designate the most relevant biological endpoints to test for *in vitro* studies (Romoser et al., 2011; Romoser et al., 2012; Berg et al., 2013).

3.3.6 Cellular uptake

Interaction of engineered nanoparticles occurs on a size

scale previously seen with the entrance of viral pathogens across the cytoplasmic membrane (Oberdorster et al., 2004; Larese et al., 2009). The uptake of nanoparticles provides a unique way of accessing intracellular compartments through intentional (i.e. drug delivery) or unintentional (i.e. occupational or consumer exposure). In either scenario, nanoparticles are capable of intracellular localization through a variety of endocytic mechanisms ranging from the clathrin-mediated endocytosis (CME) to non-specific macropinocytosis or simple passive diffusion (Qaddoumi et al., 2003; Geiser et al., 2005; Rothen-Rutishauser et al., 2006; Harush-Frenkel et al., 2007; Harush-Frenkel et al., 2008; Jiang et al., 2008). Many physicochemical characteristics such as nanoparticle size, surface coating, and surface charge have been postulated as factors influencing the endocytosis of nanoparticles. Many endocytic mechanisms are structurally size limited by the protein scaffolding lining of the vesicle on the cytoplasmic membrane. Calculations based on thermodynamic limitations and cell-ligand interactions have calculated the most efficient receptor-mediated nanoparticle endocytosis occurs when the particle is a spherical is shape and 30 nm in diameter (Freund and Lin 2004; Gao et al., 2005). When the particles aggregate, however, the resultant agglomerate is treated as larger particle. In these circumstances, phagocytosis by immune-modulator macrophages is responsible for clearance of agglomerates.

While primary particle size and agglomeration state play the primary role in directing the specific route in nanoparticle endocytosis, they are not the only factors. Surface charge also plays a role in the interactions between nanoparticles and cell membranes (Harush-Frenkel et al., 2008; Zhang, 2009). For example, negatively charged particle surfaces, such as particles coated with hydrophilic acids, and positively charged particle surfaces, such as particles coated with polymers, are more capable of incorporation into human cells than particles with little to no surface charge. The charge of a nanoparticle will also dictate the pathway through which the particle is internalized (Harush-Frenkel et al., 2008; Mayor and Pagano, 2007; Doherty and McMahon, 2009; Gould and Lippincott-Schwartz, 2009; Zhang, 2009). For example, while uptake of both positively and negatively charged particles are energy and F-actin polymerization dependent, they have been shown to undergo different pathways. Positively charged nanoparticles enter cells through macropinocytosis and CME (Qaddoumi et al., 2003; Chung et al., 2007). Negatively charged nanoparticles enter cells through dynamin-independent mechanisms (Qaddoumi et al., 2003; Schroeder et al., 2007; Partha et al., 2008; Villanueva et al., 2009). While associations between charge and mechanisms of cellular internalization have been made, further research into this topic is needed.

In addition to nanoparticle charge, a modified surface coating influences the uptake by cells. Another factor dictating nanoparticle cellular uptake and potential toxicity is the adsorption of proteins onto the surface of the particle (Chen et al., 2005; Chen et al., 2006; Huang et al., 2007; Lundqvist et al., 2008; Schellenberger et al., 2008). Proteins have been shown to coat particles when placed in cell culture media, serum, and biological fluids. The extent of the protein coating is dependent upon physical factors such as size and shape and chemical factors such as charge and other surface functionalization. Antibody conjugation onto the surface of a particle increases linearly with respect to the radius. This association between size and protein binding is due to the high rate of curvature exhibited by the surface of a small nanoparticle which sterically hinders the binding of additional antibodies. Protein adsorption may be dramatically altered as any single physicochemical property is changed—thus prohibiting many mathematical models to be used in this field. It is this protein adsorption theory, which necessitates the importance of proper characterization of nanomaterials, as well as puts forth complicating task of linking nanomaterial physicochemical properties with their biological endpoint.

4. The phases of nanomaterial characterization within a study design

The most thorough nanotoxicology studies include a thoughtful experimental design for the material characterization. The nanoparticle sample should be characterized and re-characterized for physical and chemical properties throughout the course of the designed study. When changing the matrix surrounding the material or simply measuring changes over time, a nanoparticle sample should be analyzed and labeled, as material characterization is the primary phase, the secondary phase, or the tertiary phase (**Fig. 1**).

Primary phase physical and chemical characteristics refer to those nanoscale properties immediately after the material is synthesized using liquid-phase synthesis or aerosolized synthesis. Furthermore, the characterization should be performed on both lab-synthesized and purchased material. Those properties relevant to toxicity testing include a diverse range of particle features, including: chemical composition, surface functionalization, surface area, size, size distribution, shape, crystallinity, and purity. Secondary phase characterization relevant to toxicity testing includes aggregation/agglomeration/coagulation, concentration, activity/reactivity, presence of reactive species, surface modifications, and leached ions or molecules. Properties in the tertiary phase that are relevant to toxicity testing include cellular uptake and tissue distribution, adsorption of molecules onto the surface, aggregation,

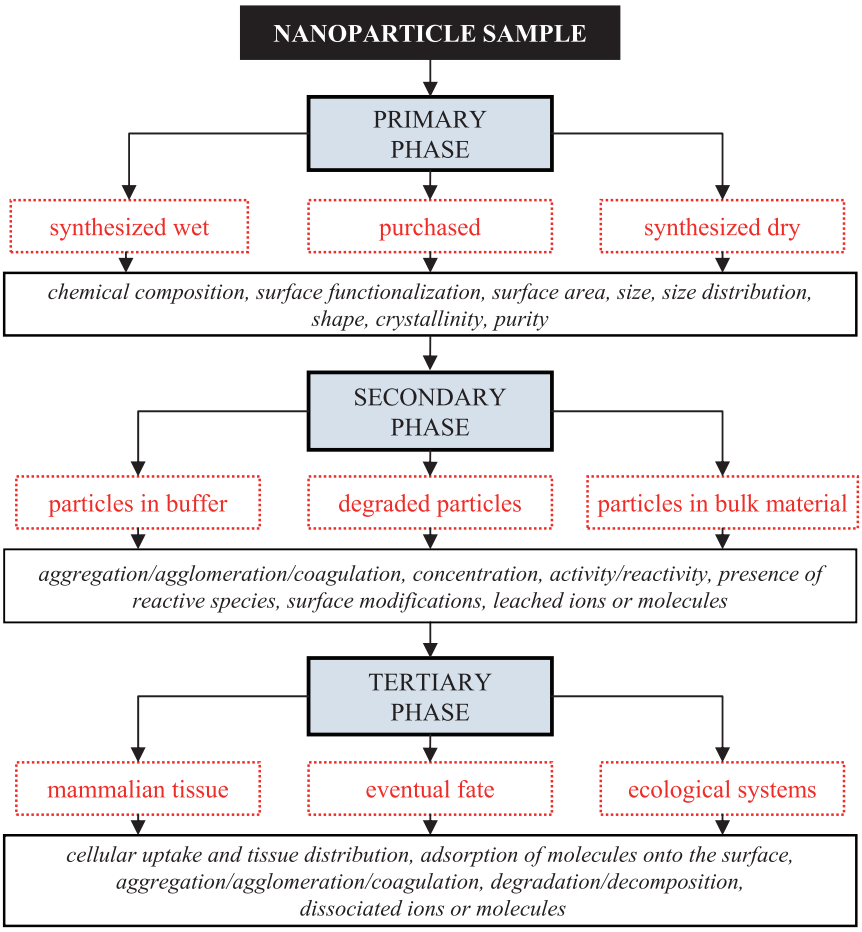

Fig. 1 The Physicochemical Characterization Required for Toxicological Evaluations.

degradation and decomposition, and dissociated ions or molecules.

There are specific characteristics regarding nanoparticle production that are most relevant to toxicologists. These issues include quantity of material produced and availability for exposure, particle composition and amount of impurities, and presence and identity of a surface coating. When performing toxicological evaluations on nanoparticles, these properties should be addressed.

One of the most frequently asked questions in nanotoxicology is: to what extent do particles aggregate (Sager et al., 2007; Murdock et al., 2008)? Particles are always attracted to each other. Forces such as van der Waals interactions, type of solvent, and Hamaker constant are all contributors for particles to aggregate. It is noteworthy, however, that aggregated particles, may not have significantly different surface areas compared to individual particles. Nanoaggregates are often referred to as "soft" aggregates. Chemical changes are needed for aggregates of nanoparticles to become permanently fixed to each other. Factors such as direct covalent attachment at grain boundaries require chemical reaction between particles. When nanoaggregates become fixed, they are often are referred to as "hard" aggregates. It is this type of aggregation (or agglomeration) that leads to much lower surface areas. Nanoparticles can be stabilized against aggregation. For example, ionic strength alters repulsion between particles by several orders of magnitude). In ionic stabilization, strong repulsive electrostatic forces are present and are dependent on the type of solvent used in the system. The strength of these electrostatic forces is affected by surface charge density. If the density of the surface charge is large in magnitude and equivalent in sign, then the repelling forces on a particle-to-particle basis can operate in relatively long ranges. Another example of prohibiting aggregation is steric stabilization. In this case, the coatings on surfaces of the nanoparticles define the extent of stabilization. Understating the interactions of the coatings with the solvent essential and ultimately can reduce van der Waals interactions.

These principles apply to nanoparticles. When characterizing a nanoparticle for any type of assessment, it is important to consider an engineered nanomaterial as a particle obeying quantum mechanics (**Fig. 2**). When the particle is aggregated into larger agglomerate, then the particle may be obeying classical mechanics. Nonetheless, particles on the nanometer size scale are different from particles on the micrometer size scale (Nel et al., 2006).

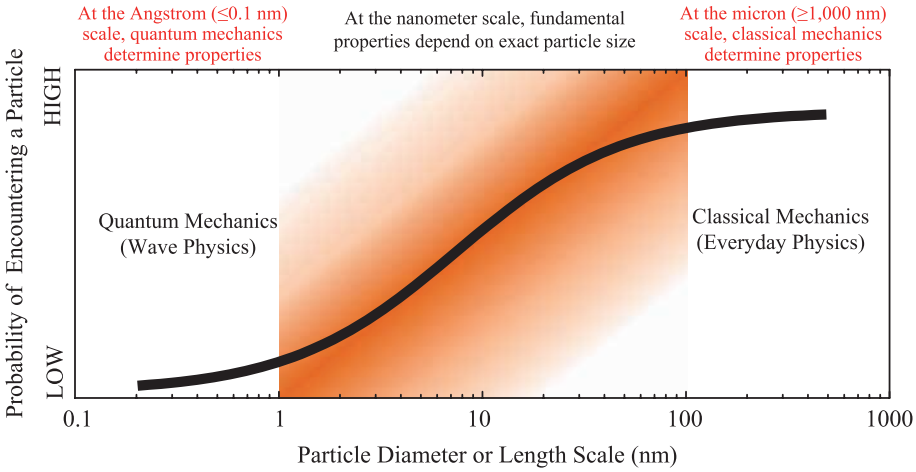

Fig. 2 The Properties Exploited in Specific Particle Size Ranges.

5. Conclusion on utility of structure-activity relationships for nanoparticles

The role of engineered nanomaterials in a variety of fields in science and engineering requires an adequate methodology for evaluating their potential impact on safety and health. Recent publications point to an increase of various biological responses, such as inflammatory or immune responses, after exposure to nanomaterials. These biological responses have been observed and reported on from either *in vitro* (cell culture based) or *in vivo* (whole animal) model systems; however, not enough effort has been placed on relating the physicochemical features of each engineered nanomaterial to the observed biological responses. Developing experimental models and methodologies that not only establish relationships between different physical structures and biological activity but also can reliably predict biological responses to nanomaterials is critical. This effort, however, requires a large and organized effort within the nanoscience community. Many data sets measuring multiple endpoints are required in order to accurately predict biological responses. The same is true for the physicochemical characterization.

The structure of a nanoparticle can be used as one of many predictors of biological responses. However, it must be noted that structure is not the only physicochemical feature that contributes to a material's potential toxicity. For example, not all nanoparticles are more toxic than their larger micrometer sized counterparts. Size, alone, is not a measure of toxicity. Surface coatings of particles have been shown to more likely influence toxicity—no matter the size or structure of the material. And particle aggregation and subsequent de-aggregation complicates the structure-activity relationship even more since this process is dynamic depending on time, suspension matrix, and temperature.

Using both analytical chemistry and biochemistry approaches, a systematic methodology is under development that will assist researchers and regulators in evaluating potential responses of a specific biological system to a specific nanomaterial exposure. While the methodology development is well underway, there is still an urgent need for new tools, standardized practices, and meaningful interpretations that help address the challenges presented by nanomaterials and nano-enabled products. Due to their complexity, nanomaterials do not fit into established structure-activity models of chemical behavior. Nonetheless, it is important to identify the trends among different nanoparticles with varying measurable physicochemical characteristics for hazard identification, exposure analyses, risk assessments, and regulatory and policy decisions. The result, ideally, would be a framework that would produce meaningful groupings of particles in an effort to generalize some of the common features and resultant common responses that so many particles on the nanometer size scale seem to induce. For instance, particles less than 10 nm in diameter not only have different optical properties, they also have different translocation tendencies in cellular systems. Metal-based nanoparticles, a.k.a. metal colloids, tend to leach metal ions at different rates and at different pH's. Crystalline materials produce more oxidant species than amorphous materials. While there are always exceptions to generalizations, these types of observations can be made when considering the literature as a whole.

References

Berg J.M., Romoser A., Banerjee N., Zebda R., Sayes C.M., The relationship between pH and zeta potential of ~30 nm metal oxide nanoparticle suspensions relevant to in vitro toxicological evaluations. Nanotoxicology, 3 (2009) 276–283.

Berg J.M., Ho S., Hwang W., Zebda R., Cummins K., Soriaga M.P., Taylor R., Guo B., Sayes C.M., Internalization of carbon black and maghemite iron oxide nanoparticle mixtures leads to oxidant production, Chemical Research in

Toxicology, 23 (2010) 1874–1882.
Berg J.M., Romoser A.A., Figueroa D.E., West C.S., Sayes C.M., Comparative cytological responses of lung epithelial and pleural mesothelial cells following in vitro exposure to nanoscale sio2, Toxicology in Vitro, 27 (2013) 24–33.
Cattley R.C., Glover S.E., Elevated 8-hydroxydeoxyguanosine in hepatic DNA of rats following exposure to peroxisome proliferators: Relationship to carcinogenesis and nuclear localization, Carcinogenesis, 14 (1993) 2495–2499.
Chen C., Kwak E.-S., Stein B., Kao C.C., Dragnea B., Packaging of gold particles in viral capsids, Journal of Nanoscience and Nanotechnology, 5 (2005) 2029–2033.
Chen C., Daniel M.-C., Quinkert Z.T., De M., Stein B., Bowman V.D., Chipman P.R., Rotello V.M., Kao C.C., Dragnea B., Nanoparticle-templated assembly of viral protein cages, Nano Letters, 6 (2006) 611–615.
Chung T.-H., Wu S.-H., Yao M., Lu C.-W., Lin Y.-S., Hung Y., Mou C.-Y., Chen Y.-C., Huang D.-M., The effect of surface charge on the uptake and biological function of mesoporous silica nanoparticles in 3t3-l1 cells and human mesenchymal stem cells, Biomaterials, 28 (2007) 2959–2966.
Cooke M.S., Evans M.D., Dizdaroglu M., Lunec J., Oxidative DNA damage: Mechanisms, mutation, and disease, The FASEB Journal, 17 (2003) 1195–1214.
Doherty G.J., McMahon H.T., Mechanisms of Endocytosis, Annu. Rev. Biochem. , 78 (2009) 31.1–31.46.
Fortner J.D., Lyon D.Y., Sayes C.M., Boyd A.M., Falkner J.C., Hotze E.M., Alemany L.B., Tao Y.J., Guo W., Ausman K.D., Colvin V.L., Hughes J.B., C60 in water: Nanocrystal formation and microbial response, Environmental Science & Technology, 39 (2005) 4307–4316.
Freund L.B., Lin Y., The role of binder mobility in spontaneous adhesive contact and implications for cell adhesion, Journal of the Mechanics and Physics of Solids, 52 (2004) 2455–2472.
Gao H., Shi W., Freund L.B., Mechanics of receptor-mediated endocytosis, Proceedings of the National Academy of Sciences of the United States of America, 102 (2005) 9469–9474.
Geiser M., Rothen-Rutishauser B., Kapp N., Schurch S., Kreyling W., Schulz H., Semmler M., Im Hof V., Heyder J., Gehr P., Ultrafine particles cross cellular membranes by nonphagocytic mechanisms in lungs and in cultured cells, Environ Health Perspect, 113 (2005) 1555–1560.
Gomes A., Fernandes E., Lima J.L.F.C., Fluorescence probes used for detection of reactive oxygen species, Journal of Biochemical and Biophysical Methods, 65 (2005) 45–80.
Gould G.W., Lippincott-Schwartz J., New Roles for Endosomes: From Vesicular Carriers to Multi-Purpose Platforms, Nature Reviews/Molecular Cell Biology, 10 (2009) 287–292.
Harington J.S., Miller K., Macnab G., Hemolysis by asbestos, Environ Res, 4 (1971) 95–117.
Harush-Frenkel O., Rozentur E., Benita S., Altschuler Y., Surface charge of nanoparticles determines their endocytic and transcytotic pathway in polarized mdck cells, Biomacromolecules, 9 (2008) 435–443.
Harush-Frenkel O., Debotton N., Benita S., Altschuler Y., Targeting of nanoparticles to the clathrin-mediated endocytic pathway, Biochem Biophys Res Commun, 353 (2007) 26–32.
Huang X., Bronstein L.M., Retrum J., Dufort C., Tsvetkova I., Aniagyei S., Stein B., Stucky G., Mckenna B., Remmes N., Baxter D., Kao C.C., Dragnea B., Self-assembled virus-like particles with magnetic cores, Nano Lett, 7 (2007) 2407–2416.
Hwang E.S., Kim G.H., Biomarkers for oxidative stress status of DNA, lipids, and proteins in vitro and in vivo cancer research, Toxicology, 229 (2007) 1–10.
Jiang W., Kim B.Y., Rutka J.T., Chan W.C., Nanoparticle-mediated cellular response is size-dependent, Nat Nanotechnol, 3 (2008) 145–150.
Larese F.F., D'agostin F., Crosera M., Adami G., Renzi N., Bovenzi M., Maina G., Human skin penetration of silver nanoparticles through intact and damaged skin, Toxicology, 255 (2009) 33–37.
Li J.J., Zou L., Hartono D., Ong C.N., Bay B.H., Lanry Yung L.Y., Gold nanoparticles induce oxidative damage in lung fibroblasts *in vitro*, Advanced Materials, 20 (2008) 138–142.
Lin W., Huang Y.W., Zhou X.D., Ma Y., In vitro toxicity of silica nanoparticles in human lung cancer cells, Toxicol Appl Pharmacol, 217 (2006) 252–259.
Lundqvist M., Stigler J., Elia G., Lynch I., Cedervall T., Dawson K.A., Nanoparticle size and surface properties determine the protein corona with possible implications for biological impacts, Proc Natl Acad Sci USA, 105 (2008) 14265–14270.
Lyon D.Y., Fortner J.D., Sayes C.M., Colvin V.L., Hughe J.B., Bacterial cell association and antimicrobial activity of a c60 water suspension, Environ Toxicol Chem, 24 (2005) 2757–2762.
Maynard A.D., Aitken R.J., Butz T., Colvin V., Donaldson K., Oberdorster G., Philbert M.A., Ryan J., Seaton A., Stone V., Tinkle S.S., Tran L., Walker N.J., Warheit D.B., Safe handling of nanotechnology, Nature, 444 (2006) 267–269.
Mayor S., Pagano R.E., Pathways of clathrin-independent endocytosis, Nat Rev Mol Cell Biol, 8 (2007) 603–612.
Murdock R.C., Braydich-Stolle L., Schrand A.M., Schlager J.J., Hussain S.M., Characterization of nanomaterial dispersion in solution prior to in vitro exposure using dynamic light scattering technique, Toxicological Sciences, 101 (2008) 239–253.
Nel A., Xia T., Madler L., Li N., Toxic potential of materials at the nanolevel, Science, 311 (2006) 622–627.
Nicholls D.G., Budd S.L., Mitochondria and neuronal survival, Physiol Rev, 80 (2000) 315–360.
Nolan R.P., Langer A.M., Harington J.S., Oster G., Selikoff I.J., Quartz hemolysis as related to its surface functionalities, Environ Res, 26 (1981) 503–520.
Oberdorster G., Sharp Z., Atudorei V., Elder A., Gelein R., Kreyling W., Cox C., Translocation of inhaled ultrafine particles to the brain, Inhal Toxicol, 16 (2004) 437–445.
Oberdorster G., Oberdorster E., Oberdorster J., Nanotoxicology: An emerging discipline evolving from studies of ultrafine particles, Environ Health Perspect, 113 (2005) 823–839.
Partha R., Mitchell L.R., Lyon J.L., Joshi P.P., Conyers J.L., Buckysomes: Fullerene-based nanocarriers for hydrophobic molecule delivery, ACS Nano, 2 (2008) 1950–1958.
Qaddoumi M.G., Gukasyan H.J., Davda J., Labhasetwar V.,

Kim K.J., Lee V.H., Clathrin and caveolin-1 expression in primary pigmented rabbit conjunctival epithelial cells: Role in PLGA nanoparticle endocytosis, Molecular Vision, 9 (2003) 559–568.

Reynolds E.S., The use of lead citrate at high ph as an electron-opaque stain in electron microscopy, J Cell Biol, 17 (1963) 208–212.

Romoser A.A., Chen P.L., Berg J.M., Seabury C., Ivanov I., Criscitiello M.F., Sayes C.M., Quantum dots trigger immunomodulation of the nfκb pathway in human skin cells, Molecular Immunology, 48 (2011) 1349–1359.

Romoser A.A., Figueroa D.E., Sooresh A., Scribner K., Chen P.L., Porter W., Criscitiello M.F., Sayes C.M., Distinct immunomodulatory effects of a panel of nanomaterials in human dermal fibroblasts, Toxicology Letters, 210 (2012) 293–301.

Rothen-Rutishauser B.M., Schurch S., Haenni B., Kapp N., Gehr P., Interaction of fine particles and nanoparticles with red blood cells visualized with advanced microscopic techniques, Environ Sci Technol, 40 (2006) 4353–4359.

Sager T.M., Porter D.W., Robinson V.A., Lindsley W.G., Schwegler-Berry D.E., Castranova V., Improved method to disperse nanoparticles for in vitro and in vivo investigation of toxicity, Nanotoxicology, 1 (2007) 118–129.

Sayes C.M., Fortner J.D., Guo W., Lyon D., Boyd A.M., Ausman K.D., Tao Y.J., Sitharaman B., Wilson L.J., Hughes J.B., West J.L., Colvin V.L., The differential cytotoxicity of water-soluble fullerenes, Nano Letters, 4 (2004) 1881–1887.

Sayes C.M., Gobin A.M., Ausman K.D., Mendez J., West J.L., Colvin V.L., Nano-c60 cytotoxicity is due to lipid peroxidation, Biomaterials, 26 (2005) 7587–7595.

Sayes C.M., Wahi R., Kurian P.A., Liu Y., West J.L., Ausman K.D., Warheit D.B., Colvin V.L., Correlating nanoscale titania structure with toxicity: A cytotoxicity and inflammatory response study with human dermal fibroblasts and human lung epithelial cells, Toxicological Sciences, 92 (2006a) 174–185.

Sayes C.M., Liang F., Hudson J.L., Mendez J., Guo W., Beach J.M., Moore V.C., Doyle C.D., West J.L., Billups W.E., Ausman K.D., Colvin V.L., Functionalization density dependence of single-walled carbon nanotubes cytotoxicity in vitro, Toxicology Letters, 161 (2006b) 135–142.

Sayes C.M., Reed K.L., Warheit D.B., Assessing toxicity of fine and nanoparticles: Comparing in vitro measurements to in vivo pulmonary toxicity profiles, Toxicological Sciences, 97 (2007) 163–180.

Schellenberger E., Schnorr J., Reutelingsperger C., Ungethüm L., Meyer W., Taupitz M., Hamm B., Linking proteins with anionic nanoparticles via protamine: Ultrasmall protein-coupled probes for magnetic resonance imaging of apoptosis, Small, 4 (2008) 225–230.

Schroeder J.E., Shweky I., Shmeeda H., Banin U., Gabizon A., Folate-mediated tumor cell uptake of quantum dots entrapped in lipid nanoparticles, Journal of Controlled Release, 124 (2007) 28–34.

Uggeri J., Gatti R., Belletti S., Scandroglio R., Corradini R., Rotoli B., Orlandini G., Calcein-am is a detector of intracellular oxidative activity, Histochemistry and Cell Biology, 122 (2004) 499–505.

Villanueva A., Cañete M., Roca A.G., Calero M., Veintemillas-Verdaguer S., Serna C.J. , Morales M. del Puerto, Miranda R., The influence of surface functionalization on the enhanced internalization of magnetic nanoparticles in cancer cells, Nanotechnology, 20 (2009) 115103.

Wang H., Joseph J.A., Quantifying cellular oxidative stress by dichlorofluorescein assay using microplate reader, Free Radic Biol Med, 27 (1999) 612–616.

Warheit D.B., Webb T.R., Colvin V.L., Reed K.L., Sayes C.M., Pulmonary bioassay studies with nanoscale and fine-quartz particles in rats: Toxicity is not dependent upon particle size but on surface characteristics, Toxicological Sciences, 95 (2007a) 270–280.

Warheit D.B., Webb T.R., Reed K.L., Frerichs S., Sayes C.M., Pulmonary toxicity study in rats with three forms of ultrafine-tio2 particles: Differential responses related to surface properties, Toxicology, 230 (2007b) 90–104.

Zhang L.W., Monteiro-Riviere N.A., Mechanisms of quantum dot nanoparticle cellular uptake, Toxicological Sciences, 110 (2009) 138–155.

Author's short biography

Christie M. Sayes

Dr. Christie M. Sayes is the Program Manager for Nanotoxicology RTI International. She was formerly a professor of toxicology at Texas A&M University. She has more than a decade of experience in the fields of nanotechnology and nanotoxicology. She has authored publications, including original research, invited reviews and book chapters. She is a member of the Society of Toxicology, the American Chemical Society, and the Society of Environmental Toxicology and Chemistry. She serves on the Editorial Boards of Nanotoxicology, Toxicological Sciences, and Toxicology Letters. Recently, she was elected onto the Executive Committee of the North Carolina Chapter Society of Toxicology.

KONA Powder and Particle Journal No. 31 (2014) 22–52/Doi:10.14356/kona.2014006 Review Paper

Nanophosphor Coatings: Technology and Applications, Opportunities and Challenges†

Roman Kubrin

[1] *Institute of Advanced Ceramics, Hamburg University of Technology, Germany*

Abstract

The particle size of conventional commercial phosphor powders used in lighting and displays is in the range from several micrometers to tens of micrometers and it is known that submicrometer-sized phosphors can facilitate a decrease in their consumption and improved resolution of phosphor screens. When the particle size becomes comparable to wavelengths of light, the optical properties of phosphor powders undergo remarkable qualitative changes so that the luminescence performance of nanophosphor screens, along with a very pronounced influence of the particle size, becomes dependent on several additional parameters such as packing density of nanoparticles, refractive index and chemical composition of the medium between them. This brings about both advantages and disadvantages which are discussed in this review of recent literature on the synthesis, deposition, and applications of nanophosphors.

Keywords: nanophosphors, lanthanide-doped nanoparticles, particle size effects, phosphor screens, transparent luminescent coatings, phosphor-converted white LEDs

1. Introduction

The general function of any phosphor is to convert a certain kind of external energy into visible light. This conversion process can serve different purposes and, from this point of view, all practical applications of phosphors can be classified into several main groups:

- Light sources (fluorescent lamps, backlights of liquid crystal displays (LCDs), light-emitting diodes (LEDs) including phosphor-converted white LEDs (pc-WLEDs), etc.).
- Information displays (plasma display panels (PDPs), field emission displays (FEDs), cathode-ray tubes (CRTs), etc.).
- Radiation converters (X-ray intensifying screens and other image intensifiers, spectral converters for solar cells, down-converters for excimer laser beam profilers and photolithography mask inspection tools, viewing screens for electron microscopy, etc.).
- Fluorescent pigments and tracers (non-destructive testing, biolabeling, security labeling, leisure goods, etc.).

Luminescent substances are very often utilized in the form of a powder coating, i.e. a continuous particulate film of relatively small thickness extended in the other two dimensions. Such a coating deposited on a transparent substrate is usually referred to as a screen, if it is used for representation of any visual information. Each application imposes an appropriate set of requirements on the properties of the phosphor coating, e.g. its chemical composition, homogeneous or patterned structure, and its thickness. Usually, a trade-off between the maximum light output for the given excitation conditions, desired transient characteristics, quality of image reproduction, mechanical and environmental stability, and costs of the phosphors and their processing has to be found.

The size of phosphor particles is one of the main parameters affecting the performance of phosphor screens. Phosphors produced by conventional methods usually consist of particles with the sizes ranging from several micrometers to several tens of micrometers, i.e. significantly larger than the wavelengths of light they emit. The reduction of phosphor particle size into the subwavelength regime could be advantageous in many applications provided that the luminescent properties of the chosen material are still appropriate and the technological route is economical.

The purpose of this review is to point out the general qualitative differences between conventional phosphors and nanophosphors and to show potential advantages of the latter. Nanophosphors can be defined as nanoparticles of transparent dielectrics (hosts) doped with optically active ions (activators), so that the emission of light happens due to the electronic transitions between the levels of the

† Accepted: June 24, 2013
[1] Denickestr. 15, 21073 Hamburg, Germany
E-mail: roman.kubrin@tuhh.de
TEL:+49-40-42878-3459 FAX: +49-40-42878-2647

impurity ions inside the bandgap of the host (characteristic luminescence). They have to be distinguished from the luminescent quantum dots as these emit light upon band-to-band transitions (bandgap luminescence) and are affected much more strongly by quantum confinement effects. Semiconductor quantum dots are not dealt with directly in this article although certain conclusions could also be applied to them. Interested readers can be directed to the reviews of physics and applications of quantum dots, such as Samokhvalov et al. (2013), Geszke-Moritz and Moritz (2013), Bera et al. (2010), Gaponik et al. (2010), and Liu et al. (2010). We will also not devote much attention to phosphor powders with particles of intermediate size between 100 nm and 1–2 μm. Their properties and synthesis were recently treated in (Kubrin, 2012) including an extended discussion of modeling methods and spray-based deposition techniques partially repeated here. Previous reviews of the physics and technology of luminescent nanoparticles can be found, e.g. in Ronda (2008), Tissue (2007), Liu and Chen (2007a), Tanner (2005), Chander (2005), and Tissue (1998).

2. Basic optics of phosphor screens

For the given excitation conditions (constant intensity of the incident X-Rays, UV-light, or an electron beam), the perceived brightness of a phosphor screen is determined by the geometrical configuration of the screen, the excitation source, and the observer. Generally, one distinguishes two different modes of screen observation. In the transmission (T-) mode, the screen is placed between the excitation source and the observer (**Fig. 1**, Observer A). In the reflection (R-) mode, the observer and the source of excitation are situated on the same side of the screen (**Fig. 1**, Observer B). The intensity of light exiting the screen in both modes depends on the screen thickness.

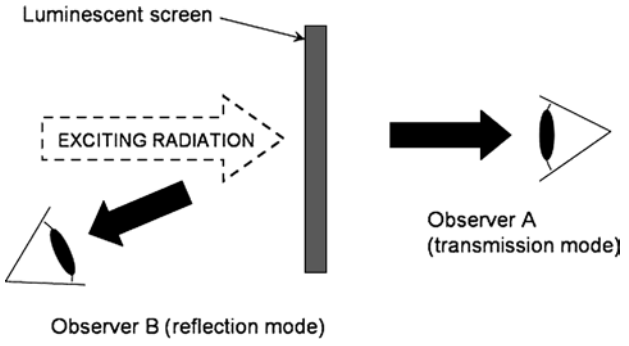

Fig. 1 Transmission and reflection modes of screen observation (Kubrin, 2012), © Cuvillier Verlag.

2.1 Perfect non-scattering screens

Let us consider the simplest model of the phosphor screen—an infinite continuous plate with even, perfectly smooth boundaries. If we assume a uniform excitation by unpolarized light (from one side of the screen), the time-averaged spatial distribution of intensity of luminescence from any volume element inside of the phosphor plate should by fully isotropic. We also assume a perfect match between refractive indices of the phosphor and surrounding medium, so that the light reflection at the boundaries of the phosphor layer can be neglected. In such cases, the intensities of light emitted forward (T-mode) and backward (R-mode) should be equal and constant everywhere outside of the screen

$$I_T = I_R, \tag{1}$$

where I_T and I_R stand for the transmission-mode and reflection-mode intensities, respectively, expressed as a number of photons emitted in a unit of time. Their sum equals the total intensity of luminescence and it can be related to the intensity of exciting radiation absorbed in the phosphor coating I'_A by the quantum efficiency q of the phosphor (number ratio of emitted and absorbed photons). From now on, symbols with a prime will be used for exciting radiation

$$I_T = I_R = q\frac{I'_A}{2}. \tag{2}$$

Exciting radiation incident on the phosphor screen is either absorbed or transmitted through the screen. The sum of corresponding contributions equals the initial intensity of excitation

$$I'_0 = I'_A + I'_T. \tag{3}$$

The part of exciting radiation transmitted through the phosphor is given by the Beer-Lambert law

$$I'_T = I'_0 \exp(-\alpha' d), \tag{4}$$

where α' is the coefficient of absorption measured in the units of inverse length and d is the thickness of the screen. We obtain the following final expression

$$I_T = I_R = q\frac{I'_0(1-\exp(-\alpha' d))}{2}. \tag{5}$$

Obviously, both R- and T-mode brightness increase for thicker phosphor screens and asymptotically approach the values corresponding to complete absorption of exciting radiation (**Fig. 2**). When considering the brightness of a perfect non-scattering screen, there is no definite optimal value of the screen thickness; the phosphor layer theoretically should be as thick as possible.

In most practical cases, the refractive index of the luminescent material is substantially higher than that of

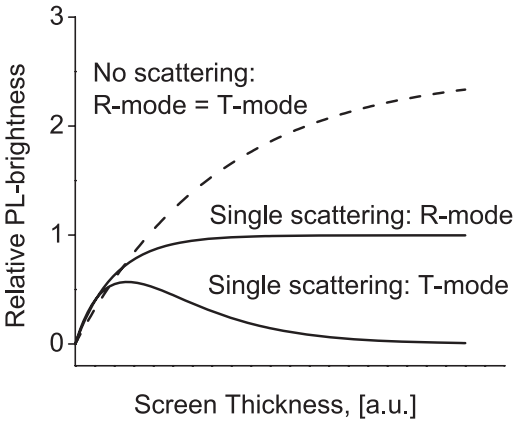

Fig. 2 Theoretical thickness dependence curves for non-scattering and single scattering models of phosphor screens.

the surrounding medium and the resulting light intensities should be corrected for the Fresnel reflection at the interface between the media. Eq. 4, which describes transmission of the exciting radiation (for the normal incidence on the screen), should now become (Nakazawa et al., 2007)

$$I'_T = \frac{(1-R_0)^2(1+\kappa^2/n^2)\exp(-\alpha' d)}{1-R_0^2\exp(-2\alpha' d)}$$

$$\approx \frac{(1-R_0)^2\exp(-\alpha' d)}{1-R_0^2\exp(-2\alpha' d)}, \quad (6)$$

where n and κ are the real and imaginary part of the refractive index, respectively; and R_0 is the normal surface reflectivity

$$R_0 = \frac{(n-1)^2+\kappa^2}{(n+1)^2+\kappa^2}. \quad (7)$$

Equation 3 should now include a part of radiation I'_R reflected from the surface of the phosphor plate

$$I'_0 = I'_A + I'_T + I'_R, \quad (8)$$

which equals

$$I'_R = R_0(1+I'_T\exp(-\alpha' d)). \quad (9)$$

The emitted light undergoes reflection from the layer boundaries and a significant fraction of all light quanta cannot escape the phosphor plate due to the total internal reflection because their angle of incidence exceeds the critical angle

$$\theta_C = \arcsin(n_A/n_P), \quad (10)$$

where n_A and n_P are the refractive indices of the ambient medium and phosphor material, respectively. Such photons experience multiple reflections inside of the phosphor plate, while propagating towards the lateral edges of the structure (this phenomenon is often referred to as waveguiding), until they are finally absorbed and transformed into heat. Eq. 2 does not hold anymore and we obtain

$$I_T = I_R < q\frac{I'_A}{2}. \quad (11)$$

The trapping of light inside of the luminescent layer (or in an adjacent transparent substrate) can have a dramatic effect on device performance. For example, the light extraction efficiency of semiconductor light-emitting diodes (LEDs) (i.e. the ratio between the intensity of light emitted into the ambience and the total intensity of light generated by the device) would come to only 2–4% if no special design measures were taken (Fujii et al., 2004; Windisch et al., 2001). Such inefficient light outcoupling results from high refractive indices of semiconductors (e.g. n[GaN] = 2.5). However, even for organic LEDs (OLEDs) which employ materials with moderate values of refractive index (n~1.5), only about 20–30% of light would escape into air (Wei et al., 2006). Refractive indices of dielectrics used as phosphor hosts fall into the range between 1.5 and 2.5 and, therefore, the brightness of any single-crystalline phosphor screen should also be strongly affected by the internal reflection. Enhancement of the light extraction can be achieved by optimization of the device structure, e.g., "flip-chip" LEDs (Krames et al., 2007) or truncated cone patterns in single-crystalline phosphor screens (Jianbo et al., 2000), and/or intentional roughening of the emitting surfaces, which is applied in order to disrupt waveguiding by means of light scattering. LEDs with extraction efficiencies of 80% have been demonstrated (Krames et al., 2007). Elimination of the effect of the total internal reflection led to a remarkable improvement in performance, so that power efficiencies of semiconductor LEDs and OLEDs could exceed that of conventional fluorescent lamps (60–70 lm/W) (Krames et al., 2007; Reineke et al., 2009). This can be considered a great success because the light extraction efficiency of the fluorescent tubes is close to unity. It has to be mentioned that the improvement of device architecture and phosphor materials already allowed the production of LEDs with luminous efficacies approaching the predicted maximum values of 260–300 lm/W (Tan et al., 2012).

2.2 Single scattering model

The fluorescent lamps and many other devices in which phosphors are used in a powder form are practically not affected by waveguiding due to the absence of sufficiently smooth layer boundaries. Intensive scattering at the surface of phosphor particles, pores, and other inhomogeneities has a drastic influence on propagation of both the exciting radiation and emitted light. The equations describing the relation between the thickness of a screen and its brightness have to be changed accordingly.

Mathematically, the simplest case of the scattering phosphor screen is when the entire intensity of scattered

light is immediately lost without any further effect on resulting screen brightness. The Beer-Lambert law for the exciting light (Eq. 4) should now include the scattering coefficient β':

$$I'_T = I'_0 \exp(-(\alpha' + \beta')d). \quad (12)$$

The scattering coefficient is not a material-specific constant; it is determined by processing-dependent properties of the phosphor powder. The absorption coefficient α' in Eq. 12 also depends on the condition of the phosphor powder and, therefore, it should be distinguished from α' for the bulk phosphor material in Eq. 4.

The assumption of equality of the T- and R-mode intensities of the emitted light (Eq. 1) does not hold anymore, especially for thick screens (i.e. when the intensity of excitation substantially changes with the screen depth) due to the effects of scattering. The T-mode intensity changes with the increasing thickness of the phosphor layer as follows

$$dI_T = aq\alpha' I'_T dx - \beta I_T dx, \quad (13)$$

where a is a fraction of light emitted in the forward direction, q is the quantum efficiency of the phosphor, β is the scattering coefficient for the light at the wavelength of emission. When combined with Eq. 12, this results in a differential equation

$$\dot{I}_T + \beta I_T = aq\alpha' I'_0 \exp(-(\alpha' + \beta')d). \quad (14)$$

The solution of Eq. 14 is

$$I_T = \frac{aq\alpha' I'_0}{\alpha' + \beta' - \beta}[\exp(-\beta d) - \exp(-(\alpha' + \beta')d)]. \quad (15)$$

This is a pulse function of the general form

$$y = A[1 - \exp(-\frac{x}{t_1})]\exp(-\frac{x}{t_2}), \quad (16)$$

which can be easily reformulated to match with Eq. 15 by setting

$$A = \frac{aq\alpha' I'_0}{\alpha' + \beta' - \beta}, \quad t_1 = \frac{1}{\alpha' + \beta' - \beta}, \quad t_2 = \frac{1}{\beta}. \quad (17)$$

For the R-mode,

$$dI_R = dI_{Rx} \exp(-\beta x), \quad (18)$$

where I_R is the intensity of light coming out from the phosphor plate in the backward direction and I_{Rx} is the intensity of light emitted in the backward direction at the depth x in the screen. Eq. 18 results in a differential equation

$$\dot{I}_R = aq\alpha' I'_0 \exp(-(\alpha' + \beta' + \beta)x), \quad (19)$$

which is solved with

$$I_R = \frac{aq\alpha' I'_0}{\alpha' + \beta' + \beta}[1 - \exp(-(\alpha' + \beta' + \beta)d)]. \quad (20)$$

The R-mode curve is a single exponential decay curve.

Fig. 2 shows the curves of the R- and T-mode brightness, which were obtained by the fitting of published experimental data (Fran and Tseng, 1999; Ozawa, 2007). This is a rather special case of the thickness dependence curves, which could only be obtained in the extremely rare conditions when the scattered photons did not reach the detector.

Even though the single scattering scenario is an oversimplification in most of the practical cases, it allows us to draw a conclusion which is generally valid. For any powder phosphor screen with non-negligible scattering which is observed in the T-mode (the usual way of operation of displays, fluorescent lamps, and phosphor-converted white LEDs), there always exists an optimal screen thickness corresponding to the maximum emission brightness at given conditions of excitation. When the exciting radiation is almost completely absorbed inside the phosphor plaque, each additional infinitesimal phosphor layer in excess of the optimal thickness introduces a net decrease of the perceived intensity because losses due to scattering exceed the intensity of light generated in this layer.

2.3 Multiple scattering of light in the powder screens

Even though the shape of the T- and R-mode curves in **Fig. 2** could be predicted by simple mathematical derivations, the obtained equations (Eqs. 15 and 20) do not describe the general case of light generation in a powder phosphor screen because usually, photons are not lost immediately upon the first scattering event and can still contribute to the light output of the screen after being scattered several times. Even for a relatively low concentration of scatterers (e.g. atmospheric aerosols), this causes significant deviations from the Beer-Lambert law (Tam and Zardecki, 1982; Wind and Szymanski, 2002). In the case of densely packed particles, the propagation of light does not practically obey the Beer-Lambert law (Dick, 1998).

Fig. 3 shows an example of the typical dependence of the intensity of photoluminescence on the thickness of the strongly scattering screen. As opposed to the single scattering model, the R-mode intensity neither obeys the exponential law nor reaches saturation when the exciting radiation is fully absorbed in the screen. Both the T- and R-mode curves have an approximately linear character in the range of large screen thickness, while the sum of the corresponding intensities stays approximately constant. The comprehensive mathematical description of the process of light generation in the layers of packed phosphor particles is rather complicated. The most frequently implemented theoretical approaches to this problem are based on Kubelka-Munk's theory and the Monte Carlo

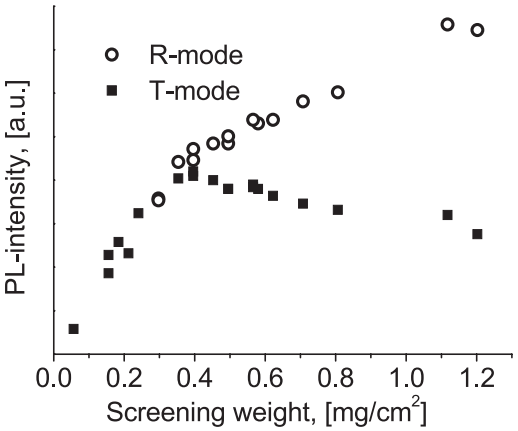

Fig. 3 Thickness dependence curves of strongly scattering Y_2O_3:Eu phosphor coatings (average phosphor particle size 440 nm, Kubrin, 2012), © Cuvillier Verlag.

method (Yen et al., 2007). In some cases, simple practical techniques for optimization of the screen weight could be developed. For example, for strongly absorbed exciting radiation, the maximum of the T-mode intensity corresponds to the minimum thickness of the powder screen fully covering the substrate (i.e. there should be no direct transmission of exciting radiation via the voids between the particles, Donofrio and Rehkopf, 1979).

In any case, it is expected that the T-mode thickness dependence curve has a maximum for a certain optimal screen thickness. Screen brightness in the R-mode asymptotically approaches a constant value, as for the non-scattering and single scattering models. However, for the multiple scattering of light emitted by a semi-infinite phosphor layer, the ratio between the light intensity detected in the R-mode and the total intensity of light generated in the screen could reach unity, if self-absorption of luminescence is negligible:

$$I_R \to qI'(0), \tag{21}$$

whereas for non-scattering screens the limit is half as small (see Eq. 2, internal reflection is disregarded):

$$I_R \to \frac{1}{2}qI'(0), \tag{22}$$

and it is even smaller in the single scattering model (see Eq. 20)

$$I_R \to \frac{\alpha'}{\alpha'+\beta'+\beta}\frac{1}{2}qI'(0). \tag{23}$$

The brightness of the non-scattering screen in the T-mode is equal to that in the R-mode and tends to the same maximum value (Eq. 22). When taking into account any losses, e.g. due to the unintended waveguiding, one obtains

$$I_T < \frac{1}{2}qI'_0. \tag{24}$$

This inequality also holds for both single and multiple scattering models because the T-mode intensity would never exceed the R-mode intensity for any given screen thickness of isotropically emitting phosphor, and their sum cannot exceed the total intensity of emitted light.

Practical calculations for the phosphor coatings of finite thickness require more rigorous treatment. The Kubelka-Munk two-flux approach, which is discussed below based on the derivation in Narita (2007), is commonly applied for various kinds of pigment coatings or any other optical coatings with non-negligible multiple scattering. Its theoretical framework can be used in many fields of application of phosphor screens. Along with modeling of the performance of fluorescent tubes (Grossman, 1998; Narita, 2007), it was successfully adopted for LEDs (Ishida et al., 2008), X-ray and vacuum UV (VUV)-excitation (Baciero et al., 1999; Jeon et al., 2000; Kandarakis et al., 1996), and cathodoluminescence (Narita, 2007). Discussion of other modeling approaches of phosphor powder coatings can be found in Yen et al. (2007) and (Kubrin, 2012).

In the approximation of the infinite screen uniformly excited from one side, scattered light produces a diffuse light flux opposite to the initial direction of propagation of the exciting radiation or emitted light. In the standard Kubelka-Munk theory, the optical properties of a particle layer (e.g. a pigment coating, Buxbaum, 2005), which is assumed to be a continuous optical medium, are completely determined by two optical constants: the absorption coefficient K and the scattering coefficient S. These coefficients correspond to the previously introduced coefficients α and β generalized to three dimensions, i.e. when incident light is diffuse and scattering takes place in all directions (Narita, 2007).

In order to perform calculations, a value of either the absorption coefficient K or the scattering coefficient S must be known. The other constant can be determined from the value of the Kubelka-Munk function $F(R_\infty)$ by the equation

$$F(R_\infty) = \frac{(1-R_\infty)^2}{2R_\infty} = \frac{K}{S}, \tag{25}$$

where R_∞ is reflectance of a semi-infinite powder layer obtained from experiments

$$R_\infty = \frac{1-\beta_0}{1+\beta_0}. \tag{26}$$

Usually, the scattering coefficient is obtained by measuring the reflectance R_0 of a relatively thin layer coated on a black plate (which has negligible reflectance)

$$S = \frac{R_\infty}{d(1-R_\infty^2)}\ln\frac{R_\infty(1-R_0R_\infty)}{R_\infty - R_0}, \tag{27}$$

where d is the thickness of the layer (Narita, 2007).

In a one-dimensional case, the light incident on the layer of non-luminescent particles is scattered in the forward and backward directions with intensities which we will denote by $I'(x)$ and $J'(x)$ instead of I'_T and I'_R, respectively. For the forward direction, the light absorbed in an infinitesimal layer of thickness dx is $\alpha' I'(x)dx$, and the scattered light is $\beta' I'(x)dx$. A part of $J'(x)$ is scattered back and has to be added to $I'(x)$. One obtains

$$\frac{dI'(x)}{dx} = -(\alpha' + \beta')I'(x) + \beta' J'(x). \tag{28}$$

For the backward direction, a similar equation can be written

$$\frac{dJ'(x)}{dx} = (\alpha' + \beta')J'(x) - \beta' I'(x). \tag{29}$$

The general solutions to this set of differential equations, known as Schuster-Kubelka-Munk equations, are

$$I'(x) = A'(1-\beta'_0)\exp(\alpha'_0 x) + B'(1+\beta'_0)\exp(-\alpha'_0 x), \tag{30}$$

$$J'(x) = A'(1+\beta'_0)\exp(\alpha'_0 x) + B'(1-\beta'_0)\exp(-\alpha'_0 x), \tag{31}$$

where constants A and B are determined by boundary conditions, and α'_0 and β'_0 are defined as

$$\alpha'_0 = \sqrt{\alpha'(\alpha' + 2\beta')}, \tag{32}$$

$$\beta'_0 = \sqrt{\alpha'/(\alpha' + 2\beta')}. \tag{33}$$

Kubelka showed that the same equations can be derived for diffuse light and scattering in all directions. As light does not always have normal incidence on the phosphor layer, the mean light path $d\xi$ is longer than dx. It was shown that

$$d\xi = 2dx. \tag{34}$$

If one defines the new coefficients K' and S' by

$$K' = 2\alpha', \; S' = 2\beta', \tag{35}$$

Eqs. 32 and 33 can be replaced with

$$\alpha'_0 = \sqrt{K'(K' + 2S')}, \tag{36}$$

$$\beta'_0 = \sqrt{K'/(K' + 2S')}, \tag{37}$$

and then, general solutions of Schuster-Kubelka-Munk equations can be expressed by Eqs. 30 and 31 again.

In the case of photoluminescence, one has to account for both exciting and emitted light. There are the following contributions to the light emitted in the forward direction (T-mode)

$$dI(x) = -dI_A - dI_S^I + dI_S^J + dI_E, \tag{38}$$

where dI_A denotes changes due to absorption of emitted light; dI_S^I and dI_S^J stand for scattering from the forward and backward modes, respectively; dI_E accounts for the process of light generation from the absorbed exciting radiation. For the backward direction, it holds

$$dJ(x) = dJ_A + dJ_S^J - dJ_S^I - dJ_E. \tag{39}$$

The intensity of the light emitted by the infinitesimal phosphor layer of thickness dx is

$$dI_E(x) + dJ_E(x) = qK'[I'(x) + J'(x)]dx, \tag{40}$$

where q is the efficiency of luminescence, K' is the absorption coefficient of the exciting radiation, and $I'(x)$ and $J'(x)$ are the intensities of the exciting light in the forward and backward directions, respectively. By combining Eqs. 30 and 31, one obtains

$$dI_E(x) + dJ_E(x) = 2qK'[A'\exp(\alpha'_0 x) + B'\exp(-\alpha'_0 x)]dx. \tag{41}$$

For infinitesimal phosphor layers,

$$dI(x)_E = dJ_E(x), \; dI_S^I = dJ_S^I, \; dI_S^J = dJ_S^J. \tag{42}$$

As a result, one obtains a set of differential equations

$$\frac{dI(x)}{dx} = -(K+S)I(x) + SJ(x) + qK'[A'\exp(\alpha'_0 x) + B'\exp(-\alpha'_0 x)], \tag{43}$$

$$\frac{dJ(x)}{dx} = (K+S)J(x) - SI(x) - qK'[A'\exp(\alpha'_0 x) + B'\exp(-\alpha'_0 x)]. \tag{44}$$

The general solutions of these equations are

$$I(x) = \frac{qK'A'}{\beta_0}\cdot\frac{\alpha'_0\beta_0 - \alpha_0}{\alpha'^2_0 - \alpha^2_0}\exp(\alpha'_0 x) - \frac{qK'B'}{\beta_0}\cdot\frac{\alpha'_0\beta_0 + \alpha_0}{\alpha'^2_0 - \alpha^2_0}\exp(-\alpha'_0 x) + A\exp(\alpha_0 x) + B\exp(-\alpha_0 x), \tag{45}$$

$$J(x) = -\frac{qK'A'}{\beta_0}\cdot\frac{\alpha'_0\beta_0 + \alpha_0}{\alpha'^2_0 - \alpha^2_0}\exp(\alpha'_0 x) + \frac{qK'B'}{\beta_0}\cdot\frac{\alpha'_0\beta_0 - \alpha_0}{\alpha'^2_0 - \alpha^2_0}\exp(-\alpha'_0 x) + \frac{A}{R_\infty}\exp(\alpha_0 x) + BR_\infty\exp(-\alpha_0 x). \tag{46}$$

The values of A and B are determined by the boundary conditions. This allows for, e.g. taking into account the

presence of the substrate or reflecting coatings, which are sometimes deposited over one side of the screen in order to increase the light output from the other side.

If absorption is not strong, the scattering coefficient S is practically independent of the absorption coefficient K. Furthermore, for conventional phosphor particles which are larger than the wavelengths of emitted light, the scattering coefficient is approximately constant over a wide wavelength range (Kortüm et al., 1963; ter Vrugt, 1965). However, in the ranges of strong absorption (e.g. for the UV-light), the described method of measuring the scattering constant cannot be used. The Kubelka-Munk theory does not predict the interdependence of K and S and requires special care when applied to the UV-range (Narita, 2007).

Another shortcoming of the Kubelka-Munk theory is that it completely disregards the size and shape of phosphor particles, as well as their mutual arrangement inside of the screen. It is known from experiments that S is reciprocally proportional to the particle size between 1 and 10 μm (Kortüm et al., 1963; Narita, 2007). In many practically relevant circumstances, the absorption coefficient K linearly depends on the volume concentration of particles f_V (volume fraction filled by particles, Buxbaum, 2005). However, the onset of multiple scattering results in a strong deviation from the linear dependence between the concentration f_V and the scattering coefficient S. It was shown that S/f_V is linearly dependent on $f_V^{2/3}$ (Buxbaum, 2005). Several authors attempted to derive the relations between the coefficients K and S and the properties of single particles (Liu et al., 2005; Mudgett and Richards, 1971).

The assumption of symmetric and semi-isotropic (two-flux) scattering made in the Kubelka-Munk theory is not always valid. In some cases, a many-flux (> 2) radiative transfer calculation procedure can produce noticeably more accurate results (Mudgett and Richards, 1971). Some further alternative approaches, such as Johnson's theory or the p-layer model, make reference to the phosphor particle size where the phosphor screen is treated as a stack of particle monolayers (Fonger, 1982a; Fran and Tseng, 1999; ter Vrugt, 1965; Yen et al., 2007). Once the reflection and transmission of such monolayers are defined, one can calculate the optical properties of the phosphor coating of any thickness. In this case, recursion formulas are used instead of differential equations. However, it should be noted that there are no strict reasons for the unit particle layer to be related to the phosphor particle size, when used for the purposes of modeling the optical properties of phosphor screens. The thickness of such an elementary layer may actually be chosen arbitrarily small. For example, a single phosphor layer can be assumed infinitesimally thin, and then the recursive formulas reduce to differential equations equivalent to the Schuster-Kubelka-Munk equations (Fonger, 1982b). In other words, Johnson's theory and other "discontinuous" models based on the notion of the particle layer are very similar to the "continuous" theory of Kubelka and Munk, and also do not explicitly account for the size and shape of phosphor particles.

The simplest bottom-up approach to modeling the collective properties of packed phosphor particles is based on stochastic computational algorithms explicitly using random numbers—generally termed as the Monte-Carlo method. It can be applied to any problem, which allows for probabilistic formulation. It was used for spherical and polyhedral particles, monosized ones and those possessing a size distribution, ordered and randomly distributed on the substrate (Konrad et al., 1999a; Soules and Klatt, 1988; Urabe, 1980). There are numerous reports on the Monte-Carlo modeling of properties of CRTs (Busselt and Raue, 1988), X-ray imaging systems (Badano, 2003; Liaparinos et al., 2006), and LEDs (Borbely and Johnson, 2005; Chang et al., 2005). Along with the possibility to explicitly account for the size, shape, and arrangement of phosphor particles on the substrate, it allows further parameters (e.g. roughness of particle surface, Konrad et al., 1999a) to be added and can be combined with theoretical methods (e.g. Mie scattering theory, Soules and Klatt, 1988; Liaparinos et al., 2006). The very important advantage of the Monte-Carlo method over the two-flux methods is that it can be used for calculations of the angular distribution of light intensity, for assessing the quality of image reproduction by the information displays and radiation converters, and can handle powder screens with a complicated structure (Urabe, 2007).

2.4 Resolution of the phosphor screens

Along with high efficiency of the conversion of external energy into visible light, phosphor screens used for acquiring or displaying any visual information have to satisfy several additional requirements. The imaging performance of a phosphor screen is determined by the amount of the information it can convey and is usually assessed by the limit of resolution, i.e. by the size of the finest structural details of an image that a display or an image converter is able to reproduce.

The smallest element of an image is a single point. In an ideal imaging system, excitation by a radiation beam of infinitesimal diameter would result in a perfect infinitesimal image point. In reality, the smallest point always has a certain finite size. Therefore, the resolution of the screen can be characterized by defining a corresponding point spread function (PSF), i.e. measuring the size of the spot produced by the point-like excitation source. The PSF is a unique characteristic of the imaging performance of a phosphor screen. The intensity distribution in the entire image, which should be considered as an aggregate

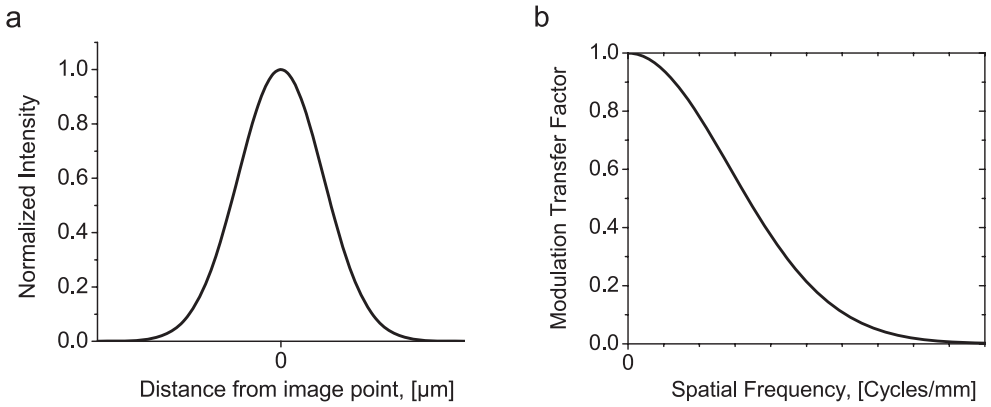

Fig. 4 Example of a point spread function (**a**) and the corresponding modulation transfer function (**b**) (Kubrin, 2012), © Cuvillier Verlag.

of image points, can be obtained by convolution of the intensity distribution of exciting radiation with the PSF of the phosphor screen. When two image points are spaced by less than the width of the PSF, they cannot be fully resolved. Such blurring of an image leads to losses of visual information.

For isotropic imaging systems, the two-dimensional point spread function is rotationally symmetric (Rossmann, 1969) and can be described by a curve for one spatial dimension (**Fig. 4a**). Often a simple Gaussian intensity profile is assumed and the full width of the PSF at half the maximum intensity (FWHM) is commonly used as the representative value. The shape of the PSF of different screens, however, may vary significantly, so that it is advisable to measure it down to at least several percent of the peak intensity (Gruner et al., 2002), and the full width corresponding to 1–5% of the maximum is sometimes specified as well (e.g., Pokric and Allinson, 2002).

Direct measurement of the PSF is quite cumbersome because it requires a point source of excitation. In many applications, it is difficult to reduce the area of the screen exposed to the exciting radiation to a vanishingly small size and to have sufficient intensity at the same time. It can be more convenient to measure the line spread function (LSF)—another transfer characteristic of phosphor screens. Similarly to the PSF, which describes the transfer of intensity distribution from the point source of excitation to its image, the LSF defines the intensity profile of the image of a line source. The LSF is related to the PSF by the expression (Gruner et al., 2002)

$$LSF(x) = \int_{-\infty}^{+\infty} PSF(x,y)\,dy\,. \tag{47}$$

The LSF is a one-dimensional function but, for the isotropic imaging systems, the two-dimensional PSF can be obtained from the single LSF by the Abel transform (Koch et al., 1998; Rossmann, 1969). If a PSF has a Gaussian shape, the corresponding LSF is a Gaussian function as well. Width of the LSF is also usually measured by its FWHM value and by the full width at some intensity in the range of several percent of the peak response (Busselt and Raue, 1988). Sometimes, the full width comprising most of the area of the integrated LSF (e.g. 90%) is applied (Koch et al., 1998).

How much overlap of the spread functions is needed for adjacent points/lines in the image to become irresolvable? There are several resolution criteria used in various fields of applied optics. The most well-known is the Rayleigh criterion, which states that two equally bright point objects can be resolved if the maximum of the PSF of the first point falls into the first minimum of the PSF of the second one (Sayanna et al., 2003). This definition of the limit of resolution was developed for diffraction-limited optical systems where the PSF is represented by the Airy pattern of concentric rings with multiple minima. For the PSFs without local minima (e.g. those of Gaussian shape), the Rayleigh criterion is ambiguous. Furthermore, it cannot be applied to the resolution of unequally bright point objects. Very often the limit of resolution is simply identified with the FWHM of the PSF. The so-defined Houston criterion can be used with the spread functions of any shape. However, it is also impractical for resolving the points/lines of different brightness. In many cases, the Sparrow criterion is preferred (Sayanna et al., 2003). Sparrow has suggested that the natural definition of resolution is the point separation at which the saddle point between the two maxima first develops, i.e. when the second derivative of the sum of the PSFs in the midpoint between the points vanishes. If the distance between the points is less or equal to the Sparrow limit, they will be perceived as a single elongated point. The same applies to the LSFs. For example, it is known that a series of equidistant Gaussian profiles separated by 2σ, where σ is a standard deviation of the spatial intensity distribution, should produce a uniform intensity ($2\sigma \approx 0.85FWHM$). This property, referred to as a merging raster, is utilized for the reproduction of images with pixelated screens, i.e. screens composed of an array of pixels (discrete picture elements). If the distance

between the lines increases, a variation of intensity with the corresponding spatial frequency will be observed as soon as this variation exceeds some perceivable threshold, i.e. the lines will be resolved.

For a general case of an arbitrary LSF, any quantitative treatment would require extensive calculations and it has long been recognized that the problem can be simplified by solving it in the (spatial) frequency domain. This approach is based on the notion of the optical transfer function (OTF), a representation of the frequency response of the optical system. The one-dimensional OTF can be obtained by the Fourier transform of the LSF (or of the PSF for two dimensions) (Koch et al., 1998; Williams and Becklund, 1989). It can also be directly measured for sinusoidal excitation patterns. As the emission and excitation of luminescence are incoherent, only the modulus of the OTF, termed modulation transfer function (MTF), has importance and its phase component (phase transfer function) can be disregarded. Modulation is defined as a ratio of the amplitude of the sinusoid to its average value and, therefore, cannot be greater than unity (Rossmann, 1969). An example of MTF is shown in **Fig. 4b**. The limit of resolution of a phosphor screen is usually associated with the spatial frequency (measured in cycles per unit length) at which the MTF decreases to 3–5%.

The contrast transfer function (CTF) is another transfer characteristic conventionally applied to phosphor screens. The CTF quantifies the frequency response of an imaging system for a square-wave input instead of the sine wave, which is more convenient for experiments (e.g. with bar charts or rectangular slits, Franks et al., 2003). For the same reason of simpler experimental procedure, the line spread function is sometimes obtained by differentiating an edge trace, i.e. intensity distribution on a boundary between "black" and "white" half-planes in the image of the knife edge (Williams and Becklund, 1989). The CTF equal to one designates perfect transfer of contrast. The limit of resolution of the imaging system is specified in lines per unit length. Such units are very convenient for pixelated displays and radiation converters where the smallest resolvable details of an image are inherently limited by the size of single pixels. However, when two neighboring lines of pixels have the same intensity, they cannot be resolved. "Black" lines should be interlaced with "white" lines, i.e. at least two lines of pixels are needed for the reproduction of each line in the image. In the sampling theory, this is justified by the Nyquist-Shannon theorem. In order to avoid confusion in the specification of resolution, the units of line pairs per unit length (e.g. lp/mm) are widely accepted. Generally, the cut-off spatial frequency for pixelated screens is in the best case approximately equal to half of the density of lines in the raster (or pixels in the line). It is somewhat worse if there is any cross-talk of the neighboring pixels, i.e. if their PSFs significantly overlap.

The resolution of homogeneous unpixelated screens is determined by several parameters. The following primitive example reveals the major factors of influence for a screen consisting of superwavelength-sized particles. Let us consider a single layer of phosphor particles deposited on the transparent substrate (**Fig. 5a**). Light emitted inside of the phosphor particle experiences multiple internal reflections and can escape the volume of the particle in any direction at an arbitrary point of its surface. Therefore, even for a single layer of phosphor particles, the smallest light emission spot would be approximately equal to the phosphor particle size. However, if neighboring particles have equal intensity, it is impossible to say whether those are two separate points or a single elongated one (Particles 1 and 2 in **Fig. 5a**). Similarly to the pixelated screens, two image points should be separated by at least one more "pixel" — in this case, another phosphor particle (Particles 2, 3, and 4 in **Fig. 5a**). The diameter D_{IP} of the smallest resolvable image point can be approximately expressed as follows:

$$D_{IP} = 2\phi + 2c\,, \tag{48}$$

where ϕ is the phosphor particle size and c is the inter-particle clearance. Obviously, both the phosphor particles themselves and the gaps between them must be kept as small as possible for improved resolution.

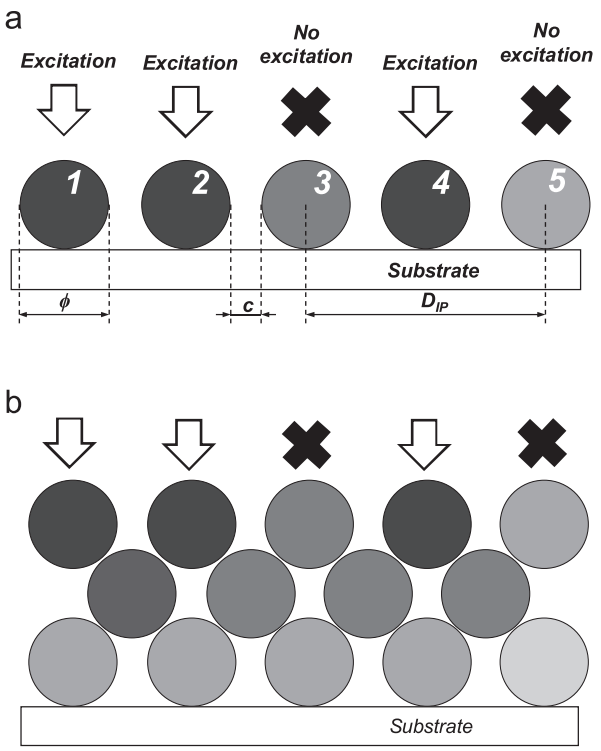

Fig. 5 Schematic illustration of the influence of phosphor particle size, packing density and screen thickness on image resolution. The darker appearance corresponds to a higher intensity of emitted light. See text for explanation.

The influence of phosphor layer thickness on screen resolution is illustrated in **Fig. 5b**. It is assumed that the coated side of the screen is exposed to excitation with electrons or strongly absorbed photons which are completely absorbed in the top layer of phosphor particles, and particles in the deeper layer(s) merely scatter emitted light without contributing to the emission of luminescence. Nearly 50 percent of produced light is emitted towards the substrate and these photons impinge upon the particles in the second and the third layers and are either reflected or refracted on their surface. Light diffuses inside of the phosphor coating in all directions until it escapes on either side of the screen. If the screen is observed in the T-mode, the light intensity pattern (the image) produced in the top particle layer undergoes gradual degradation (blur), which makes closely spaced image points unresolvable, as in the bottom layer of the screen in **Fig. 5b**. The image observed in the R-mode is much less prone to the optical blur, although light scattered back from the deeper particle layers may escape from the screen at the spots which were not excited (Particle 3 in **Fig. 5b**) and in this way slightly impair the MTF. Experiments show that for powder phosphor screens exposed to the strongly absorbed exciting radiation, the MTF in the R-mode is almost independent of the screen thickness. The reflecting CRTs have 3–4 times better resolution as compared to the conventional transmitting ones (Zege et al., 1991).

Obviously, the resolution of unpixelated screens can be improved by decreasing the thickness of the phosphor screen, increasing the packing density of phosphor particles and, finally, by reducing the phosphor particle size. This conclusion is generally valid for any cathodo- or photoluminescent powder screens as well as for those excited by X-rays. However, each parameter affecting the screen resolution can be varied only within a certain limited range determined by other application-specific requirements or available technology. For example, X-rays are weakly absorbed by phosphors, and a considerable thickness of the screen may be required for sufficient efficiency of conversion into visible light. Usually in such cases, a trade-off between better resolution and fainter emission intensity has to be found. On the other hand, the penetration depth of an electron beam into the phosphor is often much smaller than the size of a single phosphor particle. However, from the point of view of manufacturing CRTs, it is difficult to deposit such thin phosphor coatings free of voids and irregularities. The thickness of phosphor screens in conventional CRTs often has to be increased in order to assure uniformity and thus the obtained resolution is compromised due to technological constraints.

A general relation for the optimum screen density W_{opt} of CRTs, which accounts for the non-close packing of phosphor particles, was obtained by Busselt and Raue (1988)

$$W_{opt} = 2\bar{\phi}_{V50}\rho f_V^{2/3}, \tag{49}$$

where $\bar{\phi}_{V50}$ is the volume median diameter (measured by sedimentation), ρ is the phosphor density, and f_V is the packing density of the phosphor screen. In the same work, a simple relation between the width of the LSF at 5% peak intensity L_{05} and the geometric thickness d of the screen was found for practical CRT phosphors (Busselt and Raue, 1988)

$$L_{05} = 4.5d. \tag{50}$$

This equation may be rewritten for the optimum screen density W_{opt} and combined with Eq. 47 to obtain

$$L_{05} = 4.5\frac{W_{opt}}{\rho f_V} = 9\frac{\bar{\phi}_{VM}}{f_V^{1/3}}. \tag{51}$$

Therefore, an increase in the packing density of phosphor particles in the screens of optimized density leads to a "sharpening" of reproduced images. It can be considered as a general trend that screens with a high packing density of particles have a better resolution but decreased brightness (Sasaki and Talbot, 1999). It should be emphasized that Eqs. 47–49 are valid only for the T-mode of screen observation.

A combined effect of the size and packing density of phosphor particles can be expressed by the change of the scattering mean free path of the emitted photons (Busselt and Raue, 1988). Intensive optical scattering is found to suppress the tails of the spread functions, i.e. to decrease the L_{05} in Eq. 47. As a result, the MTF of the powder phosphor screens at low spatial frequencies often surpasses that of non-scattering ones (e.g. single-crystalline or glass plates, Faruqi et al., 1995; Gruner et al., 2002; Swank, 1973).

Scattering of the exciting radiation usually has a minor effect on the quality of image reproduction in most of the applications. For example, in the case of CRTs, changes of the MTF introduced by an increase of the energy of electrons from 5 to 40 keV were less than 15% (Zege et al., 1991). For the X-ray excitation, the scattering of X-rays can be completely neglected.

If the exciting radiation is weakly absorbed, the resolution of the screen is still to a large extent determined by its geometric thickness, so that the values of the MTF corresponding to the same product of spatial frequency and phosphor thickness stay unchanged (Swank, 1973). The necessity of large values of thickness for the complete absorption of X-rays leads to a relatively low resolution of powder phosphor screens, which usually is limited to the range of 10–20 lp/mm (Badano, 2003; Sklensky et al., 1975). For a given thickness of the X-ray intensifying screen, the resolution may be improved by several methods, e.g. by depositing a reflective or absorbing coating

(backing) over the rear side of the screen or by introducing small amounts of impurities which provide weak self-absorption of luminescence in the phosphor material, thus removing long tails of the LSF without strongly impairing the light output (Swank, 1973; Zege et al., 1991). Also for the X-ray excitation, the resolution of the screens in the R-mode is somewhat better than that for the T-mode (Zege et al., 1991).

Although the R-mode seems to be preferable for high-resolution imaging, it is highly impractical in most of the applications. In order to achieve superior resolution in the T-mode without sacrificing the efficiency of detection of X-rays, special structured screens are sometimes used. Columnar (needle-like) phosphor particles aligned parallel to the incident X-rays allow elimination of the strong interdependence between the width of the LSF and the screen thickness (Badano, 2003). Alternatively, a mask with an array of thin holes filled with a phosphor can be used. Screens with the resolution on the order of 1 μm were realized based on the latter approach (Flannery et al., 1987). Nonetheless, the screens with a spatial resolution close to the optical diffraction limit could be obtained only by decreasing the thickness of the phosphor film to 1 μm (Koch et al., 1998; Martin and Koch, 2006).

3. Limits of performance of the luminescent screens

Let us consider a powder phosphor screen which is excited by the UV-light (the wavelength and intensity are fixed). What can be its highest brightness and resolution?

For a semi-infinite phosphor plaque, the R-mode brightness is at most (see Sec. 2.3 and Eq. 21)

$$I_R \to qI'(0), \tag{52}$$

where q is the quantum efficiency of the phosphor and $I'(0)$ is the intensity of the incident exciting radiation. For the T-mode, the maximum achievable intensity (for the optimized screen thickness and without reflecting coatings on the rear side of the screen) would be

$$I_T \le \frac{1}{2} qI'(0). \tag{53}$$

Thus, the maximum brightness of the phosphor screen is ultimately limited by the quantum efficiency of the phosphor. The quantum efficiency of phosphors used in fluorescent lamps, PDPs, and LEDs is about 100% (Ronda, 2008). In this aspect, the performance of the state-of-the-art inorganic phosphors is quite close to the physical limits. One has to distinguish, however, between the quantum efficiency and energy efficiency of a phosphor. If luminescence is excited with photons which have energy exceeding that of the emitted photons by more than a factor of 2, the quantum efficiency may reach 200% in certain luminescent materials, i.e. two photons could be emitted per each incident exciting photon. This process is referred to as quantum cutting. Quantum-cutting phosphors have attracted a lot of attention in the past decade, particularly in the fields of photovoltaics and mercury-free fluorescent lamps (Huang et al., 2013; Meltzer, 2007; Ronda, 2008; Zhang and Huang, 2010).

Resolution of the screen is another major figure of performance. For the screens designed for observation with the naked human eye, the resolution of 20 lp/mm is usually sufficient. However, there are several imaging applications such as the excimer laser beam profiling, inspection of photolithographic masks, tunneling electron microscopy, and X-ray microtomography where the phosphor screens with a resolution beyond 1000 lp/mm would provide a definite advantage.

The resolution of the unpixelated phosphor screens is mainly determined by their geometric thickness (see Sec. 2.4). In principle, any desired resolution could be obtained with an appropriately thin phosphor coating, provided that it absorbs a sufficient amount of exciting radiation for a detectable light output. However, the ultimate limit of resolution is set by the diffraction of light and not by the screen thickness. If no special super-resolution techniques are utilized, the resolution of an optical system cannot be better than

$$k \approx \frac{2n}{\lambda}, \tag{54}$$

where k is the Abbe limit of detection (measured in spatial frequency), n is the refractive index of the surrounding medium, and λ is the wavelength of emitted light (Evanko, 2009). The highest spatial frequency that can be optically resolved (for λ=400 nm) is therefore, about 5000 cycles/mm. For longer wavelengths and a finite aperture of the detector, the limit of detection can significantly decrease. If we assume, for simplicity, that the FWHM of the LSF exactly equals the thickness of the phosphor coating (Koch et al., 1998), the corresponding thickness threshold of the diffraction-limited phosphor screen would be on the order of 200 nm. For the pixelated phosphors, this is also the value of the smallest pixel pitch that could ever be needed for the optical imaging.

On one hand, several works on phosphor screens with submicrometer resolution very close to theoretical limits were already reported (Koch et al., 1998; Martin and Koch, 2006; Martin et al., 2012), so that the room for improvement of the spatial resolution *per se* is also rather limited. On the other hand, high-resolution phosphor radiation converters in the form of non-scattering single crystal films or transparent ceramics are much more difficult to produce (Kuntz et al., 2007; Martin et al., 2012; Park et al., 2012b; Touš et al., 2007) as compared to the conventional

processing methods of phosphor powder coatings. It would be beneficial to find a means to manufacture phosphor screens with submicrometer optical resolution by simpler, more economical methods.

As follows from the discussion above, phosphor powder screens may approach diffraction-limited imaging if their thickness could be reduced below 200 nm. Obviously, the manufacturing of such screens would require the application of nanophosphors with a much smaller particle size.

The reduction of phosphor particle size in the super-wavelength regime is relatively straightforward because it does not affect the luminescent properties of particular phosphor materials. Submicrometer-sized phosphor particles are used, e.g. in plasma display panels, because they can be processed in smaller pixels than for conventional phosphors produced by solid-state firing and retain the same brightness for significantly lower screen weights (Kubrin et al., 2007; Kubrin, 2012), thus allowing for a reduced consumption of sometimes extremely costly phosphors. However, when their particle size enters the nano-range, many physical properties of solids undergo dramatic changes. These size effects are summarized in the next sections.

4. Physical implications of reducing the phosphor particle size

4.1 Independent scattering and absorption of light by nanoparticles

As discussed in Sec. 2.4, the scattering of light inside the phosphor layer degrades the resolution of powder screens. We also learned in Sec. 2.2 and 2.3 that scattering affects the thickness dependence curves of light emitted from the screen in the R- and T-modes. It is therefore desirable to derive a mathematical relation between the particle size and the scattering coefficient β (as used in Sec. 2.2 and 2.3) and to compare the behavior of conventional phosphor powders and nanophosphors.

It is convenient to introduce a quantity that specifies the ability of a single phosphor particle to scatter light. The amount of light removed from the incident light by a single phosphor particle is proportional to its geometric projected area A_P

$$C_{SCA} = Q_{SCA} A_P \tag{55}$$

where C_{SCA} is the scattering cross-section of the particle (measured in the units of area), the proportionality factor Q_{SCA} is termed scattering efficiency. In the general case of particles that both absorb and scatter, the attenuation cross-section (also called extinction cross-section) should be used instead of C_{SCA}

$$C_{ATT} = Q_{ATT} A_P = C_{ABS} + C_{SCA} = (Q_{ABS} + Q_{SCA}) A_P, \tag{56}$$

where Q_{ATT} and Q_{ABS} are the attenuation and absorption efficiencies, respectively; C_{ATT} and C_{ABS} are the corresponding cross-sections.

Calculation of the scattering and absorption efficiency factors is the central problem of the Mie scattering theory. The theory provides the exact solution of the Maxwell equations, describing the propagation of electromagnetic radiation for a plane wave incident on spherically symmetric particles. The intensity of scattered light at any angle can be calculated for a particle with the given relative refractive index n_R and size parameter x, defined by expressions

$$n_R = \frac{n_P}{n_A}, \tag{57}$$

where n_P and n_A are the refractive indices of the phosphor material and ambient medium, respectively; and

$$x = \frac{\pi\phi}{\lambda}, \tag{58}$$

where ϕ is the particle diameter and λ is the wavelength of light incident on the particle. The desired attenuation/scattering efficiency factors are obtained in the form of a series of Legendre polynomials. If no additional simplifying assumptions can be made, the required calculations are computationally quite intensive. The comprehensive description of the procedure may be found in numerous textbooks on the scattering of light by small particles, e.g. in Bohren and Huffman (2004) Mishchenko et al. (2002), or van de Hulst (2009). An important outcome is that the scattering efficiency factor asymptotically tends to a value of 2 as the size parameter increases (i.e. for particles much larger than the wavelength of light). In the range of small values of the size parameter, a steep decrease of the scattering efficiency is observed.

For particles which are much smaller than the wavelength of light (ϕ < 50 nm), the intensity and pattern of scattering can be obtained by a much simpler Rayleigh scattering theory. For such particles, the incident electromagnetic field behaves almost as an electrostatic field and is homogeneous inside of the particle. This results in the following equations for the scattering and absorption efficiencies (Mishchenko et al., 2002)

$$Q_{SCA} = \frac{8}{3} x^4 \left| \frac{n_R^2 - 1}{n_R^2 + 2} \right|^2, \tag{59}$$

$$Q_{ABS} = 4x \,\mathrm{Im}\left(\frac{n_R^2 - 1}{n_R^2 + 2} \right). \tag{60}$$

It is important to note here that the scattering efficiency scales with the fourth power of the size parameter, whereas the absorption efficiency has a linear dependence.

This means that the decrease in size of the nanoparticles strongly increases the contribution of absorption to the overall attenuation.

If the effective attenuation cross-section of phosphor particles is known, it can be used for assessing the collective optical properties of ensembles of particles. For the idealized scenario of single scattering by N particles per unit of volume (particles are assumed to be sparsely spaced), the Beer-Lambert law (see Eq. 12) can be rewritten to yield (Hinds, 1999)

$$I_T = I_0 \exp(-(\alpha + \beta)d) = I_0 \exp(-NQ_{ATT}A_P d). \quad (61)$$

Alternatively, it could be reformulated for the particle volume fraction f_V by assuming particles of spherical shape and diameter ϕ

$$f_V = \frac{\pi N \phi^3}{6}, \quad (62)$$

$$A_P = \frac{\pi \phi^2}{4}, \quad (63)$$

$$I_T = I_0 \exp(-\frac{3 f_V Q_{ATT}}{2\phi} d). \quad (64)$$

For non-absorbing particles substantially larger than the wavelength of light,

$$Q_{ATT} = Q_{SCA} = 2. \quad (65)$$

one obtains a simple relation between β and ϕ

$$\beta = \frac{3 f_V Q_{SCA}}{2\phi} = \frac{3 f_V}{\phi}. \quad (66)$$

If the volume concentration of particles (i.e. f_V) does not change, the scattering constant in the Beer-Lambert law is inversely proportional to the phosphor particle size. For nanoparticles (see Eq. 59),

$$\beta = \frac{3 f_V Q_{SCA}}{2\phi} = \frac{4 f_V}{\phi} x^4 \left|\frac{n_R^2 - 1}{n_R^2 + 2}\right|^2 = \frac{4\pi^4 f_V \phi^3}{\lambda^4} \left|\frac{n_R^2 - 1}{n_R^2 + 2}\right|^2, \quad (67)$$

it is expected that the scattering constant scales in direct proportion to ϕ^3. For the absorption constant (Eq. 60), we have

$$\alpha = \frac{3 f_V Q_{ABS}}{2\phi} = \frac{6 f_V}{\phi} x \,\mathrm{Im}\left(\frac{n_R^2 - 1}{n_R^2 + 2}\right) = \frac{6\pi f_V}{\lambda} \mathrm{Im}\left(\frac{n_R^2 - 1}{n_R^2 + 2}\right), \quad (68)$$

which seems not to be affected by the size of nanoparticles. It is important that both α and β become dependent on the wavelength light. We should also keep in mind that the refractive index is also a function of the wavelength.

For superwavelength-sized particles, expressions of the general form

$$S = \frac{const.}{\phi} \quad (69)$$

relating the scattering coefficient S with the size of phosphor particles can also be applied in the framework of the Kubelka-Munk theory (Butler, 1980). When particles are separated from each other by sufficiently large distances so that the scattering from each single particle is not affected by the proximity of its neighbors, it is possible to directly relate the parameters of the Kubelka-Munk theory with those of the Mie theory by introducing additional parameters (Liu et al., 2005)

$$K = N\overline{\xi} C_{ABS} = \frac{3 f_V}{2\phi} \overline{\xi} Q_{ABS}, \quad (70)$$

$$S = N\overline{\xi}(1 - \overline{\sigma}_d) C_{SCA} = \frac{3 f_V}{2\phi} \overline{\xi}(1 - \overline{\sigma}_d) Q_{SCA}, \quad (71)$$

where $\overline{\xi}$ is the average path-length parameter (assumed equal to 2 in the original Kubelka-Munk theory), and $\overline{\sigma}_d$ is the forward-scattering ratio for diffuse radiation (i.e. a fraction of energy that each particle scatters in the forward direction; it can also be determined by the Mie theory). It is possible to derive K and S for nanophosphors similar to Eqs. 67 and 68. However, such expressions cannot properly describe light propagation in the nanophosphor screens because the previously made assumption of independent light scattering by each particle, which requires their large separation, is never fulfilled for packed nanoparticles.

4.2 Dependent scattering and absorption in densely packed powders

In some cases, the collective optical properties of densely packed particles can still be treated as if these particles were attenuating incident light independently from each other. In many cases, however, the influence of the neighboring particles cannot be neglected. For example, effects generally termed as particle crowding play a very significant role in the technology of pigments (Auger et al., 2009; Koleske, 1995). With increasing packing density, the distances between neighboring particles decrease and more and more particles come into contact with each other. The mean free path of the photons between two successive scattering events is determined by the average interparticle spacing and thus it should decrease as well. If it becomes comparable to the particle size, the wavefront of the scattered light incident on the next particle along its path can be appreciably different from the plane wave. As a consequence, the accuracy of calculations based on the efficiency factors obtained from the Mie theory can be impaired. Furthermore, in such a case phosphor particles cannot be treated as point-like scatterers. The absorption

and scattering coefficients (see Eq. 66) should be corrected for volume scattering (Brewster, 2004)

$$\alpha = \frac{3 f_V Q_{ABS}}{(1-f_V)2\phi}, \quad \beta = \frac{3 f_V Q_{SCA}}{(1-f_V)2\phi}. \tag{72}$$

These expressions differ from those derived for the point scattering by the factor $(1–f_V)$ in denominator, which is introduced in order to account for shadowing of particles by each other for $f_V > 0.1$.

Significant qualitative changes in the interaction of light with particulate matter occur when the interparticle distances enter the size range of a single wavelength of incident light. At this scale, the scattered fields of the neighboring particles can become spatially coherent even for an incoherent radiation source. Coherent addition of the scattered light strongly affects the scattering characteristics of particles in the far field (Tien, 1988). At the same time, the near-field interactions become pronounced (McNeil et al., 2001). At a subwavelength distance from the particle surface, electromagnetic fields include contributions from non-propagating evanescent waves (Li et al., 2005; Mendes et al., 2010). Their influence on the radiation transfer is manifested, for example, by a phenomenon known as the frustrated total internal reflection, which causes transmission of light between two media with high refractive indices separated by a small gap filled with material of lower refractive index at the angles of incidence, for which the total internal reflection would occur in the absence of the second high-index medium. The near-field interactions affect both absorption and scattering of light by particulate matter (Tien, 1988).

The onset of the dependent scattering and absorption is usually determined by a 5% deviation from the independent Mie theory. It was found that this threshold is usually surpassed when the interparticle clearance decreases below approximately one half of the wavelength of the incident radiation (Tien and Drolen, 1987)

$$c_d \le 0.5\lambda, \tag{73}$$

where c_d denotes the clearance for which the dependent effects are significant, and λ is the wavelength of light in the medium between the particles (not λ_0 for vacuum). It was shown that the criterion given by Eq. 73 approximately corresponds to the clearance at which the near-field zones of scattering particles begin to overlap (Kamiuto, 1984).

Although in general particles are randomly packed and have different sizes and shapes, the ratio of the average interparticle clearance to the wavelength is very often assessed by a formula derived for a periodical rhombohedral arrangement of monosized spheres (Tien, 1988)

$$\frac{c}{\lambda} = \frac{x}{\pi}\left(\frac{0.905}{f_V^{1/3}} - 1\right), \tag{74}$$

where f_V is the particle volume fraction, x is the particle size parameter. For nanoparticles, the clearance and the distance between the centers of the particles are practically equal. The position of the boundary between the independent and dependent regimes almost does not change with the particles size parameter, and therefore for Rayleigh particles, the critical particle volume fraction of 0.006 is generally assumed.

The “dependent” effects described above result in a decrease of the effective scattering cross-section of particles. For small absorbing particles, the absorption efficiency factor was found to increase (Kumar and Tien, 1990; Prasher, 2007). In the range of Rayleigh scattering, the contribution of absorption to the total attenuation dominates over scattering, and therefore the dependent attenuation efficiency of absorbing particles increases as well (Kumar and Tien, 1990; Prasher, 2007; Siegel and Howell, 1992).

Quantitatively, the problems of radiation transfer in the regime of dependent multiple scattering are usually solved by numerical simulations (Tien and Drolen, 1987). In several cases, analytical relations between the dependent scattering efficiency factor Q_{SCA}^D and the independent (i.e. Mie-) scattering efficiency Q_{SCA}^M could be obtained. For example, the pioneering work by Hottel et al. (Hottel et al., 1971) resulted in the following empirical expression for $c/\lambda > 0.092$

$$\log\log\left(\frac{Q_{SCA}^M}{Q_{SCA}^D}\right) = 0.25 - 3.8\frac{c}{\lambda}, \tag{75}$$

which was verified for $x < 1$ (Tien and Drolen, 1987). For the size parameter $x \to 0$, an analytic relation between Q_{SCA}^D and Q_{SCA}^M could be derived for the Percus-Yevick hard-sphere model (Tien and Drolen, 1987)

$$\frac{Q_{SCA}^D}{Q_{SCA}^M} = \frac{(1-f_V)^4}{(1+2f_V)^2}. \tag{76}$$

An approximate expression for the dependent absorption efficiencies Q_{ABS}^D in the limit of Rayleigh particles (i.e. $x \to 0$) was identical for several different models (Kumar and Tien, 1990)

$$Q_{ABS}^D = 4x\,\mathrm{Im}\left(\delta\,\frac{n_R^2 - 1}{n_R^2 + 2}\right), \tag{77}$$

where

$$\delta = \left[1 - \frac{n_R^2 - 1}{n_R^2 + 2} f_V\right]. \tag{78}$$

Recently, it was shown that changes to the effective refractive index of a nanoparticulate medium should be taken into account when modeling the radiation transfer with dependent absorption and scattering (Prasher, 2007).

A turbid medium filled with particles much smaller than the wavelength of light acts upon photons, which traverse it, as an optically homogeneous medium with a refractive index determined by the refractive indices of constituting media and the particle volume fraction. From this point of view, the influence of the volume concentration of nanoparticles on the effective refractive index can be considered as a further effect of dependent scattering and absorption.

Assuming a substantial number concentration N of nanoparticles in vacuum (there should be many nanoparticles in a sphere with a radius equal to the wavelength of light), the effective refractive index n_{EFF} can be related by the Lorentz-Lorenz equation (van de Hulst, 2009), also known as the Clausius-Mossotti relation (Meltzer et al., 1999)

$$\frac{4\pi\alpha}{3}N=\frac{n_{EFF}^2-1}{n_{EFF}^2+2}, \tag{79}$$

where N is the number concentration of particles and α is the polarizability of the nanoparticles. The polarizability defines a dipole moment of the Rayleigh particles induced by an external electric field and can be used to describe their scattering. Alternatively, the effective refractive index can be derived from the volume concentration of particles f_V and their refractive index n_P

$$\frac{n_{EFF}^2-1}{n_{EFF}^2+2}=f_V\frac{n_P^2-1}{n_P^2+2}. \tag{80}$$

For particles dispersed in a medium with refractive index n_A it becomes (Klein, 1988)

$$\frac{n_{EFF}^2-1}{n_{EFF}^2+2}=f_V\frac{n_P^2-1}{n_P^2+2}+(1-f_V)\frac{n_A^2-1}{n_A^2+2}. \tag{81}$$

In many cases, however, a simplified expression below is applied (Meltzer et al., 1999; Vollath, 2008)

$$n_{EFF}=f_V n_P+(1-f_V)n_A. \tag{82}$$

The imaginary part of the effective refractive index (usually referred to as the extinction coefficient k) can be transformed into the absorption coefficient of the nanophosphor layer by the expression (Bohren and Huffman, 2004)

$$\alpha=\frac{4\pi\ \mathrm{Im}(n_{EFF})}{\lambda_0}=\frac{4\pi k_{EFF}}{\lambda_0}, \tag{83}$$

where λ_0 is the wavelength of light in vacuum.

A potentially more exact expression can be derived from Eq. 68 and 77

$$\alpha=\frac{3f_V Q_{ABS}^D}{2\phi}=\frac{6f_V}{\phi}x\,\mathrm{Im}\left(\delta\frac{n_{EFF}^2-1}{n_{EFF}^2+2}\right)$$

$$=\frac{6\pi f_V}{\lambda}\mathrm{Im}\left(\delta\frac{n_{EFF}^2-1}{n_{EFF}^2+2}\right). \tag{84}$$

For the scattering coefficient, we combine Eq. 67 and 76

$$\beta=\frac{3f_V Q_{SCA}^D}{2\phi}=\frac{4f_V}{\phi}x^4\left|\frac{n_{EFF}^2-1}{n_{EFF}^2+2}\right|^2\frac{(1-f_V)^4}{(1+2f_V)^2}$$

$$=\frac{4\pi^4 f_V\phi^3}{\lambda^4}\left|\frac{n_{EFF}^2-1}{n_{EFF}^2+2}\right|^2\frac{(1-f_V)^4}{(1+2f_V)^2}. \tag{85}$$

The coefficients K and S for the Kubelka-Munk model could be derived in similar way. However, their complexity precludes convenient comparison of the scattering and absorption properties of conventional phosphors and nanophosphors. To complete this section, the experimentally observed wavelength dependence of the attenuance of coatings made of the same phosphor with different particle sizes is shown in **Fig. 6**. One can see that the values measured in the range of strong absorption (λ < 280 nm) are very close, whereas near the main emission peaks ($\lambda \approx$ 590–650 nm), scattering of the nanophosphor coating (i.e. attenuance minus absorbance, the latter is negligible in this wavelength range) is two orders of magnitude lower than that of phosphors with larger particle sizes. Furthermore, an increase of the particle volume fraction from 0.03 to 0.1 does not practically affect the curve in the short wavelength range but the scattering in the red part of the spectra substantially decreases due to the more pronounced dependent effects. The scattering of conventional phosphors is practically independent of the wavelength. For nanophosphors, a steep decrease is observed toward longer wavelengths in agreement with the predictions of Eq. 67. A consequence of the dramatically decreased scattering can be seen in the shape of the thickness dependence curve for the T-mode intensity of luminescence in **Fig. 7**. Once the maximal value is reached, the brightness of the screen stays virtually constant for any thicker phosphor coating, very similar to the theoretically expected behavior for non-scattering screens (**Fig. 2**).

As shown above, the intensity of scattering in the nanoparticle coating dramatically decreases with increasing wavelength of scattered light, decreasing the size of particles and increasing their packing density. Theoretically it should be possible to almost completely eliminate the scattering of light emitted by nanophosphor, if the particles could be made arbitrarily small and/or the particle volume fraction in the screen could be increased to values that are as high as possible (ideally up to the bulk density of the phosphor material). In this way, non-scattering phosphor screens suitable for diffraction-limited imaging could be obtained. At the same time, nanophosphor screens are less prone to losses due to internal reflection (see Sec. 2.1) because their surface is not smooth (or can be made deliberately rough, if needed), and their effective refractive index is usually much lower than that of single crystal films or fully sintered transparent ceramic phosphor

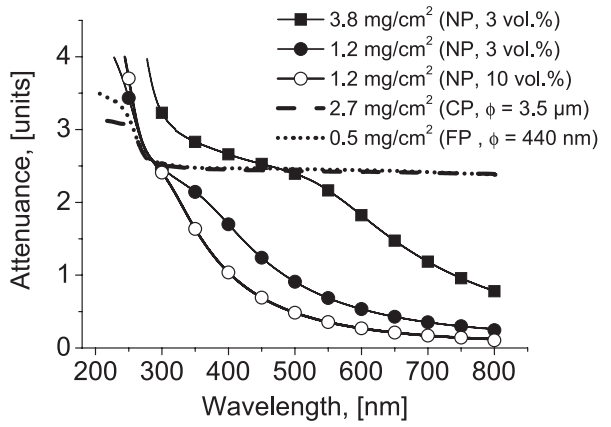

Fig. 6 Attenuance spectra Y_2O_3:Eu nanophosphor coatings (NP) of different coating densities and particle volume fractions deposited by flame aerosol deposition. For comparison, spectra of a commercial phosphor powder (CP) and a fine phosphor powder produced by flame-assisted spray pyrolysis (FP) are also shown. Their thickness was optimized for the highest T-mode output. The figure is a compilation of data published in Fig. 7 and 9, Kubrin et al. (2010), © IOP Publishing.

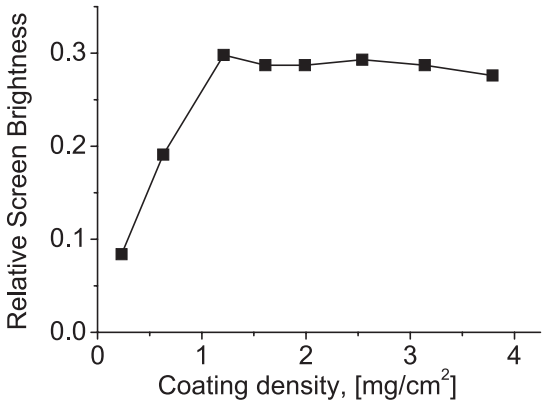

Fig. 7 T-mode thickness dependence curve of Y_2O_3:Eu nanophosphor coatings normalized to the highest brightness of the screen made of the commercial phosphor powder. The figure is a modified version of Fig. 8, Kubrin et al. (2010), © IOP Publishing.

plates. Now we can try to figure out the limiting factors, which counteract the advantages of weak light scattering by nanoparticulate matter.

4.3 Influence of particle size on emission of luminescence

How do the particle size and packing density influence the process of light emission by the particles of doped dielectrics? The quantum efficiency of a phosphor is determined by the competing processes of radiative and non-radiative relaxation of excited states. It can be expressed by the corresponding contributions to the decay times of luminescence

$$q = \frac{\tau}{\tau_R}, \tag{86}$$

where τ_R is the radiative decay time constant (without non-radiative processes) and τ is the observed emission decay time constant. In the simplest case, when both the radiative and non-radiative contributions can be represented by a first-order exponential decay, τ would change according to

$$\frac{1}{\tau} = \frac{1}{\tau_R} + \frac{1}{\tau_{NR}}, \tag{87}$$

where τ_{NR} is the non-radiative decay time constant.

Changes to the quantum efficiency and the luminescence decay time of doped phosphors are not very pronounced until they enter the size range of nanoparticles (i.e. < 100 nm). A further reduction of the size of phosphor particles usually has a profound effect on the performance of doped phosphors.

In the deep subwavelength size regime, the emission rate usually decreases with decreasing phosphor particle size. It is mainly attributed to the changes in the effective refractive index of the particulate medium (see Eqs. 80–82) (Liu and Chen, 2007a). The radiative decay time of an excited ion embedded in a medium with a refractive index n can be expressed as follows (Henderson and Imbusch, 1989; Meltzer et al., 1999)

$$\tau_R = \frac{1}{f(ED)} \frac{\lambda_0^2}{\left[\frac{1}{3}(n^2+2)\right]^2 n}, \tag{88}$$

where $f(ED)$ is the oscillator strength of the electric dipole transition. In the case of nanoparticles, the effective refractive index n_{EFF} defined in the previous section should be used. Thus it can be expected that for vanishingly small phosphor particles separated by large distances ($c > \lambda$, i.e., $f_V \to 0$), the radiative lifetime of electronic transitions can be increased from its bulk value by a factor of

$$\frac{n_P}{9}\left(n_P^2+2\right)^2. \tag{89}$$

For the magnetic dipole transitions, Equation 88 should be replaced by (Liu and Chen, 2007b)

$$\tau_R = \frac{1}{f(MD)} \frac{\lambda_0^2}{n^3}, \tag{90}$$

i.e. the radiative lifetime of the nanoparticles could differ from that of the bulk phosphor by a factor of n_P^3.

According to Eqs. 86 and 87, the decrease of the radiative decay rate due to the typically low effective refraction index can cause substantial reduction of the quantum efficiency. This effect has to be taken into account while measuring the efficiency (Mialon et al., 2009) because it

becomes dependent on the packing density of nanophosphor. Compaction of the porous nanophosphor layer from 3 to 10 vol.% particle volume fraction discussed in the previous section, not only decreased its scattering but also increased the T-mode brightness of luminescence by 13% (Kubrin et al., 2010).

The non-radiative decay time of luminescence for conventional phosphors also affects quantum efficiency. It is usually described by the temperature-dependent multiphonon relaxation rate (Liu and Chen, 2007a)

$$\frac{1}{\tau_{NR}} = C\exp\left(\frac{-\alpha\Delta E}{\hbar\omega_m}\right)\left[\frac{\exp(\hbar\omega_m/kT)}{\exp(\hbar\omega_m/kT)-1}\right]^{\Delta E/\hbar\omega_m}, \quad (91)$$

where $\hbar\omega_m$ is the maximum phonon energy of the lattice vibrations, ΔE is the energy gap between the populated state and the next low-lying state, k is the Boltzmann constant, T is the temperature, and C and α are empirical parameters characteristic for the particular crystals. In nanocrystals, the phonon density of states becomes discrete and the low-energy acoustic phonons are gradually eliminated with decreasing particle size so that the non-radiative relaxation rate of excited states and the efficiency of the phonon-assisted energy transfer in nanophosphors can be substantially reduced as compared to that in bulk materials (Liu and Chen, 2007a).

The excited state can also migrate between the activator ions in insulating hosts due to the resonant energy transfer (Liu and Chen, 2007a). However, a slight variation of the energy levels of the embedded ions due to lattice stress and defects noticeably decreases the probability of the resonant energy transfer, especially for particles with a size below 40 nm (Chen et al., 2003). As a result, both mechanisms of migration of excitation energy are inhibited in nanophosphors.

On one hand, the decreased efficiency of the phonon-assisted energy transfer impairs sensitized or upconversion luminescence (Chen et al., 2003). And on the other hand, the increase of the non-radiative lifetime of luminescence due to restricted energy transfer should favorably influence the overall quantum efficiency of conventional downconverting phosphors by postponing the onset of the concentration quenching, especially when the size of the particles approaches 1–2 nm (Mutelet et al., 2011). As a general observation, nanophosphors are significantly less efficient than their micrometer-sized counterparts (Liu and Chen, 2007a; Ronda, 2008), which means that the non-radiative decay rate either does not decrease with the size of nanoparticles or it decreases too slowly to counteract the decrease of the radiative decay rate discussed earlier in this section. It is widely accepted that the main obstacle for achieving the performance of bulk materials is constituted by the increased specific surface area of nanoparticles (i.e. by large values of surface-to-volume ratio).

In the presence of migration of excitation, the non-radiative relaxation rate is determined not only by the efficiency of the inter-ionic energy transfer but also by the concentration of lattice defects acting as emission quenchers. The particle surface itself should be considered as a distortion of the crystalline structure. Atoms within several lattice constants from the surface are displaced due to the surface reconstruction, and dangling bonds are often terminated by chemical species with high phonon frequencies (e.g. OH-, CO_3- or NH-groups) adsorbed from the ambience (Bogdan et al., 2011; Igarashi et al., 2000; Liu and Chen, 2007a; Nayak et al., 2007; Ronda, 2008). The phonon spectra of nanoparticles are further modified by the introduction of surface phonon modes which are localized at the interface with surrounding medium and can provide new channels for non-radiative relaxations (Prasad, 2004). For nanoparticles dispersed in solvents, polymers, or glasses, the effect of size confinement leading to inhibition of the energy transfer does not play any significant role and the non-radiative decay time of luminescence is usually shorter than that of the same particles not embedded in any medium (Liu and Chen, 2007a). All these effects generally referred to as surface quenching effects become more pronounced with decreasing phosphor particle size and may dramatically change the dynamics of the luminescence emission of ultrafine phosphor powders.

One of the size effects attributed to the surface quenching consists in deviation of the luminescence decay curve from single-exponential behavior (Zhang et al., 2003). It was discovered that even for relatively low concentrations of activator, the decay of emission of nanophosphors is much better fitted with a second-order exponent (Kubrin, 2012). Following the explanation proposed in Zhang et al. (2003), the shorter decay time constant should correspond to activator ions situated on or near the particle surface. However, it is very unlikely that there are only two dissimilar kinds of activator ions (on the surface and in the volume of nanoparticles) without any intermediate states. It was suggested that the decay time constants gradually increase from the surface into the depth so that it could be described by a stretched exponential function (also called Kohlrausch function)

$$I(t) = I_0\exp\left[-\left(t/\tau\right)^{\beta}\right], \quad (92)$$

where $0 < \beta \leq 1$ (Kubrin, 2012). The parameter β characterizes the width of distribution of the lifetimes and is often used as a measure of "disorder" present in the system under investigation. The Kohlrausch function is successfully applied to describe relaxation processes in many areas of physics including molecular fluorescence and luminescence of nanoscale semiconductors (Berber-

an-Santos et al., 2005; Chen, 2003; Martin and Shea-Rohwer, 2006).

Obviously, it is desirable to have a means to suppress the surface quenching. A simple strategy was proposed, which allows the quantum efficiency of nanophosphors to be improved. A thin shell of undoped host material or some other dielectric with low-as-possible maximum phonon frequency and similar lattice constant has to be grown around each nanoparticle. The external layer efficiently reduces the energy transfer to the quenching centers at the surface (Gnach and Bednarkiewicz, 2012; Liu and Chen, 2007a, Ronda, 2008, Wang et al., 2010). This strategy made it possible to achieve an exceptionally high quantum efficiency of 70% for $CePO_4$:Tb/$LaPO_4$ core-shell nanoparticles (Kömpe et al., 2003). The same method has been successfully applied for semiconductor quantum dots with a high quantum yield (Liu and Chen, 2007a). In certain cases, an undoped shell around phosphor nanoparticles can perform some further functions, e.g. protect the dopant ions from oxidation to a non-luminescent state (Buissette et al., 2006). It should be noted that "finishing" of the surface of phosphor particles is sometimes also used for conventional micrometer-sized phosphors in order to improve their maintenance or stability in suspensions (Jüstel et al., 1998). For coarse-grained phosphor powders, passivating coatings do not directly affect the luminescent properties.

Although the large surface-to-volume ratio of nanophosphors is usually a problem, it also can provide unique opportunities. For example, it has been demonstrated that the surface of Y_2O_3:Eu nanophosphor, which usually emits pure red light and is efficiently excited with only UV-light of wavelengths below 280 nm, can be passivated with organic ligands acting as a molecular antenna (Dai et al., 2011). Acetylacetonate ligands increase the absorption cross-section of phosphor nanoparticles so that the emission from Eu-ions and oxygen vacancies can be excited by a UV-LED (λ=350–370 nm) resulting in white luminescence.

The number of emitting ions inside of each nanoparticle decreases with its size and it becomes possible to observe emission from single ions of the activator. The constant intensity of emission under the constant excitation and exponential decay of luminescence, when excitation ceases, turns into discrete on-off blinking events (Barnes et al., 2000). Studies of luminescence of single phosphor nanoparticles offer additional opportunities for research. For example, they provided evidence of the dipole nature of electronic transitions involved in the emission of light (Bartko et al., 2002).

The luminescence spectra of nanophosphors are practically not affected by quantum confinement, as opposed to semiconductor quantum dots. Characteristic luminescence results from electron transitions inside of single impurity ions, which are strongly localized (this is especially true for rare earth ions predominantly used as activators for nanophosphors). As a result, the positions of the energy levels participating in radiative transitions hardly change even for nanophosphors with particle sizes well below 10 nm (Liu and Chen, 2007a; Ronda, 2008). This is the reason why the terms nanophosphors and quantum dots should not be used interchangeably. A sometimes reported broadening of the peaks in the spectra of emission is mostly attributed to distortions of the crystalline structure of nanoparticles (Lebbou et al., 2005; Tanner, 2005). The most pronounced changes related to quantum confinement of electronic states are reported for the peaks in the spectra of excitation of photoluminescence which involve the edges of the bandgap of the host material, such as shifts of the charge transfer bands (Shang et al., 2011).

4.4 Non-optical effects of reduced particle size

It is not only the optical properties of phosphors that are modified by the downscaling of phosphor particle size. There are several further particle size effects which can have implications for the technology of manufacturing and which indirectly influence the performance of the powder screens.

The increase of the surface-to-volume ratio affects the thermodynamics of the phase transformation. The Gibbs-Thomson effect favors crystallization of nanoparticles in high-pressure polymorphs due to additional hydrostatic pressure P (Dosev et al., 2006; Skandan et al., 1992)

$$P = \frac{4\gamma}{\phi}, \tag{93}$$

where γ is the surface energy (value of 1.5 J/m^2 is typical for many ceramic materials) and ϕ is the size of nanoparticle. More generally, it can be stated that reduction of the particle size decreases the temperature of phase transformations (Vollath, 2008). The melting points of nanoparticles are lower than those of the bulk substances (Kondepudi, 2008; Vollath, 2008). In addition, it can result in a particle size limit for the crystallization of some ceramic hosts (e.g. 8 nm for Al_2O_3, Vollath, 2008).

The contact mechanics of solid particles undergoes major changes when their size decreases. For nanoparticles, the adhesive forces can exceed other common forces by orders of magnitude. As a result, they stick firmly to any surface they contact (Hinds, 1999). Furthermore, such particles become cohesive, i.e. they tend to agglomerate with each other. For example, a clustering of nanoparticles dispersed in transparent matrices can cause a dramatic increase of light scattering (Vollath, 2008). Agglomeration and large interparticle friction forces are also responsible for the extremely low filling fraction of a random loose packing of fine and ultrafine powders (Valverde and Castellanos, 2006) as well as for low density

of compacted nanopowders (< 45% of the theoretical values) (Gonzalez and Piermarini, 2000).

The size of phosphor particles directly influences their stability in colloidal suspensions. A particle in a liquid of lower density settles with a velocity that is proportional to the square of its size (Stokes' law, Hinds, 1999). For well-dispersed nanoparticles, this velocity becomes extremely small. This has a strong impact on the technology of phosphor screens. On one hand, it renders screen deposition methods based on sedimentation, which are otherwise very popular in the manufacturing of monochromatic displays, highly impractical. On the other hand, by using colloidal methods, nanophosphors could be processed into special elaborate structures with the feature sizes on the order or below the wavelengths of incident/emitted light to gain additional functionality, e.g. to produce luminescent 3D photonic crystals with a morphology of inverse opal (Zhang et al., 2010). The technology-related issues will be reviewed in the next section.

5. Manufacturing of nanophosphor screens

5.1 Synthesis of nanophosphors

Many research groups all over the world are currently investigating different methods for the synthesis of nanophosphors. The most popular approaches have been reviewed several times (Chander, 2005; Dosev et al., 2008; Tan, 2012; Tanner, 2005; Tissue, 1998; Tissue, 2007) and are only briefly summarized here.

According to Tissue (2007), two main groups of synthesis methods can be defined. The first one includes different ways of producing nanophosphors in the gas phase, including synthesis in a vacuum, inert or reactive gas atmospheres. A source of heat for the vaporization of elements of the synthesized compounds is implied. This function can be performed by an electron beam, a laser beam, or a flame. Solid nanoparticles condense in the gas phase upon cooling. Such methods as laser-assisted gas-phase condensation (Bihari et al., 1997, Tissue, 2007), chemical vapor condensation (Konrad et al., 1999b; Schmechel et al., 2001), and flame spray pyrolysis (Laine et al., 2000; Camenzind et al., 2007; Kubrin et al., 2010; Sotiriou et al., 2011, 2012) fall under this category. Somewhat ambiguous is the assignment of pulsed laser deposition (Bär et al., 2005; Jones et al., 1997; Rajan and Gopchandran, 2009, Xu et al., 2011) and related laser ablation methods (Masenelli et al., 2013), which are sometimes included in this group of methods although they rather produce dense solid films and not nanopowders.

In the second group of synthesis methods, phosphor nanoparticles are obtained in a liquid solution. The group includes various realizations of chemical precipitation (Bazzi et al., 2004; Buissette et al., 2006; Khan et al., 2008; Lebbou et al., 2005; Mutelet et al., 2011; Wang et al., 2011), hydrothermal (Jacobsohn et al., 2007; Huang et al., 2012b; Riwotzki and Haase, 2001; Song et al., 2011; Zhang et al., 2010) or solvothermal (Gong et al., 2013; Kasuya et al., 2007; Nyman et al., 2009; Vorsthove and Kynast, 2011) synthesis, thermal (Si et al., 2006; Ye et al., 2010) or microwave (Dai et al., 2011) decomposition, sol-gel methods (Back et al., 2012; Dhanaraj et al., 2001; Eid et al., 2005; Gupta et al., 2010; Zhang et al., 2002), inverse micelle method (Barnes et al., 2000; Hirai et al., 2004), laser ablation in liquid media (Mhin et al., 2009; Singh et al., 2010), and combustion synthesis (Jacobsohn et al., 2007; Qi et al., 2002; Vu et al., 2007; Ye et al., 2009; Zhang et al., 2003), including flame-assisted spray pyrolysis, which is also capable of producing nanoparticles if the precursor solution is appropriately modified (Purwanto et al., 2008).

Chemical precipitation, sol-gel and some other methods of wet chemistry are very attractive because of simple and the relatively cheap process arrangement, but the collected products often require thermal post-treatment to improve their crystallinity and quantum efficiency. From this point of view, hydrothermal and solvothermal methods have a crucial advantage as they can facilitate the synthesis of well-dispersed crystalline nanoparticles at low temperatures (usually in the range 100–300°C). Another common shortcoming of many synthesis methods is a relatively low production rate of nanopowders. Upscaling of batchwise wet chemical processing is not always straightforward although for some methods this limitation is less pronounced. For example, sol-gel techniques are known for a high yield of the products. High production rates can be achieved with flame spray pyrolysis, where values on the order of 1 kg/h were already demonstrated (Mueller et al., 2003; Mueller et al., 2004).

As a next step towards the practical application of phosphors with decreased particle size, the optical performance of screens and coatings made of the new materials should be investigated. The choice of the screening technique is crucial because it affects both the optical and mechanical properties of phosphor coatings.

5.2 Deposition of separately produced nanophosphor powders

The simplest and most widely used method for depositing flat monochrome screens is gravitational settling (or sedimentation) of a suspension of phosphor particles in a solution containing a binder, e.g. potassium silicate buffered by barium nitrate or barium acetate (Sadowsky, 1949; Sasaki and Talbot, 1999; Tomita, 2007; Widdel, 1992). However, it is suitable only for large particles which settle fast. For particles smaller than 5 μm down to 1 μm, a centrifugal

force should be applied in order to reduce the sedimentation time and to increase the packing density. Settling could hardly be applied for nanophosphors.

Electrophoretic deposition (EPD) is often used with fine particle size phosphors (Sadowsky, 1949; Sasaki and Talbot, 1999; Sluzky and Hesse, 1989; Yum et al., 2003). In this method, the phosphor in liquid suspension (e.g. isopropyl alcohol) is attracted to an immersed electrode. Phosphor particles should be electrically charged (e.g. by the introduction of charging ions such as Mg^{2+}); the particles will then deposit onto the electrode of the opposite charge. Therefore, EPD requires a conductive substrate (e.g. ITO glass). Deposited samples are dried and baked. Smooth, dense phosphor layers with exceptional resolution and low noise can be deposited by EPD from conventional micrometer-sized phosphors, although the adhesive strength of EPD coatings is relatively weak (Yum et al., 2003). The deposition of luminescent nanoparticles by EPD and similar approaches has been reported (Lee et al., 2000; Smith et al., 2003; Wakefield et al., 2001; Zhang et al., 2006) but it does not seem to gain much popularity, which could be at least partly explained by the fact that the need for transparent and uniformly conductive substrates diminishes the attractiveness of the method for currently developing applications of nanophosphors other than field emission displays.

One of these applications (we will discuss them later in this review) is in phosphor-converted LEDs and there is ongoing research on the processing of nanophosphors by the corresponding standard manufacturing methods. Phosphor powders deposited onto UV- or blue LED chips are usually encapsulated by epoxy or silicone resins. This approach was successfully tested not only with epoxy (Nyman et al., 2009) and silicone (Revaux et al., 2011a) but also with poly(methyl methacrylate) (PMMA, Saladino et al., 2010), derivatives of ethyl methacrylate (Davion et al., 2011), poly-N-vinylpyrrolidone (PVP, Potdevin et al., 2012), and cyanoacrylate (Super Glue, Dai et al., 2011). In an interesting recent publication by Mutlugun et al. (2012), InP/ZnS quantum dots embedded in PMMA were processed into free-standing film with an area exceeding 50 cm × 50 cm. Requirements imposed on the encapsulation of nanophosphors and semiconductor quantum dot are very similar, so that the results obtained for the latter should be taken into account for the future work on nanophosphor-converted white LEDs. Furthermore, this knowledge could also be useful for X-Ray or UV-enhanced CCD image sensors, where similar strategies for the deposition of phosphor layers were proposed (Franks et al., 2000; Franks et al., 2003). Properties of the encapsulant are crucial because it may impair the quantum efficiency of the nanophosphor as discussed in Sec. 4.3. Nanophosphors should not agglomerate in the polymeric phase, which substantially limits the achievable particle volume fractions (e.g. < 20% w/w for CdSe quantum dots in 13 different polymers, Schreuder et al., 2008). Another related common problem is the photodegradation of encapsulants which lose their transparency under exposure to UV-light (Edwards et al., 2001; Koh et al., 2013, Narendran et al., 2004).

Thick layers of nanophosphors could be deposited with the well-known Doctor Blade method (Fujiwara et al., 2008) or by pressing a viscous paste between two substrates (Kasuya et al., 2007; Park et al., 2012a). The screen printing technique, in which a concentrated phosphor ink containing a liquid organic vehicle is applied to a substrate through a mesh screen and then calcinated to remove organic additives, could also be implemented for nanophopshor plasma display panels (Song et al., 2012a; Song et al., 2012b), field emission screens (Wang et al., 2011), and X-Ray imaging systems (Kim et al., 2007). Sol-gel coatings and pastes can be applied by dip-coating (Pang et al., 2003; Wu et al., 2007) or spin-coating (Bedekar et al., 2010; Buissette et al., 2006; Huang et al., 2012a; Khan et al., 2008; Klausch et al., 2012; Psuja et al., 2009; Revaux et al., 2011b; Song et al., 2011). Wet spraying, known for many decades (Sadowsky, 1949), could be adopted for the deposition of nanophosphors as well (Fleury et al., 2012; Revaux et al., 2011a).

In all the above-mentioned techniques, phosphor nanoparticles have to be dispersed in liquids and therefore obey the principles of colloidal chemistry. The composition of the solvent plays an extremely important role because it should prevent the agglomeration of nanoparticles (to ensure low scattering in the deposited screens and low viscosity of the phosphor slurry/ink/paste during processing) as well as the contamination of the screen by non-luminescent substances (residues of dispersants, surfactants, and chemical species adsorbed on the particle surface), which could decrease its quantum efficiency. Furthermore, the solvent is usually removed in the final step of deposition. Drying can cause substantial shrinkage of the phosphor layer potentially leading to the formation of cracks. For example, sol-gel coatings are especially prone to drying-induced cracks so that the crack-free deposits can be obtained only if the layer thickness does not exceed a certain critical value (typically on the order of 1 μm, Brinker and Scherer, 1990).

On the other hand, colloidal methods offer unique opportunities for processing nanophosphors such as shape-directed self-assembly (Si et al., 2006, Ye et al., 2010) and templating of colloidal crystals (Zhang et al., 2010). It also facilitates novel methods of the deposition of nanoparticles which are not applicable for conventional phosphors: layer-by-layer assembly (Camacho et al., 2012; Jang and Grunlan, 2005, Varahramyan and Lvov, 2006), Langmuir-Blodgett technique (Lu et al., 2005), and ink-jet printing (Fuller et al., 2002).

5.3 Simultaneous synthesis and deposition of nanophosphors

Not all methods of processing conventional coarse-grained phosphors require wet processing of powders. For example, in dry spraying, a fine spray of dry phosphor powder is blown from a gun onto the tacky surface (Sadowsky, 1949). This technique is hardly feasible for nanophosphors because dry nanoparticles tend to build agglomerates so that the advantages of reduced particle size could not be fully utilized even if spraying would succeed. However, premature agglomeration of ultrafine particles can be precluded by combining processes of gas-phase synthesis and film deposition in a single technology step. In such a way, all intermediate steps are excluded (i.e. dispersion in liquids is not required), and the deposition of phosphor coatings can be performed very rapidly. This approach is exploited in laser-assisted gas-phase condensation (Tissue, 2007) and electrostatic-directed deposition (Tsai et al., 2005), microwave plasma synthesis (Milewski et al., 1998) and hypersonic plasma particle deposition (Hafiz et al., 2004), as well as in flame aerosol deposition (FAD, Kubrin et al., 2010).

Flame aerosol deposition, also known as direct nanoparticle deposition (DND), is the best studied method as it was already tested for manufacturing advanced gas sensors (Kuehne et al., 2008; Mädler et al., 2006; Sahm et al., 2007), porous catalysts (Kavitha et al., 2007; Thybo et al., 2004), and battery electrodes (Chew et al., 2009), as well as for the deposition of anti-fogging films (Tricoli et al., 2009) and optical coatings (Pimenoff et al., 2006). It is also industrially applied in the fabrication of optical fiber preforms (Mendez and Morse, 2007; Tammela et al., 2006).

FAD is derived from flame spray pyrolysis and should be distinguished from other spray-based coating methods which could also be used for the deposition of phosphors but do not produce dispersed nanoparticles. One such method is spray deposition, where inorganic films are deposited by spraying solutions of appropriate reagents over a heated substrate. The chemical transformation occurs directly on the surface of the substrate. Phosphors can be deposited in this way (e.g. Y_2O_3:RE, Hao et al., 2001) but this method produces continuous films rather than powder coatings.

Flame spray pyrolysis (FSP) can be defined as a spray process where the high-temperature environment for chemical reactions is provided by heat released by a burning spray. FSP of flammable precursors should be opposed to the flame-assisted spray pyrolysis (FASP) of precursors that are not combustible themselves (e.g. aqueous solutions), and where heat is generated exclusively by an external flame. Different methods of synthesis of inorganic powders by FSP can be further classified into processes of direct droplet-to-particle conversion (DPC) and chemical vapor condensation (CVC). The droplet-to-particle conversion occurs when the precursor solute is not volatile. In such cases, the final weight of each single particle is proportional to the initial size of the droplet. The DPC usually produces submicrometer-sized particles. The CVC involves the combustion of volatile precursors which evaporate, react in the gas-phase, and condense to produce nanoparticles of the desired compounds. In the context of this review, both FSP and FAD refer to the CVC-type of particle formation. Latest reviews on the subject can be found in Pratsinis (2010); Teoh et al., (2010) and Strobel and Pratsinis (2007).

For the purposes of the deposition of particulate coatings, a substrate can be placed directly into the flame. Under certain conditions, this could result in the heterogeneous condensation of pyrolyzed compounds from the vapor-phase directly on the surface of the substrate, i.e. without producing free nanoparticles. This deposition technique, first published in 1993 (Hunt et al., 1993), is called combustion chemical vapor deposition (CCVD). It could also be used for the deposition of phosphors (e.g. Zn_2SiO_4:Mn, Kang et al., 2006) in the form of solid films. However, when the substrate is placed outside the reaction volume, airborne nanoparticles can be formed. In this way, the high temperature of the flame required to obtain particles with improved crystallinity is separated from the deposition zone. The substrate temperature can be decreased down to 150°C so that it can facilitate the direct deposition of nanopowders onto electronic chips (Tricoli et al., 2008).

FAD essentially shares the main strengths and weaknesses of FSP. On the one hand, it is exceptionally rapid and allows producing relatively thick deposits within minutes (Kubrin et al., 2010). From this point of view, FAD-deposited nanophosphor screens probably could compete with conventional phosphors even for applications which do not require optical transparency or high image resolution. On the other hand, due to the inherent limitation of all combustion synthesis methods, FAD/FSP is best suited for the production of oxides. Nevertheless, certain important non-oxide phosphors can still be obtained by appropriate post-treatment (Y_2O_2S:Er, Chen et al., 2003; Liu et al., 2002), flame pyrolysis in controlled inert atmosphere (ZnS:Mn, Athanassiou et al., 2010), or by simply using an appropriate halide source (NaYF:RE, Stepuk et al., 2013). The size of produced nanoparticles is controlled by parameters of the flame and, if needed, can be further decreased by charging them during the synthesis with a corona discharge (Vemury and Pratsinis, 1995). The deposits are extremely porous (particle volume fraction < 3 vol.%) but could be manually compacted to at least 10 vol.% without destroying the integrity of the phosphor layer (Kubrin et al., 2010). Further compaction should be possible through the elaboration of proper tech-

niques. Even for the thickness on the order of 100 μm, the deposits were fairly homogeneous and free of cracks. FAD should be considered a powerful tool for future studies on nanophosphors, and can certainly inspire research on other functional nanoparticle coatings and other methods for the rapid processing of nanopowders.

6. Applications of nanophosphor screens

Phosphor-converted white LEDs was probably the field where the advantage of low scattering of light was recognized first. Most of work here is focused on YAG:Ce nanophosphor, which converts blue light from the LED chip into yellow so that white light is obtained by color addition. Kasuya et al. (2007) demonstrated a 200-μm-thick nanophosphor film with 82% transparency at the emission wavelength. No absolute figures of conversion efficiency or quantum efficiency were reported, but the doubling of photoluminescence intensity by placing a mirror on the rear side of the sample was pointed out. In the case of conventional micrometer-sized phosphor, the use of the mirror had no appreciable effect on screen performance. Nyman et al. (2009) reported an increase of quantum efficiency of YAG:Ce nanopowder to 57% and its successful epoxy-encapsulation. The quantum yield of the phosphor was further increased to 60% by a "protected annealing" in porous silica by Revaux et al. (2011c). The same group investigated the incorporation of nanophosphors into a TiO_2 sol-gel coating in order to match the refractive index and thus further decrease scattering (Revaux et al., 2011a; Revaux et al., 2011b). A systematic comparison of the performance of pc-LEDs incorporating YAG:Ce with the morphology of a nanophosphor, thin-film phosphor, ceramic plate and micrometer-sized powder was performed by Park et al. (2012a), also including a 2D photonic crystal layer for improving the extraction efficiency and short-wave pass filters for recovering the light emitted backwards. Nanophosphor-based LEDs showed a conversion efficiency of 31%, packaging efficiency of 82%, and luminous efficacy of 40.2 lm/W, not much worse than that of the ceramic plate or conventional phosphor powder and outperforming the thin-film phosphor. Recently, a luminosity of 100 lm/W was obtained with ligand-passivated Y_2O_3:Eu nanophosphor (Dai et al., 2011) discussed in Sec 4.3. This performance is competitive with current commercial products.

The optical transparency of nanophosphor layers was crucial in the development of transparent plasma display devices (PDD) first published in 2010 by the group of H. Yang at the Hongik University, Seoul, Korea (Song et al., 2010). Initially starting with monochrome green-emitting nanophosphor $LaPO_4$:Ce,Tb, they reached a luminance of 97 cd/m^2 (Song et al., 2011). The transparency of the phosphor layer in the wavelength range of emission exceeded 90% and that of the fully assembled test devices was at least 40%. The work on red-emitting $Y(V,P)O_4$:Eu followed soon after (Song et al., 2012b) and finally, the full-color PDDs based on $LaPO_4$:Ce,Tb, $Y(V,P)O_4$:Eu, and blue-emitting $Y(V,P)O_4$:Tm were reported (Song et al., 2012a). The phosphors were deposited by means of screen printing and combined by line patterning. The brightness of white emission was 96 cd/m^2 and could be increased to 137 cd/m^2 by the application of a 2D photonic crystal (a monolayer of ordered polystyrene microspheres of a uniform size). Transparency could be held on the level of 30%.

The advantageous properties of nanophosphors for field emission displays (FED) were demonstrated more than a decade ago (Lee et al., 2000; Wakefield et al., 2001). In this case, however, the main benefit was the increased phosphor efficiency attributed to the improved crystallinity and surface microstructure, not the decreased scattering. New works on nanophosphors for low-voltage cathodoluminescence have occasionally been published since then (Chang et al., 2010; Shang et al., 2012; Wang et al., 2011).

There were a few reports on the application of nanophosphors for X-ray imaging (Cha et al., 2011; Kalyvas et al., 2012; Kim et al., 2007), but none of them clearly addressed the effects of phosphor particle size. A comprehensive theoretical treatment applying the Mie scattering theory and Monte Carlo simulations showed that the best imaging performance should be expected from scintillator powders with a particle size greater than 200 nm (Liaparinos, 2012). It should be concluded that there is no advantage of utilizing nanophosphor screens for conventional digital radiography with a resolution lower than 20 lp/mm. This does not apply to X-ray microtomography and other imaging applications with submicrometer resolution (discussed in Sec. 2.4.), because nanophosphors have a great potential in this area.

Another promising application of nanophosphor screens is in the technology of solar cells, which absorb electromagnetic radiation and convert it into electricity. The efficiency of this process cannot exceed a so-called Shockley-Queisser limit (usually about 30%) unless they are enhanced by appropriate spectral converters (SC, Richards, 2006; van der Ende et al., 2009). Downshifting (conventional photoluminescence) and downconverting (quantum-cutting luminescence) SCs absorb high-energy photons and convert them to photons of wavelengths more efficiently absorbed by the corresponding solar cells. Such coatings are placed in front of the cell and ideally they should not interfere with light which does not need to be converted. Obviously, transparency of the converter layer is strongly desired so that nanophosphor coatings should be preferred over conventional phosphors (Huang et al., 2012a; Khan et al., 2008; Peng et al., 2011; Takeshita et

al., 2009). Upconverting SCs perform a complimentary function of absorbing low-energy photons, for which the solar cell itself is transparent, and convert to photons of shorter wavelength so that they could also be absorbed by the solar cell. Upconverters are usually mounted on the rear side of the cell and can be processed from phosphor nanoparticles as well (Chen et al., 2012). It was predicted that the Shockley-Queisser limit for the efficiency of a single junction solar cell can be raised to 40% (using downconversion) or even 50% (using upconversion, van der Ende et al., 2009).

One more potential application of nanophosphors which relies on the transparency of powder coatings is in flat dielectric discharge lamps published recently (Klausch et al., 2012). A nanophosphor layer of YVO_4:Eu with > 90% transmittance in the visible range was tested as a prototype of a light-emitting window.

The luminescent properties of nanophosphors are affected by environmental conditions. For example, the intensity and decay time of luminescence or ratio of intensities of certain peaks in the spectra may substantially change for different ambient temperatures. Such effects further extend the list of possible applications of nanophosphor coatings, e.g. by scanning nanothermometry (Jaque and Vetrone, 2012). The options here are almost unlimited: if a high sensitivity in the physiological range is required, one can use upconverting nanoparticles (Fischer et al., 2011). In the range of extreme temperatures, nanoparticles of refractory phosphors could probably be applied even above 1000°C because the emission of bulk thermographic phosphors such as YAG:Dy can be measured up to 1700°C (Chambers and Clarke, 2009). The resolution of nanothermometry is approaching the size of the single nanoparticle and allows the temperature inside the living cells to be measured (Vetrone et al., 2010). The small size of nanoparticles facilitates numerous further ways of their utilization in biomedical imaging as fluorescent labels (Dosev et al., 2008), but these methods do not involve phosphor screens and thus will not be further discussed here.

7. Conclusions

In this review, we try to present the advantages of phosphor nanopowders for applications where continuous phosphor layers—screens—are used. The basic optics of phosphor screens is treated in detail so that the influence of particle size on the screen performance can be comprehensively explained. We discuss various further effects of particle size which modify the quantum efficiency of luminescent devices and have implications for the manufacturing technology. The most popular methods of deposition and suggested applications of phosphor screens/coatings are analyzed. Here, we summarize the main outcomes.

First of all, nanoparticles barely scatter light. This means that even relatively thick coatings can be virtually transparent and thus, nanophosphors are preferred for application as spectral converters in photovoltaics, and could potentially be applied in “augmented reality” displays including, e.g. contact lens displays (Lingley et al., 2011). Vanishingly weak scattering leads also to a dramatic qualitative change in the shape of the thickness dependence curves for the brightness of phosphor screens. Nanophosphor layers behave similarly to non-scattering screens (e.g. single crystalline films). It can be expected that their T-mode performance will only weakly depend on the thickness, both in terms of brightness and resolution, especially when excited by strongly absorbed radiation. Ideally, the excitation energy should be absorbed within some 200 nm from the exposed surface of the screen so that the emitting volume corresponding to a single image point could be kept smaller than the limit of diffraction. If emitted light was not scattered, the perfect image point could be observed from any direction, thus approaching the diffraction-limited image resolution, irrespective of the total screen thickness. For X-ray applications or other weakly absorbed radiation, the full thickness of the diffraction-limited nanophosphot screen would have to be kept below 200 nm.

The quantum efficiency of nanophosphors is usually lower than that of the corresponding bulk materials. This is explained to a large extent by the increased surface-to-volume ratio of the nanoparticles, which promotes the surface quenching effects. However, it is possible to turn this drawback into an advantage, e.g. by improving the efficiency of excitation of photoluminescence through appropriate functionalization of the particle surface with organic ligands. The same approach would not work with conventional coarse-grained phosphors.

A thorough characterization of the quantum efficiency of the luminescence lifetime of nanophosphors requires special care regarding the porosity of the deposits and refractive index of the medium filling the pores, because the observed luminescent properties are strongly affected by the effective refractive index of the surroundings of emitting ions. For example, compaction of the nanophosphor layer leads to improvement of the quantum efficiency as well as shortening of the emission decay time.

Nanophosphors offer special opportunities for processing the screens as their small particle size can facilitate untypical deposition methods such as self-assembly, templating of colloidal crystals, and ink-jet printing. Due to their cohesive nature, they could also be directly attached to a substrate in a very rapid process of flame aerosol deposition without using any adhesive or a binder. Moreover, we observed that the nanophosphor coating itself can act as an adhesive when we investigated compaction of the deposits between two substrates.

Continuous progress in the technology of nanophosphors will surely stimulate development of numerous new imaging applications. There is still 'plenty of room' spanning all possible excitation sources and all conceivable dimensions of the nanophosphor screens—starting from single nanoparticles excited by X-rays, as in recently published X-ray luminescence computed tomography (Cong et al., 2011; Carpenter et al., 2012), and ending with macroscopic volumes excited by infrared radiation, as in solid-state 3D displays (Downing et al., 1996).

References

Athanassiou E.K., Grass R.N., Stark W.J., One-step large scale gas phase synthesis of Mn^{2+} doped ZnS nanoparticles in reducing flames, Nanotechnology, 21 (2010) 215603.

Auger J.-C., Martinez V., Stout B., Theoretical study of the scattering efficiency of rutile titanium dioxide pigments as a function of their spatial dispersion, J. Coat. Technol. Res., 6 (2009) 89–97.

Baciero A., Placentino L., McCarthy K.J., Barquero L.R., Ibarra A., Zurro B., Vacuum ultraviolet and x-ray luminescence efficiencies of $Y_3Al_5O_{12}$:Ce phosphor screens, J. Appl. Phys., 85 (1999) 6790–6796.

Back M., Massari A., Boffelli M., Gonella F., Riello P., Cristofori D., Riccò R., Enrichi F., Optical investigation of Tb^{3+}-doped Y_2O_3 nanocrystals prepared by Pechini-type sol-gel process, J. Nanopart. Res., 14 (2012) 1–10.

Badano A., Optical blur and collection efficiency in columnar phosphors for X-ray imaging, Nucl. Instr. Meth. Phys. Res. A, 508 (2003) 467–479.

Bär S., Huber G., Gonzalo J., Perea A., Munz M., Pulsed laser deposition of Eu:Y_2O_3 thin films on (0001) a-Al_2O_3, Appl. Phys. A, 80 (2005) 209–216.

Barnes M.D., Mehta A., Thundat T., Bhargava R.N., Chhabra V., Kulkarni B., On−Off Blinking and Multiple Bright States of Single Europium Ions in Eu^{3+}:Y_2O_3 Nanocrystals, J. Phys. Chem. B, 104 (2000) 6099–6102.

Bartko A.P., Peyser L.A., Dickson R.M., Mehta A., Thundat T., Bhargava R., Barnes M.D., Observation of dipolar emission patterns from isolated Eu^{3+}:Y_2O_3 doped nanocrystals: new evidence for single ion luminescence, Chem. Phys. Lett., 358 (2002) 459–465.

Bazzi R., Flores M.A., Louis C., Lebbou K., Zhang W., Dujardin C., Roux S., Mercier B., Ledoux G., Bernstein E., Perriat P., Tillement O., Synthesis and properties of europium-based phosphors on the nanometer scale: Eu_2O_3, Gd_2O_3:Eu, and Y_2O_3:Eu, J. Colloid Interface Sci., 273 (2004) 191–197.

Bedekar V., Dutta D.P., Tyagi A.K., White Light Emission from Spin Coated Gd_2O_3:Dy Nano Phosphors Synthesized Using Polyol Technique, J. Nanosci. Nanotechnol., 10 (2010) 8234–8238.

Bera D., Qian L., Tseng T.-K., Holloway P.H., Quantum Dots and Their Multimodal Applications: A Review, Materials, 3 (2010) 2260–2345.

Berberan-Santos M.N., Bodunov E.N., Valeur B., Mathematical functions for the analysis of luminescence decays with underlying distributions 1. Kohlrausch decay function (stretched exponential), Chem. Phys., 315 (2005) 171–182.

Bihari B., Eilers H., Tissue B.M., Spectra and dynamics of monoclinic Eu_2O_3 and Eu^{3+}:Y_2O_3 nanocrystals, J. Lumin., 75 (1997) 1–10.

Bogdan N., Vetrone F., Ozin G.A., Capobianco J.A., Synthesis of Ligand-Free Colloidally Stable Water Dispersible Brightly Luminescent Lanthanide-Doped Upconverting Nanoparticles, Nano Lett., 11 (2011) 835–840.

Bohren C.F., Huffman D.R., Absorption and scattering of light by small particles, Wiley-VCH, Weinheim, 2004.

Borbely A., Johnson S.G., Performance of phosphor-coated light-emitting diode optics in ray-trace simulations, Opt. Eng., 44 (2005) 111308.

Brewster Q., Volume Scattering of Radiation in Packed Beds of Large, Opaque Spheres, J. Heat Transfer, 126 (2004) 1048–1050.

Brinker C.J., Scherer G.W., Sol-gel science. The physics and chemistry of sol-gel processing, Academic Press, Boston [etc.], 1990.

Buissette V., Giaume D., Gacoin T., Boilot J.-P., Aqueous routes to lanthanide-doped oxide nanophosphors, J. Mater. Chem, 16 (2006) 529–539.

Busselt W., Raue R., Optimizing the Optical Properties of TV Phosphor Screens, J. Electrochem. Soc., 135 (1988) 764–771.

Butler K.H., Fluorescent Lamp Phosphors. Technology and theory. Pennsylvania State Univ. Pr., University Park, 1980.

Buxbaum G., Industrial inorganic pigments, 3rd ed. Wiley-VCH, Weinheim, 2005.

Camacho S.A., Aoki P.H.B., Constantino C.J.L., Aroca R.F., Pires A.M., Nanostructured hybrid films containing nanophosphor: Fabrication and electronic spectral properties, J. Alloy Comp., 541 (2012) 365–371.

Camenzind A., Strobel R., Krumeich F., Pratsinis S.E., Luminescence and crystallinity of flame-made Y_2O_3:Eu^{3+} nanoparticles, Adv. Powder Technol., 18 (2007) 5–22.

Carpenter C.M., Sun C., Pratx G., Liu H., Cheng Z., Xing L., Radioluminescent nanophosphors enable multiplexed small-animal imaging, Opt. Express, 20 (2012) 11598–11604.

Cha B.K., Lee S.J., Muralidharan P., Kim J.Y., Kim D.K., Cho G., Characterization and imaging performance of nanoscintillator screen for high resolution X-ray imaging detectors, Nucl. Instr. Meth. Phys. Res. A, 633, Supplement 1 (2011) S294.

Chambers M., Clarke D., Doped Oxides for High-Temperature Luminescence and Lifetime Thermometry, Annu. Rev. Mater. Res., 39 (2009) 325–359.

Chander H., Development of nanophosphors—A review, Mater. Sci. Eng. R, 49 (2005) 113–155.

Chang C.C., Chern R.-L., Chang C.C., Chu C.-C., Chi J.Y., Su J.-C., Chan I.-M., Wang J.-F.T., Monte Carlo Simulation of Optical Properties of Phosphor-Screened Ultraviolet Light in a White Light-Emitting Device, Jpn. J. Appl. Phys., 44

(2005) 6056.
Chang H.-Y., Lee H.-D., Wu M.-L., Lin L.-J., Highly efficient cathodoluminescence of nanophosphors by solvothermal route, J. Lumin., 130 (2010) 969–975.
Chen R., Apparent stretched-exponential luminescence decay in crystalline solids, J. Lumin., 102-103 (2003) 510–518.
Chen S., Zhou G., Su F., Zhang H., Wang L., Wu M., Chen M., Pan L., Wang S., Power conversion efficiency enhancement in silicon solar cell from solution processed transparent upconversion film, Mater. Lett., 77 (2012) 17–20.
Chen X.Y., Zhuang H.Z., Liu G.K., Li S., Niedbala R.S., Confinement on energy transfer between luminescent centers in nanocrystals, J. Appl. Phys., 94 (2003) 5559–5565.
Chew S.Y., Patey T.J., Waser O., Ng S.H., Büchel R., Tricoli A., Krumeich F., Wang J., Liu H.K., Pratsinis S.E., Novák P., Thin nanostructured $LiMn_2O_4$ films by flame spray deposition and in situ annealing method, J. Power Sources, 189 (2009) 449–453.
Cong W., Shen H., Wang G., Spectrally resolving and scattering-compensated x-ray luminescence/fluorescence computed tomography, J. Biomed. Opt., 16 (2011) 66014.
Dai Q., Foley M.E., Breshike C.J., Lita A., Strouse G.F., Ligand-Passivated Eu:Y_2O_3 Nanocrystals as a Phosphor for White Light Emitting Diodes, J. Amer. Chem. Soc., 133 (2011) 15475–15486.
Davion B., Delhorbe V., Peralta S., Goubard F., Vidal F., Dispersion of Luminescent Nanoparticles in Different Derivatives of Poly(ethyl methacrylate), J. Nanosci. Nanotechnology, 11 (2011) 3208–3214.
Dhanaraj J., Jagannathan R., Kutty T.R.N., Lu C.-H., Photoluminescence Characteristics of Y_2O_3:Eu^{3+} Nanophosphors Prepared Using Sol-Gel Thermolysis, J. Phys. Chem. B, 105 (2001) 11098–11105.
Dick V.P., Applicability Limits of Beer's Law for Dispersion Media with a High Concentration of Particles, Appl. Opt., 37 (1998) 4998–5004.
Donofrio R.L., Rehkopf C.H., Screen Weight Optimization, J. Electrochem. Soc., 126 (1979) 1563–1567.
Dosev D., Guo B., Kennedy I.M., Photoluminescence of Eu^{3+}:Y_2O_3 as an indication of crystal structure and particle size in nanoparticles synthesized by flame spray pyrolysis, J. Aerosol Sci., 37 (2006) 402–412.
Dosev D., Nichkova M., Kennedy I.M., Inorganic Lanthanide Nanophosphors in Biotechnology, J. Nanosci. Nanotechnol., 8 (2008) 1052–1067.
Downing E., Hesselink L., Ralston J., Macfarlane R., A Three-Color, Solid-State, Three-Dimensional Display, Science, 273 (1996) 1185–1189.
Edwards M., Zhou Y., Wyrowski F., Comparative properties of optically clear epoxy encapsulants, Proc. SPIE, 4436 (2001) 190–197.
Eid J., Pierre A.C., Baret G., Preparation and characterization of transparent Eu doped Y_2O_3 aerogel monoliths, for application in luminescence, J. Non-Cryst. Solids, 351 (2005) 218–227.
Evanko D., Primer: fluorescence imaging under the diffraction limit, Nat. Meth., 6 (2009) 19–20.
Faruqi A.R., Andrews H.N., Henderson R., A high sensitivity imaging detector for electron microscopy. Nucl. Instr. Meth. Phys. Res. A, 367 (1995) 408–412.
Fischer L.H., Harms G.S., Wolfbeis O.S., Upconverting Nanoparticles for Nanoscale Thermometry, Angew. Chem. Int. Ed., 50 (2011) 4546–4551.
Flannery B.P., Deckman H.W., Roberge W.G., D'Amico K.L., Three-Dimensional X-ray Microtomography, Science, 237 (1987) 1439–1444.
Fleury B., Dantelle G., Darbe S., Boilot J.P., Gacoin T., Transparent Coatings Made from Spray Deposited Colloidal Suspensions, Langmuir, 28 (2012) 7639–7645.
Fonger W.H., Two-constant models of luminescence in particle layers. 1: The p-layer model, Appl. Opt., 21 (1982a) 1219–1221.
Fonger W.H., Two-constant models of luminescence in particle layers. 2: The layer luminescence, Appl. Opt., 21 (1982b) 1222–1227.
Fran Y.S., Tseng T.Y., Involvement of scattered UV light in the generation of photoluminescence in powdered phosphor screens, J. Phys. D, 32 (1999) 513.
Franks W.A.R., Kiik M.J., Nathan A., Blouke M.M., Sampat N., Williams G.M., Jr., Yeh T., Inorganic phosphor coatings for UV-responsive CCD image sensors, Proc. SPIE, 3965 (2000) 33–41.
Franks W.A.R., Kiik M.J., Nathan A., UV-responsive CCD image sensors with enhanced inorganic phosphor coatings, IEEE Trans. Electron Dev., 50 (2003) 352–358.
Fujii T., Gao Y., Sharma R., Hu E.L., DenBaars S.P., Nakamura S., Increase in the extraction efficiency of GaN-based light-emitting diodes via surface roughening, Appl. Phys. Lett., 84 (2004) 855–857.
Fujiwara R., Sano H., Harada S., Shimizu M., Takebe H., Kuwabara M., Fabrication of Electroluminescent Devices Using Nanocrystalline Oxide Phosphors, Key Eng. Mater., 388 (2008) 123–126.
Fuller S.B., Wilhelm E.J., Jacobson J.M., Ink-jet printed nanoparticle microelectromechanical systems, IEEE ASME J. Microelectromech. Syst., 11 (2002) 54–60.
Gaponik N., Hickey S.G., Dorfs D., Rogach A.L., Eychmüller A., Progress in the Light Emission of Colloidal Semiconductor Nanocrystals, Small, 6 (2010) 1364–1378.
Geszke-Moritz M., Moritz M., Quantum dots as versatile probes in medical sciences: Synthesis, modification and properties, Mater. Sci. Eng. C, 33 (2013) 1008–1021.
Gnach A., Bednarkiewicz A., Lanthanide-doped up-converting nanoparticles: Merits and challenges, Nano Today, 7 (2012) 532–563.
Gong L., Ma M., Xu C., Li X., Wang S., Lin J., Yang Q., Multicolor upconversion emission of dispersed ultrasmall cubic Sr_2LuF_7 nanocrystals synthesized by a solvothermal process, J. Lumin., 134 (2013) 718–723.
Gonzalez E.J., Piermarini G.J., Low-Temperature Compaction of Nanosize Powder. in: Nalwa, H.S. (Ed.), Handbook of nanostructured materials and nanotechnology, 1 (Synthesis and Processing), Acad. Press, San Diego, Calif., 2000, pp. 215–249.
Grossman M.W., Effect of radiation transport on the kinetics of phosphor degradation, J. Appl. Phys., 84 (1998) 1251–1262.
Gruner S.M., Tate M.W., Eikenberry E.F., Charge-coupled

device area x-ray detectors, Rev. Sci. Instrum., 73 (2002) 2815–2842.

Gupta B.K., Haranath D., Saini S., Singh V.N., Shanker V., Synthesis and characterization of ultra-fine Y_2O_3: Eu^{3+} nanophosphors for luminescent security ink applications, Nanotechnology, 21 (2010) 5607.

Hafiz J., Wang X., Mukherjee R., Mook W., Perrey C.R., Deneen J., Heberlein J.V.R., McMurry P.H., Gerberich W.W., Carter C.B., Girshick S.L., Hypersonic plasma particle deposition of Si-Ti-N nanostructured coatings, Surf. Coat. Technol., 188-189 (2004) 364–370.

Hao J., Studenikin S.A., Cocivera M., Blue, green and red cathodoluminescence of Y_2O_3 phosphor films prepared by spray pyrolysis, J. Lumin., 93 (2001) 313–319.

Henderson B., Imbusch G.F., Optical spectroscopy of inorganic solids, Oxford science publications, Clarendon Press, Oxford, 1989.

Hinds W.C., Aerosol technology. Properties, behavior, and measurement of airborne particles, 2nd ed., Wiley, New York, 1999.

Hirai T., Asada Y., Komasawa I., Preparation of Y_2O_3:Eu^{3+} nanoparticles in reverse micellar systems and their photoluminescence properties, J. Colloid Interface Sci., 276 (2004) 339–345.

Hottel H.C., Dalzell W.H., Sarofim A.F., Vasalos I.A., Optical Properties of Coatings. Effect of Pigment Concentration, AIAA J., 9 (1971) 1895–1898.

Huang C.K., Chen Y.C., Hung W.B., Chen T.M., Sun K.W., Chang W.-L., Enhanced light harvesting of Si solar cells via luminescent down-shifting using YVO_4:Bi^{3+}, Eu^{3+} nanophosphors, Prog. Photovolt: Res. Appl. (2012a), DOI: 10.1002/pip.2222.

Huang H., Zhang H., Zhang W., Lian S., Kang Z., Liu Y., Ultra-small sized Y_2O_3:Eu^{3+} nanocrystals: One-step polyoxometalate-assisted synthesis and their photoluminescence properties, J. Lumin., 132 (2012b) 2155–2160.

Huang X., Han S., Huang W., Liu X., Enhancing solar cell efficiency: the search for luminescent materials as spectral converters, Chem. Soc. Rev., 42 (2013) 173–201.

Hunt A.T., Carter W.B., Cochran J.K., Jr., Combustion chemical vapor deposition: A novel thin-film deposition technique, Appl. Phys. Lett., 63 (1993) 266–268.

Igarashi T., Ihara M., Kusunoki T., Ohno K., Isobe T., Senna M., Relationship between optical properties and crystallinity of nanometer Y_2O_3:Eu phosphor, Appl. Phys. Lett., 76 (2000) 1549–1551.

Ishida K., Mitsuishi I., Hattori Y., Nunoue S., A revised Kubelka—Munk theory for spectral simulation of phosphor-based white light-emitting diodes, Appl. Phys. Lett., 93 (2008) 241910–241913.

Jacobsohn L.G., Bennett B.L., Muenchausen R.E., Smith J.F., Wayne Cooke D., Luminescent properties of nanophosphors, Rad. Meas., 42 (2007) 675–678.

Jang W.-S., Grunlan J.C., Robotic dipping system for layer-by-layer assembly of multifunctional thin films, Rev. Sci. Instrum., 76 (2005) 103904.

Jaque D., Vetrone F., Luminescence nanothermometry, Nanoscale, 4 (2012) 4301–4326.

Jeon B.S., Hong K.Y., Yoo J.S., Whang K.-W., Studies on the Phosphor Screen Prepared by Electrophoretic Deposition for Plasma Display Panel Applications, J. Electrochem. Soc., 147 (2000) 4356–4362.

Jianbo C., Wenbin C., Kaiyu Y., High luminance YAG single crystal phosphor screen, Displays, 21 (2000) 195–198.

Jones S.L., Kumar D., Singh R.K., Holloway P.H., Luminescence of pulsed laser deposited Eu doped yttrium oxide films, Appl. Phys. Lett., 71 (1997) 404–406.

Jüstel T., Nikol H., Ronda C., New Developments in the Field of Luminescent Materials for Lighting and Displays, Angew. Chem. Int. Ed., 37 (1998) 3084–3103.

Kalyvas N., Liaparinos P., Michail C., David S., Fountos G., Wójtowicz M., Zych E., Kandarakis I., Studying the luminescence efficiency of Lu_2O_3:Eu nanophosphor material for digital X-ray imaging applications, Appl. Phys. A, 106 (2012) 131-136.

Kamiuto K., Near-field scattering by a small spherical particle embedded in a nonabsorbing medium, J. Opt. Soc. Am. A, 1 (1984) 840–844.

Kandarakis I., Cavouras D., Panayiotakis G., Agelis T., Nomicos C., Giakoumakis G., X-ray induced luminescence and spatial resolution of phosphor screens, Phys. Med. Biol., 41 (1996) 297–307.

Kang Z.T., Liu Y., Wagner B.K., Gilstrap R., Liu M., Summers C.J., Luminescence properties of Mn^{2+} doped Zn_2SiO_4 phosphor films synthesized by combustion CVD, J. Lumin., 121 (2006) 595–600.

Kasuya R., Kawano A., Isobe T., Kuma H., Katano J., Characteristic optical properties of transparent color conversion film prepared from YAG:Ce^{3+} nanoparticles, Appl. Phys. Lett., 91 (2007) 111916.

Kavitha R., Meghani S., Jayaram V., Synthesis of titania films by combustion flame spray pyrolysis technique and its characterization for photocatalysis, Mater. Sci. Eng. B, 139 (2007) 134–140.

Khan A.F., Haranath D., Yadav R., Singh S., Chawla S., Dutta V., Controlled surface distribution and luminescence of YVO_4:Eu^{3+} nanophosphor layers, Appl. Phys. Lett., 93 (2008) 073103-3.

Kim S.-y., Park J.-k., Kang S.-s., Cha B.-y., Cho S.-h., Shin J.-w., Son D.-w., Nam S.-h., Investigation of the imaging characteristics of the Gd_2O_3:Eu nanophosphor for high-resolution digital X-ray imaging system, Nucl. Instr. Meth. Phys. Res. A, 576 (2007) 70–74.

Klausch A., Althues H., Freudenberg T., Kaskel S., Wet chemical preparation of YVO_4:Eu thin films as red-emitting phosphor layers for fully transparent flat dielectric discharge lamp, Thin Solid Films, 520 (2012) 4297–4301.

Klein L.C., Sol-gel technology for thin films, fibers, preforms, electronics and specialty shapes, 4th ed., Materials science and process technology series, Noyes Publ., Park Ridge, N.J., 1988.

Koch A., Raven C., Spanne P., Snigirev A., X-ray imaging with submicrometer resolution employing transparent luminescent screens, J. Opt. Soc. Am. A, 15 (1998) 1940–1951.

Koh S., Driel W.D., Yuan C.A., Zhang G.Q., Degradation Mechanisms in LED Packages, in: van Driel, W., Fan, X. (Eds.),

Solid State Lighting Reliability, vol. 1, Springer New York, 2013, pp. 185–205.

Koleske J.V., Paint and coating testing manual, 14th ed., ASTM, Philadelphia, PA, 1995.

Kömpe K., Borchert H., Storz J., Lobo A., Adam S., Möller T., Haase M., Green-Emitting $CePO_4$:Tb/$LaPO_4$ Core-Shell Nanoparticles with 70% Photoluminescence Quantum Yield, Angew. Chem. Int. Ed., 42 (2003) 5513–5516.

Kondepudi D., Introduction to modern thermodynamics, Wiley, Chichester, 2008.

Konrad A., Almanstotter J., Reichardt J., Gahn A., Tidecks R., Samwer K., Modeling the optical properties of fluorescent powders: $Y_{1.91}Eu_{0.09}O_3$, J. Appl. Phys., 85 (1999a) 1796–1801.

Konrad A., Fries T., Gahn A., Kummer F., Herr U., Tidecks R., Samwer K., Chemical vapor synthesis and luminescence properties of nanocrystalline cubic Y_2O_3:Eu, J. Appl. Phys., 86 (1999b) 3129–3133.

Kortüm G., Braun W., Herzog G., Prinzip und Meßmethodik der diffusen Reflexionsspektroskopie, Angew. Chem., 75 (1963) 653–661.

Krames M.R., Shchekin O.B., Mueller-Mach R., Mueller G., Zhou L., Harbers G., Craford M.G., Status and Future of High-Power Light-Emitting Diodes for Solid-State Lighting, J. Display Technol., 3 (2007) 160–175.

Kubrin R., Bauhofer W., Ivankov A., No-Binder Screening of Fine Phosphor Powders by Flame Spray Pyrolysis, J. Electrochem. Soc., 154 (2007) J253-J261.

Kubrin R., Tricoli A., Camenzind A., Pratsinis S.E., Bauhofer W., Flame aerosol deposition of Y_2O_3:Eu nanophosphor screens and their photoluminescent performance, Nanotechnology, 21 (2010) 225603.

Kubrin R., Deposition of advanced phosphor coatings by flame spray pyrolysis. Cuvellier, Goettingen, 2012.

Kuehne S., Graf M., Tricoli A., Mayer F., Pratsinis S.E., Hierlemann A., Wafer-level flame-spray-pyrolysis deposition of gas-sensitive layers on microsensors, J. Micromech. Microeng., 18 (2008) 35040.

Kumar S., Tien C.L., Dependent Absorption and Extinction of Radiation by Small Particles, J. Heat Transfer, 112 (1990) 178–185.

Kuntz J.D., Roberts J.J., Hough M., Cherepy N.J., Multiple synthesis routes to transparent ceramic lutetium aluminum garnet, Scr. Mater., 57 (2007) 960–963.

Laine R.M., Hinklin T., Williams G., Rand S.C., Low-Cost Nanopowders for Phosphor and Laser Applications by Flame Spray Pyrolysis, Mater. Sci. Forum, 343–346 (2000) 500–510.

Lebbou K., Perriat P., Tillement O., Recent Progress on Elaboration of Undoped and Doped Y_2O_3, Gd_2O_3 Rare-Earth Nano-Oxide, J. Nanosci. Nanotechnol., 5 (2005) 1448–1454.

Lee M.H., Oh S.G., Yi S.C., Seo D.S., Hong J.P., Kim C.O., Yoo Y.K., Yoo J.S., Characterization of Eu‐Doped Y_2O_3 Nanoparticles Prepared in Nonionic Reverse Microemulsions in Relation to Their Application for Field Emission Display, J. Electrochem. Soc., 147 (2000) 3139–3142.

Li C., Kattawar G., Zhai P.-W., Yang P., Electric and magnetic energy density distributions inside and outside dielectric particles illuminated by a plane electromagnetic wave, Opt. Express, 13 (2005) 4554–4559.

Liaparinos P.F., Kandarakis I.S., Cavouras D.A., Delis H.B., Panayiotakis G.S., Modeling granular phosphor screens by Monte Carlo methods, Med. Phys., 33 (2006) 4502–4514.

Liaparinos P.F., Optical diffusion performance of nanophosphor-based materials for use in medical imaging, J. Biomed. Opt., 17 (2012) 126013.

Lingley A.R., Ali M., Liao Y., Mirjalili R., Klonner M., Sopanen M., Suihkonen S., Shen T., Otis B.P., Lipsanen H., A single-pixel wireless contact lens display, J. Micromech. Microeng., 21 (2011) 125014.

Liu G.K., Zhuang H.Z., Chen X.Y., Restricted Phonon Relaxation and Anomalous Thermalization of Rare Earth Ions in Nanocrystals, Nano Lett., 2 (2002) 535–539.

Liu L., Gong R., Huang D., Nie Y., Liu C., Calculation of emittance of a coating layer with the Kubelka-Munk theory and the Mie-scattering model, J. Opt. Soc. Am. A, 22 (2005) 2424–2429.

Liu G., Chen X., Spectroscopic Properties of Lanthanides in Nanomaterials, in: Gschneidner K.A., Bünzli J.-C., Pecharsky V.K. (Eds.), Handbook on the Physics and Chemistry of Rare Earths, 1 ed., Elsevier, Amsterdam, 2007a, pp. 99–169.

Liu L., Chen X., Energy levels, fluorescence lifetime and Judd-Ofelt parameters of Eu^{3+} in Gd_2O_3 nanocrystals, Nanotechnology, 18 (2007b) 255704.

Liu S.-M., Chen W., Wang Z.-G., Luminescence Nanocrystals for Solar Cell Enhancement, J. Nanosci. Nanotechnol., 10 (2010) 1418–1429.

Lu Y., Liu G.L., Lee L.P., High-Density Silver Nanoparticle Film with Temperature-Controllable Interparticle Spacing for a Tunable Surface Enhanced Raman Scattering Substrate, Nano Lett., 5 (2005) 5–9.

Mädler L., Roessler A., Pratsinis S.E., Sahm T., Gurlo A., Barsan N., Weimar U., Direct formation of highly porous gas-sensing films by in situ thermophoretic deposition of flame-made Pt/SnO_2 nanoparticles, Sens. Actuator. B, 114 (2006) 283–295.

Martin J.E., Shea-Rohwer L.E., Lifetime determination of materials that exhibit a stretched exponential luminescent decay, J. Lumin., 121 (2006) 573–587.

Martin T., Koch A., Recent developments in X-ray imaging with micrometer spatial resolution, J. Synchrotron Rad., 13 (2006) 180–194.

Martin T., Douissard P.-A., Seeley Z., Cherepy N., Payne S., Mathieu E., Schuladen J., New High Stopping Power Thin Scintillators Based on Lu_2O_3 and $Lu_3Ga_{5-x}In_xO_{12}$ for High Resolution X-ray Imaging, IEEE Trans. Nucl. Sci., 59 (2012) 2269–2274.

Masenelli B., Mollet O., Boisron O., Canut B., Ledoux G., Bluet J.-M., Melinon P., Dujardin C., Huant S., YAG:Ce nanoparticle lightsources, Nanotechnology, 24 (2013) 165703

McNeil L.E., Hanuska A.R., French R.H., Orientation dependence in near-field scattering from TiO_2 particles, Appl. Opt., 40 (2001) 3726–3736.

Meltzer R.S., Feofilov S.P., Tissue B., Yuan H.B., Dependence

of fluorescence lifetimes of Y_2O_3:Eu^{3+} nanoparticles on the surrounding medium, Phys. Rev. B, 60 (1999) R14012.

Meltzer R.S., Quantum-cutting phosphors. Phosphors for lamps, in: Yen W.M., Shionoya S., Yamamoto H. (Eds.), Phosphor handbook, 2 ed., CRC Press, Boca Raton, Fla., 2007, pp. 507–531.

Mendes M.J., Tobías I., Martí A., Luque A., Near-field scattering by dielectric spheroidal particles with sizes on the order of the illuminating wavelength, J. Opt. Soc. Am. B, 27 (2010) 1221–1231.

Mendez A., Morse T.F., Specialty optical fibers handbook, Elsevier/Academic Press, Amsterdam, 2007.

Mhin S., Ryu J., Kim K., Park G., Ryu H., Shim K., Sasaki T., Koshizaki N., Pulsed-Laser-Induced Simple Synthetic Route for $Tb_3Al_5O_{12}$:Ce^{3+} Colloidal Nanocrystals and Their Luminescent Properties, Nanoscale Res. Lett., 4 (2009) 888–895.

Mialon G., Türkcan S., Alexandrou A., Gacoin T., Boilot J.-P., New Insights into Size Effects in Luminescent Oxide Nanocrystals, J. Phys. Chem. C, 113 (2009) 18699–18706.

Milewski P.D., Streiffer S.K., Kingon A.I., Shmagin I.K., Kolbas R.M., Krishnankutty, S., Selective deposition and luminescence characterization of Eu-doped Y_2O_3 nanoparticles by microwave plasma synthesis, J. Soc. Inf. Display, 6 (1998) 143–147.

Mishchenko M.I., Travis L.D., Lacis A.A., Scattering, absorption, and emission of light by small particles, Cambridge Univ. Press, Cambridge, 2002.

Mudgett P.S., Richards L.W., Multiple Scattering Calculations for Technology, Appl. Opt., 10 (1971) 1485–1502.

Mueller R., Mädler L., Pratsinis S.E., Nanoparticle synthesis at high production rates by flame spray pyrolysis, Chem. Eng. Sci., 58 (2003) 1969–1976.

Mueller R., Jossen R., Pratsinis S.E., Watson M., Akhtar M.K., Zirconia Nanoparticles Made in Spray Flames at High Production Rates, J. Amer. Ceram. Soc., 87 (2004) 197–202.

Mutelet B., Perriat P., Ledoux G., Amans D., Lux F., Tillement O., Billotey C., Janier M., Villiers C., Bazzi R., Roux S., Lu G., Gong Q., Martini M., Suppression of luminescence quenching at the nanometer scale in Gd_2O_3 doped with Eu^{3+} or Tb^{3+}: Systematic comparison between nanometric and macroscopic samples of life-time, quantum yield, radiative and non-radiative decay rates, J. Appl. Phys., 110 (2011) 94317–94319.

Mutlugun E., Hernandez-Martinez P.L., Eroglu C., Coskun Y., Erdem T., Sharma V.K., Unal E., Panda S.K., Hickey S.G., Gaponik N., Eychmüller A., Demir H.V., Large-Area (over 50 cm × 50 cm) Freestanding Films of Colloidal InP/ZnS Quantum Dots, Nano Lett., 12 (2012) 3986–3993.

Nakazawa E., Fundamentals of Luminescence. Fundamental Properties of Phosphors. in: Yen, W.M., Shionoya, S., Yamamoto, H. (Eds.), Phosphor handbook, 2 ed. CRC Press, Boca Raton, Fla., 2007, pp. 11.20.

Narendran N., Gu Y., Freyssinier J.P., Yu H., Deng L., Solid-state lighting: failure analysis of white LEDs, J. Cryst. Growth, 268 (2004) 449–456.

Narita K., Kubelka-Munk's theory. Optical Properties of Powder Layers, in: Yen W.M., Shionoya S., Yamamoto H. (Eds.), Phosphor handbook, 2 ed., CRC Press, Boca Raton, Fla., 2007, pp. 923–936.

Nayak A., Sahoo R., Debnath R., Hydration-induced coupling of the excitonic state of Y_2O_3 with its phonon: Negative effect on the luminescence efficiency of Y_2O_3:Eu^{3+} nanophosphor, J. Mater. Res., 22 (2007) 35–39.

Nyman M., Shea-Rohwer L.E., Martin J.E., Provencio P., Nano-YAG:Ce Mechanisms of Growth and Epoxy-Encapsulation, Chem. Mater., 21 (2009) 1536–1542.

Ozawa L., Cathodoluminescence and photoluminescence. Theories and practical applications, Phosphor science and engineering, CRC Press, Boca Raton, Fla., 2007.

Pang M.L., Lin J., Cheng Z.Y., Fu J., Xing R.B., Wang S.B., Patterning and luminescent properties of nanocrystalline Y_2O_3:Eu^{3+} phosphor films by sol-gel soft lithography, Mater. Sci. Eng. B, 100 (2003) 124–131.

Park B.K., Park H.K., Oh J.H., Oh J.R., Do Y.R., Selecting Morphology of $Y_3Al_5O_{12}$:Ce^{3+} Phosphors for Minimizing Scattering Loss in the pc-LED Package, J. Electrochem. Soc., 159 (2012a) J96-J106.

Park H.K., Oh J.H., Rag Do Y., Toward scatter-free phosphors in white phosphor-converted light-emitting diodes, Opt. Express, 20 (2012b) 10218–10228.

Peng Y., Liu J., Zhang K., Luo H., Li J., Xu B., Han L., Li X., Yu X., Near-infrared luminescent and antireflective in SiO_2/YVO_4:Yb^{3+} bilayer films for c-Si solar cells, Appl. Phys. Lett., 99 (2011) 121110–121113.

Pimenoff J., Hovinen A., Rajala M., Glass Coating by Atmospheric Flame Spray Nanoparticle Deposition, in: Proc. 6th Int. Conf. on Coatings on Glass and Plastics. (Dresden, Germany, June 18–22, 2006), 2006, p. 135.

Pokric M., Allinson N.M., Testing of gadolinium oxy-sulphide phosphors for use in CCD-based X-ray detectors for macromolecular crystallography, Nucl. Instr. Meth. Phys. Res. A, 477 (2002) 353–359.

Potdevin A., Chadeyron G., Thérias S., Mahiou R., Luminescent Nanocomposites Made of Finely Dispersed $Y_3Ga_5O_{12}$:Tb Powder in a Polymer Matrix: Promising Candidates for Optical Devices, Langmuir, 28 (2012) 13526–13535.

Prasad P.N., Nanophotonics, Wiley, Hoboken, NJ, 2004.

Prasher R., Thermal radiation in dense nano- and microparticulate media, J. Appl. Phys., 102 (2007) 74316–74319.

Pratsinis S.E., Aerosol-based technologies in nanoscale manufacturing: from functional materials to devices through core chemical engineering, AIChE J., 56 (2010) 3028–3035.

Psuja P., Hreniak D., Strek W., Kovalenko D., Gaishun V., Fabrication and properties of nanocomposite ITO layer containing terbium doped yttrium aluminum garnet nanocrystallites, Proc. SPIE, 7212 (2009) 72121C.

Purwanto A., Wang W.-N., Ogi T., Lenggoro I.W., Tanabe E., Okuyama K., High luminance YAG:Ce nanoparticles fabricated from urea added aqueous precursor by flame process, J. Alloy Comp., 463 (2008) 350–357.

Qi Z., Shi C., Zhang W., Zhang W., Hu T., Local structure and luminescence of nanocrystalline Y_2O_3:Eu, Appl. Phys. Lett., 81 (2002) 2857–2859.

Rajan G., Gopchandran K.G., Enhanced luminescence from

spontaneously ordered $Gd_2O_3:Eu^{3+}$ based nanostructures, Appl. Surf. Sci., 255 (2009) 9112–9123.

Reineke S., Lindner F., Schwartz G., Seidler N., Walzer K., Lussem B., Leo K., White organic light-emitting diodes with fluorescent tube efficiency, Nature, 459 (2009) 234–238.

Revaux A., Dantelle G., Brinkley S., Matioli E., Weisbuch C., Boilot J.-P., Gacoin T., YAG:Ce nanoparticle based converter layer for white LEDs, Proc. SPIE, 8102 (2011a) 81020R.

Revaux A., Dantelle G., Decanini D., Haghiri-Gosnet A.-M., Gacoin T., Boilot J.-P., Synthesis of YAG:Ce/TiO_2 nanocomposite films, Opt. Mater., 33 (2011b) 1124–1127.

Revaux A., Dantelle G., George N., Seshadri R., Gacoin T., Boilot J.-P., A protected annealing strategy to enhanced light emission and photostability of YAG:Ce nanoparticle-based films, Nanoscale, 3 (2011c) 2015–2022.

Richards B.S., Enhancing the performance of silicon solar cells via the application of passive luminescence conversion layers, Sol. Energy Mater. Sol. Cells 90 (2006) 2329–2337.

Riwotzki K., Haase M., Colloidal YVO_4:Eu and $YP_{0.95}V_{0.05}O_4$:Eu Nanoparticles: Luminescence and Energy Transfer Processes, J. Phys. Chem. B, 105 (2001) 12709–12713.

Ronda C., Luminescence. From theory to applications, Wiley-VCH, Weinheim, 2008.

Rossmann K., Point Spread-Function, Line Spread-Function, and Modulation Transfer Function, Radiology, 93 (1969) 257–272.

Sadowsky M., The Preparation of Luminescent Screens, J. Electrochem. Soc., 95 (1949) 112–128.

Sahm T., Rong W., Bârsan N., Mädler L., Friedlander S.K., Weimar U., Formation of multilayer films for gas sensing by in situ thermophoretic deposition of nanoparticles from aerosol phase, J. Mater. Res., 22 (2007) 850–857.

Saladino M.L., Zanotto A., Chillura Martino D., Spinella A., Nasillo G., Caponetti E., Ce:YAG Nanoparticles Embedded in a PMMA Matrix: Preparation and Characterization, Langmuir, 26 (2010) 13442–13449.

Samokhvalov P., Artemyev M., Nabiev I., Basic Principles and Current Trends in Colloidal Synthesis of Highly Luminescent Semiconductor Nanocrystals, Chem. Eur. J., 19 (2013) 1534–1546.

Sasaki K.Y., Talbot J.B., Deposition of Powder Phosphors for Information Displays, Adv. Mater., 11 (1999) 91–105.

Sayanna K.R., Sagar D.K., Goud S.L., Effects of defocusing on the Sparrow limits for apodized optical systems, Opt. Commun., 217 (2003) 59–67.

Schmechel R., Kennedy M., Seggern H. von, Winkler H., Kolbe M., Fischer R.A., Xaomao L., Benker A., Winterer M., Hahn H., Luminescence properties of nanocrystalline $Y_2O_3:Eu^{3+}$ in different host materials, J. Appl. Phys., 89 (2001) 1679–1686.

Schreuder M.A., Gosnell J.D., Smith N.J., Warnement M.R., Weiss S.M., Rosenthal S.J., Encapsulated white-light CdSe nanocrystals as nanophosphors for solid-state lighting, J. Mater. Chem., 18 (2008) 970–975.

Shang C., Shang X., Qu Y., Li M., Investigation on the red shift of charge transfer excitation spectra for nano-sized $Y_2O_3:Eu^{3+}$, Chem. Phys. Lett., 501 (2011) 480–484.

Shang M., Geng D., Kang X., Yang D., Zhang Y., Lin J., Hydrothermal Derived $LaOF:Ln^{3+}$ (Ln=Eu, Tb, Sm, Dy, Tm, and/or Ho) Nanocrystals with Multicolor-Tunable Emission Properties, Inorg. Chem., 51 (2012) 11106–11116.

Si R., Zhang Y.-W., Zhou H.-P., Sun L.-D., Yan C.-H., Controlled-Synthesis, Self-Assembly Behavior, and Surface-Dependent Optical Properties of High-Quality Rare-Earth Oxide Nanocrystals, Chem. Mater., 19 (2006) 18–27.

Siegel R., Howell J.R., Thermal radiation heat transfer, 3rd ed., Hemisphere Publ., Washington, D.C., 1992.

Singh S.K., Kumar K., Rai S.B., Synthesis and spectroscopy of transparent colloidal solution of Gd_2O_3: Er^{3+}, Yb^{3+} spherical nanocrystals by pulsed laser ablation, Mater. Sci. Eng. B, 166 (2010) 180–184.

Skandan G., Foster C.M., Frase H., Ali M.N., Parker J.C., Hahn H., Phase characterization and stabilization due to grain size effects of nanostructured Y_2O_3, Nanostr. Mater., 1 (1992) 313–322.

Sklensky A.F., Buchanan R.A., Maple T.G., Bailey H.N., Resolution of X-Ray Intensifying Screens, J. Electrochem. Soc., 122 (1975) 1089–1092.

Sluzky E., Hesse K., Electrophoretic Preparation of Phosphor Screens, J. Electrochem. Soc., 136 (1989) 2724–2727.

Smith A., Belomoin G., Nayfeh M.H., Nayfeh T., Spatially selective electrochemical deposition of composite films of metal and luminescent Si nanoparticles, Chem. Phys. Lett., 372 (2003) 415–418.

Song W.-S., Choi H.-N., Kim Y.-S., Yang H., Formation of green-emitting $LaPO_4$:Ce,Tb nanophosphor layer and its application to highly transparent plasma displays, J. Mater. Chem., 20 (2010) 6929–6934.

Song W.-S., Kim Y.-S., Yang H., Construction of Highly Transparent Plasma Display Devices Using Hydrothermally Synthesized Green-Emitting $LaPO_4$:Ce,Tb Nanophosphors, J. Electrochem. Soc., 158 (2011) J137–J142.

Song W.-S., Lee K.-H., Do Y.R., Yang H., Utilization of All Hydrothermally Synthesized Red, Green, Blue Nanophosphors for Fabrication of Highly Transparent Monochromatic and Full-Color Plasma Display Devices, Adv. Funct. Mater., 22 (2012a) 1885–1893.

Song W.-S., Lee K.-H., Kim Y.-S., Yang H., Tuning of size and luminescence of red $Y(V,P)O_4$:Eu nanophosphors for their application to transparent panels of plasma display, Mater. Chem. Phys., 135 (2012b) 51–57.

Sotiriou G.A., Schneider M., Pratsinis S.E., Color-Tunable Nanophosphors by Codoping Flame-Made Y_2O_3 with Tb and Eu†, J. Phys. Chem. C, 115 (2011) 1084–1089.

Sotiriou G.A., Schneider M., Pratsinis S.E., Green, Silica-Coated Monoclinic $Y_2O_3:Tb^{3+}$ Nanophosphors: Flame Synthesis and Characterization, J. Phys. Chem. C, 116 (2012) 4493–4499.

Soules T.F., Klatt W.A., Optical Properties of Powder Coatings, Journal of the Illuminating Engineering Society, 17 (1988) 92.

Stepuk A., Krämer K.W., Stark W.J., Flame Synthesis of Complex Fluoride-Based Nanoparticles as Upconversion Phosphors, KONA Powd. Part. J., 30 (2013) 267–275.

Strobel R., Pratsinis S.E., Flame aerosol synthesis of smart

nanostructured materials, J. Mater. Chem., 17 (2007) 4743–4756.

Swank R.K., Calculation of Modulation Transfer Functions of X-Ray Fluorescent Screens, Appl. Opt., 12 (1973) 1865–1870.

Takeshita S., Nakayama K., Isobe T., Sawayama T., Niikura S., Optical Properties of Transparent Wavelength-Conversion Film Prepared from $YVO_4:Bi^{3+},Eu^{3+}$ Nanophosphors, J. Electrochem. Soc., 156 (2009) J273–J277.

Tam W.G., Zardecki A., Multiple scattering corrections to the Beer-Lambert law. 1: Open detector, Appl. Opt., 21 (1982) 2405–2412.

Tammela S., Soderlund M., Koponen J., Philippov V., Stenius P., Digonnet M.J., Jiang S., The potential of direct nanoparticle deposition for the next generation of optical fibers, Proc. SPIE, 6116 (2006) 61160G-9.

Tan S.T., Sun X.W., Demir H.V., DenBaars S.P., Advances in the LED Materials and Architectures for Energy-Saving Solid-State Lighting Toward "Lighting Revolution", IEEE Photon. J., 4 (2012) 613–619.

Tan T.T.Y. (ed), Rare earth nanotechnology. Pan Stanford Pub., Singapore (2012).

Tanner P.A., Synthesis and Luminescence of Nano-Insulators Doped with Lanthanide Ions, J. Nanosci. Nanotechnol., 5 (2005) 1455–1464.

Teoh W.Y., Amal R., Madler L., Flame spray pyrolysis: An enabling technology for nanoparticles design and fabrication, Nanoscale, 2 (2010) 1324–1347.

ter Vrugt J.W., Optical Properties of Thin Powder Layers, Philips Res. Repts, 20 (1965) 23–33.

Thybo S., Jensen S., Johansen J., Johannessen T., Hansen O., Quaade U.J., Flame spray deposition of porous catalysts on surfaces and in microsystems, J. Catalysis, 223 (2004) 271–277.

Tien C.L., Drolen B.L., Thermal radiation in particulate media with dependent and independent scattering, in: Chawla T.C. (ed.), Annual review of numerical fluid mechanics and heat transfe, vol. 1, Hemisphere Publishing, London, 1987, pp. 1–32.

Tien C.L., Thermal Radiation in Packed and Fluidized Beds, J. Heat Transfer, 110 (1988) 1230–1242.

Tissue B.M., Synthesis and Luminescence of Lanthanide Ions in Nanoscale Insulating Hosts, Chem. Mater., 10 (1998) 2837–2845.

Tissue B.M., Inorganic nanoparticles and nanostructures for phosphor applications. Methods of phosphor synthesis and related technology, in: Yen W.M., Shionoya S., Yamamoto H. (Eds.), Phosphor handbook, 2 ed. CRC Press, Boca Raton, Fla., 2007, pp. 355–380.

Tomita Y., Coating methods. Methods of phosphor synthesis and related technology, in: Yen W.M., Shionoya S., Yamamoto H. (Eds.), Phosphor handbook, 2 ed. CRC Press, Boca Raton, Fla., 2007, pp. 399–403.

Touš J., Blažek K., Pína L., Sopko B., High-resolution X-ray imaging CCD camera based on a thin scintillator screen, Rad. Meas., 42 (2007) 925–928.

Tricoli A., Graf M., Mayer F., Kuühne S., Hierlemann A., Pratsinis S.E., Micropatterning Layers by Flame Aerosol Deposition-Annealing, Adv. Mater., 20 (2008) 3005–3010.

Tricoli A., Righettoni M., Pratsinis S.E., Anti-Fogging Nanofibrous SiO2 and Nanostructured SiO_2-TiO_2 Films Made by Rapid Flame Deposition and In Situ Annealing, Langmuir, 25 (2009) 12578–12584.

Tsai D.H., Kim S.H., Corrigan T.D., Phaneuf R.J., Zachariah M.R., Electrostatic-directed deposition of nanoparticles on a field generating substrate, Nanotechnology, 16 (2005) 1856.

Urabe K., Monte Carlo Calculation on Phosphor Screens with Complicated Boundary Conditions, Jpn. J. Appl. Phys., 19 (1980) 885.

Urabe K., Monte Carlo method. Optical properties of powder layers, in: Yen W.M., Shionoya S., Yamamoto H. (Eds.), Phosphor handbook, 2 ed. CRC Press, Boca Raton, Fla., 2007, pp. 949–957.

Valverde J.M., Castellanos A., Random loose packing of cohesive granular materials, Europhys. Lett., 75 (2006) 985.

van de Hulst H.C., Light scattering by small particles, Dover classics of science and mathematics, Dover, New York, NY, 2009.

van der Ende B.M., Aarts L., Meijerink A., Lanthanide ions as spectral converters for solar cells, Phys. Chem. Chem. Phys., 11 (2009) 11081–11095.

Varahramyan K., Lvov Y., Nanomanufacturing by layer-by-layer assembly—from nanoscale coating to device applications, Proceedings of the Institution of Mechanical Engineers, Part N: Journal of Nanoengineering and Nanosystems, 220 (2006) 29–37.

Vemury S., Pratsinis S.E., Corona-assisted flame synthesis of ultrafine titania particles, Appl. Phys. Lett., 66 (1995) 3275–3277.

Vetrone F., Naccache R., Zamarrón A., Juarranz de la Fuente A., Sanz-Rodríguez F., Martinez Maestro L., Martín Rodriguez E., Jaque D., García Solé J., Capobianco J.A., Temperature Sensing Using Fluorescent Nanothermometers, ACS Nano, 4 (2010) 3254–3258.

Vollath D., Nanomaterials. An introduction to synthesis, properties and application, Wiley-VCH, Weinheim, 2008.

Vorsthove M., Kynast U., Efficiency issues in Ce^{3+} doped YAG nanocrystals, Mater. Res. Bull., 46 (2011) 1761–1765.

Vu N., Kim A.T., Yi G.C., Strek W., Photoluminescence and cathodoluminescence properties of Y_2O_3:Eu nanophosphors prepared by combustion synthesis, J. Lumin., 122-123 (2007) 776–779.

Wakefield G., Holland E., Dobson P.J., Hutchison J.L., Luminescence Properties of Nanocrystalline Y_2O_3:Eu, Adv. Mater., 13 (2001) 1557–1560.

Wang F., Wang J., Liu X., Direct Evidence of a Surface Quenching Effect on Size-Dependent Luminescence of Upconversion Nanoparticles, Angew. Chem. Int. Ed., 49 (2010) 7456–7460.

Wang X., Zhang M., Ding H., Li H., Sun Z., Low-voltage cathodoluminescence properties of green-emitting $ZnAl_2O_4:Mn^{2+}$ nanophosphors for field emission display, J. Alloy Comp., 509 (2011) 6317–6320.

Wei M.-K., Su I.L., Chen Y.-J., Chang M., Lin H.-Y., Wu T.-C., The influence of a microlens array on planar organic

light-emitting devices, J. Micromech. Microeng., 16 (2006) 368–374.
Widdel H., Color in electronic displays, Defense research series, vol. 3, Plenum Press, New York, 1992.
Williams C.S., Becklund O.A., Introduction to the optical transfer function, Wiley, New York, 1989.
Wind L., Szymanski W.W., Quantification of scattering corrections to the Beer-Lambert law for transmittance measurements in turbid media, Meas. Sci. Technol., 13 (2002) 270.
Windisch R., Rooman C., Meinlschmidt S., Kiesel P., Zipperer D., Dohler G.H., Dutta B., Kuijk M., Borghs G., Heremans P., Impact of texture-enhanced transmission on high-efficiency surface-textured light-emitting diodes, Appl. Phys. Lett., 79 (2001) 2315–2317.
Wu Y.C., Garapon C., Bazzi R., Pillonnet A., Tillement O., Mugnier J., Optical and fluorescent properties of Y_2O_3 sol–gel planar waveguides containing Tb^{3+} doped nanocrystals, Appl. Phys. A, 87 (2007) 697–704.
Xu W., Song H., Yan D., Zhu H., Wang Y., Xu S., Bai X., Dong B., Liu Y., YVO_4:Eu^{3+},Bi^{3+} UV to visible conversion nanofilms used for organic photovoltaic solar cells, J. Mater. Chem., 21 (2011) 12331–12336.
Ye X., Zhuang W., Hu Y., He T., Huang X., Liao C., Zhong S., Xu Z., Nie H., Deng G., Preparation, characterization, and optical properties of nano- and submicron-sized Y_2O_3:Eu^{3+} phosphors, J. Appl. Phys., 105 (2009) 64302–64306.
Ye X., Collins J.E., Kang Y., Chen J., Chen D.T.N., Yodh A.G., Murray C.B., Morphologically controlled synthesis of colloidal upconversion nanophosphors and their shape-directed self-assembly, Proc. Nat. Acad. Sci. USA, 107 (2010) 22430–22435.
Yen W.M., Shionoya S., Yamamoto H. (eds.), Phosphor handbook, 2nd ed., CRC Press, Boca Raton, Fla. (2007).
Yum J.-h., Seo S.-Y., Lee S., Sung Y.-E., $Y_3Al_5O_{12}$:$Ce_{0.05}$ Phosphor Coatings on Gallium Nitride for White Light Emitting Diodes, J. Electrochem. Soc., 150 (2003) H47–H52.
Zege E.P., Ivanov A.P., Kacev I.L., Image transfer through a scattering medium, Springer, Berlin, 1991.
Zhang F., Deng Y., Shi Y., Zhang R., Zhao D., Photoluminescence modification in upconversion rare-earth fluoride nanocrystal array constructed photonic crystals, J. Mater. Chem., 20 (2010) 3895–3900.
Zhang H., Cui Y., Men Y., Liu X., Strong ultraviolet emission from zinc oxide thin films prepared by electrophoretic deposition, J. Lumin., 121 (2006) 601–605.
Zhang J., Tang Z., Zhang Z., Fu W., Wang J., Lin Y., Synthesis of nanometer Y_2O_3:Eu phosphor and its luminescence property, Mater. Sci. Eng. A, 334 (2002) 246–249.
Zhang Q.Y., Huang X.Y., Recent progress in quantum cutting phosphors, Prog. Mater. Sci., 55 (2010) 353–427.
Zhang W.-W., Zhang W.-P., Xie P.-B., Yin M., Chen H.-T., Jing L., Zhang Y.-S., Lou L.-R., Xia S.-D., Optical properties of nanocrystalline Y_2O_3:Eu depending on its odd structure, J. Colloid Interface Sci., 262 (2003) 588–593.

Author's short biography

Roman Kubrin

Roman Kubrin graduated from the North-Caucasus State Technical University in Stavropol, Russia, in 2002 and received his M.Sc. degree in Microelectronics and Microsystems from the Hamburg University of Technology (TUHH) in 2005. He later worked on the technology of phosphors with reduced particle size at the Institute of Optical and Electronic Materials at the TUHH, was a visiting researcher at the Particle Technology Laboratory at the Swiss Federal Institute of Technology (ETH Zurich), and received his Ph.D. (Dr.-Ing.) in 2012. He is currently working at the Institute of Advanced Ceramics at the TUHH on the synthesis of ceramic nanostructures for high-temperature photonics.

KONA Powder and Particle Journal No. 31 (2014) 53–81/Doi:10.14356/kona.2014010 Review Paper

A Review of the Fire and Explosion Hazards of Particulates†

Saul M. Lemkowitz[1]* and Hans J. Pasman[2]

[1] *Department of Chemical Engineering, Delft University of Technology, the Netherlands*
[2] *Mary Kay O'Connor Process Safety Center, Department of Chemical Engineering of Texas A&M University, USA*

Abstract

Particulate fires and explosions cause substantial loss of life and property. With the goal of understanding, preventing, or at least mitigating particulate fire and explosion hazards, we review basics. We distinguish between 'hazard' and 'risk' and discuss the fire and explosion hazards of particulates, the many factors determining such hazards, hazard indexes, and ways to reduce fire and explosion hazards. While our primary goal is to improve safety, we briefly discuss how fundamental knowledge can be extracted from weapon technology based on particulate combustion. We review the prevention of and protection against particulate explosions and discuss ongoing and future research.

Keywords: fire, explosion, (nano)particles, hazard indexes, prevention, protection, modeling

1. Introduction; hazard versus risk

Although the basics are well understood, fires and explosions of solid particulates (powders, 'dusts') and liquid particulates ('mists'), especially the former, continue to cause considerable material damage and loss of life. Particle safety therefore remains important. In discussing particulate safety we distinguish between the concepts of 'hazard' and 'risk'.

Hazard is the potential to create an adverse effect. Typical hazards of particulates are fire and explosion. Hazards can be quantified using certain substance properties, often expressed as hazard indexes, which are discussed later. Quantitative values of hazards are always relative, never absolute.

As a technical concept, risk is composed of two quantifiable factors: an adverse effect (e.g. number of deaths) and the probability (0 to 100%) of that adverse effect occurring. If both of these factors are accurately quantified, risk can, at least in principle, have a correct absolute value. In practice, however, calculated risks are often subject to large uncertainties.

Particulate hazards include fire and explosion, which for a given particulate, are determined by its properties, such as its chemical composition, particle size distribution, etc. The risk of a given particulate is, however, not solely determined by its properties, but also by factors external to the particulate itself, such as amounts, conditions (e.g. pressure, temperature), size and strength of containment, (distance to) possible 'targets', good management, adherence to legislation, etc. Here we discuss particle hazards and their reduction. The more extensive concept of particle risk falls outside the scope of this review[1)].

2. Fire and explosion hazards of particulates: the basics

Fire is a (usually relatively continuous) combustion (burning) process consisting of exothermic (= heat-producing) chemical reactions involving a fuel and producing besides combustion products, such as water and carbon dioxide, heat and, via flame, also light. In addition to simply burning, an insidious form of fire called smoldering can occur when large volumes of a combustible powder are stored, typically in a pile for an extended time period. Through oxidation of the surface of the particulates, heat is generated, and if the rate of heat generation exceeds the rate of heat loss (as can occur in a large pile), the temperature within the pile can reach the ignition temperature. The result is a relatively slow burning (slow because oxygen must diffuse into the pile and reaction gases/vapors out). Aside from generating poisonous gases (e.g. carbon monoxide), smoldering can lead to fires and even explosions. We mention smoldering further in **Table 2** (under Minimum Ignition Temperature). In the following text, we shall focus on dust explosions.

Given the right conditions, most unoxidized materials can burn. Most substances industrially produced (e.g. plastics, oils) or processed (e.g. wood, petroleum) are unoxidized or not fully oxidized and can therefore burn. One

† Accepted: July 12, 2013
1 2628 BL Delft, The Netherlands
2 College Station, Texas 77843-3122, USA
* Corresponding author:
E-mail: s.m.lemkowitz@tudelft.nl
TEL: +31-152-789-111

must be aware that:

ALL POWDERS THAT CAN BURN CAN ALSO EXPLODE

ALL LIQUIDS THAT CAN BURN CAN—AS PARTICULATES (MISTS)—ALSO EXPLODE

No definitive, quantitative definition of the term 'explosion' exists. Characteristic of explosions are: "much energy" (Joules, J), "in a short time" ((fraction of) seconds(s); thus high power (J/s)), "in a small volume" (m^3, thus high power density (J/(s m^3)). Further: creation of a 'blast' as a pressure wave (**Fig. 1, left**) or a more destructive shock wave (**Fig. 1, right**), both of which can wound/kill people, destroy buildings, and create deadly high-velocity fragments. The energy source of explosions can be physical (e.g. lightning) or chemical (e.g. combustion). Here we discuss the explosion hazards of particulates, and therefore we consider only explosions caused by chemical reactions, i.e. combustible substances undergoing combustion in air or oxygen.

A reason why no unambiguous scientific definition of explosion exists is that the most common type of chemical explosion, the deflagration, is simply a 'very rapid burning'. How rapid? Rapid enough to create a pressure wave and, when it occurs in the open air and is rapid enough, an audible signal ('bang'). When an explosion occurs in a closed vessel and the vessel cannot sustain the pressure, it will produce a blast (i.e. destructive pressure or shock wave in the surrounding air) at the moment of bursting.

A key difference between fire and explosion is that in fire, the fuel (e.g. burning candle) and the oxidizer (air) are clearly separated. Oxygen molecules, necessary to maintain the occurrence of combustion, reach the flame largely by diffusion. By contrast, explosions are characterized by a *pre-mixing* of fuel and oxidizer. Examples of increasing intimacy of pre-mixing are: a cloud of combustible dust or mist (combustible particles suspended in air); an explosive gaseous mixture (e.g. methane molecules and oxygen molecules in air); a solid high explosive, such as TNT (atoms of fuel (carbon and hydrogen) adjacent to atoms of oxidizer (oxygen) in the same molecule). It is this pre-mixing of fuel and oxidizer, and its degree of 'intimacy' (most 'intimate' at the atomic level, as in an explosive such as TNT), that form the basic reason why explosions occur (much) more rapidly than fires do, thereby resulting in a (much) higher (volumetric) rate of energy release, i.e. power (W or W/m^3).

Explosions of powders, commonly called dust explosions and/or explosions of liquid particulates, called mist explosions[2)], are almost always a type of explosion called deflagration. The propagation mechanism of deflagration is heat conduction: heat is transferred from the hot reaction zone (the flame) to the much cooler unreacted material ahead of the flame, thus preheating it until it reaches its ignition temperature, at which it ignites and burns (combusts). Behind the flame, expanding hot, oxidized gaseous products and (possibly) unburned material are present.

Characteristic of deflagrations is that the flame speed, S_f, is always subsonic (i.e. flame propagates at less than the speed of sound, which in air at ambient conditions is ca. 330–340 m/s). At non-turbulent conditions, deflagrative flame speeds in air at ambient conditions typically range between a few m/s and about 10 m/s.

In a closed vessel filled with a flammable mixture undergoing deflagration and ignited in the center, the flame expands spherically from the vessel's center until it reaches the vessel's wall. During this process, the pressure in the vessel continuously rises. Both the pressure and the rate of pressure rise reach a maximum when the flame reaches the vessel's wall. Characteristic of deflagrations in a closed vessel are therefore a maximum explosion pressure, P_{max}, and a finite maximum rate of pressure increase, $(dP/dt)_{max}$. (In practice, pressure is often expressed as bara (= bar absolute, 1 bara (≈ atmospheric pressure) being 10^5 Pa) and rate of pressure rise expressed in bar/s.) Maximum pressure, P_{max}, and maximum rate of pressure increase, $(dP/dt)_{max}$, are found at optimal particulate concentration.

While deflagrating flames propagate less rapidly than the speed of sound, the pressure waves produced by the expanding flame propagate ahead of the flame at sonic velocity; i.e. 330–340 m/s. Therefore in deflagrations, the flame (subsonic velocity) and pressure waves (sonic velocity) are separated from one another, pressure waves preceding the flame.

Only at conditions rarely existing in industrial applications can particulates explode via a mechanism other than deflagration: the detonation. A detonation is a chemically reactive shock wave. A shock wave (**Fig. 1, at right**) is a special case of a pressure wave. Like pressure waves, shock waves have a maximum pressure, P_{max}, but differ from pressure waves by having an almost infinite rate of pressure rise, dP/dt. Additionally, the flame speed of a detonation is supersonic, i.e. faster than the speed of sound. Also in contrast to deflagrations, in which the deflagrative flame and pressure waves are separate from one another and propagate at different speeds, both the detonation flame and the shock wave propagate at the same (supersonic) speed, with the combustion occurring within the shock wave, ignited by the high temperature resulting from the sudden compression. In general, per unit mass of material exploding (e.g. per kg), detonations are much more devastating than deflagrations because detonation pressures are much higher (ca. 2 to 16 times greater) than maximum deflagration pressures and rates of pressure rise near infinite. Detonations are also much more difficult to protect against than deflagrations, since detonations propagate supersonically.

For deflagrations occurring in a closed volume at an initial pressure not far from atmospheric (i.e. ca. 0.1 to 10

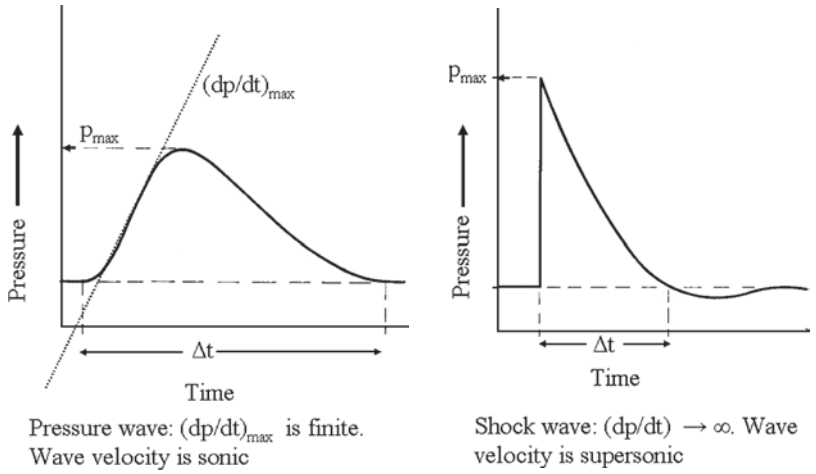

Fig. 1 Pressure wave (left) and shock wave (right) propagating in an open system (i.e. constant pressure system, such as atmospheric).

bar), the ideal gas law expresses the maximum explosion pressure simply and usually sufficiently accurately (< 10% error):

$$P_{explosion} \approx (n_{explosion}/n_{initial}) \cdot (T_{explosion}/T_{initial}) \cdot P_{initial} \quad (1)$$

where:

$P_{explosion}$ = final pressure (bara) of the explosion for given conditions of mixture composition, etc.

$(n_{explosion}/n_{initial})$ = ratio of number of gaseous moles produced by the explosion relative to the initial number, including, in both cases, the inert gas molecules; $T_{explosion}/T_{initial}$ = ratio of absolute explosion temperature (K) relative to initial temperature (K).

$P_{initial}$ = initial pressure (bara).

The presence of roughly 80% inerts (nitrogen + argon) in air causes the factor $(n_{explosion}/n_{initial})$ to be approximately unity. Therefore Equation 1 simplifies to:

$$P_{explosion} \approx (T_{explosion}/T_{initial}) \cdot P_{initial} \quad (2)$$

Under optimal conditions $P_{explosion}$ becomes the maximum possible explosion pressure P_{max}. Equation 2 predicts that the maximum possible explosion pressure of a deflagration within a closed vessel is reached when the maximum possible temperature is obtained. For gases, this occurs to a (near) stoichiometric mixture composition. For particulates, it is in a fuel-rich area. The maximum combustion temperature is the adiabatic flame temperature, 'adiabatic' referring to ideal conditions in which no heat loss occurs. The adiabatic flame temperature is a chemical thermodynamic property; i.e. it is determined solely by the chemical properties of the substances involved (e.g. its heats of combustion), mixture composition (e.g. oxygen concentration), and initial temperature and pressure of the system.

Generally the faster the explosion process, the less time to lose heat, and the closer adiabatic conditions are attained, manifesting itself as a closer approach to the theoretical maximum adiabatic explosion temperature and thus greater rate of temperature rise, dT/dt, and pressure rise, dP/dt. Maximum adiabatic flame temperatures for common organic powders (i.e. plastics, coal) and/or droplets of combustible liquids exploding in air (e.g. oils) typically range between 1,500 and 3,000 K. Eq. 2, based simply on the perfect gas law, predicts that maximum explosion pressures for particulate explosions (deflagrations) of most particulates occurring in air in closed vessels initially at atmospheric pressure (1 bara) and ambient temperature (T = ca. 300 K) should typically be in the range of ca. 5 to 10 bara (= 4 and 9 baro (baro = bar overpressure)); in practice this is indeed the case[3)].

Two parameters essential for assessing particulate explosion severity (**Table 1**) are maximum explosion pressure, P_{max}, and maximum rate of pressure rise, $(dP/dt)_{max}$, the latter usually volume-normalized and called the K_{St} factor (or simply K factor; see **Table 1**). As Eq. 2 shows, the maximum possible explosion pressure of deflagrations is largely determined by the adiabatic flame temperature.

The (volume-normalized) rate of pressure rise is largely determined by the speed of the flame, S_f. For a deflagration occurring in closed spherical equipment and ignited at its center, the time duration of the explosion, Δt, is, by approximation, simply the radius of the sphere, R_{sphere}, divided by the flame speed, S_f. Therefore the faster the flame, the quicker the explosion occurs, and thus the faster the pressure rise. Indeed, the following approximations can be easily derived[4,5,6)]:

$$dP/dt = \Delta P/\Delta t = (P_{max} - P_{initial})/(R_{sphere}/S_f) \quad (3)$$

$$K_{St} = (dP/dt)_{max} \cdot V^{1/3} \propto P_{initial} \cdot S_f \quad (4)$$

in which P_{max} and $P_{initial}$ are, resp., the maximum explosion pressure and the initial pressure, R_{sphere} the radius of the sphere in which the explosion occurs, and S_f the averaged flame speed; the symbol μ means 'proportional to'. More exact models are available, see e.g. Dahoe et al.[6)]

In the absence of turbulence, the flame speed, S_f, being the propagation velocity of the flame front, is the vector result of the laminar burning velocity, S_U, and the expansion of the hot gas. In a closed vessel, the latter is large at first, when pressure is still near the initial value, and zero at the end when maximum pressure is reached. In a tube open at one end and closed at the other, and ignited at the open end, as the flame propagates into the tube, the hot reaction gases flow out of the tube and thus in a direction opposite (i.e. countercurrently) to that of the flame. In this special case, and assuming laminar conditions: $S_f = S_U$. Like the adiabatic flame temperature, the laminar burning velocity is determined only by substance properties, mixture composition, and initial temperature and pressure conditions. Typical laminar burning velocities for gases/vapors in air at stoichiometric concentrations are roughly 0.4 m/s or less; for most powders they are less, typically roughly 0.25 m/s. However, unlike the maximum explosion pressure which follows directly from chemical thermodynamics, the laminar burning velocity is also strongly influenced by chemical kinetics (e.g. reaction mechanism). Chemical kinetics is usually much more complex than chemical thermodynamics, which is a reason why laminar burning velocities usually cannot be calculated from theory. As we discuss later, while laminar burning velocities are typically in the 1 m/s range, through turbulence flame speeds can accelerate enormously (to more than 600 m/s) causing pressure increases of several bars. Explosion behavior is determined by a complicated interplay between chemical thermodynamics, chemical kinetics, and turbulence-generated physical transfer phenomena.

Surprisingly small overpressures can cause considerable damage. An overpressure of 0.1 baro typically shatters glass windows and lethal effects start also at this pressure; 1.0 baro damages typical industrial equipment used for handling powders such as silos, and totally destroys normal buildings (houses, office blocks), causing their collapse and killing those inside. Normal structures react to even small overpressures because pressure is force/area, e.g. overpressures of 0.1 and 1 baro correspond to forces of, respectively, 1 ton/m^2 and 10 tons/m^2. Typical vertical surfaces of buildings (e.g. windows, walls) cannot withstand such huge lateral forces and are thus highly vulnerable[7)].

In dust or mist explosions, typically deflagrations, occurring in closed systems such as silos, it is the maximum pressure, P_{max}, that largely determines the explosion's destructiveness. For explosions occurring in open systems, however, such as in the open air, the situation is different. In this case it is the combination of maximum pressure, P_{max}, the duration of the explosion (shown as Δt in **Fig. 1**), and even the form of the pressure wave (e.g. its dP/dt) that determine explosion destructiveness. The combination of explosion overpressure and explosion duration, i.e. the integral of the overpressure over time, is called the explosion impulse, $I_{explosion}$:

$$\text{Explosion impulse} = I_{explosion} = \int P dt \tag{5}$$

In practice, the explosion impulse can often be approximated sufficiently accurately by assuming a right triangle for the pressure or shock wave (i.e. right-hand side of **Fig. 1**), so that

$$\text{Explosion impulse} = I_{explosion} = \int P dt \approx \tfrac{1}{2} P_{max} \cdot \Delta t \tag{6}$$

Once certain thresholds of over-pressure and impulse are reached to be able to create damage, explosion destructiveness generally increases as explosion impulse increases, i.e. increasing P_{max} and/or increasing explosion duration, Δt.

We again distinguish between an explosion occurring in a *closed system* or in an *open system* and *deflagrations* versus *detonations*. As discussed above, in a *closed system* (e.g. reactor or silo), an explosion—deflagration and detonation—manifests itself as a sudden pressure rise leading to a maximum pressure. In a completely open system, for example an explosion occurring in the open air, a typical *deflagration* generally results in a large (hot) gas volume increase, but only in a very small pressure increase (i.e. $\Delta P << 0.1$ baro)[8)]. This fact follows from the ideal gas law, as applied to an open system (i.e. constant pressure system, as in the atmosphere):

$$V_{explosion} \approx (T_{explosion}/T_{initial}) \cdot V_{initial} \tag{7}$$

By approximation, the adiabatic flame temperature and thus the explosion temperature of a given substance remains roughly the same independent of whether the system is at a constant volume (i.e. closed system) or at constant pressure (i.e. open system); i.e. the factor $(T_{explosion}/T_{initial})$ remains approximately constant. Therefore Eq. 7 shows that in an open system, the ratio of the volume of the explosion products ($V_{explosion}$) to the initial unexploded volume ($V_{initial}$) will be approximately the same as the pressure ratio obtained in a closed system, namely 5–10. It is also because deflagrations occur relatively slowly (typical flame speeds being only about 10 m/s) that deflagrations occurring in completely open areas do not usually produce large overpressures, but they can when occurring in congested areas.

However, *detonations* occurring in open air behave quite differently. Detonation pressures of particulate clouds are typically around 20 times the initial pressure in both open

and closed spaces. Also, because of aerodynamic phenomena caused by supersonic flow, pressures resulting from reflections of detonative shock waves can be much higher—ca. 40 to even 160 times the initial pressure. Because of these huge initial detonation pressures and even higher reflected pressures, detonation is much more destructive than deflagration, especially in the open air.

Concerning explosion behavior in general, Abbasi et al., 2009[9] and Mannan, 2012[10] provide detailed description of types and characteristics of explosions, including deflagrations and detonations.

3. Fire and explosion hazard indexes

The more energy released during combustion and the faster this occurs, the greater the destructiveness—the severity—of the resulting fire/explosion. The less energy needed to initiate combustion, the greater the sensitivity to ignition (to fire and/or explosion), and thus the greater the probability of a fire/explosion occurring. Fire and explosion hazards of particulates (and also of gases and vapors) are therefore expressed in terms of severity indexes and sensitivity indexes, which **Tables 1 and 2** list, along with meaning and significance.

Assessment of the fire and explosion hazards of particulates requires knowing the values of the indexes listed in **Tables 1 and 2**[11]. We stress that with the possible exception of P_{max} and S_U, which in principle are invariant, values for most explosion indexes either cannot or not yet reliably be predicted theoretically. It is essential to be aware that the index values are influenced by testing procedures and equipment (which have been standardized; e.g. for temperature, pressure, turbulence, etc.). Note further that values found in the literature are often not directly applicable to one's own case, as these index values are affected by ambient changes (e.g. temperature, pressure, turbulence)[12]. Additionally, indexes of a given type of particulate (e.g. grain dust) may vary greatly, depending on which type of grain (species and sub-species), average particle size and particle size distribution, and even weather conditions (temperature, humidity) under which the powder has been stored, and for how long (this related to possible adsorption/absorption of moisture from air and its effect on particle size). The literature gives a detailed discussion of test methods and their evaluation[13].

While test methods are standardized, research leads to new insights and improved testing improvements. Gao et al., 2013, describe examples of how sensitive explosion behavior is to variations in testing procedures[14]. This is also true for an essential explosion severity index, the K_{St} value, once thought to be invariant. Proust et al. show that the assumption that it is independent of the two standard types of testing equipment is not generally true[15].

Table 1 Hazard severity indexes of particulates dispersed in air (or other oxidative gases)

Severity index	Meaning/significance/dimensions of severity index
Tendency towards detonation	Per kg of material, detonation is the most destructive explosion type. Generally, the tendency towards detonation increases with increasing mixture reactivity and decreasing particle size.
Maximum explosion pressure, P_{max}*	For deflagrations the maximum explosion pressure is largely determined by the maximum explosion temperature (Eq. 2); (bara (absolute pressure) or baro (overpressure)). Explosion hazard increases with greater maximum explosion pressure.
Maximum rate of pressure rise, $(dP/dt)_{max}$*	Maximum rate of pressure rise, with initial conditions of 1 bara and room temperature; usually expressed as bar/s. Usually cannot be calculated and must therefore be measured. Explosion hazard increases with greater maximum rate of pressure rise.
Maximum volume-normalized rate of pressure rise, called K_{St} factor (or simply K factor), where: $K_{St} = V^{1/3} \bullet (dP/dt)_{max}$; (relationship often called 'cubic law')	Maximum rate of pressure rise (bar/s), normalized to a sphere of 1 m^3 volume, with initial conditions of 1 bara and room temperature. (This equation is called the 'cubic law'.) Since it depends on $(dP/dt)_{max}$, the K_{St} factor must be measured; usually expressed as bar $m^{-1}s^{-1}$. Explosion hazard increases with increasing value of K_{st} factor. Both the maximum rate of pressure rise and the volume-normalized rate of pressure rise are largely determined by the flame speed, S_f, see Eqs. 3 and 4.
Flame speed: Laminar burning velocity, S_U, m/s; (turbulent) flame speed, S_f; m/s	Speed of flame relative to stationary observer, S_f. Laminar burning velocity, S_U, is the speed of flame relative to the unburnt gas at completely laminar (i.e. non-turbulent) conditions and stoichiometric concentration; at constant pressure this is only possible if the expanding hot combustion gases flow away backwards countercurrently to the moving flame front. S_U is typically in the range of ca. 02–0.4 m/s. Through turbulence, the flame speed (S_f) can accelerate from a few m/s to near sonic velocities, and even to supersonic during a deflagration-detonation transition: DDT

*Note that in non-optimal composition and hence not maximum output, these quantities are indicated as P_{ex} and $(dP/dt)_{ex}$.

Table 2 Hazard sensitivity indexes of particulates dispersed in air (or other oxidative gases)

Explosion sensitivity index	Meaning/significance/dimensions of explosion sensitivity index
Lower Flammability Limit (LFL); also called Lower Explosion Limit (LEL)* or Minimum Explosive Concentration (MEC)	Lowest concentration of a substance (g/m^3 or kg/m^3) dispersed in air that can burn or explode. Is measured at initial conditions of 1 bara and room temperature. Must be measured. Fire and explosion hazard increases as LEL decreases, as even very low concentrations of particulates are still flammable and thus explosive. From here onwards all "LEL"= "LFL" and "UEL" ="UFL".
Upper Flammability Limit (UFL); also called Upper Explosion Limit (UEL)*	Highest concentration (g/m^3 or kg/m^3) of a substance dispersed in air that can burn or explode. Is measured at initial conditions of 1 bara and room temperature. Compared to gases/vapors which have a more or less definite UEL, the UEL for particulates has a more limited practical utility, as particulate concentrations tend to fall due to particulate deposition. Thus a particulate whose concentration is initially above its UEL may settle out due to gravity, causing its concentration to decrease to below the UEL and thus enter the explosive range.
Explosive range: UFL—LFL	The range of concentration (g/m^3) that is explosive. Generally the larger the explosive range, the greater the probability of ignition, and thus the greater the fire and explosion hazard.
Lower Flash point (LFP)	Lowest temperature (°C or K) at which a substance reaches a vapor pressure sufficient to form a flammable mixture in air (i.e. reach the LEL). LFP usually relates to liquids but is also applicable to solids with high vapor pressure (e.g. naphthalene, benzoic acid). A lower LFP increases fire and explosion hazard.
Minimum Ignition Energy (MIE)	Lowest amount of energy (mJ) of an electrical spark that can cause a particulate dispersed in air to explode. Fire and explosion hazard usually increase as MIE decreases, as even very weak ignition sources are then capable of causing fire and/or explosion.
Minimum Oxygen Concentration (MOC); also called Limiting Oxygen Concentration (LOC)	Lowest concentration of oxygen (mol- or volume-percent O_2) in a gas mixture that can support combustion. Below this oxygen concentration explosion is not possible. The lower the MOC, the more difficult it is to produce a carrier gas in which fire and explosion cannot occur.)
Maximum Experimental Safe Gap (MESG)	The maximum gap width (mm) that allows flame propagation of a given particulate. A smaller gap width quenches the flame, thus preventing fire/explosion propagation. The lower the MESG value, the greater the fire/explosion hazard/risk of a given particulate.
Minimum Ignition Temperature (MIT); also sometimes called: Minimum Auto-ignition Temperature (AIT)	Lowest temperature (T in °C or K) of a surface that can ignite a cloud of a particulate dispersed in air to explosion. Fire and explosion hazard increases as AIT decreases.
For powders initially dispersed in air but that have deposited on a surface forming a surface layer: Minimum Ignition Temperature (MIT); also often called Minimum Smoldering Temperature	Lowest temperature (T in °C or K) of a surface that can cause a dust layer of a given depth to catch fire or at least smolder. Fire and explosion hazard increases as surface MIT decreases,

* Note that LEL and UEL are in use in European standards while LFL and UFL are basically American terms. Wording of definition differs between America and Europe. In Europe the LEL is the highest concentration starting from zero that just does not explode, while in the USA the LFL is defined as the lowest concentration starting from zero at which the mixture can just explode. In practice, however, the meaning is the same. We use the American wording.

We concentrate here on discussing how particulate properties determine particulate hazards. Reducing hazards requires an understanding of the basics and actively applying this understanding to designing, manufacturing and handling particulates and the design and handling of relevant equipment.

4. Chemical and physical factors determining particulate hazards

4.1 Chemical factors

Particulates composed of unoxidized or not fully oxidized

substances are usually combustible; if combustible they can also explode. Here we divide combustible particulates into three categories: 1. *Unstable reactive substances*; 2. *Stable reactive substances*; 3. *Stable flammable substances*.

Unstable reactive substances are substances whose decomposition is exothermic. By themselves (e.g. no air present), unstable substance therefore tend to spontaneously decompose, and since decomposition is exothermic, heat is generated. When stored with insufficient cooling, unstable substances thus tend to heat up, causing a temperature increase. Since increased temperature generally exponentially increases the chemical reaction rate (of further decomposition, which is exothermic), a vicious cycle may result leading to increasingly fast temperature increase, increasingly fast decomposition reaction, etc., a 'run-away', ultimately causing explosion.

Examples of unstable reactive liquid substances produced in large quantities are ethylene oxide, propylene oxide, and organic peroxides; in much smaller quantities, concentrated hydrogen peroxide and nitroglycerine[16]. Examples of solid unstable substances produced in large quantities are ammonium nitrate, TNT, and other high explosives. Most large-volume unstable powders are, however, not commonly used in industry[17].

Stable reactive substances are stable in that by themselves, they do not decompose or their decomposition is endothermic (i.e. requires heat). They are reactive because they can spontaneously burn or explode—but only when in contact with air or water. *Pyrophoric* substances form a category of stable reactive substances; these spontaneously burn or explode when exposed to air. Examples are finely divided unoxidized metals, such as iron and aluminum, which spontaneously ignite when exposed to air[18]. Water-reactive substances which spontaneously react violently (burn, explode) in contact with water, form another category of stable reactive substances. Examples are the elements sodium, potassium, rubidium, and cesium and compounds such as aluminum bromide and calcium carbide[19].

The third category of substances, *stable substances*, consists of substances that by themselves do not spontaneously decompose and, in contact with air or water, do not spontaneously burn or explode. Stable materials that are non-oxidized (e.g. polyethylene powder, gasoline), or incompletely oxidized (e.g. alcohols, grain dust) are flammable, but will only burn/explode when pre-mixed with air, and additionally are *also subjected to an ignition source* (e.g. flame, spark) of sufficient energy (i.e. greater than the particulate's MIE and/or MIT). It is such substances—non-oxidized or only partially oxidized substances, and thus combustible—that by far cause the greatest number of fires and explosions.

In general, explosion sensitivity and in particular explosion severity tend to increase as certain chemical thermodynamic properties, such as heat of combustion, increase (expressed in terms of mass (e.g. kJ/kg) or, even more importantly, in terms of volume (kJ/m^3)). Higher heats of combustion usually result in higher adiabatic flame temperatures and thus (Equation 2) higher maximum explosion pressures. Since chemical reaction rates tend to increase exponentially with increasing temperature, substances with high adiabatic flame temperatures also tend to have higher laminar burning velocities and flame speeds, and thus higher rates of pressure increase, $(dP/dt)_{max}$. Finely divided reactive metals such as aluminum and magnesium have particularly high heats of combustion, thus high adiabatic flame temperatures (up to nearly 3600 K[20]), and thus high maximum explosion pressures (typically around 12 bara) and high K_{St} values (well above 300 bar m/s).

4.2 Physical factors

4.2.1 Similarities of gas/vapor and particulate explosions

Explosions of particulates (i.e. dust explosions, mist explosions) resemble gas and vapor explosions in that they also occur via chemical combustion; furthermore both deflagration and detonation are possible. Additionally, maximum explosion pressures of particulate explosions are generally similar to maximum explosion pressures of gas/vapor explosions. Thus (for deflagrations) typically 5–10 times the original pressure (Eq. 2), and for detonations roughly 20 times the initial pressure. As previously noted, this similarity is caused by the fact that the maximum adiabatic flame temperatures of common combustible particulates burning in air are usually similar to those of combustible gases/vapors, i.e. usual1y 1,500 to 3,000 K.

4.2.2 Differences: combustion mechanism of particulate explosions

The most fundamental difference between gas/vapor explosions and particulate explosions lies in their respective explosion mechanisms. Gas/vapor explosions occur *homogeneously*—within one phase, the gaseous phase. Mechanistically, gas/vapor explosions thus occur in a *premixed mixture of molecules* (e.g. methane molecules and oxygen molecules) which react with one another at a molecular level.

Relative to gas/vapor explosions, the mechanism of particulate explosions is more complex. Particulate combustion occurs *heterogeneously* (i.e. involving at least two distinctly different phases, a solid phase (solid (powder)) and/or liquid phase (e.g. mist)) and a gaseous phase (normally air)[21]. The complexity of the mechanism of particulate explosions is caused by many possible steps occurring sequentially in time:

1. Heating of the unreacted particles due to radiant heat from the approaching flame and/or conductive/convective heating via hot unburned gases.
2. Heating of the particle surface and, via heat conduction,

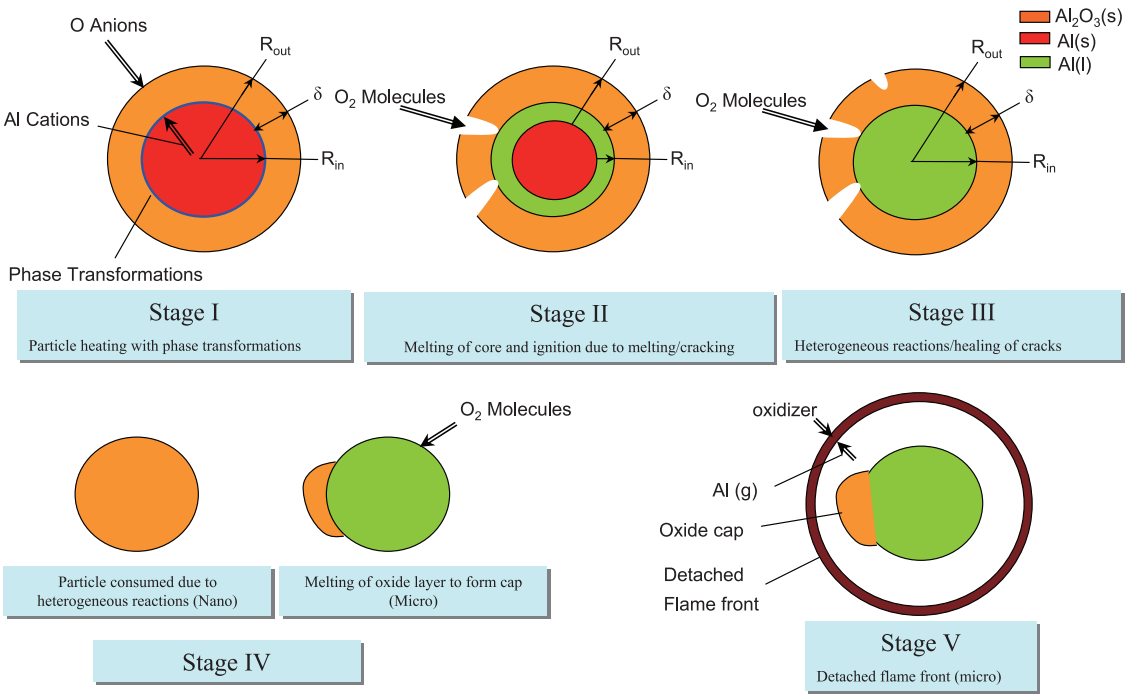

Fig. 2 Schematic presentation of various stages of the combustion (explosion) mechanism of burning aluminum particles: an example of the possible complexity of particulate explosion mechanisms according to Puri and Yang[23].

heating of the particle interior (particle volume).

3. Depending on the temperature reached by heating and the volatility of the particles (e.g. melting and boiling points), either no, partial or complete vaporization of the particles before the flame reaches them.
4. For relatively volatile substances (e.g. diesel fuel, polyethylene), complete vaporization and subsequent ignition and combustion of the resulting vapors which have been pre-mixed into the gaseous phase. This is essentially a gas explosion.
5. For partially vaporized particles, ignition of the combustible vapors formed (e.g. aluminum vapor boiling off molten aluminum particles) followed by ignition of the particles and further combustion at their surface. For such burning particles, diffusion of oxygen to the combusting surface zone and diffusion of combustion products (e.g. carbon dioxide, water vapor) into the bulk gaseous phase.
6. For substances of very high sublimation, melting and/or boiling points (e.g. graphite, tungsten) combustion exclusively on the surface of the particles. Various phase transformations depending on the melting and boiling points of oxides formed relative to the adiabatic flame temperature of the particles[22].
7. Eventually: further combustion on the surface of the charred remains of out-gassed organic particles (e.g. coal). Reaction rate controlled by diffusion to, from, and within the particle.

Mechanistically, of all these steps, gas/vapor explosions involve only step 4. Due to all this, the three-zone burning model has been developed, Dahoe et al.[6] for a dust explosion.

Diffusion is the rate-determining step of the heterogeneous combustion mechanism process pictured in **Fig. 2**: oxygen molecules must diffuse in from the bulk gaseous phase to the particle surface, and reaction products from the burning particles must diffuse out into the bulk gaseous phase. Diffusion usually occurs much more slowly than the rate of chemical reaction, whose rate tends to increase exponentially with temperature.

The complex mechanism of particulate combustion is influenced by many chemical and physical parameters such as: chemical composition; particle size (distribution); phase(s) of the particulates involved (solid and/or liquid); for liquids, volatility (vapor pressure as function of temperature (e.g. boiling point)); for solids, idem, including sublimation, melting, and boiling point; surface structure/specific surface area; heat conductivity and heat capacity; for substances forming liquid or solid oxides (e.g. coal, many metals, such as aluminum, magnesium, iron), melting and boiling points of the oxides; turbulence (affects rate of mass transfer (e.g. diffusion versus mixing via convection)); flame temperature (K) and thermal intensity (kW/m^2) of the combustion process (affects rate and mechanism of heat transfer).

Fig. 2 illustrates the sequential steps of a mechanism proposed for the ignition and combustion process occurring

in the explosion of aluminum particles[23].

Point number 4 listed above is the simplest mechanism of the explosion of particulates: the rapid combustion (deflagration) of small liquid droplets of a volatile combustible liquid (e.g. a mist of gasoline droplets) or cloud of small particles of an easily volatilized combustible solid (e.g. polyethylene) in turbulent air. Well before the flame of the explosion reaches such particles, the explosion's heat completely evaporates them into the vapor phase, and the turbulence pre-mixes the vapor molecules with the oxygen molecules of air. The ensuing explosion thus occurs homogeneously, i.e. as a gas/vapor explosion.

More complicated, and typical of many particulate explosions, is the case of droplets of a complex organic heavy liquid (e.g. heavy tar oil) or particles of a complex organic solid (e.g. bituminous coal). Also in this case, particulates of organic materials undergoing fire or explosion are first (partially) evaporated and/or (partially) pyrolyzed, i.e. pre-heated and thus brought into the gaseous/vapor phase as molecules, which chemically react further. Like the previous case, this evaporation/pyrolysis (pre-heat) is brought about by the heat of the approaching flame. The difference with the previous case in which the combustion process occurs completely in the gaseous/vapor phase (i.e. homogeneously), is that here the combustion process which began in the gaseous phase continues on the surface of the particles, i.e. this combustion occurs heterogeneously.

Because of the existence of two distinct phases, gaseous/vapor and solid (or liquid), the pre-heat zone and the flame zone of particulate explosions are much thicker than in gas explosions (cm versus mm). Furthermore, once the combustion process is going, it may become even more violent due to micro-mist formation as a result of the drag on liquid particulates by the faster-flowing gas[24].

4.2.3 Particle size and particle size distribution: smaller particles = greater hazard

Reducing particle size tends to increase the particulate hazard, as expressed by both explosion severity and explosion sensitivity indexes. **Figs. 3**[25] **and 4** show examples of the huge effect of the particle size on, respectively, LEL and MIE (explosion sensitivity); **Fig. 5** shows the effect of particle size on maximum pressure and rate of pressure rise (explosion severity).

Given the decisive effects of particle size on the particulate explosion hazard it is surprising that many, especially older (ca. pre-2000), studies presenting explosion behavior as a function of the particle size are neither clear as to how the particle size is defined nor how it is measured. Already in 1980, Ballal[29] noted this hiatus, commenting: "Clearly, from the point of view of fundamental combustion studies, it is the Sauter mean diameter (SMD)[30], particle size

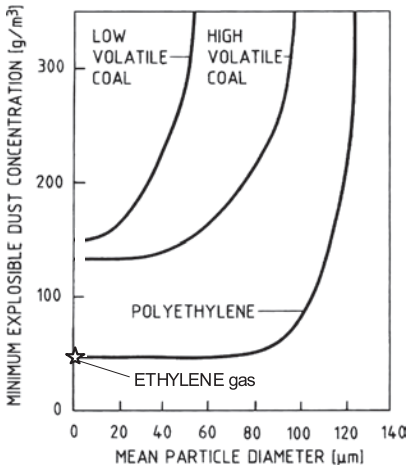

Fig. 3 Effect of mean particle diameter on Lower Explosion Limit (LEL; here expressed as 'Minimum Explosive Dust Concentration') of polyethylene powder and high- and low-volatile coal (Dobashi[25]).

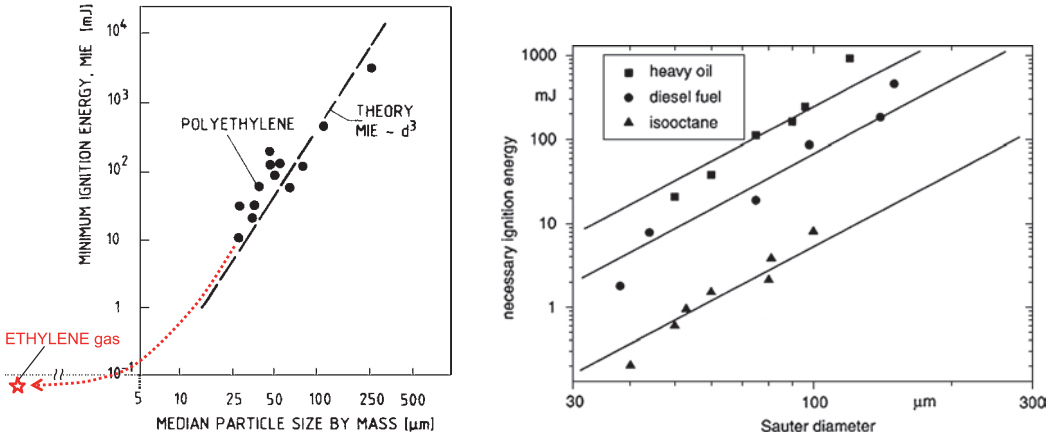

Fig. 4 Effect of particle size on Minimum Ignition Energy (MIE). At *left*[26]: effect of median particle size by mass on the Minimum Ignition Energy (MIE) of polyethylene powder. At *right*: effect of particle size (Sauter Diameter) on the MIE of three mists[27]. Results seem to indicate that within this size range, MIE increases with the third power of increasing particle diameter.

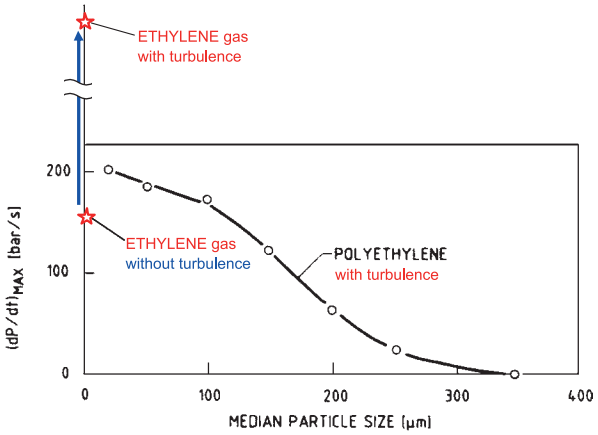

Fig. 5[28] Effect of median particle size by mass on explosion severity: maximum rate of pressure rise of powdered polyethylene as a function of particle size. (Section 4.2.4, which discusses the importance of turbulence, explains why ethylene gas is also included here.)

distribution, and equivalence ratio that are of great importance." Yet even in Eckhoff's 2003 text[31], presently perhaps the best single general source on dust explosions, the Sauter mean diameter is not mentioned[32]. Föster explicitly discusses the importance of how the particle size is measured and expressed, including the Sauter diameter[33]. Experimental results that do not clearly state how the particle size is expressed should be viewed with circumspection.

Particulates with the same average particle size often have different particle size distributions, which can result in significantly different particulate explosion hazards. For example, a powder having a broad particle size distribution may exhibit high explosion sensitivity and severity, whereas the same powder—with exactly the same chemical composition, but with a much more narrow particle size distribution around the same median size—may (at standard test conditions) not explode at all. The reason is that the first powder contains a significant fine fraction which is much more sensitive to ignition than the coarse fraction. These fines are easily ignited, and the ensuing combustion is sufficiently energetic to ignite the coarser fraction. Particle size distributions should therefore not be characterized by median size or an undefined mean size, but by a well-chosen mean size, such as the Sauter mean diameter. During size measurements, the size of so-called equivalent spheres is determined which is dependent on both particle shape and measurement principle[34]. We stress that measurement results should be critically reviewed when comparing results coming from different techniques.

Particles are often assumed to be spheres. However, in general practice particles may well have irregular shapes, resulting in a larger surface area than the corresponding sphere with the same volume. Not surprisingly, increasing specific particle surface area (m^2/g) generally increases powder explosion hazards, explosion sensitivity and severity.

Note that the diameter axis of **Figs. 3, 4** (left), and **6** (from Dobashi, 2008) extends to (near) zero and thus to molecular size. These figures suggest that while explosion hazards generally strongly increase as the particle diameter decreases, below a certain diameter value, the explosion hazard increases much more slowly, or hardly at all, the limiting value occurring at particle diameters of zero, i.e. molecular diameter. We return to this question when discussing nanoparticles in Section 7, Current and future research.

4.2.4 Effects of turbulence

By turbulence we mean the highly irregular motion of fluids (here gas) in which instantaneous velocities (i.e. speed and direction of fluid motion) exhibit rapid, irregular, and apparently random fluctuations. Superimposed on the net velocity of the fluid are separate small pockets of fluid called eddies or vortexes, whose size and (rotational) velocity similarly exhibit rapid, irregular, and apparently random fluctuations. Turbulence is a prime example of so-called complex behavior: i.e. behavior in a system in which a seemingly negligible change in a part of the system can greatly change the whole system's behavior, making accurate and precise prediction impossible. Complex behavior is not deterministic; it is stochastic (i.e. probabilistic).

Turbulence is essential for the occurrence of particulate explosions, being necessary to disperse particulates, mix them with air, and keep them suspended. Additionally, turbulence has a complex effect on the dust explosion hazard. On the one hand, *increased turbulence reduces the hazard by reducing explosion sensitivity* (e.g. increasing MIT, MIE, LEL, etc.)[35]. This effect is due to the fact that at the limits of ignition (i.e. at the conditions of MIT, MIE, LEL, etc.), increased turbulence hampers ignition by dispersing ignition energy. The physical reason for this is that increased turbulence mixes more cold fluid into the just-barely ignitable kernel of air plus particulates, and this quenching effect prevents ignition.

On the other hand, for an already ignited, highly energy-rich particle-air mixture (e.g. an already ignited polyethylene-air mixture in the middle of its explosive range), *increased turbulence vastly increases the hazard by increasing explosion severity* (i.e. especially by increasing flame speed, S_f, and thus $(dP/dt)_{max}$ and the K_{St} factor). Reasons for this effect are firstly, that greater turbulence tends to increase the surface area of the flame of a burning mixture. Turbulent eddies cause an initially flat (two-dimensional) flame to transform into a (severely) 'wrinkled' three-dimensional flame, thus greatly increasing the flame's surface area. Since the flame's surface is the area on which energy is being released (W/m^2), an increase in surface area increases the total rate of energy release. That turbulence increases the explosion severity applies not only for dust and mist explosions, but also for gaseous

explosions occurring in energy-rich mixtures, as **Fig. 5** illustrates for the effect of turbulence on deflagrations of ethylene gas. Turbulence is the mechanism that can accelerate the flame speeds of deflagrations from ca. 10 to hundreds of meters per second and even cause deflagrations to transit into detonations.

A second reason is that turbulence also tends to decrease the slowing effect of diffusion, diffusion being a factor inherently reducing the rate of combustion of multi-phase (i.e. heterogeneous) mixtures. One can consider each particle to be enveloped in a thin laminar 'film' of a given thickness, through which diffusion takes place[36]. Increased turbulence reduces the thickness of this laminar film, thereby reducing the time it takes for diffusion through the film to occur. When diffusion is the rate-determining step, faster diffusion speeds up the rate of energy release, thus increasing the severity of the explosion. (However, at a high turbulence intensity, this effect can be countered by flame quenching and extinction due to a high cooling rate.)

Through turbulence, a particulate explosion can become self-feeding; i.e. a small explosion starting somewhere in a plant grows due to the settled/deposited dust (or a liquid film) on floors and machinery being stirred up by the pressure waves and turbulence generated before the flame arrives. Explosions can in such cases propagate from one plant or installation to another—with devastating effects. Many disastrous dust explosions of this kind—in which a primary explosion generates and ignites one or more secondary explosions—are known[37]. Dust deposits of only a few millimeters thickness or less, usually caused by bad house-keeping[38] (and thus ultimately poor management), are sufficient to raise dust concentrations into the explosive range (i.e. above the LEL).

Additionally, inside a process installation a small, incipient explosion can, as it propagates through piping connecting vessels within the installation, generate increasing turbulence. It is this self-generated turbulence that can cause flame speeds to accelerate dramatically. In the extreme case, flame acceleration accelerates the flame speed from values typical of a deflagration, i.e. ca. 10 m/s, to supersonic velocities: a detonation. This feared phenomenon is called a *deflagration-to-detonation-transition:* DDT[39].

Another dangerous phenomenon associated with turbulence as an explosion propagates between interconnected vessels is *pressure piling*[40]. Effects pressure piling causes in a secondary vessel are pressure increase, temperature rise (due to this compression), turbulence caused by the flow into the secondary vessel from a primary vessel, and possibly also flame-jet ignition as the explosion propagates from the primary to the secondary vessel. These factors can result in vastly increased explosion pressures and rates of pressure rise in secondary vessels. It is for these reasons that the propagation of incipient explosions must be prevented (e.g. via compartmentalization; see **Table 4**).

Theoretically, turbulent flow can be analytically predicted using Newton's Laws of motion applied three-dimensionally (i.e. Navier-Stokes equations). In practice, however, turbulence is 'too complex' for analytical solution. This is frustrating, considering the importance of predicting the behavior of turbulent systems, such as the weather, fluid flow of all types (e.g. around automobiles, ships, aircraft), combustion of fuel in engines (e.g. diesels, jet turbines), and explosive combustion. The great breakthrough in calculating turbulent behavior was the development of Computational Fluid Dynamics (CFD), made possible by the advent of (super-)computers. A great breakthrough in directly measuring turbulence before and during particle explosions, e.g. in testing equipment, was the development and application of Laser Doppler Anemometry[41,42].

Computational Fluid Dynamics (CFD) has led to breakthroughs in modeling and thus predicting gas/vapor explosions, and more recently, particulate explosions. We return to CFD in Section 7, Current and future research.

4.3 Combined chemical and physical effects

4.3.1 Effects of humidity

Chemical composition determines not only combustibility, but also whether and to what degree a particulate is hydrophilic ('water-loving') or hydrophobic ('water-hating'). Hydrophilic powders tend to adsorb/absorb air moisture, thus forming a layer of water molecules on the particle surface. This layer causes particles to stick together (agglomerate), which can strongly increase the virtual particle size and thus reduce the specific surface area. The specific surface area plays an important role in chemical kinetics and adsorption/absorption kinetics and therefore strongly influences the explosion hazard. In particular the Minimum Ignition Energy of hydrophilic powders is often strongly reduced by reducing the concentration of adsorbed/absorbed water. In particular, MIE values may decrease by a factor of 100 or even more[43].

Additionally, a layer of adsorbed water tends to increase the electrical conductivity of powders, thereby reducing the tendency to generate and retain a static electrical charge, thus reducing the hazard of ignition by static electricity[44].

4.3.2 Upper explosion limit, explosive range, volumetric explosion energy

Mixtures of combustible gases and vapors with air generally have sharply defined explosion limits (LEL and UEL values) and thus sharply defined explosive ranges (UEL – LEL). Additionally, the UEL values of gases and vapors at ambient pressure and temperature are typically roughly two times the stoichiometric concentration.

By contrast, particulates have less sharply delineated explosion limits; in particular, the upper explosion limits

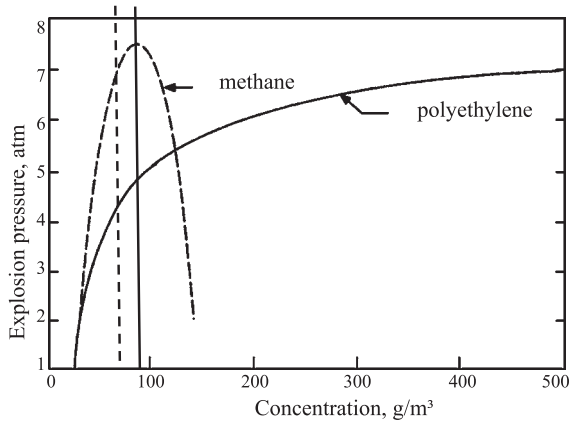

Fig. 6 Comparison of explosion limits for a gas explosion (methane) and a dust explosion (polyethylene powder) in air. Stoichiometric concentration of methane = 67.8 g/m^3 (vertical striped line); stoichiometric concentration of polyethylene in air = 87.1 g/m^3 (solid vertical line).

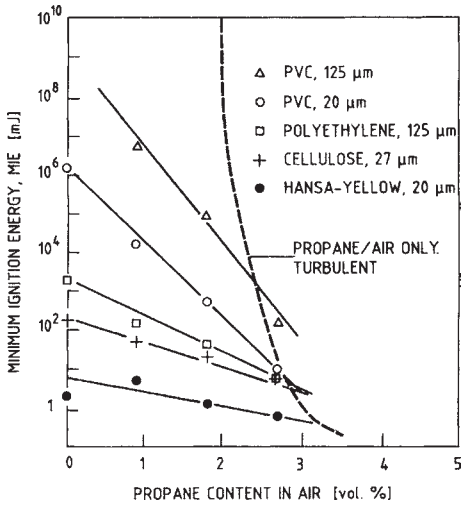

Fig. 7 Hybrid mixture: Effect of adding flammable gas (propane). Minimum Ignition Energies (MIEs) of various powders.

(UELs) of particulates are poorly defined for two reasons. Firstly, a particulate-air mixture initially above the UEL-concentration will, through deposition caused by gravity, eventually enter the explosive range. For this reason the UEL value for a particulate usually has little practical significance and can even be dangerous by engendering false confidence.

Secondly, while a gas/vapor explosion takes place between molecules, a particulate explosion involves the surface of the particles. As the mass concentration of the powder in a powder-air mixture increases to (far) above the theoretical (mass-based) stoichiometric concentration, the powder particles simply burn to a thinner depth. Thus, while gas/vapor explosions generally show a sharp maximum explosion severity at roughly the stoichiometric concentration, and explosion severities fall sharply past this concentration, the dust explosion severity is generally reached (far) above the (mass-based) stoichiometric concentration and, additionally, it falls off slowly (often far) above the stoichiometric concentration. **Fig. 6** illustrates this effect graphically, contrasting the sharply defined explosion severity of methane in air compared with the much flatter behavior of polyethylene powder in air, as a function of concentration[45].

Energy content increases with substance amount. Common gases typically have a density of roughly 1 kg/m^3 (at STP). Solids and liquids generally have a much higher density, typically 1,000 kg/m^3 or more, thus at least about 1,000 greater than gases. Therefore a typical powder-air mixture often contains more energy per unit volume (i.e. volumetric energy content, J/m^3) than a gaseous mixture. This greater amount of energy manifests itself in that a particulate explosion lasts longer in time than gas explosions. Important to note is that, for these reasons, explosions of aerosols (dusts, mists) also tend to cause more fire damage than explosions of gases.

Furthermore, since particulate explosions can occur at concentrations far above stoichiometric concentrations, a particulate explosion occurring in and rupturing closed equipment within a factory can emit large quantities of hot unburned material. Upon contact with air this hot unburned material can explode, resulting in a second explosion occurring inside the factory.

4.4 Hybrid mixtures

Hybrid mixtures are mixtures of combustible solid particles and air containing a combustible gas and/or vapor. Minimum ignition energies (MIEs) of typical flammable gas/vapor mixtures (e.g. methane in air, gasoline vapor in air), which are mixtures of individual molecules, are often very low (e.g. MIE values typically between 0.1 to 1 mJ; by comparison a human body can generate a static electric spark of 10 mJ); such low MIE values of gases/vapors lead to a large ignition hazard. Many common powders, however, have MIEs at least an order of magnitude higher than flammable gases/vapors, i.e. above 10 mJ. The insidious hazard of hybrid mixtures, first clearly discussed by Bartknecht already in 1980[46] and illustrated in **Figs. 7**[47] **and 8**[48], is that the presence of even low concentrations of flammable gases/vapors (e.g. originating from traces of evaporated solvents) can greatly increase the explosion sensitivity by reducing LEL values and drastically reducing MIE values; idem for the explosion severity, in particular the rate of pressure rise. Mixtures of combustible solid particles and air containing a combustible gas and/or vapor (hybrid mixtures) thus combine the worst hazards of dust explosions and gas explosions: the high explosion sensitivity of gas explosions, the high energy density of dust explosions, the high rate of pressure rise of gas/vapor

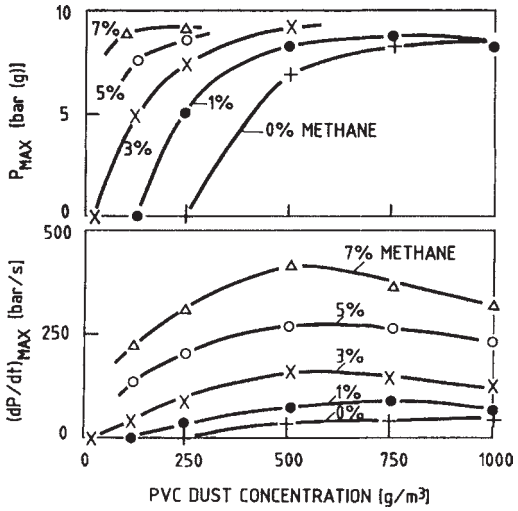

Fig. 8 Hybrid mixture: Effect of adding flammable gas (methane) on Lower Explosion Limit (LEL), maximum explosion pressure (P_{max}) and maximum rate of pressure rise, $(dP/dt)_{max}$, of PVC-powder.

explosions, and explosion pressures as high as those of gas/vapor explosions.

We discuss recent research on hybrid explosions in Section 7, Current and Future Research.

5. Knowledge of the explosion behavior of particulates applied in fuel air explosive (FAE) weapon technology

5.1 General

So far we have reviewed scientific and technological knowledge with the goal of identifying and reducing particulate fire and explosion hazards. But such science can also be used for military goals, and additionally, understanding the technology can lead to safety improvements.

As noted, the most powerful explosions are detonations. Detonations of explosive solids such as TNT occur at supersonic velocities (flame speeds between 5,000 to almost 10,000 m/s) and produce extraordinarily high maximum explosion pressures (between 200,000 to nearly 500,000 baro). However, from a military standpoint, conventional high-explosives such as TNT have some inherent limitations. Firstly, while the maximum explosion pressures generated are enormous, they decrease rapidly with distance, since the TNT explosion is by approximation a 'point source'. Thus the destructive effect is restricted to a relatively small area and volume. Secondly, the extraordinarily high pressures developed are actually much too high for a number of military purposes. Thirdly, conventional explosives such as TNT contain oxygen within their molecule. This oxygen is necessary to sustain the detonation process, but it also makes up a substantial part of the weight of the explosive. But oxygen is freely available in air. By using atmospheric oxygen, rather than having oxygen within the explosive itself, the destructive effect of a given mass of explosive can be substantially increased.

From a military standpoint, a useful explosive device (e.g. bomb) would have the following properties (**Table 3**).

Perhaps ironically, and partly as a result of investigating accidental industrial explosions such as the devastating vapor cloud explosion at Flixborough (UK) in 1974, with the goal of preventing such explosions and increasing industrial safety, scientific discoveries were made that facilitated the creation and further development of weapons meeting all the above-mentioned specifications; these are called Fuel-Air Explosives (FAEs)[49].

A typical fuel-air explosive (FAE) such as a bomb, consists of a container of fuel and two separate explosive charges. After the bomb is dropped the first explosive

Table 3 Possible general requirements for a particle-based bomb as shown feasible in open sources

1.	Generate a maximum pressure wave of approximately 15 to 20 bar overpressure, as such pressures are 100% lethal to humans, obliterate conventional buildings, destroy communication antennae, and severely damage and/or overturn vehicles.
2.	Generate this overpressure over a large surface area and large pie-like volume. Generate and maintain this pressure for a sufficiently long time duration (Δt), giving it more time to do damage (i.e. by creating a larger explosion impulse, $\int P dt$ (Eqs. 5–6)). Additionally, create a flame with the highest possible temperature to generate more lethality and damage.
3.	Produce the above-mentioned effects with a device of minimum volume and weight (e.g. by using the oxygen available in air).
4.	When used within an enclosed area such as bunkers or caves, consume the oxygen in the air, and by the nature of the combustion process sustaining the explosion, generate toxic gases such as carbon monoxide to poison those not killed by blast. Additionally, due to the rapid cooling of the hot explosion gases within the enclosed area, subsequently create a significant underpressure that can fatally damage lungs (i.e. create a partial vacuum, also called rarefaction).
5.	Be cheap to produce and safe to store and to transport.

charge bursts open the container and disperses the fuel into a cloud of fine particulates (droplets and/or dust) that mix with atmospheric oxygen. This cloud flows around objects and penetrates into structures. The second charge then detonates the entire fuel-air cloud[50], which has a substantial volume and is thus certainly not a 'point source'. The detonation, which occurs throughout the whole cloud, generates a blast wave of ca. 20 bar overpressure within the cloud which completely destroys unreinforced buildings and kills 100% of exposed people (e.g. soldiers in foxholes). Outside the fuel-air cloud the explosion blast wave attenuates, but since overpressures of even some tenths of a bar can cause severe damage, the 'death-and-destruction diameter' of an FAE (i.e. inside and outside the fuel-air cloud) can be very large relative to normal bombs; e.g., for a 500 kg bomb ca. 100 m, thus an area of ca. 8,000 square meters[51]. For obtaining a blast and flame, FAEs are the most powerful non-nuclear bombs. It was once thought that they might even be used to simulate nuclear explosions[52]. (We add, however, that in addition to offensive use, FAEs are important defensively. Through their low detonation pressure and long explosion duration, FAEs are used to clear minefields, thus obviating the need for manual clearance.)

A problem with FAEs is that their initiation to detonation is quite difficult, requiring an ignition energy typically up to a million times greater than that needed to ignite a deflagration[53]. Additionally, to ensure complete detonation in the entire fuel-air cloud, the particle concentration must vary little around an optimum value. (This fact can also help to increase civil safety by designing measures that reduce the chance of accidental detonations.)

The nature of FAEs is such that up-to-date information continually appears in (in the authors' opinion) relatively reliable websites such as Wikipedia, IMAS (International Mine Action Standards), and Global Security.

6. Preventing and mitigating particulate explosion hazards

An abundance of literature exists describing course, prevention and mitigation of particulate explosions, including not only scientific and technological aspects, but also relevant standards, norms, legislation, and proper management (e.g. see Appendix). Here we divide prevention/mitigation into four categories:

1. Good management
2. Reducing the hazard of the particulate itself
3. Reducing the hazard of the system producing the particulate
4. Combinations of Points 1 to 3

6.1 Reducing hazard through good management

It is now known that poor management is the root cause of the overwhelming majority of industrial fires and explosions, as shown by countless investigations[54]. Not the lack of knowledge, but unawareness or not properly applying it. It is for this reason that comprehensive safety management systems have been developed over the last three decades. Indeed, Points 2 to 4 above follow from good management. It is beyond our scope to discuss this extensive topic; here we merely cite two representative publications[55] and discuss this point a bit further in 6.4.

6.2 Reducing the hazard of the particulate itself

Most technical methods to reduce particulate hazards follow logically from the basics described in previous sections, being simply negations of causative or exacerbating factors; e.g. since smaller particles increase the hazard, increase the size of particles. Most of these methods are thus 'scientifically trivial'—but nevertheless effective: e.g. "increasing particle size", "increasing particle humidity", "preventing hybrid mixtures", etc. Such measures have been known for decades and are described in detail in literature (e.g. see Appendix).

6.3 Reducing the hazard by improving the system in which the particulate is produced, stored, transported

The hazard is reduced by firstly preventing explosions from occurring and secondly, mitigating their effects should an explosion nevertheless occur. Prevention is achieved largely by, where possible, eliminating sources of fuel (e.g. practicing 'good housekeeping') and eliminating possible ignition sources such as (static) electrical and mechanical sparks and hot spots[56]. The indexes listed in **Table 2**, which relate to ignition, logically suggest possible preventive measures: e.g. keeping particulate concentrations below LEL; through inertization, reducing oxygen concentrations ideally to below LOC; maintaining all surface temperatures below MIT; etc. Protective measures relate to hindering the propagation of an explosion. We briefly summarize a number of these measures in **Table 4**. Our discussion is necessarily superficial; in addition to extensive description in textbooks (see Appendix), excellent reviews of prevention and mitigation also exist[57].

6.4 Combinations of Points 1 to 3: Inherently Safer Design (ISD), Layers of Defense Approach (LOPA), 'Holistic' Approaches—components of 'Loss Prevention'

Over the past decades, new design methodologies called

Table 4 Some important mitigative measures

Type	Working principle
Compartmentalization	Prevent an explosion occurring in one part of the system from propagating into other parts of the system; e.g. by placing quick-acting valves in interconnecting piping
Explosion-proof construction	Build equipment strong enough to withstand maximum explosion pressure
Explosion suppression	Rapidly disperse materials that stop explosion at very early stage
Explosion venting	Provide system with weak spots that burst open to the atmosphere at low overpressures occurring at the beginning stage of deflagration, thus preventing development of maximum explosion pressure

Inherently Safer Design (ISD) and Layers of Protection Analysis (LOPA) have been developed that systematically avoid or at least mitigate chemical hazards like fire and explosion. Inherently Safer Design (ISD) is based on the logical negation of basic factors causing and exacerbating a hazard[58]. ISD uses keywords such as: Reduce, Substitute, Attenuate, and Simplify. Layers of Protection Analysis, whose starting point in the ideal case is Inherently Safer Design, is based on designing successive rings of 'protective layers' ("Layers of Protection") around a process[59]. Each layer offers protection and/or mitigation in the event of disturbances and failure of a preceding layer. ISD and LOPA are examples of the systematic, comprehensive, and science-based discipline known as Loss Prevention[60], which has been developing since the 1980s. The ISD- and LOPA-concepts date from approximately the end of the 20th century, but apparently only during this last decade have they been specifically applied to controlling dust explosion hazards[61] and, most recently, explosion hazards of nano-particles[62]. Incorporating the ISD and LOPA design methodologies into computer-based 'Expert Systems', which also include explosion indexes (**Tables 1 and 2**) for the materials used and produced, represents a formidable new tools for achieving safety through basic process design[63]. Perhaps even more promising are 'holistic' approaches to process safety. These include systematic technical approaches (e.g. ISD, LOPA, Quantitative Risk Analysis (QRA)), but expand considerably to include broad social-economic factors affecting top management such as the 'emergent' (i.e. 'complex') nature of society. A key goal is to find a proper balance between the pressure to increase profitability and (the costs of) adequate safety, and to provide top management with effective tools[64].

7. Current and future research

7.1 General

A plethora of knowledge already exists concerning the fire and explosion hazards of particulates and their effective control. Once again we emphasize that awareness, dissemination, and proper application of existing knowledge, i.e. the key responsibilities of management, are sufficient to prevent the overwhelming majority of industrial incidents.

Nevertheless research continues, with interesting and useful results. Particulate explosion falls within the much larger field of particle combustion, which is of major importance because a significant part of total world energy generation occurs through particulate combustion (e.g. diesels, jet engines, coal-based electric power generation). Up-to-date reviews of state-of-the-art particle combustion science and technology of this type therefore regularly appear in textbooks[65]. Combustion science also relates to achieving advanced (military) goals such as powering hypersonic aircraft using detonation-based engines, possibly fueled by aluminum nanoparticles[66].

Here we concentrate on the particulate research relating to industrial hazards. Many excellent reviews of particulate fire and explosion hazards have appeared over the years[67]. A general line of progress in research has been firstly, an increasing knowledge and insight into particulate explosion behavior and explosion mechanisms and better quantitative description and prediction. Secondly, stimulated through further development of CFD, better modeling, enabling more accurate prediction of fire and explosion ignition and propagation and the design of more cost-effective preventive and protective measures. Below we summarize some interesting areas in which progress and, for particulate explosion modeling, certain breakthroughs have been made.

We divide our discussion into particles themselves (nanoparticles and hybrid mixtures) and systems containing particles.

7.2 Effects of reducing particle size towards the size of molecules: Nanoparticles

Spherical nanoparticles are defined as those having a diameter of less than 100 nm (0.1 micron); non-spherical nanoparticles are defined as those having at least two dimensions smaller than 100 nm. Due to their special properties, the production and use of nanoparticles is strongly increasing. Interest in health and safety aspects of

nanoparticulates has grown recently because of their ability to penetrate into the deepest parts of the lung[68] and their suspected heightened explosion hazards[69].

In discussing the effects of reduced particle size it is useful to distinguish between different groups of materials that may exist in the nano range such as:

1. Natural organic materials (e.g. grain, linen, sugar, etc.)
2. Synthetic organic materials (e.g. plastics, pigments, pharmaceuticals, etc.)
3. Carbon, coal and peat
4. Stable reactive substances such as reactive metals (e.g. Al, Mg, Si, Ti, etc)
5. Unstable reactive substances such as high explosives (e.g. TNT, HMX, CL-20)
6. Unstable mixtures composed of different powdered substances (e.g. gunpowder)

(Note that 'Stable reactive substances' and 'Unstable reactive substances' are defined in Section 4.1.)

In a thorough review, Eckhoff[70] compares the explosion behavior of nano- versus micron-sized particles and presents a number of general conclusions:

1. For all commonly used powders (Groups 1 to 4), the explosion hazards, as expressed by the explosion severity (our **Table 1**) and explosion sensitivity indexes (our **Table 2**), increase strongly as the particle size decreases from mm values to the lower end of the micron range (roughly 1 to 10 microns (see our **Figs. 3–5**).
2. Nearly all experimental data on nanoparticle explosion hazards are available only in the upper-end of the nano range, i.e. around 100 nm or not much lower (usually >> 10 nm; lowest values found were 15 nm[71]).
3. Explosion sensitivity, particularly as expressed in the MIE value, continues to increase as particle size decreases down into the (higher end) of the nano range; i.e. MIE values continue to decrease with decreasing particle size into the nano range.
4. By contrast, explosion severity, as expressed by P_{max}- and K_{St} values, appears **not** to increase as particle size decreases from the micron range into the (high) nano range.

Point 1 above follows logically from the fact that specific surface area increases as particle size decreases (e.g. wooden logs do not explode, but finely powdered sawdust does; the finer the sawdust, the greater the explosion hazard).

Concerning Points 2 and 4 above, Eckhoff notes inherent physics-based limitations in creating true nanoparticles and dispersing them into stable clouds of true nanoparticles[72]. Coagulative forces such as van der Waals' forces increase significantly as particle size decreases from the micron into the nanometer range. Thus nanoparticles inherently tend to coagulate into conglomerates of multi-particles. Also due to strong coagulative forces, it is difficult to disperse nanoparticles as nanoparticles, and even once dispersed into a cloud, true nanoparticles will, through collisions, tend to rapidly (e.g. before ignition occurs) coagulate into larger, micron-sized conglomerate particles.

With this explanation in mind, Eckhoff explains the apparent anomaly of Point 3 (explosion sensitivity, expressed as MID) by theorizing that the electric spark, inherent to the MIE testing procedure, may be powerful enough to cause eventually formed conglomerates to break up into true nanoparticles.

Concerning Group 4 powders mentioned above (Stable reactive metals such as aluminum), Eckhoff briefly mentions another factor affecting explosion severity and sensitivity: the degree to which reactive metal particles are covered with an oxide layer. An oxide layer is completely non-reactive and is a heat sink, thus tending to inert the powder. Obviously the finer the particles, the greater the relative mass of even a thin oxide layer and thus the greater the reduction of explosion hazard[73]. This phenomenon was widely known already decades ago, since the production of fine powders of reactive metals.

Nanoparticles of reactive metals form a special case as more explosion research has been done on them than on any other type of nano-particulates. This is due to their widespread (military) use—past, present, and future—as components of pyrotechnics, rocket propellants, and (fuel-air) explosives. It has long been known, for example, that if sufficiently fine and sufficiently pure (e.g. free of oxide film), many metals are so reactive that if suddenly dispersed in air they will spontaneously—without any external ignition source—burn/explode; i.e. they are pyrophoric[74]. Being pyrophoric, their MIE is zero and their MIT is below ambient temperature. Whether pyrophoricity occurs in practice depends on a heat balance involving factors like exothermicity of the oxidation reaction, particle size, thickness of oxide layer, and boiling points of metal and oxide relative to adiabatic flame temperature[75,76]. The pyrophoric nature of fine powders of reactive metal, especially those in the nano range, complicates testing procedures to determine explosion indexes, requiring modification of standard dust explosion testing equipment and procedures for explosion severity[77] and explosion sensitivity[78].

Experimental measurements, complemented with theoretical studies, suggest some very interesting particle combustion and explosion phenomena unique to sub-micron/nano-sized particles. The following figures illustrate some of this behavior.

For powders that do not readily volatilize such as carbon and metals with high melting points, **Fig. 9** illustrates the change in reaction mechanism as the particle size decreases from the low mm range to below roughly about 1–10 μm: the combustion mechanism changes from being diffusion-controlled in the region of large particles to being

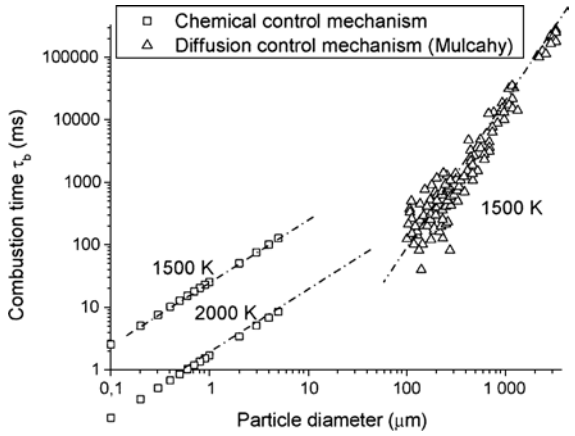

Fig. 9 Combustion time (ms) versus particle diameter (micron) of carbon[79].

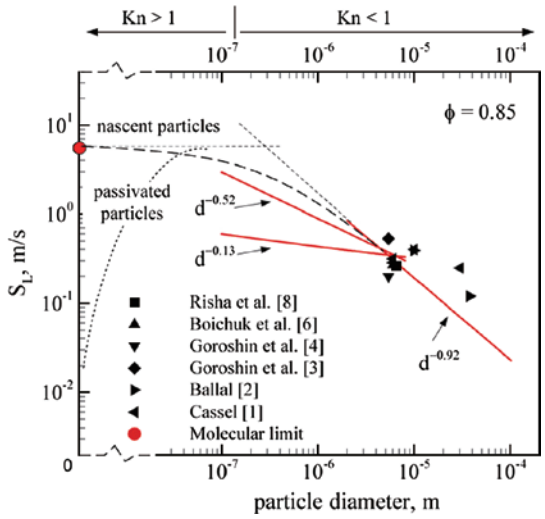

Fig. 10 Effect of decreasing particle size on laminar burning velocity (S_U) of reactive (i.e. non-pre-oxidized; here called 'nascent') aluminum particles[81].

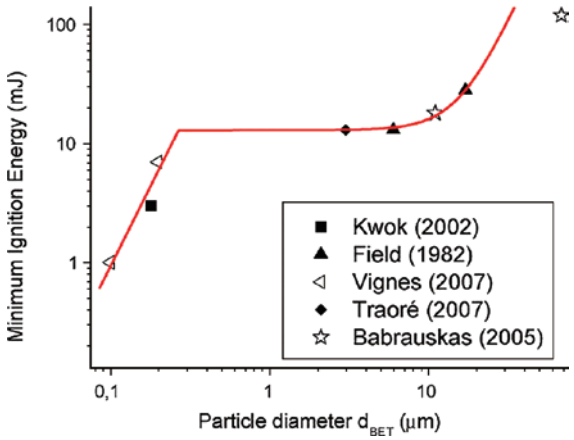

Fig. 11 Effect of reduction of the particle diameter on the Minimum Ignition Energy (MIE) of powdered aluminum (chemical-kinetically controlled at small particle sizes and diffusion controlled at larger sizes)[83].

chemical-kinetically controlled in the region of increasingly smaller particles[80]. As previously noted in Section 4.2.2, gas/vapor explosions, which occur between molecules, are chemical-kinetically controlled and dust explosions of large particles are diffusion-controlled. But as particle size decreases and begins to approach that of gas molecules, it is to be expected that powder explosions will progressively become more like gas/vapor explosions.

Huang et al. (**Fig. 10**)[81] also illustrate the transition from diffusion control to chemical-kinetic control of the reaction rate as particle size decreases from the micron range into the nanometer range (Bidabadi et al. present nearly identical results and conclusions[82].) As already noted, a fundamental property of the flame of a given mixture of a combustible substance in air at given conditions is its laminar burning velocity, S_U. Also as mentioned before, hydrocarbon fuels in air exhibit laminar burning velocities of tens of centimeters per second or somewhat higher. Highly reactive combustible gases such as hydrogen and acetylene have laminar burning velocities in air typically in the meters-per-second range. Reactive combustible particulates in the micron range have laminar burning velocities in air that are typically approximately a factor of ten smaller. **Fig. 10** illustrates the effect of decreasing particle size on the laminar burning velocity (S_U) of powdered aluminum in air, with extrapolation into the nanometer range and even to the particle size range of molecules. Huang et al.[81] thus predict that as the particle size decreases and eventually reaches the molecular range, the laminar burning velocities of aluminum, a highly reactive metal with a very high adiabatic flame temperature, will be quite similar to those of reactive gases and vapors (i.e. ca. 5 m/s for aluminum versus 3 m/s for hydrogen).

This same line of reasoning—nanosized particles in the homogeneous, chemical-kinetically controlled regime, and micron-sized particles in the heterogeneous, diffusion controlled regime—can also be applied to the *ignition* of fine metallic particles (i.e. their MIE and MIT), as is shown in **Fig. 11** for the Minimum Ignition Energy (MIE) of aluminum particles[83]. That is: As the particle diameter approaches the molecular diameter, the MIE values of particulates approach those of gases/vapors, i.e. for reactive metal powders, MIE values below 1 mJ. (And, as noted above, very fine powders of non-oxidized stable reactive metals are pyrophoric: MIE = 0; MIT below ambient temperature.)

Concerning Group 5 powders (unstable substances such as high explosives), it appears that reducing particle size from the micro to the nano range increases (military) usefulness by increasing explosive power while reducing sensitivity to ignition (the latter as expressed by impact sensitivity). This was found for one of the most powerful explosives known, CL-20[84], as well as the explosives TATB and HMX[85] (all these explosives are more powerful

than TNT).

Concerning Group 6 powders (unstable mixtures such as gunpowder), it is reported that, at least for flash powder used in fireworks, reducing particle size from the micro to the (upper) nano range increases explosive power but in contrast to results reported above for a number of high explosives, also increases ignition sensitivity (as expressed by impact sensitivity)[86].

We conclude this section by commenting that more research needs to be done in the lower regions of nano-sized particulates (i.e. << 100 nm) to be certain about the explosion behavior of particles closely approaching molecular size. It would seem reasonable to these authors (SML and HJP) to assume for the time being that for such particles, their explosion indexes as expressed in Tables 1 and 2 will increasingly resemble those of gases/vapors with a similar basic molecular structure, as chemical kinetics starts to control the rate of overall reaction. But this must be experimentally verified, because pyrolysis and diffusion rates in the case of organic dusts and the breaching of oxidized surfaces of metal particles can stretch reaction times. Such effects will mitigate explosion index values.

7.3 Hybrid mixtures

Recent research largely validates but also complements Bartknecht's basic findings (e.g. **Figs. 7–8**) by providing additional information[87] and a more fundamental description of relevant explosion phenomena, linking hybrid mixture behavior with modern safety analysis methods, modeling hybrid explosion behavior, and even modifying industrial standards. Dufaud et al.[88] comment on how better knowledge of hybrid explosion behavior is used to modify an important industrial norm (NFPA 68; venting of deflagrations). Dufaud et al.[89] study effects of pyrolysis gases/vapors evolving during dust explosions of organic powders and develop a predictive model. Garcia-Agreda et al.[90] develop an insightful way of graphically presenting hybrid explosion behavior in terms of measured K_{St} values and 5 combustion regimes: non-explosive, dust-driven, gas/vapour-driven, gas-gas/vapour-driven, and 'synergistically' driven. Denkevits performed unique experiments, namely combining a highly reactive gas, hydrogen, with a much less reactive substance (tungsten)[91], or a very much less reactive element, pure carbon (graphite)[92]; both pure carbon and tungsten are, for practical purposes, non-volatile. Previous researchers had combined flammable gases/vapors with powders that volatilize (i.e. most organic materials). Especially interesting are the results with graphite, which show that a hybrid explosion with a highly reactive substance (hydrogen) and a combustible substance of low reactivity (e.g. graphite) can occur in two distinct stages: initial fast explosion of the reactive substance, followed by a second, relatively slow explosion of the inactive substance, ignited by the initial explosion. On the subject of approaching hybrid explosion hazards with new methods, using polyethylene production as an example, Abuswer et al.[93] combine controlling the hazard (and risk) of hybrid dust explosions with Inherent Safer Design (ISD, described in Section 6.3), Quantitative Risk Analysis (QRA, e.g. employing Fault Tree Analysis), and CFD modeling using DESC (described below in Section 7.5).

7.4 Predicting values of particulate hazard severity (Table 1) and sensitivity (Table 2) indexes

Reyes et al. predict dust severity indexes (P_{max} and K_{St} value) using Quantitative Structure Property Relations (QSPRs) relations[94]. Such an approach (also commonly called Quantitative Structure Activity Relations: QSARs) is used with increasing success to predict a whole host of the physical, chemical, and even physiological-medical (e.g. anti-carcinogenic) effects of substances, thus obviating, or at least greatly reducing, the need for (expensive) testing. We caution, however, that even P_{max}, which theoretically is a chemical thermodynamic entity and thus invariant, can depend strongly on how it is measured (e.g. degree of turbulence)[95]. The reason is that at higher heat loss, maximum temperatures are lower, resulting in slower kinetics, which in turn hampers reaching the equilibrium reaction product composition and thus the adiabatic flame temperature.

7.5 Modeling the propagation of particulate explosions using computational fluid dynamics (CFD)

Particle technology engineers are used to applying Discrete Element Modeling (DEM) when they want to study particle flow in various situations. As regards dust dispersion, even a combination of DEM and Computational Fluid Dynamics (CFD) proves very useful, as shown by Hilton and Cleary[96]. However, so far computer capabilities fall short of depicting model heating, gasification and combustion around discrete elements; only a code based on differencing a continuum is capable of modeling flow and flame (reactive gas dynamics). Norwegian Gexcon, a spin-off of Bergen University, obtained over a period of at least 20 years considerable experience in modeling vapor cloud explosions by developing the CFD-code FLACS (Flame Acceleration Simulator). For instance, applying this code, Gexcon was able to successfully simulate the surprisingly high pressures which occurred in the explosion of a gasoline components cloud resulting from an overflowing storage tank at the Buncefield site near London in 2005[97]. The FLACS code simulates the flame speed-overpressure dynamics of an exploding cloud by solving the Navier-Stokes conservation flow equations, the gas equation of state, a sub-grid scale turbulence model

and the combustion energy release rate. The latter is dependent on the turbulent intensity which an advancing flame faces. This turbulence is generated by the flow ahead of the flame, pushed forward by the expansion of hot gases behind the front and the interaction and friction of the flow with obstacles and congestion in the environment. This phenomenon of turbulence in the unburnt gas by which the expanding hot reaction products accelerates the flame is called a feedback mechanism. The results of runs of the code have been extensively validated against explosion test results at various scales.

Already in 1996, Van Wingerden[98] of Gexcon clearly listed the necessity and possibility of applying Computational Fluid Dynamics (CFD) for creating an overall model of propagating dust explosions within a contained space such as a process plant, and using this model to optimally design safeguarding measures. In analogy to vapor cloud explosion modeling, the Norwegian-based Gexcon company initiated in 2003 a multi-partner European research project DESC, an acronym which stands for Dust Explosion Simulation Code[99]. Additional problems with dust explosions are, however, that flame propagation occurs with an even more complex mechanism than in gas explosions and that the flame in a dust explosion is also "feeding itself" by whirling up settled dust. This dust dispersion part is still not fully developed and further experimental work is being carried out in shock tubes to investigate all relevant parameters, with the aim of being able to more reliably model the dust concentration and turbulence intensity into which the explosive flame propagates. More advanced codes apply large-eddy simulation but are limited with respect to the space dimensions they can cover. Nevertheless, compared to the capabilities of CFD to successfully model gas explosion behavior, at this moment CFD modeling for particulate explosions is still in its infancy. In his 2010 lecture, Skjold presents a detailed and frank evaluation of the state of CFD for modeling dust explosions[100], concluding that: "There remains much to be done before dust explosions are adequately understood". Meanwhile, Castellanos et al.[101] have recently published an interesting application of DESC in a model calculation of a vented dust explosion with and without a duct and comparing it with experimental findings and calculation results based on guidelines and standards and empirical correlations.

As regards flame propagation in a dust cloud, there has been a long quest to unravel the mechanism and to be able to describe it in fundamental terms. An obstacle is the inhomogeneous conditions of testing the explosiveness of a dust. The instrument by choice is the 20-litre vessel, but the concentration of the dust cloud generated in this vessel and the turbulence intensity decrease rapidly as a function of time and space. There have been several attempts to measure the laminar burning velocity, S_U, of a homogeneous dust-air mixture, e.g. by applying a vertical tube in which dust particles float statically in position by an up-going flow of air, as in a fluidized bed[102]. A recent and more successful series of experiments measuring the laminar burning velocity of coal dust-methane-air mixtures has been performed by Xie et al.[103] The measurement takes place on the principle of obtaining a steady-state flame fed by a continuous flow of fuel-air and observing the flame cone by applying a shadow-graph technique, for which special equipment had to be developed. The methane serves to stabilize the flame. The dust concentration is varied over quite a wide range. The experimental results were compared to calculated ones based on a straightforward one-dimensional heat balance deflagration model and applying a devolatilization rate model of coal particles as a function of temperature. The devolatilization also acts as a heat sink. The model yields a devolatilization zone thickness and a burning velocity. This approach is rather promising; it can also be applied on controlled turbulent intensity flames as shown by Rockwell and Rangwala[104], and can be expected to be applied on a variety of dust-fuel-air systems.

Di Benedetto and Russo[105] tackled the aspect of combustion after the devolatilization stage of organic dusts, which is very important to the burning velocity of the dust-air mixture, and hence to the K_{St} value. By applying devolatilization test results from various sources, carried out by thermogravimetry with attached chromatographic analysis of the pyrolysis gas produced, the composition as well as the rate of formation of flammable gas at various temperature levels was obtained from a number of dusts, namely cornstarch, polyethylene, and cellulose. The authors then used the CHEMKIN Premix module to calculate the laminar burning velocity given the gas composition and the known GRI-Mech 3.4 kinetic combustion mechanism. In addition, they applied a relation between the pressure increase in a closed vessel, its radius, and the ratio of specific heats developed by Dahoe and De Goey[106] to calculate the rate of pressure rise. Subsequently, they derived the K_{st} value or deflagration index from the rate of pressure rise and the cube root of the vessel volume. Although the results did not cover the experimental values very accurately, the trends of the effect of concentration with the K_{st} value fitted the experimental ones surprisingly well. To obtain the best fit, the pyrolysis composition to be used in the model must be determined at the highest temperature and heating rate of the thermogravimetric apparatus. Low-temperature gasification kinetics differ from higher-temperature ones. The missing link is now the relation between the burning velocity and turbulent intensity. As mentioned above by the work of Rockwell and Rangwala, there is some progress also in this direction, albeit slow.

An interesting further step is modeling the effect of particle size on dust explosion indices. Di Benedetto et al.[107] performed a study of the effect of particle size on the deflagration index. As explained above, devolatilization can

be measured by performing thermogravimetric experiments over a certain range of temperatures. In this study it was also modeled. This was done as a two-step kinetic rate process: first step is the formation of a molten phase, while the second step is a pyrolysis (cracking) and volatilization. Mass and energy balances in differential form were derived for the conversions under influence of convected and radiant heat. The volatilization depends on the dimensionless Biot number, *Bi*, being the ratio of the time constant of heat conducting into the particle and that of the external heat transfer. Two cases were considered: one in which the external heat transfer dominated ($Bi << 1$) and the other in which internal heat transfer controls ($Bi >> 1$). For the first case, the dimensionless Damköhler number, *Da*, is considered, being the ratio of the external heat transfer time constant and the characteristic pyrolysis conversion time. Next, two regimes are distinguished: regime I in which the external heat transfer controls the pyrolysis ($Bi << 1$ and $Da >> 1$), and a second (II) where the pyrolysis is the slowest ($Bi << 1$ and $Da << 1$). For the second case ($Bi >> 1$), the dimensionless Thiele number, *Th*, is applicable, being the ratio between conducted heat time constant and the characteristic pyrolysis time. This results in a third and fourth regime (III and IV) with pyrolysis controlled rate ($Bi >> 1$ and $Th << 1$) and conversion controlled by internal conduction ($Bi >> 1$ and $Th >> 1$), respectively. Particle size appears in the nominator of both *Bi* and *Th* number. A third dimensionless number, *Pc*, is defined as the ratio between the time constants of pyrolysis and combustion. This ratio is equal to the quotient of the product of density and laminar burning velocity, and the product of particle size and flame thickness. If *Pc* is larger than unity and if pyrolysis is controlled by conversion kinetics (regimes II and III), the pyrolysis reaction rate controls the explosion. Alternatively, at a *Pc* smaller than one, the combustion of volatiles controls. In the case of regime I, the product of $Da \cdot Pc$ should be evaluated, and in the case of regime IV $Th \cdot Pc$. Depending on the particle size, one or the other regime dominates. When the particle size is smaller than a certain critical value depending on the dust material, heating and devolatilization rates are relatively high (*Pc*, $Da \cdot Pc$ and $Th \cdot Pc << 1$) and combustion kinetics determine flame propagation which can be considered to produce a maximum K_{st} value. The other regimes can be defined by evaluating the dimensionless numbers. On this basis, simulations were performed which gave further insight. For instance, the simulations yielded for the four regimes the ratio of maximum volatiles production rate at any particle size and at a particle size near zero as a function of particle size. The model was applied to polyethylene dust. The particle size was varied between 10 and 900 microns. Compared with experimental results of the K_{st} values, the simulated ones were in fair agreement. More dust types should be investigated.

Finally, Di Benedetto et al.[108] accomplished a CFD study to simulate the dust dispersion in the 20-liter explosion vessel. The dust concentration variation in time and space after its injection into this vessel, being the standard test equipment used by many, is still unknown. This is important, because the 20-liter vessel is supposed to produce the same results as a 1-m^3 vessel and for that purpose, the ignition delay time and pressure difference ratio which determine the pre-ignition turbulence and dust dispersion have been carefully selected. How large the margin is, is uncertain. Measuring of the turbulence level with a laser velocimeter (also named Laser Doppler Anemometer) as in the case of gas is not possible with dust. The dust concentration selected was 250 g/m^3, the dust density 2100 kg/m^3, so that it appeared possible to apply an Eulerian approach to the time-averaged Navier-Stokes equations for the gas phase and a Lagrangian one for the dust particles. A solution was obtained with the ANSYS Fluent code. The solid-phase flow was simulated by means of the (Lagrangian) Discrete Phase Model. It appears that multiple vortex structures develop which push the dust towards the walls. Hence the concentration is far from uniform. The turbulence level at the center near the ignition is rather high. Further studies will be needed to investigate the effect of particle size distribution and of other particle characteristics.

8. Summary and Conclusions

Particulate hazards include fire and explosion. The key difference between fire and explosion is that the rates of physical and chemical processes occurring during explosions are much faster than those occurring during fires because during a fire, fuel and air are clearly separated, while in explosions fuel is 'pre-mixed' with air. Particulate explosions, like particulate fires, produce flames, intense heat, and high temperatures, but unlike fire, particulate explosions produce a 'blast', a destructive pressure or shock wave, and sometimes also high-velocity fragments caused by bursting equipment. It is essential to be aware that:

ALL COMBUSTIBLE POWDERS AND MISTS CAN EXPLODE

Characteristics of explosions are the propagation velocity (called flame speed, S_f), maximum pressure; P_{max}, maximum rate of pressure rise, $(dP/dt)_{max}$; time duration of the explosion, Δt; and the integral of explosion overpressure over time, $\int P dt$, called explosion impulse, I_{exp}. Most particulate explosions occur as a deflagration, which is simply a very rapid burning. Deflagrations propagate at less than the speed of sound and produce pressure waves which have finite $(dP/dt)_{max}$ values. Typical P_{max} values for particulate deflagrations at optimum composition are ca. 5–10 times the initial pressure, and flame speeds (S_f values) are typically around 10 m/s. Under certain circumstances of

confinement, however, the flow of unburnt mixture over obstacles can greatly increase turbulence by creating large numbers of pockets of rapidly moving/rotating fluid called eddies. Eddy formation can greatly increase the surface area of the flame, which in turn leads to flame acceleration. Due to increased turbulence intensity, flame speeds can even accelerate to supersonic velocities, at which a deflagration transits into a detonation. Detonations produce a special type of pressure wave called a shock wave, characterized by a (near) infinite rate of pressure rise, dP/dt. Detonations propagate supersonically (up to 2000–3000 m/s) and produce much higher P_{max} values than deflagrations. Therefore they are much more hazardous than deflagrations.

Most particulate explosions are deflagrations; safety measures aim to ideally prevent deflagrations, or should they occur, mitigate their effects. A key safety design priority is furthermore to prevent deflagrations from transforming into the much more deadly detonation. However, fundamental explosion knowledge can be used not only to increase safety, but also to cause particulate clouds in air to directly detonate, forming the basis of Fuel-Air Explosives (FAEs), a powerful, relatively new, blast weapon.

The hazards of a given particulate are characterized by two types of fire and explosion indexes. The first type, fire and explosion sensitivity indexes, relates to the probability of fire and/or explosion occurring (i.e. probability of ignition). Examples are: Lower and Upper Explosion Limits (LEL and UEL), Minimum Explosion Temperature and Energy (MIT and MIE), and Limiting Oxygen Concentration (LOC). The second type of indexes, explosion severity indexes, relates to the magnitude of adverse effects caused by explosions. Such indexes include the type of explosion occurring (deflagration of detonation), P_{max}, and $(dP/dt)_{max}$, the latter volume normalized and called the K_{St} factor. In general, particulates produce roughly the same maximum explosion pressures (i.e. 5–10 times initial pressure) as gas explosions, but their rate of pressure rise is usually (much) less than that of gas/vapor explosions. On the other hand, because of the much greater density of particulates relative to gases/vapors, particulate-air mixtures contain more energy per unit volume than mixtures of combustible gas/vapor with air. This manifests itself in a longer explosion time duration (Δt) than gas/vapor explosions, and thus a larger explosion impulse, I, which can cause more damage.

The explosion hazards of a given particulate, as expressed by values of its explosion sensitivity and explosion severity indexes, are determined by the particulate's chemical and physical properties. Increasing chemical reactivity (e.g. higher combustion energy, J/kg, leading to higher adiabatic flame temperature) tends to increase all fire and explosion indexes (e.g. lower MIT and MIE; higher S_f, P_{max} and K_{St} factor), and thus to increase the hazard. The most important physical property affecting fire and explosion parameters is particle size (particle size and particle size distribution). In general, the finer the particles, the greater their hazard. The explosion mechanism of most particulates is controlled by diffusion (of oxygen to and reaction products away from the particle's surface). Diffusion control is typical of a heterogeneous (i.e. multi-phase) chemical reaction. The rate of gas and vapor explosions which occur homogeneously (i.e. within one phase: gas) is determined not by diffusion, but by chemical kinetics. Compared to rates of chemical reaction, which increase exponentially with temperature, diffusion is a relatively slow process. This is the basic reason why explosions of the most commonly used particulates which are in the upper micron region generally proceed more slowly than gas/vapor explosions (i.e. similar P_{max}, but slower dP/dt).

However, even low concentrations of flammable gases or vapors (the latter possibly originating from the evaporation of traces of solvents) present in particulate-air suspensions (called 'hybrid mixtures') can greatly increase both the explosion sensitivity and severity of particulate explosions (hybrid explosions).

Turbulence has a complex effect on particulate explosions. Turbulence is essential for creating and maintaining particle clouds in air, and increased turbulence tends to increase all particulate explosion severity indexes. As previously mentioned, turbulence can even cause a deflagration to transit into the vastly more hazardous explosion type, the detonation, a phenomenon known as a deflagration-detonation transition (DDT). By contrast, however, increased turbulence tends to reduce most particulate explosion sensitivity indexes. A breakthrough in the ability to describe turbulent flow, a highly 'complex' area of physics, and predict flame speed and pressure build-up has been the development of Computational Fluid Dynamics (CFD). In spite of considerable progress, application to dust explosions is, however, still in its infancy.

Various chemical and physical properties of particulates are aggregated to form an internationally used fire and explosion index, that of the National Fire Protection Agency (NFPA).

A plethora of information exists concerning the basics of particulate fires and explosions and ways of preventing and/or mitigating the fire and explosion hazards (see Appendix). Extensive analysis of industrial accidents shows that it is not lack of knowledge that is the most general cause of accidents, but rather unawareness and/or non- or improper application of such knowledge, thus management failure. Therefore, while we outline the basics of prevention and protection, we stress that the generic cause of most particulate fires and explosions is poor management. To tackle this problem, modern safety management systems are evolving. Such management systems are being combined with new design methods such as Inherently Safer Design (ISD) and Layers of Defense Analysis

(LOPA) to create even more integrated and 'holistic' management methodologies. These tools and methods are part of the systematic, integrative, and comprehensive safety science field known as Loss Prevention.

While an abundance of knowledge (data, theory) exists, research on the fire and explosion hazards of particulates nevertheless continues, with interesting and useful results. One important area is nanoparticles, whose production and use are increasing rapidly. Research so far shows that reducing the particle size down from the mm range to the 1-micron range (1000 nm) strongly increases both the explosion severity and explosion sensitivity. Further reduction into the (high) nanometer range shows a continuing explosion sensitivity increase (i.e. lower MIE), but no further increase in explosion severity (i.e. P_{max} and K_{St} values remain constant, or even increase slightly with further particle size reduction). We note, however, that nearly all research has been restricted to the high end of nanoparticle size; i.e. to particles around 100 nm or somewhat smaller (≥ ca. 15 nm). Creating smaller nanoparticles and dispersing them into clouds is hampered by strong cohesive forces (e.g. van der Waals' forces). Research on reactive metallic nanoparticles is further complicated by their tendency to spontaneously oxidize or even exhibit pyrophoric behavior. Nevertheless, it is clear that as the particle size decreases from the micron range into the nanometer range, the mechanism of particulate explosions increasingly resembles the mechanism of gas/vapor explosions; i.e. the reaction rate is less controlled by diffusion and more by chemical kinetics. Various researchers theorize and extrapolate or calculate that in the extreme case, when particulates approach the size of individual molecules, their explosion mechanism will become identical with that of gases and vapors, namely controlled exclusively by chemical kinetics. At these low nanodiameters, the fundamental explosion parameters such as laminar burning velocity and sensitivity and explosion severity indexes will increasingly resemble those of gases and vapors (e.g. indexes of smaller and smaller (nano-sized) polyethylene particles increasingly resembling those of ethylene gas; aluminum (a stable but reactive metal) nanoparticles, although chemically very different, having a laminar burning velocity increasingly close to that of acetylene (a highly reactive gas)).

Another important area of research is acquiring a deeper understanding of particulate fire and explosion reaction mechanisms, and through such knowledge being able to better quantitatively describe and predict fire and explosion behavior. Making use of Computational Fluid Dynamics (CFD), powerful models are being developed to predict the course of (particulate) explosions (e.g. S_f, P_{max}, Δt, dP/dt, these as functions of time, location, and initial conditions), both inside and outside installations. Such models enable more cost-effective safety design and operation. Present CFD modeling of dust explosion behavior, however, still requires further development to reach the reliability presently achieved for modeling gas/vapor explosions.

Symbols and Abbreviations

AIT	Auto-Ignition Temperature (usually Minimum Auto-Ignition Temperature)
bara	bar absolute pressure
baro	bar overpressure
CCPS	Center for Chemical Process Safety (USA)
DDT	Deflagration-Detonation Transition
DIN	Deutsches Institut für Normung (German Institute for Standardization)
ISD	Inherently Safer Design
LEL	Lower Explosion Limit (= LFL: Lower Flammability Limit)
LOC	Limiting Oxygen Concentration (below which explosion is not possible)
LOPA	Layer of Protection Analysis
MESG	Maximum Experimental Safe Gap
MIE	Minimum Ignition Energy
MIT	Minimum Ignition Temperature
NFPA	National Fire Protection Association (USA)
PVC	Polyvinylchloride
SMD	Sauter Mean Diameter ($D_{3,2}$)
STP	Standard Temperature and Pressure
TNT	TriNitroToluene
UEL	Upper Explosion Limit (= UFL: Upper Flammability Limit)
D	Particle size (note: for non-spherical particles: measured size depends upon technique)
$D_{3,2}$	Area-weighted Sauter mean diameter
K_{st}	Volume-normalized maximum rate of pressure rise in a vessel ($= V^{1/3} \cdot (dP/dt)_{max)}$
P	Pressure
$\int P dt$	Integral of explosion overpressure and time=explosion impulse
S_U	Laminar burning velocity
S_f	Flame speed
t	Time
Δt	Time duration of explosion
T	Temperature
V	Volume of a vessel

Appendix. Some recommended literature sources

1. Bartknecht, W. (1993): "Explosionsschutz—Grundlagen und Anwendung", Springer-Verlag, (ISBN: 3-540-55464-5).
2. Bartknecht, W. (1989): "Dust Explosions: Course, Prevention, Protection", Springer-Verlag, (ISBN: 3-540-50100-2).
3. Bartknecht, W., (1981): "Explosions", Springer-Verlag, (ISBN: 3-540-10216-7).

4. Barton, J. (2002): "Dust explosion prevention and protection—A Practical Guide", Institution of Chemical Engineers, (ISBN 0-85295-410-7).
5. Britton, L. G. (1999): "Avoiding Static Ignition Hazards in Chemical Operations," Center for Chemical Process Safety, American Institute of Chemical Engineers (ISBN: 0-8169-0800-1).
6. Bjerketvedt, D., Bakke, J. B., and van Wingerden, K. (1997): Gas Explosion Handbook, Journal of Hazardous Materials No. 52, pp. 1–150. (In spite of title, much information also relevant to explosions of particulates.)
7. Center for Chemical Process Safety (2005): "Guidelines for Safe Handling of Powders and Bulk Solids, 2005, American Institute of Chemical Engineers (ISBN 0-521-03339-7).
8. Crowl, D. A. (2003): "Understanding Explosions, Center for Chemical Process Safety", American Institute of Chemical Engineers, (ISBN 0-8169-0779-X).
9. Dahoe, A. E. (2000): "Dust Explosions: A Study of Flame Propagation", Ph.D. Dissertation, Delft University of Technology, 297 pages (ISBN: 90-90-13706-8).
10. Eckhoff, R. K. (2003): "Dust Explosions in the Process Industries", Third Edition, Butterworth-Heinemann, (ISBN: 0-7506-7602-7).
11. Eckhoff, R. K. (2005): "Explosion Hazards In The Process Industries—Why Explosions Occur And How To Prevent Them, With Case Histories", Golf Publishing Company.
12. Glor, M. (1988): "Electrostatic Hazards in Powder Handling", Wiley, (ISBN: 0-471-92024).
13. M. Hattwig, M. and Steen, H. (2004): "Handbook of Explosion Prevention and Protection", Wiley-VCH, 2004, (700 pages; ISBN: 3-527-30718-4).
14. Hetzberg, M. and Cashdollar, K. L. (Eds.) (1987): "Industrial Dust Explosions Symposium on Industrial Dust Explosions", (ASTM Special Technical Publication), (ISBN-10: 0803109571, ISBN-13: 978-0803109575).
15. Mannan, S. (Ed.): Lees' Loss Prevention in the Process Industries, Third Edition, Elsevier Butterworth Heinemann, 2005. (Set ISBN: 0-7506-7555-1; Set consists of Volumes 1, 2, and 3 (ca. 3,000 pages) discussing in great detail a broad scale of topics and issues related to loss prevention (e.g., fire and explosion prevention and protection) in the process industries. Note that a Fourth Edition is being prepared. Presently (2013) Volumes 1 (ISBN-10: 0123971896) and 2 (ISBN-13: 978-0123971890) of the three volume series have been published.
16. Nolan, D. P. (2011): "Handbook of Fire and Explosion Protection Engineering Principles for Oil, Gas, Chemical and Related Facilities", Second Edition, Elsevier, (ISBN: 978-1-4377-7857-1).
17. UKELG 46th (2010): "Meeting on Causes, severity and mitigation of aerosol and particulate explosions", Dept. Chem. Eng., Imperial College, London, 22nd Sept. 2010. Lectures available at: http://ukelg.ps.ic.ac.uk/UKELG46.htm

End notes and cited literature

1) Lemkowitz, S. M. and Pasman, H. J. (2013): discuss particulate fire and explosion risks in "Assessment and Control of Fire and Explosion Hazards and Risks of Particulates", Chapter 4, Merkus, H. G. and Meesters, G. M. H. (Editors), "Particulate Products—Design Properties for Performance Optimization", pp. 77–120, .Springer, 2013 (ISBN: 978-3-319-00713-7).
2) While dust explosion hazards are extensively studied, much less is available for mist explosions. Examples are: Gant, S, Bettis, R., Santon, R., Bickland, I., Bower, Ph. and Kay, P. (2012), "Generation of Flammable Mists from High Flashpoint Fluids: Literature Review", presented at Institution of Chemical Engineers, XXIII Conference, Southport, UK, 12–15 November 2012, available as: http://s177835660.websitehome.co.uk/research/gant_bettis_santon_buckland_bowen_kay_2012_mists_lit_review_preprint.pdf, 19 pages; Förster, H. (2004), Chapter 5, "Properties of Flammable Mists and Foams", p. 419–480, from M. Hattwig, M. and Steen, H., "Handbook of Explosion Prevention and Protection", Wiley-VCH, 2004 (ISBN: 3-527-30718-4); Krishna, K., Rogers, W. J. and Mannan, M. S. (2003), "The use of aerosol formation, flammability, and explosion information for heat-transfer fluid selection", Journal of Hazardous Materials 104, pp. 215–226; Holness, M. H. and Smith, B. J. (2002), "Oil Mist and Machinery Space Fires", Marine Technology, 39(1), 2002, pp. 62–66; Britton, L. G. (1999), "Avoiding Static Ignition Hazards in Chemical Operations," Center for Chemical Process Safety, American Institute of Chemical Engineers, pp. 83–96, 209–211.
3) See for example, Eckhoff, "R. K. (2003), "Dust Explosions in the Process Industries", Third Edition, Elsevier, (ISBN: 0-7506-7602-7), in particular Table A.1, pages 686–699, which lists explosion severity and sensitivity indexes, including P_{max}, for ca. 600 different powders.
4) Lemkowitz, S. M. and Scholten, R. M. (1999), "Explosion theory for dummies", NPT Process Techniek, 2, pp. 19–24. Derivation is based on assumptions that flame thickness is small relative to vessel diameter and that flame speed is independent of temperature and pressure.
5) Hertzberg et al, 1986 derive a formula very similar to Eq. 4 applied to gases, i.e. for flames whose thickness is small relative to the radius of vessels in which explosion occurs. Hertzberg, M., Cashdollar, K. L., and Zlochower, I. A. (1986), "Flammability Limit Measurements For Dusts and Gases: Ignition Energy Requirements and Pressure Dependences", Twenty-first Symposium (International) on Combustion, the Combustion Institute, pp. 303–313; see Eq. 5, page 307. Cashdollar (2000) obtains the same equation as Hertzberg et al. (1986), but applies it to dust explosions, commenting that the equation is probably more valid in the standard 1000 liter testing sphere than in the, also standard, 20 liter sphere due to the greater radius of the 1000 liter sphere, relative to dust flame thickness. Cashdollar, K. L. (2000), "Overview of dust explosibility characteristics", Journal of Loss Prevention in the Process Industries, 13, pp. 183–199. See Eqs. 6–7, page 188.
6) Dahoe et al. (1996, 2003) derive more realistic—and considerably more complex—equations describing flame speed effects on pressure rise and K factor for thick dust flames,

which are typical of particulate explosions. Dahoe, A. E. and de Goey, L. P. H. (2003), "On the determination of the laminar burning velocity from closed vessel gas explosions", Journal of Loss Prevention in the Process Industries, 16, pp. 457–478; Dahoe, A. E., Zevenbergen, J. F., Lemkowitz, S. M., and Scarlett, B. (1996), "Dust explosions in spherical vessels: the role of flame thickness in the validity of the 'cube-root-law'", Journal of Loss Prevention in the Process Industries, 9, pp. 33–44

7) Center for Chemical Process Safety (2012), "Guidelines for Evaluating Process Plant Buildings for External Explosions, Fire, and Toxic Releases", Second Edition, Wiley (ISBN 978-0-470-64367); see p. 62.
8) Center for Chemical Process Safety (1994), "Guidelines for Evaluating the Characteristics of Vapor Cloud Explosions, Flash Fires, and BLEVEs", first edition, American Institute of Chemical Engineers; see Table 4.1a, p. 72.
9) Abbasi, T., Pasman H. J., Abbasi S. A. (2010), A scheme for the classification of explosions in the chemical process industry, Journal of Hazardous Materials, 174, pp. 270–280.
10) Mannan, S. editor (2012), "Lees' Loss Prevention In The Process Industries, Fourth Edition, Chapter 17, "Explosion", Elsevier, ISBN 978-0-123-971890
11) Using such indexes (Tables 1 and 2), in combination with chemical thermodynamic data and data from practice (e.g., accidents), the National Fire Protection Agency (NFPA) ranks hazards of powders in terms of Health, Fire, and Instability. See Center for Chemical Process Safety, (2005), "Guidelines for Safe Handling of Powders and Bulk Solids".
12) On the basis of a number of simplifying assumptions, and using only secondary school chemistry and physics, Lemkowitz and Scholten correctly derive, in terms of trends, how changes in ambient temperature, pressure, and flow (turbulence) affect nearly all important fire and explosion indexes: Lemkowitz, S. M. and Scholten, R. M. (1999), op cit.
13) Detailed discussions of test methods for powders and their evaluation are given in: J. Barton (2002)), "Dust Explosion Prevention and Protection—A Practical Guide", Institution of Chemical Engineers; see Chapter 2: "Determination of dust ignitability, flammability and explosibility characteristics", pp. 8–20; Eckhoff, R. (2003), "Dust Explosions in the Process Industries", Third Edition, Butterworth-Heinemann, see Chapter 7, "Assessment of ignitability, explosibility, and related properties of dusts by laboratory-scale tests; pp. 473–548.
14) Gao, W., Zhong, S., Miao, N., and Liu, H. (2013), "Effect of ignition on the explosion behavior of 1-Octadecanol/air mixtures", Powder Technology, 241, pp. 105–114.
15) Proust, Ch., Accorsi, A., and Dupont, L. (2007), "Measuring the violence of dust explosions with the "20 l sphere" and the standard "ISO 1 m^3 vessel—Systematic comparison and analysis of the discrepancies", Journal of Loss Prevention in the Process Industries, 20, pp. 599–606.
16) Detailed descriptions of hazards of unstable liquids and their control are given by L. A. Medard (1989) in: "Accidental Explosions" Volumes 1 (ISBN 0470215305) and Volume 2 (ISBN 0-7458-0436-5). Ellis Horwood Ltm (English translations of the original French language text of 1987).
17) Powdered ammonium nitrate, mixed with an inert compound such as calcium carbonate to reduce its explosion hazard ('phlegmatizing' it), is a widely used fertilizer. In spite phlegmatizing inerts, a number of serious explosions of large piles of powdered ammonium nitrate have nevertheless occurred.
18) Examples of pyrophoric substances are found in Johnson, R. W., Rudy, S. W., and Unwin, S. D. (2003), "Essential Practices for Managing Chemical Reaction Hazards", Center for Chemical Process Safety, American Institute of Chemical Engineering, Table 3.2, page 45.
19) The above source also lists common water-reactive substances (Table 3.4, page 50) as also does 'Common Water Reactive Chemicals', http://www.esd.uga.edu/chem/pub/waterreactivemat.pdf.
20) Going, J. E. and Snoeys, J. (2002), "Explosion Protection with Metal Dust Fuels", Process Safety Progress, 21(4), pp. 305–312.
21) In some cases, such as explosions of finely divided metals (e.g., powdered aluminum), even three phases can be simultaneously present: a solid phase (solid aluminum oxide), a liquid phase (molten aluminum), and a gaseous phase (air, even vaporized aluminum).
22) P. Puri, P. (2008), "Multiscale modelling of ignition and combustion of micro and nano aluminum particles", PhD Dissertation, The Pennsylvania State University, In his 235 page thesis Puri discusses combustion mechanisms of metal particles in great detail, including many splendid color figures. Full dissertation available via: http://search.proquest.com/docview/231495775
23) Lecture of Puri, P. and V. Yang, V. (2005), "Multi-Scale Modeling of Nano Aluminum Particle Ignition and Combustion", Sheet 6, lecture presented in 2005 at MURI NEEM Program Review, Aberdeen, Maryland; full lecture available as: http://soliton.ae.gatech.edu/people/vigor.yang/projects/Nano%20Aluminum...(Puneesh)/ARO-MURI%20NEEM%20Website-(11-16-05).pdf. See also Yang, V., Sundaram, D., and Puni, P. (2010), "Multi-Scale Modeling of Nano Aluminum Particle Ignition and Combustion", lecture presented in 2010 MURI NEEM Program Review, Aberdeen, Maryland, March 15, 2010. Sheet 3. Lecture available as: http://www.neem.psu.edu/2010%20Review%20Meeting/GeorgiaTech_Yang_NEEM_MURI_Final_Review_15_March_2010.pdf
24) Kobiera, A., Szymczyk, J., Wolanski, P., and Kuhl, A (2009), "Study of the shock-induced acceleration of hexane droplets", Shock Waves, 18.4, pp. 475–485.
25) Dobashi, R. (2008), "Risk of dust explosions of combustible nanomaterials", Journal of Physics: Conference Series, IOP Publishing, 170, Figure 3 on page 3.
26) R. Dobashi, R. (2008), "Risk of dust explosions of combustible nanomaterials", sheet 19 of lecture presented at Nanosafe 2008, International Conference on Safe Production and Use of Nanomaterials; lecture available as: http://www.nanosafe.org/home/liblocal/docs/2008_Oral%20presentations/PL7_Dobashi.pdf
27) Föster, H. (2004), "Properties of Flammable Mists and

Foams", Chapter 5 of "Handbook of Explosion Prevention and Protection", edited by Hattwig, M. and Steen, H. Wiley-VCH Verlag, 2004 (ISBN: 3-527-30718-4), Figure 5.1-6, page 435.

28) Dobashi, R. (2008), op cit, sheet 20 from 2008 lecture of Dobashi

29) Ballal, D. R. (1980), "Ignition and Flame Quenching of Quiescent Dust Clouds of Solid Fuels", Proceedings of the Royal Society of London. Series A, Mathematical and Physical Sciences, 369, pp. 479–500.

30) The Sauter mean diameter (SMD, d_{32} or D[3, 2]) is an average of particle size. It is defined as the diameter of a sphere that has the same volume/surface area ratio as the particle of interest.

31) Eckhoff, R. K. (2003), op cit, page 479

32) Eckhoff does, however, mention (p. 490) a related essential point, namely that a measured particle size distribution may be quite different from that occurring in practice, due to how in practice a powder is dispersed and suspended.

33) Föster, H. (2004), op cit., see pages 423–425 and 235.

34) Merkus, H. G. (2009), "Particle Size Measurements—Fundamentals, Practice, Quality", Springer (ISBN: 978-1-4020-9015-8 en e-ISBN: 978-1-4020-9016-5). See pp 140–146.

35) Amyotte, P. R., Chippett, S., and Pegg, M. J. (1989), "Effects of Turbulence on Dust Explosions", Progress in Energy and Combustion Science, 14, pp. 293–310; see also Lemkowitz and Scholten, 1999, op cit.

36) A detailed discussion of film theory in describing heterogeneous combustion is given in: Annamalei, K. et al. (1994), "Interactive Processes in Gasification and Combustion-Part III: Coal/Char Particle Arrays, Streams and Clouds", Prog. Energy Combust. Sci. 20, 487–618; see especially pages 491–494.

37) For detailed discussion of secondary dust explosions see: Taveau, J. (2012), "Secondary Dust Explosions: How to Prevent Them or Mitigate Their Effects", Process Safety Progress, 31(1), pp. 36–50.

38) A comprehensive and detailed analysis (85 pages) of such an explosion, caused in part by poor housekeeping, is given in: U.S. Chemical Safety and Hazard Investigation Board, Sugar Dust Explosion and Fire (14 Killed, 36 Injured), Investigation Report No. 2008-05-I-GA, September 2009; available as: http://www.csb.gov/assets/document/Imperial_Sugar_Report_Final_updated.pdf

39) Proust discusses DDTs through flame acceleration in connecting pipe work: Proust, Ch. (1996), "Dust explosions in pipes: a review", Journal of Loss Prevention in the Process Industries, 4(9), pp. 267–277.

40) R. K. Eckhoff, R. K. (2003), op cit, pages 74 and 525; see also Crowl, D. A. (2003), "Understanding Explosions", Center for Chemical Process Safety, American Institute of Chemical Engineers, (ISBN 0-8169-0779-X), pp. 63–64.

41) See for example, Dahoe, A. E., Cant, R. S., Pegg, M. J. and Scarlett, B. (2001), "On the transient flow in the 20-liter explosion sphere", Journal of Loss Prevention in the Process Industries 14, pp. 475–487

42) For more detail see: Dahoe, A. E., "Dust Explosions: A Study of Flame Propagation", PhD Dissertation, Delft University of Technology, 2000, 297 pages (ISBN: 90-90-13706-8); see especially pages 174–181.

43) van Laar, G. F. M. and Zeeuwen, J. P. (1981), "On the Minimum Ignition Energy of Dust-Air Mixtures", Archivum Combustionis, 5, pp. 145–159R. A extensive study of effects ab//adsorbed water of explosion indexes is: J. P. Zeeuwen and G. F. M. van Laar (1983), "An overview of the research at TNO in the dust explosion field over the last decade", Figure 6, page 83, of VDI-Berichte 494 (1983), "Sichere Handhabung brennbarer Stäube", VDI-Verlag GmbH, Verlag des Vereins Deutscher Ingenieurs, Düsseldorf.

44) Glor, M. (1988), "Electrostatic Hazards in Powder Handling", Chapter 2, Charging of particles, Chapter 3, Ignition of particles, Wiley (ISBN: 0-471-92024).

45) Hertzberg, M. and Cashdollar, K. L. (1987), "Introduction to Dust Explosions", from Hertzberg, M. and Cashdollar, K. L. (editors), "Industrial Dust Explosions", ASTM (American Society for Testing Materials), 1987 (ISBN: 0-8031-0957-1); modified version of Figure 5, page 14.

46) Bartknecht, W., (1981), "Explosions", Springer-Verlag, 1981 (ISBN: 3-540-10216-7), pp. 49–55. Many of Bartknecht's original figures continually reappear in modified form in standard works on dust explosions, such as Eckhoff's 2003 textbook.

47) Modified from Pellmont, G. (1979), "Explosions- und Zündverhalten von Hybriden Gemischen aus brennbaren Stäuben und Brenngasen", PhD thesis, No. 6498, ETH Zürich. Figure 7 here is taken from Eckhoff, R. K. (2003), op cit, Figure 1.60, p. 52.

48) Modified from Bartknecht, W. (1981), "Explosions—Course, Prevention, Protection", Springer-Verlag, Fig. 1-5.4, p. 51. Figure 8 here is taken from Eckhoff, R. K. (2003), op cit, Figure 1.65, p. 55.

49) Lavoie, L. (1989), "Fuel-Air Explosives, Weapons, and Effects", Military Technology—MILTECH, 9, pp. 64–70.

50) Rao, A. A., (1987), "Fuel Air Explosives", Defence Science Journal, 37(1), pp. 23–28; Liu, G., Hou, F., Cao, B., Xie, L., Shen, Zh., and Zhou, T. (2008), "Experimental Study of Fuel-Air Explosive", Combustion, Explosion, and Shock Waves, 44(2), pp. 213–217.

51) Dearden, P., (2001), "New Blast Weapons", Journal of the Royal Army Medical Corps, 147 (1), 2001, 80–86. Available as: http://www.ramcjournal.com/content/147/1/80.full.pdf+html; Wildegger-Gaissmaier, A. E., "Aspects of thermobaric weaponry", ADF Health (Health Journal for the Australian Department of Defence—Joint Health Command), 4, pp. 3–6, 2003; article available as: http://www.defence.gov.au/health/infocentre/journals/ADFHJ_apr03/ADFHealth_4_1_03-06.pdf

52) Pierce, T. H., Sedgwick, R. T. and Groethe, M. A. (1982), "Investigation of a Reusable Fuel-Air Explosive Nuclear Airblast Simulator", Defense Nuclear Agency (Washington D.C.), 133 pages.

Abstract available as:
http://oai.dtic.mil/oai/oai?verb=getRecord&metadataPrefix=html&identifier=ADA149473

53) Direct ignition of detonations of gaseous fuel-air mixtures requires high energies, typically (more than) a million times greater than those required to ignite deflagrations.

See for example, Center for Chemical Process Safety (2010), "Guidelines for Vapor Cloud Explosion, Pressure Vessel Burst, BLEVE and Flash Fire Hazards", Second Edition, Wiley, (ISBN 978-0-470-25147-9), Table 4.2, page 55.

54) The generic nature of management failure in causing industrial explosions is clearly shown in, for example, many publications of the United States Chemical Safety Board. (http://www.csb.gov/), like the investigation of the 2009 explosion at the Imperial Sugar plant that killed 14 workers and totally destroyed the plant. Other publicly available investigations of industrial disasters (e.g., Flixborough, Seveso, Piper Alpha, Chernobyl, BP Texas City explosion, BP Deepwater Horizon oil spill) all show management failure, not lack of scientific knowledge, to be the basic cause of disasters.

55) For example: Center for Chemical Process Safety: (2011), "Guidelines for Auditing Process Safety Management Systems, 2nd Edition", Wiley (ISBN: 978-0-470-28235-9); (2008) Guidelines for the Management of Change for Process Safety, Wiley (ISBN: 978-0-470-04309-7)

56) For example see: Britton, L. G. (1999), "Avoiding Static Ignition Hazards in Chemical Operations", Center for Chemical Process Safety (ISBN: 0-8169-0800-1); and Glor, M. (1988), op cit.

57) For example: Vijayaraghavan, G. (2011), "Review Article: Dust Explosions - A Major Industrial Hazard", International Journal of Advanced Engineering Technology, Vol. II/Issue IV, pp. 83–87; Amyotte, P. R. and Rolf K. Eckhoff, P. R. (2010), "Dust explosion causation, prevention and mitigation: An overview", Journal of Chemical Health & Safety, pp. 15–28; Eckhoff, R. K. (2009), "Understanding dust explosions: The role of powder science and technology", Journal of Loss Prevention in the Process Industries, 22, pp. 105–116; Eckhoff, R. K. (2009), "Dust Explosion Prevention and Mitigation, Status and Developments in Basic Knowledge and in Practical Application", International Journal of Chemical Engineering, pp. 1–12; Abbasi, T and Abbasi, S. A., (2007) "Dust explosions—Cases, causes, consequences, and control", Journal of Hazardous Materials, 140, pp. 7–44; Amyotte, P. R., Pegg, M. J., Khan, F. I., Nifuku, M., and Yingxin, T., (2007) "Moderation of dust explosions", Journal of Loss Prevention in the Process Industries, 20, pp. 675–687; Pekalski, A. A., Zevenbergen, J. F., Lemkowitz, S. M. and Pasman, H. J., (2005), "A Review of Explosion Prevention and Protection Systems Suitable as ultimate Layer of Protection in Chemical Process Installations", Trans IChemE, Part B, Process Safety and Environmental Protection, 83(B1), pp. 1–17;

58) Center for Chemical Process Safety (2009), "Inherently Safer Chemical Processes: A Life Cycle Approach", 2nd Edition (ISBN: 978-0-471-77892-9). Layer of Protection Analysis (LOPA) and Inherently Safer Design (ISD) are examples of parts of the systematic, science-based discipline of Loss Prevention.

59) Center for Chemical Process Safety (CCPS), Layer of Protection Analysis—Simplified Process Risk Assessment, American Institute of Chemical Engineers, 2001 (ISBN 0-8169-0811-7).

60) For an overview of Loss Prevention, see, for example, Mannon, Ref. 15 in the Appendix.

61) See, for example, Chapter 13, "The Role of Inherently Safer Design in Dust Explosion Prevention and Mitigation", from Kletz, T. and Amyotte, P. (2010), "Process Plants: A Handbook for Inherently Safer Design", Second Edition, CRC Press, ISBN: 978-1-4398-0455-1, pp. 289–318; Amyotte, P. R., Pegg, M. J. and Khan, F. I. (2009), "Application of inherent safety principles to dust explosion prevention and mitigation", Process Safety and Environmental Protection, 87, pp. 35–39; Dufaud, O., Perrin, L. and Laurent, A. (2010), "State of the art: promotion of early inherently safer design against dust explosions", paper presented at CISAP4, 4th International Conference on Safety and Environment, Florence, Italy; available as: http://www.aidic.it/CISAP4/webpapers/74Dufaud.pdf

62) Vignes, A., Muñoz, F., Bouillard, J., Dufaud, O., Perrin, L., Laurent, A. and Thomas, D. (2012), "Risk assessment of the ignitability and explosivity of aluminum nanopowders", Process Safety and Environmental Protection, 90, p. 304–310.

63) Zhang, Q., Zhong, S. and Jiang, G. (2011), "Development of an Expert System for Dust Explosion Risk Management Based on ASP. Net and Prolog", Journal of Software, 6(9), pp. 1857–1865.

64) Pasman, H. J., Knegtering, B., and Rogers, W. J. (2013), "Review: A holistic approach to control process safety risks: Possible ways forward", Reliability Engineering and System Safety, 117, pp. 21–29

65) See, for example, Baukal, C. E. (2013), "The John Zink Hamworthy Combustion Handbook", Second Edition: Volume 1—Fundamentals, CRC Press. ISBN: 978-1-4398-3962-1.

66) For example: Veyssiere, B., Khasainov, B. A., and W. Ingignoli, W. (2010), "Shock Initiation of Detonations in Aluminum-Oxygen Mixtures", pp. 297–310, in Roy, G. D. and Frolov, S. M. (editors) "Deflagrative and Detonation Combustion", Torus Press (ISBN: 978-5-94588-071-9).

67) Examples being: Proust, Ch. (2006), "A few fundamental aspects about ignition and flame propagation in dust clouds", Journal of Loss Prevention in the Process Industries, 19, pp. 104–120; Eckhoff, R. K. (2005), "Current Status and Expected Future Trends in Dust Explosion Research", Journal of Loss Prevention in the Process Industries, 18, pp. 225–237; Eckhoff, R. K. (1993), "Dust explosion research. State-of-the-art outstanding problems", Journal of Hazardous Materials, 35, pp. 103–117; Kauffman, C. W., Sichel, M. and Wolanski, P. (1992), "Research on dust explosions at the University of Michigan", Powder Technology, 71, pp. 119–134.

68) Hinkley, G. K. and Stephen M. Roberts, S. M. (2013), Chapter 5, pp. 121–149, "Particle and Fiber Toxicology", from Merkus, H. G. and Meesters, G. M. H. (Editors), "Particulate Products—Design Properties for Performance Optimization", Springer, 2013 (ISBN: 978-3-319-00713-7)

69) Safety and health issues are central in the Nanosafe: Safe Production and Use of Nanomaterials. International conferences held biannually in Grenoble, France in 2008, 2010, and 2012. Noticeable is that while in 2008 and 2010 fire and explosion safety issues were discussed in many lectures, since then these issues seem relatively clear, in comparison with health issues, which in 2012 still received much atten-

tion. Lectures available on the web.
For 2008: http://www.nanosafe.org/scripts/home/publigen/content/templates/show.asp?P=96&L=EN&ITEMID=42.
For 2010: http://www.nanosafe.org/scripts/home/publigen/content/templates/show.asp?P=118&L=EN.
For 2012: http://www.nanosafe.org/scripts/home/publigen/content/templates/show.asp?P=124&L=EN

70) Eckhoff, R. K. (2012), "Does the dust explosion risk increase when moving from µm-particle powders to powders of nm-particles?", Journal of Loss Prevention in the Process Industries, 25, p. 448–459
71) Wu, H-C, Chang, R-C, and Hsiao, H-C. (2009), "Research of minimum ignition energy for nano Titanium powder and nano Iron powder", Journal of Loss Prevention in the Process Industries, p. 21–24
72) Eckhoff, R. K. (2013), "Influence of dispersibility and coagulation on the dust explosion risk presented by powders consisting of nm-particles", Powder Technology, 239, p. 223–230.
73) Yetter, R. A., Risha, G. A., and Son, S. F. (2009), "Metal particle combustion and nanotechnology", Proceedings of the Combustion Institute 32, p. 1819–1838; e.g. see p. 1822.
74) Evans, J. P., Borland, W. and Mardon, P. G. (1976) "Pyrophoricityof fine metal; powders", Powder Metallurgy, 1, p. 17–21.
75) Mohan, S., Ermoline, A. and Dreizin, E. L. (2012), "Pyrophoricity of nano-sized aluminum particles", Journal of Nanoparticle Research, 14(2), p. 1–6.
76) Sundaram, D. S., Puri, P. and Yang, V. (2013), "Pyrophoricity of nascent and passivated aluminum particles at nanoscales", Combustion and Flame, in press.
77) Krietsch, A., Romahn, T., Scheid, M. and Krause, U. (2013), "Modified Setup of 20-L-Sphere for the Determination of Safety Characteristics of Nano Powders", Chemical Engineering Transactions, 31 (online).
78) Randeberg, E. and Eckhoff, R. K., (2007), "Measurement of minimum ignition energies of dust clouds in the <1 mJ region", Journal of Hazardous Materials, 140, p. 237–244
79) Bouillarda, J., Vignesa, A., Dufaud, O, Perrinb, L, and Thomas, D. (2010), "Ignition and explosion risks of nanopowders", Journal of Hazardous Materials, 181, pp. 873–880. Fig. 4, p. 875;
80) See also: Lecture of O. Dufaud, A. Vignes, F. Henry, L. Perrin, and J. Bouillard (2010), "Ignition and explosion of nanopowders: Something new under the dust", Sheet 8; lecture presented at Symposium Nanosafe 2010: Safe Production and Use of Nanomaterials, 16–18 November 2010, Grenoble, France. Complete lecture available on web as: http://www.nanosafe.org/home/liblocal/docs/Nanosafe%202010/2010_oral%20presentations/O11-1_Vignes.pdf
81) Huang, Y., Risha, G. A., Yang, V. and Yetter, R. A. (2009), "Effect of particle size on combustion of aluminum particle dust in air, Combustion and Flame 156 (2009), pp. 5–13 (Figure 11, p. 11). See also lectures of P. Puri, T. Lui, Ying, Huang, and V. Yang, "Modeling and Simulation of Supercritical Fluid Processing of Nano Energetic Materials": Sheet 22, lecture presented in 2006 at MURI NEEM Program Review at Pennsylvania State University. Lecture available on web as: http://www.neem.psu.edu/2006%20Review%20Meeting/Yang%20MURI%20NEEM%20Year%202%20PSU%20Nov%202006.pdf
82) Bidabadi, M., Fereidooni, J., Hosseini, S. N. and Asadollahzadeh, P. (2012), "Investigation of particle size effect on flame velocity in the combustion of nano/micron-sized aluminum particles in air", Proceedings of the Institution of Mechanical Engineers, Part G: Journal of Aerospace Engineering, p. 1–8)
83) Bouillarda, J., Vignesa, A., Dufaud, O, Perrinb, L, and Thomas, D. (2010), "Ignition and explosion risks of nanopowders", Journal of Hazardous Materials, 181, pp. 873–880. Fig. 9, p. 878.
84) Yadollah Bayat, Y. and Zeynali, V. (2011), "Preparation and Characterization of Nano-CL-20 Explosive", Journal of Energetic Materials", 29: p. 281–291
85) Yan-fei, X, Jiang, Y, Chang-fu, X and Yan-feng, G. (2012), "The Study On Ultrafine Explosives' Sensitivity", Advanced Materials Research", 631–632, p. 395–398
86) Selvakumar, N, Azhagurajan, A. and Suresh, A. (2012), "Experimental analysis on nano scale flash powder composition in fireworks manufacturing", Journal of Thermal Analysis and Calorimetry (published online).
87) See for example: Dufaud, O., Perrin, L., Traore, M. Chazelet, S., and Thomas, D. (2009), "Explosions of vapour/dust hybrid mixtures: A particular class", Powder Technology, 190, pp. 269–273
88) Dufaud, O., Perrin, L., Traoré, M (2008), "Dust/vapour explosions: Hybrid behaviors?", Journal of Loss Prevention in the Process Industries, 21, pp. 481–484.
89) Dufaud, O., Poupeau, M., Khalili, I., Cuervo, N., Christodoulou, M., Olcese, R., Dufour, A., and Perrin, L. (2012), "Comparing Pyrolysis Gases and Dusts Explosivities: A Clue to Understanding Hybrid Mixtures Explosions?", Industrial & Engineering Chemistry Research, 51, pp. 7456–7662.
90) Garcia-Agreda, A., Di Benedetto, Russo, P., Salzano, E., and Sanchirico, R. (2011), "Dust/gas mixtures explosion regimes", Powder Technology 205, pp. 81–86.
91) Denkevits, A. (2010), "Hydrogen/dust explosion hazard in ITER: Effect of nitrogen dilution on explosion behavior of hydrogen/tungsten dust/air mixtures", Fusion Engineering and Design, pp. 1059–1063
92) Denkevits, A. (2007), Explosibility of hydrogen–graphite dust hybrid mixtures, Journal of Loss Prevention in the Process Industries 20 (2007) 698–707
93) Abuswer, M., Amyotte, P. and Khan, F. (2013), "A quantitative risk management framework for dust and hybrid mixture explosions", Journal of Loss Prevention in the Process Industries, 26, pp. 283–289.
94) Reyes, O. J., Patel, S. J. and M. Sam Mannan, M. S. (2011), "Quantitative Structure Property Relationship Studies for Predicting Dust Explosibility Characteristics (K_{st}, P_{max}) of Organic Chemical Dusts", Ind. Eng. Chem. Res., 50, pp. 2373–2379
95) Dahoe, A. E., van der Nat, K., Braithwaite, M., and Scarlett, B. (2001), "On the sensitivity of the maximum explosion pressure of a dust deflagration to turbulence", KONA, 19, pp. 178–195.
96) Hilton, J. E. and Cleary, P. W. (2013), "Dust modelling

using a combined CFD and discrete element formulation", International Journal for Numerical Methods in Fluids; 72: 528–549

97) Bakke, J. R., Van Wingerden, K., Hoorelbeke, P., Brewerton, B. (2010): "A study on the effect of trees on gas explosions", Journal of Loss Prevention in the Process Industries, 23, pp. 878–884.

98) Van Wingerden, K. (1996), "Simulations of dust explosion using a CFD-code", Proceedings of the 7th International Colloquium on Dust Explosions, Bergen Norway, pp. 6.42–6.51. Paper available as: http://www.t-solutionglobal.com/ts-upfiles/file/other/2009-1-4/Simulation_of_dust_explosions_using_a_CFD.pdf

99) Skjold, T. (2007), "Review of the DESC project," Journal of Loss Prevention in the Process Industries, 20, pp. 291–302.

100) Skjold, T. (2010), "Modelling of industrial dust explosions in complex geometries," lecture presented at UKELG 46th Meeting on Causes, severity and mitigation of aerosol and particulate explosions, Dept. Chem. Eng., Imperial College, London, 22nd Sept. 2010. Full lecture of Skjold available at: http://ukelg.ps.ic.ac.uk/46TS.pdf

101) Castellanos, D., Skjold, T., van Wingerden, K., Eckhoff, R. K., and Mannan, M. S. (2013), "Validation of the DESC Code in Simulating the Effect of Vent Ducts on Dust Explosions", Industrial & Engineering Chemistry Research, 52, 6057–6067.

102) Proust, Ch. (2006), "On the sensitivity of the maximum explosion pressure of a dust deflagration to turbulence," Journal of Loss Prevention in the Process Industries, 19, pp. 104–120.

103) Xie, Y., Raghavan, V., Rangwala, A. S. (2012), "Study of interaction of entrained coal dust particles in lean methane–air premixed flames", Combustion and Flame, 159, pp. 2449–2456

104) Rockwell, S. R. and Rangwala, A. S. (2013), "Influence of coal dust on premixed turbulent methane–air flames", Combustion and Flame, 160, pp. 635–640.

105) Di Benedetto, A., and Russo, P. (2007), "Thermokinetic modeling of dust explosions", Journal of Loss Prevention in the Process Industries, 20, pp. 303–309.

106) Dahoe, A, and De Goey, L. P. H. (2003): "On the determination of the laminar burning velocity from closed vessel gas explosion experiments", Journal of Loss Prevention in the Process Industries, 16, pp. 457–478.

107) Di Benedetto, A., Russo, P., Amyotte, P., Marchand, N. (2010), Modelling the effect of particle size on dust explosions, Chemical Engineering Science, 65, pp. 772–779.

108) Di Benedetto, A., Maccariello, A., Russo, P. Sanchiricco, R., Di Sarli, V. (2013), "CFD simulations of turbulent fluid flow and dust dispersion in the 20 liter explosion vessel", AIChE Journal, DOI: 10.1002/aic.14029.

Author's short biography

Saul M. Lemkowitz

Saul Lemkowitz studied chemical engineering (B.Sc.) at Rutgers University in the United States. After working at Allied Chemical Europe in The Netherlands, he studied chemical engineering at Delft University of Technology (M.Sc. Ph.D.). He remained at Delft University, as an associate professor of loss prevention and austainability, researching dust explosions and teaching explosion safety (later together with Prof. Hans Pasman). For almost 30 years he has also taught explosion safety to industry. While being formally retired, Dr. Lemkowitz still actively teaches at Delft University and to industry and publishes articles.

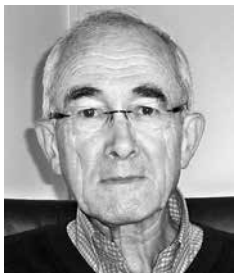

Hans J. Pasman

Dr.Ir. Hans J. Pasman is a research professor at Mary Kay O'Connor Process Safety Center of the Department of Chemical Engineering of Texas A&M University and emeritus professor chemical risk management of the Delft University of Technology in the Netherlands. He has also been a member of the Dutch Council of Hazardous Substances until this council was disbanded in 2012.

Graduated in chemical technology at Delft University of Technology in 1961, and finishing a doctor's thesis in 1964 while employed by Shell, he joined the Dutch organisation for applied research, TNO, in 1965, performing research in reactive materials, gas, dust and energetic material explosions, investigation of industrial accidents and risk analysis, while also managing part of the organization. He has been a member of the Working Party on Loss Prevention and Safety Promotion in the Process Industries since 1972, and has been chairman of the International Group on Unstable Substances for 10 years, of the European Study Group on Risk Analysis (1980–1985), of a NATO Group on Explosives (1982–1992), and chairman of the EFCE Working Party on Loss Prevention (1986–2004). In this latter capacity, he was instrumental in founding the European Process Safety Centre in 1992. He is active in writing and reviewing process safety articles and has obtained numerous awards.

KONA Powder and Particle Journal No. 31 (2014) 82–91/Doi:10.14356/kona.2014014 Review Paper

Design of Optimum Sampling Plans for Dry Powders and Slurries †

Hassan El-Shall[1]* and Brij M. Moudgil[1, 2]

[1] *Materials Science and Engineering, University of Florida, USA*
[2] *Particle Engineering Research Center, University of Florida, USA*

Abstract

Generally, in order to learn about a certain quality of a population, a small portion (sample) is extracted and analyzed for the desired property. In order to obtain accurate information, the sample has to represent the stream it is taken from (plant feed, intermediate product, and/or final product). In materials processing sampling of materials (powders or slurries) is very important to the quality control and quality assurance purposes. This sample can be too large and has to be further subdivided, or too small and a two-stage sampler has to be introduced. In most cases, the desired property is determined by analyzing a sample as small as a few milligrams. In this regard, obtaining a representative sample is not as straightforward as it sounds. For homogeneous materials, it is easy to use statistical probabilities to estimate numbers and sizes of samples that accurately represent the whole population. However, this is not so easy in the actual practice especially dealing with inhomogeneous materials. Therefore, sampling representativeness, perhaps the most important aspect of sampling practice is emphasized in this paper. Sampling strategies and equipment for dry materials and slurries are discussed with links to related literature and sampling equipment manufacturers.

Keywords: sampling, representative samples, dry powders, slurries, sampling errors, sampling equipment, sampling rules

1. Introduction

In order to learn about a certain quality of a population, a small portion is extracted and analysed for the desired property. If the sample is extracted correctly (representative of the population), it can provide information that is used to describe the population. In powder production, as in any materials processing operations, sampling is very critical to the quality control and for quality assurance purposes. Such sampling could be done on the feed stream, the intermediate products, and/or the final products. If this sample is too large then it has to be further subdivided, and if it is too small then a two-stage sampler has to be introduced. In most cases, the desired property is determined by analysing a sample as small as a few milligrams. Using a defined statistical parameter, we can determine if the sample is representative of the larger quantity. We can utilize automatic analysis equipment in process-control sampling to minimize detrimental time delays. The sampling process is as follows:

1. Take a gross sample from bulk material.
2. Divide the sample into smaller weights as required by the subsequent processing step. Sample crushing and/or grinding may be needed during such step.
3. Conduct required tests.

2. Sample Weight

Variations in materials quality dictate sampling techniques. For example, materials containing wide size distributions will require more rigorous sampling than those of close size distributions. In addition, coarse material needs to be sampled more carefully as the desired valuable mineral could be non-uniformly distributed in all the particles. Thus, finer materials may require less sampling than course ones as shown in **Table 1**.

To specify minimum sample size for estimating particle distributions within allowed variance, we use a simple approach based on a screening process in terms of binomial distribution. The particles will either pass through the screen or not. This is clear from examining the following example given in Perry's Chemical Engineering handbook (1997). The sample weight needed for screen analysis can be calculated as follows:

† Accepted: August 1, 2013
[1, 2] P.O. Box 116135, Gainesville, FL 32611, USA.
* Corresponding author:
E-mail: helsh@ad.ufl.edu
TEL: 1-352-846-3557 FAX: 1-352-846-1196

Table 1 Minimum Weight of Samples as a Function of Particle Size
http://www.mine-engineer.com/mining/sample_1.htm

Particle Diameter In Inches	Minimum Weight of Sample (pounds)
0.04	0.0625
0.08	0.5
0.16	4
0.32	32
0.64	256
1.25	2048
2.5	16348

$$W = G\,(100 - G)\,w/V \tag{1}$$

Where:

G = % weight did not pass the desired screen

w = weight of one particle remaining on that screen

V = variance = (Standard error)^2

Another example is given by Allen (2003) and summarized by Davies (2009) relating a minimum weight for the sample depending to the particle size and the variance of the tolerated sampling errors as expressed in the following equation:

$$M_s = 1/2\{\rho/\varphi^2\}\{1/W_\lambda - 2\}d^3_\lambda \times 10^3 \tag{2}$$

Where:

M_s is the limiting weight in grams

ρ is the powder density in gm/cm^3

Φ is the variance of the tolerated sampling error

W_λ is the fractional mass of the largest size class in the bulk

d_λ is the arithmetic mean of the cubes of the largest diameter in the size class in cm^3

3. Number of Samples

In practice, there will always be some differences between the sample and the population. Repeated samples from the same population may also yield different results. Therefore, it is important to answer questions such as "What are the sources of such variations?", "What is the optimum number of samples?", and "How to minimize the errors?" The answers to these questions are very important so that cost effective and efficient sampling plans can be designed to achieve the desired information. These sampling principles are covered by the Theory of Sampling (TOS) which, if properly applied, can lead to information gathering at a minimum cost and in the shortest possible time. For materials processing, there are several challenges encountered due to the nature of the material and/or the processing methods (Gy, 1998). Various sampling errors are discussed in details by Petersen et al. (2005) and will be summarized later in this paper.

In statistics it is convenient to use the term *population* for the aggregate of all possible measurements or observations of a given type. Of course, one sample ($n = 1$) drawn from a population would not give enough information. However, more samples ($n = 100$ for example), if properly drawn, could be very informative about that population. Important statistical information can be derived from the observations. For example, the average and the variance can be calculated as shown below.

Usually, the population is characterized by value of the mean η, and the variance σ^2. The information in the sample is unfolded by calculating the *average*, y_{av}.

$$y_{av} = (y_1 + y_2 + \ldots + y_n)/n = [\Sigma\, y_i]/n \tag{3}$$

$i = 1$

In practical situations we have a sample, from which we estimate the average, as mentioned above, and the variance as:

$$s^2 = [\Sigma\,(y_i - y)^2]/(n-1) \text{ or}$$

$$s^2 = [\Sigma\, y_i^2 - (\Sigma\, y_i)^2/n]/(n-1)s^2 \tag{4}$$

Where:

$\Sigma\, y_i^2$ = Crude Sum of Squares.

$(\Sigma\, y_i)^2/n$ = the Correction Factor.

$[\Sigma\, y_i^2 - (\Sigma\, y_i)^2/n]$ = the Corrected Sum of Squares

$(n-1) = v$ = the degrees of freedom

Thus, s^2 = the Corrected Sum of Squares/degrees of freedom.

$\sqrt{s^2}$ = standard error (s.e.)

From the Central Limit Theorem, if $y_1, y_2 \ldots y_n$ is a random sample of size n from a distribution with mean η and variance σ^2, then $y_{av} = \eta$ and the variance $V = \sigma^2/n$. It should be noted that increasing the number of observations (samples) can lead to reduction in the variance. The implications related to sampling materials will be clarified later.

Variation in a particular result may be contributed by a number of different sources.

For example, the yield of a chemical process on a particular day might be determined by taking one small sample of the product and submitting that sample to a single laboratory test. Variation in the resulting observed yield would be contributed by:

1) the intrinsic day-to-day variability of the process,

2) the sampling error, and

3) the analytical error.

Before efforts can be directed at reducing the over-all variation it is necessary to know the relative importance of these different potential sources of variation.

To estimate these sources of variation a special hierarchical (or nested) design may be run in which two or more samples are taken on each of a number of days, and two more chemical analyses are run on each sample.

An analysis of variance of the results (ANOVA) makes it possible to isolate and estimate the separate components of variance associated with:

1) variation of the process alone,
2) the sampling error alone, and
3) the analytical testing error alone

As a result of such a special study, the researcher who is interested in reducing over-all variation can direct her/his inquiries to the process itself, to the sampling technique, or to the analytical method, as appropriate. Alternatively, she/he may increase the number of samples, or the number of analytical tests, so that through the process of averaging the variance, contribution by any component may be reduced.

Therefore, it is important to be aware of the sources of errors in any sampling plan. These errors are summarized below and explained in details by Petersen, et al. (2005).

4. Sampling Errors

In addition to particle size, all the constituent elements of the stream should have an equal probability of being represented in the sample. Thus, good sampling plans are designed to avoid the following errors (Petersen et al. 2005):

- Compositional error: variations caused by temporal differences in the chemical nature of the bulk material give rise to this error. This error is usually reduced by milling the sampling stream and taking many sample increments from the resulting production cycle.
- Segregation error: this depends on the nature of the material and the ranges of size, shape and density distributions present. Thus, it is directly related to the amount of segregation in a lot. It can be minimized a) by mixing or building up a well-mixed composite sample from a large number of increments and b) by a correct design of the sampling system.
- Statistical error: it is the only sampling error that cannot be suppressed and occurs even in ideal sampling. It can be estimated beforehand and reduced by increasing the sample size (number of samples) as explained above.

In this paper, we will focus on mechanical extraction of representative samples of proper weight and numbers. Manual sampling methods are also used in practice; however mechanical sampling techniques should be used as much as possible to obtain best results with minimum errors. In addition, a good sampling strategy should involve important unit operations as emphasized by several authors (Allen, 2003, Minnitt et al., 2007, and Petersen et al., 2005) including:

- Heterogeneity characterization of new materials
- Sampling bulk material or powder only when in motion.
- Sampling the whole of the moving material stream in many short increments, rather than part of the stream for the whole of the time.
- Mixing (homogenization) well before all further sampling steps
- Composite sampling
- Particle size reduction (comminution or milling) whenever necessary
- Representative mass reduction

5. Sampling Practice of Particulate Materials

5.1 Sampling/mass reduction tools and methods

There are several sampling tools and methods that may be used to extract the primary sample. The choice of particular method depends on many factors including the relative reliability, type of lot to be sampled, etc. Mass reduction is often done via scooping devices or using specific mass reduction devices. Some common mass reduction techniques and devices include: grab sampling, alternate shoveling, fractional shoveling, spoon method, riffle splitters, and rational splitters. Examples of these tools are given below for free and non-free flowing materials.

5.2 Thief or spear sampling

- There are several companies that produce and/or sell such equipment including Samplers direct, Sampling Systems Ltd. UK, EET Corporation, etc. (Specific sampling equipment supplier names are provided for information purposes only and do not necessarily imply endorsement of the equipment by the author) Links to these companies' web sites are given at the end of the paper. Sampling steps generally include,
- Thrusting the spear into the bulk (**Fig. 1**).
  (Powder falls through holes into the spear.)
- Rotating handle and extracting spear with enclosed sample

5.3 Coning and Quartering

Sampling of small heaps is frequently done by coning

Fig. 1 Thief or spear sampling. (Courtesy of EET Corporate, www.eetcorp.com)

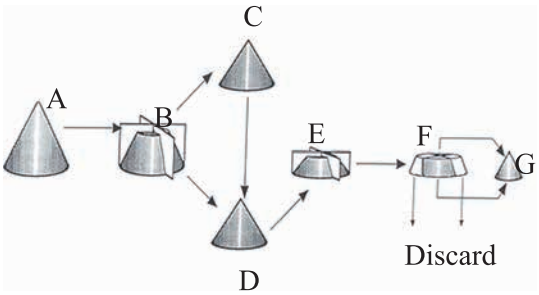

Fig. 2 Coning and quartering as described by Davies (2009).

and quartering. The heap is flattened and separated into four equal parts by a sharp edged tool, opposite quadrants are recombined, half the heap is discarded, and the remaining half is quartered again (**Fig. 2**). This process is repeated until the desired sample mass is achieved. Quartering should not be used for the sampling of free flowing powders. It is more accurate to sample the powder while it is being poured into a heap rather than after. It is not recommended to sample stationary free-flowing powder due to segregation. However, if it must be done, samples should be taken and analyzed separately to determine the degree of segregation. Fine particles will be concentrated in the center of the heap while coarser particles will be located in the outer portions.

5.4 Laboratory Spinning Rifflers

There are several companies producing such splitters. Among them is Quantachrome Instruments Company. A

Fig. 3 A photograph of a micro Riffler. (Courtesy of Quantachrome Instruments, www.quantachrome.com)

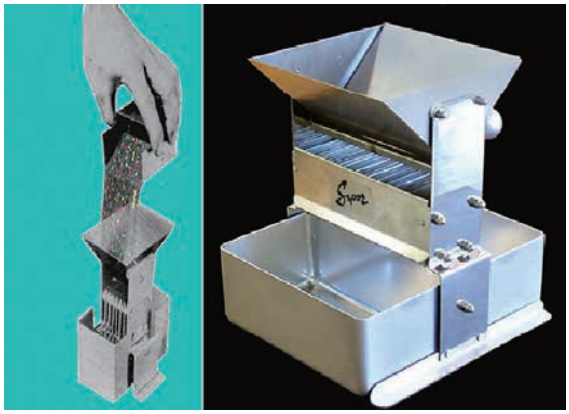

Fig. 4 A picture of Chute Rifflers. (Courtesy of Sepor, www.sepor.com)

picture of a Micro Riffler is given in **Fig. 3**. There are a couple of videos on the company's web site showing the operation of such splitters. For particles of larger size and samples of larger mass, chute rifflers are used. A couple of these rifflers are shown in **Fig. 4**.

It should be noted that reliability of some of these methods is low as shown in the following **Table 2**.

5.5 Sampling non-free flowing stored material

The following points should be taken into consideration before sampling takes place:

- It is usually assumed that the material is well mixed, but this assumption is often incorrect and

Table 2 Reliability of some sampling/mass reduction techniques

Method	Estimated Maximum error (%)
Cone & Quartering	22.7
Scoop Sampling	17.1
Table Sampling	7.0
Chute Riffling	3.4
Spinning Riffling	0.42

biased sampling results.

- Surface sampling by scoop is unreliable.
- Better accuracy is obtained if samples are taken from the body of the material by the use of a sampling spear or thief.
- A template should be devised so that samples can be withdrawn from various parts of the material volume.
- Never take scoop samples if at all possible from heaps. If it must be done, use coning and quartering or chute riffling of the whole heap.
- Sampling materials in bags, bins, wagons, bottles should not be done using scoop or spatula samples. Try to sample the materials when the containers are being filled.
- Expect large sampling errors from stored material sampling.

5.6 Sampling from a hopper/silo

Examples of point samplers for free-flowing and non-free-flowing materials from gravity lines and hoppers are also given in the web site of Sentry Equipment Corporation. A picture of this sampler in operation is given in **Fig. 5** below.

The sampler takes a sample when a gear motor-driven auger draws the product to the discharge point. A schematic of similar operation is shown in **Fig. 6** below (After Davies 2009).

5.7 Sampling Flowing Streams

In this case, Terry Allen's Golden Rules of Sampling should be applied as suggested by Davies (2009):

- A bulk material or powder should only be sampled when in motion.
- The whole of the moving material stream should be sampled in many short increments, rather than part of the stream for the whole of the time.
- The sampling cutter should be designed to introduce no bias in the sampling of the largest particles present, and the cutter must never be allowed to overflow.
- To sample a moving stream the gross sample is made up of a series of increments. In this case, the minimum incremental weight is given by multiplying the flow rate times the cutter width (for a traversing cutter) and the cutter velocity. The cutter width should be large enough (about 10 times the largest particle diameter) so that a biased sample deficient of coarse particles may be avoided.

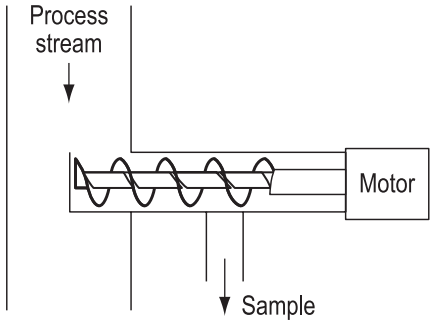

Fig. 5 Screw Sampler. (Courtesy of Sentry Equipment, www.sentry-equip.com)

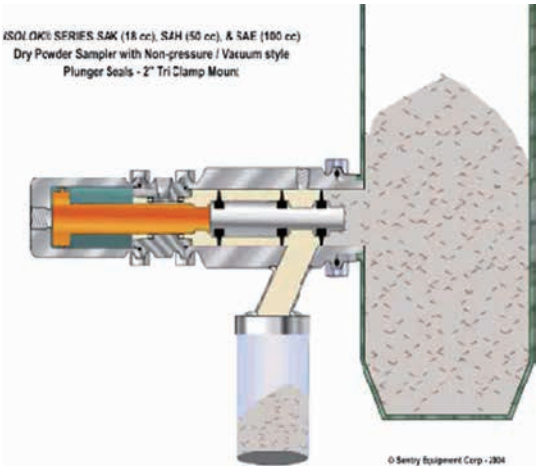

Fig. 6 Schematic of a Screw Sampler. (Courtesy of Sentry Equipment, www.sentryequip.com)

When sampling from a conveyor belt, it is best to sample material as it cascades over the end of the conveyor belt as shown in **Fig. 7**. If this is not possible samples must be taken from the belt itself. Some automatic samplers have a moving arm that sweeps across the belt collecting all of the materials within a particular area. Sampling from a moving stream can be done continually or intermittently. Poor and good sampling procedures are shown below. A schematic drawing is shown in **Fig. 8** to illustrate the reasons for such classification (Courtesy of Davies, 2009).

In **Fig. 8** (**a**) the sample will not represent the whole size distribution as the course particles will not be collected together with the fine particles. However, this does not happen in part (**b**). There are several samplers that can be used for Belt Conveyor sampling such as the ones sold by Sentry Equipment Corporation [www.sentry-equip.com] and Intersystems Company [www. intersystems.com]. The picture of this machine is shown below. The company's web site contains more details as well as a video for this sampler and others.

Point samplers for sampling granules from a screw conveyor are also among the automatic sampling devices sold by various manufacturers. An example is the one sold by Sentry Equipment Corporation [www.sentry-equip.com] shown in **Fig. 9** below. Their web site contains more details as well as a video of an operating sampler.

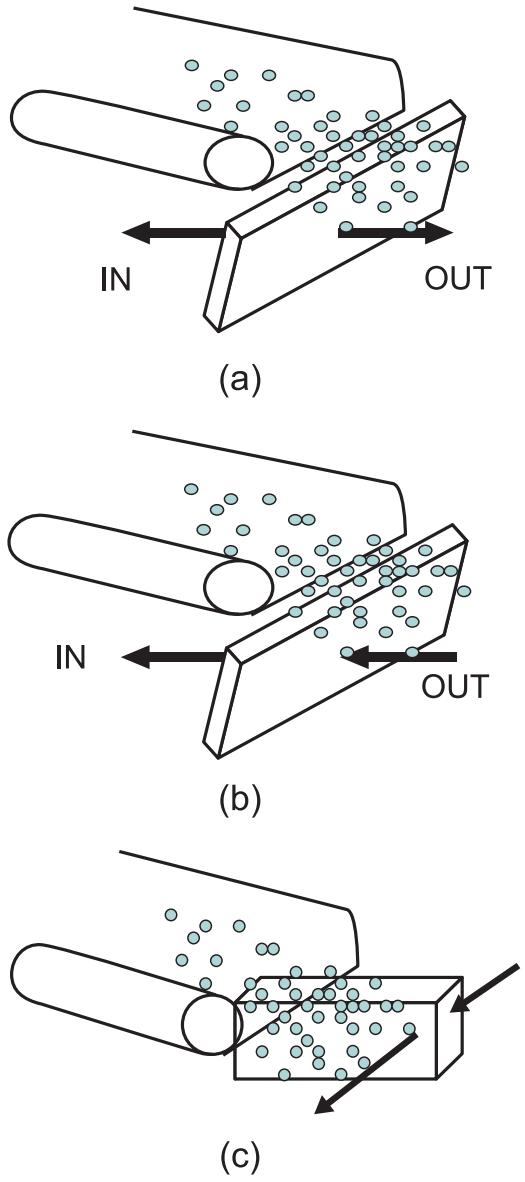

Fig. 7 Sampling from falling conveyors: (**a**) bad sampling technique, (**b**) good sampling technique, (**c**) sampling procedure to be adopted for high mass flow rate. (Courtesy of Reg Davies, 2009)

6. Slurry Sampling

Slurries (a mixture of liquid and solid) are generally easier to sample than solids. Since slurries can be pumped

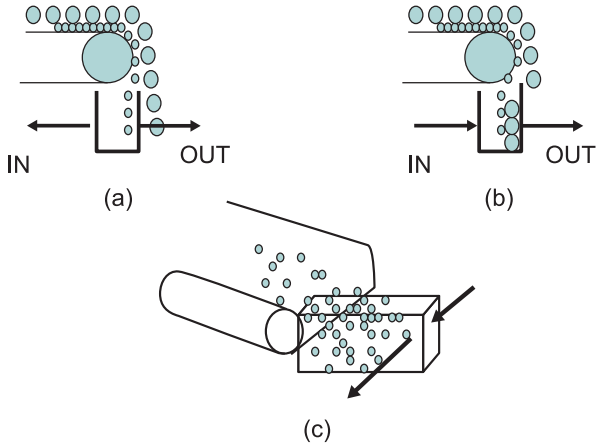

Fig. 8 A schematic drawing explaining the reasons for good and bad sampling techniques. (Courtesy of Reg Davies, 2009)

Fig. 9 Sampling a moving belt.
(Courtesy of Sentry Equipment, www.sentry-equip.com)

through pipes and are in constant motion, we can almost get a perfect representative sample. However, getting a complete cross section can be difficult due to the pipes being round. In-pipe samplers do not adequately extract particles at the pipe walls and thus you must consider both the location and the type of sampler in order to obtain a representative sample.

For accurate primary sampling, it is recommended that you sample at a dumping point. Samples are taken at a pipe discharge point using a cross stream sampler along with a slurry cutter. For secondary sampling, the primary sample can be split using a vezin sampler discussed on the web site of Multotec Company, 2012 (www.multotec.com.au.). Fine particles can be reduced by using a 2% cutter, reducing the primary sample by 98%. Two or three vezins can be used to split larger samples to final lab size volumes for the quality control testing.

In order to assure a representative sample, all material in a process flow should have an equal probability of being part of the sample. Typical process streams require a turbulent flow to keep the slurry in suspension (speed >1.5 m/s) as turbulence keeps the slurry well mixed. Lighter and finer solids in slurry require a greater level of mixing. When particles are above 100 μm in size and/or of high specific gravity material, mixing still produces the desired effect in the horizontal direction. We can use several mechanical sampling equipment, as discussed below, to obtain representative samples.

6.1 Mechanical sampling equipment

For slurry that flows by gravity through launders and sloped pipes, samples are taken from the point of discharge. Samples can also be taken at an open discharge from a vertical gravity pipe. There are two basic mechanical sampler designs for sampling material from a gravity flow such as sampling with linear cutter motion and sampling with radial cutter motion. When equipment is properly designed and operated, both designs produce the same result. Based on flow quantity, we can determine the mechanical installation factors. Equipment suppliers should be consulted to provide the proper design for any particular application. For helpful information, you may consult Perry's Handbook of Chemical Engineering (1999).

6.2 Sampling from Pipes

In Florida phosphate industry, sampling equipment is either home-custom made or obtained from suppliers such as in **Fig.10** from Sentry Equipment Corp. The following is a general description of sampling slurries either flowing under pressure or by gravity.

Fig. 10 Sampling a Screw Conveyor. (Courtesy of Sentry Equipment, www.sentry-equip.com)

6.2.1 Pressure Flow

We must determine the primary sample flow for process streams under pressure. This is done by finding the balance between sampler pressure head and sample pipe friction. Outokumputechnology.com (2011) offers a full description of primary samplers and criteria relating sampler specifications to pipe size and flow rates. In addition, sentry-equipment.com offers a wide array of sampling equipment that can be used for slurry sampling from pipes under pressure flow or gravity flow. **Fig. 11** shows an example of such equipment (ISOLOK® SAA Automatic Fixed Volume Sampler).

6.2.2 Gravity Flow

Gravity flowing slurries either through in launders, sloped pipes or vertical gravity flow pipe, should be sampled at the point of discharge. A vertical sample cutter can be used for process streams at/around ambient pressure. In order to obtain a proper sample using this technique, you must ensure that the cutter used has an opening many times larger than the largest particle size of sample slurry (preferably greater than 20 mm, no less than 8 mm). You can use an adjustable cutter opening to adjust sample flow for pipe sizes up to 400 mm. Several sampling steps or innovative sampling designs are required

Outokumputechnology.com (2011). In addition to Outokumputechnology (now Outotec), Sentry Equipment Corporation and other suppliers have several samplers that can be used for this purpose. These companies' web sites are given below to guide you to choose the best sampler for your application. Another example of samplers that can be used for flowing streams either under pressure or under gravity is shown in **Fig. 11** as published by Sentry Equipment Corporation (2011).

There are other types of samplers using linear and rotary traverse mechanisms. The following is an example of how to calculate amount of sample in every increment

ISOLOK® SAA Automatic Fixed Volume Sampler
Captures 3 or 8 cc per cycle of liquids and slurries

Fig. 11 In-line Sampling Equipment for Pressure Flows. (Courtesy of Sentry Equipment www.sentry-equip.com)

ISOLOK® SAB Automatic Fixed Volume Sampler
Captures 10 or 25 cc per cycle of liquids and slurries

Fig. 12 Automatic Sampler for Tanks, Mixers, and Reactors. (Courtesy of Sentry Equipment www.sentry-equip.com)

as mentioned in Perry's Handbook of Chemical Engineering (1997).

6.2.3 Slurry Sampling by Rotary Traverse of Gravity Flow

Given the following information, the quantity of slurry extracted by one rotation, S, can be calculted.

S = increment volume (quantity of slurry extracted by one rotation)

B = bulk slurry flow, in volume/unit time

R = rotation of cutter, in rpm

D = cutter angle opening, $D/360$ = extraction ratio for continuous cutter rotation

$$S = D \times B/360 \times R \quad (5)$$

In addition to mechanical sampling equipment, hand sampling can be used to obtain samples from gravity flowing material from chutes, vibrating screens, belts, etc. When sampling from such streams, it is best to sample material as it cascades over the end of the equipment as explained earlier in the case of belt conveyors.

Suppliers of sampling equipment are eager to help in choosing the proper samplers for specific applications. Another example of such equipment is presented in **Fig. 12** as a courtesy of Sentry Equipment Corp. The *ISOLOK®* SAB operates when compressed air forces the plunger into the process line to capture a fixed volume of material. Compressed air then acts on the opposite side of the piston to retract the plunger to a position which allows the sample to drop by gravity into a container. The operator is isolated from the process at all times by the sampler's seal design, and the sample captured in the container is "locked out" from external influences. The reader is advised to consult the manufacturer catalogue for further details.

6.2.4 Calculation of Sample Extraction Increments

Cooper in Perry's Handbook of Chemical Engineering (1997) presents clearly several examples illustrating calculation of incremental weights obtained by three commonly used sampling methods. These methods include: (a) Linear Traversing Trajectory Cutter, (b) Slurry Sampling by Rotary Traverse of Gravity Flow as explained above, and (c) Cross-Belt Sampling of Solids from Conveyors

6.2.5 Processing Wet Samples

Collected samples are dried in air and/or ovens provided that drying does not affect the chemistry of the sample contents. The dried samples then will be treated as dry powder sampling procedure explained earlier.

7. Summary Highlights of Sampling Rules

Several authors including Allen 2003, Davies 2009, Gy 1998, 2004a, 2004b, Minnitt et al. 2007, and Petersen et al. 2005 stressed the importance of the following points:

There are several sampling tools and methods that may be used to extract the primary sample. The choice of particular method depends on many factors including the relative reliability, type of lot to be samples, etc. It should be noted that reliability of some of these methods is low.

It is usually assumed that the material is well mixed, but this assumption is often incorrect and biased sampling results.

Select general guidelines for obtaining reliable sampling results are as follows.

- Never take scoop samples if at all possible from heaps. If it must be done, use coning and quartering or chute riffling of the whole heap.
- Sampling materials in bags, bins, wagons, bottles should not be done using scoop or spatula samples.

Try to sample the materials when the containers are being filled.

- A bulk material or powder should only be sampled when in motion.
- The whole of the moving material stream should be sampled in many short increments, rather than part of the stream for the whole of the time.
- When sampling from a conveyor belt. It is best to sample material as it cascades over the end of the conveyor belt. If this is not possible samples must be taken from the belt itself.

Acknowledgements, Copy right statement and disclaimer

Financial support of this work was provided by the Center for Particulate and Suspension Systems (CPaSS) a NSF I/UCRC (NSF Grant #0749481). Opinions expressed are those of the authors and do not necessarily represent the views of the NSF or the CPaSS Industry Members. Commercial suppliers of the various equipment are provided for information purposes only and do not necessarily imply endorsement of the specific equipment by the authors.

References

Allen T., Powder sampling and particle size determination, first ed., Elsevier, New York, 2003.

Cooper H., Sampling of Solids and Slurries in Solid-Solid Operations and Equipment, section 19, Perry's Handbook of Chemical Engineering, seventh edition, McGraw-Hill, 1997.

Davies R., Sampling Particulate Materials, A short course at Particle Engineering Research Center, University of Florida, (April 2009).

Gy P., Sampling for analytical purposes, John Wiley & Sons, New York, 1998.

Gy P., Sampling of discrete materials, A new introduction to the theory of sampling: I. Qualitative approach, Chemometrics and Intelligent Laboratory Systems, 74(1) (2004a) 7–24.

Gy P., Sampling of discrete materials: A Quantitative approach—sampling of zero-dimensional objects, Chemometrics and Intelligent Laboratory Systems, 74(1) (2004b) 25–38.

Minnitt R.C.A., Rice P.M., Spangenberg C., Part 1: Understanding the components of the fundamental sampling error: A key to good sampling practice, Journal of the South African Institute of Mining and Metallurgy, 107(8) (2007) 505–511.

Petersen L., Minkkinen P., Esbensen K.H., Representative sampling for reliable data analysis: Theory of sampling, Chemometrics and Intelligent Laboratory Systems, 77(1-2) (2005) 261–277.

Links to Literature

● The Accuracy of Systematic Sampling from Conveyor Belts:
http://www.jstor.org/stable/pdfplus/2985832.pdf
● Sampling equipment:
http://www.powderandbulk.com/analyzers/samplers.htm
● Belt conveying equipment:
http://www.powderandbulk.com/conveying/belt.htm
http://www.directindustry.com/industrial-manufacturer/bulk-and-powder-handling-and-equipment-152/conveyor-belt-61357.html
http://www.ktron.com/products/pneumatic_conveyors/index.cfm
http://www.flexicon.com/us/products/PneumaticConveyingSystems/index.asp
http://www.vac-u-max.com/pneumatic.html

Author's short biography

Hassan El-Shall

Dr. El-Shall is a professor emeritus at the Department of Materials Science and Engineering of University of Florida. He has been serving as an associate professor of Materials Science and Engineering and Associate Director for Research at The Particle Engineering Research Center of University of Florida since 1994. He also served as Associate Director for beneficiation research at the Florida Institute of Phosphate Research from 1986–1992. In the early 80's, he has served as assistant professor of Mineral Processing at Montana Tech from 1980 to 1986. He posses thirty nine years of diverse experience in research (both basic and applied), management, as well as hands-on experience in the areas of Applied Surface and Colloid Chemistry, Mineral Processing, Chemical Metallurgical Engineering, and related environmental services. His work related to industrial minerals such as phosphate, gypsum, clay, etc is recognized by his peers allover the world. In addition, he has extensive and practical experience in the development of training and teaching programs for both undergraduate and graduate students in the above fields. His major research interests include interfacial phenomena and its applications in mineral industry, and waste treatment in various industries. He expanded his research efforts to include mineral modifications for medical applications.

Dr. El-Shall has published over 165 publications including: 11 patents, 9 edited books, one authored manual, 19 chapter contributions to books, over 50 Refereed articles in prestigious journals such as Powder Technology, Mineral and Metallurgical Processing, International Journal of Mineral Processing, and others, in addition to many industrial reports.

Dr. El-Shall is a dedicated teacher in the fields of Mineral processing Engineering, Materials Science and Engineering, and Chemical Engineering. He has served as chair, co-chair, or a member of over 50 graduate committees for M.S. and Ph.D. students including his own 15 M.Sc. and 13 Ph.D. students who are currently employed by various industries.

BRIJ M. MOUDGIL

Dr. Brij M. Moudgil is a Distinguished Professor of Materials Science and Engineering, Director of the Particle Engineering Research Center (PERC), and the Center for Particulate and Surfactant Systems (CPaSS–NSF I/UCRC) at the University of Florida, Gainesville, FL. Dr. Moudgil also serves as the Director of the UF Mineral Resources Research Center. He received B.E. (Metallurgy) degree from the Indian Institute of Science (IISc), Bangalore, and M.S. and Eng.Sc.D. Degrees in Mineral Engineering from the Henry Krumb School of Mines, Columbia University, New York, NY. His research and professional leadership accomplishments are recognized by several major awards including his election to the National Academy of Engineering (NAE), U.S.A. He has been also elected as Foreign Fellow of the Indian National Academy of Engineering. He is recipient of the 2003 Distinguished Alumni Award of the Indian Institute of Science, Bangalore. He served as 2006 President of the Society for Mining Metallurgy and Exploration, Inc. (SME). His current research interests include engineered particulate systems for enhanced performance in nano and bio technologies, advanced materials and minerals, microelectronics, photocatalytic degradation of hazardous microbes, nanotoxicity, and greener reagents and particle technologies.

KONA Powder and Particle Journal No. 31 (2014) 92–110/Doi:10.14356/kona.2014015 Review Paper

Versatile Fabrication of Complex Shaped Metal Oxide Nano-Microstructures and Their Interconnected Networks for Multifunctional Applications†

Yogendra Kumar Mishra[1]*, Sören Kaps[1], Arnim Schuchardt[1], Ingo Paulowicz[1], Xin Jin[1], Dawit Gedamu[1], Sebastian Wille[1, 2], Oleg Lupan[1, 3] and Rainer Adelung[1]

[1] *Functional Nanomaterials, Institute for Materials Science, University of Kiel, Germany*
[2] *Department of Prosthodontics, Propaedeutics and Dental Materials, University Medical Center Schleswig-Holstein, Germany*
[3] *Department of Microelectronics and Semiconductors Devices, Technical University of Moldova, Republic of Moldova*

Abstract

Metal oxide nano-microstructures are applied in photocatalytic surfaces, sensors or biomedical engineering, proving the versatile utilization of nanotechnology. However, more complex or interconnected nano-microstructures are still seldomly met in practical applications, although they are of higher interest, due to enhanced structural, electronic and piezoelectric properties, as well as several complex biomedical effects, like antiviral characteristics. Here we attempt to present an overview of the novel, facile and cost-efficient flame transport synthesis (FTS) which allows controlled growth of different nano-microstructures and their interconnected networks in a scalable process. Various morphologies of nano-microstructures synthesized by FTS and its variants are demonstrated. These nano-microstructures have shown potential applications in different fields and the most relevant are reviewed here. Fabrication, growth mechanisms and properties of such large and highly porous three-dimensional (3D) interconnected networks of metal oxides (ZnO, SnO_2, Fe_2O_3) nano-microstructures including carbon based aerographite material using FTS approaches are discussed along with their potential applications.

Key words: Flame transport synthesis, metal oxide, ZnO, SnO_2, Fe_2O_3, nano-microstructures, nanorods, nanowires, interconnected tetrapods networks, multifunctional applications, aerographite

1. Introduction

Metal oxide nano-microstructures such as nanorods, nanowires, nanobelts, nanotetrapods and others are being significantly investigated due to their new and extraordinary properties appropriate for versatile nanotechnological applications[1–3]. Fabrication of several nanostructures from various metal oxides like ZnO, SnO_2, TiO_2, and Fe_2O_3 has already been performed using several growth techniques and their properties have been reported[1–4]. Among them, ZnO is one of the most investigated materials in the last decades, because of its wide and direct bandgap of ~3.37 eV, large exciton binding energy ~60 meV and simplicity in growth[1–3, 5]. Due to its hexagonal-wurtzite crystal structure, Zn and O terminated polar surfaces, different growth rates of the diverse crystal planes, quasi-1-Dimensional (Q1D) nanostructures and complex morphologies from ZnO can be synthesized. The direct bandgap which lies in the near ultraviolet -(UV) spectral region and alternating Zn and O stacking layers enable ZnO nanostructures to exhibit exceptional optical, luminescent[6, 7] and electrical properties[5, 8–11]. Bendability is also a very important property required for different applications but bulk ceramics or metal oxides are brittle in nature[1–3]. However, their Q1D structures can bent elastically to larger curvatures once their thickness is in the nanoscopic range[1–3, 12]. Nanorods and nanowires from ZnO have already shown interesting piezoelectric properties for energy or mechanical applications[1–3, 13]. Illumination of ZnO nanostructures with UV light creates electron-hole pairs and thus changes their conductivity and enables its uses for photodetectors[14–19]. Additionally ZnO nano-microstructures are extensively investigated for light emitting diodes and gas sensing applications[14, 20–22]. By doping with different elements it is possible to enhance the sensing performances of ZnO nanostructures[23, 24]. ZnO nanostructures have also been considered as biocompatible material and

† Accepted: August 20, 2013
1 Kaiser Str. 2, D-24143, Kiel, Germany
2 Campus Kiel, Arnold-Heller-Str. 3 - Haus 26, D-24105, Kiel, Germany
3 168 Stefan cel Mare Blvd., MD-2004, Chisinau, Republic of Moldova
* Corresponding author:
E-mail: ykm@tf.uni-kiel.de
TEL: +49-431-880-6195 FAX :+49-431-880-6124

therefore have been significantly employed in biomedical applications[25–29]. Furthermore, the interconnected nanostructures can build up microstructures or even highly porous 3D interconnected macroscopic networks which avoid risks of toxicity as a result from nanoscale particles. However, several issues like actual effect and cytotoxicity are still open[25, 30]. In general, various physical and chemical properties of different metal oxide nanostructures depend not only on their sizes and morphologies, but also on the synthesis techniques and experimental conditions (or technological 'history'). Despite of such interesting applications, the scientific community is still looking for appropriate synthesis techniques, which can facilitate the versatile fabrication of different networked metal oxide nano-microstructures for practical applications in a cost-effective and scalable process.

Several synthesis methods have been utilized for growing different metal oxide nano-microstructures. Vapor-liquid-solid (VLS) mechanism[31] has been a very common process for controlled growth of ZnO nanostructures like nanorods[32, 33], nanowires[34], nanotrees[35], and interpenetrating ZnO nanosails bridge[36] at junctions, etc. Other methods like hydrothermal synthesis[37–39], chemical vapor deposition (CVD)[40], microwave chemistry[41], combustion synthesis[42], plasma process[43, 44], electrochemical deposition[14, 45, 46], gas phase synthesis[47] and flame based synthesis[48–51] have been employed to grow metal oxide nanostructures, especially ZnO nanostructures. Thus, an easy scalable, cost-effective and facile synthesis method which can produce large amounts of different metal oxide nano-microstructures is still a highly demanded aspect for various applications.

Although most of the mentioned synthesis methods enable controlled growth of metal oxide nanostructures, but they lack with the feature of *in-situ* integration of such nanostructures directly on the chip in form of device. One requires nanoscale electrical contacts and this further hinders their application. To overcome such technological limitations a thin film fracture approach[52] was invented recently. It allows direct fabrication of desired metal or metal oxide nanostructures between the electrical contacts on the sensor or device chip[53–55]. However, most desirable technological procedures are based on facile growth and direct integration of nanostructures on chip in a single step. Fabrication of large and porous 3D networks from interconnected metal oxide nanostructures might be an ideal choice for utilizing its nanoscale properties at macroscopic scale for different industrial technologies. It is important to mention that it has not been explored in details yet. Only few groups[56, 57] have reported fabrication of 3D networks from metal oxide nanostructures using different techniques.

Recently Adelung and co-workers[58, 59] have introduced a very simple and novel flame transport synthesis (FTS) approach which allows facile fabrication of versatile metal oxide nano-microstructures and their macroscopic networks. These FTS synthesized metal oxide nano-microstructures have already shown promising applications in different directions[60–66]. ZnO nanoseaurchin and tetrapod type structures grown by FTS approach exhibit strong potential of blocking the viral (herpes simplex virus type-1 and type-2) entry into the cells[60, 61]. The submicron size tetrapods can be utilized for advanced linking technologies[64] and designing multifunctional composites, e.g., new concept of self-reporting material[65]. In this context, FTS approach offers a simple way to fabricate large size 3D networks from interconnected metal oxide nano-microstructures with desired porosity and mechanical strength. These 3D networks are stable at high temperatures (up to ~1400°C), electrically conducting and therefore can be used in advanced technological applications[57]. Recently, such 3D interconnected ZnO tetrapods networks were used as templates for the guided growth of the carbon based new aerographite material, which is currently one of the least dense materials in the world[67]. In this paper, we present the growth of different metal oxide nano-microstructures and their interconnected 3D networks by FTS approach and its variants. Different morphologies, growth mechanisms and properties of nanomaterials are presented and discussed in detail.

2. Experimental

2.1 Materials Requirements

Flame transport synthesis (FTS) method and its variants[59] mainly require microscale diameter spherical metal particles as precursor materials, sacrificial polymer (e.g., polyvinyl butyral (PVB), etc.) and ethanol for mixing homogeneously in slurry form. In our works[59], different metal particles powders (Zn, Fe, Sn, Bi, Al, Si etc.) with diameters in the range from 3 μm to 45 μm have been used (purchased from GoodFellow UK, purities 99.9% to 99.99%). PVB powder (supplied by Kuraray Europe GmbH, Germany) was used as sacrificial polymer for the presented experiments. A simple muffle type furnace which can rapidly heat up to high temperatures was used for our experiments. Also, in these experiments, no gas control or vacuum equipment is necessary because it works in normal air environment. Some ceramic plates, crucibles, and cylinders and conventional burner type equipments are required for different variants of FTS approach[59].

2.2 Flame transport approach and its variants

The first variant of FTS approach (**Fig. 1a**) enables the fabrication of nanoseaurchin type structures[59]. For this process the slurry mixture of precursor metal -microparticles, PVB powder and ethanol is prepared in appropriate ratio

and coated on desired substrates (Si, Aluminum etc.). After drying the coated layer on the substrate, it is heated at different temperatures (depending upon the type of precursor metal microparticles) and formation of nanoseaurchin type structures occurs. For example, to synthesize ZnO nanoseaurchins, a temperature above 550°C is sufficient. According to our experimental evidence for iron oxide nanoseaurchins, the optimum temperature is about 900°C. By increasing the precursor metal particle ratio versus PVB in the slurry and by increasing the thickness of the coated layer, it was possible to fabricate a 3D network from nanoseaurchins (**Fig. 2a**) in a similar manner. The second variant of FTS approach allows direct transformation of precursor metal microparticles into metal oxide nano-microstructures in powder form (**Fig. 3a–3d**). The mixture Zn:PVB with ratio 1:2 was filled in the ceramic crucible and heated up to 900°C, which results in formation of different ZnO nano-microstructures in form of powder. These nano-microstructures can be harvested from the furnace and accordingly utilized for desired applications[59]. The yield per experiment mainly depends on the several factors like ratio of Zn to PVB, amount of Zn and PVB mixture and temperature of the furnace etc. In each standard experiment for ZnO tetrapods production (Zn:PVB = 1:2, 900°C, 30 minutes) the yield was around 30–40% and in each experiment and we harvest about 15–20 grams of ZnO tetrapods depending upon initial conditions. The third variant of FTS approach utilizes an in-house ceramic cylinder arrangement (**Fig. 5a**) and it enables controlled synthesis of different quasi-1D nano-microstructures and their networked bridges. The fourth variant utilizes a simple burner approach (**Fig. 6a**) in which the precursor metal microparticles are directly inserted into the oxygen and propane gas mixture inside the burner tube. On their way in the flame, these precursor metal microparticles are converted into various metal oxide nano-microstructures within milliseconds and can be collected in form of powder or *in-situ* integrated on the substrate/chip as per requirements[59]. The main aim of this paper is to provide an overview of different structures, which can be synthesized using proposed FTS approaches for practical applications. More technical details about ratios, growth conditions, temperature time and substrate positions can be found in previous works[58, 59].

2.3 Characterizations:

The obtained nano-microstructures by FTS approach were characterized using scanning electron microscope (20 keV Philips-FEI XL30 equipped with LaB_6 filament). Electromechanical measurements of Q1D, 2D and 3D networks were performed by using a home made setup which includes a micro-manipulator, a Keithley 2400 Sourcemeter, and a computer-controlled laboratory balance with the help of a LabView program[59].

3. Results and discussions

3.1 Growth of metal oxide nanoseaurchin structures using first variant of FTS approach

Fig. 1 demonstrates the growth mechanism of nanoseaurchin type structure and few examples of already synthesized nanoseaurchins from different metal oxides (ZnO, SnO_2, Fe_2O_3, Al_2O_3, Bi_2O_5). To grow ZnO nanoseaurchins, a dilute slurry mixtures from Zn, PVB and ethanol [Zn:{PVB:Ethanol}=1:3{1:2}] was prepared and coated on Si substrates. After drying the slurry coated substrate was heated at 600°C in the muffle furnace for 2 hours. Depending upon the requirements the ratios of Zn, PVB and ethanol were varied and the coated substrates were heated above 600°C for different durations to synthesize various types of seaurchins[59]. In similar manner, nanoseaurchins of several other metal oxides have been successfully grown and can be found in previous work[59].

For the growth of core-spike nanoseaurchins (**Fig. 1**), the crystalline quality of precursor metal micro-particles as well as processing temperature play very important roles. The sacrificial polymer (PVB) and ethanol mixture exhibit double roles: (i) it maintain necessary separation between precursor microparticles which prohibits the agglomeration of metal microparticles and (ii) during heating it provides necessary local environmental control for nanospike growth on the surface of microscopic core. Also above certain temperature (below the nanospike growth) the PVB decomposes entirely and leaves no fingerprints behind in the grown seaurchins or nanostructures, since it contain only C and O. The heating ramp rate of the furnace is the most important parameter for growth of nanoseaurchins, e.g., faster heating rates result in a better growth of such micro-nanostructures (we used furnace with ramp rate above 100°C/min). It has been observed that the metal oxide nanospikes were synthesized on the surface of precursor metal microparticles only when the growth condition is far from thermal equilibrium. Under such circumstances, the kinetic growth processes dominate and it leads to a nanospike growth on the substrate/crucible surface. This type of the spherical precursor microparticles exhibit surface defects, like reconstructed surface and grain boundaries[68]. It seems that the grain boundaries most likely offer the energetically favorable nucleation sites to initiate the nanospike growth[68]. These nanospikes were investigated in details using cross-sectional high resolution transmission electron microscopy along with precession electron diffraction studies and it was observed that they consist of twin boundary propagating along the *c*-axis[69]. Such ZnO nanoseaurchin structures show their promising application as potential candidate for blocking the viral (HSV-1) entry into the cells[60]. Further work on this kind of micro-nanostructures is in progress.

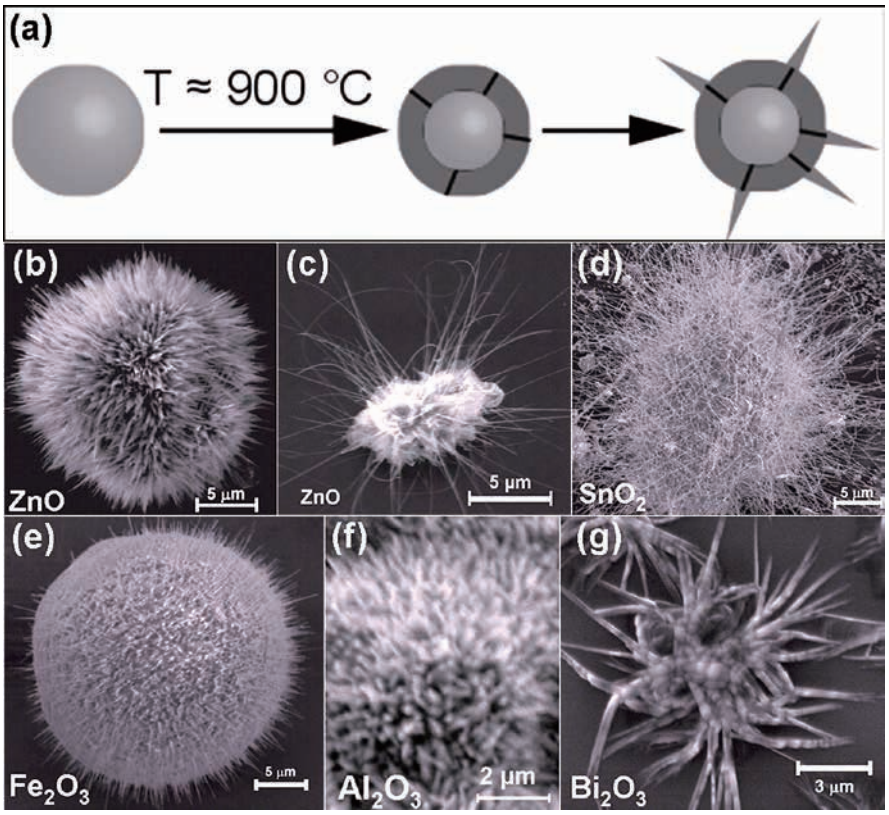

Fig. 1 (**a**) Schematic drawing demonstrating the formation of core-spike nanoseaurchin type structure. (**b**)–(**g**) Nanoseaurchins of different metal-oxides (ZnO, SnO_2, Fe_2O_3, Al_2O_3, Bi_2O_3) grown by using FTS approach. (**b**) & (**c**) Two typical examples of ZnO nanoseaurchins grown at 900°C. (**d**) Tin oxide nanoseaurchin structure grown at 950°C. (**e**) Core-spike nanoseaurchin from iron-oxide obtained at 900°C. (**f**) Aluminum oxide nanoseaurchin grown by FTS approach (shown in **1a**). (**g**) Bismuth oxide nanooctopus type structure with branched nanoscopic arms fabricated at 900°C. [Partially reproduced from Fig. 1 with permission from[59)]].

As mentioned already that growth of 3D interconnected network from metal oxide nanostructures is a highly demanded aspect for practical applications. Using the growth concept of nanoseaurchins, we have successfully grown large 3D interconnected networks from core-spike nanoseaurchins. The schematic drawing for 3D network growth is demonstrated in **Fig. 2a** in which a thick layer of slurry mixture is coated on the substrate. The ratio of metal microparticles, PVB and ethanol is kept in such a manner that the precursor metal particles are homogenously dispersed in the slurry and during coating they are well separated by sacrificial polymer layer (mixed with ethanol). After drying the substrate with slurry is heated rapidly up to higher temperature (typically ~600°C for ZnO, and ~900°C for Fe_2O_3, SnO_2, Bi_2O_3 and Al_2O_3)[59)]. Because of rapid heating process, the growth of nanospikes on surface of precursor metal particles is initiated like demonstrated in **Fig. 1**. The sacrificial polymer layer plays a crucial role here as it maintains the necessary separation between microscopic particles and at the same time nanospikes grow and form interconnecting bridges between individual cores[59)]. These interconnecting nanospike bridges provide mechanical strength to the network[59)]. Using this concept, large 3D interconnected networks from ZnO nanoseaurchins were successfully grown and are shown by zoom-in series of SEM images in **Fig. 2(b–d)** (from left to right). The interconnecting nanospike bridges can be clearly seen in high magnification SEM image in **Fig. 2d**.

A large 3D network from ZnO nanoseaurchins grown on Aluminum substrate (shown in **Fig. 2e**) following a similar FTS approach. Such kind of networks were investigated by SEM and confirmed that it is entirely made from interconnecting core-spike nanoseaurchins, as presented in **Fig. 2(f)**. Its corresponding higher magnification SEM image is shown in **Fig. 2(g)**. The 3D networks from ZnO nanoseaurchins have been successfully grown and optimized. However experiments for other metal oxide 3D networks are currently under progress.

The second variant of FTS approach enables direct conversion of precursor metal microparticles into nanostructures within the flame created due to burning of sacrificial polymer (PVB). The mixture of precursor metal microparticles and PVB (1:2 ratio by weight) is filled in the ceramic crucible which is placed inside the furnace and heated

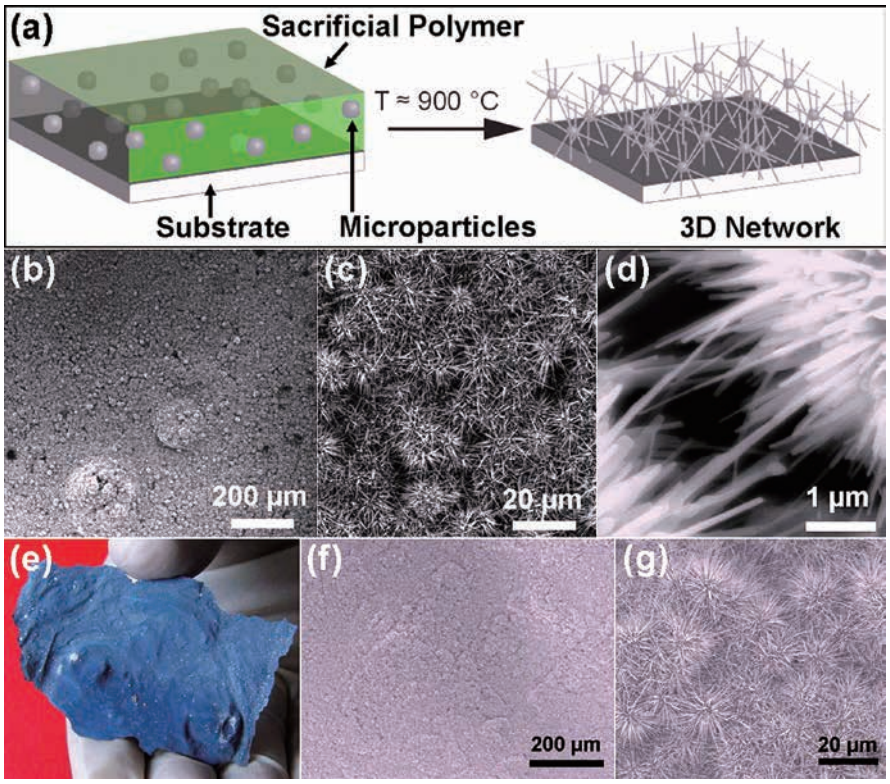

Fig. 2 (**a**) Fabrication principle of 3D interconnected networks by assembling nanoscale seaurchins. The precursor metal microparticles are mixed with sacrificial polymer and ethanol and then coated on substrate. During heating, the sacrificial polymer decomposes completely and at the same time the nanospikes grow and establish the interconnections among microscopic cores which provide the mechanical strength to the network. (**b**)–(**d**) SEM images from a 3D interconnected ZnO nanoseaurchins network at increasing magnifications (from left to right) synthesized by approach described in (**a**). (**e**) Digital camera image a 3D ZnO nanoseaurchins network synthesized using Aluminum substrate. (**f**) and (**g**) SEM images from the 3D interconnected network (shown in **e**) at higher magnifications (left to right). [Partially reproduced from Fig. 1 with permission from[59)]].

rapidly up to temperature of 900°C (for Zn microparticles). Because of high heating rate the PVB starts burning and creates intense flame[59)]. Then, the precursor metal microparticles travel in the flame stream and due to of high flame temperature are converted in ZnO nano-microstructures. After reaching 900°C, the temperature of the furnace is maintained constant for different time spans (ranging from 30 minutes to 4 hours depending upon the requirements) for proper growth of specific nano-microstructures. The role of sacrificial polymer (PVB) is very important in FTS process, as it maintains the separation of metal microspheres, creates the flame and also enables necessary environmental conditions for nano-microstructures growth[59)].

The conversion principle of precursor metal microparticles into the flame is demonstrated in **Fig. 3a**. For simplicity reasons only two types of structures (tetrapods and multipods) are shown in the schematic however structures with various complex morphologies have been grown. **Fig. 3b** shows the digital camera image of the on going FTS process and the intense yellow flame in the centre shows the turbulent stream of flame in which microparticles are being converted into nano-microstructures. Once the process time is achieved, the furnace was turned off. After cooling one can see the crucibles and the base of the furnace are entirely covered with snowflake type white powder (**Fig. 3c**). These snowflake type powders consist of tetrapods, multipodes, branched ZnO nano-microstructures depending upon the location in the furnace. The snowflake type powder was harvested from positions 1 and 2 (**Fig. 3c**) was analyzed inside SEM. Morphological studies of the powder harvested from position 1 **(Fig. 3c**), i.e., from the crucible, revealed that it mainly consists of ZnO tetrapod structures with different sizes as shown by SEM images in **Fig. 3(d–f)** at increasing magnifications (from left to right). However, the fluffy powder at the base (position 2, **Fig. 3c**) consists of ZnO tetrapods, ZnO multipodes and several other complicated shapes as evident by SEM images in **Fig. 3(g–i)** at increasing magnifications (from left to right). The ZnO tetrapod and multipode structures can be harvested and can be utilized accordingly for desired applications. The ZnO tetrapods have shown promising applications, as antiviral agents[60, 61)], in advanced linking

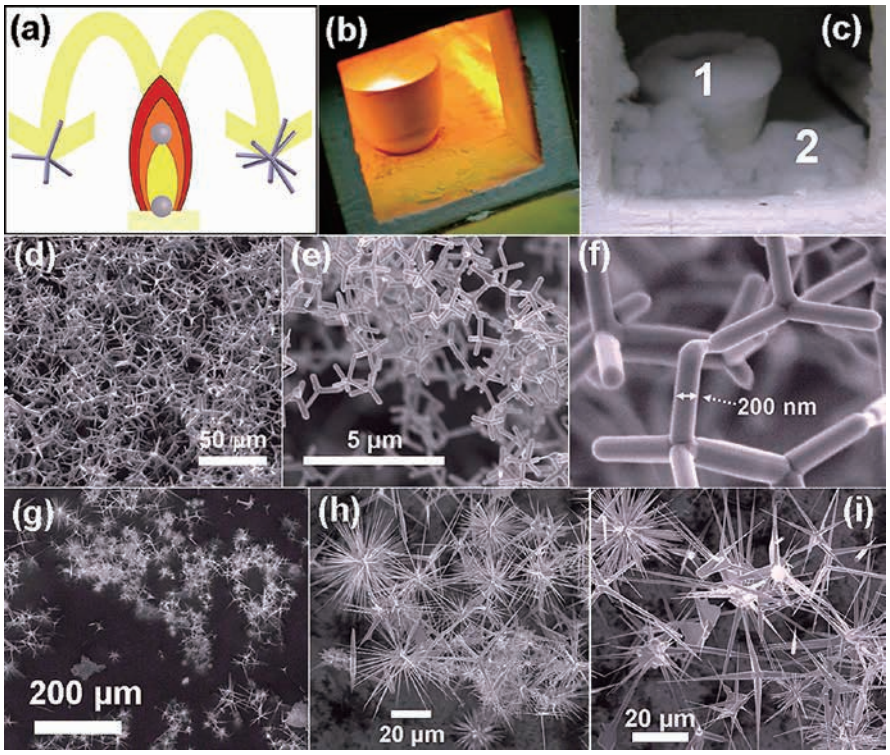

Fig. 3 Flame transport synthesis of different nano-microstructures: (**a**) Schematic drawing showing the conversion principle of precursor metal microparticles into different nanostructures by flame; (**b**) digital photograph of ongoing flame transport process in the furnace. The mixture of precursor metal microparticles and sacrificial polymer powder are filled (~60% by volume) into ceramic crucible and then heated in the furnace at 900°C. The intense yellow flame in the centre of crucible shows the ongoing flame transport process. (**c**) Digital photograph of the furnace chamber after the flame transport process. The converted nano-microstructures are deposited everywhere inside the furnace. These structures can be harvested from different locations (e.g., 1 and 2 within the crucibles and at its base). (**d**)–(**f**) SEM images of ZnO tetrapods at increasing magnifications (from left to right) harvested from location 1. (**g**)–(**i**) Zoom series (from left to right) of SEM images from the fluffy powder harvested from the base of the furnace (location 2 in image **c**) showing formation of tetrapod, multipods and their mixed structures. [Partially reproduced from permission from[59]].

technology[64] and designing self-reporting composites[65].

Since growth of desired 3D networks was the strong motivation for our research, the harvested ZnO tetrapods from second variant of FTS were further processed to synthesize different interconnected networks[59]. Appropriate amounts of tetrapods were filled in open cylindrical ceramic scaffolds, pressed and reheated at high temperature (~1150°C) for 4 hours. Such a reheating results in the formation of interconnections between tetrapod arms providing mechanical strength to the entire network[59]. For example, the 3D ZnO networks fabricated using this approach is shown in **Fig. 4a**. These 3D networks were analyzed inside SEM in details to study the underlying growth process. **Fig. 4(b–d)** shows the SEM images taken inside the network at different magnifications. It is clearly visible that at some places the tetrapod arms interpenetrate fully (**Fig. 4d** is a high magnification of **Fig. 4b**) and at some places they interpenetrate partially (**Fig. 4c**). It seems that formation of interconnections initiates from the positions where the arms are touching each other during re-heating. However, further investigations for understanding the exact mechanism of arms's interpenetrations are under progress[59].

Based on proposed approach macroscopic and highly porous (up to 98%) 3D interconnected networks were fabricated using ZnO tetrapods[59]. These networks are electrically conducting and high temperatures stable (up to 1400°C). Flexibility of 3D porous networks is a very important property which enables their use for various applications. It was observed that by varying the density, one can tune the elastic modulus of these networks from few kPa to rubber elastic region (less than 100 MPa) and thus they fall in the category of flexible ceramics[59]. These flexible conducting highly porous 3D interconnected networks exhibit potential applications for new advanced technologies. Recently, these 3D networks have been used as templates for guided growth of carbon based aerographite material[67].

The third variant of FTS offers controlled growth of different Q1D metal oxide nano-microstructures employing the cylindrical arrangement as shown in **Fig. 5(a)**. The precursor metal microparticles, sacrificial polymer and ethanol mixture (in form of slurry) is placed in the crucible and the substrates can be mounted at positions 1 to 4 (**Fig. 5a**) for

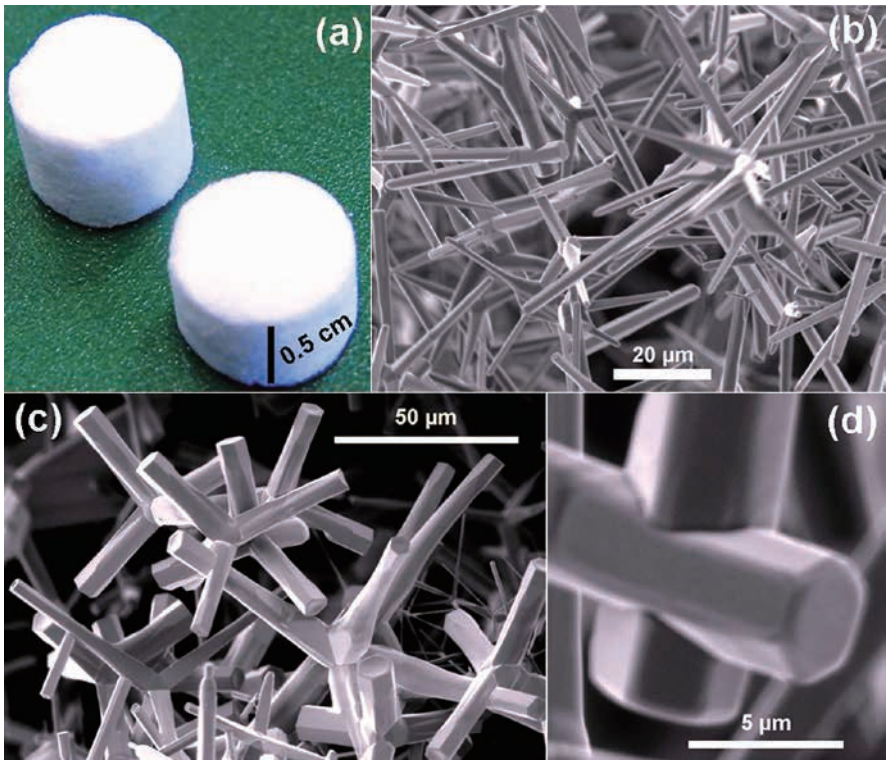

Fig. 4 Fabrication of the 3D interconnected networks from the ZnO tetrapod powder (shown in **Fig. 3d**). Appropriate amounts of ZnO tetrapods were filled in ceramic crucible and re-heated at high temperatures (between 1100°C to 1200°C) for 4–5 hours. (**a**) Digital camera image of the 3D network tablets obtained after heating the ZnO tetrapods in the ceramic scaffolds (at 1150°C for 4 hours). (**b**)–(**d**) SEM images from these 3D network tablet confirming the formation of interconnections between the tetrapod arms. Formation of partial (**c**) and full (**d**) interpenetrations between the tetrapod arms can be seen. [Partially reproduced from permission from[59)]].

different nano-microstructures. The cylindrical arrangement is inserted into the furnace and heated at high temperatures in air environment. The cylinder arrangement enables further control on the nanostructure growth process and Q1D nanostructures, like nanorods, nanowires, nanonails and their large arrays can be grown in a controlled manner[59)]. The conversion mechanism of precursor microparticles in the flame is similar like mentioned in **Fig. 3(a)** but inclusion of ceramic cylinder adds extra features. At positions 1 and 4 (**Fig. 5a**), the nanostructure growth process is almost similar to that demonstrated in **Fig. 3**.

Nano-microstructures grown at position 2 and 3 (**Fig. 5a**) are quite different, because position 3 is located inside the cylinder at the base surrounding the crucible and position 2 on the top holes, where substrates are mounted vertically downwards. SEM studies from structures deposited on position 1 (**Fig. 5a**) confirmed the growth of different types of ZnO tetrapods, as shown in **Fig. 5b** and **Fig. 5c**. Growth of different Q1D nanorods and their arrays occurs on substrates mounted at position 2, (**Fig. 5a**). On substrates at position 3, located inside the cylinder, more converted nano-microstructures are deposited during growth process and therefore 3D networks are formed. These 3D networks are quite different as compared to those obtained by reheating the tetrapods (**Fig. 4**). Since growth and interpenetration simultaneously occur at position 3, these 3D networks are much stiffer and exhibit relatively higher elastic modulus[59)].

The fourth variant of FTS approach utilizes a burner equipped with Oxygen and Propane gases for the flame as shown in **Fig. 6a**[59)]. The precursor Zn microparticles are inserted into the gas stream in controlled manner and they travel along with the flame when coming out from the nozzle. During their travel, these precursor metal microparticles are converted into nano-microstructures because of very high flame temperature of the flame. These nano-microstructures can be deposited on the substrates or collected in form of powder depending upon the requirement.

The 3D interconnected networks can be synthesized if process is continued for longer durations at same locations[59)]. The conversion of Zn microparticles into nano-microstructures depends on transport time within the flame and transformation stages as marked by positions 1, 2 and 3 (**Fig. 5a**). A large copper plate coated with ZnO tetrapods using burner approach is shown in **Fig. 6b**. The SEM images (1–3) presented in **Fig. 6** correspond to particle transformation stages shown in **Fig. 6a**. The image 4 in **Fig. 6** shows SEM of a single ZnO nanotetrapod, which

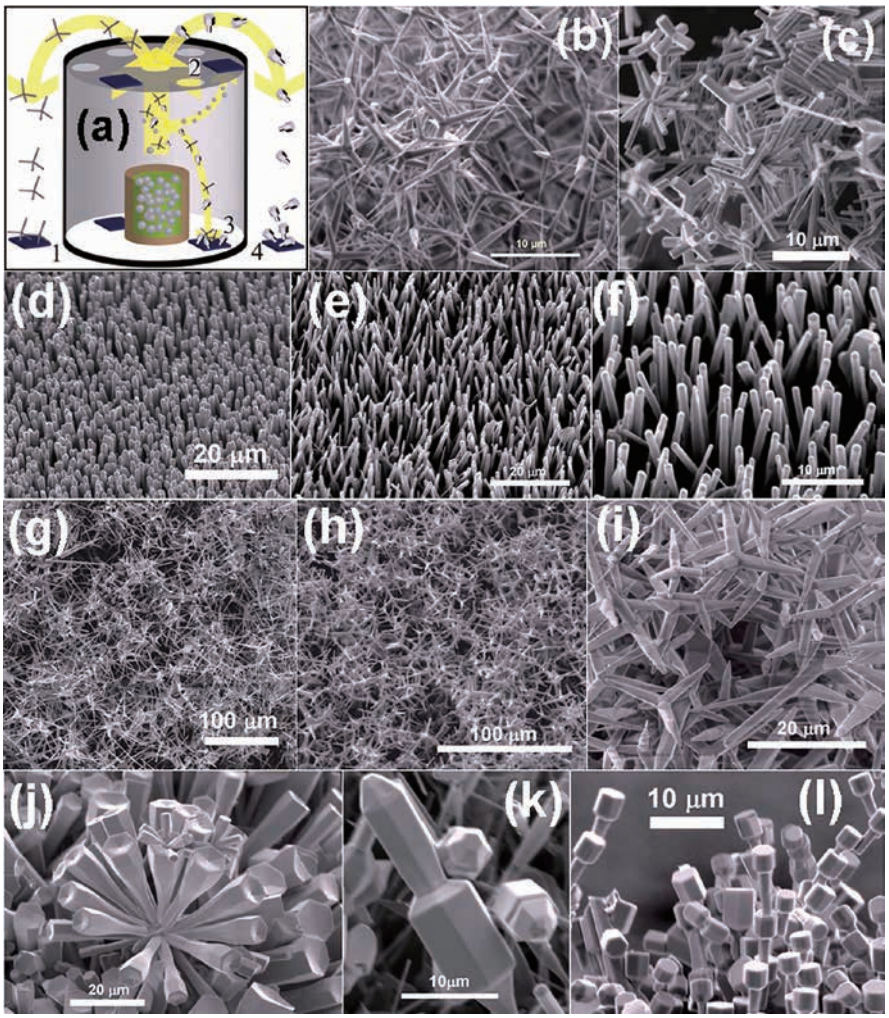

Fig. 5 (**a**) Schematic drawing demonstrating the controlled variant of FTS approach using a ceramic cylinder. The crucible in centre contains the slurry mixture and the substrates are mounted at positions 1 to 4. (**b**) & (**c**) SEM images for different ZnO tetrapod structures grown at substrate mounted at position 1. At position 2 (top cover of cylinder having holes) the substrates are symmetrically mounted with the desired surface pointing vertically downwards towards the crucible. Typically quasi-1D nano-microstructures and their arrays grow at position 2. (**d**)–(**f**) SEM images of different ZnO nanorods array grown on Si substrate at position 2. (**g**)–(**i**) SEM images of different types ZnO tetrapods networks grown at position 3 inside the cylinder. (**j**)–(**l**) SEM images of different types of ZnO structures i.e., flowers, dumbbells, bolts and other morphologies were grown at substrate mounted at position 4. Nano-microstructure grown at positions 1 and 4 are almost same. For demonstration reasons, only few structures are shown here. [Partially reproduced from Fig. 2 with permission from[59]].

was coated on copper plate. More details about different experiments are elaborated in previously published paper[59] and experiments are still under progress to optimize the growth of other metal oxide nano-microstructures. The FTS grown nano-microstructures have already shown promising applications and few are summarized in the next section. Recently using burner-FTS approach, an interconnected ZnO nanotetrapods network bridge was directly integrated between electrodes in a chip for UV photodetector applications which demonstrated very fast photodetection response[70].

4. Applications of the ZnO networked structures

4.1 Antiviral activity of ZnO nanoseaurchins and tetrapods against HSV-1

The synthesized structures by FTS approach were tested for antiviral applications and it was observed that ZnO nanoseaurchins and tetrapods (shown in **Fig. 7a** and **7b**) block the HSV-1 viral entry into cells[60]. The confocal microscopy images (A–C) in **Fig. 7c** confirm the attachment of viruses on the surface of ZnO structures. The plot D in **Fig. 7c** shows the HSV-1 entry level into the cells in presence of unilluminated and illuminated ZnO structures with

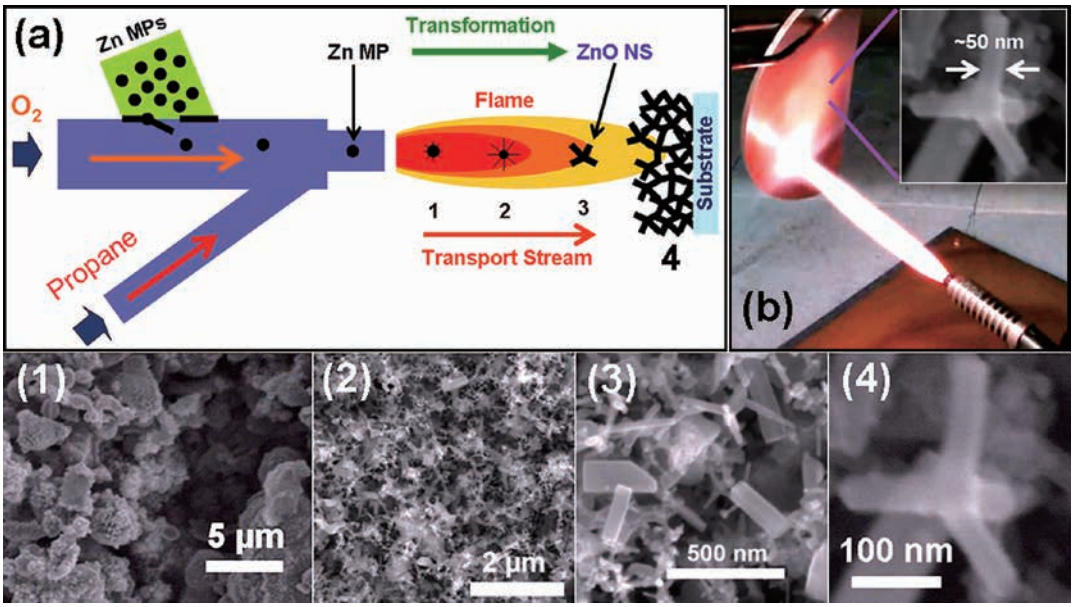

Fig. 6 (**a**) Modified FTS technology using burner approach. The precursor metal microparticles are inserted into the burner, which are transported and converted to metal oxide nano-microstructures in the flame. The transformation of precursor microparticles depends on their time of travel in the flame which are marked 1–3 and at 4 corresponds to substrate where converted structures are collected (for simplicity only tetrapod shape is shown but typically various shapes can be obtained). (**b**) Digital camera image of a copper plate coated with ZnO tetrapods. Inset in (**b**) shows the SEM image of nanoscale ZnO tetrapod deposited on the Cu plate. SEM images (1–4) shows the transformation of precursor ZnO microparticles into ZnO nanostructures. [Partially reproduced from Fig. 4 with permission from[59)]].

UV light. It was observed that in presence of such ZnO structures, the HSV viral entry level goes down as some viruses get attached on the ZnO surface. After UV illumination of these ZnO structures, the HSV-1 viral entry into the cells is significantly decreased because of enhanced attachment of viruses on the ZnO surface[60)].

The HSV-1 entry mechanism into the cells is demonstrated by schematic drawing shown in **Fig. 7d**. The HSV-1 virus exhibits heparan sulfate (HS) groups as virion envelop which interacts with gD-receptors on the cells and enter into the cells. The presence of ZnO nano-microstructures screens the HSV-1 entry into the cells as some viruses are attracted by the oxygen deficient surfaces of ZnO nano-microstructures. After preparation, the ZnO nano-microstructures are several times under sun-shine, it is sufficient to create oxygen vacancies[60)]. After UV illumination, further O vacancies are created in such ZnO structures which enhance the virus attachments on the ZnO surface and results in the significantly decreased HSV-1viral entry into the cells decreased. More details can be found in previous work[60)].

4.2 Antiviral activity of nano-micro ZnO tetrapods against HSV-2

Since herpes simplex virus type 2 (HSV-2) is more fatal as compared to HSV-1 and antiviral community is still waiting for appropriate treatments. We utilized the ZnO tetrapods to study the HSV-2 viral entry into the cells[61)] and its antiviral activity is demonstrated in **Fig. 8**. The SEM images of ZnO tetrapods used for experiments with HSV-2 are shown in **Fig. 8(a–c)** at increasing magnifications (from top to bottom). The confocal microscopy results of ZnO tetrapods without and with HSV-2 viruses are shown in **Fig. 8(d)** and **Fig. 8(e, f)**, respectively.

The HSV-2 viruses were labeled with green markers using a dye. The viral entry mechanism of HSV-2 viruses into the cells in presence of ZnO tetrapods is demonstrated in **Fig. 8(g–i)**. As mentioned above, in presence of ZnO tetrapods, some viruses are attached at the surface of ZnO tetrapod arms due to inherent oxygen vacancies (**Fig. 8g**). In absence of ZnO tetrapods, the HSV-2 viruses make normal entry into the cells in natural manner (**Fig. 8h**). After UV illumination on such ZnO tetrapods, the HSV-2 viral entry into the cells goes significantly down (**Fig. 8i**) because more viruses are attached on the surface of ZnO tetrapods arms due to additional oxygen vacancies created by UV illumination[61)]. Few studies relating to blocking capability of these ZnO tetrapods have already reported in recently published articles[60, 61, 63)]. Further in-vivo experiments are under progress to understand the process in more details. Similar phenomenon was observed in case of SnO_2 nanowire networks, synthesized by FTS approach shows strong potential of blocking the HSV-1 entry into the cells[62)]. For biomedical applications of different nano-microstructures, cytotoxicity

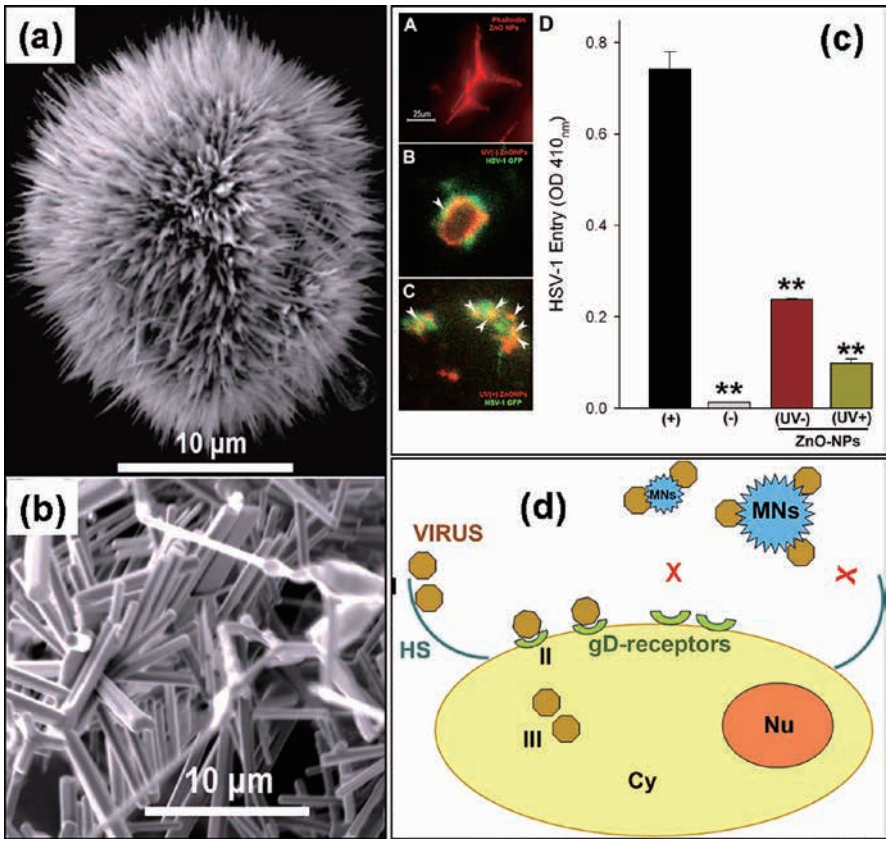

Fig. 7 Antiviral activity of the ZnO nanoseaurchins and tetrapods against herpes simplex virus type -1 (HSV-1). The SEM images (**a**) & (**b**) show morphology of the ZnO nano-microstructures used for HSV-1 experiments. (**c**) Confocal microscopy results (**A**–**C**) and antiviral activity (**D**) of ZnO structures: Image (**A**) shows the confocal microscopy image of ZnO tetrapods. The confocal microscopy images in (**B**) and (**C**) shows the attachment of HSV-1 with ZnO structures (viruses were leveled with green markers). Plot in (**D**) demonstrates the antiviral activity of ZnO nano-microstructures without and with UV illumination. (**d**) Schematic model demonstrating the blocking of HSV-1 entry into cells by ZnO structures. When illuminated with UV light, these ZnO structures significantly bind HSV-1. [Reproduced with permission from[60]].

is very important issue and these nano-micro scale ZnO tetrapods exhibit very low level of cytotoxicity as compared to conventional spherical nanoparticles and $ZnCl_2$ reference[71], which implies towards better utilization in biomedical engineering.

4.3 ZnO nano-micro tetrapods for advanced linking technology

A brand new method of joining polymers with low surface energy was developed by the utilization of the ZnO nano-micro tetrapods (**Fig. 9**) produced by the second FTS variant shown before[59]. This method employs the convex shape of tetrapodal microparticles which works as an anchor to mechanically interlock two polymer layers together. Its efficiency was demonstrated by joining two extremely difficult-to-join polymer layers, namely the poly(tetrafluorethylene) (PTFE) and cross-linked poly(dimethylsiloxane) (PDMS)[64]. Both polymers have very low surface energies and it was difficult to find a single report describing that both polymers can be strongly joined by any technique. Even PTFE alone is notoriously difficult to modify. The surface modification methods developed before, such as plasma treatment and ion beam treatment, require specific instruments. Chemical treatments are difficult and involve hazardous chemicals with PTFE, which is highly chemically inert. The new method achieved a peeling strength of 220 N/m by an easy applicable approach, without modification of the chemical composition of each polymer layers[64].

Fig. 9a demonstrates the adhesion technology between two polymer layers employing ZnO tetrapods (T-ZnO) at the interface between two layers. It was observed that with the T-ZnO at the interface the peeking strength was improved significantly (**Fig. 9b**). In order to compare the effect of shape, some ZnO tetrapods (**Fig. 9c**) were ground (G-ZnO), which resulted in microrod type structures (**Fig. 9d**). These G-ZnO (ground ZnO tetrapods) structures were also embedded at the interface between two polymer layers and peeling strengths from both (T-ZnO and G-ZnO) were

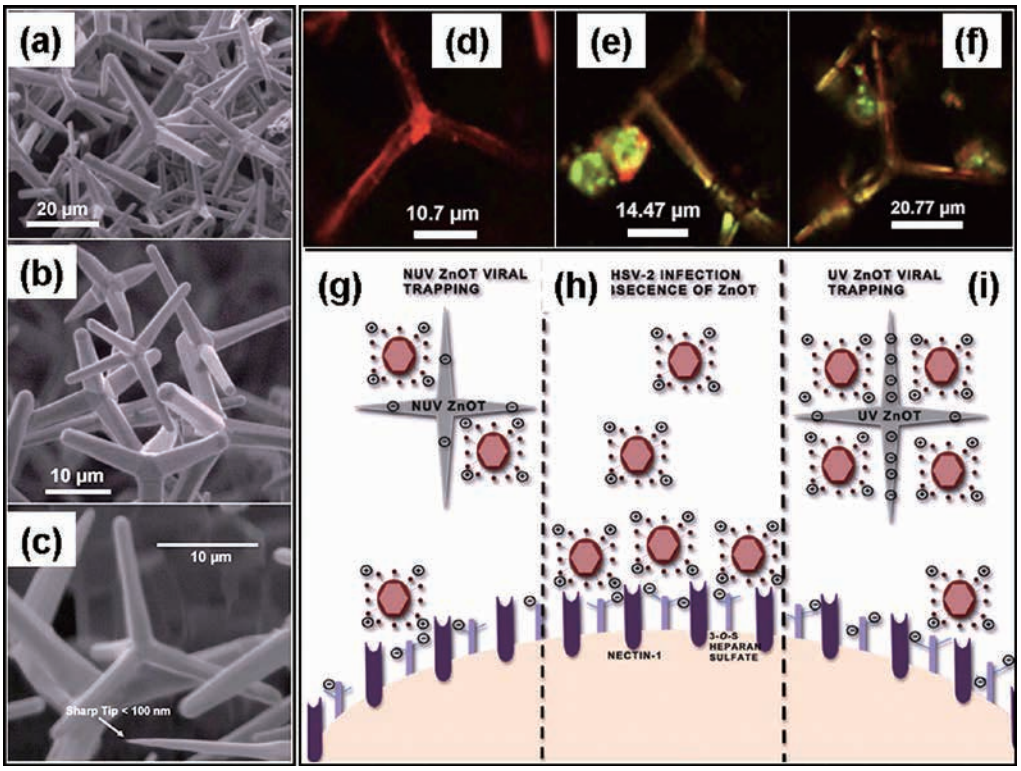

Fig. 8 Antiviral activity of ZnO tetrapods against herpes simplex virus type -2 (HSV-2). (**a**)–(**c**) SEM images of ZnO tetrapods utilized for HSV-2 experiments. (**d**)–(**f**) Confocal microscopy images of ZnO tetrapod (**d**) without and (**e**, **f**) with HSV-2. The viruses are leveled with green markers and confocal microscopy images in (**e**) and (**f**) show that they are attached with ZnO tetrapods. (**g**)–(**i**) Schematic drawings show the role of ZnO tetrapods in HSV-2 entry into the cells. (**h**) In absence of ZnO tetrapods viruses enter into the cells in normal manner. (**g**) In presence of ZnO tetrapods some viruses are attached with ZnO tetrapods and thus their entry into cell decrease. When these ZnO tetrapods are illuminated with UV light, more viruses are attached with tetrapods and this further reduces the viral entry into cells. [Reproduced with permission from[61)]].

compared which are shown in **Fig. 9e**. It can be clearly seen that employing T-ZnO gives much better adhesion as compared to G-ZnO. Since there was no chemical treatment applied to ZnO structures and polymer surfaces, the strong adhesion is purely due to mechanical interlocking. Therefore the concave shaped particles such as tetrapods produced by FTS approach has shown unique potential in improving the mechanical adhesion of polymer laminates[64)]. More details can be found in report by Jin et al.[64)]

4.4 ZnO nano-micro tetrapods as fillers for fabricating self-reporting composites

Semiconducting tetrapod type structures have already shown interesting stress dependent luminescent responses[72, 73)]. An important possible application of tetrapodal shaped ZnO nano-microstructures in polymers is the development of a new concept for self-reporting materials[65)]. The concept assumed that, the deformation of the crystals induces changes in the photoluminescence (PL) signal of the ZnO nano-microtetrapods and therefore it can be used to indicate the stress state of the material. This concept was tested by embedding the tetrapodal particles in an elastomeric matrix as shown in **Fig. 10a**. Typical SEM image of ZnO tetrapods used in the experiments are shown in **Fig. 10b** and digital camera image of the final prepared T-ZnO: PDMS (Polydimethylsiloxane) composite is shown as inset in **Fig 10b**. Desired size and shape of composite can be fabricated as reported by Jin et al.[65)] The PL spectra of T-ZnO: PDMS composites with respect to tensile stress are shown in **Fig. 10c**. It can be seen that the intensity of blue PL peak (from UV excitons in ZnO) remains constant but intensity of green PL peak (~523 nm) has increased which most likely appears from surface defects in ZnO[10, 11)].

A strong correlation between the tensile stress and green PL signal was observed as shown in **Fig. 10d**. Furthermore, the polymer was reinforced by the addition of tetrapodal microparticles, which was not the case in other stress-sensing mechanisms involving photoluminiscent particles as fillers[65)]. Detailed analysis revealed that the formation of network of tetrapodal micro-particles is important for such correlations and a detailed monitoring of

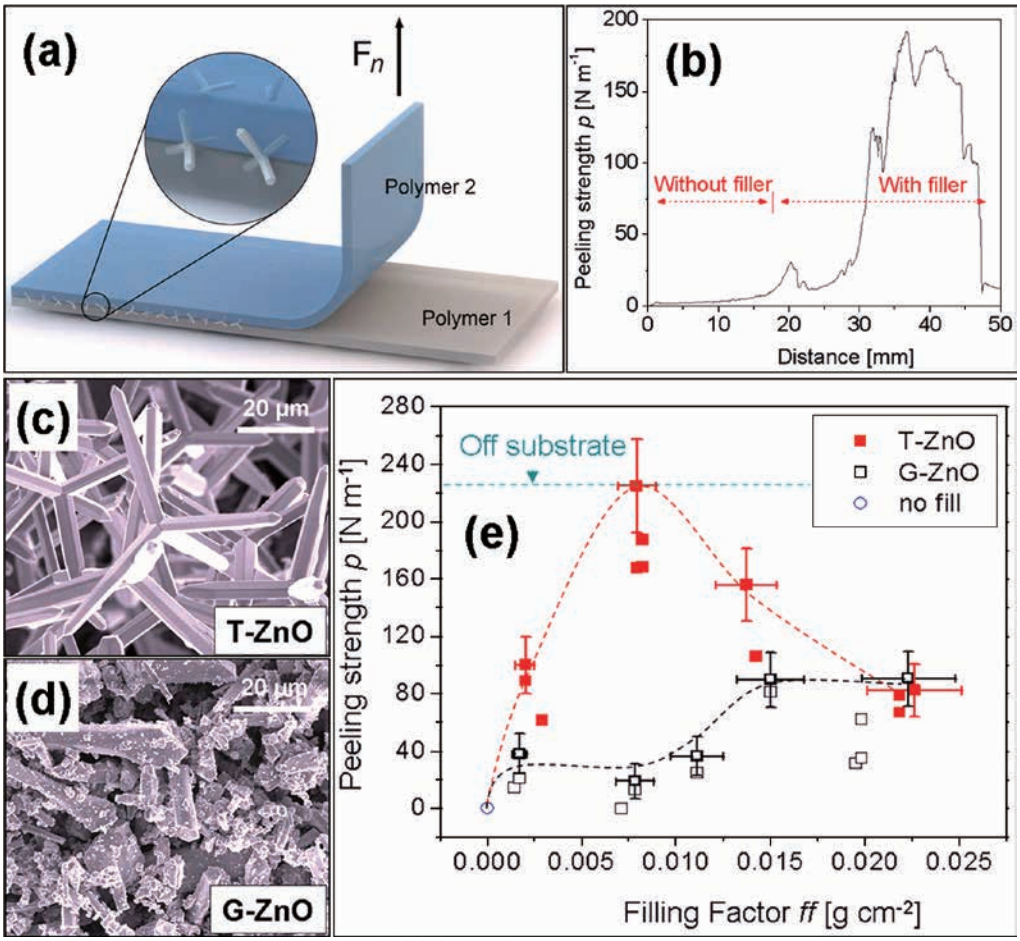

Fig. 9 ZnO tetrapods used as cross-linkers for joining the least surface energy polymers (PDMS and PTFE). (**a**) Schematic drawing demonstrating the experiment for testing the adhesion strength between two polymer layers with tetrapods at the interface as cross-linkers. (**b**) Peeling strength between PTFE and PDMS polymer layers without and with ZnO tetrapods. (**c**) & (**d**) SEM images of ZnO tetrapods (T-ZnO) and ground ZnO tetrapods (G-ZnO). (**e**) Peeling strength between PDMS and PTFE layers when filled with T-ZnO and G-ZnO as fillers. Utilizing ZnO tetrapods as cross-linkers, the peeling strength between PDMS and PTFE layers significantly increased. [Reproduced with permission from[64]].

intensity ratio one might be able to extract to damage informations inside the composites. Further details can be found in the article by Jin et al.[65]

4.5 ZnO 3D networks as templates for growth of ultra light weight aerographite material

The 3D interconnected metal oxide nano-microstructures networks are extremely important for practical applications. Next, we demonstrate an example of growing new carbon based Aerographite material (shown in **Fig. 11**), which is one of lightest solid materials so far[67]. The interconnected networks from ZnO tetrapods were used as templates inside CVD chamber for growth of aerographite material. It was observed that the material growth follows exactly the tetrapods morphology and the existing interconnections in the 3D ZnO network template. The hydrogen gas flowing in the CVD chamber plays main role in the transformation of ZnO into aerographite as it etches ZnO from the surface of ZnO tetrapods and simultaneously deposits carbon at this place[67]. It was reported that belt like early stage growth is most likely responsible for this type of transformation of ZnO tetrapods into aerographite material[67]. This is an ultralight weight material with lot of interesting physical and chemical properties suitable for different applications[67]. Just for demonstration, SEM images from the fabricated aerographite material and some of its properties are summarized in **Fig. 11**.

The 3D aerographite networks with desired sizes can be grown by proposed technique. For example digital camera image of a large cylindrical (1.4 cm diameter large with 1 cm height) aerographite network is shown in **Fig. 11a** and corresponding low and high magnification SEM images are shown **Fig. 11b** and **Fig. 11c** respectively. The high magnification SEM image (**Fig. 11c**) confirms the hierarchical hollow framework networks of microtubes inside aerographite network. **Fig. 11e** and **d** display mechanical data of aerographite material. In **Fig. 11d**, a mechanical load cycle

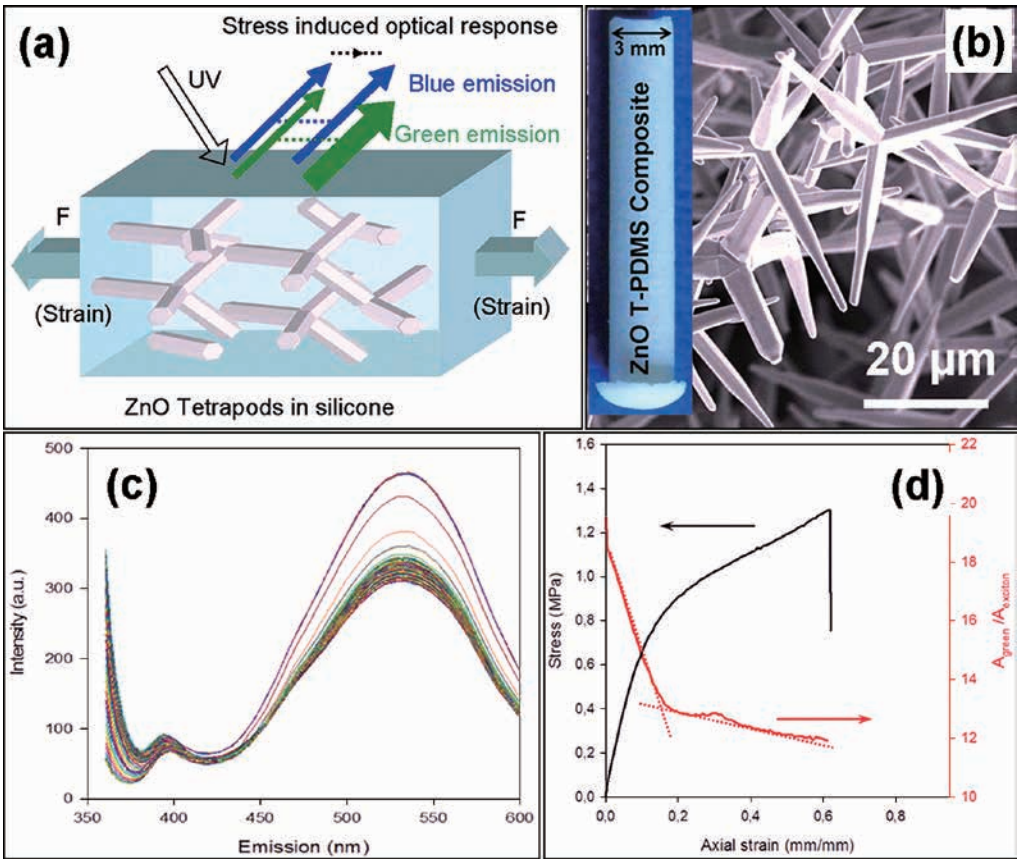

Fig. 10 Use of luminescence features of ZnO tetrapods (T-ZnO) for designing self-reporting composites: (**a**) Schematic drawing showing the change in luminescent response from ZnO tetrapods under tensile stress. (**b**) SEM image of ZnO tetrapods. The inset in (**b**) shows a digital camera image of the fabricated T-ZnO:PDMS composite. (**c**) Photoluminescence spectra (raw data for plot d) from the T-ZnO: PDMS composite (50 weight % T-ZnO) under tensile stress (at every 2.5 s interval, 100 spectra were collected during tensile test and 85 spectra are plotted here in which a clear change of intensity of PL peak ~ 523 nm is visible). (**d**) Stress-strain plot of the T-ZnO:PDMS (50 weight % T-ZnO) composite (left side) and variation of intensity ratio of green to blue PL emissions regions with respect to strain. [Reproduced with permission from[65]].

containing compressive and tensile load is shown. The inset in **Fig. 11d** shows how the electrical conductivity increases during the mechanical compression in a similar experiment. **Fig. 11e** is an Ashby material selection map[74] as it is a convenient guideline in modern lightweight engineering. It compares the specific modulus and density for a plenty of materials (including aerographite) because these two properties are very crucial to build stiff and light parts from an individual material. The here demonstrated Aerographite material exhibits interesting electro-mechanical properties (**Fig. 11d**) and material selection map (shown in **Fig. 11e**) suggests it to be a potential candidate for material engineering applications[67]. It is among one of the extremely porous materials (porosity > 99.9%) and still superhydrophobic in nature[67]. The aerographite material possesses a lot of other interesting features suitable for various advanced applications and more details can be found from the previous paper by Mecklenburg et al.[67]

5. Conclusion

In conclusion, we point out that proposed flame transport synthesis FTS and its approaches offer really facile, cost-effective and scalable synthesis processes for versatile micro-nanostructures of various metal oxides. It also enables successful fabrication of different 3D interconnected networks with desired sizes, porosities, electrical conductivities etc. The tunable elastic modulus of these 3D networks in the range of rubber elastic region enables them as flexible ceramics for various technological applications. Three-dimensional interpenetrated micro-nanostructures can be used as appropriate networks for controlled growth different other structures for example and ultralight weight aerographite material. The nano-micro-scale ZnO tetrapods have already proved their promising applications in the direction of biomedical engineering, advance linking technologies and designing self-reporting composites etc. The controlled variant of FTS technology offers facile growth

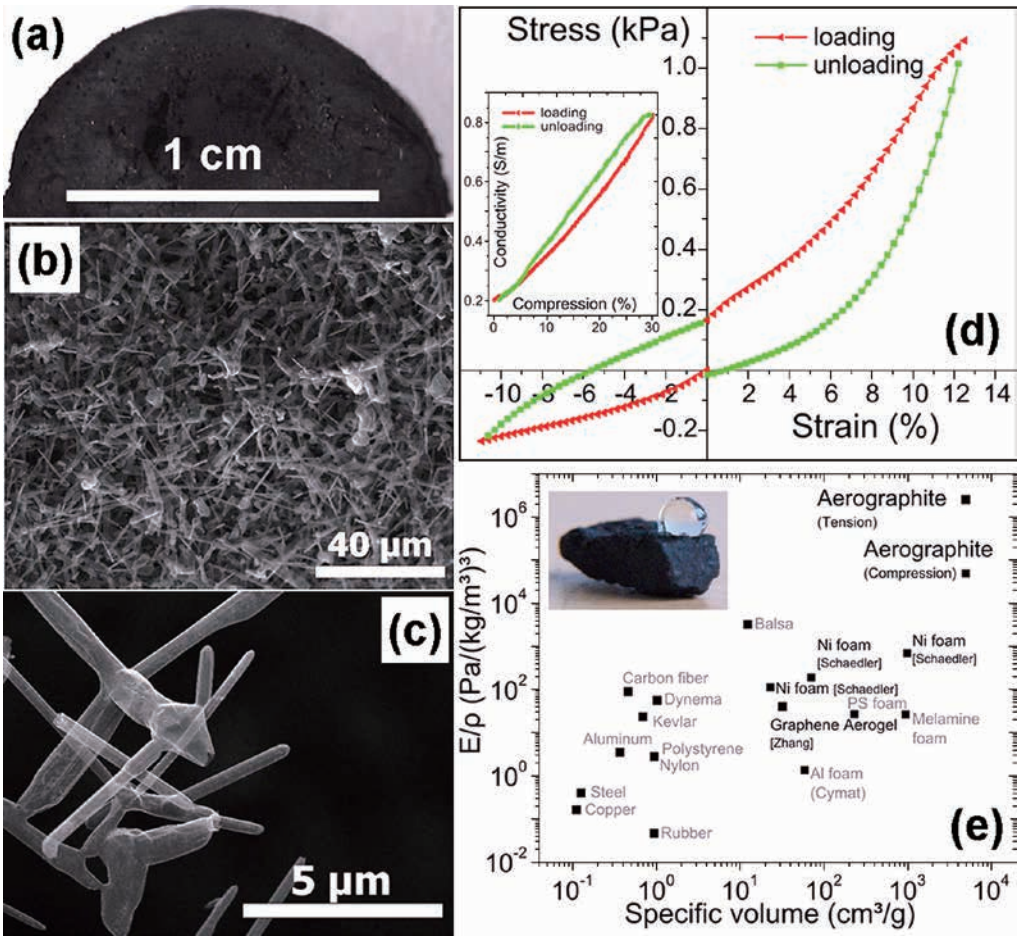

Fig. 11 (**a**) Digital camera image of half-tablet of aerographite material. (**b**) & (**c**) SEM images of aerographite material at low (**b**) and high (**c**) magnifications. (**d**) Loading and unloading stress-strain response of aerographite demonstrates elastic behaviour under compressive and tensile stresses. During compression, a reversible increase of conductivity can be observed, see inset. (**e**) Specific modulus versus density map comparison of aerographite with respect to other light weight engineering materials. This materials selection map shows the theoretical superior properties of aerographite for the case of a minimized bending of a free standing bar with defined weight[74]. [Reproduced with permission from[67]].

of quasi-1D nanostructures and their arrays. Preliminary experiments using ultralong single crystalline ZnO needles have shown promising features for applications in various fields. Most relevant applications of the metal oxide micro-nanostructures grown by FTS approach and its variants have been summarized in this paper and several others are under progress.

Acknowledgements

YKM sincerely thanks to Prof. Sotiris E. Pratsinis (Particle Technology Laboratory, ETH-Zurich) for kind invitation to write the article and to Ms. Natalie Winzer (HOSOKAWA ALPINE Aktiengesellschaft, Germany) for her enormous patience in terms of deadline extensions and reviewing. This project was funded by German Research Foundation (DFG) under the schemes SFB 855-A5 and partially by SFB 677-C10 and Ad/183/10-1. YKM and OL acknowledge the researcher fellowships from Alexander von Humboldt Foundation at the University of Kiel, Institute of Materials Science, Germany.

References

1) Wang, Z. L. (2009): ZnO nanowire and nanobelt platform for nanotechnology, Mat. Sci. & Eng. R, Vol. 64, pp. 33–71.
2) Wang, Z. L. (2012): From nanogenerators to piezotronics-A decade-long study of ZnO nanostructures, MRS Bulletin, Vol. 37, pp. 814–827.
3) Zhou, W. and Wang, Z. L. (2011): "Three dimensional nano-architectures: Designing next generation devices", Springer Publications, 233 Spring, New York, NY 10013, US, ISBN 978-1-4419-9821-7.
4) Devan, R. S., Patil, R. A., Lin, J. H. and Ma, Y. R. (2012): One dimensional metal-oxide nanostructures: Recent developments in synthesis, characterization, and applications,

Adv. Funct. Mater., Vol. 22, pp. 3326–3370.
5) Özgur, U., Alivov, Y., Liu, C., Take, A., Reshchhikov, M. A., Dogan, S., Avrutin, V., Cho, J. S. and Morkoc, H. (2005): A comprehensive review of ZnO materials and devices, J. Appl. Phys., Vol. 98, pp. 41301.
6) Zeng, H., Duan, G., Li, Y., Yang, S. and Cai, W. (2010): Blue luminescence of ZnO nanoparticles based on non-equilibrium processes: Defect origins and emission controls, Adv. Funct. Mater., Vol. 20, pp. 561–572.
7) Aubert, T., Nerambourg, N., Saito, N., Haneda, H., Ohashi, N., Mortier, M., Cordier, S. and Grasset, F. (2013): Tunable visible emission of luminescent hybrid nanoparticles incorporating two complementary luminophores: ZnO nanocrystals and $[Mo_6Br_{14}]^{2-}$ nanosized cluster units, Part. Part. Syst. Charact., Vol. 30, pp. 90–95.
8) Lupan, O., Pauporte, T. and Viana, B. (2010): Low-voltage UV-electroluminescence from ZnO-nanowire array/p-GaN light-emitting diodes. Adv. Mater., Vol. 22, pp. 3298–3302.
9) Lupan, O., Chai, G., Chow, L., Emelchenko, G. A., Heinrich, H., Ursaki, V. V., Gruzintsev, A. N. and Redkin, A. N. (2010): Ultraviolet photoconductive sensor based on single ZnO nanowire, Phys. Status Solidi A, Vol. 207, pp. 1735–1740.
10) Lupan, O., Pauporté, T., Ursaki, V. V. and Tiginyanu, I. M. (2011): Highly luminescent columnar ZnO films grown directly on n-Si and p-Si substrates by low-temperature electrochemical deposition, Opt. Mater., Vol. 33, pp. 914–919.
11) Lupan, O., Pauporté, T., Tiginyanu, I. M., Ursaki, V. V., Heinrich, H. and Chow, L. (2011): Optical properties of ZnO nanowire arrays electrodeposited on n- and p-type Si (1 1 1): Effects of thermal annealing, Mater. Sci. Eng. B, Vol. 176, pp. 1277–1284.
12) Hoffmann, S., Utke I., Moser, B., Michler, J., Christiansen S. H., Schmidt, V., Senz, S., Werner, P., Gösele, U. and Ballif, C. (2006): Measurement of the bending strength of vapor−liquid−solid grown Silicon nanowires, Nano Lett., Vol. 6, pp. 622–625.
13) Desai, A. V. and Haque, M. A. (2007): Mechanical properties of ZnO nanowires, Sensor and Actuat. A-Phys., Vol.134, pp. 169–176.
14) Zhai, T. Y., Fang, X. S., Liao, M. Y., Xu, X. J., Zeng, H. B., Bando, Y. and Golberg, D. (2009): A comprehensive review of one-dimensional metal-oxide nanostructure photodetectors, Sensors Vol. 9, pp. 6504–6529.
15) Fang, X. S., Bando, Y., Gautam, U. K., Zhai, T. Y., Zeng, H. B., Xu, X. J., Liao, M. Y. and Golberg, D. (2009): ZnO and ZnS nanostructures: Ultraviolet-light emitters, lasers, and sensors, Critical Rev. Solid State & Mat. Sci., Vol. 34, pp. 190–223.
16) Lupan, O., Pauporté, T., Bahers, T. L., Viana, B. and Ciofini, I. (2011): Wavelength-emission tuning of ZnO nanowire-based light-emitting diodes by Cu doping: Experimental and computational insights, Adv. Funct. Mater., Vol. 21, pp. 3564–3572.
17) Chai, G. Y., Chow, L., Lupan, O., Rusu, E., Stratan, G. I., Heinrich, H., Ursaki, V. V. and Tiginyanu, I. M. (2011): Fabrication and characterization of an individual ZnO microwire-based UV photodetector, Solid State Sci., Vol. 13, pp. 1205–1210.
18) Hu, L., Yan, J., Liao, M., Xiang, H., Gong, X., Zhang, L. and Fang, X. (2012):An optimized ultraviolet-A light photodetector with wide-range photoresponse based on ZnS/ZnO biaxial nanobelt, Adv. Mater., Vol. 24, pp. 2305–2309.
19) Chow, L., Lupan, O., Chai, G. Y. (2010): FIB fabrication of ZnO nanotetrapod and cross-sensor, Phys. Status Solidi-B., Vol. 247, pp. 1628–1632.
20) Lupan, O., Pauporté, T., Bahers, T. L., Ciofini, I. and Viana, B. (2011): High Aspect Ratio Ternary $Zn_{1-x}Cd_xO$ Nanowires by Electrodeposition for Light-Emitting Diode Applications, J. Phys. Chem. C., Vol. 115, pp. 14548–14558.
21) Lupan, O., Ursaki, V.V., Chai, G., Chow, L., Emelchenko, G. A., Tiginyanu, I. M., Gruzintsev, A. N. and Redkin, A. N. (2010): Selective hydrogen gas nanosensor using individual ZnO nanowire with fast response at room temperature, Sensor and Actuat. B-Chem., Vol. 144, pp. 56–66.
22) Lupan, O., Chow, L., Pauporté, T., Ono, L. K., Cuenya, B. R. and Chai, G. (2012): Highly sensitive and selective hydrogen single-nanowire nanosensor, Sensor and Actuat. B-Chem., Vol. 173, pp. 772–780.
23) Shishiyanu, S. T., Lupan, O., Monaico, E. V., Ursaki, V. V., Shishiyanu, T. S. and Tiginyanu, I. M. (2005): Photoluminescence of chemical bath deposited ZnO:Al films treated by rapid thermal annealing, Thin Solid Films, Vol. 488, pp. 15–19.
24) Chow, L., Lupan, O., Chai, G., Khallaf, H., Ono, L. K., Cuenya, B. R., Tiginyanu, I. M., Ursaki, V. V., Sontea, V. and Schulte, A. (2013): Synthesis and characterization of Cu-doped ZnO one-dimensional structures for miniaturized sensor applications with faster response, Sensor and Actuat. A, Vol. 189, pp. 399–408.
25) Wahab, R., Kaushik, N. K., Verma, A. K., Mishra, A., Hwang, I. H., Yang, Y. B., Shin, H. S. and Kim, Y. S. (2011): Fabrication and growth mechanism of ZnO nanostructures and their cytotoxic effect on human brain tumor U87, cervical cancer HeLa, and normal HEK cells, J. Biol. Inorg. Chem., Vol. 16, pp. 431–442.
26) Gunawan, C., Teoh, W. Y., Ricardo, Marquis, C. P. and Amal, R. (2013): Zinc oxide nanoparticles induce cell filamentation in E. coli, Part. Part. Syst. Charact., Vol. 30, pp. 375–380.
27) Wahab, R., Dwivedi, S., Umar, A., Singh, S., Hwang, I., Shin, H. S., Musarrat, J., Al-Khedhairy, A. A., Kim, Y. S. (2013): ZnO nanoparticles induce oxidative stress in Cloudman S91 melanoma cancer cells. J. Biomed. Nanotechnol., Vol. 9, pp. 441–449.
28) Wahab, R., Kaushik, N. K., Kaushik, N., Choi, E.H., Umar, A., Dwivedi, S., Musarrat, J. and Al-Khedhairy, A. A. (2013): ZnO nanoparticles induces cell death in malignant human T98G gliomas, KB and non-malignant HEK cells, J. Biomed. Nanotechnol., Vol. 9, pp. 1181–1189.
29) Umar, A., Chauhan, M., Chauhan, S., Kumar, R., Sharma, P., Tomar, K. J., Wahab, R., Al-Hajry, A. and Singh, D. (2013): Applications of ZnO nanoflowers as antimicrobial agents for Escherichia-Coli and enzyme-free glucose sensor, J. Biomed. Nanotechnol., Vol. 9, pp. 1794–1802.
30) Nie, L., Gao, L., Feng, P., Zhang, J., Fu, X., Liu, Y., Yan, X.

and Wang, T. (2006): Three-dimensional functionalized tetrapod like ZnO nanostructures for plasmid DNA delivery, Small, Vol. 2, pp. 621–625.
31) Wagner, R. S. and Ellis, W. C. (1964): Vapor liquid solid mechanism of single crystal growth, Appl. Phys. Lett., Vol. 4, pp. 89.
32) Mishra, Y. K., Mohapatra, S., Singhal, R., Avasthi, D. K., Agarwal, D. C. and Ogale, S. B. (2008): Au-ZnO: A tunable localized surface plasmonic nanocomposite, Appl. Phys. Lett., Vol. 92, pp. 43107.
33) Mishra, Y. K., Chakravadhanula, V. S. K., Hrkac, V., Jebril, S., Agarwal, D. C., Mohapatra, S., Avasthi, D. K., Kienle, L. and Adelung, R. (2012): Crystal growth behaviour in Au-ZnO nanocomposite under different annealing environments and photoswitchability, J. Appl. Phys., Vol. 112, pp. 064308.
34) Yang, P., Yan, H., Mao, S., Russo, R., Yan, H., Saykally, R., Morris, N., Pham, J., He, R. and Choi, H. J. (2012): Controlled growth of ZnO nanowires and their optical properties, Adv. Fun. Mater., Vol. 12, pp. 323-331.
35) Dick, K. A., Deppert, K., Larsson, M. W., Martensson, T., Seifert, W., Wallenberg, L. R. and Samuelson, L. (2004): Synthesis of branched 'nanotrees' by controlled seeding of multiple branching events, Nat. Mater., Vol. 3, pp. 380–384.
36) Jebril, S., Kuhlmann, H., Müller, S., Ronning, C., Kienle, L., Duppel, V., Mishra, Y. K. and Adelung, R. (2010): Epitactically interpenetrated high quality ZnO nanostructured junctions on microchips grown by the vapor-liquid-solid method, Cryst. Growth Des., Vol. 10, pp. 2842–2846.
37) Lupan, O., Chow, L., Chai, G. and Heinrich, H. (2008): Fabrication and characterization of Zn-ZnO core-shell microspheres from nanorods, Chem. Phys. Lett., Vol. 465, pp. 249–253.
38) Chow, L., Lupan, O., Heinrich, H. and Chai, G. (2009): Self-assembly of densely packed and aligned bilayer ZnO nanorod arrays, Appl. Phys. Lett., Vol. 94, pp. 163105.
39) Peng, Y., Huo, D., Zheng, L. and Qian, Z. (2012): A simple hydrothermal method for the growth of ZnO crystals, Part. Syst. Charact., Vol. 29, pp. 3–7.
40) Lupan, O., Emelchenko, G. A., Ursaki, V. V., Chai, G., Redkin, A. N., Gruzintsev, A. N., Tiginyanu, I. M., Chow, L., Ono, L. K., Cuenya, B. R., Heinrich, H. and Yakimov, E. E. (2010): Synthesis and characterization of ZnO nanowires for nanosensor applications, Mat. Res. Bull., Vol. 45, pp. 1026–1032.
41) Bilecka, I. and Niederberger, M. (2010): Microwave chemistry for inorganic nanomaterials synthesis, Nanoscale Vol. 2, pp. 1358–1374.
42) Patil, K. C., Aruna, S. T. and Mimani, T. (2002): Combustion synthesis: an update, Curr. Opin. Solid St. M., Vol. 6, pp. 507–512.
43) Ostrikov, K., Neyts, E. C. and Meyyappan, M. (2013): Plasma nanoscience: from nano-solids in plasmas to nano-plasmas in solids, Adv. Phys., Vol. 62, pp. 113–224.
44) Ostrikov, K., Seo, D. H., Mehdipour, H., Cheng, Q. and Kumar, S. (2012): Plasma effects in semiconducting nanowire growth, Nanoscale, Vol. 4, pp. 1497–1508.
45) Elias, J., Clement, C. L., Bechelany, M., Michler, J., Wang, G. Y., Wang, Z. and Philippe, L. (2010): Hollow urchin-like ZnO thin films by electrochemical deposition, Adv. Mater., Vol. 22, pp. 1607–1612.
46) Lupan, O., Pauporté, T. and Viana, B. (2010): Low-temperature growth of ZnO nanowire arrays on p-Silicon (111) for visible-light-emitting diode fabrication, *J. Phys. Chem. C.,* Vol. 114, pp. 14781–14785.
47) Schilling, C., Theissmann, R., Notthoff, C. and Winterer, M. (2013): Synthesis of small hollow ZnO nanospheres from gas phase, Part. Part. Syst. Charact., Vol. 30, pp. 434–437.
48) Strobel, R. and Pratsinis, S. E. (2007): Flame aerosol synthesis of smart nanostructured materials, J. Mater. Chem., Vol. 17, pp. 4743–4756.
49) Yang, S., Jang, Y. H., Kim, C. H., Hwang, C., Lee, J., Chae, S., Jung, S. and Choi, M. (2010): A flame metal combustion method for production of nanoparticles, Powder Technol., Vol. 197, pp. 170–176.
50) Camenzind, A., Caseri, W. R. and Pratsinis, S. E. (2010): Flame-made nanoparticles for nanocomposites, Nano Today, Vol. 5, pp. 48–65.
51) Stepuk, A., Krämer, K. W. and Stark, W. J. (2013): Flame synthesis of complex fluoride-based nanoparticles as up-conversion phosphors, KONA Powder and Particle Journal, Vol. 30, pp. 267–275.
52) Adelung, R., Aktas, O. C., Franc, J., Biswas, A., Kunz, R., Elbahri, M., Kanzow, J, Schürmann, U. and Faupel, F. (2004): Strain-controlled growth of nanowires within thin-film cracks, Nat. Mater., Vol. 3, pp. 375–379.
53) Jebril, S., Elbahri, M., Titazu, G., Subannajui, K., Essa, S., Niebelschutz, F., Röhlig, C. C., Cimalla, V., Ambacher, O., Schmidt, B., Kabiraj, D., Avasti, D. and Adelung, R. (2008): Integration of thin-film-fracture-based nanowires into microchip fabrication, Small, Vol. 4, pp. 2214–2221.
54) Gedamu, D., Jebril, S., Schuchardt, A., Elbahri, M. Wille, S., Mishra, Y. K. and Adelung, R.(2010): Examples for the integration of self-organized nanowires for functional devices by a fracture approach, Phys. Status Solidi-B, Vol. 247, pp. 2571–2580.
55) Gedamu, D., Paulowicz, I., Jebril, S., Mishra, Y. K. and Adelung, R. (2012): Procedures and properties for a direct nano-micro integration of metal and semiconductor nanowires on Si chips, Journal of Nanotechnology, Vol. 2012, pp. 325732.
56) Zhou, J., Ding, Y., Deng, S. Z., Gong, L., Xu, N. S. and Wang, Z. L. (2005): Three-dimensional tungsten oxide nanowire networks, Adv. Mater., Vol. 17, pp. 2107–2110.
57) Shi, J., Hara, Y., Sun, C., Anderson, M. A. and Wang, X. (2011): Three-dimensional high-density hierarchical nanowire architecture for high-performance photoelectrochemical electrodes, Nano Lett., Vol. 11, pp. 3413–3419.
58) Adelung, R., Kaps, S., Mishra, Y. K., Claus, M., Preusse, T. and Wolpert, C. (2011): German Patent WO2011-116751, European Patent 2013, EP2550241.
59) Mishra, Y. K., Kaps, S., Schuchardt, A., Paulowicz, I., Jin, X., Gedamu, D., Freitag, S., Wille, S., Claus, M., Kovalev, A., Gorb, S. N. and Adelung, R. (2013): Fabrication of macroscopically flexible and highly porous 3D semiconductor networks from interpenetrating nanostructures by simple flame transport approach, Part. Part. Syst. Charact., Vol.

30, pp. 775–783.
60) Mishra, Y. K., Adelung, R., Röhl, C., Shukla, D., Spors, F. and Tiwari, V. (2011): Virostatic potential of micro-nano filopodia-like ZnO structures against herpes simplex virus-1, Antiviral Res., Vol. 92, pp. 305–312.
61) Antoine, T., Mishra, Y. K., Trigilio, J., Tiwari, V., Adelung, R. and Shukla, D. (2012): Prophylactic, therapeutic and neutralizing effects of zinc oxide tetrapod structures against herpes simplex virus type-2 infection, Antiviral Res., Vol. 96, pp. 363–375.
62) Trigilio, J., Antoine, T., Paulowicz, I., Mishra, Y. K., Adelung, R. and Shukla, D. (2012): Tin oxide nanowires suppress herpes simplex virus-1 entry and cell-to-cell membrane fusion, PLoS ONE, Vol. 7, pp. e48147.
63) Adelung, R., Mishra, Y. K., Röhl, C., Shukla, D., Spors, F. and Tiwari, V. (2012):Virus Traps, US Patent, Serial No. 13593934 (Pending).
64) Jin, X., Strueben, J., Heepe, L., Kovalev, A., Mishra, Y. K., Adelung, R., Gorb, S. N. and Staubitz, A. (2012): Joining the un-joinable: Adhesion between low surface energy polymers using tetrapodal ZnO linkers, Adv. Mater., Vol. 24, pp. 5676–5680.
65) Jin, X., Götz, M., Wille, S., Mishra, Y. K., Adelung, R. and Zollfrank, C. (2013): A novel concept for self-reporting materials: stress sensitive photoluminescence in ZnO tetrapod filled elastomers, Adv. Mater., Vol. 25, pp. 1342–1347.
66) Bhowmick, S., Stauffer, D., Guo, H., Kaps, S., Mishra, Y. K., Hrkac, V., Warren, O., Adelung, R., Minor, A. and Kienle, L. (2013): In-situ electromechanical study of ZnO nanowires, Microscopy and Microanalysis, Vol. 19, pp. 434–435.
67) Mecklenburg, M., Schuchardt, A., Mishra, Y. K., Kaps, S., Adelung, R., Lotnyk, A., Kienle, L. and Schulte, K. (2012): Aerographite: Ultra lightweight, flexible nanowall, carbon microtube material with outstanding mechanical performance, Adv. Mater., Vol. 24, pp. 3486–3490.
68) Lipowsky, P., Bowick, M. J., Meinke, J. H., Nelson, D. R. and Bausch, A. R. (2005): Direct visualization of dislocation dynamics in grain-boundary scars, Nat. Mater., Vol. 4, pp. 407–411.
69) Hrkac, V., Kienle, L., Kaps, S., Lotnyk, A., Mishra, Y. K., Schürmann, U., Duppel, V., Lotsch, B. V. and Adelung, R. (2013): Superposition twinning supported by texture in ZnO nanospikes, J. Appl. Crystallogr., Vol. 46, pp. 396–403.
70) Gedamu, D., Paulowicz, I., Kaps, S., Lupan, O., Wille, S., Haidarschin, G., Mishra, Y. K. and Adelung, R. (2013): Rapid fabrication technique for interpenetrated ZnO nanotetrapod networks for fast UV-sensors, Adv. Mater. 10.1002/adma.201304363.
71) Papavlassopoulos, H., Mishra, Y. K., Kaps, S., Paulowicz, I., Abdelaziz, R., Elbahri, M., Maser, E., Adelung, R. and Röhl, C. (2013): Toxicity of functional zinc oxide nano-micro-tetrapods: Impact of cell culture conditions, cellular age, and material properties, PLoS ONE (Unpublished Result).
72) Choi, C. L., Koski, K. J., Olson, A. C. K. and Alivisatos, A. P. (2010): Luminescent nanocrystal stress gauge, Proc. Natl. Acad. Sci. U.S.A., Vol. 107, pp. 21306–21310.
73) Raja, S. N., Olson, A. C. K., Thorkelsson, K., Luong, A. J., Hsueh, L., Chang, G., Gludovatz, B., Lin, L., Xu, T., Ritchie, R. O. and Alivisatos, A. P. (2013): Tetrapod nanocrystals as fluorescent stress probes of electrospun nanocomposites, Nano Lett., Vol. 13, pp. 3915–3922.
74) Ashby, M. F. (2005): Materials selection in mechanical design, Pergamon Press (ISBN-13: 978-0750661683), Oxford.

Author's short biography

Yogendra Kumar Mishra

Yogendra Kumar Mishra is currently working as a senior research assistant and habilitant in the Functional Nanomaterials Group at the Institute for Materials Science in the University of Kiel, Germany. He received his Ph.D. in physics (plasmonics) from Jawaharlal Nehru University, New Delhi, in September 2008, and since October 2008 has been working in the Functional Nanomaterials Group. During February 2009 to February 2011, he worked as an Alexander von Humboldt fellow in the group. At Kiel, he introduced a new fabrication technique called 'Flame Transport Synthesis' which allows the versatile fabrication of different metal oxide nano-microstructures and their interconnected 3D networks.

Author's short biography

Sören Kaps

Sören Kaps studied materials science at the University of Kiel and received his diploma in 2008. He joined the group of Prof. Rainer Adelung (Functional Nanomaterials) as a Ph.D. candidate in 2008. His research is focused on the application of ZnO in magneto-electric sensors as in the DFG project SFB 855 *Biomagnetic Sensing*.

Arnim Schuchardt

Arnim Schuchardt received his B.Sc. (materials science) in 2008 at the University of Kiel. In 2010 he received his M.Sc. (materials science) at the University of Kiel. Since 2010, he has been a Ph.D. student in the Functional Nanomaterials Group, Institute for Materials Science in the University of Kiel, Germany. He is mainly working on the fabrication and electromechanical characterization of highly porous carbon-based 3D networks (aerographite).

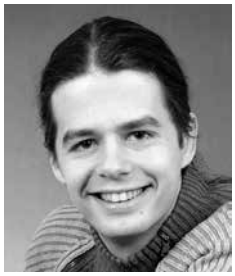

Ingo Paulowicz

Ingo Paulowicz is currently working as a Ph.D. candidate in the Functional Nanomaterials Group at the Institute of Materials Science, University of Kiel, Germany. He finished his M.Sc. in 2010 at the very same place on the synthesis and characterization of tin oxide nanostructures. He prepared his B.Sc. at Hochschule Bonn-Rhein-Sieg on the topic of laser-sintered titanium dioxide, which he finished in 2008. His present field of work is mainly the synthesis of zinc oxide, in particular via a modified burner approach synthesis (m-BAS).

Xin Jin

Xin Jin studied Physics at the East China Normal University in Shanghai. She obtained her Master's degree (2010) in material science and engineering from the University of Kiel. Since 2010 she has been a Ph.D. candidate in the group of Prof. Dr. Rainer Adelung (Functional Nanomaterials), University of Kiel, Kiel, Germany. She is working mainly on the DFG project SFB677 which focuses on photoswitchable adhesives. She recently introduced the new concept of joining the un-joinable polymers employing ZnO tetrapods as linkers.

Author's short biography

Dawit Gedamu

Dawit Gedamu is a Ph. D. candidate. in materials science at the Functional Nanomaterials Group, Institute for Materials Science, University of Kiel. His research interest mainly includes the synthesis of different metal and metal oxide nanowires and their potential for various nanoelectronic devices and sensors. He received an M.Sc. in material science and engineering in 2008 from the University of Kiel, Kiel, Germany.

Sebastian Wille

Sebastian Wille is currently working as a leader of the dental materials group in the Department of Prosthodontic, Propaedeutics and Dental Materials at the UKSH in Kiel on various projects about dental materials. A key topic is the aging of dental zirconia ceramics. He received a Ph.D. degree in materials science (Dr.-Ing.) from the University of Kiel in May 2009. He continued working in the group of Functional Nanomaterials in Kiel until December 2012 as a scientist, concentrating mainly on several projects about the application and synthesis of metal oxide micro- and nanostructures.

Oleg Lupan

Oleg Lupan is a research fellow supported by the Alexander von Humboldt Foundation at the University of Kiel, Institute of Materials Science, Functional Nanomaterials. He received his M.S. in microelectronics from the Technical University of Moldova (TUM) in 1993. He received his Ph.D. in solid-state electronics, microelectronics and nanoelectronics from the Institute of Applied Physics, Academy of Sciences of Moldova in 2005. His post-doctorate research activities were carried out at the CNRS, Paris, France, and the University of Central Florida, USA. He received his doctor habilitate degree in 2011. He is an associate professor at the TUM. His current research interests include nanosensors and optoelectronic devices.

Rainer Adelung

Rainer Adelung is a full professor and chairholder of the Functional Nanomaterials Group established in 2007 at the Institute for Materials Science, University of Kiel, Germany. He received his Ph.D. (rer. net) in physics in 2000 from the Institute of Experimental and Applied Physics, University of Kiel, and during 2001–2002, he was at Case Western Reserve University in Cleveland (USA) as a Feodor Lynen (Alexander von Humboldt) Research Fellow. In 2006 he finished habilitation at the Institute for Materials Science in Kiel and then continued as a Heisenberg Professor (DFG grant) with his own Functional Nanomaterials Group until 2012.

KONA Powder and Particle Journal No. 31 (2014) 111–125/Doi:10.14356/kona.2014018 Review Paper

Aerosol Processing of Graphene and Its Application to Oil Absorbent and Glucose Biosensor †

Sun Kyung Kim[1,2], Hankwon Chang[1], Jeong-Woo Choi[2], Jiaxing Huang[3] and Hee Dong Jang[1]***

[1] *Rare Metals Research Center, Korea Institute of Geoscience and Mineral Resources, Korea*
[2] *Interdisciplinary Program of Integrated Biotechnology, Sogang University, Korea*
[3] *Department of Materials Science and Engineering, Northwestern University, USA*

Abstract

Graphene (GR) is a flat monolayer of sp^2-bonded single carbon atoms densely packed into a honeycomb crystal lattice. Due to its unique characteristics, GR is expected to contribute to enhanced nano-electronic, bio-electronic devices, etc. in the near future. However, the single-layered GR sheets have a tendency to form irreversible aggregates or even to restack easily due to strong attraction between sheets. Preventing of aggregation and restacking of GR is achieved by the dimensional transition from flat sheets to fractal-dimensional, nearly spherical crumpled balls using aerosol spray pyrolysis. This review first introduces the fabrication of crumpled GR and GR-composite by aerosol spray pyrolysis, and then discusses the material properties of GR: strain-hardening, compression and aggregation-resistant behavior. Finally, we introduce effective applications of hollow crumpled GR balls for oil absorbent and crumpled GR-composites for glucose biosensor, respectively.

Keywords: graphene, crumpled graphene, composite materials, aerosol spray pyrolysis, biosensor, oil absorbent

1. Introduction

Graphene (GR) is a flat monolayer of sp^2-bonded single carbon atoms densely packed into a honeycomb crystal lattice[1)]. GR can be synthesized by various methods such as mechanical exfoliation of graphite, chemical vapor deposition from carbon based precursor, and chemical oxidation and reduction of graphite. **Fig. 1** shows structural models of GR, GR oxide (GO) and reduced GO (r-GO). r-GO is often mentioned as chemically modified GR. So here, we use GR and r-GO interchangeably for convenience. The structure of GR has been demonstrated to have a high specific surface area, high thermal conductivity, excellent mechanical stiffness, high optical transparency, good biocompatibility, and fast electron transportation[2–7)]. The unique characteristics of GR have attracted tremendous interest for many applications. GR-based polymer nanocomposites exhibit improved mechanical, thermal, and electrical properties[8–15)]. GR is also able to replace metal conductors in electronic and electrical devices due to its excellent electrical conductivity and mechanical flexibility[16–18)]. A few ongoing studies have reported that GR can replace brittle and chemically unstable indium tin oxide in flexible displays and touch screens. Due to its excellent electronic properties, GR can be used in an enzyme immobilization matrix in the construction of a biosensor. In addition, GR as an electronic circuit material is considered to be potentially superior to other carbon-based nanofillers[19–21)]. Therefore, GR is expected to contribute to enhancing nano-electronic and bio-electronic devices in near future[22)]. It is obvious that these excellent properties are relevant at the nanoscale and the manufacture of nanocomposites is highly dependent on the single-layered GR in the matrices.

However, single-layered GR sheets have a tendency to form irreversible aggregates or even restack easily due to π-π stacking and van der Waals attraction if the sheets are not well separated from each other[23)]. Preventing aggregation and restacking is essential for GR sheets because the unique properties are only associated with individual sheets. Restacking and aggregation of GR sheets not only reduce their effective application but also compromise their properties, such as accessible surface area. Making exfoliated GR sheet materials will help to standardize the materials and their performance for various applications. Many methods for preventing aggregation in solution have been developed

† Accepted: September 8, 2013
[1] Daejeon, 305-350, Korea
[2] Seoul, 121-742, Korea
[3] Evanston, Illinois 60208, USA
* Corresponding author:
E-mail: hdjang@kigam.re.kr
TEL: +82-42-868-3612 FAX: +82-42-868-3415
** Corresponding author:
E-mail: jiaxing-huang@northwestern.edu
TEL: +1-847-491-5940 FAX: +1-847-491-7820

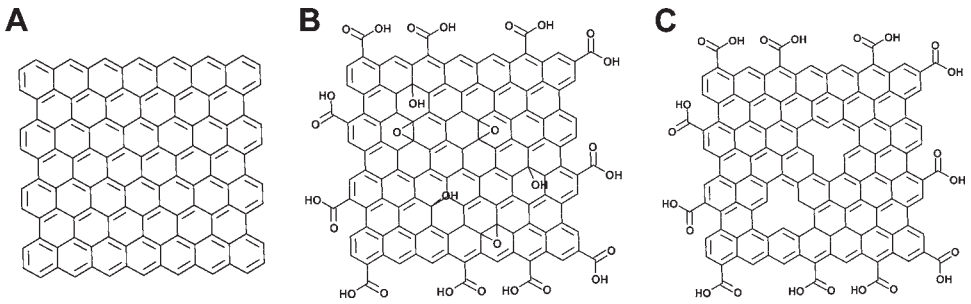

Fig. 1 Structural model of (**A**) graphene, (**B**) GO and (**C**) r-GO.

and typically include reducing the size of the sheets, tailoring the solvent-GR interactions, employing dispersing agents and attaching functional groups[24–29]. However, once the dispersions are dried, preventing aggregation of the solid state GR products and making them re-dispersible have been challenging topics[23].

It will also be beneficial to develop crumpled paper balls because the dimensional transition technology from flat sheets to near three-dimensional (3D) crumpled balls can resist compression and aggregation properties. Like crumpled paper balls, crumpled GR is capable of tight packing into a near three-dimensional (3D) form without significantly losing surface area[30].

In order to make crumpled GR, the free-standing aqueous droplets containing exfoliated graphene oxide (GO) in an inert atmosphere are evaporated. Then, the soft GO sheets can be compressed to form a near-spherical particle just like a crumpled paper ball and are then converted into r-GO by thermal reduction at high temperature[31]. This concept has been experimentally achieved by an aerosol-assisted capillary compression process called aerosol spray pyrolysis (ASP).

All the previous studies employed a liquid phase reaction that included many time consuming unit operation stages, such as liquid-solid separation, washing, and drying, in order to synthesize the GR[32–40]. On the other hand, the ASP has many advantages in fabricating of crumpled GR from GO because it is a very fast, simple and continuous process for fabricating self assembled composites as a one-step method[41]. It also takes a very short time of several seconds for crumpling and reducing of GO together and does not require any post heat treatment, purification or reduction agents[23,41–43]. The size of the crumpled particles and the degree of crumpling can be tuned with the concentration of GO in the aerosol droplets. The as-prepared crumpled GR by ASP is compression-resistant just like paper balls as compressive stress makes them stiffer and harder, and it has consistently higher and much more stable surface areas after the same processing steps compared to the GR sheets[23]. In addition, an anode modified by the crumpled GR exhibits enhanced performance in electricity generation over those covered with activated carbon and regular GR sheets, which lead to a significantly high short-circuit current and maximum power density[44].

As mentioned above, GR-supported composites have attracted a great deal of attention for their enhanced material properties, such as their high electrical and thermal conductivity, and so on. Many materials such as polymers, metal oxides and noble metals have been used widely to fabricate functional GR composites[31,45]. When the crumpled GR-based composite is fabricated, improved material properties for many applications are expected.

In this review, we introduce the aerosol processing of GR and demonstrate the superior properties and interesting potential applications for crumpled GR. We first introduce the fabrication of crumpled GR and its composite by ASP. The material properties of crumpled GR, such as strain-hardening, compression and aggregation-resistant behavior, are then discussed. Applications for crumpled GR balls and GR-composite such as oil absorbent and glucose biosensor are also introduced, respectively.

2. Fabrication of Crumpled GR

2.1 Graphene Oxide

To fabricate crumpled GR by ASP, a colloidal solution of exfoliated graphene oxide (GO) is prepared as an aerosol precursor. The colloidal GO is generally prepared by oxidation of graphite powder using a modified Hummers' method as follows[46–49]. In the first step, graphite, $K_2S_2O_8$, and H_2SO_4 are stirred together in an 80°C oil bath for the pre-oxidation process. Then, for the oxidation process, $KMnO_4$ is slowly added in 30°C oil bath. Once mixed, the solution is transferred to an ice bath and forms a thick paste. Next, distilled water is carefully added, and the solution is stirred for 30 min while the temperature is maintained below 50°C. Finally, H_2O_2 is slowly added, turning the color of the solution from dark brown to yellow. The warm colloidal mixture is then filtered, washed with distilled water and dried. The dried filter cake is then dispersed in distilled water under ultra-sonication for the exfoliation process. Low-speed centrifugation is done at

3000 rpm for 15 min. It is repeated until all visible particles are removed (about 5 times) from the precipitates. The supernatant then undergoes two more high-speed centrifugation steps at 8000 rpm for 30 min to remove small GO pieces and water-soluble by-products. The final sediment is re-dispersed in distilled water using an ultrasonic bath, giving a colloidal solution of exfoliated GO[47].

Fig. 2 demonstrates how the GO is successfully synthesized from graphite by the modified Hummers' method. The X-ray photo emission spectroscopy (XPS) spectrum of the as-prepared GO shows that C and O peaks appeared at 285 and 533 eV, respectively (**Fig. 2(A)**). Further, the C1s spectrum shows two peaks at 284.7 and 286.6 eV, which are attributed to C-C and C-OH/C=O, respectively[31]. According to the result of the XRD analysis, the peak of GO appears at 10.21° (**Fig. 2(B)**). The Raman spectrum of the as-prepared GO shows a G band at 1600 cm^{-1} and a D band at 1337 cm^{-1} (**Fig. 2(C)**)[45]. The G band of the GO is broadened compared to graphite, mainly due to the extensive oxidation. The UV-Vis spectrum of the GO dispersion shows a peak at 225 nm (**Fig. 2(D)**).

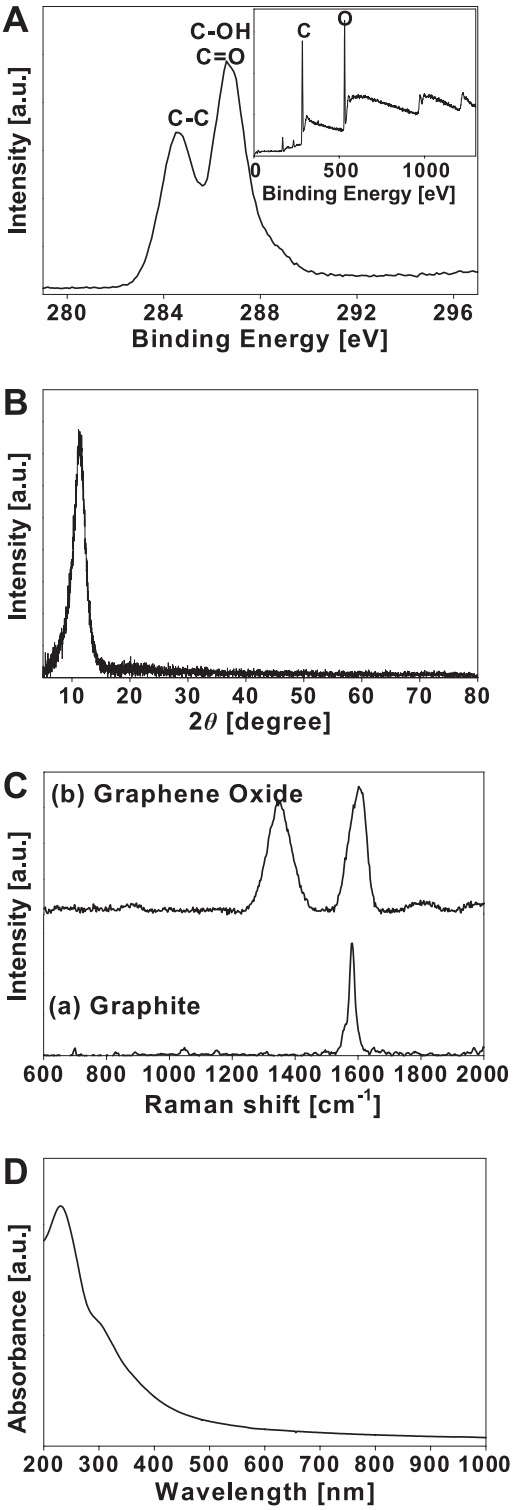

Fig. 2 **A**: X-Ray photoelectron spectroscopy of the GO. Reprinted with permission from ref 31. Copyright 2012 ELSEVIER. **B**: The x-ray diffraction of patterns of the GO. **C**: Raman spectra of (**a**) graphite and (**b**) GO. Reprinted with permission from ref 45. Copyright 2013 ELSEVIER. **D**: UV-Vis spectrum of GO.

2.2 Crumpled GR

Fig. 3 shows a schematic illustration of aerosol process for fabricating crumpled GR from a colloidal GO solution. Since exfoliated GO sheets are essentially soft, water-dispersible, and in single atomic layers, crumpled GR can be easily fabricated from the GO colloid using the ASP process. The experimental apparatus for the ASP process consists of an ultrasonic atomizer, an electrical tubular furnace, and a filter sampler. An aqueous colloid of micron size GO sheets is sprayed to generate many aerosol droplets of micron size and flowed through a tube furnace preheated at 800°C by inert carrier gas (nitrogen or argon). Rapid evaporation of the solution causes shrinkage of the droplets, first concentrating the GO sheets and subsequently compressing them into crumpled balls of sub-micrometer scale. By heating, the GO is thermally reduced to GR as indicated by the color change from brown to black. It takes only several seconds to prepare the crumpled GR and there is no need for any post-heat-treatment or purification steps[23].

Field emission scanning electron microscopy (FE-SEM) images indicate morphology of crumpled GR by the ASP (**Fig. 4**). The samples reveal the near three-dimensional crumpled ball-like structures with many ridges and vertices[23].

2.3 Hollow GR

The fabrication of hollow GR has been studied because of their promising properties, such as large specific surface area, low density, and high porosity[50–63]. Accordingly, various methods such as the sol-gel and hydrothermal methods have been developed to synthesize hollow particles of inorganic materials using templates and a series of many steps for treatment[64–69].

However, when the ASP technique is employed, rapid

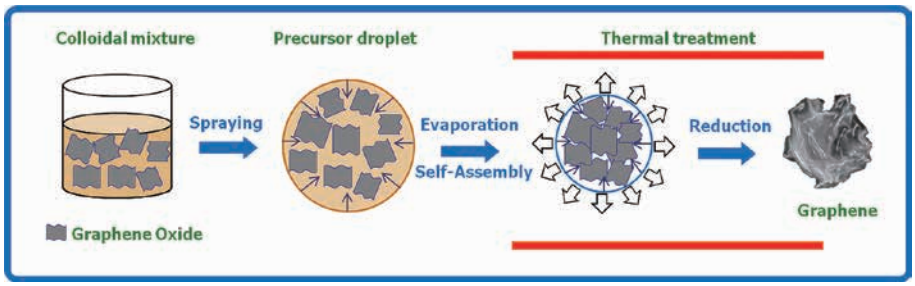

Fig. 3 Schematic illustration of the formation of crumpled GR from GO via aerosol spray pyrolysis.

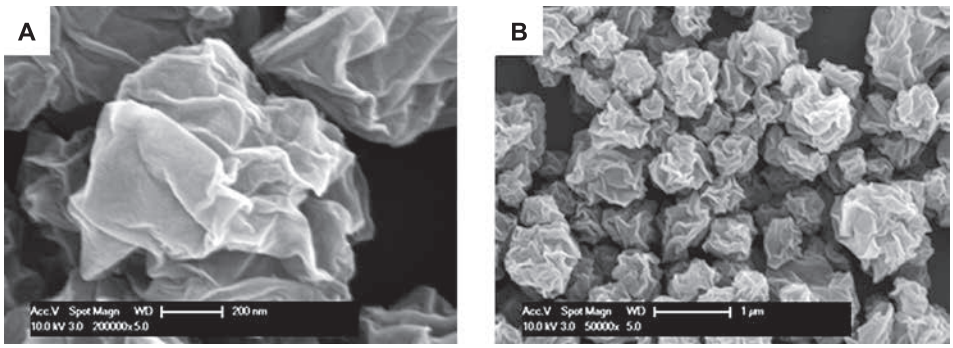

Fig. 4 FE-SEM images of GR as shown in the (**A**) representative high magnification single particle and (**B**) low magnification overview.

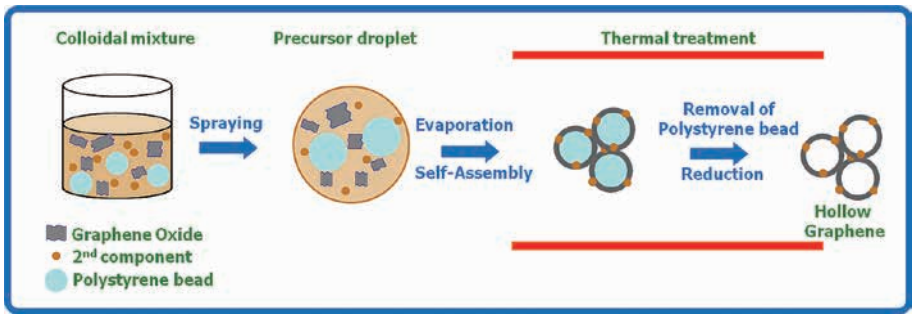

Fig. 5 Schematic illustration showing the preparation of hollow GR capsules.

formation of hollow GR balls can be achieved by capillary molding and template removal in one step and a continuous mode of production. The schematic drawings in **Fig. 5** illustrate the process for fabricating hollow GR capsules. Aqueous aerosol droplets containing GO sheets and polystyrene (PS) colloids are first generated by an ultrasonic atomizer, and then flowed into a preheated tube furnace by argon carrier gas. As they pass through the heating zone, the aerosol droplets first rapidly evaporate. Then hollow GR balls are eventually shaped by wrapping PS beads by GO, GO reduction and PS evaporation. The low magnification scanning electron microscopy (SEM) image in **Fig. 6(A)** gives an overview of the sample morphology, which clearly shows their spherical shape and hollow nature. The transmission electron microscopy (TEM) image shows that the diameter of the capsules is around 580 nm, which is similar to that of PS templates. When a second component, such as metal or metal oxide nanoparticles, is added to the colloidal precursor, metal or metal oxide nanoparticles decorated by hollow GR composites can be easily synthesized (**Fig. 6(B)**)[43].

2.4 Crumpled GR Composite

For the synthesis of the crumpled GR-metal oxide or crumpled GR-noble metal composite by ASP, a colloidal mixture as a precursor must be prepared with the as-prepared GO colloid and sub materials (metal oxide particles (TiO_2) or noble metal precursor ($H_2PtCl_6 \cdot 6H_2O$ and $HAuCl_4 \cdot 3H_2O$)[31,45]. The experimental apparatus for crumpled GR can be employed to synthesize the crumpled GR composite. An ultrasonic atomizer is used to generate micron-sized droplets

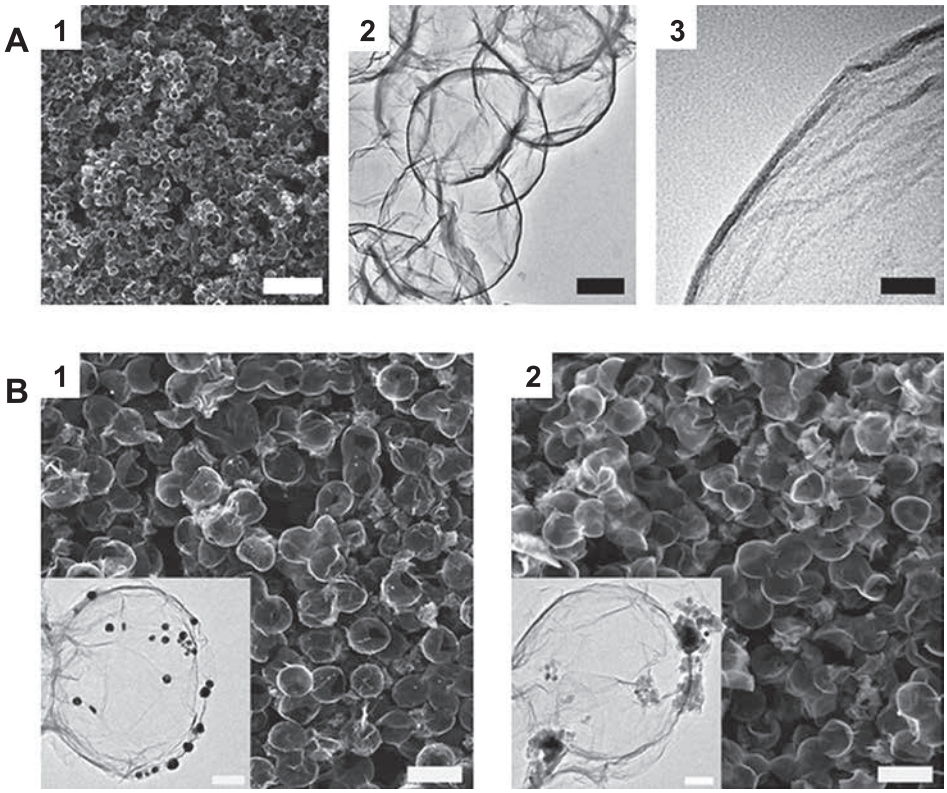

Fig. 6 **A**: (1) SEM image showing an overview of the hollow GR capsules. (2) The hollow nature of the spheres can be clearly seen in the TEM image. (3) High resolution TEM image taken at the edge of a capsule. Scale bars: (1) 4 mm; (2) 200 nm; (3) 20 nm. **B**: SEM (1 and 2) and TEM (inset) images showing hollow GR capsules decorated by (1) Au and (2) Fe_3O_4 nanoparticles, respectively. Scale bars: (1 and 2) 1 mm; (inset) 100 nm. Reprinted with permission from ref 43. Copyright 2012 The Royal Society of Chemistry.

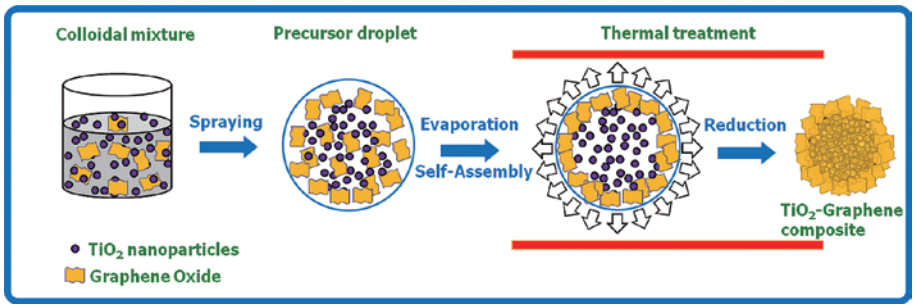

Fig. 7 Schematic illustration of the formation of TiO_2-GR composite from colloidal mixture of TiO_2 nanoparticles and GO via aerosol spray pyrolysis.

of the metal oxide-GO or noble metal-GO colloidal precursor. The droplets are then carried into a tubular furnace by argon gas. Crumpled GR composites are formed in the furnace and then collected by a Teflon membrane filter.

Figs. 7 and **8** show the schematic drawing of the formation of a crumpled GR-TiO_2 composite and a crumpled GR-noble metal composite by the ASP process. For the synthesis of the crumpled GR-TiO_2 composite, rapid evaporation of water, self-assembly between GO and TiO_2, and thermal reduction of GO are carried out in series in the furnace (**Fig. 7**). In case of the crumpled GR-noble metal composite, the evaporation of water, formation of crumpled GO, thermal reduction of crumpled GO and the noble metal precursor, and the self-assembly between crumpled GR and noble metal nanoparticles are carried out (**Fig. 8**)[45].

In **Fig. 9**, the FE-SEM image shows the morphology of a crumpled GR-TiO_2 composite according to the concentration of the GO colloid. The TiO_2 nanoparticles are encapsulated by the GR. The GO accumulates at the water surface of a sprayed droplet during evaporation and finally

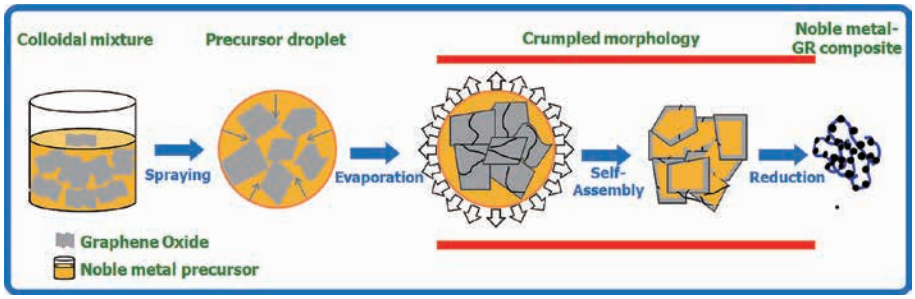

Fig. 8 Schematic illustration of the formation of noble metal-GR composite from colloidal mixture of noble metal precursor and GO via aerosol spray pyrolysis. Reprinted with permission from ref 45. Copyright 2013 ELSEVIER.

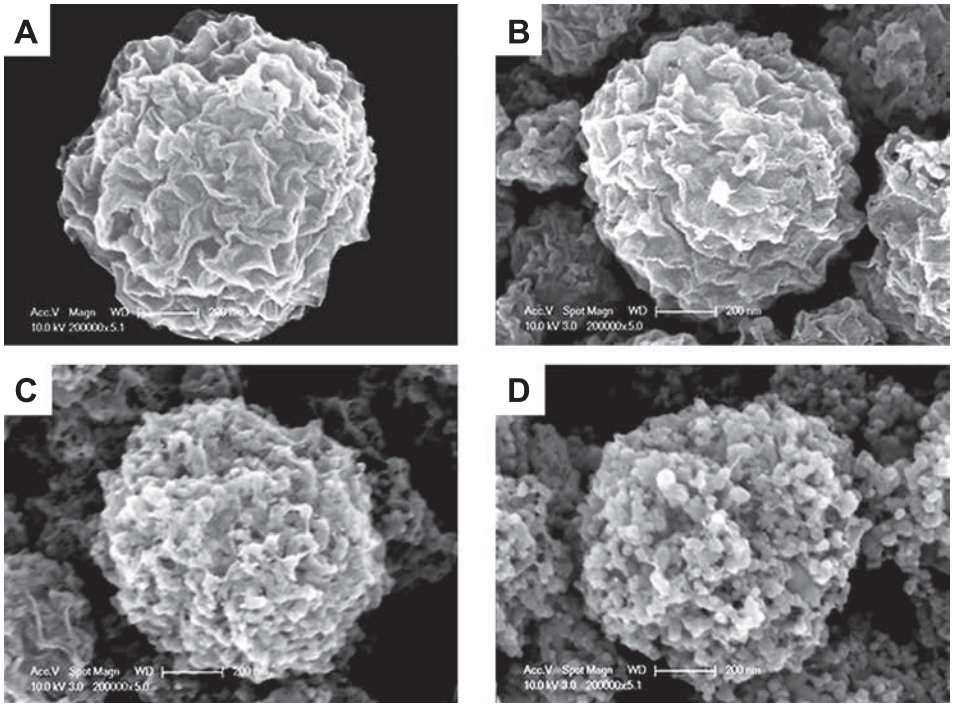

Fig. 9 FE-SEM images of TiO_2-GR composite at different weight ratios of GO/TiO_2 (**A**) 2, (**B**) 0.5, (**C**) 0.1, (**D**) 0.05 at TiO_2: 0.1 wt%. Reprinted with permission from ref 31. Copyright 2012 ELSEVIER.

forms a GR ball. In contrast, hydrophilic TiO_2 nanoparticles are agglomerated and positioned inside of the GR ball during the evaporation process. Further, as the GO concentration decreases from high to low concentration, a decrease in the degree of coverage of GR to TiO_2 is clearly observed. **Fig. 10(A)** shows the X-ray photoemission spectroscopy (XPS) spectra of TiO_2-GR composites. The C, Ti and O peaks are measured at 285, 480 and 533 eV, respectively. As the concentration of GO decreases, the intensity of C becomes lower whereas that of Ti and O become higher. This occurs because TiO_2 is exposed at a lower concentration of GR. These results prove that the as-prepared crumpled GR composites can be harmoniously made from every piece of precursor by the ASP process. Additionally, according to the XRD analysis, the diffraction patterns of the crumpled GR-TiO_2 composite show the anatase and rutile phase of TiO_2 only. Although the GR content in the composite varies, the intensity of the TiO_2 phases does not change because the intensity of the GR phase is much lower than that of TiO_2 (**Fig. 10(B)**)[31].

Fig. 11(A, B) reveals that the morphology of the crumpled GR-noble metal composites is generally the shape of a crumpled paper ball and that noble metal nanoparticles are deposited on the surface of the GR crumples. TEM analysis shows that Pt and Au nanoparticles 3 and 5 nm in diameter, respectively, are uniformly deposited on GR sheets. **Fig. 11(C)** shows the diffraction patterns of the noble metal-GR composites according to the XRD analysis. The crystallinity of the as-prepared composites synthesized at 800°C indicates the same peaks as those of the noble metal reference. The peak detected at around 25 degrees is GR. The crystallite sizes that are calculated by

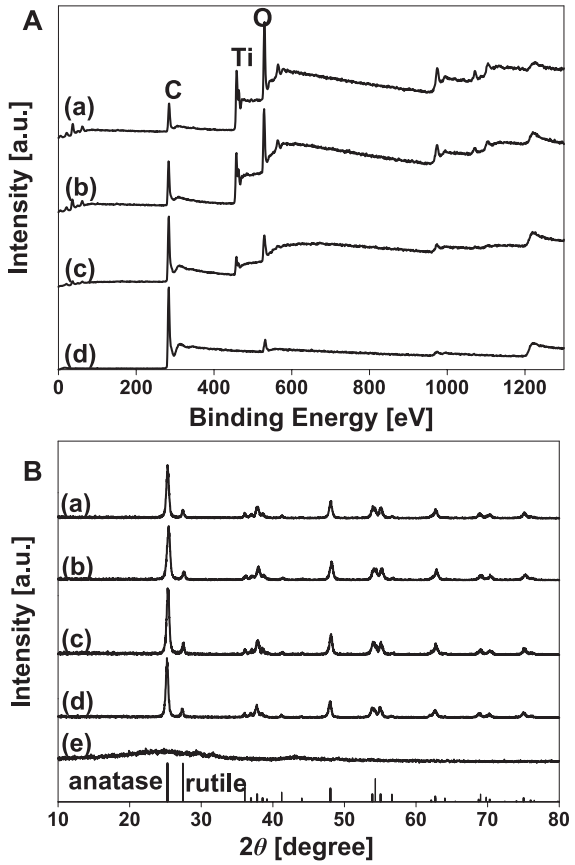

Fig. 10 **A**: X-ray photoelectron spectra of TiO_2-GR composite prepared at different GO/TiO_2 weight ratio (a) 0.5, (b) 0.1, (c) 0.5, and (d) pure GO at TiO_2: 0.1 wt%. **B**: XRD patterns of TiO_2-GR composite with different GO/TiO_2 weight ratio (a) 0.05, (b) 0.1, (c) 0.5, (d) 2, and (e) pure GO at TiO_2: 0.1 wt%. Reprinted with permission from ref 31. Copyright 2012 ELSEVIER.

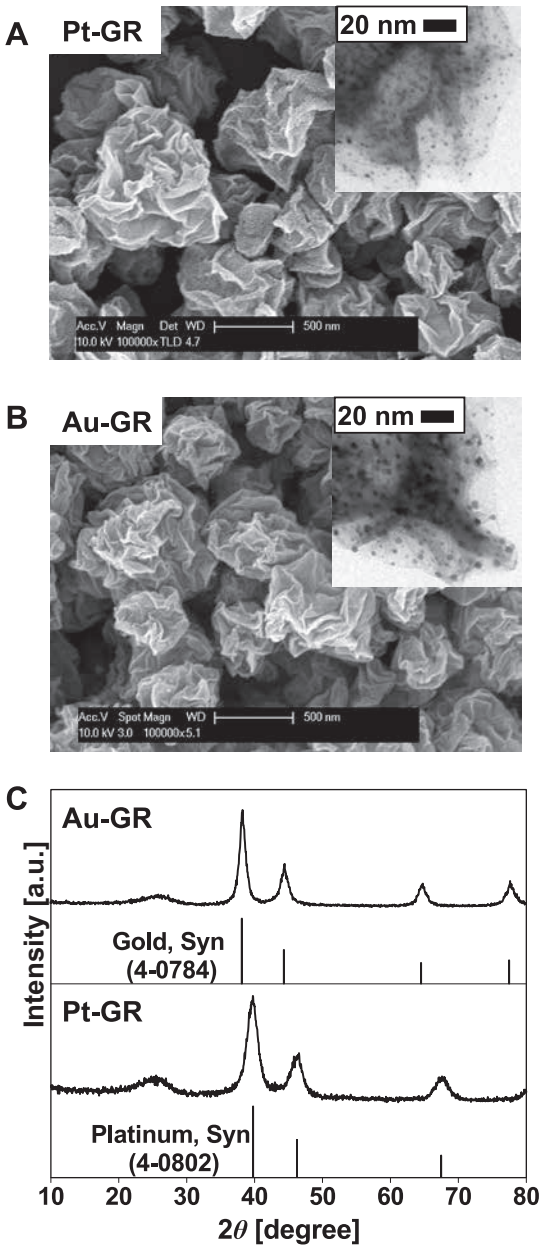

Fig. 11 **A**: FE-SEM and TEM images of as-prepared crumpled Pt-GR composites. **B**: FE-SEM and TEM images of as-prepared crumpled Au-GR composites. **C**: The x-ray diffraction of patterns of as-prepared noble metal-GR composites (above: Au-GR and below: Pt-GR). Reprinted with permission from ref 45. Copyright 2013 ELSEVIER.

the Scherrer equation are 3.3 and 5.5 nm in Pt and Au, respectively[45].

3. Properties of Crumpled GR

In a crumpled paper, the crumpled structure is stabilized by plastically deformed ridges made of kinked paper fibers, which prevent the structure from unfolding. The microstructure analysis of the crumpled GR reveals that the plastic deformation in the crumpled graphene particles is due to strong π-π stacking at the ridges[70–72]. It is also found that the crumpled GR particles are compression-resistant because compressive stress makes them stiffer and harder.

The crumpled GR balls were remarkably stable against aggregation in solution as well as in a solid state due to the π-π stacked ridges and strain-hardening properties. When pelletized, crumpled GR formed a piece of isotropic, black solid with rough microstructures at both the surface and the cross section (**Fig. 12(A, B)**). In contrast, flat GR formed an anisotropic, shiny pellet with very smooth, nearly featureless surface but with a laminated microstructure at the cross section (**Fig. 12(C, D)**). Moreover, the strongly compressed pellet of crumpled GR was readily redispersed in solvents upon shaking by hand (**Fig. 12(E)**). An SEM image of redispersed particles (**Fig. 12(F)**) shows that the crumpled GR morphology is not largely affected by the compression. However, pellets of the flat GR under the same pressure were not redispersed

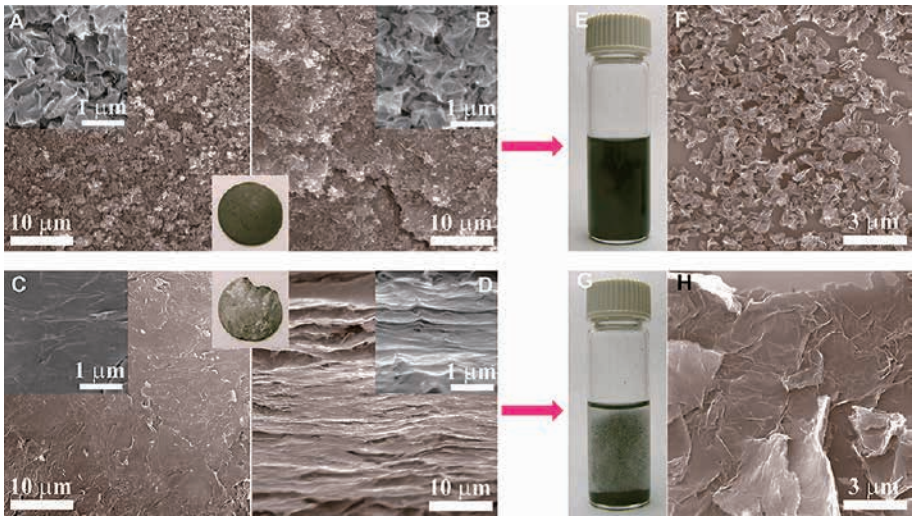

Fig. 12 Compressed pellet of crumpled GR particles (inset of panels A and B) has rough and isotropic microstructures as shown in the SEM images taken at both (**A**) the surface and (**B**) cross section due to their near-spherical, pointy shape. In contrast, flat GR sheets restack along the compressing direction, resulting in a highly anisotropic pellet (inset of **C**, **D**) with (**C**) very smooth surface and (**D**) lamellar cross section. (**E**, **F**) The pellet of the crumpled particles can be readily dispersed by gentle hand-shaking after being compressed at 55 MPa. (**G**, **H**) However, the pellet of regular GR sheets cannot be redispersed due to extensive aggregation. Reprinted with permission from ref 23. Copyright 2011 American Chemical Society.

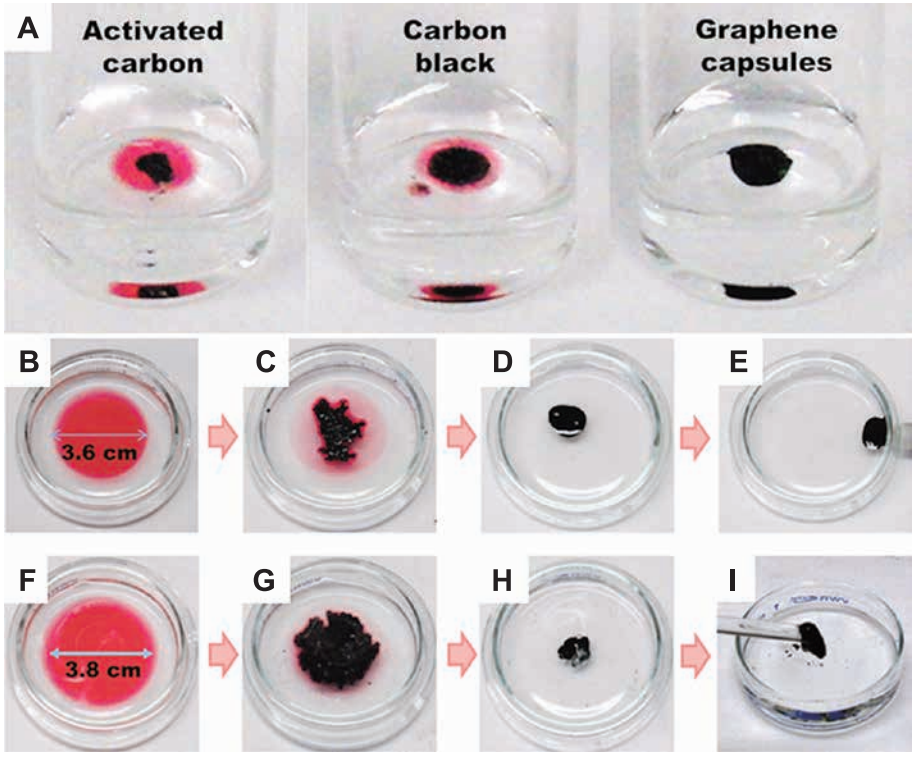

Fig. 13 **A**: Photos showing oil absorption capability of the 3 carbon particles. In each vial, 1.0 mg of carbon particles was added to 17.5 ml of vegetable oil colored with a red dye. The oil-carbon blends were suspended on water for better view. **B**-**E**: Photos showing 100 ml of dyed vegetable oil absorbed by 10 mg of Fe_3O4 decorated magnetic r-GO hollow capsules. **F**-**I**: 150 ml of dyed vegetable oil absorbed by 10 mg of r-GO hollow capsules. Reprinted with permission from ref 43. Copyright 2012 The Royal Society of Chemistry.

even after sonication due to extensive irreversible stacking (**Fig. 12(G, H)**). The electrical conductivity at the surface of crumpled GR pellets was similar to that of a flat GR. This reveals that crumpled GR can help to prevent aggregation without decreasing the overall electrical characteristics[23].

4. Application of Crumpled GR

4.1 Oil Absorbent

The hollow GR balls exhibit properties such as hydrophobic structure, light weight, large free volume, and many small pores on the surfaces. Those features make the hollow GR balls attractive for oil absorption and recovery[43].

In order to compare the oil absorption capability of hollow GR balls against some high surface area carbon materials, such as commercial activated carbon (Norit Darco G60) and commercial carbon black powders (Cabot Vulcan XC-72), we performed a set of control experiments using vegetable oil colored with a red dye (**Fig. 13**). The specific surface areas of the hollow GR balls, carbon black and activated carbon were 84 m^2/g, 230 m^2/g, and 789 m^2/g, respectively. The oil absorption experiments showed that the hollow GR had the highest oil absorption capacity among the three samples (**Fig. 13(A)**). The result demonstrates that a high specific surface area is advantageous for molecular adsorption, but not necessarily for oil absorption. This result also suggests a basic design principle for oil absorption materials, which can be used to prepare as high a free volume as possible. After oil absorbing, the oil filled GR balls were aggregated on the water surface. **Fig. 13 (B–E)** demonstrates that initially vegetable oil colored with a red dye was spread on the water surface. Then, hollow GR balls decorated with magnetic nanoparticles were dropped onto the oil film, which quickly shrank within a few minutes (**Fig. 13(C)**), and eventually transformed into a thick carbon-oil droplet (**Fig. 13(D)**), which could be recovered by a magnet. When undecorated hollow GR balls were used, the resulting blend could be directly picked up and removed by a glass rod (**Fig. 13(F–I)**)[43].

Therefore, the hollow GR balls prepared by the ASP process have a high free volume determined by the size of the template, and show promising oil absorption properties. In addition, hollow GR balls with many opening pores with a hydrophobic structure have an excellent oil absorption ability[43].

4.2 Glucose biosensors

As GR is expected to enhance bio-electronic devices in the near future, many studies have been conducted to find potential applications of GR[73]. Chen et al. (2008) showed

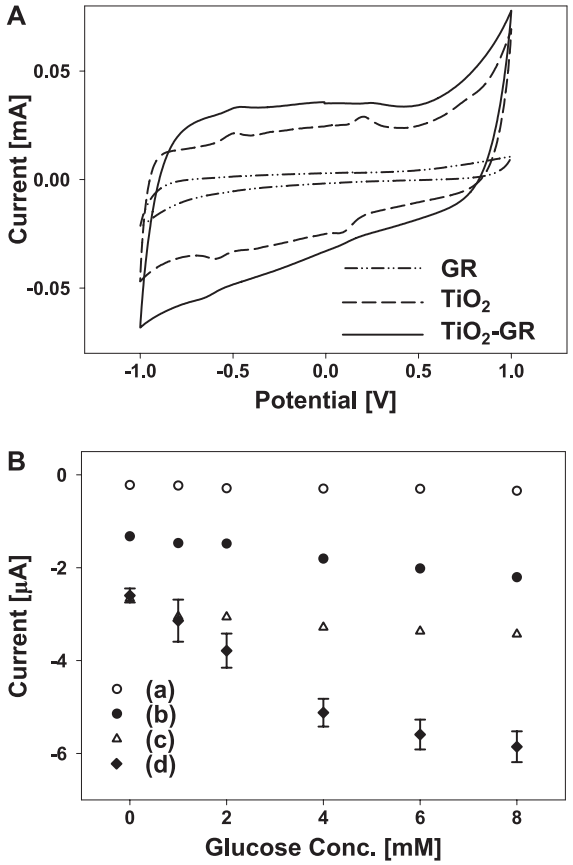

Fig. 14 **A**: Cyclic voltammograms of glucose biosensors prepared with GR, TiO_2, and TiO_2-GR composite, respectively. **B**: Amperometric responses of the glucose biosensor based on TiO_2-GR composite prepared at different weight ratios of GO/TiO_2 (b) 0.5, (d) 0.1, (a) pure TiO_2, and (c) pure GO. Reprinted with permission from ref 31. Copyright 2012 ELSEVIER.

that GR sheets may be biocompatible and therefore suitable for biomedical applications based on the cell culture experiments[74]. Yang et al. (2011) showed that no obvious toxicity of GR was observed in blood biochemistry, hematology, or histology analysis[75]. Park et al. (2010) proved that GR sheets are noncytotoxic to mammalian cell lines[76]. Thus, GR is expected to play an important role in improving the catalytic performance of biosensor applications due to its biocompatibility and unique properties.

Recently, glucose biosensors fabricated with GR and GR-based composites have been a great concern among enzyme-based biosensors since they can monitor blood glucose for the treatment and control of diabetes[77,78].

In case of glucose biosensors fabricated with GR, Nafion-flat GR/GOD film-modified electrodes were developed for the detection of glucose and showed good stability. The glucose sensor exhibited a linear response in the range of 2.0×10^{-6} to 1.0×10^{-4} M with a detection limit of 1.0×10^{-6} M. The good response was due to the fast electron transfer in the GR composite film[79]. The self-assembled GR platelet-GOD nanostructures were reported as an enhanced

glucose biosensor. The linear detection range of their sensor was estimated to be from 2 to 22 mM, and the detection limit was estimated to be 20 μM, which revealed that the GR platelet-GOD had a notable catalytic performance for detection of glucose[80].

In case of glucose biosensors fabricated with a GR-based composite, Chitosan-flat GR/Au nanocomposite films were also reported as a potential glucose biosensor due to their good amperometric response to glucose with wide linear ranges[81]. The glucose biosensor fabricated with Pt-graphite nanoplatelets was suggested as an enhanced glucose biosensor as well and showed a high sensitivity and selectivity[82]. The results revealed that the graphite nanoplatelets incorporated into the biosensor interface increased the effective electrode surface area. Using a fabricated Au-flat GR composite, a prominent electrochemical response to glucose with wide linear ranges and a high sensitivity due to the synergistic effect of GR and Au nanoparticles was reported[83,84].

In the above studies, flat GR and graphite platelets were employed to fabricate a GR or metal-GR composite-based biosensor electrode and improved properties for glucose biosensors were obtained. Therefore, if the glucose biosensor with the crumpled GR is used, more enhanced properties are expected.

Recently, it has been reported that a glucose biosensor fabricated with a crumpled GR-TiO_2 composite demonstrated enhanced properties such as sensitivity and stability[31]. When cyclic voltammogram of glucose biosensors prepared with crumpled GR, TiO_2, and the crumpled GR-TiO_2 composite was measured, the biosensor prepared with the crumpled GR-TiO_2 composite had the highest current flow as well as clear oxidation, with reduced peaks at −0.5 V and −0.6 V (**Fig. 14(A)**). The amperometric response by the glucose biosensor based on the crumpled GR-TiO_2 composite was linear against the concentration of glucose ranging from 0 to 8 mM at −0.6 V (**Fig. 14(B)**). The highest sensitivity of the glucose biosensor based on the crumpled GR-TiO_2 composite was about 6.2 μA/mM·cm^2. This reveals the synergistic effect of TiO_2 nanoparticles with crumpled GR as the electrode materials for biosensors[31].

Furthermore, a crumpled GR-noble metal composite was developed for glucose biosensor application[45]. **Fig. 15(A)** shows the cyclic voltammetry result of the glucose biosensor prepared with the crumpled GR-noble metal composites. The current flow of the biosensor prepared by the crumpled GR-Pt was higher than other composites, crumpled GR-Au or crumpled GR. The redox peak of the electrochemical reaction by the crumpled GR-Pt was the strongest at −0.07 and −0.25 V among the three electrodes. The sensitivity was 62 and 15 μA/mM·cm^2 for the crumpled GR-Pt and the crumpled GR-Au composites, respectively (**Fig. 15(B)**). This result showed that the noble

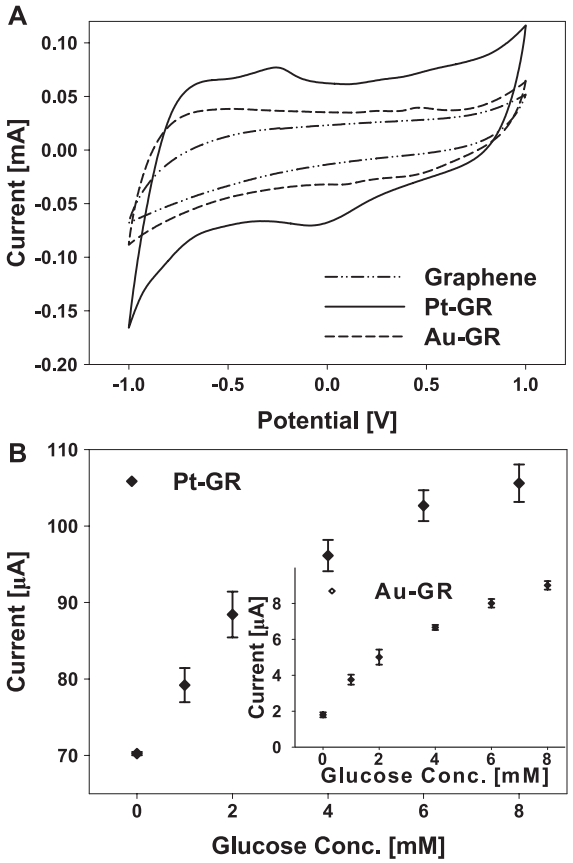

Fig. 15 **A**: Cyclic voltammograms of the glucose biosensor prepared by noble metal-GR (Pt-GR and Au-GR). **B**: Amperometric responses of the glucose biosensor based on Pt-GR composite, Inset graph indicate that of Au-GR composite. Reprinted with permission from ref 45. Copyright 2013 ELSEVIER.

metal-crumpled GR composite covered with uniformly distributed noble metal nanoparticles had higher electrochemical activity, as noble metals can enhance the electron transfer between the enzyme and the electrode[45]. The superior electrochemical activity could have originated from the crumpled GR that can tightly pack without significantly reducing the area of accessible surface and can also deliver much higher specific capacitance ability and better rate performance[44].

5. Summary

This review first introduced crumpled GR and its composite fabricated by aerosol spray pyrolysis (ASP). We then discussed the material properties of crumpled-GR such as strain-hardening, compression and aggregation-resistant behavior. Finally, we introduced potential applications of a crumpled GR ball and its composite such as oil absorbent and glucose biosensors.

In the section on the fabrication of crumpled GR, we

described the preparation of colloidal GO by the oxidation of graphite powder using a modified Hummers' method. Then, we presented the experimental apparatus and schematic procedure of ASP for fabrication of crumpled GR, hollow GR, and GR-based composites.

In the section on the materials properties of crumpled GR, we demonstrated that crumpled GR is stabilized by external influences, and thus does not unfold or collapse during various types treatments. We further discussed the difference in specific surface area between flat GR and crumpled GR processed under the same conditions. Finally, we discussed strain-hardening behaviors of crumpled particles, which make them remarkably resistant to aggregation in both solution and dried states.

In the section on the applications of crumpled GR, first, we discussed application of hollow GR balls for oil absorption and recovery since the hollow GR balls have properties, such as hydrophobic structure, light weight, large free volume, and many small pores on the surfaces, and introduced the superior capacity for oil absorption of hollow GR capsules. Second, we introduced glucose biosensors fabricated with crumpled GR-TiO_2 and crumpled GR-noble metal composites since GR-supported composites are known for their superior biocompatibility, electrical conductivity, and chemical and electrical properties. The biosensor prepared with the crumpled GR-Pt composite showed the highest current flow as well as clear oxidation, which results in high sensitivity. The results for the biosensor prepared with the crumpled GR-noble metal composite showed that the noble metal-crumpled GR composite covered with uniformly distributed noble metal nanoparticles had higher electrochemical activity, as noble metals can enhance the electron transfer between the enzyme and the electrode.

Acknowledgements

This research was supported by the General Research Project of the Korea Institute of Geoscience and Mineral Resources (KIGAM) funded by the Ministry of Science ICT and Future Planning. J.H. thanks supports from the Initiative for Sustainability and Energy at Northwestern (ISEN) through an Early Career Investigator Award (initial seed fund) and the Office of Naval Research (ONR-N000141310556).

References

1) Slonczewski, J. C. and Weiss, P. R. (1958): Band Structure of Graphite, Physical Review, Vol. 109, pp. 272–279.
2) Ritter, K. A. and Lyding, J. W. (2009): The Influence of Edge Structure on the Electronic Properties of Graphene Quantum Dots and Nanoribbons, Nature Materials, Vol. 8, pp. 235–242.
3) Ubbelohde, A. R. and Lewis, L. A. (1960): "Graphite and Its Crystal Compounds", London, Oxford University Press.
4) Thompson, T. E., Falardeau, E. R. and Hanlon, L. R. (1977): The Electrical Conductivity and Optical Reflectance of Graphite-SbF5 Compounds, Carbon, Vol. 15, pp. 39–43.
5) Fuzellier, H., Melin, J. and Herold, A. (1977): Conductibilité Électrique des Composés Lamellaires Graphite-SbF_5 et Graphite-$SbCl_5$, Carbon, Vol. 15, pp. 45–46.
6) Shenderova, O. A., Zhirnov, V. V. and Brenner, D. W. (2002): Carbon Nanostructures, Critical Reviews in Solid State and Materials Sciences, Vol. 27, pp. 227–356.
7) Krishnan, A., Dujardin, E., Treacy, M. M. J., Hugdahl, J., Lynum. S. and Ebbesen, T. W. (1997): Graphitic Cones and the Nucleation of Curved Carbon Surfaces, Nature, Vol. 388, pp. 451–454.
8) Land, T. A., Michely, T., Behm, R. J., Hemminger, J. C. and Comsa, G. (1992): STM Investigation of Single Layer Graphite Structures Produced on Pt(111) by Hydrocarbon Decomposition, Surface Science, Vol. 264, pp. 261–270.
9) Nagashima, A., Nuka, K., Itoh, H., Ichinokawa, T., Oshima, C. and Otani, S. (1993): Electronic States of Monolayer Graphite Formed on TiC(111) Surface, Surface Science, Vol. 291, pp. 93–98.
10) Forbeaux, I., Themlin, J. M. and Debever, J. M. (1998): Heteroepitaxial Graphite on 6H-SiC(0001): Interface Formation through Conduction-Band Electronic Structure, Physical Revew B, Vol. 58, pp. 16396–16406.
11) Berger, C., Song, Z. M., Li, T. B., Li, X. B., Ogbazghi, A. Y., Feng, R., Dai, Z., Marchenkov, A. N., Conrad, E. H., First, P. N. and Heer, W. A. (2004): Ultrathin Epitaxial Graphite: 2D Electron Gas Properties and a Route toward Graphene-Based Nanoelectronics, The Journal of Physical Chemistry B, Vol. 108, pp. 19912–19916.
12) Berger, C., Song, Z., Li, X., Wu, X., Brown, N., Naud, C., Mayou, D., Li, T., Hass, J., Marchenkov, A. N., Conrad, E. H., First, P. N. and Heer, W. A. (2006): Electronic Confinement and Coherence in Patterned Epitaxial Graphene, Science, Vol. 312, pp. 1191–1196.
13) Ohta, T., Bostwick, A., Seyller, T., Horn, K. and Rotenberg, E. (2006): Controlling the Electronic Structure of Bilayer Graphene, Science, Vol. 313, pp. 951–954.
14) Novoselov, K. S., Geim, A. K., Morozov, S. V., Jiang, D., Zhang, Y., Dubonos, S. V., Grigorieva, I. V. and Firsov, A. A.(2004): Electric Feld Effect in Atomically Thin Carbon Films, Science, Vol. 306, pp. 666–669.
15) Fukushima, H. and Drzal, L. T., (2003): A Carbon Nanotube Alternative: Graphite Nanoplatelets as Reinforcements for Polymers, Annual Technical Conference-ANTEC, Vol. 2, pp. 2230–2234.
16) Kelly, B.T. (1981): Physics of Graphite, Applied Science, London, pp.475.
17) Kotov, N. A. (2006): Materials Science: Carbon Sheet Solutions, Nature, Vol. 442, pp. 254–255.
18) Stankovich, S., Dikin, D. A., Piner, R. D., Kohlhaas, K. A., Kleinhammes, A., Jia, Y., Wu, Y., Nguyen, S. T. and Ruoff, R. S. (2007): Synthesis of Graphene-Based Nanosheets via Chemical Reduction of Exfoliated Graphite Oxide, Carbon, Vol. 45, pp. 1558–1565.

19) Eda, G., Fanchini, G. and Chhowalla, M. (2008): Large-Area Ultrathin Flms of Reduced Graphene Oxide as a Transparent and Flexible Electronic Material, Nature Nanotechnology, Vol. 3, pp. 270–274.
20) Becerril, H. A., Mao, J., Liu, Z., Stoltenberg, R. M., Bao, Z. and Chen, Y. (2008): Evaluation of Solution-Processed Reduced Graphene Oxide Films as Transparent Conductors, ACS Nano, Vol. 2, pp. 463–470.
21) Blake, P., Brimicombe, P. D., Nair, R. R., Booth, T. J., Jiang, D., Schedin, F., Ponomarenko , L. A., Morozov, S. V., Gleeson, H. F., Hill, E. W., Geim, A. K. and Novoselov, K. S. (2008): Graphene-Based Liquid Crystal Device, Nano Letters, Vol. 8, pp. 1704–1708.
22) Zhang, Y., Tan, Y. W., Stormer, H. L. and Kim, P. (2005): Experimental Observation of the Quantum Hall Effect and Berry's Phase in Graphene, Nature, Vol. 438, pp. 201–204.
23) Luo, J., Jang, H. D., Sun, T., Xiao, L., He, Z., Katsoulidis, A. P., Kanatzidis, M. G., Gibson, J. M. and Huang, J. (2011): Compression and Aggregation-Resistant Particles of Crumpled Soft Sheets, ACS Nano, Vol. 5, pp. 8943–8949.
24) Li, D., Muller, M. B., Gilje, S., Kaner, R. B. and Wallace, G. G. (2008): Processable Aqueous Dispersions of Graphene Nanosheets, Nature Nanotechnology, Vol. 3, pp. 101–105.
25) Tung, V. C., Allen, M. J., Yang, Y. and Kaner, R. B. (2009): High-Throughput Solution Processing of Large-Scale Graphene, Nature Nanotechnology, Vol. 4, pp. 25–29.
26) Luo, J., Cote, L. J., Tung, V. C., Tan, A. T. L., Goins, P. E., Wu, J. and Huang, J. (2010): Graphene Oxide Nanocolloids, Journal of the American Chemical Society, Vol. 132, pp. 17667–17669.
27) Hamilton, C. E., Lomeda, J. R., Sun, Z., Tour, J. M. and Barron, A. R. (2009): High-Yield Organic Dispersions of Unfunctionalized Graphene, Nano Letters, Vol. 9, pp. 3460–3462.
28) Yang, X., Zhu, J., Qiu, L. and Li, D. (2011): Bioinspired Effective Prevention of Restacking in Multilayered Graphene Films: Towards the Next Generation of High-Performance Supercapacitors, Advanced Materials, Vol. 23, pp. 2833–2838.
29) Korkut, S., Roy-Mayhew, J. D., Dabbs, D. M., Milius, D. L. and Aksay, I. A. (2011): High Surface Area Tapes Produced with Functionalized Graphene, ACS Nano, Vol. 5, pp. 5214–5222.
30) Xiao, L., Damien, J., Luo, J., Jang, H. D., Huang, J. and He. Z. (2012): Crumpled Graphene Particles for Microbial Fuel Cell Electrodes, Journal of Power Sources, Vol. 208, pp. 187–192.
31) Jang, H. D., Kim, S. K., Chang, H., Roh, K. M. and Choi, J. W. (2012): A Glucose Biosensor Based on TiO_2-Graphene Composite, Biosensors and Bioelectronics, Vol. 38, pp.184–188.
32) Stankovich, S., Dikin, D. A., Dommett, G. H. B., Kohlhaas, K. M., Zimney, E. J., Stach, E. A., Piner, R. D., Nguyen, S. T. and Ruoff, R. S. (2006): Graphene-Based Composite Materials, Nature, Vol. 442, pp. 282–286.
33) Li, D. and Kaner, R. B. (2008): Graphene-Based Materials, Science, Vol. 320, pp. 1170–1171.
34) Si, Y. and Samulski, E. T. (2008): Exfoliated Graphene Separated by Platinum Nanoparticles, Chemistry of Materials, Vol. 20, pp. 6792–6797.
35) Xu, C.,Wang, X. and Zhu, J. (2008): Graphene-Metal Particle Nanocomposites, The Journal of Physical Chemistry C, Vol. 112, pp. 19841–19845.
36) Li, Y., Tang, L. and Li, J. (2009): Preparation and Electrochemical Performance for Methanol Oxidation of Pt/Graphene Nanocomposites, Elecrochemistry Communications, Vol. 11, pp. 846–849.
37) Williams, G. and Kamat, P. V. (2009): Graphene-Semiconductor Nanocomposites: Excited-State Interactions between ZnO Nanoparticles and Graphene Oxide, Langmuir, Vol. 25, pp. 13869–13873.
38) Yoo, E., Okata, T., Akita, T., Kohyama, M., Nakamura, J. and Honma, I. (2009): Enhanced Electrocatalytic Activity of Pt Subnanoclusters on Graphene Nanosheet Surface, Nano Letters, Vol. 9, pp. 2255–2259.
39) Zhang, Y., Li, H., Pan, L., Lu, T. and Sun, Z. (2009): Capacitive Behavior of Graphene-ZnO Composite Film for Supercapacitors, Journal of Electroanalytical Chemistry, Vol. 634, pp. 68–71.
40) Kou, R., Shao, Y., Wang, D., Engelhard, M. H., Kwak, J. H., Wang, J., Viswanathan, V. V., Wang, C., Lin, Y., Wang, Y., Aksay, I. A. and Liu, J. (2009): Enhanced Activity and Stability of Pt Catalysts on Functionalized Graphene Sheets for Electrocatalytic Oxygen Reduction, Electrochemistry Communications, Vol. 11, pp. 954–957.
41) Jang, H. D., Kim, S. K., Chang, H., Choi, J. W., Luo, J. and Huang, J. (2013): One-Step Synthesis of Pt-Nanoparticles-Laden Graphene Crumples by Aerosol Spray Pyrolysis and Evaluation of Their Electrocatalytic Activity, Aerosol Science and Technology, Vol. 47, pp. 93–98.
42) Luo, J., Zhao, X., Wu, J., Jang, H. D., Kung, H. H. and Huang, J. (2012): Crumpled Graphene-Encapsulated Si Nanoparticles for Lithium Ion Battery Anodes, The Journal of Physical Chemistry Letters, Vol. 3, pp. 1824–1829.
43) Shon, K., Na, Y. J., Chang, H., Roh, K. M., Jang, H. D. and Huang, J. (2012): Oil Absorbing Graphene Capsules by Capillary Molding, Chemical Communication, Vol. 48, pp. 5968–5970.
44) Luo. J., Jang, H. D. and Huang, J. (2013): Effect of Sheet Morphology on the Scalability of Graphene-Based Ultracapacitors, ACS Nano, Vol. 7, pp.1464–1471.
45) Jang, H. D., Kim, S. K., Chang, H., Choi, J. W. and Huang, J. (2013): Synthesis of Graphene Based Noble Metal Composites for Glucose Biosensor, Materials Letters, Vol. 106, pp. 277–280.
46) Cote, L. J., Silva, R. C. and Huang, J. (2009): Flash Reduction and Patterning of Graphite Oxide and Its Polymer Composite, Journal of the American Chemical Society, Vol. 131, pp. 11027–11032.
47) Cote, L. J., Kim, F. and Huang, J. (2009): Langmuir-Blodgett Assembly of Graphite Oxide Single Layers, Journal of the American Chemical Society, Vol. 131, pp. 1043–1049.
48) Hummers, W. S. and Offeman, R. E. (1958): Preparation of Graphitic Oxide, Journal of the American Chemical Society, Vol. 80, pp. 1339.
49) Kim, F., Luo, J., Silva, R. C., Cote, L. J., Sohn, K. and Huang, J. (2010) Self-Propagating Domino-like Reactions in

Oxidized Graphite, Advanced Functional Materials, Vol. 20, pp. 2867–2873.
50) Feng, Z., Li, Y., Niu, D., Li, L., Zhao, W., Chen, H., Li, L., Gao, J., Ruan, M. and Shi, J. (2008): A Facile Route to Hollow Nanospheres of Mesoporous Silica with Tunable Size, Chemical Communications, Vol. 44, pp. 2629–2631.
51) Wang, J. G., Li, F., Zhou, H. J., Sun, P. C., Ding, D. T. and Chen, T. H. (2009): Silica Hollow Spheres with Ordered and Radially Oriented Amino-Functionalized Mesochannels, Chemical Communications, Vol. 21, pp. 612–620.
52) Zhu, J., Tang, J., Zhao, L., Zhou, X., Wang, Y. and Yu, C. (2010): Ultrasmall, Well-Dispersed, Hollow Siliceous Spheres with Enhanced Endocytosis Properties, Small, Vol. 6, pp. 276–282.
53) Du, L., Liao, S., Khatib, H. A., Stoddart, J. F. and Zink, J. I.: Controlled-Access Hollow Mechanized Silica Nanocontainers, Journal of the American Chemical Society, Vol. 131, pp. 15136–15142.
54) Qi, G., Wang, Y., Estevez, L., Switzer, A. K., Duan, X., Yang, X. and Giannelis, E. P. (2010): Facile and Scalable Synthesis of Monodispersed Spherical Capsules with a Mesoporous Shell, Chemistry of Materials, Vol. 22, pp. 2693–2695.
55) Lebret, V., Raehm, L., Durand, J. O., Smaïhi, M., Werts, M. H. V., Blanchard-Desce, M., Méthy-Gonnod, D. and Dubernet, C. (2010): Folic Acid-Targeted Mesoporous Silica Nanoparticles for Two-Photon Fluorescence, Journal of Biomedical Nanotechnology, Vol. 6, pp. 176–180.
56) He, N., Deng, Y., Xu, L., Li, Z. and Li, X. (2010): Preparation of Silicotungstenic Acid-Containing Mesoporous Materials, Journal of Biomedical Nanotechnology, Vol. 10, pp. 8463–8466.
57) Shokrgozar, M. A., Mottaghitalab, F., Mottaghitalab, V. and Farokhi, M. (2011): Fabrication of Porous Chitosan/Poly (vinyl alcohol) Reinforced Single-Walled Carbon Nanotube Nanocomposites for Neural Tissue Engineering, Journal of Biomedical Nanotechnology, Vol. 7, pp. 276–284.
58) Singh, K. P., Panwar, P., Kohli, P. and Sanjesh. (2011): Liposome-Mesoporous Silica Nanoparticles Fused Cores: A Safer Mode of Drug Carrier, Journal of Biomedical Nanotechnology, Vol. 7, pp. 60–62.
59) Yiu, H. H. P., McBain, S. C., Lethbridge, Z. A. D., Lees, M. R., Palona, I., Olariu, C. I. and Dobson, J. (2011): Novel Magnetite-Silica Nanocomposite (Fe_3O_4-SBA-15) Particles for DNA Binding and Gene Delivery Aided by a Magnet Array, Journal of Nanoscience and Nanotechnology, Vol. 11, pp. 3586–3591.
60) Jung, W. Y., Lee, G. D., Park, S. S., Lim, K. T., Lee, M. S. and Hong, S. S. (2011): Synthesis of TiO_2 Supported on SBA-15 Using Different Method and Their Photocatalytic Activity, Journal of Nanoscience and Nanotechnology, Vol. 11, pp. 7446–7450.
61) Wang, M., Zhang, J., Yuan, Z., Yang, W., Wu, Q. and Gu, H. (2012): Targeted Thrombolysis by Using of Magnetic Mesoporous Silica Nanoparticles, Journal of Biomedical Nanotechnology, Vol. 8, 624–632.
62) He, N., Xu, L., Wang, T., Du, J., Li, Z., Deng, Y., Li, S. and Ge, S. (2009): Determination of Paracetamol with Porous Electrochemical Sensor, Journal of Biomedical Nanotechnology, Vol. 5, pp. 607–610.
63) Xu, L., Du, J., Deng, Y. and He, N. (2012): Electrochemical Detection of E. coli O157:H7 Using Porous Pseudo-Carbon Paste Electrode Modified with Carboxylic Multi-Walled Carbon Nanotubes, Glutaraldehyde and 3-Aminopropyltriethoxysilane, Journal of Biomedical Nanotechnology, Vol. 8, pp. 1006–1011.
64) Liu, C., Ge, C., Wang, A., Yin, H., Ren, M., Zhang, Y., Yu, L. and Jiang, T. (2011): Synthesis of Porous Hollow Silica Spheres using Functionalized Polystyrene Latex Spheres as Templates, Korean Journal of Chemical Engineering, Vol. 28, pp. 1458–1463.
65) Yang, J., Lee, J., Kang, J., Lee, K., Suh, J. S., Yoon, H. G., Huh, Y. M. and Haam, S. (2008): Hollow Silica Nanocontainers as Drug Delivery Vehicles, Langmuir, Vol. 24, pp. 3417–3421.
66) Trewyn, B. G., Slowing, I. I., Giri, S., Chen, H. T. and Lin, V. S. Y. (2007): Synthesis and Functionalization of a Mesoporous Silica Nanoparticle Based on the Sol-Gel Process and Applications in Controlled Release, Accounts of Chemical Research, Vol. 40, pp. 846–853.
67) Lay, C. L., Liu, H. Q., Wu, D. and Liu, Y. (2010): Poly (ethylene glycol)-Graft-Hollow Silica Vesicles for Drug Delivery, Chemistry—A European Journal, Vol. 16, pp. 3001–3004.
68) Chen, H., He, J., Tang, H. and Yan, C. (2008): Porous Silica Nanocapsules and Nanospheres: Dynamic Self-Assembly Synthesis and Application in Controlled Release, Chemistry of Materials, Vol. 20, pp. 5894–5900.
69) Kim, J., Lee, J., Choi, J. W. and Jang, H. D. (2013): Synthesis and Characterization of Hollow Silica Particles from Tetraethyl Orthosilicate and Sodium Silicate, Journal of Nanoscience and Nanotechnology, Vol. 13, pp. 2284–2288.
70) Tallinen, T., Astrom, J. A. and Timonen, J. (2009): The Effect of Plasticity in Crumpling of Thin Sheets, Nature Materials, Vol. 8, pp. 25–29.
71) Matan, K., Williams, R. B., Witten, T. A. and Nagel, S. R. (2002): Crumpling a Thin Sheet, Physical Review Letters, Vol. 88, pp. 076101.
72) Lobkovsky, A., Gentges, S., Li, H., Morse, D. and Witten, T. A. (1995): Scaling Properties of Stretching Ridges in a Crumpled Elastic Sheet, Science, Vol. 270, pp. 1482–1485.
73) Kuila, T., Bose, S., Khanra, P., Mishra, A. K., Kim, N. H. and Lee, J. H. (2011): Recent Advances in Graphene-Based Biosensors, Biosensors and Bioelectronics, Vol. 26, pp. 4637–4648.
74) Chen, H., Muller, M. B., Gilmore, K. J., Wallace, G. C. and Li, D. (2008): Mechanically Strong, Electrically Conductive, and Biocompatible Graphene Paper, Advanced Materials, Vol. 20, pp. 3557–3561.
75) Yang, K., Wan, J., Zhang, S., Zhang, Y., Lee, S. T. and Liu, Z. (2011): In Vivo Pharmacokinetics, Long-Term Biodistribution, and Toxicology of PEGylated Graphene in Mice, ACS Nano, Vol. 5, pp. 516–522.
76) Park, S., Mohanty, N., Suk, J. W., Nagaraja, A., An, J., Piner, R. D., Cai, W., Dreyer, D. R., Berry, V. and Ruoff, R. S. (2010): Biocompatible, Robust Free-Standing Paper Com-

posed of a TWEEN/Graphene Composite, Advanced Materials, Vol. 22, pp. 1736–1740.
77) Wang, J., (2008): Electrochemical Glucose Biosensors. Chemical Reviews, Vol. 108, pp. 814–825.
78) Wang, Y., Shao, Y., Matson, D. W., Li, J. and Lin, Y. (2010): Nitrogen-Doped Graphene and Its Application in Electrochemical Biosensing, ACS Nano, Vol. 4, pp. 1790–1798.
79) Chen, X., Ye, H., Wang, W., Qiu, B., Lin, Z. and Chen, G. (2010): Electrochemiluminescence Biosensor for Glucose Based on Graphene/Nafion/GOD Film Modified Glassy Carbon Electrode, Electroanalysis, Vol. 22, pp. 2347–2352.
80) Liu, S., Tian, J., Wang, L., Luo, Y., Lu, W. and Sun, X. (2011): Self-assembled graphene platelet-glucose oxidase nanostructures for glucose biosensing, Biosensors and bioelectronics, Vol. 26, pp. 4491–4496.
81) Shan, C., Yang, H., Han, D., Zhang, Q., Ivaska, A. and Niu, L. (2010): Graphene/AuNPs/chitosan nanocomposites film for glucose biosensing, Biosensors and bioelectronics, Vol. 25, pp. 1070–1074.
82) Lu, J., Do, I., Drzal, L. T., Worden, R. M. and Lee, I. (2008): Nanometal-Decorated Exfoliated Graphite Nanoplatelet Based Glucose Biosensors with High Sensitivity and Fast Response, ACS Nano, Vol. 2, pp. 1825–1832.
83) Baby, T. T., Aravind, S. S. J., Arockiadoss, T., Rakhi, R. B. and Ramaprabhu, S. (2010): Metal Decorated Graphene Nanosheets as Immobilization Matrix for Amperometric Glucose Biosensor, Sensors and Actuators B: Chemical, Vol. 145, pp. 71–77.
84) Chen, Y., Li, Y., Sun, D., Tian, D., Zhang, J. and Zhu, J. J. (2011): Fabrication of Gold Nanoparticles on Bilayer Graphene for Glucose Electrochemical Biosensing, Journal of Materials Chemistry, Vol. 21, pp. 7604–7610.

Author's short biography

Sun Kyung Kim

Sun Kyung Kim received her B.S. (2006) and M.S (2010) degrees from Chungnam National University and Sogang University in Korea, respectively. She is currently working toward her Ph.D. degree in Rare Metals Research Center at Korea Institute of Geoscience and Mineral Resources and Interdisciplinary Program of Integrated Biotechnology at Sogang University. Her current research interests include aerosol synthesis of nano-materials and their applications for electrochemical sensors.

Hankwon Chang

Hankwon Chang received his B.S. (1998) and M.S. (2000) degrees from Yeungnam University, Korea and Ph.D. (2003) degree in Chemical Engineering from Hiroshima University. In 2004, he returned home country, Korea and joined in Nano-Materials Research Team of Korea Institute of Geoscience and Mineral Resources (KIGAM) as a Senior Researcher. He is now a Principal Researcher in Rare Metals Utilization Research Team of KIGAM and an Associate Professor of Nanomaterials Science and Engineering Major of University of Science and Technology (UST). As a societal service, he has been working as an Editorial Board Member of Advanced Powder Technology from 2009 and a Chair for Nano-Materials Division of the Korean Association for Particle and Aerosol Research (KAPAR) from 2012. His current research interests include aerosol synthesis of functional nano-materials and their applications for energy conversion and storage materials.

Author's short biography

Jeong-Woo Choi

Jeong-Woo Choi received his B.S. (1982) and M.S. (1984) at Sogang University, Korea, and Ph.D. (1990) at Rutgers University, USA. He worked at the IBM Almaden Research Center and Mitsubishi Electronics Advanced Technology R&D Center as a visiting researcher from 1993 to 1996. He also received D. Eng. (2003) from Tokyo Institute of Technology, Japan, as well as MBA (2005) from the University of Durham, UK. He has been a Professor of the Department of Chemical & Biomolecular Engineering, Sogang University, South Korea, after 1990. His main research area is nanobioelectronics including biomemory device, nanoprotein chips, and cell chips based on nanotechnology. He has published over 313 peer-reviewed papers including in Angewandte Chemie, Advanced Materials, Biomaterials, Biosensor and Bioelectronics, etc. His current research interest is the application of nanoparticles to nanobioelectronic device.

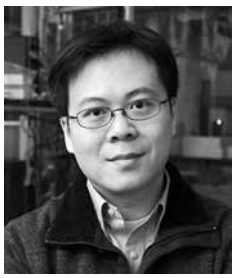

Jiaxing Huang

Jiaxing Huang is an Associate Professor of Materials Science and Engineering at Northwestern University. He received a B.S. in Chemical Physics from University of Science and Technology of China (USTC) in 2000 and a Ph.D. in chemistry from the University of California, Los Angeles (UCLA) in 2004, and became a Miller Research Fellow at the University of California, Berkeley before joining Northwestern in 2007. His research interest is in the general area of materials chemistry, processing and manufacturing. Some materials of interests include 2D materials, organic crystals and metal nanostructures. He has been a recipient of the IUPAC Young Chemist Prize, the Alfred P. Sloan Research Fellowship, the NSF CAREER Award, the inaugural ISEN Early Career Investigator Award at Northwestern, and the Gustav Olling Outstanding Young Manufacturing Engineers Award from the Society of Manufacturing Engineers.

Hee Dong Jang

Hee Dong Jang received his B.S. (1982), M.S. (1984), and Ph.D. (1993) at Sogang University in Korea, and Dr. Eng. (2005) at Hiroshima University in Japan. He has worked as a postdoctoral researcher at the University of California at Los Angeles from 1996 to 1997 and a visiting scholar at the Northwestern University from 2009 to 2010. He has been appointed as a President of Korea Association for Aerosol and Particle Research from 2012, and an Executive Editor of Advanced Powder Technology from 2009. He has been working at Korea Institute of Geoscience and Mineral Resources (KIGAM) from 1985, and he is currently a distinguished principal researcher and a Director of Rare Metals Research Center at KIGAM, and Professor in the Nano-Materials Science and Engineering Major of University of Science and Technology. His area of expertise is the aerosol processing and application of nanostructured materials. His current interests involve the synthesis of Graphene based nanocomposite materials and their application for energy, environmental and biomaterials.

KONA Powder and Particle Journal No. 31 (2014) 126–134/Doi:10.14356/kona.2014019 Review Paper

Physicochemical Properties and Factors that Induce Asbestos-Related Respiratory Disease †

Hiroto Izumi * and Yasuo Morimoto

[1] *Institute of Industrial Ecological Sciences, University of Occupational and Environmental Health, Japan*

Abstract

It is thought that inhaled dusts such as asbestos and man-made mineral fibers in the lung repeatedly induce persistent inflammation and finally lead to pulmonary fibrosis and respiratory cancer. There have been many studies about whether a variety of factors, such as oxidative stress including free radicals, chemokines, inflammatory cytokines, and fibrosis-related cytokines are related to pulmonary fibrosis, lung cancer and malignant mesothelioma. In this paper, we introduce the relationship between these factors and these diseases. It is important to determine what physicochemical properties of fibrous materials such as asbestos are related to asbestos-related diseases. We show the relationship between the physicochemical properties of not only asbestos but also other fibrous materials and inflammation, fibrosis and biopersistence in the lung.

Keywords: asbestos, lung cancer, malignant mesothelioma, cumulative exposure

Asbestos exposure and respiratory tumor

It is thought that a high concentration of asbestos exposure induces lung cancer[1)]. There are some reports that a cumulative exposure of 25–100 fiber-years induced the onset of lung cancer caused by asbestos, and the Helsinki criteria showed that a cumulative exposure of 25 fiber-years, the minimum cumulative exposure level, is necessary for the onset of lung cancer induced by asbestos[2)]. Cumulative exposure correspond to a 2-fold risk of lung cancer. The indexes of the risk of lung cancer are 1) retained fiber levels of 2 million amphibole fibers (> 5 μm) per gram of dry lung tissue or 5 million amphibole fibers (> 1 μm) per gram of dry lung tissue measured by electron microscopy, (**Fig. 1**); 2) 5000 asbestos bodies per gram of dry tissue measured by light microscopy, or 5 asbestos bodies per milliliter of bronchoalveolar lavage fluid measured by light microscopy (**Fig. 2**); and 3) a profusion score of 1in a chest x-ray finding, which means early asbestosis. Henderson et al.[3)] proposed, as a revised version of the Helsinki criteria, that a cumulative exposure of 20 fiber-years for amphibole asbestos, cumulative exposure of 25 fiber-years for asbestos yarn spinning, cumulative exposure of 200 fiber-years for chrysotile asbestos only (work in chrysotile mine quarrying, crushing and friction materials production in Canada) , or cumulative exposure of more than 25 fiber-years for the combined exposure of chrysotile and amphibole asbestos is necessary for the onset of lung cancer induced by asbestos.

The onset of malignant mesothelioma is thought to be induced by a low concentration of asbestos exposure, although there is no significant evidence of a relationship between the occurrence of mesothelioma and the amount of exposure to asbestos. Previous studies[4)] reported that malignant mesothelioma was contracted by workers who were engaged in indirect asbestos exposure in a shipyard or in the vehicle manufacturing industry developed malignant mesothelioma, a person who washed workers' clothes, to which asbestos was attached, and neighboring inhabitants around asbestos mines and the asbestos product man-

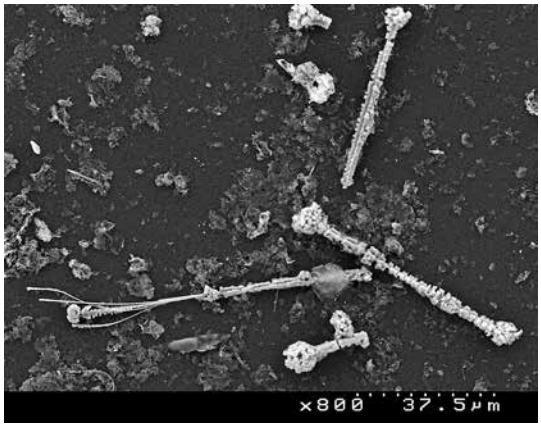

Fig. 1 Scanning electron microscope of asbestos bodies

† Accepted: September 18, 2013
[1] 1-1, Iseigaoka, Yahata-nishi-ku, Kitakyushu, Fukuoka, 807-8555, Japan
* Corresponding author:
E-mail: h-izumi@med.uoeh-u.ac.jp
TEL: +81-93-691-7466 FAX: +81-93-691-4284

Fig. 2 Light microscope of asbestos bodies

ufacturing industry. Therefore, asbestos exposure other than in occupation induced the disease. For that reason, in examining asbestos-related diseases, it is very important to know not only the occupational history of workers but also the residential history of families. It is thought that from cohort studies the degree of risk of developing mesothelioma by asbestos depends on the kind of asbestos, namely when the strength of chrysotile, amosite and crocidolite is 1: 100: 500, respectively[5]. In addition, the onset is unrelated to smoking.

Relationship between size of asbestos and asbestos-related tumor

The physicochemical properties of asbestos in the induction of lung cancer are thought to be 1) fibers with low solubility and 2) fibers which are thin and long.

If fibers reach the lung, some of them melt in body fluid and some are divided into small fragments. These fibers, which become small, are phagocytized by alveolar macrophages and are excreted outside the lungs with mucociliary escalator. Even if fibers have low solubility, short fibers are also excreted by alveolar macrophages. However, it is difficult for macrophages to phagocytize the fiber physically, particularly when fibers with low solubility are longer than the diameter of the macrophages. Thus fibers with low solubility and long length are deposited in the lung in the long term and will influence the lung continuously without being excreted. It is thought that fibers which are not excreted from the lung have a physically and chemically harmful effect on the lung.

Solubility tests (in vitro test to examine how fibers dissolve in medium) and inhalation studies of not only asbestos but also man-made mineral fibers have been performed[6]. The solubility in the solubility test is associated with pathological lesions in acute and chronic inhalation studies. In the solubility test, fibers with low solubility, such as crocidolite and amosite, induced a long half-life of the fiber in an acute inhalation study and developed pulmonary fibrosis and cancer in a chronic inhalation study. On the other hand, fibers with high solubility, such as slagwool and HT stone wool, reduced the half-time of the fiber and caused no significant pathological lesions.

Taken together, the physicochemical properties of asbestos which affect the lung tissue are its length and solubility. Long and thin fibers with low solubility induce biopersistence in the lung and finally cause lung disorders. From the clinical point of view, the length of the fiber affects the development of lung cancer. There are regulations based on the length of fiber, such as more than 1 μm or 5 μm, to measure the number of asbestos fibers in lung tissue in order to examine whether or not lung cancer is related to asbestos exposure. This may show that the length of fibers is related to the onset of lung cancer induced by asbestos.

In malignant mesothelioma, the association between physicochemical properties and the development of mesothelioma is unclear, but it has been reported that short fibers induce malignant mesothelioma. In the case of malignant mesothelioma, it may be important that the onset of mesothelioma is associated with the movement of the asbestos to the parietal pleura. The physical limitation of phagocytosis of the fibers by the macrophages may be related to the shortness of the fibers.

Lung damage by free radicals and inflammation

Inhalation of fibers can cause inflammation in the respiratory tract and pulmonary alveolar space in not only the acute phase but also in the chronic phase[7] These inflammations, especially continuous inflammation, progress to fibrosis of the lungs and pleura, or lung tumor (malignant mesothelioma and lung cancer)[7, 8]. We performed intratracheal instillation of different mineral fibers to rat, and examined lung inflammation from 3 days up to 6 months[9]. Harmful respirable particles like crystalline silica or crocidolite asbestos, which are kinds of asbestos, caused persistent inflammation from the initial instillation until six months. However, transient inflammation was only observed early in the instillation when less harmful titanium dioxide of micron size was inhaled. In the inhalation exposure examination to rat with chrysotile for 20 days, continuous inflammation and fibrosis containing mainly neutrophils were observed[10]. Continuous inflammation causes lung injury, and free radicals play a central role in this injury. There are two types of free radicals, one is reactive oxygen species and the other is reactive nitrogen

species[11, 12]. In the reactive oxygen species, there are a superoxide ion (O_2^-), hydroxyl radicals (·OH), hydrogen peroxide (H_2O_2), and singlet oxygen ($^1O_2$). On the other hand, in the reactive nitrogen species, there are nitric oxide (NO), nitrosonium ion (NO^+), nitrite ion (NO_2^-), and peroxynitrite ($ONOO^-$).·OH and $ONOO^-$ have the highest reactivity in each species. There are two main production locations of the free radicals. One is produced directly from the surface of the asbestos[13], and the other is produced indirectly from cells. Free radicals can attack DNA and proteins including cell membranes[14,15]. Free radicals have not only cytotoxic activity but also functions of signaling molecules against immunoreaction[16], remodeling of extracellular matrix[17,18], regulation of cell proliferation[19] and malignant transformation[20].

It is known that exposure to asbestos induces cell dysfunction, such as cell death, DNA damage and protein damage. Apoptosis is one kind of cell death, and asbestos exposure induces apoptosis of epithelial cells[21]. We have reported that chrysotile induces apoptosis of A549 lung epithelial cancer cell lines in a dose-dependent manner and that this mechanism occurs through the activation of caspase 3 and 9[22]. In an animal model using rats, we also observed that intratracheal instillation of chrysotile induced apoptosis of alveolar epithelial cells and alveolar macrophages and that the activation of caspase 3 and 9 was sustained. These findings suggest that epithelial cells can protect the lung from inflammation and fibrosis, and that apoptosis of epithelial cells by asbestos is involved in fibrosis and tumor progression. Anti-oxidative stress enzymes, such as heme oxygenase-1 (HO-1) and macrophage inflammatory protein-2 (MIP-2), a transcription factor involved in inflammation such as NF-κB, have been studied as indications of oxidative stress. HO-1 is useful as an indicator of oxidative stress because it has the ability to inhibit the production of active oxygen and its expression is increased in response to the amount of active oxygen[23,24]. We have reported that the protein expression of HO-1 was enhanced continuously up to six months when chrysotile or crocidolite was injected intratracheally to rat[25,26]. Driscoll et al.[27] reported that exposure to crocidolite induced the expression of MIP-2 and NF-κB in alveolar epithelial cells and that this induction was suppressed by administering an antioxidant. Fattman et al.[28] using knockout mice with deleted EC-SOD gene, which can eliminate active oxygen, reported that free radicals advance the inflammation and fibrosis of asbestos. These results suggest that the oxidative stress caused by asbestos might promote inflammation and fibrosis.

As for DNA damage, it has been reported that 8-hydroxy deoxyguanosine and 8 nitroguanine are generated by asbestos[29,30]. 8 nitroguanine was generated in airway epithelial cells of mouse lung tissue by intratracheal injection of chrysotile and crocidolite. At the protein level, it has been reported that the tumor suppressor gene p53 is phosphorylated by chrysotile and crocidolite in vitro[31]. This might indicate that asbestos exposure can repress the tumor suppressor function.

Genetic abnormality of malignant pleural mesothelioma and lung cancer

Asbestos is known as a carcinogen, and it can cause malignant pleural mesothelioma and lung cancer[32]. However, the mechanism of carcinogenesis has not been sufficiently clarified. Its oncogenesis might be influenced by complicated factors, such as diversity of the asbestos (type, geometry, dose of the fiber, and so on), individual sensitivity, and synergistic effects with other carcinogens like cigarette. Abnormality of gene expression is broadly classified into genetic abnormality and epigenetic abnormality[33–35]. Genetic abnormality is a disorder which is directly caused by a mutation in the nucleotide sequence of the gene. On the other hand, epigenetics is a study that reveals the diversity of gene expression inherited even after cell division without a change in the nucleotide sequence. Both genetic abnormality and epigenetic abnormality are associated with not only oncogenesis but also malignant progression. In cancer cells, there are two types of mutations. One is passenger mutations, which are accumulated only by chance, and the other is oncogenic driver mutations, which occur in important genes involved in the phenotype of cancer[36]. Oncogenic driver mutations have been found in the EGF receptor, K-ras, HER2, AKT1, etc. (**Table 1**). In addition, there is a cancer that is completely dependent on the oncogenic signal associated with cell proliferation and survival of cancer by only one mutated gene. This is called oncogene addiction, and its representative example is L858R mutation in the EGFR gene[37].

In the genetic abnormality of asbestos-related lung cancer, mutations of the k-ras and TP53 (p53) have been reported[38–48]. K-ras mutation is an oncogene that plays an important role in the signal transduction of the epidermal growth factor receptor (EGFR). Husgafvel-Pursiainen et al.[42] reported that asbestos exposure alone was not significantly associated with an increased occurrence of K-ras mutations. However, a strong and significant association was found between adenocarcinoma and K-ras mutation in a group of combined smoking and asbestos exposure[42,47,48]. Nelson et al.[40] suggested that asbestos exposure increases the likelihood of mutation at K-ras codon 12 and that this process occurs independently of the induction of interstitial fibrosis. Mutant p53 proteins acquire oncogenic properties that enable them to promote invasion, metastasis, proliferation and cell survival[49]. Wang X et al. reported that p53 mutations occurred significantly more frequently in patients with a history of occupational exposure to

Table 1 Oncogenic driver mutations for lung cancer

	Entrez GeneID
KRAS (Kirsten rat sarcoma viral oncogene homolog)	3845
EGFR (epidermal growth factor receptor)	1956
HER2 (v-erb-b2 avian erythroblastic leukemia viral oncogene homolog 2)	2064
BRAF (v-raf murine sarcoma viral oncogene homolog B)	673
MET (met proto-oncogene, hepatocyte growth factor receptor)	4233
AKT1 (v-akt murine thymoma viral oncogene homolog 1)	207
MAP2K1 (mitogen-activated protein kinase kinase 1)	5604
PIK3CA (phosphatidylinositol-4,5-bisphosphate 3-kinase, catalytic subunit alpha)	5290
EML4-ALK*[1]	27436/238

*[1] EML4-ALK is a product of the fusion gene lined the N-terminus of EML4 (echinoderm microtubule associated protein like 4, GeneID 27436) and the C-terminus of ALK (anaplastic lymphoma receptor tyrosine kinase, GeneID 238).

asbestos[46]. It has also been reported that the mutation of p53 gene is common in asbestos associated cancers[43].

An analysis of specific gene copy number changes in asbestos-related lung cancer revealed some allelic imbalances[50]. In particular, allelic imbalances of 19p[51], 9q33[52], and 2p16[53] were important in asbestos-related lung cancer. FHIT, a candidate tumor suppressor gene, contains the FRA3B common fragile site and is highly susceptible to carcinogen damage[54]. Deletion of the FHIT gene in the chromosome 3p14.2 and reduced expression of the FHIT protein are correlated with malignant non-small cell lung cancer. It has also been indicated that these mutations are associated with smoking and asbestos exposure[55, 56].

There are many reports about the genetic abnormality of malignant pleural mesothelioma. Mutations of K-ras and p53 in malignant pleural mesothelioma have been reported in the same way as other malignant tumors[57, 58]. However, association with malignant pleural mesothelioma and the BRCA1 associated protein-1 (BAP1), the cyclin-dependent kinase inhibitor 2A (p16/CDKN2A), neurofibromin 2 (NF2), and EGFR genes have been well investigated. BAP1 binds to BRCA1 and acts as a tumor suppressor[59, 60]. p16/CDKN2A acts as a negative regulator of the proliferation of normal cells by interacting strongly with CDK4 and CDK6[61] and is associated with cellular senescence and tumor suppressor[62]. NF2 is associated with a signaling pathway that plays a pivotal role in tumor suppression by restricting proliferation and promoting apoptosis[63]. Frequent mutations of the BAP1, p16/CDKN2A and NF2 genes are detected in malignant mesothelioma cells[64, 65]. There are reports of mutation[66, 67] and overexpression[68, 69] of EGFR in malignant pleural mesothelioma. Downstream of EGFR signaling is activated in both cases, and mutations in EGFR downstream pathways are not rare in malignant pleural mesothelioma[58]. Murthy and Testa reported that specific sites of chromosome arms are deleted in malignant mesothelioma and that p16/CDKN2A at 9p21 and NF2 at 22q12 are frequently altered[70].

The status of DNA methylation, structural changes in the chromatin by chemical modification of histones (**Table 2**), the action of non-coding RNA, etc., are important in epigenetic abnormality[71]. For the methylation of DNA, guanine and cytosine rich regions as the promoter of the gene (CpG island) are easily transferred by the addition of a methyl group by a specific enzyme. Transcription factor can not bind to the methylated promoter and transcriptional activity is suppressed. For example, when the promoter or cording region of a tumor suppressor gene is methylated, tumor suppressor proteins can not be synthesized and the tumor suppression effect is attenuated. Same reported DNA-hypermethylated tumor suppressor genes are, p16/CDKN2A, mutL homologue 1 (MLH1), epithelial-cadherin (E-cadherin), runt-related transcription factor 3 (RUNX3), adenomatous polyposis coli (APC), O(6)-methylguanine-DNA methyltransferase (MGMT), Ras association domain family 1A (RASSF1A), death-associated protein kinase (DAPK), cell adhesion molecule 1 (CADM1), retinoic acid receptor beta (RARB), metalloproteinase inhibitor 3 (TIMP3), and FHIT[72–75]. Hypermethylation of tumor suppressor genes is also involved in malignant mesothelioma and lung cancer caused by asbestos. When Dammann et al.[76] analyzed the methylation from the lung tissue of lung cancer patients, hypermethylations of p16 were observed in 47% of lung cancer tissue and in 14% of normal lung tissue of patients. They also reported that there is a correlation between inactivation of p16 and asbestos exposure. On the other hand, Fujii et al.[77] reported that hypermethylation of p16 was observed in 7.7% of malignant pleural mesothelioma, which was lower than 30.4% of lung cancer. Further

Table 2 Epigenetic regulation of gene expression

1) Modification of promoter region	
	Gene expression
Demethylation in CpG island	On
Methylation in CpG island	Off
2) Modification of histone	
	Gene expression
Acetylation	On
Deacetylation	Off
Phosphorylation	On or Off
Ubiquitination	On or Off
Methylation	On or Off
SUMOylation	On or Off

investigation is required to clarify the relationship between asbestos exposure and DNA methylation.

Structural changes in the chromatin by the chemical modification of histones are also involved in epigenetic regulation[78]. Histone acetylation induces transcription, while deacetylation of histone suppresses transcription (**Table 2**). There are few reports about the association of malignant progression of mesothelioma and histone acetylation. However, a number of molecular-targeted agents that are currently under evaluation for mesothelioma, such as the Histone deacetylase (HDAC) inhibitors, have demonstrated promising anticancer activity[79].

Micro RNA is a non-coding RNA which binds to the target mRNA and reduces the protein expression by inhibiting translation. An association between miRNA and malignant pleural mesothelioma has been reported. From an analysis of miRNA expression in mesothelioma tissue, it has been suggested that miRNAs could be potential biomarkers of prognosis and therapeutic targets[80–87]. Benjamin H et al.[87] reported that Hsa-miR-193-3p was overexpressed in malignant pleural mesothelioma, while hsa-miR-200c and hsa-miR-192 were overexpressed in peripheral lung adenocarcinoma and carcinomas that frequently metastasize to lung pleura. This indicates that this diagnostic assay might be a useful tool in the differential diagnosis of malignant pleural mesothelioma from other malignancies in the pleura. Interestingly, there have been attempts to diagnose malignant mesothelioma by measuring the miRNA in serum, and some useful miRNAs have been reported[81, 82, 86]. Some reports indicate the target genes of miRNA and the effects on cell transformation[88–93]. There are few reports of miRNA in asbestos-related lung cancer[94]. Previous studies have reported that miRNA expression is not affected by asbestos exposure[82].

Conclusion

It is thought that asbestos inhaled into the lungs causes inflammation and eventually leads to pulmonary fibrosis and tumors. In this inflammation, free radicals such as those produced by reactive oxygen species and reactive nitrogen oxide species induce not only cell and tissue damage but also the progression of fibrosis and inflammation. These observations are forming a consensus that continuous inflammation is important in the formation of pathogenesis. It is believed that additional mutations in the bronchial-alveolar epithelial cells and pleural mesothelial cells cause the onset of lung cancer and pleural mesothelioma, respectively. The characteristics of the fibers that are related to fibrosis and carcinogenicity are low solubility and thin-long type. It is necessary to elucidate the molecular mechanisms of asbestos-related lung cancer and malignant pleural mesothelioma. The development of biomarkers using serum miRNA is also required. In particular, the development of biomarkers to distinguish between asbestos-related and non asbestos-related lung cancer and biomarkers for early detection of malignant pleural mesothelioma is anticipated.

References

1) The comittee report on the regulation for authorization of asbestos-related disease. (2012): Ministry of Health, Labour and Welfare.
2) Asbestos, asbestosis, and cancer: the Helsinki criteria for diagnosis and attribution. (1997): Scand J Work Environ Health 23, pp. 311–316.
3) Henderson, D. W. and Leigh, J. (2011): "Chapter 6. Asbestos and Carcinoma of the Lung. In: Dodson, R. F., Hammar, S. P., (eds.), Asbestos. Risk assessment, epidemiology and health effects, second edition" , CRC press, pp. 269–306.
4) Kurumatani, N. and Kumagai, S. (2008): Mapping the risk of mesothelioma due to neighborhood asbestos exposure, American Journal of Respiratory and Critical Care Medicine, Vol. 178, pp. 624–629.
5) Hodgson, J. T. and Darnton, A. (2000): The quantitative risks of mesothelioma and lung cancer in relation to asbestos exposure, Annals of Occupational Hygiene, Vol. 44, pp. 565–601.
6) IARC monographs on the evaluation of carcinogenic risks to humans. Volume 81 Man-made vitreous fibres. (2002): IARC press
7) Mossman, B. T., Lippmann, M., Hesterberg, T. W., Kelsey, K. T., Barchowsky, A. and Bonner, J. C. (2011): Pulmonary endpoints (lung carcinomas and asbestosis) following inhalation exposure to asbestos, Journal of Toxicology and Environmental Health. Part B, Critical Reviews, Vol. 14, pp. 76–121.
8) Ardies, C. M. (2003): Inflammation as cause for scar cancers of the lung, Integrative Cancer Therapies, Vol. 2, pp. 238–246.

9) Ogami, A., Morimoto, Y., Myojo, T., Oyabu, T., Murakami, M., Nishi, K., Kadoya, C. and Tanaka, I. (2007): Histopathological changes in rat lung following intratracheal instillation of silicon carbide whiskers and potassium octatitanate whiskers, Inhalation Toxicology, Vol. 19, pp. 753–758.
10) Quinlan, T. R., BéruBé, K. A., Marsh, J. P., Janssen, Y. M., Taishi, P., Leslie, K. O., Hemenway, D., O'Shaughnessy, P. T., Vacek, P. and Mossman, B. T. (1995): Patterns of inflammation, cell proliferation, and related gene expression in lung after inhalation of chrysotile asbestos, American Journal of Pathology, Vol. 147, pp. 728–739.
11) Roberts, R. A., Smith, R. A., Safe, S., Szabo, C., Tjalkens, R. B. and Robertson, F. M. (2010): Toxicological and pathophysiological roles of reactive oxygen and nitrogen species, Toxicology, Vol. 276, pp. 85–94.
12) Gius, D. and Spitz, D. R. (2006): Redox signaling in cancer biology, Antioxidants & Redox Signaling, Vol. 8, pp. 1249–1252.
13) Fubini, B. and Hubbard, A. (2003): Reactive oxygen species (ROS) and reactive nitrogen species (RNS) generation by silica in inflammation and fibrosis, Free Radical Biology & Medicine, Vol. 34, pp. 1507–1516.
14) Dizdaroglu, M. and Jaruga. P. (2012): Mechanisms of free radical-induced damage to DNA, Free Radical Research. Vol. 46, pp. 382–419.
15) Hawkins, C. L., Morgan, P. E. and Davies, M. J. (2009): Quantification of protein modification by oxidants, Free Radical Biology & Medicine, Vol. 46, pp. 965–988.
16) Fialkow, L., Wang, Y. and Downey, G. P. (2007): Reactive oxygen and nitrogen species as signaling molecules regulating neutrophil function, Free Radical Biology & Medicine, Vol. 42, pp. 153–164.
17) Kar, S., Subbaram, S., Carrico, P. M. and Melendez, J. A. (2010): Redox-control of matrix metalloproteinase-1: a critical link between free radicals, matrix remodeling and degenerative disease, Respiratory Physiology & Neurobiology, Vol. 174, pp. 299–306.
18) Kliment, C. R. and Oury, T. D. (2010): Oxidative stress, extracellular matrix targets, and idiopathic pulmonary fibrosis, Free Radical Biology & Medicine, Vol. 49, pp. 707–717.
19) Chan, E. C., Jiang, F., Peshavariya, H. M. and Dusting, G. J. (2009): Regulation of cell proliferation by NADPH oxidase-mediated signaling: potential roles in tissue repair, regenerative medicine and tissue engineering, Pharmacology & Therapeutics, Vol. 122, pp. 97–108.
20) Azad, N., Iyer, A., Vallyathan, V., Wang, L., Castranova, V., Stehlik, C. and Rojanasakul, Y. (2010): Role of oxidative/nitrosative stress-mediated Bcl-2 regulation in apoptosis and malignant transformation, Annals of the New York Academy of Sciences, Vol. 1203, pp. 1–6.
21) Liu, G., Cheresh, P. and Kamp, D. W. (2013): Molecular basis of asbestos-induced lung disease, Annual Review of Pathology, Vol. 8, pp. 161–187.
22) Kido, T., Morimoto, Y., Asonuma, E., Yatera, K., Ogami, A., Oyabu, T., Tanaka, I. and Kido, M. (2008): Chrysotile asbestos causes AEC apoptosis via the caspase activation in vitro and in vivo, Inhalation Toxicology, Vol. 20, pp. 339–347.
23) Was, H., Dulak, J. and Jozkowicz, A. (2010): Heme oxygenase-1 in tumor biology and therapy, Current Drug Targets, Vol. 11, pp. 1551–1570.
24) Raval, C. M. and Lee, P. J. (2010): Heme oxygenase-1 in lung disease, Current Drug Targets, Vol. 11, pp. 1532–1540.
25) Nagatomo, H., Morimoto, Y., Oyabu, T., Hirohashi, M., Ogami, A., Yamato, H., Kuroda, K., Higashi, T. and Tanaka, I. (2005): Expression of heme oxygenase-1 in the lungs of rats exposed to crocidolite asbestos, Inhalation Toxicology, Vol. 17, pp. 293–296.
26) Nagatomo, H., Morimoto, Y., Ogami, A., Hirohashi, M., Oyabu, T., Kuroda, K., Higashi, T. and Tanaka, I. (2007): Change of heme oxygenase-1 expression in lung injury induced by chrysotile asbestos in vivo and in vitro, Inhalation Toxicology, Vol. 19, pp. 317–323..
27) Driscoll, K. E., Carter, J. M., Howard, B. W., Hassenbein, D., Janssen, Y. M. and Mossman, B. T. (1998): Crocidolite activates NF-kappa B and MIP-2 gene expression in rat alveolar epithelial cells. Role of mitochondrial-derived oxidants, Environmental Health Perspectives, Vol. 5, pp. 1171–1174.
28) Fattman, C. L., Tan, R. J., Tobolewski, J. M. and Oury, T. D. (2006): Increased sensitivity to asbestos-induced lung injury in mice lacking extracellular superoxide dismutase, Free Radical Biology & Medicine, Vol. 40, pp. 601–607.
29) Murata, M., Thanan, R., Ma, N. and Kawanishi, S. (2012): Role of nitrative and oxidative DNA damage in inflammation-related carcinogenesis, Journal of Biomedicine & Biotechnology, Vol. 2012, Article ID.623019. doi: 10.1155/2012/623019.
30) Hiraku, Y., Kawanishi, S., Ichinose, T. and Murata, M. (2010): The role of iNOS-mediated DNA damage in infection- and asbestos-induced carcinogenesis, Annals of the New York Academy of Sciences, Vol. 1203, pp. 15–22.
31) Matsuoka, M., Igisu, H. and Morimoto, Y. (2003): Phosphorylation of p53 protein in A549 human pulmonary epithelial cells exposed to asbestos fibers, Environmental Health Perspectives, Vol. 111, pp. 509–512.
32) Mineo, T. C. and Ambrogi, V. (2012): Malignant pleural mesothelioma: factors influencing the prognosis, Oncology, Vol. 26, pp. 1164–1175.
33) Chiba, T., Marusawa, H. and Ushijima, T. (2012): Inflammation-associated cancer development in digestive organs: mechanisms and roles for genetic and epigenetic modulation, Gastroenterology, Vol. 143, pp. 550–563.
34) Wen, J., Fu, J., Zhang, W. and Guo, M. (2011): Genetic and epigenetic changes in lung carcinoma and their clinical implications, Modern Pathology, Vol. 24, pp. 932–943.
35) Risch, A. and Plass, C. (2008): Lung cancer epigenetics and genetics, International Journal of Cancer, Vol. 123, pp. 1–7.
36) Suda, K., Tomizawa, K. and Mitsudomi, T. (2010): Biological and clinical significance of KRAS mutations in lung cancer: an oncogenic driver that contrasts with EGFR mutation, Cancer Metastasis Reviews, Vol. 29, pp. 49–60.
37) Bean, G. R., Ganesan, Y. T., Dong, Y., Takeda, S., Liu, H., Chan, P. M., Huang, Y., Chodosh, L. A., Zambetti, G. P., Hsieh, J. J. and Cheng, E. H. (2013): PUMA and BIM are

required for oncogene inactivation-induced apoptosis, Science Signaling, Vol. 6, pp.:ra20. doi: 10.1126/scisignal.2003483.
38) Ahrendt, S. A., Decker, P. A., Alawi, E. A., Zhu, Yr. YR., Sanchez-Cespedes, M., Yang, S. C., Haasler, G. B., Kajdacsy-Balla, A., Demeure, M. J. and Sidransky, D. (2001): Cigarette smoking is strongly associated with mutation of the K-ras gene in patients with primary adenocarcinoma of the lung, Cancer, Vol. 92, pp. 1525–1530.
39) Sioris, T., Husgafvel-Pursiainen, K., Karjalainen, A., Anttila, S., Kannio, A., Salo, J. A., Perhoniemi, V., Heikkilä, L. and Vainio, H. (2000): Survival in operable non-small-cell lung cancer: role of p53 mutations, tobacco smoking and asbestos exposure, International Journal of Cancer, Vol. 86, pp. 590–594..
40) Nelson, H. H., Christiani, D. C., Wiencke, J. K., Mark, E. J., Wain, J. C. and Kelsey, K. T. (1999): k-ras mutation and occupational asbestos exposure in lung adenocarcinoma: asbestos-related cancer without asbestosis, Cancer Research, Vol. 59, pp. 4570–4573.
41) Mayall, F. G., Jacobson, G. and Wilkins, R. (1999): Mutations of p53 gene and SV40 sequences in asbestos associated and non-asbestos-associated mesotheliomas, Journal of Clinical Pathology, Vol. 52, pp. 291–293.
42) Husgafvel-Pursiainen, K., Karjalainen, A., Kannio, A., Anttila, S., Partanen, T., Ojajärvi, A. and Vainio, H. (1999): Lung cancer and past occupational exposure to asbestos. Role of p53 and K-ras mutations, American Journal of Respiratory Cell and Molecular Biology, Vol. 20, pp. 667–674.
43) Liu, B. C., Fu, D. C., Miao, Q., Wang, H. H. and You, B. R. (1998) p53 gene mutations in asbestos associated cancers, Biomedical and environmental sciences, Vol. 11, pp. 226–232.
44) Husgafvel-Pursiainen, K., Kannio, A., Oksa, P., Suitiala, T., Koskinen, H., Partanen, R., Hemminki, K., Smith, S., Rosenstock-Leibu, R. and Brandt-Rauf, P. W. (1997): Mutations, tissue accumulations, and serum levels of p53 in patients with occupational cancers from asbestos and silica exposure, Environmental and Molecular Mutagenesis, Vol. 30, pp. 224–230.
45) Kannio, A. (1996): A molecular and epidemiological study on bladder cancer: p53 mutations, tobacco smoking, and occupational exposure to asbestos, Cancer Epidemiology, Biomarkers & Prevention, Vol. 5, pp. 33–39.
46) Wang, X., Christiani, D. C., Wiencke, J. K., Fischbein, M., Xu, X., Cheng, T. J., Mark, E., Wain, J. C. and Kelsey, K. T. (1995): Mutations in the p53 gene in lung cancer are associated with cigarette smoking and asbestos exposure, Cancer Epidemiology, Biomarkers & Prevention, Vol. 4, pp. 543–548.
47) Vainio, H., Husgafvel-Pursiainen, K., Anttila, S., Karjalainen, A., Hackman, P. and Partanen, T. (1993): Interaction between smoking and asbestos in human lung adenocarcinoma: role of K-ras mutations, Environmental Health Perspectives, Vol. 3, pp. 189–192.
48) Husgafvel-Pursiainen, K., Hackman, P., Ridanpää, M., Anttila, S., Karjalainen, A., Partanen, T., Taikina-Aho, O., Heikkilä, L. and Vainio, H. (1993): K-ras mutations in human adenocarcinoma of the lung: association with smoking and occupational exposure to asbestos, International Journal of Cancer, Vol. 53, pp. 250–256.
49) Muller, P. A. and Vousden, K. H. (2013): p53 mutations in cancer, Nature Cell Biology, Vol. 15, pp. 2–8.
50) Nymark, P., Wikman, H., Ruosaari, S., Hollmén, J., Vanhala, E., Karjalainen, A., Anttila, S. and Knuutila, S. (2006): Identification of specific gene copy number changes in asbestos-related lung cancer, Cancer Research, Vol. 66, pp. 5737–5743.
51) Wikman, H., Ruosaari, S., Nymark, P., Sarhadi, V. K., Saharinen, J., Vanhala, E., Karjalainen, A., Hollmén, J., Knuutila, S. and Anttila, S. (2007): Gene expression and copy number profiling suggests the importance of allelic imbalance in 19p in asbestos-associated lung cancer, Oncogene, Vol. 26, pp. 4730–4737.
52) Nymark, P., Kettunen, E., Aavikko, M., Ruosaari, S., Kuosma, E., Vanhala, E., Salmenkivi, K., Pirinen, R., Karjalainen, A., Knuutila, S., Wikman, H. and Anttila, S. (2009): Molecular alterations at 9q33.1 and polyploidy in asbestos-related lung cancer, Clinical Cancer Research, Vol. 15, pp. 468–475.
53) Kettunen, E., Aavikko, M., Nymark, P., Ruosaari, S., Wikman, H., Vanhala, E., Salmenkivi, K., Pirinen, R., Karjalainen, A., Kuosma, E. and Anttila, S. (2009): DNA copy number loss and allelic imbalance at 2p16 in lung cancer associated with asbestos exposure, British Journal of Cancer, Vol. 100, pp. 1336–1342.
54) Palumbo, E., Tosoni, E., Matricardi, L. and Russo, A. (2013): Genetic instability of the tumor suppressor gene FHIT in normal human cells, Genes, Chromosomes & Cancer, Vol. 52, pp. 832–844.
55) Nelson, H. H., Wiencke, J. K., Gunn, L., Wain, J. C., Christiani, D. C. and Kelsey, K. T. (1998): Chromosome 3p14 alterations in lung cancer: evidence that FHIT exon deletion is a target of tobacco carcinogens and asbestos, Cancer Research, Vol. 58, pp. 1804–1807.
56) Pylkkanen, L., Wolff, H., Stjernvall, T., Tuominen, P., Sioris, T., Karjalainen, A., Anttila, S. and Husgafvel-Pursiainen, K. (2002): Reduced Fhit protein expression and loss of heterozygosity at FHIT gene in tumours from smoking and asbestos-exposed lung cancer patients, International Journal of Oncology, Vol. 20, pp. 285–290.
57) Metcalf, R. A., Welsh, J. A., Bennett, W. P., Seddon, M. B., Lehman, T. A., Pelin, K., Linnainmaa, K., Tammilehto, L., Mattson, K., Gerwin, B. I. and Harris, C. C. (1992): p53 and Kirsten-ras mutations in human mesothelioma cell lines, Cancer Research, Vol. 52, pp. 2610–2615.
58) Mezzapelle, R., Miglio, U., Rena, O., Paganotti, A., Allegrini, S., Antona, J., Molinari, F., Frattini, M., Monga, G., Alabiso, O. and Boldorini, R. (2013): Mutation analysis of the EGFR gene and downstream signalling pathway in histologic samples of malignant pleural mesothelioma, British Journal of Cancer, Vol. 108, pp. 1743–1749.
59) Ventii, K. H., Devi, N. S., Friedrich, K. L., Chernova, T. A., Tighiouart, M., Van Meir, E. G. and Wilkinson, K. D. (2008): BRCA1-associated protein-1 is a tumor suppressor that requires deubiquitinating activity and nuclear localization, Cancer Research, Vol. 68, pp. 6953–6962.

60) Murali, R., Wiesner, T. and Scolyer, R. A. (2013): Tumours associated with BAP1 mutations, Pathology, Vol. 45, pp. 116–126.
61) Li, J., Poi, M. J. and Tsai, M. D. (2011): Regulatory mechanisms of tumor suppressor P16(INK4A) and their relevance to cancer, Biochemistry, Vol. 50, pp. 5566–5582.
62) Rayess, H., Wang, M. B. and Srivatsan, E. S. (2012): Cellular senescence and tumor suppressor gene p16, International Journal of Cancer, Vol. 130, pp. 1715–1725.
63) Harvey, K. F., Zhang, X. and Thomas, D. M. (2013): The Hippo pathway and human cancer, Nature Reviews. Cancer, Vol. 13, pp. 246–257.
64) Sekido, Y. (2013): Molecular pathogenesis of malignant mesothelioma, Carcinogenesis, Vol. 34, pp. 1413–1419.
65) Ladanyi, M., Zauderer, M. G., Krug, L. M., Ito, T., McMillan, R., Bott, M. and Giancotti, F. (2012): New strategies in pleural mesothelioma: BAP1 and NF2 as novel targets for therapeutic development and risk assessment, Clinical Cancer Research, Vol. 18, pp. 4485–4490.
66) Enomoto, Y., Kasai, T., Takeda, M., Takano, M., Morita, K., Kadota, E., Iizuka, N., Maruyama, H., Haratake, J., Kojima, Y., Ikeda, N., Inatsugi, N. and Nonomura, A. (2012): Epidermal growth factor receptor mutations in malignant pleural and peritoneal mesothelioma, Journal of Clinical Pathology, Vol. 65, pp. 522–527.
67) Okuda, K., Sasaki, H., Kawano, O., Yukiue, H., Yokoyama, T., Yano, M. and Fujii, Y. (2008): Epidermal growth factor receptor gene mutation, amplification and protein expression in malignant pleural mesothelioma, Journal of Cancer Research and Clinical Oncology, Vol. 134, pp. 1105–1111.
68) Rena, O., Boldorini, L. R., Gaudino, E. and Casadio, C. (2011): Epidermal growth factor receptor overexpression in malignant pleural mesothelioma: prognostic correlations, Journal of Surgical Oncology, Vol. 104, pp. 701–705.
69) Destro, A., Ceresoli, G. L., Falleni, M., Zucali, P. A., Morenghi, E., Bianchi, P., Pellegrini, C., Cordani, N., Vaira, V., Alloisio, M., Rizzi, A., Bosari, S. and Roncalli, M. (2006): EGFR overexpression in malignant pleural mesothelioma. An immunohistochemical and molecular study with clinico-pathological correlations, Lung Cancer, Vol. 51, pp. 207–215.
70) Murthy, S. S. and Testa, J. R. (1999): Asbestos, chromosomal deletions, and tumor suppressor gene alterations in human malignant mesothelioma, Journal of Cellular Physiology, Vol. 180, pp. 150–157.
71) Dawson, M. A. and Kouzarides, T. (2012): Cancer epigenetics: from mechanism to therapy, Cell, Vol. 150, pp. 12–27.
72) Zhao, C. and Bu, X. (2012): Promoter methylation of tumor-related genes in gastric carcinogenesis, Histology and Histopathology, Vol. 27, pp. 1271–1282.
73) Díez-Pérez, R., Campo-Trapero, J., Cano-Sánchez, J., López-Durán, M., Gonzalez-Moles, M. A., Bascones-Ilundain, J. and Bascones-Martinez, A. (2011): Methylation in oral cancer and pre-cancerous lesions (Review), Oncology Reports, Vol. 25, pp. 1203–1209.
74) Phé, V., Cussenot, O. and Rouprêt, M. (2009): Interest of methylated genes as biomarkers in urothelial cell carcinomas of the urinary tract, BJU International, Vol. 104, pp. 896–901.
75) Wentzensen, N., Sherman, M. E., Schiffman, M. and Wang, S. S. (2009): Utility of methylation markers in cervical cancer early detection: appraisal of the state-of-the-science, Gynecologic Oncology, Vol. 112, pp. 293–299.
76) Dammann, R., Strunnikova, M., Schagdarsurengin, U., Rastetter, M., Papritz, M., Hattenhorst, U. E., Hofmann, H. S., Silber, R. E., Burdach, S. and Hansen, G. (2005): CpG island methylation and expression of tumour-associated genes in lung carcinoma, European Journal of Cancer, Vol. 41, pp. 1223–1236.
77) Fujii, M., Fujimoto, N., Hiraki, A., Gemba, K., Aoe, K., Umemura, S., Katayama, H., Takigawa, N., Kiura, K., Tanimoto, M. and Kishimoto, T. (2012): Aberrant DNA methylation profile in pleural fluid for differential diagnosis of malignant pleural mesothelioma, Cancer Science, Vol. 103, pp. 510–514.
78) Sawan, C. and Herceg, Z. (2010): Histone modifications and cancer, Advances in Genetics, Vol. 70, pp. 57–85.
79) Ramalingam, S. S. and Belani, C. P. (2008): Recent advances in the treatment of malignant pleural mesothelioma, Journal of Thoracic Oncology, Vol. 3, pp. 1056–1064.
80) Maki, Y., Asano, H., Toyooka, S., Soh, J., Kubo, T., Katsui, K., Ueno, T., Shien, K., Muraoka, T., Tanaka, N., Yamamoto, H., Tsukuda, K., Kishimoto, T., Kanazawa, S. and Miyoshi, S. (2012): MicroRNA miR-34b/c enhances cellular radiosensitivity of malignant pleural mesothelioma cells, Anticancer Research, Vol. 32, pp. 4871–4875.
81) Kirschner, M. B., Cheng, Y. Y., Badrian, B., Kao, S. C., Creaney, J., Edelman, J. J., Armstrong, N. J., Vallely, M. P., Musk, A. W., Robinson, B. W., McCaughan, B. C., Klebe, S., Mutsaers, S. E., van Zandwijk, N. and Reid, G. (2012): Increased circulating miR-625-3p: a potential biomarker for patients with malignant pleural mesothelioma, Journal of Thoracic Oncology, Vol. 7, pp. 1184–1191.
82) Santarelli, L., Strafella, E., Staffolani, S., Amati, M., Emanuelli, M., Sartini, D., Pozzi, V., Carbonari, D., Bracci, M., Pignotti, E., Mazzanti, P., Sabbatini, A., Ranaldi, R., Gasparini, S., Neuzil, J. and Tomasetti, M. (2011): Association of MiR-126 with soluble mesothelin-related peptides, a marker for malignant mesothelioma, PLoS One, Vol. 6, pp. e18232.
83) Pass, H. I., Goparaju, C., Ivanov, S., Donington, J., Carbone, M., Hoshen, M., Cohen, D., Chajut, A., Rosenwald, S., Dan, H., Benjamin, S. and Aharonov, R. (2010): hsa-miR-29c* is linked to the prognosis of malignant pleural mesothelioma, Cancer Research, Vol. 70, pp. 1916–1924.
84) Weber, D. G., Johnen, G., Bryk, O., Jöckel, K. H. and Brüning, T. (2012): Identification of miRNA-103 in the cellular fraction of human peripheral blood as a potential biomarker for malignant mesothelioma – a pilot study, PLoS One, Vol. 7, pp. e30221.
85) Busacca, S., Germano, S., De Cecco, L., Rinaldi, M., Comoglio, F., Favero, F., Murer, B., Mutti, L., Pierotti, M. and Gaudino, G. (2010): MicroRNA signature of malignant mesothelioma with potential diagnostic and prognostic implications, American Journal of Respiratory Cell

and Molecular Biology, Vol. 42, pp. 312–319.
86) Tomasetti, M., Staffolani, S., Nocchi, L., Neuzil, J., Strafella, E., Manzella, N., Mariotti, L., Bracci, M., Valentino, M., Amati, M. and Santarelli, L. (2012): Clinical significance of circulating miR-126 quantification in malignant mesothelioma patients, Clinical biochemistry, Vol. 45, pp. 575–581.
87) Benjamin, H., Lebanony, D., Rosenwald, S., Cohen, L., Gibori, H., Barabash, N., Ashkenazi, K., Goren, E., Meiri, E., Morgenstern, S., Perelman, M., Barshack, I., Goren, Y., Edmonston, T.B., Chajut, A., Aharonov, R., Bentwich, Z., Rosenfeld, N. and Cohen, D. (2010): A diagnostic assay based on microRNA expression accurately identifies malignant pleural mesothelioma, Journal of Molecular Diagnostics, Vol. 12, pp. 771–779.
88) Khodayari, N., Mohammed, K. A., Goldberg, E. P. and Nasreen, N. (2011): EphrinA1 inhibits malignant mesothelioma tumor growth via let-7 microRNA-mediated repression of the RAS oncogene, Cancer Gene Therapy, Vol. 18, pp. 806–816.
89) Kubo, T., Toyooka, S., Tsukuda, K., Sakaguchi, M., Fukazawa, T., Soh, J., Asano, H., Ueno, T., Muraoka, T., Yamamoto, H., Nasu, Y., Kishimoto, T., Pass, H. I., Matsui, H., Huh, N. H. and Miyoshi, S. (2011): Epigenetic silencing of microRNA-34b/c plays an important role in the pathogenesis of malignant pleural mesothelioma, Clinical Cancer Research, Vol. 17, pp. 4965–4974.
90) Ghawanmeh, T., Thunberg, U., Castro, J., Murray, F. and Laytragoon-Lewin, N. (2011): miR-34a expression, cell cycle arrest and cell death of malignant mesothelioma cells upon treatment with radiation, docetaxel or combination treatment, Oncology, Vol. 81, pp. 330–335.
91) Ivanov, S. V., Goparaju, C. M., Lopez, P., Zavadil, J., Toren-Haritan, G., Rosenwald, S., Hoshen, M., Chajut, A., Cohen, D. and Pass, H. I. (2010): Pro-tumorigenic effects of miR-31 loss in mesothelioma, Journal of Biological Chemistry, Vol. 285, pp. 22809–22817.
92) Balatti, V., Maniero, S., Ferracin, M., Veronese, A., Negrini, M., Ferrocci, G., Martini, F. and Tognon, M. G. (2011): MicroRNAs dysregulation in human malignant pleural mesothelioma, Journal of Thoracic Oncology, Vol. 6, pp. 844–851.
93) Guled, M., Lahti, L., Lindholm, P. M., Salmenkivi, K., Bagwan, I., Nicholson, A. G. and Knuutila, S. (2009): CDKN2A, NF2, and JUN are dysregulated among other genes by miRNAs in malignant mesothelioma -A miRNA microarray analysis, Genes, Chromosomes & Cancer, Vol. 48, pp. 615–623.
94) Nymark, P., Guled, M., Borze, I., Faisal, A., Lahti, L., Salmenkivi, K., Kettunen, E., Anttila, S. and Knuutila, S. (2011): Integrative analysis of microRNA, mRNA and aCGH data reveals asbestos- and histology-related changes in lung cancer, Genes, Chromosomes & Cancer, Vol. 50, pp. 585–597.

Author's short biography

Hiroto Izumi

Hiroto Izumi M.D. & Ph.D. is an associate professor in Department of Occupational Pneumology, Institute of Industrial Ecological Sciences, University of Occupational and Environmental Health, Japan. He graduated from Oita Medical University in 1988 and obtained doctorate in 1996. He joined Department of Molecular Biology, University of Occupational and Environmental Health Japan, in 1996. He was visiting Researcher at Institute of Anatomy and Cell Biology, Göteborg University in Sweden from 1997 to 1999. From 2013, he joined current department. Research theme is the analysis of the biological properties of cancer. In particular, he has focused on the analysis of mechanisms of the anti-cancer drug resistance.

Yasuo Morimoto

Yasuo Morimoto graduated from Kagoshima University, Faculty of Medicine at 1986. He received his Ph.D. at 1993 from University of Occupational and Environmental Health, Japan (UOEH). Since 2000 he is professor of Institute of Industrial Ecological Sciences, UOEH. His topics of research are hazard assessment and pulmonary toxicity of environmental particles including nano and fibrous materials.

KONA Powder and Particle Journal No. 31 (2014) 135–145/Doi:10.14356/kona.2014003 Original Research Paper

Transient Flow Induced by the Adsorption of Particles†

Naga Musunuri, Bhavin Dalal, Daniel Codjoe, Ian S. Fischer and Pushpendra Singh*

[1] *Department of Mechanical and Industrial Engineering, New Jersey Institute of Technology, USA*

Abstract

The paper describes the physics of particle adsorption and the spontaneous dispersion of powders that occurs when they come in contact with a fluid-liquid interface. The dispersion can occur so quickly that it appears explosive, especially for small particles on the surface of mobile liquids like water. Our PIV measurements show that the adsorption of a spherical particle at the interface causes an axisymmetric streaming flow about the vertical line passing through the particle center. The fluid directly below the particle rises upward, and near the surface, it moves away from the particle. The flow, which develops within a fraction of second after the adsorption of the particle, persists for several seconds. The flow strength, and the volume over which it extends, decrease with decreasing particle size. The streaming flow induced by the adsorption of two or more particles is a combination of the flows which they induce individually. The flow not only causes particles sprinkled together onto a liquid surface to disperse, but also causes a hydrodynamic stress which is extensional in the direction tangential to the interface and compressive in the normal direction. These stresses can cause the breakup of particle agglomerates when they are adsorbed on a liquid surface.

Keywords: dispersion, powders, agglomerates, particle image velocimetry (PIV), interfacial tension.

1. Introduction

The focus of the paper is to describe the physics of particle adsorption and the spontaneous dispersion of powders that occurs when they come in contact with a fluid-liquid interface. While past studies have been concerned with understanding the mechanisms by which particles already trapped on fluid-liquid interfaces interact leading to their self-assembly into monolayered patterns (Kralchevsky and Nagayama, 2000; Kralchevsky et al., 1992; Nicolson, 1949), (Singh et al., 2010, and the references therein), the sudden dispersion of particles coming into contact with a fluid-liquid interface described in this paper has not been considered prior to our recent study (Singh et al., 2009) and (Gurupatham et al., 2011, 2012).

It was shown in (Singh et al., 2009) that (i) particles sprinkled over a small area almost instantaneously spread over an area that can be several orders of magnitudes larger (see **Fig. 1**); (ii) a newly-adsorbed particle causes particles already trapped on the interface to move away creating a particle-free region around itself (see **Fig. 2**); and (iii) dispersion influences the nature, e.g., structure and porosity, of the monolayer clusters that are formed. These phenomena have importance in a wide range of applications, such as pollination in hydrophilous plants, transportation and spreading of microbes and viruses, and the self-assembly of particles leading to the formation of novel nano-structured materials, stabilization of emulsions, etc. (Aveyard et al., 2003; Binks and Horozov, 2006; Cox, 1988; Cox and Knox, 1989; Dryfe, 2006; Gust et al., 2001; Pickering, 1907; Tang et al., 2006; Wasielewski, 1992).

The dispersion can occur so quickly that it appears *explosive*, especially on the surface of mobile liquids like water. An experiment showing this can be performed easily in a household kitchen by filling a dish partially with water

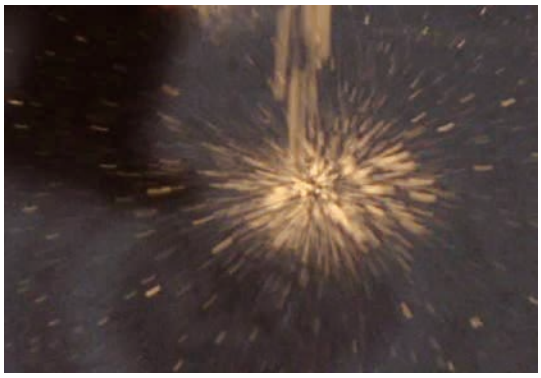

Fig. 1 Sudden dispersion of flour sprinkled onto water in a dish. Streaklines were formed due to the radially-outward motion of the particles emanating from the location where they were sprinkled. The size of flour particles was ~2–100 μm. Taken from (Gurupatham et al., 2011)

† Accepted: June 1, 2013
[1] Newark, New Jersey 07102, USA
* Corresponding author:
E-mail: singhp@njit.edu
TEL: +1-973-596-3326 FAX: +1-973-642-4282

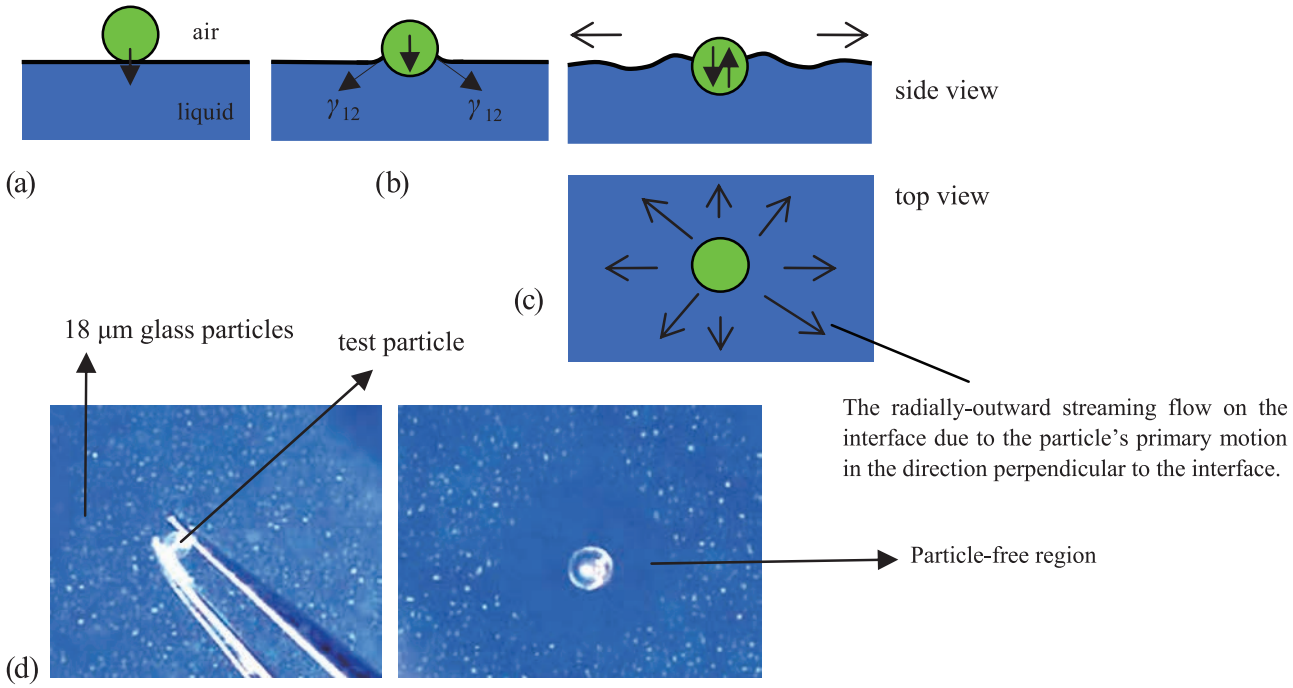

Fig. 2 Trapping (or adsorption) of particles at an interface. (**a**) The particle comes in contact with the interface. (**b**) The particle is pulled downwards by the interfacial force (γ_{12}). (**c**) The particle oscillates about the equilibrium height within the interface causing a radially outward flow on the interface. Both the side and top views are shown. The lengths of the arrows are *not* proportional to the flow strength. (**d**) (Left) A glass sphere of diameter 1.1 mm being dropped onto a monolayer of 18 μm tracer glass particles on the surface of a 60% glycerin in water. (Right) The flow on the surface causes all of the nearby tracer particles to move away so that a roughly circular, particle-free region is created.

and then sprinkling a small amount of a finely-ground powder such as wheat or corn flour onto the water surface. The moment the flour comes in contact with the surface it quickly disperses into an approximately-circular shaped region, forming a monolayer of dispersed flour particles on the surface (see **Fig. 1**). The interfacial forces that cause this sudden dispersion of flour particles are, in fact, so strong that a few milligrams of flour sprinkled onto the surface almost instantaneously covers the entire water surface in the dish.

It was shown by (Singh et al., 2009) and (Gurupatham et al., 2011) that the initial dispersion of particles is due to the fact that when a particle comes in contact with the interface, the vertical capillary force pulls it into the interface, thereby causing it to accelerate in the direction normal to the interface (see **Fig. 2**). The maximum velocity increases with decreasing particle size; for nanometer-sized particles, e.g., viruses and proteins, the velocity on an air-water interface can be as large as ~47 m/s. Also, since the motion of a particle on the surface of mobile liquids like water is inertia dominated, it oscillates vertically about its equilibrium height before the viscous drag causes it to stop. This gives rise to a *streaming* flow on the interface away from the particle (see **Fig. 2c**).

The energy needed to pull a particle into the interface and to induce the streaming flow comes from the net *decrease* in the interfacial energy (W_a) due to the adsorption of the particle (Singh et al., 2009). By assuming that the particle floats without significantly deforming the interface, it can be shown that W_a for a spherical particle of radius R is

$$W_a = \pi R^2 \gamma_{12} (1+\cos\theta)^2 \tag{1}$$

where θ is the contact angle and γ_{12} is the interfacial tension between the upper and lower fluids (see Binks and Horozov, 2006 and Tsujii, 1998).

Therefore, when two or more particles are simultaneously adsorbed at the interface, each of the particles causes a streaming flow on the interface away from itself thereby causing the other particles to move away. When two particles are adsorbed the maximum distance by which they move apart is about a few diameters. However, as the number of particles being adsorbed increases, the distance travelled by a particle, especially if it is near the outer periphery of the cluster, can be very large—several orders of magnitude larger than any dimension of the area over which particles are sprinkled. For example, as noted above, a few milligrams of flour sprinkled over a very small area on the water surface almost spontaneously disperses to cover the entire water surface in the dish.

The dispersion phase, which lasts for a short period of time (about one second for the case described in **Fig. 1**), is followed by a phase that is dominated by attractive lateral-capillary forces during which particles slowly

come back to cluster. The latter phase has been a focus of many past studies (Fortes, 1982; Kralchevsky et al., 1992; Lucassen, 1992; Nicolson, 1949). Particles trapped at a fluid-fluid interface generally interact with each other via attractive capillary forces that arise because of their weight. A common example of this capillarity-driven self-assembly is the clustering of breakfast-cereal flakes floating on the surface of milk. This mechanism is widely used for two-dimensional assembly of particles at liquid surfaces. However, if the buoyant weight of particles is negligible, as is the case for colloidal particles, then the particles will only disperse since the attractive capillary forces between them are negligible (Aubry et al., 2008; Bresme and Oettel, 2007; Singh and Joseph, 2005; Stamou and Duschl, 2000).

One may postulate that the gradient of particle concentration gives rise to a (Maringoni) force that causes particles to disperse because the concentration of particles in the region in which they are sprinkled is larger than in the surrounding region. However, this is clearly not the case, as the dispersed particles cluster again under the action of lateral capillary forces. This shows that the gradient of particle concentration does not give rise to a dispersion force and that particles disperse only when they come in contact with the interface for the first time (during which each of the particles gives rise to a flow away from itself as they are pulled into the interface).

Also, one may postulate that the dispersion is because of the presence of contaminants on the surface of particles which are released into the liquid when they come in contact with the interface and their presence in fact causes particles to disperse. If this is the case, then the intensity with which the particles disperse should diminish when they are washed. We ruled out this possibility by repeatedly washing the particles and showing that their dispersive behavior did not change when the experiments were repeated (Gurupatham et al., 2011).

Particles also disperse on liquid-liquid interfaces. In fact, as **Fig. 3** shows, the dispersion forces can break apart agglomerates of micron-sized particle that remain intact in the upper liquid (Gurupatham et al., 2012). This breakup and spreading of particle clumps (agglomerates) on liquid surfaces is important in various processes in the pharmaceutical and food industries such as wet granulation and food processing (Nguyen et al., 2010; Tüskea et al., 2005; Zajic and Buckton, 1990).

The sudden dispersion of particles plays an important role also in some physical processes occurring on fluid-fluid interfaces, including the rate at which germs/microbes disperse on a water surface. An example in botany is the formation by hydrophilous (water-pollinated) plants of floating porous pollen structures called “pollen rafts” (Cox, 1988; Cox and Knox, 1989). A crucial first step in their formation is the initial dispersion of pollen that occurs after it comes in contact with the water surface (if it did not disperse, it would remain clumped/agglomerated).

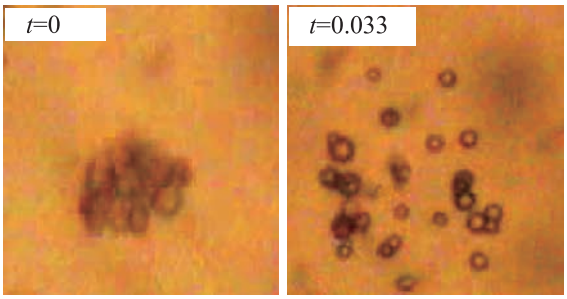

Fig. 3 Breakup and dispersion of agglomerate on the interface of corn oil and water, looking down from above (500x mag.). The size of glass particles of the agglomerate was ~4 μm. (left) An agglomerate sedimented through corn oil and was captured at the interface. (right) After coming in contact with the interface it *breaks apart explosively* dispersing radially-outward into an approximately-circular region. Notice that some of the particles remained agglomerated. Taken from (Gurupatham et al., 2012).

In the next section, a description of the forces that act on a particle during adsorption and of the pertinent dimensionless parameters is given. The experimental set-up and results of our PIV measurements are presented in Sections 3 and 4. Finally, we summarize and conclude in Section 5.

2. Governing equations and dimensionless parameters

As discussed above, when a particle comes in contact with a fluid-liquid interface it is pulled inwards from the upper fluid into the interface with the lower fluid by the capillary force to its equilibrium position in the interface. It is crucial to understand this motion of the particle in the direction normal to the interface, as it gives rise to the streaming flow on the interface away from the particle.

The motion of the particle can be obtained by solving the governing equations for the two fluids and the momentum equation for the particle, which are coupled, along with the interface stress condition and a condition for the contact line motion on the particle surface. This is a formidable problem because the capillary force at the line of contact of the three phases on the particle surface depends on the slope of the interface which in general requires the solution of the aforementioned equations (Pillapakkam and Singh, 2001; Singh et al., 2003; Singh and Joseph, 2005). However, a decoupled momentum equation for a particle can be derived by modeling the forces that act on the particle (Singh et al., 2011; Singh et al., 2009). These forces are: the vertical capillary force ($\mathbf{F}_{st}$), the buoyant weight ($\mathbf{F}_{g}$), the Brownian force ($\mathbf{F}_{B}$),

and the viscous drag ($\mathbf{F}_D$). A decoupled equation for the motion of the particle under the action of these forces can be written as:

$$m\frac{dV}{dt} = \mathbf{F}_{st} + \mathbf{F}_D + \mathbf{F}_g + \mathbf{F}_B \tag{2}$$

where m is the effective mass of the particle which includes the added mass contribution (Currie, 1974), V is the velocity, $\mathbf{F}_{st} = 2\pi R\gamma_{12}\sin(\theta_c)\sin(\theta_c+\alpha)$ is the capillary force, α is the contact angle, and θ_c is the particle position in the interface. The Brownian force in Eq. (2) is negligible compared to the capillary force (Singh et al., 2011; Singh et al., 2009).

The added mass and the drag calculations are complicated by the fact that the fraction of the particle that is immersed in the upper and lower fluids changes as the particle moves in the direction normal to the interface. We will assume that the added mass is one half of the mass of the fluid displaced, but this result is for a particle fully immersed in a fluid (Currie, 1974). The drag force will be assumed to be given by $\mathbf{F}_D = 6\pi\mu RV\,f_D$, where μ is the viscosity of the lower liquid, and f_D is a parameter that accounts for the particle being immersed in both upper and lower fluids.

2.1 Governing dimensionless parameters

Let the characteristic velocity, length and time be given by $U = \gamma_{12}/\mu$, R, and R/U, respectively. Then, Eq. (2) can be nondimensionalized to give (Singh et al., 2011):

$$We\cdot m'\frac{\rho_p}{\rho}\frac{dV'}{dt'} = \sin(\theta_c)\sin(\theta_c+\alpha) + 3V'f_D + \frac{2}{3}B\frac{\rho_p-\rho_c}{\rho}f_b. \tag{3}$$

Here the primed variables are dimensionless. f_b is the dimensionless buoyancy which is O(1) but depends on the profile of the deformed interface. ρ and ρ_a are the densities of the lower and upper fluids, ρ_c is the effective density of the volume displaced by the particle, and ρ_p is the particle density. The dimensionless parameters in the above equation are: the Weber number $We = \frac{2}{3}\frac{\rho R\gamma_{12}}{\mu^2}$, the Bond number $B = \rho R^2 g/\gamma_{12}$, $\frac{\rho_p}{\rho}$, and the contact angle α. The Weber number is the ratio of inertia forces to capillary forces, and the Bond number is the ratio of gravitational forces to surface tension forces.

For an air-water interface, the parameters have the values: $\mu = 0.001$ Pa.s, $\rho = \rho_p = 1000$ kg/m^3, $\frac{\rho_p-\rho_c}{\rho} = 0.1$ and $\gamma_{12} = 0.07$ N/m. Let us assume that $\mu_a = \rho_a = 0$, $m' = 1.5$, $f_D = 0.5$ and $f_b = 1$. Then, $We = \sim 10^8 R$ and $B = \sim 10^5 R^2$, where R is in meters. Therefore, the role of particle inertia becomes negligible only when R is *much smaller* than 10 nm because only then We is much smaller than one. The influence of gravity becomes negligible when $R < \sim 1$ mm in the sense that such small particles float so that the interfacial deformation is negligible. However, even a negligibly-small deformation of the interface gives rise to attractive lateral capillary forces which, even though small, cause floating particles to cluster. This happens because a particle floating on a liquid surface is *free* to move laterally. The only resistance to its lateral motion is the hydrodynamic drag which can slow the motion but *cannot* stop it. Consequently, only very-small particles, for which lateral capillary forces are smaller than Brownian forces, do not cluster.

3. Experimental Setup

The setup consisted of a square Petri dish which was partially filled with Millipore water (see **Fig. 4**). The cross-section of Petri dish was 10 × 10 cm, and the depth was 1.5 cm. PIV measurements were performed in a vertical plane (normal to the camera axis) illuminated by a laser sheet. The vertical position of the camera was in line with the water surface, providing an undistorted view of the volume directly below the water surface. The test particles were released very close to the liquid surface, about 1 mm from the surface, in an area near the intersection of the laser sheet and the camera axis.

A high-speed camera was used to record the motion of seeding particles visible in the laser sheet. A Nikon 1 series V1 camera equipped with a 30 mm Kenko automatic extension tube and a Tamron SP AF 60 mm 1:1 macro lens was used to provide the required magnification. The laser sheet was generated using a ZM18 series 40 mw solid state diode laser of wavelength 532 nm (green color). Movies were recorded at a resolution of 1280 × 720 pixels. For the particle size range considered (~500 μm to 2 mm), the optimal recording speed for performing the PIV analyses was found to be 60 frames per second. This was determined by a trial and error procedure.

The water was seeded with silver-coated hollow glass spheres of density around 1 gm/cc and average size of around 8–12 μm. The density of seeding particles closely

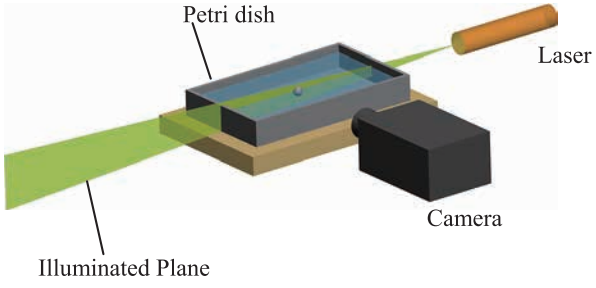

Fig. 4 Schematic diagram of the experimental setup.

matched the water density, but there was a small particle-to-particle variation. Consequently, some particles sedimented and some rose slowly giving us ample time to record their motion when a flow was induced due to the adsorption of one or more test particles. The seeding particles were silver coated which ensured that the intensity of the scattered light was sufficient to track their motion.

An open-source code, PIVlab, was used for performing the time-resolved PIV analysis. PIVlab is a MatLab-based software which analyzes a time sequence of frames to give the velocity distribution for each of the frames. A MatLab code for post-processing and plotting results was written.

4. Results

We first discuss our PIV measurements of the transient flow on a water surface that was induced due to the adsorption of a single test particle. Glass particles of three different diameters, 2.0, 1.1, and 0.65 mm were used to obtain the qualitative nature of the flow, and determine how the strength and time duration of the induced flow vary with the particle size.

In agreement with the analytic results obtained in (Gurupatham et al., 2011), test particles in all cases oscillated vertically before reaching their equilibrium positions in the interface. The frequency of oscillation increased, and the adsorption time decreased, with decreasing particle size in agreement with the analytic results. For example, the frequencies for the diameters 2.0, 1.1 and 0.65 mm were 25 Hz, 50 Hz and 85.71 Hz respectively.

The adsorption of a test particle caused a flow on the air-water interface, which caused tracer particles trapped on the surface to move away from the adsorbed test particle. Consequently, the water surface near the test particle had few tracer particles which made fluid velocity measurement at and near the water surface difficult. Also, the air-water interface near the test particles was deformed since their density was larger than the water density. In fact, the center of particles was a fraction of radius below the position of the undeformed interface. The deformation of the interface made viewing of the interface by a camera mounted on a side difficult (see **Fig. 4**). Therefore, in our PIV measurements, the velocity was measured only in the region below a horizontal line passing through the point of contact of the interface with the particle which was a fraction of the particle radius below the undeformed interface (see **Fig. 5**).

Although the water near the test particle started to move as soon as the particle came in contact with the surface, the adsorption-induced streaming flow intensity developed over a period of time. The intensity reached a maximal strength after a fraction of a second and then it decreased. In the time interval after which the streaming flow reached its maximal strength, the vertical oscillations of the test particle were already negligible. The PIV measurements show that the streaming flow was approximately axisymmetric about the vertical line passing through the center of the test particle (see **Fig. 5**). Tracer-particles in the region below the test particle moved upwards, and

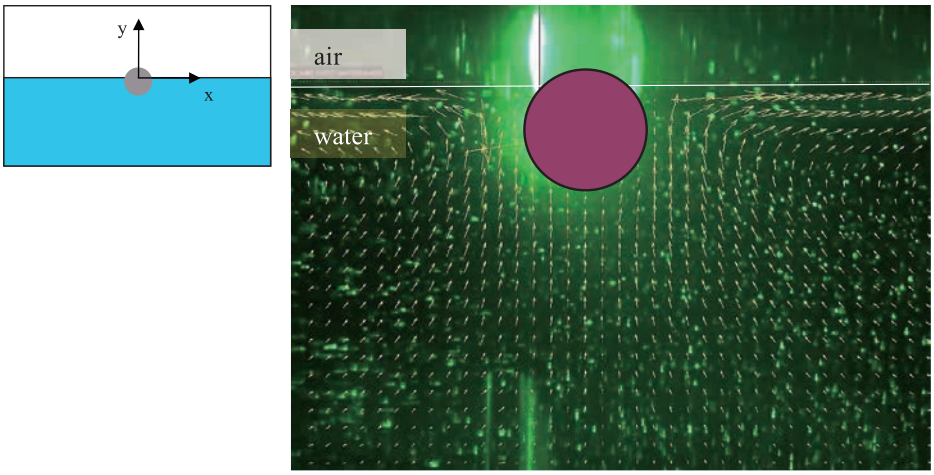

Fig. 5 (Left) The origin of the coordinate system was at the intersection of the vertical lines passing through the center of the test particle and the horizontal line passing through the point of contact of the interface with the particle. The center of the test particle was a fraction of particle radius below the position of the undeformed interface. (Right) Velocity vectors for the streaming flow induced by a 2 mm test particle 0.67s after it came in contact with an air-water interface. The particle was dropped in a vertical plane illuminated by a thin sheet of laser light. The velocity vectors of tracer particles have been superimposed on the PIV image, and the interface is marked by a horizontal white colored line. A purple-colored mask was used in the PIV analysis to define the region occupied by the test particle. The velocity distribution was approximately axisymmetric about the vertical passing through the center of the particle.

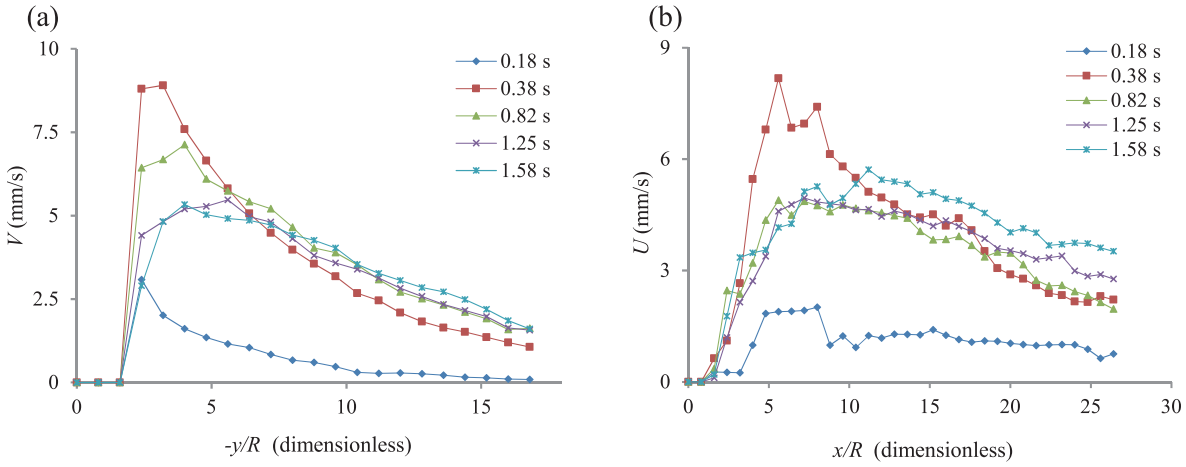

Fig. 6 Temporal evolution of the streaming flow induced by the adsorption of a 650 μm particle. The velocity is shown at five different time intervals after the test particle came in contact with the water surface. (**a**) The vertical component of velocity (V) is shown as a function of $-y/R$. (**b**) The horizontal component of velocity (U) is shown as a function of x/R.

those near and in the water surface moved away from the test particle. The trajectories of fluid particles were qualitatively similar to that for a stagnation point flow, with the center of the test particle being the stagnation point. This implies that the stress on the test particle due to the induced flow was extensional in the horizontal plane near the water surface, and compressive in the direction normal to the surface.

Since the induced velocity field was approximately axisymmetric, it can be conveniently quantified in terms of its y-component along the vertical line passing through the center of the test particle and the x-component along the x-axis as defined in **Fig. 5**. Time was measured from the instant at which the test particle came in contact with the water surface and the distance was measured from the origin of the coordinate system. The former was identified by a frame-by-frame analysis the movie images. **Fig. 6a** shows the y-component of velocity for a 650 μm test particle along the vertical line passing through its center at five different times; the x-component of velocity along this line was relatively small. The y-component of velocity was positive, indicating that the flow was in the upward direction towards the particle. The fluid velocity near the surface of the test particle was small, as the test particle was not moving, and increased with increasing distance from the particle reaching a maximal strength at a distance of about one particle radius from the surface. The velocity then decreased with increasing distance from the particle, but remained significant for a distance of several diameters.

The figure also shows that the fluid velocity did not develop instantaneously after the particle was adsorbed. For example, at $t = 0.167$ s, the maximum velocity of 3.10 mm/s was at a distance of 0.78 mm from the particle, and the velocity at a distance of 5.5 mm was only 0.09 mm/s. The velocity increased with time to reach the maximum value of 8.9 mm/s at $t = 0.37$ s and $y = -1.04$ mm. At $y = -5.5$ mm, the velocity at this time was 1.07 mm/s. After reaching the maximum strength, the fluid velocity started to decrease. The decrease first occurred closer to the test particle, while it was still increasing farther away from the particle. For example, the maximum velocity at $t = 0.82$ s was 7.12 mm/s at $y = -1.3$ mm, and at $t = 1.25$ s and $y = -1.82$ it was 5.47 mm/s. The velocity at larger distances from the particle continued to increase for a longer time interval before starting to decrease. At a distance of $y = -5.5$ mm, the velocity at $t = 1.58$ s was 1.60 mm/s, which was larger than the velocity at this location at $t = 0.37$ s. The streaming flow slowly reduced in strength but continued for several seconds.

Fig. 6b shows the x-component of velocity for a 650 μm test particle along a horizontal line at five different times; the y-component of velocity along this line was negligible. The velocity was positive which means that the water near the surface was moving away from the particle. As in **Fig. 6a**, the fluid velocity near the test particle was small because it was not moving, and increased with increasing distance from the particle and then after reaching a maximal value it decreased with increasing distance. However, the maximal velocity was at a distance of about two particle diameters from the particle surface, whereas below the particle the maximum was reached at a distance of one particle radius. The velocity remained significant for a distance of several diameters. The maximum water velocity near the surface was comparable to the maximum velocity below the test particle.

The temporal evolution of streaming flow near the water surface was qualitatively similar to that in the water below the test particle. The flow started when the particle touched the water surface, and reached a maximal value after a time interval which was comparable to that below the particle. At $t = 0.167$ s, the maximum velocity of

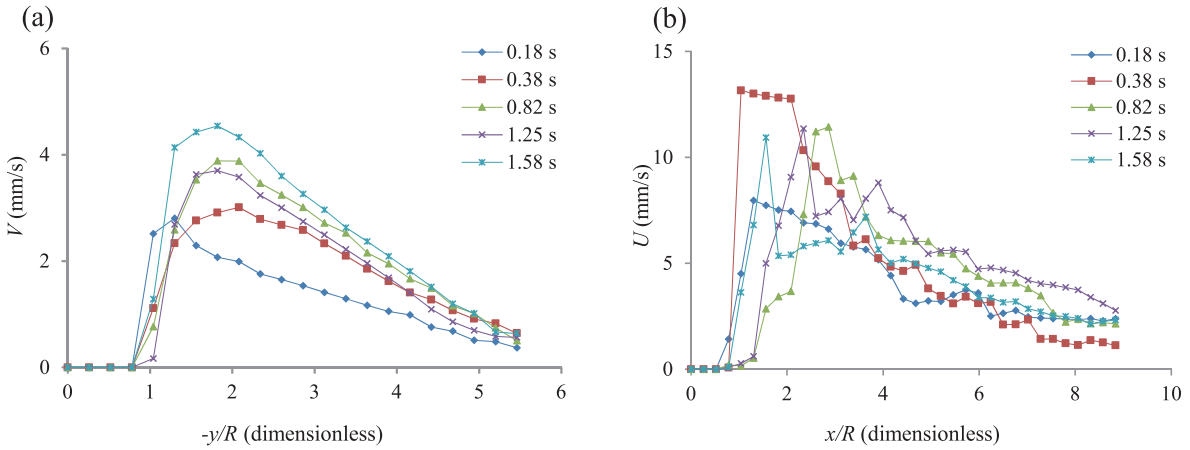

Fig. 7 Temporal evolution of the streaming flow induced by the adsorption of a 2 mm particle. The velocity is shown at five different time intervals after the test particle came in contact with the water surface. (**a**) The vertical component of velocity (V) is shown as a function of $-y/R$. (**b**) The horizontal component of fluid velocity (U) is shown as a function of x/R.

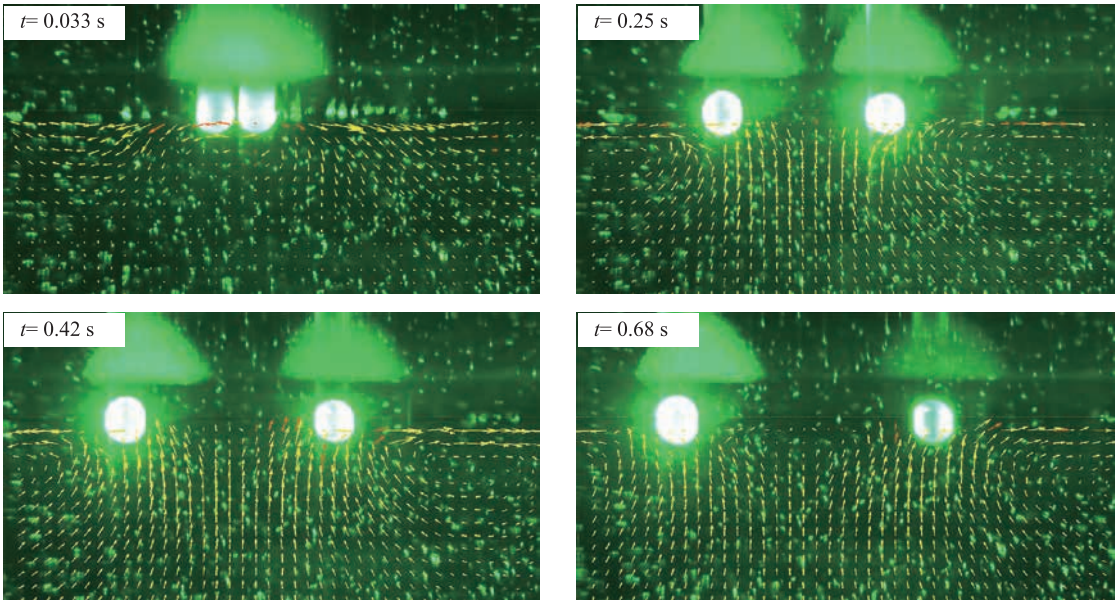

Fig. 8 The figure shows the streaming flow induced by two 650 μm test particles after they came in contact with an air-water interface. The particles were dropped in a vertical plane illuminated by a thin sheet of laser light. The velocity vectors have been superimposed on the PIV images. The flows induced by the particles caused them to move apart. The size of velocity vectors is arbitrary, and for clarity a larger magnification is used in the plot at $t = 0.033$ s than in the later plots.

1.91 mm/s was at a distance of 2.1 mm from the particle, and the velocity at a distance of 5.5 mm was 1.1 mm/s. The velocity increased with time to reach the maximum value of 8.2 mm/s at $t = 0.37$ s and $x = 1.82$ mm. At this time, the velocity at $x = 5.5$ mm was 4.4 mm/s. This shows that the velocity near the water surface was more intense over a larger area than below the particle. The strength of the streaming flow then decreased with time with the decrease first occurring closer to the test particle.

The time interval after which the streaming flow attained the maximal intensity and the volume over which the flow extended varied with the particle size. The velocity distribution for a 2 mm particle is shown **Fig. 7**. The figure shows that the streaming flow evolution was qualitatively similar to that for a 650 μm particle described above. However, it developed relatively more slowly. The maximum velocity of 13.5 mm/s was reached 1.58 s after the particle came in contact with the water surface. For a 650 μm particle, on the other hand, the maximal velocity was reached at $t = 0.38$ s. For a 2 mm particle, not only the maximum velocity was larger, it occurred at a larger distance of 1.38 mm from the test particle, and so the

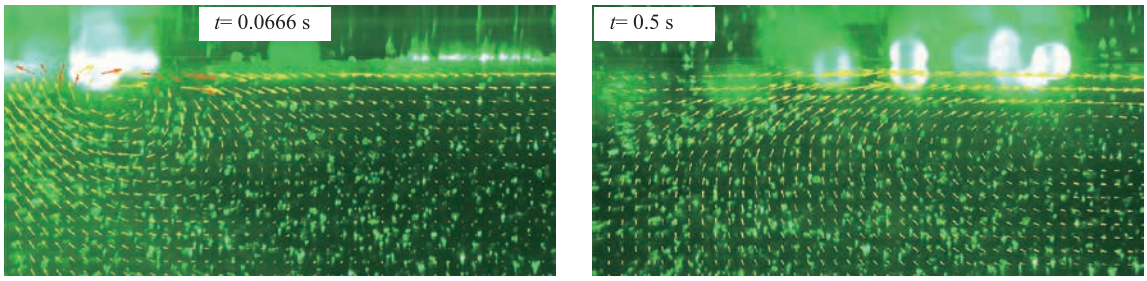

Fig. 9 The figure shows the streaming flow induced by about 20, 650 μm particles after they came in contact with an air-water interface. The particles were dropped in and near a vertical plane illuminated by a thin sheet of laser light, and towards the left side of the photographs. The figure shows the motion of the particles that moved to the right side (some of the particles moved in other directions and so are invisible in the photographs). The velocity vectors have been superimposed on the PIV images. The size of velocity vectors is arbitrary.

volume over which the flow was intense was larger than for a 650 μm particle. Our PIV measurements of the three particle sizes considered show that the time interval after which the maximal flow strength was attained, the volume over which the flow intensity extends, as well as the time interval for which the flow persists, increase with increasing particle size.

4.1 Adsorption of two or more particles

We next consider the case in which two 650 μm particles were simultaneously adsorbed at an air-water interface. The particles were dropped onto the interface such that the line joining their centers was in the plane of the laser sheet. This ensured that the induced flow was approximately symmetric about the vertical plane passing though the centers of the two particles, and also about the vertical plane bisecting the line joining their centers. **Fig. 8** shows that each of the particles induced a streaming flow which was similar to that which was induced by a single particle. The combined flow below the particles was in the upward direction and near the water surface the flow was away from the particles. In the region between the particles, the horizontal flow contributions approximately cancelled and the vertical contribution added. Thus, the combined streaming flow was approximately the sum of the flows induced by the two particles individually, and thus stronger than the flow induced by one particle. The combined flow developed in about 0.4 s which was comparable to the time in which the streaming flow developed for a single 650 μm particle.

For the case shown in **Fig. 8**, the two particles were initially close to each other and so the streaming flow induced by the first particle caused the second one to move away, and vice versa. The symmetry of the streaming flow with respect to the laser sheet ensured that the two particles remained in the plane of the laser sheet while they moved apart. However, when the particles were dropped so that the angle between the line joining their centers and the laser sheet was not small, the streaming flow carried them away out of the plane of the laser sheet, and so they were visible only for the time duration for which they were illuminated. For the case shown in **Fig. 8**, the speed at $t = 0.167$ s was approximately 12.3 mm/s. The speed decreased as they moved farther apart, and also with time as the streaming flow intensity diminished with time. In fact, after the distance between them was about $10R$ their speeds became negligible.

We also considered cases where about 10–30 particles were dropped onto an air-water interface in and near the laser sheet (see **Fig. 9**). Again, each of the particles induced a streaming flow in the water that was similar to the flow induced by a single particle. These flows induced by the particles caused neighboring particles to move away, and so the net result was that particles moved radially outward from the location where they were dropped. Experiments show that clusters of particles disperse radially outward from the center (see **Fig. 1** which shows streak lines), and that when the cluster size was larger the radius of the approximately-circular area over which its particles dispersed and the dispersion velocity were larger. This increase in the dispersion velocity with increasing number of particles was also seen in our direct numerical simulations (Singh et al., 2009). The PIV measurements show that the water rises in the region below the particles and on the surface it moves away from the particle.

5. Conclusion and discussion

When a particle comes in contact with a fluid-liquid interface the vertical capillary force pulls it into the interface which gives rise to a transient streaming flow. The PIV measurements show that the liquid below a newly-adsorbed particle rises upwards and the liquid near

the surface moves away from the particle. The induced flow for a spherical particle was axisymmetric about the vertical line passing through the particle center. Also, the flow strength is not established immediately after the particle comes in contact with the interface, but builds up over a short time interval. For a 650 μm glass sphere the maximum flow strength occurred about 0.4 s after the particle come in contact, and for a 2 mm sphere after about 1.5 s. We also considered 1.1 mm, 850 mm and 550 mm glass spheres for which the maximal flow strength occurred after 0.75 s, 0.47 s and 0.18 s, respectively. These results show that the time interval after which the maximal flow strength occurred decreased with decreasing particle size.

When two or more particles were simultaneously adsorbed, the streaming flow was a combination of the flows induced by the particles individually and so the flow strength increased with increasing number of particles. Consequently, the distance travelled by the particles near the outer periphery of a cluster sprinkled on a liquid surface can be several orders of magnitude larger than any dimension of the area over which the particles were sprinkled. This can be important for some physical processes occurring on a water surface, such as the pollination of hydrophilous plants, and the transportation and rate of spread of microbes and viruses on a water surface. Furthermore, the streaming flow can break apart agglomerates of particles when they are adsorbed at a fluid-liquid interface which is important in various processes in the pharmaceutical and food industries such as wet granulation and food processing.

Acknowledgements

We gratefully acknowledge the support of the National Science Foundation (CBET-1236035).

References

Aubry N., Singh P., Janjua M., Nudurupati S., Assembly of defect-free particle monolayers with dynamically adjustable lattice spacing. In Proceedings of the National Academy of Sciences (Vol. 105, pp. 3711–3714), 2008.

Aveyard R., Clint J.H., Horozov T.S., Aspects of the stabilization of emulsions by solid particles: Effects of line tension and monolayer curvature energy. Phys. Chem. Chem. Phys., 5 (2003) 2398–2409.

Binks B.P., Horozov T.S., Colloidal particles at liquid interfaces: An introduction:, Cambridge University Press, 2006.

Bresme F., Oettel M., Nanoparticle at fluid interfaces, J. Phys.: Condens. Matter, 19 (2007).

Cox P.A., Hydrophilous pollination, Annu. Rev. Ecol, Syst, 19 (1988) 261–280.

Cox P.A., Knox R.B., Two-dimensional pollination in hydrophilous plants: Convergent evolution in the genera Halodule (Cymodoceaceae), Halophila (Hydrocharitaceae), Ruppia (Ruppiaceae), and Lepilaena (Zannichelliaceae), Amer. J. Bot, 176 (1989) 164–175.

Currie I.G., Fundamentals mechanics of fluids, New York, McGraw Hill, 1974.

Dryfe R.A.W., Modifying the liquid/liquid interface: pores, particles and deposition, Phys. Chem. Chem. Phys., 8 (2006) 1869–1883.

Fortes M.A., Attraction and repulsion of floating particles, Can. J. Chem, 60 (1982) 2889.

Gurupatham S.K., Dalal B., Hossain M., Fischer I., Singh P., Joseph D.D., Particles Dispersion on Fluid-Liquid Interfaces, Particuology, 9 (2011) 1–13.

Gurupatham S.K., Dalal B., Hossain M., Fischer I., Singh P., Joseph D.D., Breakup of particle clumps on liquid surfaces, Powder Technology, 217 (2012) 288–297.

Gust D., Moore T.A., Moore A.L., Mimicking Photosynthetic Solar Energy Transduction, Acc. Chem. Res., 34 (2001) 40.

Kralchevsky P.A., Nagayama K., Capillary interactions between particles bound to interfaces, liquid films and biomembranes, Advances in Colloid and Interface Science, 85 (2000) 145–192.

Kralchevsky P.A., Paunov, V.N., Ivanov I.B., Nagayama K., Capillary Meniscus Interactions between Colloidal Particles Attached to a Liquid—Fluid Interface, J. Colloid Interface Sci, 151 (1992) 79–94.

Lucassen J., Capillary forces between solid particles in fluid interfaces, Coll. Surf, 65 (1992) 131.

Nguyen T.H., Eshtiaghi N., Hapgood K.P., Shen W., An analysis of the thermodynamic conditions for solid powder particles spreading over liquid surface, Powder Technology, 201 (2010) 306–310.

Nicolson M.M., The interaction between floating particles, Proc. Cambridge Philosophical Soc., 45 (1949) 288.

Pickering S.U., Emulsions, Journal of the Chemical Society, London, 91 (1907) 2001.

Pillapakkam S.B., Singh P., A Level Set Method for computing solutions to viscoelastic two-phase flow, J. Computational Physics, 174 (2001) 552–578.

Singh P., Hesla T.I., Joseph D.D., A Modified Distributed Lagrange Multiplier/Fictitious Domain Method for Particulate Flows with Collisions, Int. J. of Multiphase Flows, 29 (2003) 495–509.

Singh P., Joseph D.D., Fluid dynamics of Floating particles, J. of Fluid Mech., 530 (2005) 31.

Singh P., Joseph D.D., Aubry N., Dispersion and Attraction of Particles Floating on fluid-Liquid Surfaces, Soft matter, 6 (2010) 4310–4325.

Singh P., Joseph D.D., Fischer I., Dalal B., The role of particle inertia in adsorption at fluid-liquid interfaces, Physical Review E83 041606 (2011).

Singh P., Joseph D.D., Gurupatham S.K., Dalal B., Nudurupati S., Spontaneous dispersion of particles on liquid surfaces, Proceedings of the National Academy of Sciences, 106 (2009) 19761–19764.

Stamou D., Duschl C., Long-range attraction between colloidal spheres at the air-water interface: The consequence of an irregular meniscus, Physical Review (2000) 5263–5272.

Tang Z., Zhang Z., Wang Y., Glotzer S.C., Kotov N.A., Self-Assembly of CdTe Nanocrystals into Free-Floating Sheets, Science, 314 (2006) 274–278.

Tsujii K., Surface Activity: Principles, Phenomena, and Applications, San Diego, Academic Press, 1998.

Tüskea Z., G R.J., Erős I., Srčičb S., Pintye-Hódi K., The role of the surface free energy in the selection of a suitable excipient in the course of a wet-granulation method, Powder Technology, 155 (2005) 139–144.

Wasielewski M.R., Photoinduced electron transfer in supramolecular systems for artificial photosynthesis, Chem. Rev, 92 (1992) 435.

Zajic L., Buckton G., The use of surface energy values to predict optimum binder selection for granulations, International Journal of Pharmaceutics, 55 (1990) 155–164.

Author's short biography

Naga Musunuri

Naga A Musunuri is a graduate student in the department of Mechanical and Industrial Engineering at New Jersey Institute of Technology (NJIT), New Jersey, USA. He received his B.S. from Jawaharlal Nehru Technological University (JNTU), India in 2009 and M.S. from New Jersey Institute of Technology (NJIT) in 2011. His current research interests include PIV measurements, adsorption, fluid mechanics, biological fluid mechanics, microfluidics, and Micro Electro Mechanical Systems (MEMS).

Bhavin Dalal

Bhavin Dalal completed his Ph.D. in Mechanical Engineering from the New Jersey Institute of Technology in 2012. He received his M.S. from Bradley University, Illinois, USA and his B.S. from Gujarat, India.

Daniel Codjoe

Daniel Codjoe graduated for St. Augustine's College at Cape Coast in Ghana. He received his B.S. in Mechanical Engineering form New Jersey Institute of Technology in 2013. He is interested in working on the water and electricity issues in his native country Ghana, and other related mechanical engineering related problems.

Author's short biography

Ian S. Fischer

Ian S. Fischer is Professor of Mechanical Engineering at New Jersey Institute of Technology. He received his B.S. from Columbia University in 1970, his M.S.E. from Princeton University in 1973, and his D. Eng. Sci. from Columbia University in 1985. His research interests include the flow of solid particles on fluid interfaces, and the dual-number modeling of mechanical systems. He is a member of the American Society of Mechanical Engineers.

Pushpendra Singh

Pushpendra Singh is Professor of Mechanical Engineering at New Jersey Institute of Technology. He received his B.S. form IIT Kanpur in 1985, and M.S. and Ph.D. from the University of Minnesota in 1989 and 1991, respectively. His research interests include Newtonian and non-Newtonian fluid mechanics, biological fluid mechanics, microfluidics, direct numerical simulations and modeling of multiphase flows, including those on fluid-liquid interfaces, and electrohydrodynamics. He is a fellow of the American Physical Society and the American Society of Mechanical Engineers.

KONA Powder and Particle Journal No. 31 (2014) 146–155/Doi:10.14356/kona.2014004 Original Research Paper

Characterization of Oxide-Dispersion-Strengthened (ODS) Alloy Powders Processed by Mechano-Chemical-Bonding (MCB) and Balling Milling (BM)†

Longzhou Ma[1]*, Bruce S.-J. Kang[2], Mary A. Alvin[3] and C. C. Huang[4]

[1] *Harry Reid Center for Environmental Studies, University of Nevada, USA*
[2] *Department of Mechanical and Aerospace Engineering, West Virginia University, USA*
[3] *US DOE National Energy Technology Laboratory, USA*
[4] *Hosokawa Micron Powder Systems, USA*

Abstract

Two types of powder processing techniques, Mechano-Chemical-Bonding (MCB) and MCB plus ball- milling (BM) with reduced time, have been employed to process the nickel-based oxide-dispersion-strengthened (ODS) alloy powders with composition of Ni-20Cr-5A1-3W-1.5Y_2O_3 to explore the alternate routes for fabricating, homogenizing and mechanical alloying (MA) the ODS alloy powders, which are usually processed by a prolonged ball-milling or rod-milling technique. In order to examine and evaluate the microstructure, morphology, blending homogeneity and MA effect of alloying powders, the commercial ball-milled ODS MA 956 alloy powders and experimental alloy powders processed by MCB only and MCB plus BM were subjected to microscopic and spectroscopic characterization and analysis using X-ray diffraction (XRD), scanning electron microscopy (SEM), and transmission electron microscopy (TEM). A FIB (focus ion beam) lift-out technique was employed to prepare the TEM cross-section samples of processed powders. The results showed that the MCB plus BM with reduced time could produce the ODS alloying powders with homogeneous lamellate structure similar to MA 956 powders processed by conventional BM technique with a prolonged period of time. The ODS alloy powders processed by MCB plus BM are to be utilized to fabricate the bulk ODS alloy product in the further research phase.

Keywords: oxide-dispersion-strengthened (ODS) alloy, Mechano-Chemical-Bonding (MCB), ball-milling (BM), X-ray diffraction (XRD), scanning electron microscopy (SEM), transmission electron microscopy (TEM), lamellate structure

1. Introduction

Nickel-based oxide-dispersion-strengthened (ODS) superalloys such as MA 956 or MA 6000, synthesized via mechanical alloying (MA) and consolidation process, exhibit the intermediate temperature strength as well as elevated temperature strength and creep resistance by means of the combined strengthening of gamma prime precipitates and nano-sized yttrium oxide (Y_2O_3) particles (Chou and Bhadeshia, 1993; Haghi and Anand, 1990; Howson et al., 1980). The Ni-based ODS superalloys are very promising for use in aircraft and advanced gas turbine engines due to their mechanical property and environmental resistance at high temperature. Also since yttria particles serve for interfacial pinning of the moving dislocations as well as yttria can be transformed to the nano-sized cluster during manufacturing, ODS alloys offer not only the improved creep resistance at elevated temperatures (up to 1200°C) but also low void swelling at condition of high energy high speed neutron irradiation. For example, recent extensively studied ferritic ODS alloys, MA 957 and 14WYT alloy with nominal composition of Fe-14Cr-1Ti-0.3Mo-0.3Y_2O_3 and Fe-14Cr-1Ti-3W-0.3Y_2O_3, respectively, are being considered for a number of advanced nuclear reactor applications at temperature of 500–600°C as well as in neutron irradiation higher than 300 dpa and elevated gas (Helium) concentration level owing to their high temperature strength and low void swelling (Odette et al., 2008; Schaublin et al., 2006; Ukai et al., 1998). Fabrication of ODS alloys is a complicated, costly and time-consuming process, which involves the

† Accepted: June 1, 2013
[1] Las Vegas, Box 454009, 4505 Maryland Parkway, Las Vegas, NV89154, USA
[2] Morgantown, WV26506, USA
[3] Pittsburgh, PA15236, USA
[4] Summit, NJ07901, USA
* Corresponding author:
E-mail: lma@nanosteelco.com
TEL: +1-702-217-2966 FAX: +1-208-552-2923

mechanical alloying (MA) powder metallurgical process, consolidation by hot deformation and post heat treatment (Gilman and Benjamin,1983; Suryanarayana, 2008). The MA process is the core step to fabricate ODS alloys, involving that the elemental alloying powders or oxide compounds are subjected to the high energy ball milling or rod milling for up to 60–72 hours to allow the nano-sized yttria particles to be dispersed homogenously throughout the master particles. After MA processing, the blended and alloyed powders are degassed, canned and consolidated by hot isostatic pressing (HIP) or hot extrusion. The consolidated material is then hot worked to semi-finished products. The hot worked material is further annealed and aged to yield the desired microstructure and properties for various applications. The complicated fabrication process has become a major barrier to commercially produce the ODS materials, leading to an extremely high raw material cost. For example, it costs about $345/kg for Ni-based ODS MA 956 alloy, however it only costs about $30–35/kg for Ni-based superalloys such as INCONEL 718 and 617 (Busby, 2009). In addition, numerous hours of MA milling time can cause high levels of contamination from milling debris and gaseous environment.

Recently developed Mechano-Chemical-Bonding (MCB) technology is an effective approach to blend alloying powders, forming the composite particles consisting of the hosting particles as core and small particles or fibres that are coated around the core. The MCB-induced particle bonding process takes place in the solid state without needing solvents or external heating avoiding potential contaminations and reactions. During MCB processing, the starting powder mixtures are subjected to high compression, shear, and impact forces as they pass through a narrow gap in a high speed rotating device. As a result, the particles are dispersed, mixed, shaped, and bonded together, consequently forming the composite particles composed of various combinations of the starting ingredients (Du Pasquier et al., 2009; Murata et al., 2004; Nam and Lee, 1999; Welham et al., 2000). So far, the green MCB technology has been utilized to make various composite particles used in the fields of functional gradient materials, batteries, cermets, fuel cells, polymers, cosmetics, and pharmaceuticals. Preliminary studies showed that utilization of MCB processing to blend ODS alloying powders was able to homogenously disperse yttrium oxides on the base particles to form the composite structure (Kang et al., 2010). Also, the newly developed MCB processing technique is simple, environmentally friendly, and can be scaled up to 300 litres per batch. Thus, MCB or its combination technique is considered as an enhancement or alternative to the conventional mechanical alloying (MA) process using balling milling or rod milling.

In this study, the technique of MCB as well as MCB plus BM with reduced time were employed to process the ODS alloying powders to explore the alternative method of the conventional time-consuming ball milling or rod milling technique. The processed alloying powders were examined and analyzed microscopically and spectroscopically using TEM, SEM and XRD to identify the mechanical alloying effects such as powder microstructure, morphology, and chemical homogeneity. In order to compare the blending effects, commercial ODS MA 956 alloy powders processed by conventional BM were examined in parallel as a benchmark, while it is iron-based. As a preliminary research phase, the goal of this study is to examine the mechanical alloying effects produced by the proposed techniques, MCB only and MCB plus BM. The processed ODS alloying powders will be either used as spray powders for advanced coating or followed by canning, HIP, hot rolling and annealing to form final ODS products in the next research phase. This study is an attempt to fabricate the ODS alloying powders using the proposed techniques as a substitute or to simplify and improve the MA processes.

2. Materials and Experiments

2.1 Materials

Commercial metallic and ceramic powders including Y_2O_3 (< 50 nm, 99.99% pure), Al (4.5–7 μm, 97.5% pure), Cr (7.5–10 μm, 99.5% pure), and Ni (4–8 μm, 99.9% pure) were purchased from Sigma Aldrich Inc. Saint Louis, MO., Alfa Aesar, Ward Hill, MA, F.W. Winter Inc. & Co. Camden, NJ, and Atlantic Equipment Engineers, Bergenfield, NJ, respectively. These powders were stored separately in an inert environment in sealed bottles full of argon gas. Considering the short time milling as well as no ball-powder-ball collision involved during MCB only process, the average sizes of all starting powder constituents ranged from 0.5 to 15 microns in this study (Du Pasquier et al., 2009; Nam and Lee, 1999; Welham et al., 2000). For conventional ball milling or rod milling MA process, however, the starting powders usually have average diameters ranging from 30 to 500 microns (Suryanarayana, 2008). The starting powders were initially mechanically blended under gas protection inside a glove box chamber according to the nominal composition (wt%) of Ni-20Cr-5Al-3W-1.5 Y_2O_3. The just-blended powders were then placed into bottles that were sealed and filled with argon gas to prevent oxidation of powders. Each bottle containing the just-blended ODS alloying powder sample weighed approximately 200 g. To compare the effects of different processing techniques, the commercial ODS MA 956 alloy powders, which have a nominal composition of Fe-20Cr-4.5Al-0.5 Y_2O_3-0.5 Ti and have been subjected to conventional BM at 200 RPM (rota-

tion per minute) for 72 hours, was obtained from Special Metals Co., Huntington, WV, as a benchmark material.

2.2 Powder Processing

Two types of processing technique, MCB only and MCB plus BM, were employed to process the as-just-blended starting powders to fabricate the experimental ODS alloy powders. For MCB only procedure, the starting powders were MCB processed at a speed to 4000 RPM for only 30 minutes. It was expected to have Y_2O_3 nanoparticles dispersed and bonded onto the surfaces of larger hosting particles such as Ni and Cr particles, which in turn created oxide dispersion and MA (mechanical alloying) effects. After MCB processing, the powders were stored in the sealed bottles filled with argon gas. The MCB processing was conducted in Hosokawa Micron Powder Systems, Summit, NJ. Following MCB processing, a portion of MCB-processed powders (200 g) was then conducted ball milling (BM) at 200 rpm for 20 hours under inertial gas protection condition. Considering the powders have been processed using high speed MCB for 30 minutes, the BM processing time was reduced to 20 hours in comparison with conventional BM time of 70 hours for MA processing. The BM processing was performed at West Virginia University, Morgantown, WV. After processing, small amount of powders (5–10 g) were taken for micro-structural analysis using TEM (transmission electron microscopy), SEM (scanning electron microscopy) and XRD (X-ray diffraction), and the rest of powders were stored for the next research phase use. The micro-structural analysis of experimental powders was conducted at University of Nevada Las Vegas, NV.

2.3 Characterization

2.3.1 X-Ray Diffraction (X-RD) Analysis

The processed powders were characterized by X-ray powder diffraction (XRD) using a PANalytical X'Pert PRO X-ray diffractometer with a CuKα radiation (45 kV, 40 mA), and a multiple-strip solid state detector (X'Celerator®). The sample was prepared by suspending 2–3 g powders in ethanol to make slurry. The slurry was then set on a low-background silicon sample holder. The XRD patterns were recorded at room temperature with step-sizes of 0.017°, 2θ, and 46 s per step. The phase constitution and crystallographic parameters were characterized using the International Center for Diffraction Database (ICDD) for powder diffraction data. The analysis of line broadening effect would be conducted to measure the mechanical deformation and crystal size.

2.3.2 Electron Microscopy (EM) Analysis

The microstructure, morphology, topology and elemental chemical distribution of the processed powder samples were studied by EM techniques including scanning electron microscopy (SEM) and transmission electron microscopy (TEM). SEM imaging was performed on a JEOL scanning electron microscope, JSM-5610 SEM, equipped with secondary electron (SE) and backscattered electron (BE) detectors and an Oxford ISIS EDS system. The acceleration voltage used in SEM was 15–18 kV using the SEM BE and SE mode. In order to improve the conductivity and image contrast, the powder samples were coated with a layer of gold. Gold-coated samples were suspended on the double-sided carbon tapes for SEM observation and imaging. Also, SEM images of processed powders were employed to measure the size of powder particle using an image processing software, Image J with version of 1.46. Note that since most particles showed round morphology, the particle size indeed referred to an equivalent diameter of a particle. Following the particle analysis procedure of Image J, 10 SEM images totally at least containing about 200 sampling particles were analysed to obtain the particle size at different processing conditions.

A TECNAI-G2-F30 transmission electron microscope with a 300 keV field emission gun was used to characterize the powder samples. Samples were analyzed using the conventional bright field (BF), selected-area diffraction (SAD) and high-angle annular dark-field scanning-transmission electron microscopy (HAADF-STEM) mode for defects, diffraction and Z-contrasting imaging, respectively. All TEM images were recorded using a Gatan SC 200 CCD camera with resolution of 2k × 2k. The elemental distribution of each sample was also determined using the corresponding X-ray energy dispersive spectrometry (EDX) under the STEM mode. For STEM/EDX mode, the electron probe with a size of 0.2 nm was used to examine the dedicated area of sample. In order to examine the internal microstructure of processed powders using TEM in a finer scale, the cross-sectioned TEM sample of experimental powders was prepared, involving that 4–6 mg of powders were mixed with spur resin in a micro-vial, which was then solidified by furnace drying at 60°C overnight. The spur resin used for these samples was a mixture of 10.0 g of ERL (vinylcyclohexene dioxide), 4.0 g of DER (a diglycidyl ether of polypropylene glycol), 26.0 g of NSA (nonenyl succinic anhydride), and 0.4 g of DMAE (dimethylaminoethanol). The powders embedded in the resin was then thinned into membranes with a thickness of 50–80 nm using a FEI Nova 200 FIB (focus ion beam) system, which combines the FIB technology with SEM in a single tool. This system can provide SEM imaging in order to monitor the whole process during FIB milling. A FIB cross-section lift-out technique based on a TEM-wizard program in FIB system was used to obtain the cross-sectioned TEM sample of powders (Giannuzzi and Stevie, 1999; Stevie et al.,

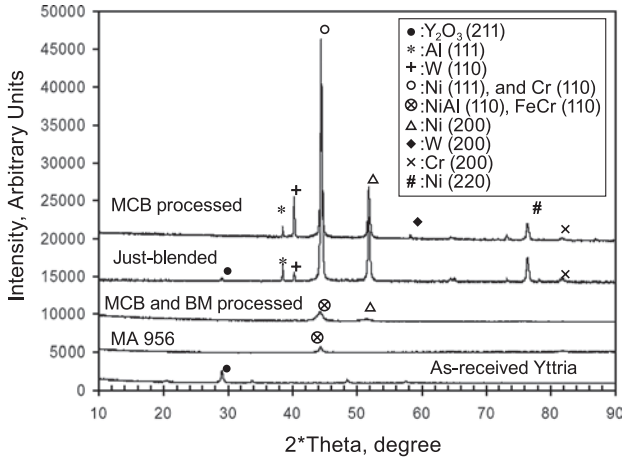

Fig. 1 XRD patterns of starting and processed powders.

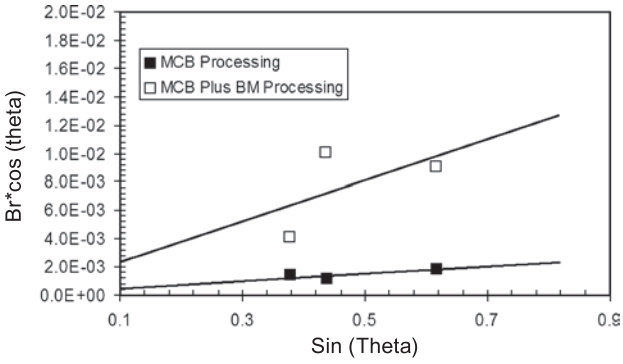

Fig. 2 Analysis of line-broadening effect.

2001). The preparation of TEM cross-sectioned samples by FIB was conducted at Arizona State University, Tempe, AZ.

3. Results and Discussions

3.1 X-RD Analysis

Fig. 1 presented the X-RD spectrum of all experimental powder samples including as-received Y_2O_3 powder, as-blended starting powder, MCB processed powder, MCB plus BM processed powder, and commercial MA 956 powder samples. For as-received yttria and just-blended starting powders, the typical sharp diffraction peaks of all alloying constituents, Al, Cr, Ni, W and Y_2O_3 were observed in X-RD spectrum. The spectrum of as-received Y_2O_3 particles displayed the line-broadening effects due to nano-scaled size of yttria. For MCB processed sample, all individual alloying elemental peaks are still observed with identical intensities relative to the spectrum of just-blended sample. Also the line broadening effect was noticed in spectrum of MCB processed sample, suggesting small deformation occurred during MCB processing. However, for MA 956 and MCB plus BM processed samples, only major elemental peaks with substantially reduced intensities, NiAl (110) and FeCr (110) peaks, were observed, suggesting significant change of crystallographic structure due to formation of solidified phase and presence of defects compared to the spectrum of as-blended sample. Also, extensive line-broadening effects were evident for MA 956 and MCB plus BM processed samples, suggesting extensive plastic deformation involved during processing. Using the peak width of just-blended powders as a reference, the line-broadening effect could be used to estimate the micro-strain and crystal size of powder. X-RD line broadening effect is usually contributed from micro-strain, fine crystal size, and systematic error of instrument. The following equation can be written to account for these contributions (Cullity and Stock, 2001; Suryanarayana and Norton, 1998):

$$B_r \cos\theta = \frac{k\lambda}{L} + \eta \sin\theta \tag{1}$$

Where, B_r is peak FWHM (full width at half maximum); θ is diffraction angle; k is a constant (0.89–1.39); λ is X-ray wavelength; L is the average crystal size; and η is micro-strain of crystal.

Using the average width at FWHM, B_r, and corresponding diffraction angle, θ, obtained from spectrum, **Fig. 2** presents $B_r \times \cos(\theta)$ as a function of $\sin(\theta)$ based on equation (1). The slop and intercept of the fitting line represent the micro-strain and crystal size of powder, respectively. From **Fig. 2**, the powders processed by MCB have micro-strain of 0.26% and crystal size of 720 nm, and the powders processed by MCB plus BM have micro-strain of 1.45% and crystal size of 177 nm. The X-RD broadening analysis suggests that MCB plus BM produced larger strain and smaller crystal size than MCB only. X-RD spectrum analysis of powders processed by MCB indicates that the MCB process in this study would not remarkably change the crystallographic structure and powder size, and MCB could disperse the nano-sized Y_2O_3 particle resulting in the disappearance of Y_2O_3 peak in XRD spectrum.

3.2 SEM Microscopy

SEM imaging was conducted on the experimental powder samples showing the morphology, topology, and dimension. **Fig. 3** presents SEM micrographs of MA 956 powders and experimental powders processed by MCB and MCB plus BM, indicating that conventional BM and MCB plus BM processing produced the random shaped particles, **Fig. 3 (a)** and **(b)**. The insets in **Fig. 3 (a)** and **(b)** show that the powders processed by BM and MCB plus BM contain numerous lamellate structures, suggesting that large deformation, cold-welding, and fracture

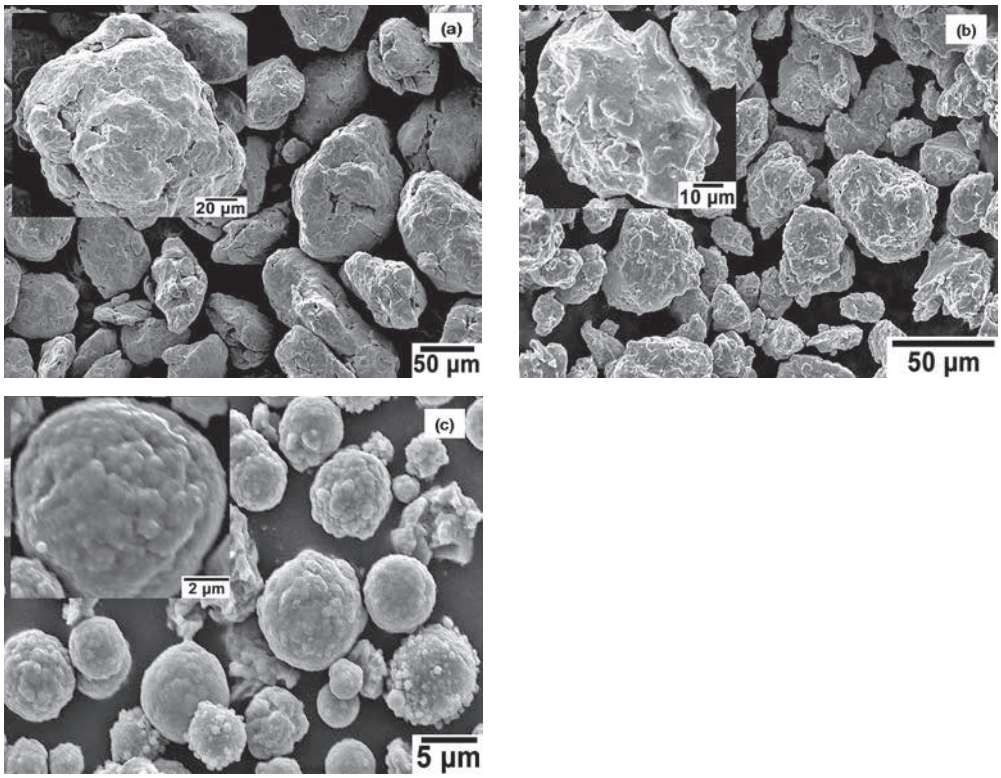

Fig. 3 SEM micrographs of processed powders. (**a**) Powders of MA 956, (**b**) Powders processed by MCB plus BM and (**c**) Powders processed by MCB only.

occurred during processing. For powders processed by MCB only, the powder size almost kept unchanged comparing to the starting size, **Fig. 3 (c)**. However the composite structure and topography was observed, indicating small particles were bonded with master particle forming the composite one as seen in insets. All MCB processed powders keep spherical, suggesting small crystal microstrain. Based on the SEM observation results, particle analysis of processed powders was conducted to statistically measure the distribution of effective particle size. **Fig. 4** plots histogram of particle size distribution for powders subjected to different processing, indicating that MA 956 alloy powders, powders processed MCB plus BM, and powders processed by MCB have mean effective particle size of 121.50, 28.42, and 5.40 μm, respectively.

3.3 TEM Microscopy and Spectroscopy

As an example, **Fig. 5** presents SEM micrographs of TEM cross-sectioned powder sample prepared by a FIB lift-out technique procedure for the powders processed by MCB, showing powder particles were mounted by the spur resin and particle area in resin specimen was delineated and protected from sputtering by deposition of a platinum line. Then, trenches were cut and milled in front and back of the deposited line until an electron-transparent membrane was available, **Fig. 5 (a)**. The thin membrane was cut at all ends, lift out by a needle, and welded on a grid for TEM observation, **Fig. 5 (b)** and **(c)**. **Fig. 6** presents TEM micrographs of the cross-sectioned powder sample of MA 956 alloy powders. TEM BF image in **Fig. 6 (a)** showed numerous of defects and lamellar structures, and inset with high magnification showed the lamellar structures contained lots of moiré fringes, indicating heavy deformation occurred during powder BM processing. The overall microstructure of MA 956 powder is very uniform. The corresponding SAD image in **Fig. 6 (b)** reflects the ring patterns with Fe, Cr and solid-solution phase (FeCr) contribution. The Fe-matrix produced diffuse rings, suggesting fine grains of heavily deformed. The FeCr phase was identified which was consistent with XRD results.

Fig. 7 and **Fig. 8** show TEM micrographs of samples processed by MCB plus BM and MCB, respectively. Compared to the well-defined lamellar structures of MA 956 alloy powders, TEM BF image of powder sample processed by MCB plus BM displays numerous deformed fragments and defects, **Fig. 7 (a)**. Some layered structures still appeared and inset shows numerous moiré fringes. **Fig. 7 (b)** represents the corresponding SAD pattern including Ni-matrix diffuse ring, faint rings and spots associated with reflections of Ni, Cr, NiCr, and yttria, suggesting formation of secondary phase, NiAl, and the presence of some un-deformed metals. For powder sample

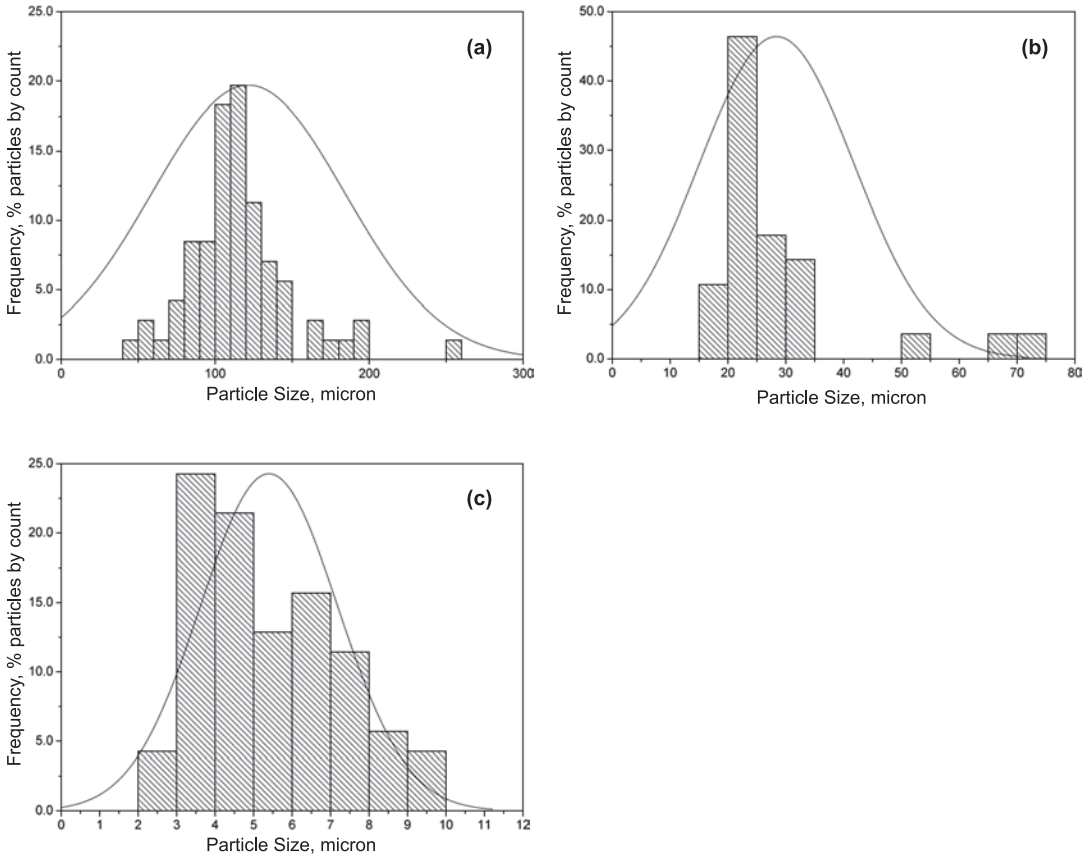

Fig. 4 Histogram of size distribution of processed powders. (**a**) Powders of MA 956, (**b**) Processed by MCB plus BM, and (**c**) Processed by MCB only.

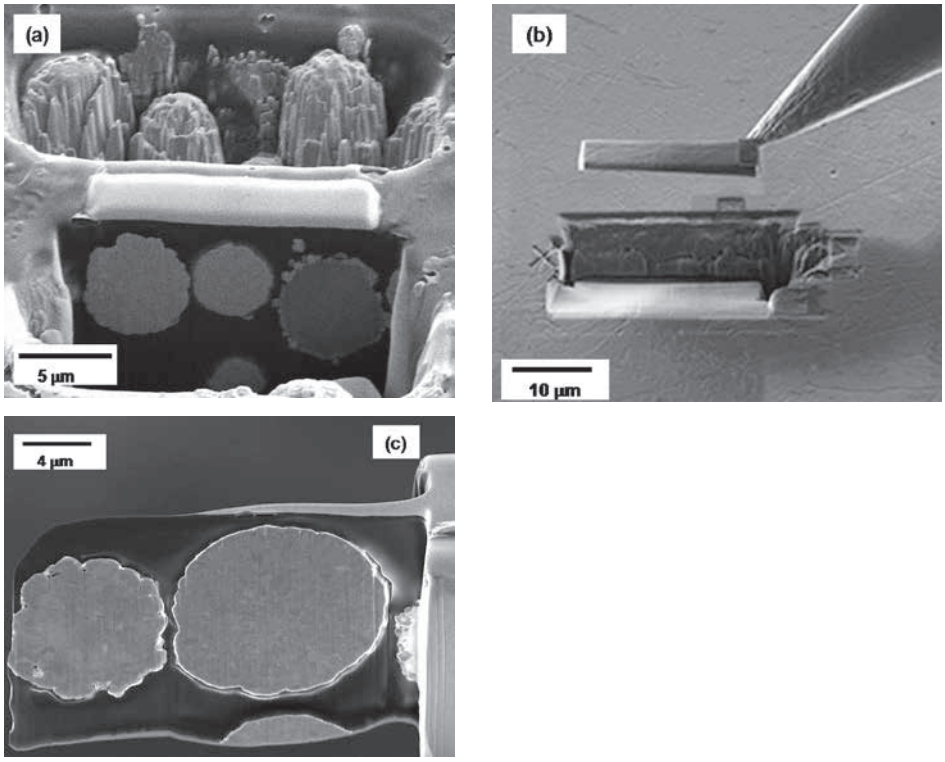

Fig. 5 Powder TEM cross-section sample preparation by FIB Lift-out procedure. (**a**) A metal line was deposited over region of interest and trenches were milled in the front and back side of deposited line. (**b**) A membrane was cut and picked out. (**c**) A TEM cross-section sample of powders processed by MCB.

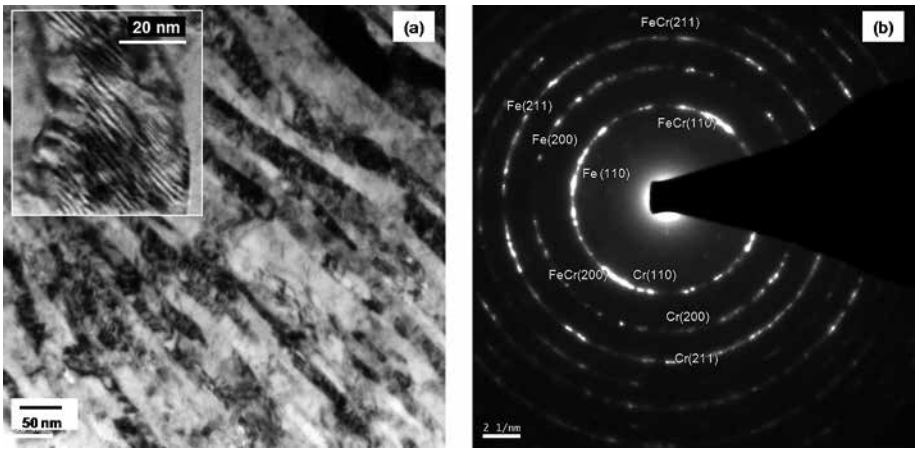

Fig. 6 TEM micrographs of MA 956 powder sample. (**a**) TEM BF image, (**b**) Corresponding SAD image.

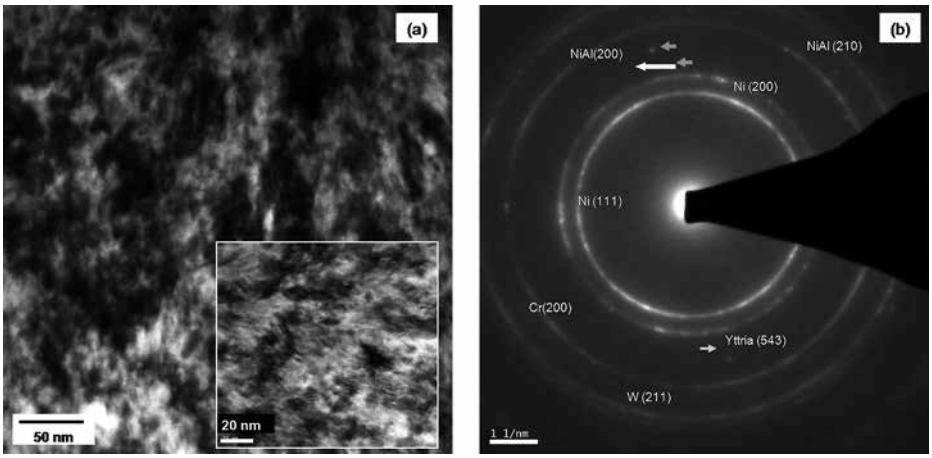

Fig. 7 TEM micrographs of powders processed by MCB plus BM. (**a**) TEM BF image, (**b**) Corresponding SAD image.

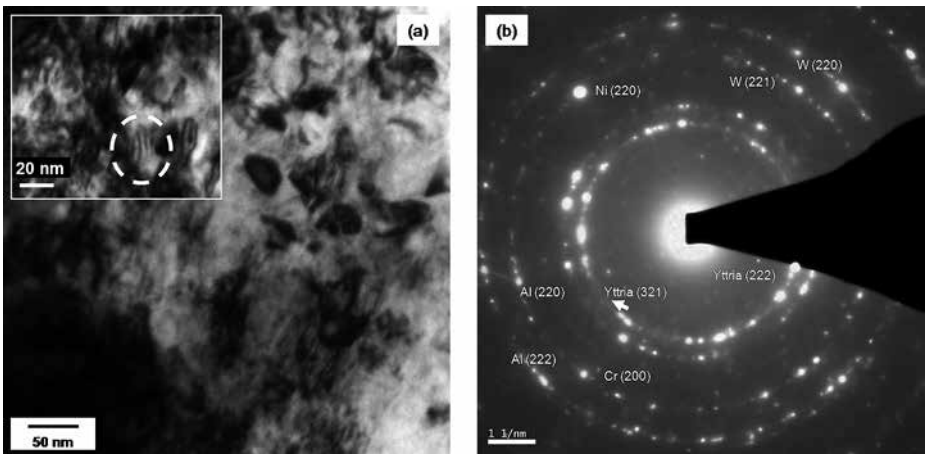

Fig. 8 TEM micrographs of powders processed by MCB. (**a**) TEM BF image, (**b**) Corresponding SAD image.

processed by MCB only, lamellar structure did not appear in TEM BF image, **Fig. 8 (a)**. Instead, lots of nano-sized particles distributed on the Ni-matrix and moiré fringes are still visible, but amount is less than samples processed by BM and MCB plus BM. SAD pattern in **Fig. 8 (b)** shows lots of individual spots associated with Ni, Al, Cr, and yttria reflection, indicating lots of metal particle were bonded with matrix, but solid-solution phase wasn't formed yet. Therefore, powders processed by MCB plus BM have similar microstructure to MA 956 powder, while

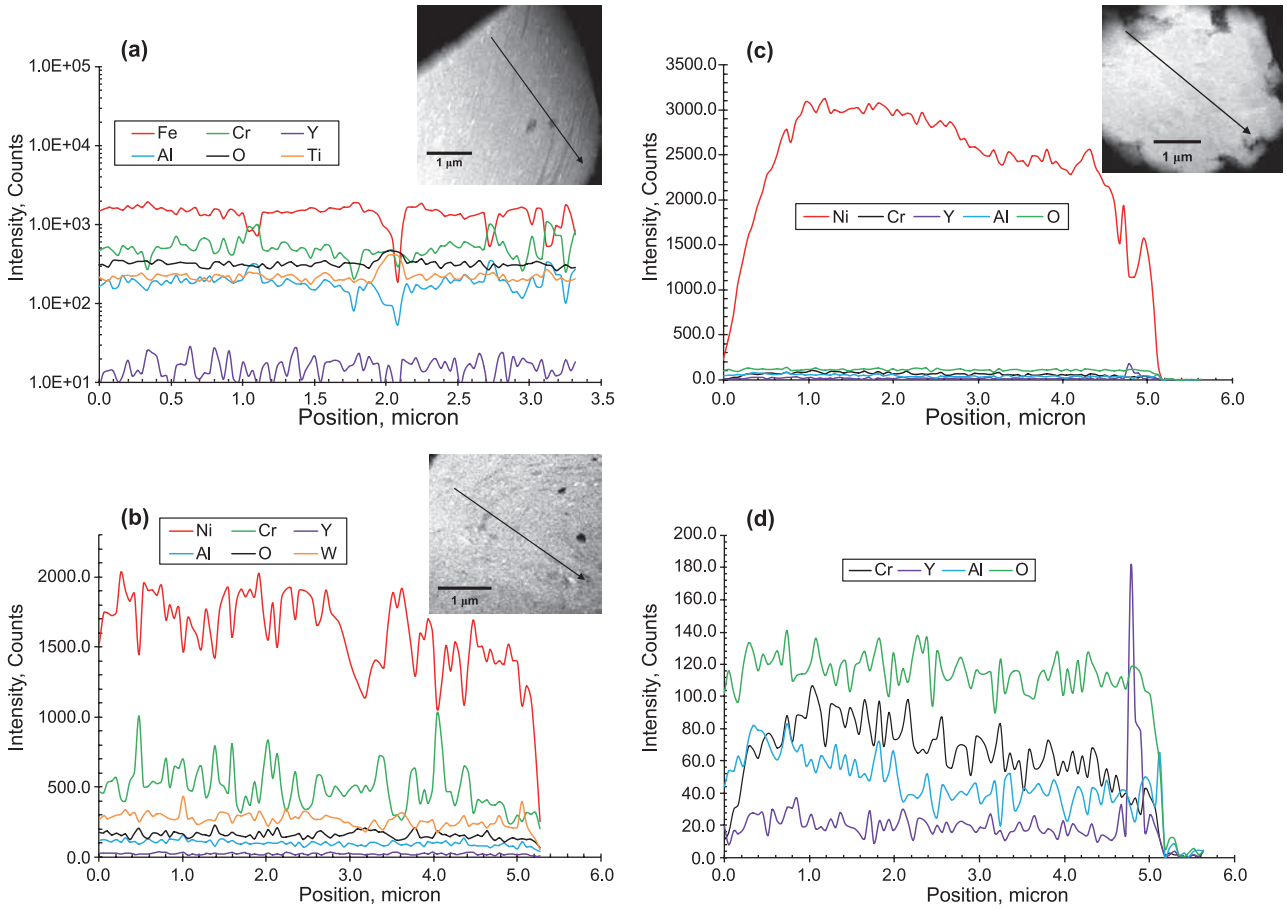

Fig. 9 STEM/EDX line-scanning analysis. (**a**) MA 956 powder sample, (**b**) MCB plus BM processed sample, (**c**) MCB processed powder sample, and (**d**) Close-viewed plot of (**c**).

the latter has more uniform lamellar structure. To get better MA and dispersion effects using MCB plus BM route, a proper combination of the starting powder sizes, energy input, and MCB processing time should be optimized.

In order to examine the chemical homogeneity of alloying elements across the powder cross-section, STEM Z-contrast imaging and EDX line-scanning analysis were conducted. **Fig. 9** presents the results of EDX line-scanning analysis and the insets show Z-contrast imaging and scanning direction. For MA 956 and MCB plus BM processed powder sample, EDX line scanning results show the alloy elements and Y_2O_3 have been dispersed homogeneously throughout the matrix, and Fe-Cr and Ni-Cr could be exchangeable, **Fig. 9 (a)** and **(b)**. The inset images show the homogeneous contrast profile, indicating the homogeneous distribution of elements. For powder sample processed by MCB as seen in **Fig. 9 (c)**, Ni-matrix particle displays strong intensity and other elements are relatively weak but detectable. **Fig. 9 (d)** was the close-view of EDX spectrum with weak counts in **Fig. 9 (c)**, indicating that yttrium was detected distributing around the edge of particle as highlighted by circle. Z-contrast image of hosting particle show deformation occurred around particle edge.

4. Conclusions

A Mechano-Chemical-Bonding (MCB) as well as MCB plus ball milling (BM) with reduced time technique was used to fabricate, blend and homogenize the oxide dispersion-strengthened (ODS) nickel-based superalloy powders. The processed powders and MA 956 alloy powders have been characterized using X-RD, SEM and TEM. The results suggested the following conclusions:

1. As a benchmark material, MA 956 alloy powders subjected to prolonged BM processing contained numerous uniform lamellar structures, moiré fringes, and defects. The solid solution phase, FeCr, has been formed during BM, and alloying elements have been homogeneously dispersed.

2. Utilization of MCB and MCB plus BM technique to blend the ODS alloying powders could introduce the lattice strain, and defects. The technical route of MCB plus BM generated larger strain and smaller crystal size than MCB.

3. The MCB processing could produce composite particles bonded with other small particles such as nano-sized yttria.

4. MCB plus BM with reduced time could produce the homogeneous lamellate structure and chemical homoge-

neity similar to MA 956 alloy powders. As an alternate, MCB plus BM process is possible to be employed to prepare ODS powders with reduction of BM time. Further exploring the effects of MCB plus BM processing parameters on microstructure and morphology of ODS alloying powders would be necessary to optimize the process. Also, follow-up work to produce surface coating or to fabricate ODS alloy final products by HIP, hot deformation and heat treatment using the MCB processed powders are necessary to validate this technical route.

5. MCB technique is potential to be employed to disperse only nano-sized yttria particles on the pre-alloyed micron-sized hosting particles to fabricate ODS alloying powders.

Acknowledgements

This research is supported by US Department of Energy, National Energy Technology Laboratory (NETL), and Advanced Research Materials (ARM) Program under RDS Contract DE-AC26-04NT41817.606.01.01. The encouragement and support by Patricia Rawls and Robert Romanosky, Program Managers, are very much appreciated. Thanks are also due to TRP (Transmutation Research Program), University of Nevada, Las Vegas, for supporting X-RD, SEM and TEM analysis in instrument usage and working time.

References

Busby J.T., Economic benefits of advanced materials in nuclear power systems, Journal of Nuclear Materials, 392 (2009) 301–306.

Chou T.S., Bhadeshia H.K.D.H., Crystallographic texture in mechanically alloyed oxide dispersion-strengthened ma956 and ma957 steels, Metallurgical Transactions A, 24 (1993) 773–779.

Cullity B.D., Stock S.R., Elements of X-Ray Diffraction, 3rd ed., Prentice—Hall, New Jersey, 2001, pp. 174–177.

Du Pasquier A., Huang C.C., Spitler T., Nano $Li_4Ti_5O_{12}$–2no $_2O_4$ batteries with high power capability and improved cycle-life, Journal of Power Sources, 186 (2009) 508–514.

Giannuzzi L.A., Stevie F.A., A review of focused ion beam milling techniques for tem specimen preparation, Micron, 30 (1999) 197–204.

Gilman P.S., Benjamin J.S., Mechanical alloying, Annual Review of Materials Science, 13 (1983) 279–300.

Haghi M., Anand L., High-temperature deformation mechanisms and constitutive equations for the oxide dispersion-strengthened superalloy ma 956, Metallurgical Transactions A, 21 (1990) 353–364.

Howson T.E., Mervyn D.A., Tien J.K., Creep and stress rupture of a mechanically alloyed oxide dispersion and precipitation strengthened nickel-base superalloy, Metallurgical Transactions A, 11 (1980) 1609–1616.

Kang B., Ogawa K., Ma L.-Z., Alvin M.A, Smith G., ODS coating development by cold spray method using powder mix prepared by combined MCB and ball milling processes, 24th Annual Conference on Fossil Energy Materials, Pittsburgh, PA, USA, May 25–27, 2010.

Murata K., Fukui T., Huang C.C., Naito M., Abe H., Nogi K., Composite powders processed by an advanced mechanical method for the fabrication of cermet anodes of solid oxide fuel cells, Journal of Chemical Engineering of Japan, 37 (2004) 568–571.

Nam J.G., Lee J.S., Mechano-chemical synthesis of nanosized stainless steel powder, Nanostructured Materials, 12 (1999) 475–478.

Odette G.R., Alinger M.J., Wirth B.D., Recent developments in irradiation-resistant steels, Annual Review of Materials Research, 38 (2008) 471–503.

Schäublin R., Ramar A., Baluc N., De Castro V., Monge M.A., Leguey T., Schmid N., Bonjour C., Microstructural development under irradiation in european ods ferritic/martensitic steels, Journal of Nuclear Materials, 351 (2006) 247–260.

Stevie F.A., Vartuli C.B., Giannuzzi L.A., Shofner T.L., Brown S.R., Rossie B., Hillion F., Mills R.H., Antonell M., Irwin R.B., Purcell B.M., Application of focused ion beam lift-out specimen preparation to tem, sem, stem, aes and sims analysis, Surface and Interface Analysis, 31 (2001) 345–351.

Suryanarayana C., Recent developments in mechanical alloying, Reviews on Advanced Materials Science, 18 (2008) 203–211.

Suryanarayana C., Norton M.G., X-Ray Diffraction: A Practical Approach, Plenum Press, New York, 1998. pp. 207–221.

Ukai S., Nishida T., Okuda T., Yoshitake T., R&d of oxide dispersion strengthened ferritic martensitic steels for fbr, Journal of Nuclear Materials, 258–263, Part 2 (1998) 1745–1749.

Welham N.J., Willis P.E., Kerr T., Mechanochemical formation of metal–ceramic composites, Journal of the American Ceramic Society, 83 (2000) 33–40.

Author's short biography

Longzhou Ma

Dr. Longzhou Ma is formerly a research scientist of Materials Engineering at Harry Reid Center for Environmental Studies, University of Nevada Las Vegas. Currently, Dr. Longzhou Ma is a senior research engineer of R & D, NanoSteel Company, Inc., Idaho Falls, ID83404. His expertise includes microstructure characterization using transmission electron microscopy (TEM), scanning electron microscopy (SEM), optical microscopy. Dr. Ma is also known for his expertise in dislocation analysis in materials structure and crack propagation analysis in metallic materials. Over the years, he has published over 35 peer-reviewed papers. Dr. Ma has affiliation with numerous engineering society including TMS, MRS, MSA. As a PI or co-PI, he ever involved several US DOE-sponsored research projects. Dr. Ma can be reached at lma@nanosteelco.com.

Bruce S.-J. Kang

Dr. Bruce Kang is a Professor at the Mechanical and Aerospace Engineering Department, West Virginia University. Dr. Kang's current research activities include: (1) SOFC and CO2 re-use, (ii) Biomass energy conversion, (iii) high temperature materials for advanced power systems, (iv) experimental and multi-scale computational modeling analyses of metallic and intermetallic alloys, and (vi) surface material property evaluation using micro/nano indentation.

Mary A. Alvin

Mary Anne Alvin, DOE NETL: Ms. Alvin currently serves as a Division Director for the Office of Research and Development (ORD), Department of Energy's National Energy Technology Laboratory. She also leads ORD's advanced gas turbine engine materials development and heat transfer research efforts for land-based power generation. Prior to joining DOE NETL in 2005, Ms. Alvin had thirty years of experience at Westinghouse and Siemens Westinghouse, working in the area of advanced energy system. Ms. Alvin was awarded the Siemens Westinghouse Eagle Award in 1999, which is the highest corporate award at Siemens that is granted to an employee. She currently holds twenty-six patents with additional pending.

C. C. Huang

Dr. C. C. Huang is the Director of Business & Technology Development at Hosokawa Micron Powder Systems, an operating unit of Hosokawa Micron International Inc., a global supplier of systems and equipment related to material sciences and engineering. He holds an M.S. degree in engineering from Illinois Institute of Technology and a Ph.D. degree in chemical engineering from West Virginia University. Dr. Huang specializes in powder and nanoparticle processing, powder characterization, powder granulation, and fluidization. He has published over 30 articles and 8 patents, chaired several meetings, and is an active member in a number of scientific and engineering societies.

KONA Powder and Particle Journal No. 31 (2014) 156–162/Doi:10.14356/kona.2014005 Original Research Paper

Synthesis of Calcium Carbonate Particles in Octylamine/Water Bilayer Systems †

Jun Wang [1,2]*, William B. White [1] and James H. Adair [1]

[1] *NSF Particulate Materials Center, Department of Materials Science and Engineering, The Pennsylvania State University, USA*
[2] *A123 Systems, LLC, USA*

Abstract

Calcium carbonate particles with various shapes and morphologies were prepared via precipitation in an octylamine/water self-assembly bilayer systems. Crystal structure and shape of the $CaCO_3$ particles were determined by the water to octylamine molar ratio R of the bilayer. At R = 16.0, phase pure calcite particles with a "hopper crystal" morphology were formed, the average particle size of the hopper crystal is 10 μm with well-defined edges on the hopper faces. Decrease the R ratio to 7.2 eventually leads to the formation of 3 μm tabular $CaCO_3$ particles which are predominated by vaterite structure. For an intermediate R of 10.8, spherical vaterite aggregates and rhombohedral calcite particles were produced. Thermal decomposition of the $CaCO_3$ particles was observed at around 710°C. The mechanism of particle evolution in the self-assembly bilayer, particularly the formation of "hopper crystal" calcite was discussed.

Keywords: powder, ceramics, chemical synthesis, Raman spectroscopy, crystal structure

1. Introduction

Calcium carbonate is one of the most abundant minerals on earth and finds its increasing applications in pigments, water treatment, biomineralization and energy storage (Colfen, 2003). It is equally important in scientific research and much attention had been focused on the crystal growth and morphology development under a number of conditions (Adair and Suvaci, 2000; Meldrum, 2003). McCauley and Roy (1974) extensively explored the processing parameters that affected the crystal growth of $CaCO_3$ polymorphs precipitated from aqueous solutions. The growth of $CaCO_3$ crystals was intertwinedly determined by solution pH, reactant concentration, and impurity ions at ambient conditions. This effort was extended by Wang et al. (1999) in the precipitation of Ca ions with urea at 90°C, and by Jung et al. (2000) for calcium carbonate formed in a Couette-Taylor reactor. A theoretical understanding of the crystallization habit of precipitated $CaCO_3$ was carried out by de Leeuw and Parker (1998) using atomistic simulation, which indicated the surface and hydration energy may directly control the formation of favored crystal structures. More recently, the precipitation of calcium carbonate particles was incorporated with polymeric additives (Archibald et al., 1996; Osman and Suter, 2002; Park and Meldrum, 2002; Rock et al., 1997; Rudloff and Colfen, 2004; Wei et al., 2004; Xu et al., 2005) and gold nanoparticle template (Lee et al., 2001) so as to gain adequate control of the crystallization and morphology development.

The crystallization of $CaCO_3$ particles under confined environment was initially studied by Mann et al. (1991), Rajam et al. (1991) and Heywood et al. (1991) using compressed Langmuir monolayers of stearic acid and octadecylamine. The structure and morphology of the $CaCO_3$ particles were significantly dedicated by the type of surfactant molecule as well as Ca^{2+} concentration (Walker et al., 1991). Analogy to the monolayer-confined synthesis, octylamine/water bilayer systems was employed by Adair et al. (1998) to grow a number of nanoscale platelets including CdS, (Adair and Suvaci, 2000; Adair et al., 1998) Ag (Yener et al., 2002) and SiO_2 (Wang et al., 2006) at ambient condition. When mixed with water under appropriate weight ratio, the amines will orient in such a way that allows organic layer and aqueous layer to alternate in the solution, mainly because of the amphiphilic nature of the organic molecules (Adair et al., 1998; Ralston et al., 1942). The thickness of each layer is directly related to the amine to water weight ratio, which provides an effective pathway to manipulate the template thereby the nanoparticle thickness during synthesis. This approach is applicable to numerous materials where

† Accepted: June 3, 2013
[1] University Park, PA 16802, USA
[2] 200 West Street, Waltham, MA 02451, USA
* Corresponding author:
E-mail: junwang@a123systems.com
TEL: +1-617-972-3456 FAX: +1-617-924-8910

chemical reactions such as precipitation, redox, and hydrolysis are feasible in aqueous media.

Previous studies demonstrated that crystal structure and shape of the $CaCO_3$ particles are sensitive to a number of processing parameters (Colfen, 2003; McCauley and Roy, 1974; Walsh et al., 1999), thus preparation of $CaCO_3$ with desired phase and shape may require precise control over the experimental procedures. Therefore, the intent of this work is to report the preliminary study on $CaCO_3$ particles precipitated from octylamine/water bilayer systems, an interesting crystal habit known as hopper crystal was observed. The possible mechanisms responsible for shape and morphology changes were discussed.

2. Experimental Procedure

2.1 Particle Synthesis

All chemicals involved in the synthesis were reagent grade and used as-received without further purification. $CaCl_2$ (99$^+$%, J. T. Baker, NJ) and Na_2CO_3 (99$^+$%, J. T. Baker, NJ) were used as the precursors for $CaCO_3$. Octylamine (99%), amylamine and polyethylenimine were purchased from Aldrich (Aldrich Chemical Co., Milwaukee, WI), while ethanol (94.4%, 188.8 proof), nitric acid and glacial acetic acid were obtained from J. T. Baker Chemicals. Deionized water was used (specific conductivity = 0.4×10^{-7} S/m) for all experiments.

The procedure used to prepare $CaCO_3$ particles is similar to that applied to produce platelet-like CdS particles in the octylamine/water bilayer systems (Adair et al., 1998). The general procedure can be described as follows, 25 mL 0.05 M $CaCl_2$ and 0.05 M Na_2CO_3 aqueous solutions were mixed with 31.97 mL octylamine and 1.33 mL amylamine to form two individual batches of self-assembled bilayers (amylamine is able to stabilize the octylamine/water bilayer and provide a well-defined bilayer structure) (Yener et al., 2002). After shaking for 10 minutes, the two bilayers were mixed together and shaken for 24 hours. Precipitation and condensation of $CaCO_3$ particles takes place in the octylamine/water bilayer during vigorous shaking. The bilayer system was subsequently broken by adding 60 mL 0.5 M HNO_3/ethanol solution and 1.25 mL 0.1 wt% PEI/ethanol solution (1 w/w PEI). The washing step was repeated 5 times by simply collecting $CaCO_3$ particles on the bottom of the beaker and removing the supernatant. It is important to control pH of the suspension close to pH 9 in each washing step, which allows the maximum yields of $CaCO_3$ (McCauley and Roy, 1974). The final suspension of $CaCO_3$ particles in ethanol has a concentration of 3.0 mg/mL and a pH close to pH 9. A schematic flow sheet for the entire procedure is shown in **Fig. 1**.

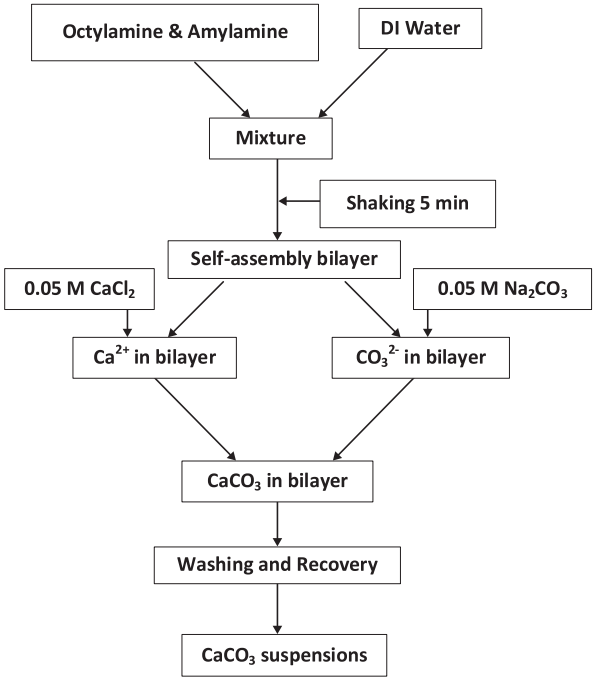

Fig. 1 Flow sheet of $CaCO_3$ particles synthesized from octylamine/water bilayer systems. The pH of the bilayer is controlled at pH 10. The octylamine to amylamine weight ratio is 25 (Yener et al., 2002).

2.2 Characterization

The morphology of the $CaCO_3$ particles was analyzed with scanning electron microscope (SEM, Hitachi S-3000H, Tokyo, Japan). Structural analysis for $CaCO_3$ particles was carried out with powder X-ray diffraction (XRD, Scintag pad V, Cu K_α 1.5418 Å). Raman spectra of the $CaCO_3$ powders were obtained using an ISA microfocus Raman spectrometer (Spectra Physics 164 Ar^+ laser, $\lambda = 514$ nm), $CaCO_3$ powders were placed on a zero background glass slide for each scan. Thermogravimetric analysis (TGA, TA 2050, TA Instruments, USA) was used to study the thermal stability and decomposition of $CaCO_3$ powders as a function of temperature under constant air flow.

3. Results

Fig. 2 shows the morphologies of the $CaCO_3$ particles with various processing conditions. At R = 16.0 (water to octylamine molar ratio), $CaCO_3$ particles precipitated in the bilayers are about 10 μm and form the so-called "hopper" crystals (**Fig. 2a**) (Buckley, 1952), each face of the crystal showing an inverse growth pyramid. The same hopper crystal morphology was observed in $CaCO_3$ precipitated from alcohol/water solution (Dickinson and McGrath, 2003) and in calcium iodate monohydrate (Shitole and Saraf, 2002) grown by silica gel technique. Decrease the R

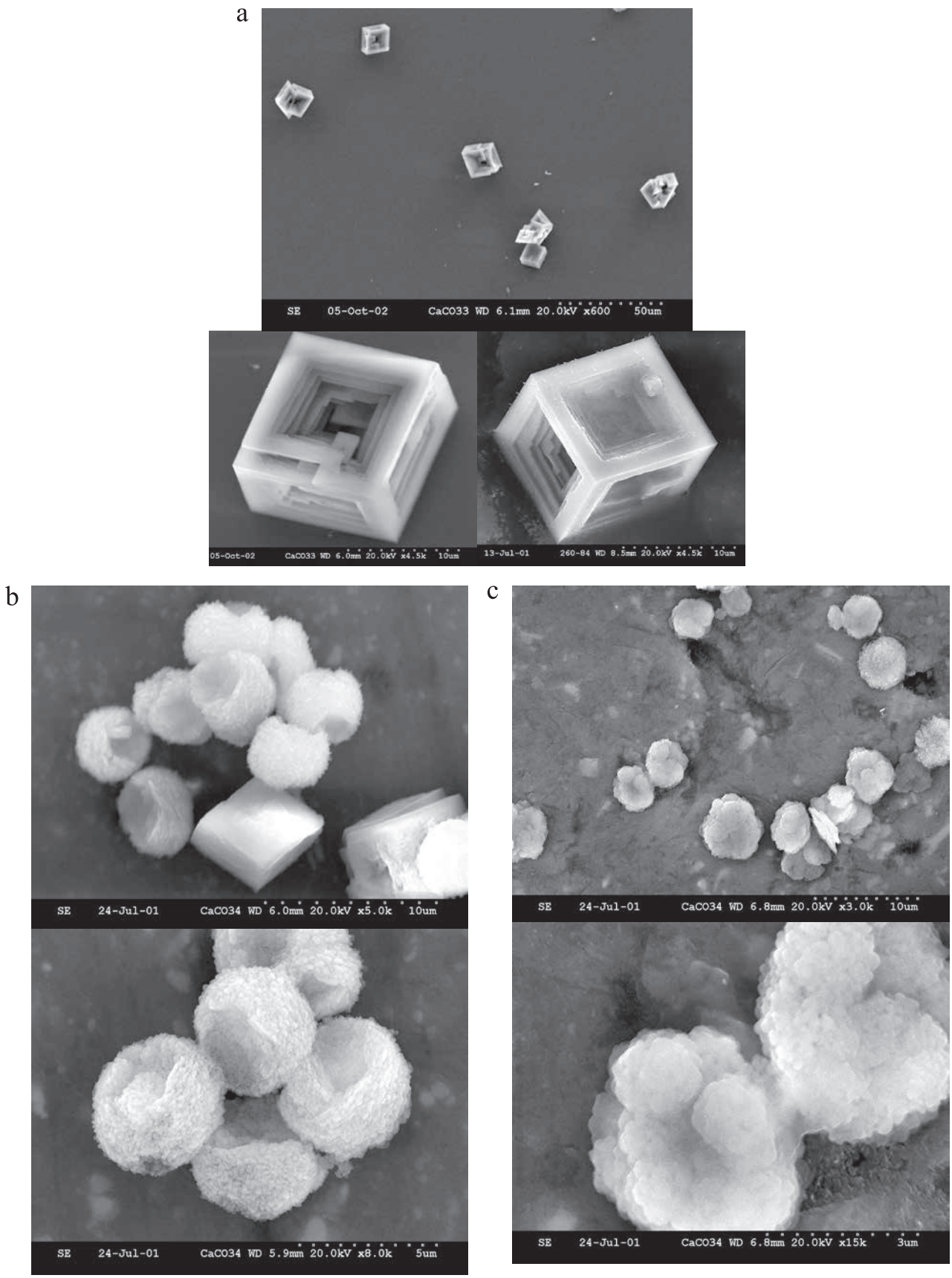

Fig. 2 SEM micrographs of $CaCO_3$ particles prepared from octylamine/water bilayer systems. (**a**) R = 16.0, hopper crystals of calcite, (**b**) R = 10.8, sphere-like and rhombohedral $CaCO_3$ particles, (**c**) R = 7.2, tabular $CaCO_3$ particle aggregate. R is the molar ratio of water to octylamine.

ratio to 10.8, the thickness of the aqueous layer is compressed due to a reduced amount of water, particle size decreases accordingly. It is obvious that the particle shape changes as revealed by the SEM analysis in **Fig. 2b**, two types of particles, sphere-like and rhombohedral coexist in this condition. **Fig. 2c** shows that tabular $CaCO_3$ particles can be produced when R ratio is 7.2, corresponding to 70 wt% octylamine in the bilayer. Average face diameter of the tabular $CaCO_3$ particles is about 3 μm. The thickness of the primary tabular particle is unknown because of the agglomerated nature of the particles as well as the limitation of the SEM. A well-defined crystal morphology is formed with R = 16.0, although particles show hopper habit of sharp growth edges. However, at low R values with thinner aqueous layers, the morphologies of the $CaCO_3$ particles are poorly-evolved, resulting agglomerated sphere-like (R = 10.8) and tabular (R = 7.2) shapes. More precisely, the morphology at R = 10.8 is a mixture of near perfect rhombohedra and sphere-like particle aggregates.

The various crystal morphologies of $CaCO_3$ shown in **Fig. 2** actually belong to different crystal structures as illustrated by XRD analysis in **Fig. 3**. The hopper crystal of $CaCO_3$ particles takes on calcite at R = 16.0, and the dominant peak at around 30 degrees is assigned to the calcite (104) face. At R = 10.8, the XRD result of those particles shows a mixed pattern of calcite and vaterite structures, which is consistent with the SEM results in **Fig. 2b**. There are two kinds of particles produced in the bilayer under this condition, sphere-like and rhombohedral. The rhombohedral particles can be assigned to calcite, whose space group is R3c. Obviously, the crystal structure of the sphere-like particles is vaterite. A supportive evident for this assignment is achieved at R = 7.2, where tabular $CaCO_3$ particle aggregates are the dominant morphology. The XRD pattern indicates that the crystal structure for the tabular particles remains the same, but the intensity of calcite (104) peak decreases significantly, which suggests the ratio of calcite to vaterite decreases. Based on the SEM and XRD measurements, combined with the crystallographic information available for $CaCO_3$ polymorphs, the sphere-like particles in **Fig. 2b** and the tabular aggregates in **Fig. 2c** are vaterite (Dickinson et al., 2002). The other polymorph of $CaCO_3$, aragonite, is not observed for all the synthetic powders (Sunagawa, 1987).

The laser Raman scattering results of $CaCO_3$ particles are shown in **Fig. 4**. The Raman spectrum of $CaCO_3$ is sharp for hopper crystals prepared at R = 16.0 than that of tabular $CaCO_3$ particles at R = 7.2, which is primarily due to different crystal structures. Five normal modes for calcite are observed in the hopper crystal $CaCO_3$, with the most intense A_1g mode at 1086 cm^{-1}, the rest vibration frequencies at 155, 281, 712 and 1435 cm^{-1} are associated with the Eg modes, their frequencies are well consistent with those reported by Rutt and Nicola (1974). The

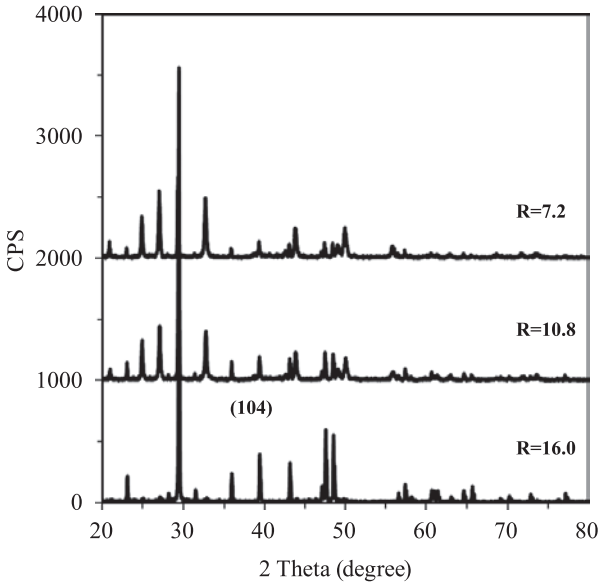

Fig. 3 X-ray diffraction patterns of $CaCO_3$ particles prepared from octylamine/water bilayer systems. Note the intensity decrease from calcite to vaterite. Miller indices from JCPDS ICDD 5-0586 (calcite) and JCPDS ICDD 33-268 (vaterite).

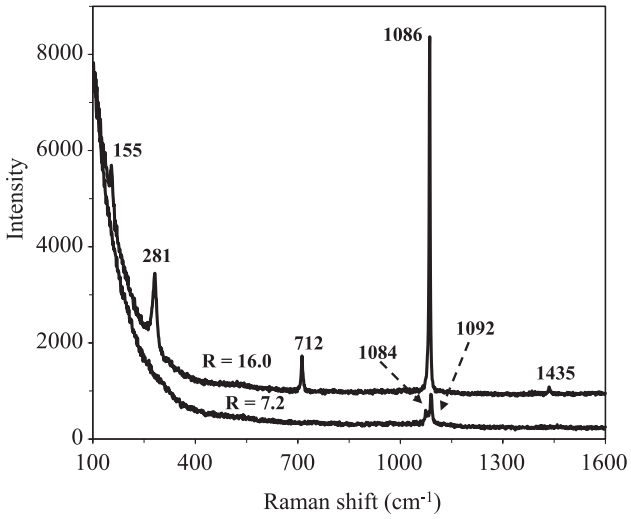

Fig. 4 Raman Scattering of $CaCO_3$ particles prepared from octylamine/water bilayer systems. The excitation line wavelength is 514 nm (Ar^+ laser). Only the two most intense bands were observed in tabular $CaCO_3$ vaterite due to poor crystallinity.

tabular $CaCO_3$ particles show only two weak over-lapped bands at 1084 and 1092 cm^{-1} because of the low crystallinity of the particles. The spectral profile at 1084 and 1092 cm^{-1} is the characteristics of vaterite structure (Behrens et al., 1995; Boughriet et al., 2000; Lee et al., 2001), which verifies the crystal structure of the tabular $CaCO_3$ particles determined by SEM and XRD analyses.

Thermal stability of tabular $CaCO_3$ particles (R = 7.2) is measured by TGA and illustrated in **Fig. 5**. The

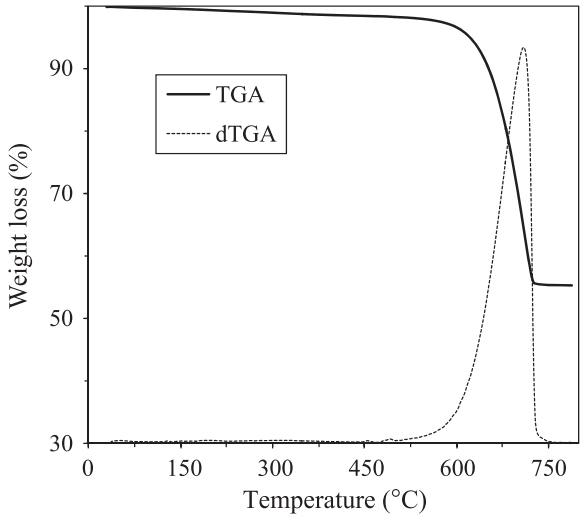

Fig. 5 Thermal stability of $CaCO_3$ particles measured by TGA (R = 10.8). The maximum weight loss occurs at 710°C as shown in the dTGA curve. The total weight loss is less than 4% at temperatures lower than 600°C.

as-synthesized particles are quite stable below 600°C, a total of about 3.4% weight loss is found which indicates the removal of the bilayer template during washing. When temperature goes above 600°C, a distinct weight loss of about 44% takes place from 600°C to 750°C. The maximum weight loss occurs at 710°C as determined by the derivative of the TGA curve, which is related to the decomposition of $CaCO_3$ that yields CO_2. The TGA measurements on hopper crystal and sphere-like $CaCO_3$ particles follow a similar trend.

4. Discussion

The formation of $CaCO_3$ with various morphologies under variable R ratio is quite understandable because of the nature of the self-assembly bilayer template as well as the particle growth mechanisms in confined environment (Adair and Suvaci, 2000; Mann et al., 1991; Walsh et al., 1999; Yener et al., 2002). However, the presence of hopper crystal calcite with square-like hopper faces is something beyond the expectation. There are two possible mechanisms responsible for the growth of hopper crystal calcite (Buckley, 1952; Dickinson and McGrath, 2003), thermodynamic control based on a screw dislocation and kinetic control linked to the diffusivity of constitute ions. Kinetic control may be a favorable process in this case according to Dickinson and McGrath (2003). Under kinetic model, the growth rate is different in various directions during crystallization, rapid growth appears to accentuate the differences between the preferred and other direction (Buckley, 1952). In the octylamine/water bilayer of pH 10, rapid growth of $CaCO_3$ crystals is feasible because of the high supersaturation of Ca^{2+}. The growth rate along body diagonal direction is faster than any other crystal directions, which explains the face-centered cavity formation as observed in SEM analysis. The apparent contradiction is that none of the three polymorphs of $CaCO_3$ belongs to the cubic system, specifically, XRD shows the hopper crystal of $CaCO_3$ is calcite, which means the cavity should be triangular instead of square since the crystal is rhombohedral with a space group R3c. Furthermore, Dickinson and McGrath (2003) claimed that higher viscosity (>1.6 mPa.s) alcohol water solution would promote the formation of hopper crystal calcite, unfortunately, an opposite trend is observed in the octylamine/water bilayer systems. Current results are far away from determining the dominant mechanism including viscosity effect as well as other contributions from solution pH, Ca^{2+} concentration and interaction of octylamine and Ca^{2+}. However, the hopper crystal calcite may be used as a host material for inclusion chemistry where large cavity is required (Stucky and Macdougall, 1990).

5. Conclusions

Hopper crystal of calcite particles with square-like face-centered cavity are prepared in the octylamine/water self-assembly bilayer systems at R = 16.0. The morphology and crystal structure of the $CaCO_3$ particles demonstrate significant dependence on the R ratio, with vaterite tabular aggregate achieved at R = 7.2. The mechanism of particle formation in alkaline self-assembly bilayer system is discussed with an emphasis on the observation of unique hopper crystal particles in rhombohedral calcite.

References

Adair J.H., Li T., Kido T., Havey K., Moon J., Mecholsky J., Morrone A., Talham D.R., Ludwig M.H., Wang L., Recent developments in the preparation and properties of nanometer-size spherical and platelet-shaped particles and composite particles, Mater. Sci. Eng. Rep., 23 (1998) 139–242.

Adair J.H., Suvaci E., Morphological control of particles, Current Opinion in Colloid & Interface Sci., 5 (2000) 160–167.

Archibald D.D., Qadri S.B., Gaber B.P., Modified calcite deposition due to ultrathin organic films on silicon substrates, Langmuir, 12 (1996) 538–546.

Behrens G., Kuhn L., Ubic R., Heuer A.H., Raman spectra of vateritic calcium carbonate, Spec. Lett., 28 (1995) 983–995.

Boughriet A., Gengembre L., Laureyns J., Recourt P., Langelin H.R., Nacer A., Generation of uranyl/carbonate/hydroxide "coatings" at the vaterite surface, Phys. Chem. Chem. Phys., 2 (2000) 1059–1068.

Buckley H.E., Crystal Growth, John Wiley and Sons, New York, 1952.

Colfen H., Precipitation of carbonates: recent progress in controlled production of complex shapes, Current Opinion in Colloid & Interface Sci., 8 (2003) 23–31.

De Leeuw N.H., Parker S.C., Surface structure and morphology of calcium carbonate polymorphs calcite, aragonite, and vaterite: an atomistic approach, J. Phys. Chem. B., 102 (1998) 2914–2922.

Dickinson S.R., Henderson G.E., McGrath K.M., Controlling the kinetic versus thermodynamic crystallisation of calcium carbonate, J. Cryst. Growth, 244 (2002) 369–378.

Dickinson S.R., McGrath K.M., Switching between kinetic and thermodynamic control: calcium carbonate growth in the presence of a simple alcohol, J. Mater. Chem., 13 (2003) 928–933.

Heywood B.R., Rajam S., Mann S., Oriented crystallization of $CaCO_3$ under compressed monolayers. Part 2.—Morphology, structure and growth of immature crystals, J. Chem. Soc. Faraday Trans., 87 (1991) 735–743.

Jung W.M., Kang S.H., Kim W., Choi C.K., Particle morphology of calcium carbonate precipitated by gas-liquid reaction in a Couette-Taylor reactor, Chem. Eng. Sci., 55 (2000) 733–747.

Lee I., Han S.W., Choi H.J., Kim K., Nanoparticle-directed crystallization of calcium carbonate, Adv. Mater., 13 (2001) 1617–1620.

Mann S., Heywood B.R., Rajam S., Walker J.B.A., Structural and stereochemical relationships between Langmuir monolayers and calcium carbonate nucleation, J. Phys. D: Appl. Phys., 24 (1991) 154–164.

McCauley J.W., Roy R., Controlled nucleation and crystal growth of various $CaCO_3$ phases by the silica gel technique, American Mineralogist, 59 (1974) 947–963.

Meldrum F.C., Calcium carbonate in biomineralisation and biomimetic chemistry, International Materials Review, 48 (2003) 187–223.

Osman M.A., Suter U.W., Surface treatment of calcite with fatty acids: structure and properties of the organic monolayer, Chem. Mater., 14 (2002) 4408–4415.

Park R.J., Meldrum F.C., Synthesis of single crystals of calcite with complex morphologies, Adv. Mater., 14 (2002) 1167–1169.

Rajam S., Heywood B.R., Walker J.B.A., Mann S., Davey R.J., Birchall D.B., Oriented crystallization of $CaCO_3$ under compressed monolayers. Part 1.—Morphological studies of mature crystals, J. Chem. Soc. Faraday Trans., 87 (1991) 727–734.

Ralston A.W., Hoerr C.W., Hoffman E.J., Studies on high molecular weight aliphatic amines and their salts. VII. The systems octylamine-, dodecylamine- and octadecylamine-water, J. Am. Chem. Soc., 64 (1942) 1516–1523.

Rock M.L., Tranchitella L.J., Pilato R.S., Control of calcium carbonate particle size and shape by precipitation from CTAB/alcohol/hexadecane mixtures, Colloid & Polymer Sci., 275 (1997) 893–896.

Rudloff J., Colfen H., Superstructures of temporarily stabilized nanocrystalline $CaCO_3$ particles: morphological control via water surface tension variation, Langmuir, 20 (2004) 991–996.

Rutt H.N., Nicola J.H., Raman spectra of carbonates of calcite structure, J. Phys. C: Solid State Phys., 7 (1974) 4522–4528.

Shitole S.J., Saraf K.B., Growth, Structural and microtopographical studies of calcium iodate, monohydrate crystals grown in silica gel, Cryst. Res. & Tech., 37 (2002) 440–452.

Stucky G.D., Macdougall J.E., Quantum confinement and host/guest chemistry: probing a new dimension, Science, 247 (1990) 669–678.

Sunagawa I., Morphology of Crystals, Part B, Terra Scientific Publishing, Tokyo, 1987.

Walker J.B.A., Heywood B.R., Mann S., Oriented nucleation of $CaCO_3$ from metastable solutions under Langmuir monolayers, J. Mater. Chem., 1 (1991) 889–890.

Walsh D., Lebeau B., Mann S., Morphosynthesis of calcium carbonate (vaterite) microsponges, Adv. Mater., 11 (1999) 324–328.

Wang J., White W.B., Adair J.H., High surface area microporous tabular SiO_2 nanoparticles synthesized from octylamine/water bilayer systems, Colloids and Surfaces A., 286 (2006) 27–32.

Wang L., Sondi I., Matijevic E., Preparation of uniform needle-like aragonite particles by homogeneous precipitation, J. Colloid Interface Sci., 218 (1999) 545–553.

Wei H., Shen Q., Zhao Y., Zhou Y., Wang D., Xu D., Effect of anionic surfactant-polymer complexes on the crystallization of calcium carbonate, J. Cryst. Growth, 264 (2004) 424–429.

Xu A.W., Yu Q., Dong W.F., Antonietti M., Colfen H., Stable amorphous $CaCO_3$ microparticles with hollow spherical superstructures stabilized by phytic acid, Adv. Mater., 17 (2005) 2217–2221.

Yener D.O., Sindel J., Randall C.A., Adair J.H., Synthesis of nanosized silver platelets in octylamine-water bilayer systems, Langmuir, 18 (2002) 8692–8699.

Author's short biography

Jun Wang

Jun Wang started his professional career with Saint-Gobain Northboro R&D center in 2004 prior to joining A123 Systems in 2011, where he is currently senior development engineer in the innovations solutions group. Dr. Wang holds a BS degree from University of Science and Technology of China, a MS from Shanghai Institute of Ceramics and a Ph.D. in material science from Penn State University. His research interests include novel nanoparticle synthesis and dispersion, nanoabrasives for chemical mechanical planarization and nanomaterials for energy storage. Dr. Wang has published over 30 research papers and 4 patents.

William B. White

William B. White is professor emeritus of geochemistry in the Department of Geosciences and the Materials Research Institute at the Pennsylvania State University. He holds a BS degree in chemistry from Juniata College (Huntingdon, PA, USA) and a Ph.D. in geochemistry from Penn State. He joined the Penn State faculty in 1962 and remained there until his retirement in 2002. Dr. White has wide-ranging research interests in materials synthesis, crystal chemistry, glass science, phosphor materials, mineralogy, and hydrogeology. He has published more than 400 research papers and 13 books.

James H. Adair

James H. Adair is a Professor in Materials Science and Engineering, Bioengineering and Pharmacology at Penn State University. His research and teaching interests include biological-nanoscale composite particulates for nanomedical applications, colloid and interfacial chemistry, material chemistry, particle synthesis and characterization, and ceramic and metal particulate processing. Dr. Adair is the author or co-author of over 240 publications, thirteen patents, several copyrights on computer software and co-editor of ten books.

KONA Powder and Particle Journal No. 31 (2014) 163–170/Doi:10.14356/kona.2014007 Original Research Paper

Development of a Particulate Solids Thermal Mass Flowmeter †

Mary Kato, John Pugh and Don McGlinchey *

[1] *Glasgow Caledonian University, UK*

Abstract

An ideal mass flow meter should have the following properties: it should be non-invasive so as not to disrupt the flow profile; it should be easily installed on the conveying line to provide on-line and continuous measurements; it should be able to provide an accurate indication of the mass flow rate regardless of the orientation of the measurement section, inhomogeneities in the solids' distribution, irregularities in the velocity profile, or variations in particle size, moisture content and material properties.

A mass flow meter as described in this paper has been developed which uses a thermal method, a direct, non-invasive approach to measuring the mass flow rate. The thermal method uses the principle of heat transfer to solid particles in a flowing fluid to determine the mass flow rate of particles. The mass flow meter is designed such that temperature sensors are located at two ends of a heated pipe section. In the experiments carried out, measurements of gas and solids' temperature were taken and used to calculate the heat transferred to the solids. The mass flow rate obtained using the thermal mass flow meter was compared to that using load cells. The results obtained are analysed and presented in this paper.

Keywords: gas-solids, pneumatic conveying, heat transfer, thermal mass flow meter

Introduction

Pneumatic conveying has proven to be an efficient and useful method for applications requiring the transportation of bulk solids within processing plants. The process is completely enclosed, using pipes and vessels where the solids are stored. The transporting gas, usually air, is released through a filter at the end of the process. This ensures there is no release of solids into the environment, making it a clean and safe procedure. Another advantage of this process is the fact that the air used as a transporting gas is readily available and does not react with the solids being conveyed. In situations where the use of air is inappropriate, a non-reacting gas such as nitrogen can be used. In various processing plants where pneumatic conveying is employed, the conveying pipes can be constructed in such a way that they span several kilometres and can be installed in a variety of ways, vertically and horizontally. This means any number of plant configurations can make use of the method including multi-storey buildings, or plants with different sections located at a distance from each other.

In pneumatic conveying plants, as in any other system, optimal control of the processes is achieved by monitoring the parameters within the system. A prerequisite is knowledge of the pressures, temperatures, velocities of gas and solids, the volume of solids within the gas, and the mass flow rate of solids being conveyed. The measurement of the mass flow rate of solids on-line presents quite a number of difficulties. One method of determining the quantity of solids being conveyed is to use a "gain-in-weight" or "loss-in-weight" system where the mass of solids is measured using load cells located at the feed or receiving vessel, respectively. This method is unable to determine the amount of solids passing through a conveying pipe at a given period or position on the line, and is more suitable for batch systems than for continuous flow systems where the mass flow rate is required as the product is being conveyed. The advantage of measuring mass flow rate on-line is the possibility of detecting problems within the conveying line as they occur, for instance a reduction in the mass flow rate along the line may suggest a pipe blockage or solids deposition beginning to occur somewhere along the line. Therefore the possibility of having a device which can determine the mass of solids at any given time during a process is quite attractive.

Research has been ongoing for a number of years towards the development of an "ideal" mass flow meter. For a mass flow meter to be described as ideal it should have the following properties: it should be non-invasive so as not to disrupt the flow profile; it should be easily

† Accepted: June 26, 2013

[1] 70 Cowcaddens Road, Glasgow, G4 0BA, United Kingdom

* Corresponding author:
E-mail: d.mcglinchey@gcu.ac.uk
TEL: +44-14-1331-3713

installed on the conveying line to provide on-line and continuous measurements; it should be able to provide a reliable and accurate indication of the mass flow rate regardless of the orientation of the measurement section, inhomogeneities in the solids' distribution, irregularities in the velocity profile, or variations in the particle size, moisture content and material properties (Yan, 1996; Arakaki et al., 2006). Finding all of these properties in one single instrument has not been achieved yet, but research is still ongoing.

The mass flow rate can be measured in two basic ways, directly or inferentially. A direct mass flow meter is one whose sensing element responds to the mass flow rate of solids passing through it, while an inferential mass flow meter obtains the mass flow rate from a calculation of velocity and concentration of solids measured by its sensor (Yan, 1996; Beck et al., 1987). A variety of methods exist for the measurement of solids' concentration and velocity using the inferential method (Carter et al., 2005; Arko et al., 1999; Hrach et al., 2008; Huang et al., 2001), as this has proved to be more easily achievable than obtaining a direct measurement of the mass flow rate. Certain limitations experienced with the use of inferential methods have been presented in the review paper of Zheng and Liu (2010).

The thermal mass flowmeter

The thermal method of mass flow rate measurement uses the principle of heat transfer to solid particles in a flowing fluid-solid mixture to determine the mass flow rate of particles. Two approaches are used; the first involves a measurement of temperature difference at sensors located before and after a heated region with a constant heat supplied to the system, while in the second method, a constant temperature difference is maintained within the heated region and the heat required to maintain this difference is measured (Zheng and Liu, 2011; Yan, 1996). The mass flow rate is deduced from the relationship between the rate of heat transferred, the measured temperatures, the heat transfer coefficient and the material's thermal conductivity. In his review of mass flow rate measurement methods, Yan (1996) stated that the problems with this method have been found to be poor repeatability of the instrument and a slow dynamic response time. Experiments conducted by Moriyama (1996) using three different measurement methods—cross-correlation, heat transfer and acoustic emission—showed the heat transfer method to have the highest time constant of the three methods. However, research is ongoing to develop the thermal method as it is non-intrusive and expected to provide reliable, on-line, continuous estimates of the mass flow rate. A thermal mass flow meter has been developed which is non-invasive and employs the use of infrared sensors for the temperature measurement of solids (Zheng et al., 2008).

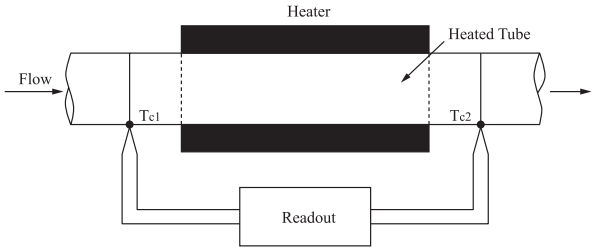

Fig. 1 A thermal mass flow meter (Yan, 1996).

Thermal mass flow meters have been developed commercially for use in the measurement of liquid and gas mass flow rates (Viswanathan et al., 2002a, 2002b; Han et al., 2005; Kim et al., 2007). A schematic diagram of a thermal mass flow meter is shown in **Fig. 1**.

Heat transfer to gas-solid systems

In a study carried out by Farber and Morley (1957), it was established that the addition of solid particles to a flowing gas increased heat transfer rates when compared to a single phase flow of gas. Using a suspension of air and alumina-silica particles, with carbon tetrachloride vapour as the heat transfer medium, the heat transfer processes occurring in the suspension were investigated. The authors observed an influence of the solids on the gas boundary layer and the heat capacity of the suspension. They concluded that for a constant gas flow rate, the ratio of the increase in the solids' temperature to the increase in gas temperature was a constant and independent of the solids' loading ratio, but increased with increasing gas flow rates or decreasing particle residence times. However, it is important to note that the solids' temperature increase was not a measured value, but was estimated by subtracting the enthalpy increase of the air from the net heat transferred, and dividing this quantity by the weight of the solids flowing and the specific heat of the solids (Farber and Morley, 1957).

The effect of particle size on heat transfer in a gas-solid mixture of air and spherical glass particles was investigated by Farber and Depew (1963). In their study, varying particle sizes of 30, 70, 140 and 200 microns were added to air flowing in a borosilicate glass tube. Using a vertically mounted tube, heat was transferred to the medium using carbon tetrachloride vapour as the heat transfer medium. The results showed a substantial increase in the gas-side heat transfer coefficient for the 30-micron particles, and no visible increase in the heat transfer coefficient for the 200-micron particles; showing that the heat transfer coefficient increased with decreasing particle size. This effect was explained as being due to the fact that increasing solids' sizes prolonged the thermal entry

length, with larger particle sizes having a longer thermal entry length approaching the tube length, therefore the thermal boundary layer was not fully developed within the tube length.

The heat transfer characteristics of a turbulent, dilute, air-solids suspension flow was studied using a uniformly heated pipe and glass beads (Aihara et al., 1997). Measurements of the bulk air-solid suspension temperatures were made using thermocouples at a region stated to be hydrodynamically and thermally fully developed. The results of the Nusselt number showed a dependence on the solids' loading ratio as well as the air flow rates. A decrease in the Nusselt number was observed upon addition of the glass beads to the air flow; however, after reaching a minimum at a critical loading ratio, it began to increase with increasing solid loading ratios.

This effect was also observed by Rajan et al. (2008). Gas-to-particle heat transfer coefficients decreased with solids' feed rate at lower solids' feed rates typical of dilute flow regimes or fast fluidization regimes in packed beds. The same was found to increase with increasing solid feed rates as dense flow regime was approached. Experiments were carried out in a pneumatic conveying test rig consisting of a galvanized iron duct of 54 mm inner diameter and 2.2 m height, fitted with 3 heaters of 5 kW heating capacity. Gypsum was used as the solid medium and hot air as the gas medium (Rajan et al., 2008). Results showed an increase in the air-solid heat transfer coefficient with increasing air velocity in the range between 4.3 m/s and 5.8 m/s; this reached a maximum before decreasing with a further increase in air velocity of about 6.3 m/s. Thermal conductance, defined as the ratio of the heat transfer rate to driving force, was found to increase with solids' feed rate and air velocity (Rajan et al., 2010).

Previous work

Research is ongoing at the Centre for Industrial Bulk Solids Handling in Glasgow on the development of a thermal instrument for solids' mass flow rate measurement. The instrument is made up of a 1-m long pipeline section which is referred to as the heated section. Thermocouples are located upstream and downstream of this section for measurement of the gas temperatures, while infrared sensors are located at similar locations for measurement of the solids' temperatures. The pipe surface temperature is measured using a thermocouple. The heat transferred to the system is controlled within a set band, giving a pulsed heat signal in which the heater is turned off when the pipe wall temperature is above a fixed point, and then turned on when the temperature falls below a fixed value. The instrument described is shown schematically below.

The operation of a thermal mass flow meter is based on the principle of heat transfer to a medium; in this case a mixture of solids in air. To provide an understanding of this, a study was carried out on the heat transfer mechanisms to solids flow. Zheng et al. (2008) reports the results of a numerical analysis and experimental studies carried out to analyse the heat transferred to a flowing gas from the heated wall, and then from the heated gas to a single particle passing through the region. This study proposed that the heat generated was transferred along the pipe wall axially and radially by conduction, and then from the pipe wall to the gas and then to the solid particle by convection.

In another study, the heat transfer coefficient from a heated wall to a gas-particulate plug flow was investigated experimentally and numerically (Zheng et al., 2007). The results showed that the heat transfer coefficient increased approximately linearly with the solids' loading ratio, this being consistent with Zheng et al.'s hypothesis that a higher solids loading provides more carriers for heat

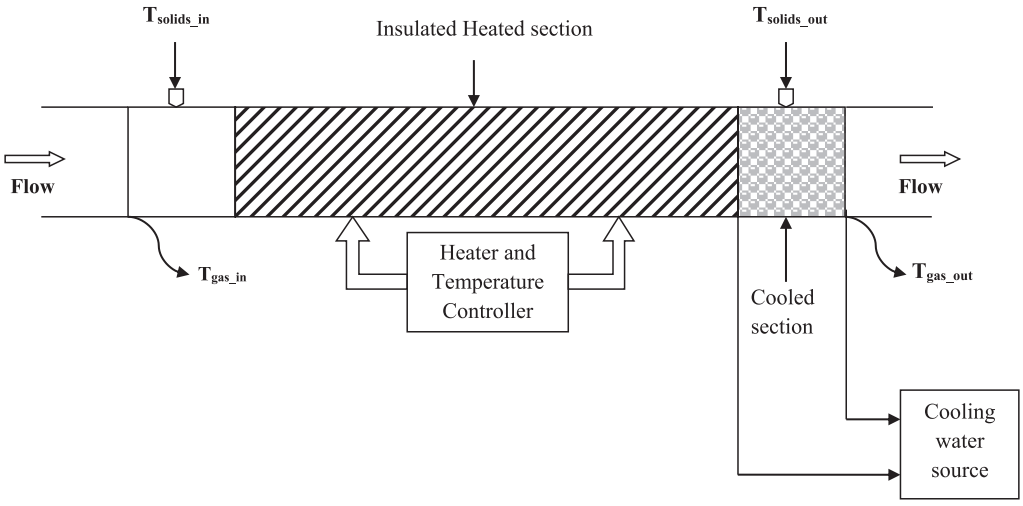

Fig. 2 Schematic diagram of the thermal mass flow meter.

transfer.

The operation of the thermal mass flow meter was further investigated with experiments conducted under dilute phase flow conditions, conveying ordinary Portland cement on an industrial-scale pneumatic rig (McGlinchey et al., 2010; McGlinchey et al., 2013). Using an energy balance approach between the heat entering the system and the heat taken by the gas-particulate mixture, a measure of the mass flow rate was obtained which was then compared to measurements obtained from load cells. The results showed good agreement between the thermal mass flow meter and the load cells; however, some important observations were made. The analysis showed that the temperature of solids being measured by the infrared sensors was affected by the ambient temperature around the sensor (Kato et al., 2012). Therefore a method to control the infrared sensor temperature was developed using cooling water which was passed through a copper pipe coiled around the steel conveying line.

The following section describes further measurements carried out on the industrial-scale pneumatic conveying rig as a means to further understand the principle of operation of the thermal mass flow meter under development.

Experimental procedure

A schematic diagram of the experimental rig used is shown in **Fig. 3**.

The experimental system is the same as that described in a previous publication (McGlinchey et al., 2013). The pipeline is of mild steel nominal bore 50 mm, with a total length of about 50 m, of which 5 m is vertically up, the remainder in the horizontal plane, and included five 90-degree standard radius bends. The measurement system as shown in **Fig. 2** was positioned at least 5 m from any bend. Ordinary Portland cement with a mean particle size of 25 mm was conveyed in a range of dilute phase conditions with mass flow rates of air ranging from 0.4 kg/s to 0.14 kg/s and solid loading ratios in the range 4 to 136. The thermal properties of ordinary Portland cement are listed in **Table 1**. The mass flow rate of solids used to compare the results from the thermal instrument was obtained from load cells at the receiving vessel.

The experimental procedure was as follows. Compressed air was supplied to the test rig via the pressure control valve PRV1 shown in **Fig. 2**. The gas mass flow rate at the outset was determined using a combination of a

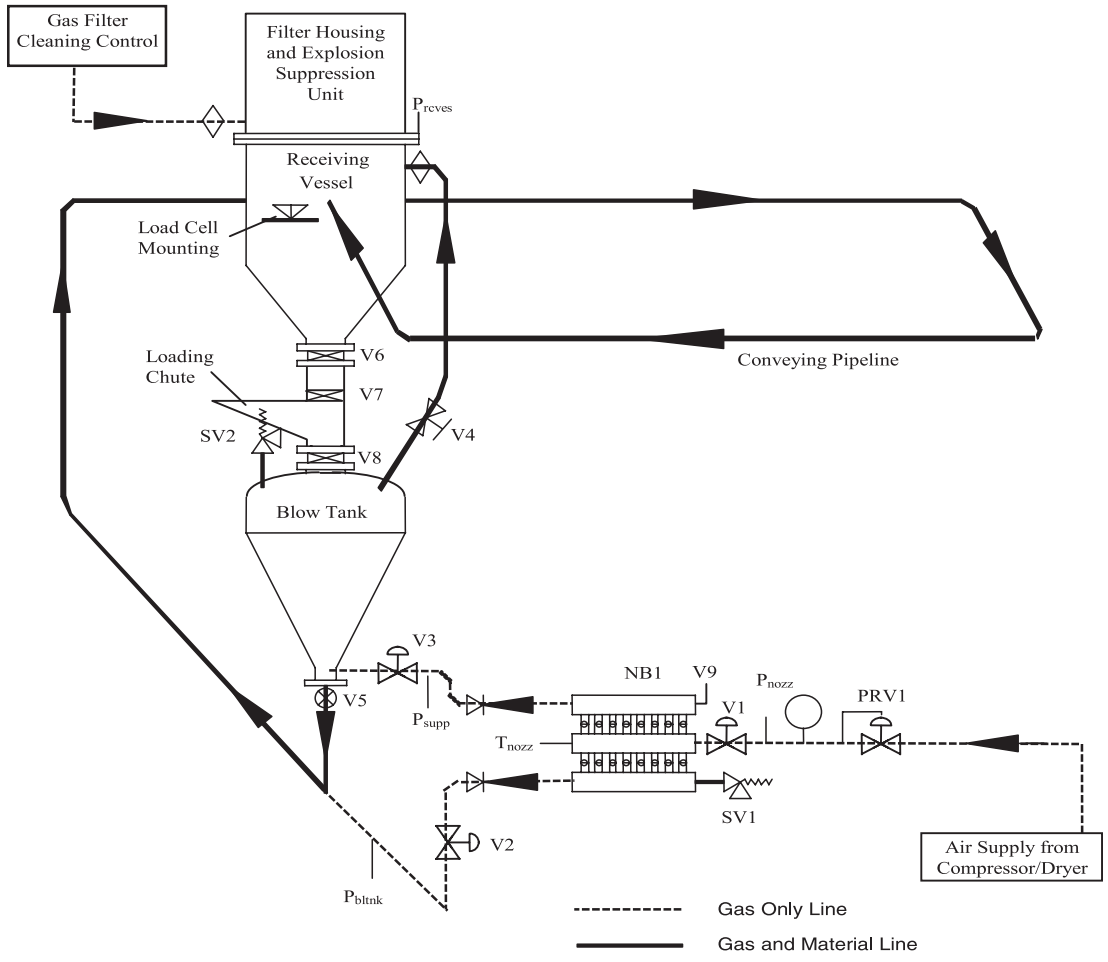

Fig. 3 Schematic diagram of industrial-scale test rig.

Table 1 Properties of Granular Material

Properties of Ordinary Portland Cement	
Particle size	25 mm
Density	1500 kg/m^3
Thermal conductivity	0.29 W/mK
Specific heat capacity	0.84 kJ/kgK

Source: Holman, 2010

number of nozzles to achieve the required flow rate. Once the gas flow rate had been established, the measurement and data acquisition system was turned on. A program developed using LabVIEW and the National Instruments DAQ system was used to control the heater to maintain the pipe wall temperature within a fixed band. After the system had reached a stable condition, solids were inserted into the conveying line from the blow tank. A record of the temperatures of the pipe wall, the gas and solids was acquired, as well as the pressure drop within the system and the mass of solids obtained from load cells located at the receiving vessel.

Results and analysis

The amount of heat transferred to a system is defined as a product of the mass of the system, its specific heat capacity and the difference in temperatures measured before and after heat is transferred. The heat transferred to a gas-solid suspension is a function of the specific heat capacity of the suspension, the temperature difference and also the mass flow rate of the suspension.

Using the energy balance method (McGlinchey et al., 2013), the following equation was used to calculate a factor corresponding to the mass flow rate of solids measured by the thermal instrument. The rate at which heat is transferred to the system is given by:

$$Q = \dot{E}_{\text{in}} + S_{\text{heater}} m_{\text{heater}} \frac{\Delta T_{\text{heater}}}{\Delta t} \tag{1}$$

and the rate at which heat is taken up by the gas-solids suspension is given by:

$$Q = S_{\text{susp}} \frac{m_{\text{susp}}}{\Delta t} \Delta T_{\text{susp}} \tag{2}$$

where $\dot{E}_{in}$ is the energy supplied to the heating system.

At a time when the electrical input to the heater is off ($\dot{E}_{\text{in}} = 0$) and the pipe wall temperature change is approximately linear with time, and if we assume the specific heats of the heater and the suspension to be relatively constant, the mass flow rate of the suspension can be obtained by equating (1) and (2) and rearranging the result to give:

$$\dot{m}_{\text{susp}} = Const * \frac{\Delta T_{\text{heater}} / \Delta t}{\Delta T_{\text{susp}}} \tag{3}$$

where the constant value is given by:

$$Const = \frac{S_{\text{heater}} m_{\text{heater}}}{S_{\text{susp}}} \tag{4}$$

Assuming a value of –1 kgs for the constant (so that the results can be viewed in the positive graph axes), the following results were obtained for tests carried out over a range of air mass flow rates and varying solid loading ratios. Results shown have been made dimensionless by dividing by corresponding air mass flow rates.

The results above show the thermal instrument's response to varying air flow rates and solid loading ratios. The mass flow rate factor from the thermal instrument was obtained using **Eqn. 3**. The graph shows three distinctive regions: Region 1, where an approximately linear relationship can be observed between the thermal instrument and the load cells; Region 2, where a very low solids' temperature difference causes the measured mass flow rate to be uncharacteristically high for the given solids' loading; and Region 3, where we can observe a gradual approach to dense phase flow conditions.

This factor obtained from the thermal instrument is dependent on the change in wall surface temperature with time, as well as the heat taken in by the solids which is measured by the infrared sensors, assuming the specific heats of the heater and the suspension remain constant. According to the equation, a high mass flow rate is recorded by the thermal instrument when the change in wall temperature with time is high. This gradient should increase with increasing air mass flow rates. In addition to this, if the heat taken in by the solids as measured by the temperature difference is a low value, then a high mass flow rate should also be observed. An increasing solids' loading ratio will reduce the relative air mass flow rate influence and hence the temperature gradient per time at the wall for a given test, however, this does not fully explain the observed results. This may be due to the measurement method of the infrared sensors. For accurate temperature measurement of moving solids using an infrared sensor, it is necessary for the solids to completely fill the viewing window of the sensor. At low solids loading ratios, it is possible that this requirement is not met, and therefore the results obtained in this range are being affected by the temperature of the inner pipe wall. See **Fig. 4**, Region 2. At high solids loading ratios the measurement may be biased to detection of a solids fraction in non-suspension mode which would be hotter than a bulk temperature. See **Fig. 4**, Region 3.

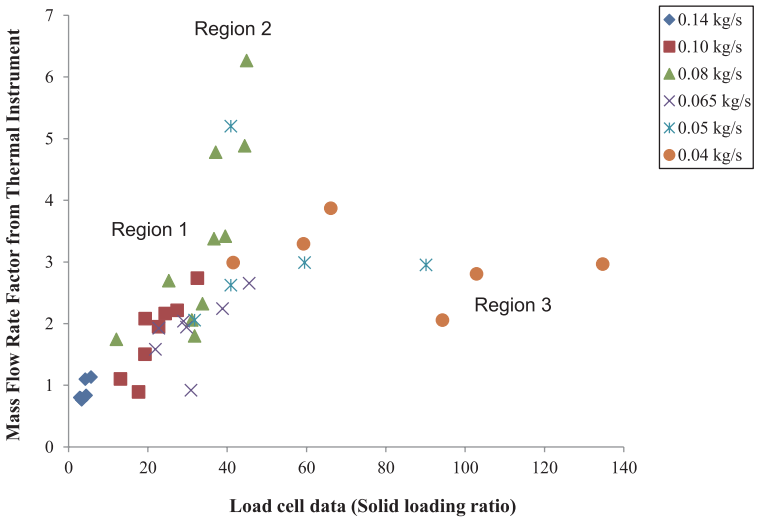

Fig. 4 Results obtained for the mass flow rates of solids using the thermal instrument. The legend shows the different air mass flow rates used.

Conclusions

Investigation of the operation of a thermal mass flow meter was carried out by analysing tests performed on a pneumatic conveying rig with air flow rates between 0.04 kg/s to 0.14 kg/s, and solid loading ratios in the range 4 to 136. Results have shown a dependency of the mass flow rate measurements on the solid loading ratio. The thermal mass flow meter shows promise as a direct mass flow rate measurement instrument. Further tests and investigations are ongoing to characterise the operation of the mass flow meter.

Nomenclature

$\dot{E}_{in}$	electrical input rate to heater (W)
m_{heater}	mass of heater (kg)
m_{susp}	mass of gas-solids suspension (kg)
$\dot{m}_{susp}$	mass flow rate of gas-solids suspension (kg/s)
Q	heat energy rate (W)
S_{heater}	specific heat capacity of heater (J/kgK)
S_{susp}	specific heat capacity of gas-solids suspension (J/kgK)
Δt	change in time (s)
ΔT_{heater}	change in temperature of heated wall (K)
ΔT_{susp}	change in temperature of gas-solids suspension (K)

References

Aihara T., Yamamoto K., Narusawa K., Haraguchi T., Ukaku M., Lasek A., Feuillenois F., Experimental study on heat transfer of thermally developing and developed, turbulent, horizontal pipe flow of dilute air-solids suspensions, Heat and Mass Transfer, 33 (1997) 109–120.

Arakaki C., Ghaderi A., Datta B.K., Lie B., Non-intrusive mass flow measurements in pneumatic transport, CHoPS-05, Proceedings, 5th International Conference for Conveying and Handling of Particulate Solids, Sorrento, Italy, 2006.

Arko A., Waterfall R.C., Beck M.S., Dyakowski T., Sutcliffe P., Byars M., Development of Electrical Capacitance Tomography for solids mass flow measurement and control of pneumatic conveying systems, Proceedings, 1st World Congress on Industrial Process Tomography, Buxton, Greater Manchester, 1999.

Beck M.S., Green R.G., Thorn R., Non-intrusive measurement of solids mass flow in Pneumatic Conveying, Journal of Physics E: Scientific Instruments, 20 (1987) 835–840.

Carter R.M., Yan Y., Cameron S.D., On-line measurement of particle size distribution and mass flow rate of particles in a pneumatic suspension using combined imaging and electrostatic sensors, Journal of Flow, Measurement & Instrumentation, 16 (2005) 309–314.

Farber L., Depew C.A., Heat transfer effects to gas-solids mixtures using solid spherical particles of uniform size, Industrial & Engineering Chemistry Fundamentals, 2 (1963) 130–135.

Farber L., Morley M.J., Heat transfer to flowing gas-solids mixtures in a circular tube, Industrial & Engineering Chemistry, 49 (1957) 1143–1150.

Han I.Y., Kim D-K., Kim, S.J., Study on the transient characteristics of the sensor tube of a thermal mass flow meter, Int'l Journal of Heat & Mass Transfer, 48 (2005) 2583–2592.

Holman J.P., Heat Transfer, tenth ed., McGraw-Hill Inc., 2010.

Hrach D., Fuchs A., Zangl H., Capacitive flow meter for gas-solids flow applications exploiting spatial frequency, Proceedings, IEEE Sensors Application Symposium, Atlanta GA, 2008.

Huang Z., Wang B., Li H., An intelligent measurement system for powder flow rate measurement in pneumatic conveying system, Proceedings, IEEE Instrum. & Meas. Tech. Conference, Budapest, Hungary, 2001.

Kato M., Pugh J.R., McGlinchey D., The influence of windows on infra-red temperature measurements for solids' mass flow rate determination, Journal of Flow, Measurement & Instrumentation, 27 (2012) 99–103.

Kim D-K., Han I.Y., Kim S.J., Study on the steady-state characteristics of the sensor tube of a thermal mass flow meter, Int'l Journal of Heat & Mass Transfer, 50 (2007) 1206–1211.

McGlinchey D., Pugh J.R., Knight E.A., Kumaraperumal A., Samaila I., Ibn Mohammed T., Operation of a novel Industrial Scale Thermal Solids Mass Flow meter, Bulk Europe 2010 & IMechE Symposium New Frontiers in Bulk Materials Handling, Glasgow, Scotland, 2010.

McGlinchey D., Pugh J., Knight L., Cowell A., Zheng L., Liu Q., Analysis and measurements from a prototype in-line thermal solids mass flow meter in an industrial scale dilute phase pneumatic conveying system, Particulate Science & Technology, 31 (2013) 271–276.

Moriyama T., Non-intrusive measuring methods on mass flow rate for moved bed gravity flow of the new plants, Proceedings, IEEE Instrum. & Meas. Tech. Conference, Brussels, Belgium, 1996.

Rajan K.S., Srivastava S.N., Pitchumani B., Dhasandhan K., Experimental study of thermal effectiveness in pneumatic conveying heat exchanger, Applied Thermal Engineering, 28 (2008) 1932–1941.

Rajan K.S., Srivastava S.N., Pitchumani B., Surendivan V., Thermal conductance of pneumatic conveying preheater for air-gypsum and air-sand heat transfer, Int'l Journal of Thermal Sciences, 49 (2010) 182–186.

Viswanathan M., Kandaswamy A., Sreekala S.K., Sajna K.V., Development, modelling and certain investigations on thermal mass flow meters, Journal of Flow, Measurement & Instrumentation, 12 (2002a) 353–360.

Viswanathan M., Rajesh R., Kandaswamy A., Design and development of thermal mass flow meters for high pressure applications, Journal of Flow, Measurement & Instrumentation, 13 (2002b) 95–102.

Yan Y., Mass flow measurement of bulk solids in pneumatic pipelines, Measurement, Science & Technology, 7 (1996) 1687–1706.

Zheng Y., Li Y., Liu Q., Measurement of mass flow rate of particulate solids in gravity chute conveyor based on laser sensing array, Optics & Laser Tech., 39 (2007) 298–305.

Zheng Y., Pugh J.R., McGlinchey D., Ansell R.O., Simulation and experimental study of gas-to-particle heat transfer for non-invasive mass flow measurement, Measurement, 41 (2008) 446–454.

Zheng Y., Liu Q., Review of certain key issues in indirect measurements of the mass flow rate of solids in pneumatic conveying pipelines, Measurement, 43 (2010) 727–734.

Zheng Y., Liu Q., Review of techniques for the mass flow rate measurement of pneumatically conveyed solids, Measurement, 44 (2011) 589–604.

Author's short biography

Mary Kato

Mary Kato is a research student at Glasgow Caledonian University, working with the Centre for Industrial Bulk Solids Handling where she is investigating heat transfer in particulate systems at the PhD research level. With a background in chemical engineering, she proceeded to study applied instrumentation & control and completed an MSc. She has published works on the influence of windows on infra-red temperature measurement towards the development of a thermal mass flow meter.

John Pugh

John Pugh is a professor at Glasgow Caledonian University. He has pursued an interest in instrumentation and measurement for over thirty five years—with at least twenty years in the area of instrumentation for bulk solids handling. Current research work is on the development of solids' two-phase mass flow measurement, and he also maintains an interest in industrial weighing. He is vice-president (Learned Society matters) of the Institute of Measurement and Control in the UK, and chair of the institute's Learned Society Board. He has published over eighty papers and conference proceedings—around 30 in the area of solids handling.

Don Mcglinchey

Professor Don McGlinchey is the head of the Centre for Industrial Bulk Solids Handling at GCU. He is an academic of international standing in the particulate solids handling community. He has undertaken consultancy projects for both multinational companies and small to medium enterprises, and has delivered short courses in Sweden, USA and the UK. Don has also presented at international academic conferences in China, India and Europe. He is a chartered physicist with a PhD on the subject of the effect of vibration on particulate materials. Don is the editor of two books and has authored over 50 research articles.

KONA Powder and Particle Journal No. 31 (2014) 171–180/Doi:10.14356/kona.2014008 Original Research Paper

The use of Highly Ionized Pulsed Plasmas for the Synthesis of Advanced Thin Films and Nanoparticles†

Iris Pilch [1]*, Daniel Söderström [1], Daniel Lundin [2] and Ulf Helmersson [1]

[1] *Plasma & Coatings Physics Division, Department of Physics, Chemistry and Biology (IFM), Sweden*
[2] *Ionautics AB, Sweden*

Abstract

Pulsed plasma processes open up the possibility of using very high plasma densities and modulated deposition in the synthesis of thin films and nanoparticles. The high plasma densities lead to a high degree of ionization of the source material, which creates new possibilities for surface engineering. Ions can, in contrast to atoms, be easily controlled with regard to their energy and direction, which is beneficial for thin film growth. Furthermore, ions can also increase the trapping probability of material on nanoparticles growing in the gas phase. The pulsed sputter ejection of source material also has other consequences: the material in the plasma and the material arrival on the growth surface will fluctuate strongly resulting in high level of supersaturation during pulse-on time. In this paper, an overview of the generation and properties of highly ionized pulsed plasmas is given. In addition, the use and importance of these types of discharges in the fields of thin-film and nanoparticle growth are also summarized.

Keywords: HiPIMS, HPPMS, IPVD, sputtering, thin films, nanoparticle synthesis

1. Introduction

The processing of materials and surfaces is today very important in many industrial branches. This includes thin-film deposition to functionalize surfaces with different properties such as wear resistance, color changes, corrosive protection, catalytic behavior, or electrical and optical properties. The properties of thin films can further be improved by, for instance, the incorporation of nanoparticles in solar cell applications (Atwater and Polman, 2010). Nanoparticles are also of great interest in catalysis (Cuenya, 2010) due to their large surface-to-volume ratio or plasmonics (Garcia, 2011), where the plasmon frequency is a function of the size of the nanoparticle.

For fabricating thin films or nanoparticles, the material that condenses onto the surface or into nanoparticles can be provided by different means—e.g. thermic evaporation, arc evaporation or pulsed laser evaporation. Another method is to utilize a plasma discharge where the vapor is removed from a target (source) by sputtering the material, which is the focus of the present article. A plasma consists of ions, electrons and neutral atoms. Plasmas used for material processing typically have a low ionization degree, which is the fraction of the density of ions to the sum of the ion and neutral density. The target material is sputtered by ions that collide with the surface, which leads to the removal of surface atoms. The sputtered material is subsequently transported out into the bulk plasma and eventually condenses on all surfaces. For thin-film deposition, a magnetic field configuration is commonly used in a way that the plasma is confined in front of the target to enhance the sputtering process (Window and Savvides, 1986). This technique is called magnetron sputtering.

For improving the properties and structure of deposited thin films, one needs to control, for instance, the energy and the deposition rate of atoms and ions that condense on the substrate (coated object). The motion of sputtered atoms is governed by ballistic transport as well as diffusion, but ions can be manipulated by electric or magnetic fields, which allow the energy of the ions reaching the substrate surface to be tailored. It is therefore desirable to have a high ionization degree of the vapor material. A way of increasing the ionization degree is to increase the plasma density, which can be achieved by increasing the power supplied to the sputter target. The maximum average power possible is defined by the melting temperature and heat conductivity of the target material. Very high plasma densities can be achieved—without exceeding the maximum average power—by supplying the power in short, high-power pulses with a low duty factor. A

† Accepted: July 1, 2013
[1] SE-581 83 Linköping, Sweden
[2] Linköping, Sweden
* Corresponding author:
E-mail: iripi@ifm.liu.se
TEL: +46-13-286617

technique that utilizes this approach to reach very high ionization degrees of the sputtered material is high-power impulse magnetron sputtering (HiPIMS) (Kouznetsov et al., 1999, Lundin and Sarakinos, 2012).

The same approach has also recently been applied to synthesize nanoparticles (Pilch et al., 2013). A high ionization degree is beneficial because the collection probability of the sputtered material—i.e. ions and atoms—on a nanoparticle is a function of the collection cross-section. For atoms, the cross-section is given by the geometric cross-section of the nanoparticle but for ions, the collection cross-section can be much larger. The reason for this is that nanoparticles attain a negative charge which is defined by the equilibrium of electron and ion currents to the nanoparticle (floating condition), and this increases the ion flux of positively charged ions onto the nanoparticle. Two consequences follow in the case of negatively charged nanoparticles. First, the collection probability of positively charged ions becomes larger than the collection probability of atoms and this leads to a faster growth, which is the reason of having a plasma with a high ionization degree. Second, the agglomeration of nanoparticles in the gas phase is inherently prevented when the nanoparticles are negatively charged.

In this contribution, results from both the deposition of thin film and the synthesis of nanoparticles using high-power pulses are presented. In Section 2 an overview on the pulsed plasma is given. Thin-film deposition and its applications using HiPIMS is presented in Section 3, and details on nanoparticles using a pulsed hollow cathode are presented in Section 4. A summary of the article is given in Section 5.

2. Pulsed plasmas

2.1. High-power pulsed plasmas

There are many methods for pulsed plasma processing and it is therefore appropriate to briefly discuss the most common techniques. We will thereby come to understand what distinguishes high-power pulsed plasmas (HiPP), discussed in the present article, from other types of pulsed plasmas.

The introduction of pulsed magnetron sputtering in the mid-90s boosted the deposition of dielectrics such as alumina, titania and silica (Kelly and Bradley, 2009). The reason is that DC discharges applied to cathodes using source materials with poor conductivity charge up the cathode surface positively during the discharge. This is due to the loss of electrons as the bombarding ions are neutralized at the cathode, and thus eventually extinguish the discharge or generate detrimental arc discharges. With the use of AC discharges, it is possible to neutralize the positive charge accumulated during one half-cycle by electron bombardment during the following half-cycle (Chapman, 1980). The most common operation constitutes asymmetric bipolar discharges, where the voltage $U_d(t)$ during pulse-off is reversed (positive) to approximately 10% or less of the magnitude of $U_d(t)$ during pulse-on at frequencies in the range 20–350 kHz and a duty cycle of about 50% (Kelly and Bradley, 2009). The technique is often referred to as mid-frequency pulsed DC sputtering.

Another pulsed sputtering technique is radio frequency (RF) sputtering. Here, a high-frequency (13.56 MHz) power is applied to achieve sputtering of the target material. This will also allow sputtering of isolators. However, the deposition rates for sputtering dielectrics are typically lower compared to mid-frequency pulsed DC sputtering (Glöß et al., 2005).

In HiPP discharges, the power is applied to the cathode in unipolar pulses at a low duty factor (< 10%) and low frequency (< 10 kHz), leading to peak cathode power densities of the order of several kW cm^{-2} while keeping the average target power density low enough to avoid heat damage to the cathode. In many ways, HiPP processes are similar to the above-described pulsed DC discharges, but they operate at a lower duty factor and considerably higher instantaneous pulse power. This means that setting up a system is fairly straightforward in the sense that it only involves changing the power supply.

An early description of the HiPP technology for material processing was provided by Kouznetsov et al. in 1999, where they used magnetron sputtering for thin-film deposition. The technique has since been commonly referred to as high-power impulse magnetron sputtering (HiPIMS) or sometimes high-power pulsed magnetron sputtering (HPPMS). It is also in this domain where we find a more strict definition distinguishing this technique from other pulsed plasma processes (Anders, 2011): *HiPIMS is pulsed magnetron sputtering, where the peak power exceeds the time-averaged power by typically two orders of magnitude*. This is very different from what one finds in, for example DC, pulsed DC or RF discharges, and has a dramatic influence on the plasma characteristics and hence the sputtered material, as will become apparent in the next section.

Recently, HiPP technology using the same power supplies as in HiPIMS has been investigated in the case of hollow cathodes for plasma-enhanced chemical vapor deposition (PECVD) of thin films (Pedersen et al., 2012) as well as for nanoparticle synthesis (Pilch et al., 2013). The deposition of thin films and the synthesis of nanoparticles depend on the pulse parameters: frequency, pulse width, and current, as well as other process parameters, such as operating gas pressure. The principles behind the plasma generation remain the same. Finally, a typical discharge pulse is seen in **Fig. 1**.

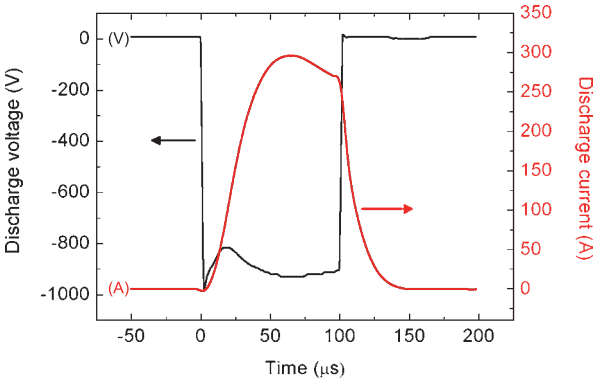

Fig. 1 A typical discharge voltage-current plot in a HiPIMS discharge. This discharge was generated using a 6" circular magnetron equipped with a Cu target operated at 1.33 Pa Ar pressure. The peak current density is about 1.6 A cm^{-2} and the peak power density is approximately 1.5 kW cm^{-2} averaged over the entire cathode area. The time-averaged power density is 5.5 W cm^{-2}.

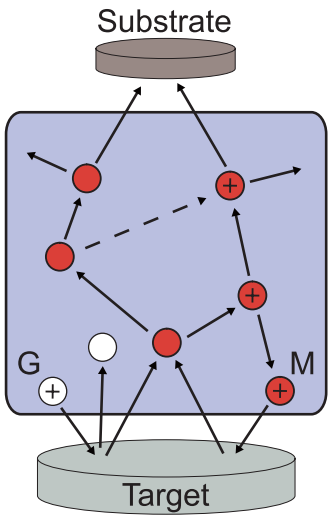

Fig. 2 Schematic of the sputtering process based on the target material pathway model by Christie (Christie, 2005). The letters G and M stand for gas and metal, respectively. Adapted from Lundin (Lundin, The HiPIMS process, 2010).

2.2. Pulsed plasmas for generating highly ionized material fluxes

In glow discharge processes such as magnetron sputtering, it is often difficult to achieve a large fraction of ionized sputtered material reaching the substrate (Christou and Barber, 2000, Rossnagel and Hopwood, 1994, Konstantinidis et al., 2004). When the deposition flux consists of more ions than neutrals, the process is referred to as ionized physical vapor deposition (PVD) or IPVD (Helmersson et al., 2006).

Commonly used IPVD techniques are inductively coupled discharges (ICP) where the plasma density is increased by inserting an antenna in the plasma and feeding it with RF-power (Hopwood, 2000), but also the industrially widespread method of cathodic arc evaporation (Johnson, 1991), which in some cases also operates in pulsed mode (Rosén et al., 2007). A drawback with arc evaporation is the formation of macro-particles through explosions caused by overheated spots on the sources. The HiPP technology also belongs to the IPVD group.

The high instantaneous power densities applied to the cathode used for HiPP plasma generation result in a strong increase of charge carriers in front of the cathode during the discharge pulse. As an example, in a HiPIMS discharge, the electron density in the region close to the cathode target surface is on the order of 10^{18}–10^{19} m^{-3} (Gudmundsson et al., 2009, Bohlmark et al., 2005). For an electron density around 10^{19} m^{-3}, the ionization mean free path of a sputtered metal atom is about 1 cm, while for an electron density of 10^{17} m^{-3}, commonly observed in a steady-state DC magnetron sputtering (DCMS) discharge, the ionization mean free path is approximately 50 cm for typical discharge conditions (Gudmundsson, 2010). Thus, given the high electron density in the HiPP discharge a significant fraction of the sputtered material is ionized, which has also been reported in a great number of publications [see Gudmundsson et al. (2012) and references therein]. In **Fig. 2**, we schematically illustrate the sputter ejection of neutral material atoms by ions from the volume plasma. The sputtered particles are then transported out into the deposition chamber and may undergo an ionizing collision depending on the plasma conditions. A fraction of the sputtered material eventually reaches the substrate, either as neutrals or as ions.

Worth pointing out is that although the ionized flux fraction typically reaches > 50% (IPVD), there are, however, substantial differences in the degree of ionization of the sputtered material depending on the target material, ranging from only a few percent to almost fully ionized (DeKoven et al., 2003, Bohlmark et al., 2005). The reason for this behavior is mainly related to the fact that the ionization potential is material-dependent and for commonly used metals is in the range E_{IP} = 5.99 eV (Al) to E_{IP} = 11.26 eV (C), meaning that Al is more easily ionized than C.

In the plasma discharge model by Samuelsson et al. (2010), these trends are investigated in more detail in the case of HiPP discharges by HiPIMS. As a reference, for direct current discharges such as DCMS, the degree of ionization of sputtered material is found to be 5% or less independent of the target material used (Hopwood, 2000).

3. Thin film growth by high-power impulse magnetron sputtering

The use of ionized deposition fluxes when growing thin

films opens up several opportunities. It includes guiding the deposition material to use the ions for substrate pre-treatment, and using the ions for generating effects on the growing film through self-ion-bombardment. Below, we go through some of the most attractive features.

Guiding the material flux is a great advantage for coating complex-shaped surfaces and for trench filling applications (Kouznetsov et al., 1999). On the microscopic scale, the electric field present in the sheath between the plasma and the substrate can be used. Since this field is perpendicular to the substrate surface, it will guide the ions to arrive with an angle close to the surface normal. This minimizes self-shadowing—a mechanism that promotes surface roughening—and smoother and denser films can be grown. This was demonstrated by Alami et al. (2005) by growing films on the wall inside of a 10-mm-wide and 10-mm-deep trench, see **Fig. 3**. The use of an ionized flux for deposition made a dramatic difference, going from a low-density tilted columnar structure when mainly neutral atoms were deposited by DCMS, to a dense microstructure with columnar grains parallel to the substrate normal when the deposition material was ionized by HiPIMS. Similar results have been demonstrated for cutting tool edges, where good film quality is achieved on both sides of the edge when using HiPIMS (Bobzin et al., 2009).

For very narrow trenches, where the plasma cannot penetrate into the small structures, the situation is different. Here, the flux of deposition ions will be channeled down the trench and an improved bottom coverage can be achieved. In this case, sidewall coverage can be achieved by increasing the substrate bias—allowing the incoming ions to accelerate to higher energies and sputter material of the deposited coating at the entrance and at the bottom of the trench. The sputtered material can then be re-deposited on the side walls. This has been elegantly demonstrated and simulated by Hamaguchi and Rossnagel (Hamaguchi and Rossnagel, 1995). On a large scale, the ionized deposition fluxes can be guided and directed by using magnetic fields. An example of this is illustrated by Bohlmark et al. (2006b) where they focus the deposition flux towards the substrate position. The guiding can also be used for filtering away neutrals to increase the degree of ionization of the deposition material (Kouznetsov, 2004).

Ion bombardment during thin film growth is of great importance when it comes to controlling the microstructure of the film. The ions generated in HiPP processes have been found to have energy distributions shifted towards higher energies than are expected from the commonly accepted Thompson sputter energy distribution (Thompson, 1968, Bohlmark et al., 2006a). From ion energy measurements in HiPIMS discharges, it has been reported that the average ion energy is around 20 eV without using any substrate bias (Lundin et al., 2008). As

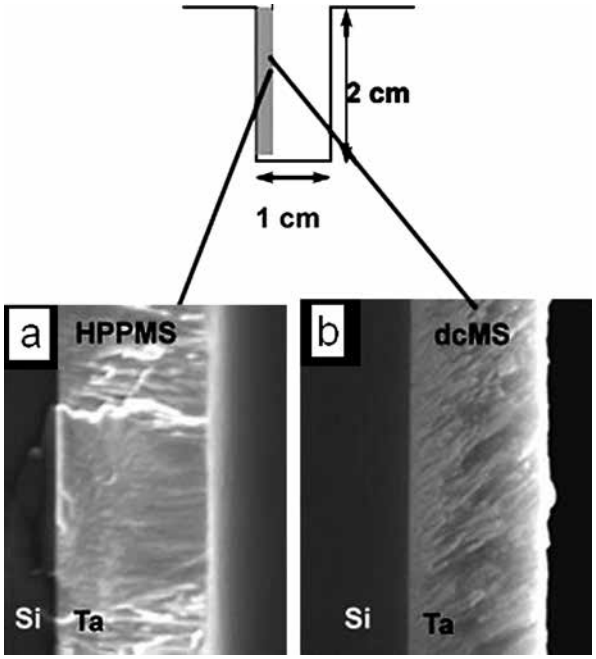

Fig. 3 Cross-sectional scanning electron microscope (SEM) images of Ta films grown by (a) HiPIMS and (b) DCMS on a Si substrate clamped on the side of a trench with an area of 1 cm^2 and a depth of 2 cm. The HiPIMS-deposited film is dense with columns growing perpendicular to the Ta/Si interface. The DCMS-deposited films have a porous microstructure with columns inclined toward the flux direction. [Reprinted with permission from Alami et al. (2005). Copyright 2005, AVS.]

it turns out, ion energies in the range 20–30 eV have been shown to have a densifying effect on thin films (Eriksson et al., 2006), since the ion flux enhances the surface mobility of the film-forming species on the growth surface and thereby reduces film porosity. Several research groups have demonstrated that HiPIMS results in denser films [see Samuelsson et al. (2010) and references therein]. Ion-bombardment is also often used in non-IPVD techniques. However, in this case the bombarding species are ions of the inert sputtering gas. For reasons not yet fully understood, bombarding the growth surface with the film-forming species is more efficient than using inert gas ions. The former also minimizes the incorporation of gas into the film.

The ion bombardment of the growing film can also be used for phase-tailoring. Alami et al. (2007) demonstrated that it was possible to grow thermodynamically stable bcc-Ta. Commonly during film growth, the more brittle tetragonal-Ta phase is formed. A similar case is the one published by Aiempanakit et al. (2011). They found that TiO_2 films with anatase and rutile phases can be controllably grown at room temperature using different HiPIMS conditions. X-ray diffraction patterns of the TiO_2 films where the change from the anatase to the rutile phase can

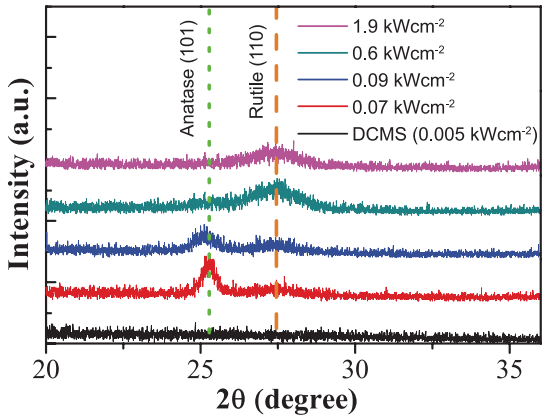

Fig. 4 X-ray diffraction patterns of TiO_2 films grown on Si substrates by HiPIMS at various values of peak target power. The increase of the peak target power and the subsequent increase in the number of ions available during deposition promote the formation of the rutile at the expense of the anatase phase. [Adapted from Aiempanakit et al. (2011).]

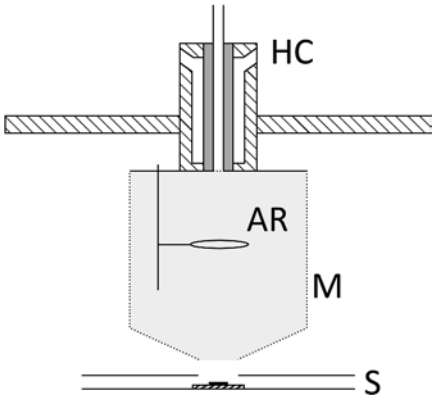

Fig. 5 Sketch of the experimental set-up, HC: hollow cathode, AR: anode ring, M: mesh, and S: substrate.

be seen in **Fig. 4**. A third example is Al_2O_3 that can form a number of phases, but only one, the corundum phase, is thermodynamically stable and desired in many wear-protection applications (Selinder et al., 2009). However, for the corundum phase to form, usually very high substrate temperatures of up to 1000°C are needed. This limits the type of substrates that can be used and thereby the number of applications. Ion bombardment during growth reduces the temperature needed to grow this phase and with HiPIMS, it is possible to grow the corundum phase at a growth temperature of 575°C (Wallin et al., 2008).

4. Nanoparticle Synthesis

There is a wide variety of gas-phase techniques to synthesize nanoparticles, e.g. flame synthesis (Wegner and Pratsinis, 2000), thermal evaporation (Granqvist and Buhrman, 1976), and plasma synthesis (Vollath, 2007; Binns, 2001). The technique presented in this article is a plasma-based technique based on high-power pulses similar to what is used in the HiPIMS discharge. HiPP discharges for nanoparticle synthesis have not been studied in detail; however, Straňák et al. (2011) used a pulsed magnetron technique where the size of the clusters could be varied, and Werner et al. (2011) synthesized nanoparticles with different shapes using a DC magnetron with long pulse-off times.

To investigate the effect of high-power pulses and a high ionization degree on the nanoparticle synthesis, a hollow cathode was used as a sputter target which has been shown to be suitable for nanoparticle synthesis (Ishii et al., 1999). A sketch of the set-up is shown in **Fig. 5** and more details of the experimental procedure can be found in Pilch et al. (2013). The nanoparticle synthesis was carried out in a stainless steel vacuum chamber in an argon atmosphere at a pressure of 106 Pa. The process gas was routed through the hollow cathode at a flow rate of 60 sccm. Typical pulse parameters used for the nanoparticle synthesis were: frequency $f = 125$ to 1300 Hz, peak current $I_H = 3$ to 20 A, and pulse width $t_{PW} = 10$ to 100 µs.

With the present set-up, it was possible to synthesize nanoparticles by sputtering different metals: Cu, Ag, Ti, Mo, and Zr. Examples of SEM micrographs of Ag and Cu nanoparticles are shown in **Fig. 6**. In both examples, a wide spread in sizes is found and two size populations were synthesized. The Ag nanoparticles have a diameter of around 60 nm and the shape of the nanoparticles is facetted; even cubic nanoparticles were found. Nanoparticles smaller than 5 nm (not seen in the image) were also synthesized. The Cu nanoparticles are spherical and two size populations were found, one with a diameter of 20 nm and the other of around 10 nm. TEM micrographs of the Cu nanoparticles are shown in **Fig. 7**.

To control the characteristics of nanoparticles, both their shape and size need to be controlled. For Ag it has been shown that nanoparticles with different shapes can be synthesized. Similar results for cubic Cu nanoparticles were also found. However, further control is needed to be able to synthesize nanoparticles with a specific shape. The change in size of Cu nanoparticles by adjusting the pulse parameters was studied in detail with the present set-up (Pilch et al., 2013). In **Fig. 8**, the variation of the nanoparticle diameter is shown for (a) varying peak current and (b) varying frequency (at constant average power). The two size populations shown in **Fig. 7(b)**—note that this is not the same data as shown in **Fig. 8**—can be avoided by choosing appropriate pulse parameters. By increasing the peak current, the nanoparticles with the smaller size become less and finally disappear. The nanoparticle size can also be changed when the frequency is varied and the average power is kept constant, see **Fig. 8(b)**. To keep the average

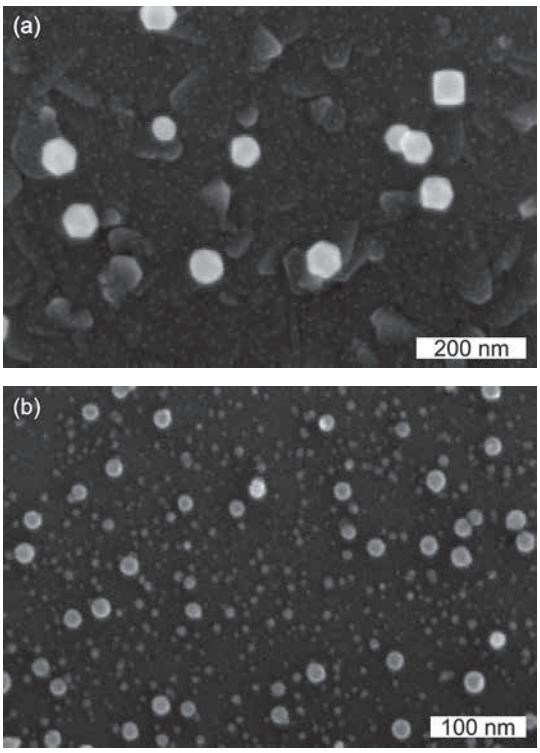

Fig. 6 SEM micrographs of (**a**) silver and (**b**) copper nanoparticles. The silver nanoparticles have cubic and facetted shapes whereas the copper nanoparticles are spherical and, in this case, with a wide spread of the size distribution.

power constant when the frequency was increased, the energy per pulse was lowered by decreasing the peak current. The possibility of synthesizing nanoparticles with different sizes at constant average powers allows one to optimize the nanoparticle synthesis with respect to power consumption.

The increased control of the growth of the nanoparticles comes from the interaction and timing of the pulses, and the amount of ions also plays an important role for the growth of nanoparticles. The properties and dynamics of the discharge were modeled by Hasan et al. (2013) for an Al target. It was found that the sputtered atoms become almost fully ionized with an ionization degree of 85% at the end of the pulse. To transfer this result from Al to Cu, which has a slightly higher ionization potential, the results from modeling the ionization degree for HiPIMS discharges can be used for comparison (Samuelsson et al., 2010). Assuming the same ratio of the ionization degrees for Al (49% for HiPIMS) and Cu (27% for HiPIMS), a high ionization of about 50% for Cu is still reasonable. The high ionization degree is required to be able to effectively utilize the charge of the nanoparticles to collect ions and enhance the growth speed of nanoparticles due to the larger collection cross-section of ions (Pilch et al., 2013).

During each pulse it was found that a cloud of ions and neutrals of the sputtered species emanates from the

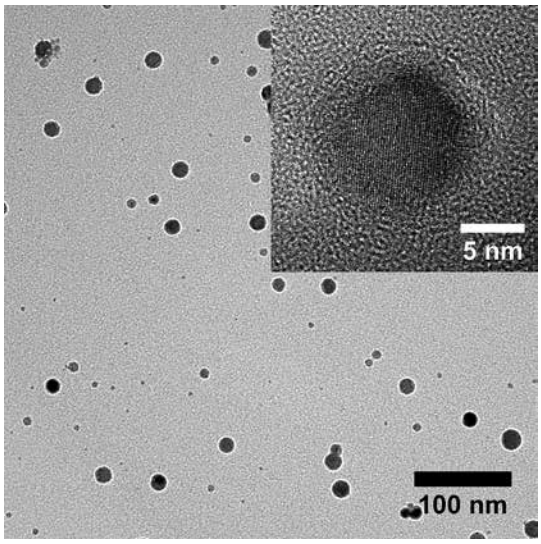

Fig. 7 TEM micrographs of copper nanoparticles. The inset shows a high-resolution micrograph of a nanoparticle with crystalline structure.

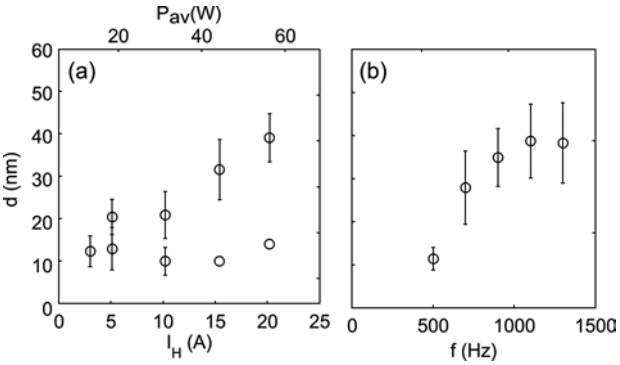

Fig. 8 Variation of the size of copper nanoparticles by changing a pulse parameter: (**a**) peak current (energy per pulse) and (**b**) frequency at constant average power. [Reprinted with permission from Pilch et al. (2013). Copyright 2013, AIP Publishing LLC.]

hollow cathode. The expansion and diffusion of the ion and the atom cloud diverge because the motion of ions is governed by ambipolar diffusion, which is a faster process than the diffusion of neutrals in the background gas. Due to the periodical ejection of material and the pulsing of the discharge, four mechanisms that affect the growth have been proposed (Pilch et al., 2013): pulse strength, neutral overlap, ion overlap, and discharge overlap.

The pulse strength is a measure of the density of the sputtered material that is available for the growth of nanoparticles. The sputtered material that is blown out of the hollow cathode condenses into small clusters, which may coalesce into larger clusters depending on the density of the small clusters. Consecutive pulses provide more material to the region outside the hollow cathode. The ejected neutral clouds can overlap and merge whereas the

ejected ion cloud flows, due to ambipolar diffusion, through the growth region providing material for nanoparticle growth. The ion overlap becomes particularly important when the nanoparticles attain a net negative charge. The charged nanoparticles will repel each other and coalescence and agglomeration of nanoparticles are prevented. Hence the nanoparticles grow by accretion of atoms and ions, whereas the process of collecting ionized material is more efficient than the collection of atoms. The higher collection probability of ions is due to a larger cross-collection of ions which is given by (Pilch et al., 2013):

$$\sigma_{\mathrm{coll}} = \sigma_0 \left(1 + k \frac{T_\mathrm{e}}{T_\mathrm{i}} \right),$$

with the geometric collection cross-section for atoms $\sigma_0 = \pi r^2$, r being the radius of a nanoparticle, the electron temperature T_e, ion temperature T_i, and a factor k that is a function of electron and ion temperature and ion mass. For a temperature ratio of $T_\mathrm{e}/T_\mathrm{i} \approx 100$, the collection cross section for ions is about two orders of magnitude larger than the geometric collection cross-section for atoms. The dependency of the collection cross-section of ions on the electron temperature is affected by the proposed discharge overlap. In the growth region outside the hollow cathode, a plasma is generated between the hollow cathode and the anode ring which leads to electron heating and possibly also ionization. A higher electron temperature will increase the collection cross-section of ions, and ionization will increase the density of ions in the growth region. Both effects can enhance the growth of nanoparticles by ions.

The increase in the size of nanoparticles when changing the peak current can be explained by an increase in pulse strength which leads to a higher density of sputtered material available for growth. In the case of varying the frequency but keeping the average power constant by reducing the pulse strength (i.e. the peak current), it can be assumed that the average density remains constant when increasing the frequency, though the density of sputtered material ejected during each pulse becomes less. Thus, the size increase can be ascribed to the overlapping of consecutive pulses. From the presented results it is not possible to deduce which one of the overlaps—neutral, ion or discharge overlap—is the most important one.

Comparing the pulsed process to a DC discharge, it was found that the pulse process can provide more tools to control the properties of the plasma environment for the growth of nanoparticles. The high power density leads to ejection of a cloud with a high density of sputtered material, which favors the nucleation of nanoparticles. Short, high-power pulses increase the ionization of the sputtered material substantially compared to a DC discharge. This is beneficial when the growth of nanoparticles is limited to the accretion of atoms and ions.

5. Summary and Conclusions

High-power pulses have been shown to be able to generate plasmas with a high degree of ionized material. The ionized material can be guided by electric and magnetic fields and the energy can be controlled by, for instance, the substrate bias. The thin-film deposition by ions rather than by atoms has shown to be capable of improving film properties such as higher density or better coverage of trench walls.

For the synthesis of nanoparticles, it was shown that the pulsing allows the sizes of nanoparticles to be controlled. The mechanism of size increase can be ascribed to the pulsing which causes a periodical ejection of source material. Nanoparticles of different metals were synthesized and in the case of Ag, it was shown that different shapes can be synthesized. This offers the possibility of obtaining a shape-selected growth by further manipulation of the growth zone—e.g. by applying an additional cooling source to quench the growth.

Acknowledgements

The authors thank Robert Boyd for providing the TEM micrographs. The work was financially supported by the Swedish Research Council under grant no. 2008-6572 through the Linköping Linneaus Environment LiLi-NFM and by the Knut and Alice Wallenberg foundation through grant no. 2012.0083.

References

Aiempanakit M., Helmersson U., Aijaz A., Larsson P., Magnusson R., Jensen J., Kubart T., Effect of peak power in reactive high power impulse magnetron sputtering of titanium dioxide. Surf. Coat. Technol., 205 (2011) 4828–4831.

Alami J., Persson P., Bohlmark J., Gudmundsson J., Music D., Helmersson U., Ion-assisted physical vapor deposition for enhanced film properties on nonflat surfaces. J. Vac. Sci. Technol. A, 23 (2005) 278–280.

Alami J., Eklund P., Andersson J., Lattermann M., Wallin E., Bohlmark J., Persson, P., Helmersson, U., Phase tailoring of Ta thin films by highly ionized pulsed magnetron sputtering. Thin Solid Films, 515 (2007) 3434–3438.

Anders A., Discharge physics of high power impulse magnetron sputtering. Surf. Coat. Technol., 205 (2011) S1–S9.

Atwater H.A., Polman A., Plasmonics for improved photovoltaic devices. Nature Materials, 9 (2010) 205–213.

Binns C., Nanoclusters deposited on surfaces. Surface Science Reports, 44 (2001) 1–49.

Bobzin K., Bagcivan N., Immich P., Bolz S., Alami J., Cremer R., Advantages of nanocomposite coatings deposited by high power pulse magnetron sputtering technology. J. Materials

Processing Technol., 209 (2009) 165–175.
Bohlmark J., Gudmundsson J., Alami J., Lattemann M., Helmersson U., Spatial electron density distribution in a high-power pulsed magnetron discharge. IEEE Trans. Plasma Sci., 33 (2005) 346–347.
Bohlmark J., Lattemann M., Gudmundsson J.T., Ehiasarian A., Gonzalvo Y.A., Brenning N., Helmersson U., The ion energy distributions and ion flux composition from a high power impulse magnetron sputtering discharge. Thin Solid Films, 515 (2006a) 1522–1526.
Bohlmark J., Östbye M., Lattemann M., Ljungcrantz H., Rosell T., Helmersson U., Guiding the deposition flux in an ionized magnetron discharge. Thin Solid Films, 515 (2006b) 1928–1931.
Chapman, Glow discharge processes, John Wiley & Sons, 1980.
Christie D.J., Target material pathways model for high power pulsed magnetron sputtering. J. Vac. Sci. Technol. A, 23 (2005) 330–335.
Christou C., Barber Z.H., Ionization of sputtered material in a planar magnetron discharge. J. Vac. Sci. Technol. A, 18 (2000) 2897–2907.
Cuenya B.R., Synthesis and catalytic properties of metal nanoparticles: Size, shape, support, composition, and oxidation state effects. Thin Solid Films, 518 (2010) 3127–3150.
DeKoven B., Ward P., Weiss R., Christie D., Scholl R., Sproul W.D., Tomasel F., Anders A. (2003). Carbon Thin Film Deposition Using High Power Pulsed Magnetron Sputtering. Society of Vacuum Coaters 46th Annual Technical Conference Proceedings, p. 158–165, San Francisco, CA, USA, May 3–8.
Eriksson F., Ghafoor N., Schäfers F., Gullikson E., Birch J., Interface engineering of short-period Ni/V multilayer X-ray mirrors. Thin Solid Films, 500 (2006) 84–95.
Garcia M.A., Surface plasmons in metallic nanoparticles: fundamentals and applications. J. Phys. D: Appl. Phys, 44 (2011) 283001.
Glöß D., Frach P., Zywitzki O., Modes T., Klinkenberg S., Gottfried C., Photocatalytic titanium dioxide thin films prepared by reactive pulse magnetron sputtering at low temperature. Surf. Coat. Technol., 200 (2005) 967–971.
Granqvist C.G., Buhrman R.A., Ultrafine metal particles. J. Appl. Phys., 47 (1976) 2200–2219.
Gudmundsson J., Sigurjonsson P., Larsson P., Lundin D., Helmersson U., On the electron energy in the high power impulse magnetron sputtering discharge. J. Appl. Phys., 105 (2009) 123302.
Gudmundsson J., The high power impulse magnetron sputtering discharge as an ionized physical vapor deposition tool. Vacuum, 84 (2010) 1360–1364.
Gudmundsson J., Brenning N., Lundin D., Helmersson U., High power impulse magnetron sputtering discharge. J. Vac. Sci. Technol. A, 30 (2012) 030801.
Hamaguchi S., Rossnagel S., Simulations of trench-filling profiles under ionized magnetron sputter metal deposition. J. Vac. Sci. Technol. B, 13 (1995) 183–191.
Hasan M.I., Pilch I., Söderström D., Lundin D., Helmersson U., Brenning N., Modeling the extraction of sputtered metal from high power impulse hollow cathode discharges. Plasma Sources Sci. Technol., 22 (2013) 035006.
Helmersson U., Lattemann M., Bohlmark J., Ehiasarian A., Gudmundsson J., Ionized physical vapor deposition (IPVD): A review of technology and applications. Thin Solid Films, 513 (2006) 1–24.
Hopwood J., In J. Hopwood (Ed.), Thin Films: Ionized Physical Vapor Deposition, Academic Press, San Diego, 2000.
Ishii K., Amano K., Hamakake H., Hollow cathode sputtering cluster source for low energy deposition: Deposition of Fe small clusters, Journal of Vacuum Science & Technology A: Vacuum, Surfaces, and Films, 17 (1999) 310–313.
Johnson P.C., In Kern J.L. (Ed.), Thin Film Processes II, Academic Press, New York, 1991.
Kelly P.J., Bradley J.W., Pulsed magnetron sputtering—process overview and applications. J. Optoelectron. Adv. Mater., 11 (2009) 1101–1107.
Konstantinidis S., Ricard A., Ganciu M., Dauchot J.P., Ranea C., Hecq, M., Measurement of ionic and neutral densities in amplified magnetron discharges by pulsed absorption spectroscopy. J. Appl. Phys., 95 (2004) 2900–2905.
Kouznetsov V., Macák K., Schneider J., Helmersson U., Petrov I., A novel pulsed magnetron sputter technique utilizing very high target power densities. Surf. Coat. Technol. 122 (1999) 290–293.
Kouznetsov V., Patent No. US20040020760, US patent, 2004.
Lundin D., Larsson P., Wallin E., Lattemann M., Brenning N., Helmersson U., Cross-field ion transport during high power impulse magnetron sputtering. Plasma Sources Sci. Technol., 17 (2008) 035021.
Lundin D., The HiPIMS process, PhD thesis (Linköping University, Sweden), 2010.
Lundin D., Sarakinos K., An introduction to thin film processing using high-power impulse magnetron sputtering. J. Mater. Res., 27 (2012) 780–792.
Pedersen H., Larsson P., Aijaz A., Jensen J., Lundin D., A novel high-power pulse PECVD method. Surf. Coat. Technol., 206 (2012) 4562–4566.
Pilch I., Söderström D., Brenning N., Helmersson U., Size-controlled growth of nanoparticles in a highly ionized pulsed plasma. Appl. Phys. Lett., 102 (2013) 033108.
Rosén J., Ryves L., Persson P., Bilek M., Deposition of epitaxial Ti_2AlC thin films by pulsed cathodic arc. J. Appl. Phys., 101 (2007) 056101.
Rossnagel S., Hopwood J., Metal ion deposition from ionized mangetron sputtering discharge. J. Vac. Sci. Technol. B, 12 (1994) 449–453.
Samuelsson M., Lundin D., Jensen J., Raadu M.A., Gudmundsson J.T., Helmersson U., On the film density using high power impulse magnetron sputtering. Surf. Coat. Technol., 205 (2010) 591–596.
Selinder T., Coronel E., Wallin E., Helmersson U., α-Alumina coatings on WC/Co substrates by physical vapor deposition. Int. Journal of Refractory Metals & Hard Materials, 27 (2009) 507–512.
Straňák V., Block S., Drache S., Hubička Z., Helm C.A., Jastrabík L., Tichý M., Hippler R., Size-controlled formation of Cu nanoclusters in pulsed magnetron sputtering

system, Surface and Coatings Technology, 205 (2011) 2755–2762.
Thompson M.W., II. The energy spectrum of ejected atoms during the high energy sputtering of gold. Philos. Mag., 18 (1968) 377–414.
Wallin E., Selinder T., Elfwing M., Helmersson U., Synthesis of α-Al_2O_3 thin films using reactive high-power impulse magnetron sputtering. Europhys. Lett., 82 (2008) 36002.
Wegner K., Pratsinis S.E., Aerosol Flame Reactors for the Synthesis of Nanoparticles. Kona Particle and Powder Journal, 18 (2000) 170–182.
Werner R., Höche T., Mayr S.G., Synthesis of shape, size and structure controlled nanocrystals by pre-seeded inert gas condensation. Cryst. Eng. Comm., 13 (2011) 3046–3050.
Window B., Savvides N., Charged particle fluxes from planar magnetron sputtering sources. J. Vac. Sci. Technol. A, 4 (1986) 196–202.
Vollath D., Plasma synthesis of nanoparticles. Kona Powder and Particle Journal, 25 (2007) 39–55.

Author's short biography

Iris Pilch

Iris Pilch received her Ph.D. degree from Christian-Albrechts-Universität in Kiel, Germany in 2010 where she studied the dynamics of dust-density waves and dust particles in a complex plasma. After her Ph.D., she joined the Plasma and Coatings Physics Division at Linköping University, Sweden, as a post doc to investigate the growth of nanoparticles in highly ionized pulsed plasmas. Her research interests include plasma physics, complex plasmas, nanoparticle synthesis and the diagnostics of nanoparticles during growth.

Daniel Söderström

Daniel Söderström is an assistant professor in the Plasma and Coatings Physics Division, Linköping University, Sweden. He received his Ph.D. from Uppsala University, Sweden, in 2008, after which he joined the Linköping group as a post doc to develop a plasma source for nanoparticle synthesis. His research interests include hollow cathode discharges, complex plasmas, and nanoparticle physics.

Daniel Lundin

Daniel Lundin received his Ph.D. in 2010 from Linköping University, Sweden, focusing on plasma characterization and process optimization in high-power impulse magnetron sputtering (HiPIMS). His research on the HiPIMS process won the Institute of Physics Prize for novelty, significance and potential impact on future research in 2008. He is one of the founders of the company Ionautics, which provides academia and industry with HiPIMS coatings recipes as well as hardware. In 2009, he was ranked as one of Sweden's young 'Supertalents' by the Swedish business journal Veckans Affärer for his work on commercializing HiPIMS.

Author's short biography

Ulf Helmersson

Dr. Ulf Helmersson, head of the Plasma & Coatings Physics division at Linköping University (LiU), has focused his research on the complex relationship between thin-film growth kinetics, microstructural evolution, and physical properties. Ulf started as an electron microscopist, using the tools to investigate materials physics (i.e. nanoscience) rather than using the microscope as an end in itself. Over the last several years, Ulf has truly pioneered the development of High-Power Impulse Magnetron Sputtering (HiPIMS), the most significant development in physical vapor deposition over the last decade. In 2008, Ulf become a fellow in the AVS Technology Society (former American Vacuum Society).

KONA Powder and Particle Journal No. 31 (2014) 181–199/Doi:10.14356/kona.2014009 Original Research Paper

Photophoresis – a Forgotten Force ??†

Helmuth Horvath

[1] *University of Vienna, Faculty of Physics, Aerosols and Environmental Physics, Austria*

Abstract

In general a force will act on a particle illuminated by light or other radiation and absorbing part of the flux, and as a consequence a motion will result. It is caused by the interaction of gas molecules with the particle's surface, which is hotter than the surroundings. This surface must be inhomogeneous with respect to accommodation and/or temperature. Gas molecules, impacting and reflected from the particle's surface with accommodation, transfer some momentum from the particle and thus cause the force. For a temperature variation on the particle's surface, the force points from the hot to the cold part, thus in the direction of the incident radiation, and under very special conditions it can be the opposite. A particle's surface having a variation in accommodation coefficient will cause a force from the locations of higher to lower accommodation. Usually this will cause both a linear force and a torque. The latter in combination with Brownian rotation will result in a zero net force. But it is possible that an external torque acting on the particles causes an orientation. The torque can be caused by magnetic or electric fields on magnetic or electric dipoles in the particles or by gravity orienting inhomogeneous particles. For micrometer- and nanometer-sized particles, the photophoretic force can exceed gravity. Photophoresis is important for levitation in the stratosphere and for planet formation, it can also be used for on-line particle separation, or in clean-room technology or in geo-engineering.

Keywords: levitation, radiation pressure, accommodation, disorientation, orientation, temperature gradient

Introduction

Particles illuminated by a beam of light or infrared radiation, having sufficient flux density, can move in various directions. This phenomenon has been mentioned by Thoré (1877), first described and later intensively studied by Ehrenhaft (1918) and co-workers/students. Since light is the cause for the motion, the expression "photophoresis" has become common. Preining (1966) gives a concise description of the important factors influencing photophoretic motion: *"This motion can depend on the illumination, color, structure and shape of the light beam, on pressure and composition of the gas, on the particle's size, shape and material, and on additional fields such as electric, magnetic, and so on."*

The motion of the particles can range between simple to very complex, and depends both on the particle and the external forces (see **Fig. 1**). The simplest motion is **(a)** positive photophoresis, in which case the particles move in the direction of the light beam; motion in the opposite direction is possible, this is called **(b)** negative photophoresis. For particles having the right surface and volume properties, a motion in or against the direction of an external field is possible, this is called **(c)** gravito-, electro-, or magneto-photophoresis, depending on the field. Illuminated particles may perform an irregular motion, similar to an enhanced Brownian motion, called **(d)** irregular photophoresis. In the case of inhomogeneous illumination and/or inhomogeneous fields, the particles may undergo **(e)** circular photophoresis, having circular or elliptical orbits, or **(f)** complex photophoresis, which can be a combination of several motions. Finally no photophoresis can occur, i.e. the illumination by light causes no motion in addition to the motion without light.

The photophoretic force can be larger than gravity for particle sizes comparable to the mean free path of the gas molecules and thus can cause a motion against gravity, leading to the formation of aerosol layers in the stratosphere, photophoresis also plays an important role in planet formation. For geo-engineering, the photophoretic force can help to keep particles suspended longer. In intense laser light, absorbing and non-absorbing particles can be separated on-line, the microchip production zone can be kept particle-free, and single particles can be handled by a photophoretic trap. Photophoresis will slow coagulation. Whenever strong light flux and microparticles occur simultaneously, photophoresis cannot be neglected, such as during combustion of fuel droplets.

† Accepted: July 9, 2013
1 Boltzmanngasse 5, 1090 Vienna, Austria
E-mail: Helmuth.Horvath@univie.ac.at
TEL: +43-142-775-1177 FAX: +43-142-779-511

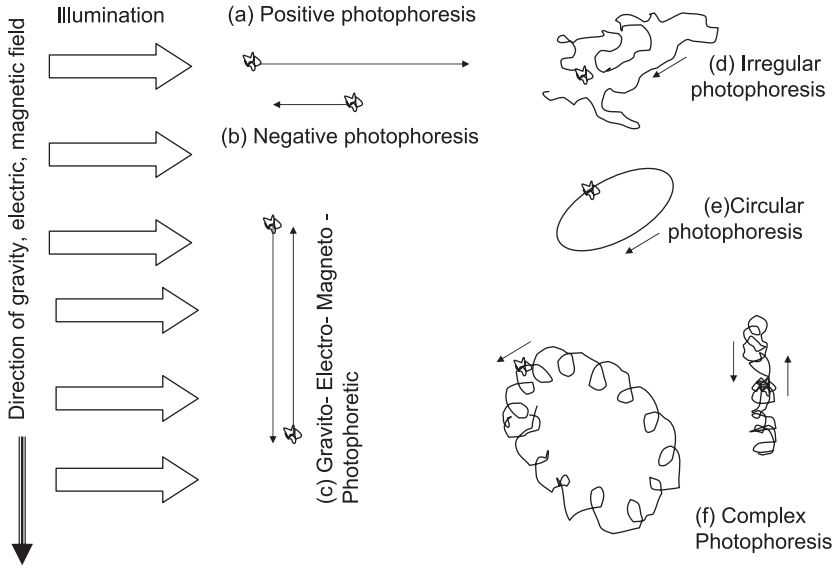

Fig. 1 Types of photophoresis. When illuminated, particles can move in or opposite to the direction of light (**a**, **b**), move in the direction of external fields (**c**), move similar to Brownian motion but more vigorously (**d**), move in closed loops (**e**) or perform complex motions.

The photophoretic force

The momentum transferred by photons hitting a surface and absorbed or deflected obviously exerts a force on a particle in the direction of the photon motion. Using the classic electromagnetism interpretation of radiation pressure, it amounts to

$$p = \frac{I}{c}(1+R) = \frac{< S >}{c}(1+R) \qquad (1)$$

with I the intensity (flux density), S the Poynting vector, c the speed of light, and R the reflectivity for electromagnetic waves (Landau and Lifschitz, 1988, p. 133). Corresponding formulas exist for the quantum point of view.

The force exerted by incident light can easily be demonstrated with a radiometer. It consists of a rotor with vanes (made of aluminum or mica which are dark on one side, and reflecting on the other) in a partial vacuum. When exposed to radiation the light mill turns (for a motion picture see, e.g. http://en.wikipedia.org/wiki/File:Radiometer_9965_Nevit.gif). A schematic of the radiometer can be seen in **Fig. 2**. The reflected photons cause a higher momentum than the absorbed ones, thus the rotor should turn counterclockwise. In reality the opposite is the case. Applying formula (1) the motion should be very slow (see, e.g. the problem 59 in chapter 29 of Tipler, 1991); it would need several years until a few revolutions per second are reached, in reality the wheel immediately turns after switching on the light. Except for extremely intense radiation, this direct photophoresis (radiation pressure) is of minor importance for the radiometer and also for aerosol science, and thus can be neglected. The indirect photophoretic force, as treated below, is much stronger, but needs the presence of gas molecules which are available in the radiometer and are always present in an aerosol.

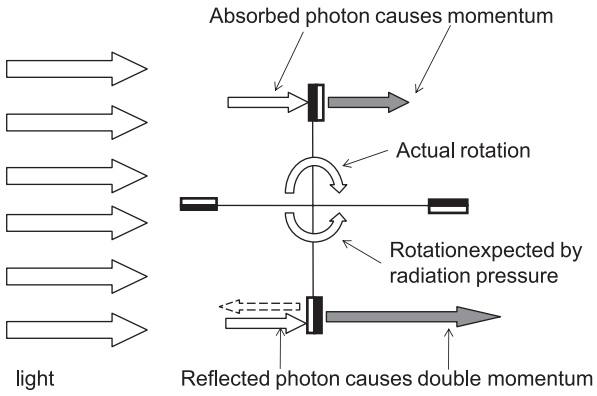

Fig. 2 Schematics of the radiometer wheel.

On a microscopic scale, gas molecules impacting on the surface are reflected. The reflection can be specular (approximately 10% of the molecules) or diffuse (90%, Fuchs 1964, p. 22), obviously with conservation of energy. The diffuse reflection is accompanied by a more or less complete accommodation (see below). For a particle moving through a gas, the molecules impacting at the front side are reflected with a higher velocity compared to the backside. This asymmetry in velocities leads to a momentum transfer to the particle and causes the friction force acting on the particles when moving through a gas.

The reflection of gas molecules at the particle's surface

with accommodation is of special importance for photophoresis. A surface of a particle which absorbs radiation (visible of IR) is heated to a higher temperature T_s than the temperature T_0 of the surrounding gas. A gas molecule hitting the particle's surface can acquire some of the thermal energy of the hot particle and be "reflected" with a velocity corresponding to a temperature, T, that is higher than the surrounding gas. The probability of taking up additional thermal energy is characterized by the accommodation coefficient $\alpha = \frac{T - T_0}{T_s - T_0}$, with $\alpha = 0$ for no, and $\alpha = 1$ for full accommodation (Knudsen, 1911). The value of α depends on both the material forming the particles as well as its surface structure and the gas. Values between $\alpha = 0.3$ and 0.8 have been reported in the literature (Angelo, 1951; Rohatschek, 1955). For example, glazed platinum has $\alpha = 0.315$, whereas platinum black, with a very structured surface, has $\alpha = 0.72$. This can be understood by the multiple reflections of the molecules on the complex surface of platinum black, giving a bigger chance to pick up the surfaces' temperature. For surfaces with linear dimensions considerably smaller than the mean free path of the gas molecules, the pressure exerted by molecules, reflected with accommodation, can be determined from basic formulas of gas kinetics: Gas molecules exert a pressure on any wall due to elastic reflection and thus transfer of momentum. The value of the pressure can be obtained from the equation $p.V = R.T$. The mean velocity of the gas molecules depends on the temperature, i.e. $\bar{c} \propto \sqrt{T}$. In a gas having a higher temperature, the velocity of the molecules is higher and thus the momentum transferred to the surface is larger, and therefore the pressure. Using $p = \frac{R \cdot T}{V}$, the increase in pressure dp caused by an increase in temperature dT is $dp = \frac{R}{V} dT = \frac{p}{T} dT$. For molecules impacting on the surface with a velocity equivalent to T_0 and reflected after accommodation with a velocity corresponding to a temperature $T_0 + dT$, only half of the pressure increase can be taken, yielding $dp = \frac{1}{2} \frac{p}{T} dT$. For the reflection of molecules of temperature T_0 on a wall with temperature T_w, the temperature of the molecules after reflection with accommodation is $T = T_0 + \alpha(T_w - T_0)$, thus $dT = \alpha(T_w - T_0)$ or $dT = \alpha \cdot \Delta T$ with $\Delta T = T_w - T_0$. Thus the additional pressure due to reflection with accommodation is $\Delta p = \frac{1}{2} \frac{p}{T_0} \cdot \alpha \cdot \Delta T$ and the force on a circular surface with diameter d amounts to

$$F = \frac{\pi}{8} \cdot d^2 \cdot p \cdot \alpha \cdot \frac{\Delta T}{T_0} \qquad (2)$$

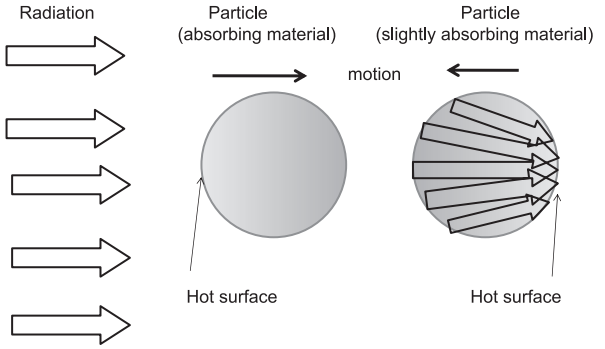

Fig. 3 Explanation of positive and negative photophoresis (Rubinowitz, 1920). The surface of a strongly absorbing particle is hotter on the side facing the radiation, thus photophoresis is in the direction of the radiation. A particle that slightly absorbs light focuses the light to the rear side, which consequently is hotter, thus the particle moves in the opposite direction.

Types of photophoresis

If the accommodation coefficient α of the surface of the particles is $\alpha > 0$ and the particle is heated by radiation, a photophoretic force can act on the particle. Two different idealized extremes can be distinguished: (a) Variation in temperature on the surface of the particles (ΔT force) and (b) variation of accommodation and constant temperature ($\Delta\alpha$ force):

Case (a): Constant accommodation coefficient but variation in surface temperature (ΔT-photophoretic force)

Let us assume a spherical particle of diameter d consisting of a light-absorbing material with a thermal conductivity k_p and immersed in a gas with pressure p, viscosity η, and molecular weight M and illuminated by visible or infrared light. The surface facing the radiation source is warmer than the backside (see **Fig. 3**); due to accommodation, the molecules on the warmer side leave the surface faster, resulting in a force away from the light source (positive photophoresis). This was found to take place, e.g. for particles consisting of Au, Ag, Hg, Cd, K, Na, Mg, soot produced by the combustion of turpentine, or camphor (Ehrenhaft, 1918).

For a slightly absorbing particle, a force in the opposite direction has been observed. The maximum absorption may be at the backside, causing the reversal of the force. The early interpretation is the lens effect, see **Fig. 3**: The convex surface of the particle acts like a lens, concentrating the rays on the backside (Rubinowitz, 1920), which becomes hotter than the surface facing the radiation, resulting in a motion towards the light source (negative photophoresis). For particles comparable to the

wavelength of light, the lens effect as a simplification may not be permitted, but strictly applying Maxwell's equation to an absorbing spherical particle leads to the same results (Dusel et al., 1979; Figure 4.31 of Barber and Hill, 1990). Negative photophoresis has been observed, e.g. for spheres of S, Se, J, Bi, Th, P, Pb, Te, As, Sb, for tobacco or wood smoke particles (Ehrenhaft, 1918).

The direction of the photophoretic force is determined by the direction of the radiation and is almost independent of the orientation of the particle, thus the force is called space-fixed, the movement is called longitudinal photophoresis and since the temperature difference causes the force, it is called ΔT force. Although all particles perform Brownian rotation, the rotation is slow compared to the time needed to establish the temperature gradient within the particle (Fuchs, 1964, p. 62). The "ideal" particles would have a low thermal conductivity and heat capacity.

In the free molecular regime, calculation of the force is simple: Molecules impacting on the particle are reflected with a larger velocity due to accommodation. Using considerations similar to the radiometer which was considered above, Rubinowitz (1920) determined the force on a spherical particle with diameter d at gas pressure p as:

$$F_{\text{free}} = \frac{\pi}{24} \cdot \alpha \cdot d^2 \cdot p \cdot \frac{\Delta T}{T} = \frac{\pi}{12} \cdot \alpha \cdot d^3 \cdot p \cdot \frac{gradT}{T} \qquad (3)$$

For the derivation in the continuum regime one has to consider the thermal creep flow around the particle and the resulting viscous forces. In contrast to the free molecular regime, the gas molecules around the particle have temperatures similar to those on the surface of the particle (see **Fig. 4**). A gas molecule impacting on the surface from the left (hot) side thus has a larger velocity than the molecule impacting from the colder side. After accommodation, the molecules have a symmetric velocity distribution with respect to the perpendicular direction of the surface, therefore the warmer molecule coming from the left side transfers to the particle a larger momentum to the right than the colder molecule to the left. This results in a net force on the particle which directs from the hot to the cold side. The gas loses this momentum, thus a creep flow around the particle from the cold side to the hot side occurs simultaneously which has its maximum flow at a distance to the mean free path of the gas (Knudsen, 1910a, b; Hettner, 1924; Fuchs, 1964, p.57). Solving the hydrodynamic equations (similar to Stokes Law), the following formula for the photophoretic force is obtained (Hettner, 1926)

$$F_{\text{cont}} = \frac{3\pi}{2} \cdot \frac{\eta^2 \cdot d \cdot R \cdot gradT}{p \cdot M} \qquad (4)$$

with R the gas constant, η the viscosity of the gas, M the molecular weight of the gas molecules, p the gas pressure and d the diameter of the particle.

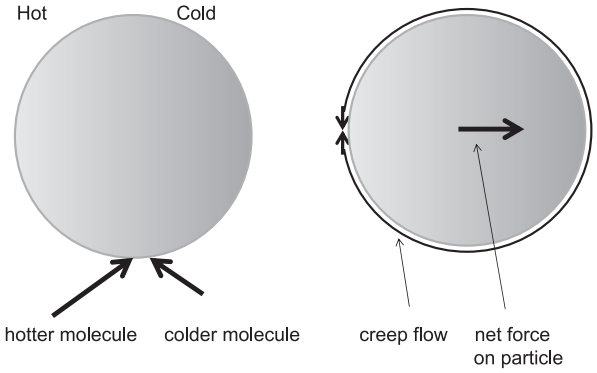

Fig. 4 Photophoretic force on a particle in the continuum regime. The particle is hotter on the left side and in the immediate vicinity of the surface, the gas molecules have the same temperature as the surface. Molecules impacting on the particle from the left are faster than those coming from the right, transferring a momentum to the right onto the particle. This momentum is lost in the gas, thus a thermal creep flow of the gas molecules to the left occurs.

Formula (3) is valid for the free molecular range, i.e. the particles must be considerably smaller than the mean free path of the gas molecules (λ = 66 nm at standard conditions, with decreasing pressure the mean free path increases), whereas formula (4) is only valid for the continuum range, i.e. for particles much larger than λ. Magnitudes influencing the force are the diameter of the particle and the temperature gradient both proportional to the force in formulas (3) and (4), the accommodation coefficient only in (4) and the pressure in (3) and (4). The force is proportional to the pressure in the free molecular regime (3) and inversely proportional to it in the continuum regime (4), i.e. a maximum force occurs in between, which is the most important range for photophoresis. Similar to Stokes' Law, an interpolation is used for the intermediate range, as proposed by Hettner (1926): $\frac{1}{F} = \frac{1}{F_{\text{free}}} + \frac{1}{F_{\text{cont}}}$, or in detail:

$$F = \frac{\frac{\pi}{4} \cdot d^2 \cdot \eta \cdot \sqrt{\frac{\alpha \cdot R}{M \cdot T}} \cdot gradT}{\frac{p}{p_0} + \frac{p_0}{p}} \quad \text{with} \quad p_0 = \frac{6\eta}{d}\sqrt{\frac{RT}{M\alpha}} \quad \text{or}$$

$$d_0 = \frac{6\eta}{p}\sqrt{\frac{RT}{M\alpha}} \qquad (5)$$

The pressure-dependent force for a given particle size has a maximum for $p = p_0$, or for a given pressure the maximum photophoretic force is for particle diameter d_0. The pressure for the maximum photophoretic force depends on the gas properties, the particle size and the accommodation coefficient. For a pressure of 1 bar the

optimum particle size is 229 nm for $\alpha = 0.8$ and 375 nm for $\alpha = 0.3$. For a pressure of 5500 Pa (20 km a.s.l.), the corresponding diameters are 6.8 and 4.1 µm.

The viscosity of the gas, η, is obviously decisive for the photophoretic force in (4). The viscosity of a gas is mainly determined by the mean free path, λ, of the gas molecules and the pressure. Using the relation $\eta = \sqrt{\frac{8M}{9\pi RT}} \cdot p \cdot \lambda$ (see, e.g. Hinds, 1982). Inserting this in (4), the size for the maximum photophoretic force is obtained as $d_0 = 4 \cdot \sqrt{\frac{2}{\pi}} \cdot \frac{1}{\sqrt{\alpha}} \cdot \lambda = \frac{3.19}{\sqrt{\alpha}} \cdot \lambda$, therefore optimal photophoretic effects will be found if the particle size is in the order of the mean free path of the gas molecules.

Denoting the maximum force at p_0 with F_0, (5) can be written as

$$\frac{F}{F_0} = \frac{2}{\frac{p}{p_0} + \frac{p_0}{p}} . \qquad (6)$$

This formula has been tested by many authors. Various particle materials, particle sizes, gases and pressures have been used. Usually the accommodation coefficient and the particle size are not known exactly, whereas the temperature gradient is completely unknown. The experimental procedure is quite elaborate, since the motion of one and the same particle is measured for pressures varying over three orders of magnitudes, lifting the particle up in between. Formula (6) contains only magnitudes that are experimentally accessible. Since the size of the particle in relation to the mean free path of the surrounding gas is important, it is also possible to make photophoretic analogy experiments with centimeter-sized particles, as long as the mean free path of the particles is large enough. This requires a high vacuum but offers the advantage that the particle can be fixed, and the force can be measured with a torsion balance. In this way many data points can be gathered, without the fear of losing the particle during pressure change (Schmitt, 1961). Compared to the experiments with sub-micrometer-sized particles, the distance to the walls of the container is much smaller, and wall effects cannot be neglected. A summary of various experiments is shown in **Fig. 5**. Particles consisting of Te, Se (Mattauch, 1928), Se (Reiss, 1935), CdS (Arnold et al., 1980) and also 1-cm polystyrene particles at correspondingly low pressures (Schmitt, 1961), all show the same behavior for gases such as H_2, A, O_2, N_2, CO_2. All data demonstrate the maximum photophoretic force at an intermediate pressure.

Once the size and the photophoretic force of the particle is known, equation (4) can be used to estimate the temperature difference between the hot and cold side of the particle. Ehrenhaft (1918) and Parankiewicz (1918)

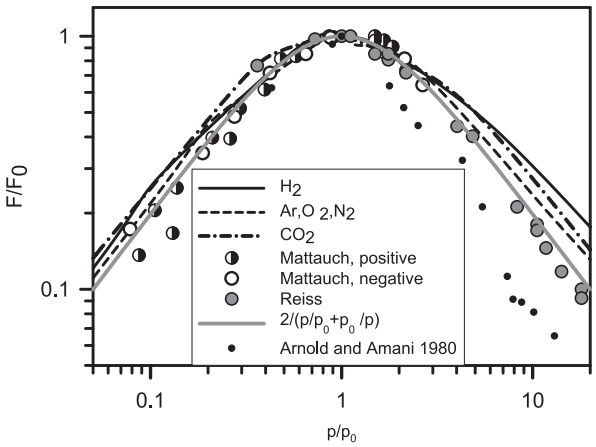

Fig. 5 Experimentally determined photophoretic forces as a function of pressure. All data show a maximum photophoretic force at an intermediate pressure as postulated by theory. The dark lines are results of model measurements with cm-sized spheres in vacuum, the points result from measurements made with individual micro- or nanometer-sized particles consisting of various materials, the gray line is theory (6).

have measured the photophoretic forces: They are in the order of 10^{-16} to 10^{-15} N for particle radii ≤ 100 nm of various materials in N_2 and Ar. The estimate for the temperature difference across the particles is 10^{-4} to 10^{-2} K (Hettner, 1926).

For calculation of the photophoretic force in (3) and (4), the temperature gradient in the particle is needed. For this, both the inhomogeneous heat production within the particle, the heat conduction to the surface, and the momentum transfer at the surface has to be solved. Fuchs (1964, p. 58) remarks: *"The main difficulty in calculating the radiometric force on a particle is the determination of the temperature gradient in the particle itself."* For simple shapes such as spheres this appears possible (see below), but many particles showing photophoresis are not spheres. A first attempt for spheres has been made by Rubinowitz (1920) yielding $gradT = \frac{S}{2(k_p + k_g)}$, with S the flux density of the illumination and k_p and k_g the thermal conductivities of the material forming the particle and the gas. In the meantime, several investigators have treated the problem in depth: Reed (1977) for low Knudsen numbers, Yalamov et al (1976), Arnold and Lewittes (1982) close to the continuum range, Akhtaruzzaman and Lin (1977) for the free molecular range, Chernyak and Beresnev (1993) and Mackowski (1989) for the whole range of Knudsen numbers.

Using all available theories, Rohatschek (1995) formulated an empirical model. For the free molecular and the continuum regime, the force on a particle with diameter d illuminated by a flux density S is obtained as

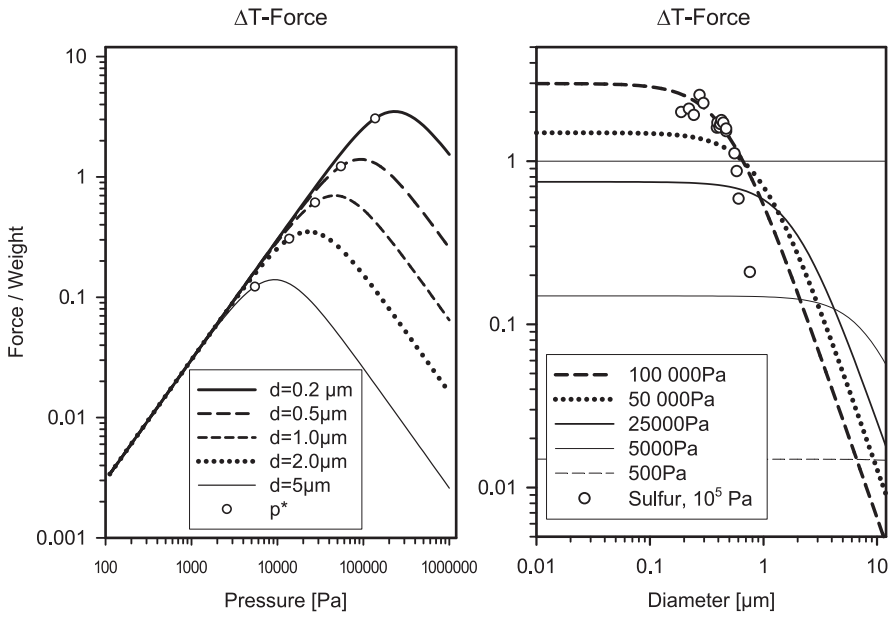

Fig. 6 Photophoretic ΔT force as a function of pressure for various particle diameters. The force is given relative to the weight of the particle. The data points in the right graph are for sulfur spheres (Parankiewicz, 1918)

$$F_{\text{free}} = D \cdot \frac{p}{p^*} \cdot d^2 \cdot \frac{\alpha \cdot J_1}{4k_{\text{p}}} \cdot S \quad \text{and}$$

$$F_{\text{cont}} = \frac{D \cdot J_1}{2k_{\text{p}}} \cdot \frac{p^*}{p} \cdot d^2 \cdot S \tag{7}$$

$$\text{with} \quad D = \frac{\pi}{2}\sqrt{\frac{\pi}{3}\kappa} \cdot \frac{\bar{c} \cdot \eta}{T} \quad \text{and}$$

$$p^* = \frac{1}{d}\sqrt{3\pi\kappa} \cdot \bar{c} \cdot \eta = \frac{6}{\pi} \cdot D \cdot \frac{T}{d} \; . \tag{7a}$$

With k_{p} the thermal conductivity of the particle, J_1 the asymmetry parameter for light absorption (½ for opaque particles, J_1 has the opposite sign if absorption is mainly at the backside, e.g. for negative photophoresis), D a factor only containing the gas properties, thus independent of particle size and pressure, κ the thermal creep coefficient (κ = 1.14 for a fraction of 0.1 of the specular-reflected molecules, Bakanov, 1992), and p^* a reference pressure. (The pressure for the maximum force is obtained by $p_0 = \sqrt{2/\alpha} \cdot p^*$) Combining the forces for the two regimes (7) as above, a formula for the ΔT force is obtained for the entire pressure range: $\frac{1}{F} = \frac{1}{F_{\text{free}}} + \frac{1}{F_{\text{cont}}}$. As an example, the ΔT forces on particles at various pressures are plotted in **Fig. 6**. The following properties of the particles have been assumed: Accommodation coefficient α = 0.7, density ρ_{p} = 1000 kg/m^3, thermal conductivity k_{p} = 1 $Wm^{-1}K^{-1}$. The pressures p^* for each particle size are indicated as data points on the curves. The maximum force and the decrease both for lower and higher pressures are clearly visible. The thermal conductivity appears in the denominator and thus strongly influences the photophoretic force. The value chosen for the graph may be representative, but it depends greatly on the particle's material. For example, crystalline graphite (Pedraza and Klemens 1993) has a thermal conductivity of 1200 $Wm^{-1}K^{-1}$ parallel to the layer planes, it thus reduces the temperature difference in the particle considerably as well as the photophoretic force. On the other hand perpendicular to the layer plane, the conductivity is only 6 $Wm^{-1}K^{-1}$. But agglomerates of carbon particles are more likely. For soot the thermal conductivity has values of 3, or even below 1 $Wm^{-1}K^{-1}$. Thus the photophoretic force very much depends on the microstructure of the particle. A few data points for sulfur spheres are added to the graph on the right side. The values have been measured by Parankiewicz (1918) for a pressure of 100 kPa; unfortunately she did not specify the flux density of the illumination. Sulfur has a thermal conductivity of 0.205 $Wm^{-1}K^{-1}$, thus the force should be five times higher than in the graph. On the other hand, sulfur only slightly absorbs light and thus shows negative photophoresis, consequently the force is considerably less since only a small fraction of the light causes a temperature increase. So these data points can be considered merely as an indication, nevertheless they still show the rapid drop of the relative force for increasing particle size.

Case (b): Variable accommodation coefficient on the surface but constant temperature (Δα-photophoretic force)

As a simple model we assume a spherical particle of diameter d consisting of a light-absorbing material immersed in a gas with pressure p, and temperature T (mean molecular velocity $\overline{c}$). The particle's surface shall have a variation in the accommodation coefficient, e.g. be caused by a difference in surface roughness or by different materials forming the particle. For this simple model, one half of the sphere's surface shall have the accommodation coefficient α_1, the other α_2 (see **Fig. 7**). At the location of larger accommodation coefficients, the molecules are reflected with a higher average velocity, resulting in a thrust on the particle from the location of the higher accommodation coefficient to the location of the lower one. This can be considered similar to the jet of an airplane: this thrust has a fixed direction relative to the airplane, approximately in the plane of symmetry of the airplane; if the airplane changes direction the thrust vector changes as well. Likewise the direction of the force on the particle is determined by the orientation of the particle and is independent of the direction of the illumination (the direction of the force is thus given in a body axis system, we call it body-fixed or particle-fixed force). Upon a change of orientation of the particle, the direction of the force likewise changes. Since all particles perform Brownian rotation, the direction of the force is distributed randomly, and the motion of the particles can be considered as a strongly enhanced Brownian motion (see **Fig. 1d**). This has been observed by various authors, e.g. Ehrenhaft (1907) and Steipe (1952), and was named the "trembling effect". It only occurred if no orienting field was present, therefore, e.g. for iron particles, the earth magnetic field had to be compensated completely. Obviously the average (net) force is zero, due to Brownian rotation.

The instantaneous Δα-photophoretic force on the particle in the direction from higher to lower accommodation coefficients amounts to (Rohatschek, 1995)

$$F = \frac{1}{2\cdot\overline{c}}\cdot\frac{\gamma-1}{\gamma+1}\cdot\frac{1}{1+(p/p^*)^2}\frac{\Delta\alpha}{\overline{\alpha}}\cdot H \text{ , or for air:}$$

$$F = \frac{1}{12\cdot\overline{c}}\cdot\frac{1}{1+(p/p^*)^2}\frac{\Delta\alpha}{\overline{\alpha}}\cdot H \qquad (8),$$

with $\Delta\alpha = \alpha_2 - \alpha_1$, $\overline{\alpha} = \frac{1}{2}(\alpha_1+\alpha_2)$, $\gamma = c_p/c_v$ the ratio of the specific heats of the gas, and H the net energy flux transferred by the gas molecules. This flux is obtained by an energy balance for the particle: Absorbed light flux $A.S$ plus infrared E_{abs} must equal the power H transferred to the molecules due to accommodation plus the emitted infrared radiative flux E_{emitt}. For pressures above 100 Pa, there are sufficient molecules available to dissipate the absorbed radiation thus E_{abs} and E_{emitt} can be considered equal, and $A.S = H$. At lower pressures, the particle's temperature increases due to a lack of sufficient energy transfer by the reflected gas molecules undergoing accommodation, and thus E_{emitt} rises, therefore $H < A.S$. To determine the absorbed light flux, the absorption cross-section A can be obtained, e.g. for spherical particles by the absorption efficiency factor Q_a of the Mie theory as $A = \frac{1}{4}\cdot d^2\cdot Q_a$ (Bohren and Huffman, 1983).

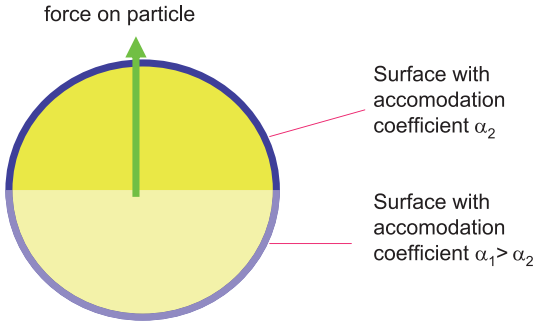

Fig. 7 Photophoretic Δα force. A particle, hotter than the surrounding air, has a larger accommodation coefficient on the lower hemisphere. Consequently the molecules reflected by the lower hemisphere are faster than the ones on the upper hemisphere, resulting in an upward-directed thrust.

As an example, the photophoretic Δα force (formula (8)) for particles having Δα = 0.1 and α = 0.7, consisting of an absorbing material with a refractive index $m = 1.6 - 0.66\,i$ and a density of 2000 kgm^{-3}, illuminated by 1000 Wm^{-2} at 550 nm at a temperature of 293 K, is shown in **Fig. 8** (left). For better comparison, the force is given as a ratio to the weight of the particle. Similar to the ΔT force, it decreases with increasing pressure, but there is no decrease for low pressures. The force is considerable, for particles of 0.2 µm it is more than 10 times the weight, causing, e.g. the trembling motion as observed, e.g. by Steipe (1952).

But this force continuously changes direction due to the Brownian rotation of the particle. The mean square angle of rotation $\overline{\theta^2}$ of a spherical particle with diameter d in time t is (Fuchs, 1964, p.245): $\overline{\theta^2} = \frac{2}{\pi}\cdot\frac{kT}{\eta d^3}\cdot t$, with k the Boltzmann constant and T the temperature. A few values of average revolutions per second are given below:

Diameter [µm]	0.1	0.2	0.5	1	2
Average revolutions in 1 second $\left[\frac{1}{2\pi}\cdot\sqrt{\overline{\theta^2}}\right]$	61.	21	5.44	1.92	0.68

Considering the vigorous rotation, it is immediately evident that none of the above particles will perform a reasonably straight motion.

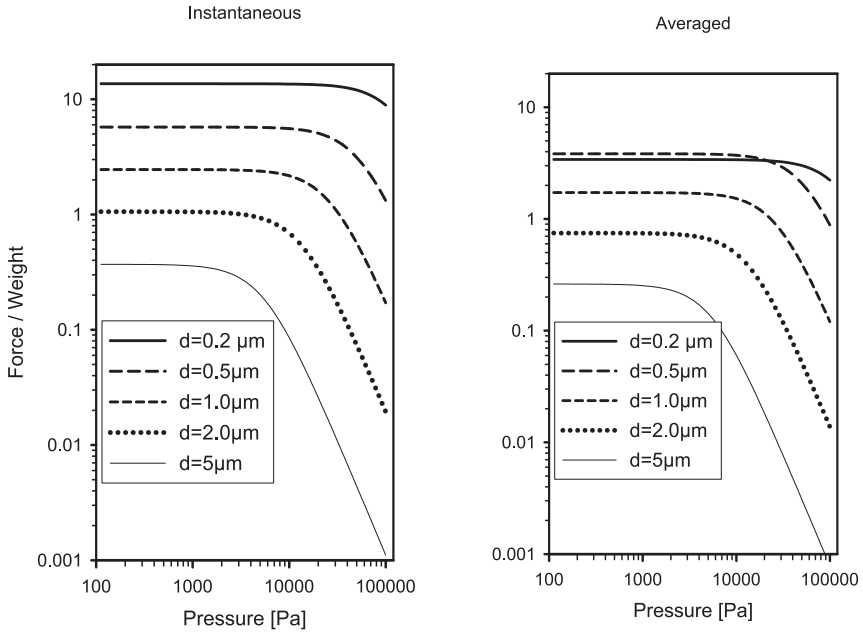

Fig. 8 Photophoretic $\Delta\alpha$ force as a function of pressure for various particle sizes. The force is given relative to the weight of the particle. Left side: Force on a particle, which is assumed to be fixed in space. Right side: average force for a particle oriented by a magnetic field, but disturbed by Brownian rotation.

The situation changes immediately if the particle orientation is forced in a certain direction. For our considerations we will assume the particle is located in a magnetic field **B** and has some remanent magnetism characterized by the magnetic momentum **m** (**Fig. 9**). The particle orients itself such that its magnetic momentum points in the direction of the magnetic field. The direction of the photophoretic force does not usually coincide with the direction of the magnetic moment and the angle between the two is δ. The particle can still freely rotate around the axis of the magnetic moment, therefore all force vectors are located on a cone with an opening angle of $2\cdot\delta$. But Brownian rotation is stochastic, thus the photophoretic force will cause a quasi-helical motion (see insert of **Fig. 9**). The averaged force on the direction of the field is obtained by multiplying the instantaneous force (8) with cos δ. Brownian rotation is not only around the axis of the magnetic momentum, but it will also disturb the orientation of the force vector, which we have so far assumed to be at angle δ to the magnetic field line. The stronger the magnet, the less deviations from this direction will be possible. The competition between orienting torque by the magnetic field and the disorientation by thermal disturbance is very similar to the orientation of magnetic dipoles in the theory of paramagnetism (see, e.g. Brand and Dahmen, 2005, pp. 290–294): The magnetic dipole with magnetic moment **m** in the magnetic field **B** has a potential energy, **m**·**B**, its thermal energy is kT. The ratio $x = \frac{m \cdot B}{k \cdot T}$ of the maximum potential energy $E_p = m \cdot B$ and the thermal energy $E_{th} = k \cdot T$ is a measure for the strength of orientation. No orientation means no magnetic field or moment, or $T \to \infty$, which implies $x = 0$. Perfect orientation would be for $m \cdot B \to \infty$ or $T \to 0$ signifying $x \to \infty$. The theory of paramagnetism yields for the magnetization M the expression $M = \hat{M}(\coth x - \frac{1}{x}) = \hat{M} \cdot L(x)$ (Brand and Dahmen, 2005, p. 293), with $\hat{M}$ the saturation magnetization and $L(x) = \frac{1}{\tanh x} - \frac{1}{x}$ the Langevin function. The asymptotic behavior of $L(x)$ is: $L(x) = \frac{1}{3}x$ for $x \ll 1$, i.e. almost no orientation for small magnetic field and/or moment, and $L(x) = 1 - \frac{1}{x}$ for $x >> 1$ which means perfect orientation for a strong dipole and/or field.

Using the formalism of paramagnetism, the projected force is multiplied with the Langevin function $L(x)$, i.e. the average projected force in the direction of the magnetic field using (8) is

$$F = \frac{1}{12 \cdot \bar{c}} \cdot \frac{1}{1 + (p/p^*)^2} \frac{\Delta\alpha}{\bar{\alpha}} \cdot H \cdot \cos\delta \cdot L(x)$$, with

$x = \frac{m \cdot B}{kT}$. (see, e.g. Preining, 1966). This has been done for the considered particles, assuming the material to have a volume magnetization of 0.02 T/μ_0, and a magnetic field of 7.10^{-5} T (earth's magnetic field). The mean projected force is shown in **Fig. 8** (right side). Besides the factor cos 45°, there is little difference to the instantaneous force

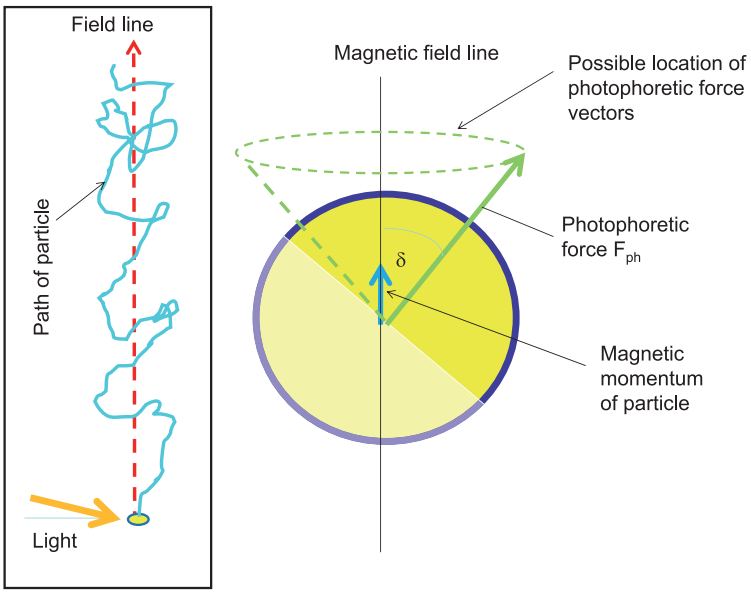

Fig. 9 Particle containing a magnetic dipole in a magnetic field. The particle is oriented such that the magnetic dipole moment points in the direction of the magnetic field. Rotation around the axis is possible, and the photophoretic force vectors are positioned on a cone with an opening angle of 2δ (right). Due to the stochastic manner of Brownian rotation, the particle performs a quasi-helical motion (left).

for the particles of 5 and 2 µm in diameter since the magnetic moment is sufficiently large to orient the particles. For the smaller sizes disorientation is essential, e.g. for 0.2-µm particles, the averaged force only is 25% of the instantaneous one. Nevertheless the averaged photophoretic force can be larger than gravity, as is the case for the 0.2- to 1-µm particles, thus levitation by sunlight in the earth's magnetic field is possible. **Fig. 10** shows the size dependence of the relative force for various air pressures. For particles smaller than 0.1 µm, the Brownian rotation prevents levitation, for particles larger than 1 to 5 µm, depending on pressure, orientation would be optimal, but the weight increases $\propto d^3$ whereas the photophoretic force $\propto d^2$, thus the relative force decreases.

The $\Delta\alpha$ force can be channeled around one direction if an orienting torque exists. This has been shown above for magnetic orientation, but is also possible by electric fields or by gravity. A typical everyday example of orienting torque by gravity would be a fishing float which usually stands upright in the water, when disturbed it will return to its initial position due to the uneven distribution of mass. An inhomogeneous distribution of mass will orient the particle in the same way. This can be seen in **Fig. 11**: Assume a particle having different accommodation coefficients on the two hemispheres causing a photophoretic force to upwards right. (a) The center of gravity is displaced from the center of the photophoretic force by a vector **q**. Gravity and photophoretic force vectors jointly cause a motion of the particle to the right and slightly upwards; (b) the motion of the particle causes a friction force which is added to the photophoretic force. Now gravity and the other forces are balanced and a stationary state is reached; but, due to the offset of the center of gravity and the center of photophoretic plus friction force, a torque acts on the particle, rotating it counterclockwise until the center of photophoretic force is above the center of gravity. This results in an upward motion, since the photophoretic force is larger than the weight (c).

The orientation of the particle is disturbed by Brownian rotation, the important magnitude is the ratio of the potential energy $E_p = m \cdot g \cdot q$ to the thermal energy $E_{th} = k \cdot T$, i.e. the value given by eq. (8) has to be multiplied by $L(x)$ with $x = \frac{m \cdot g \cdot q}{k \cdot T}$. Using the same procedure as above, the average force for particles of various sizes and at different pressures has been calculated and results can be seen in **Fig. 10** (right). The assumed density is $\rho_p = 1000$ kgm^{-3} and the center of gravity is displaced by $q = 0.2 \cdot d$. The only difference to magnetic orientation is the smaller force and the larger diameter at which the relative force peaks. Levitation is only possible at lower pressures. Since the force is directly proportional to the flux density of the radiation, levitation at atmospheric pressures is possible at flux densities which can be achieved easily by lasers or by intense illumination.

The $\Delta\alpha$-photophoresis needs an orienting field, thus it is called field photophoresis, specifically gravito-, magneto- or electro-photophoresis. For optimum $\Delta\alpha$-photophoresis, the particles should have a considerable variation of the accommodation coefficient on the surface and a high thermal conductivity, in order to have a homogeneous temperature on the surface.

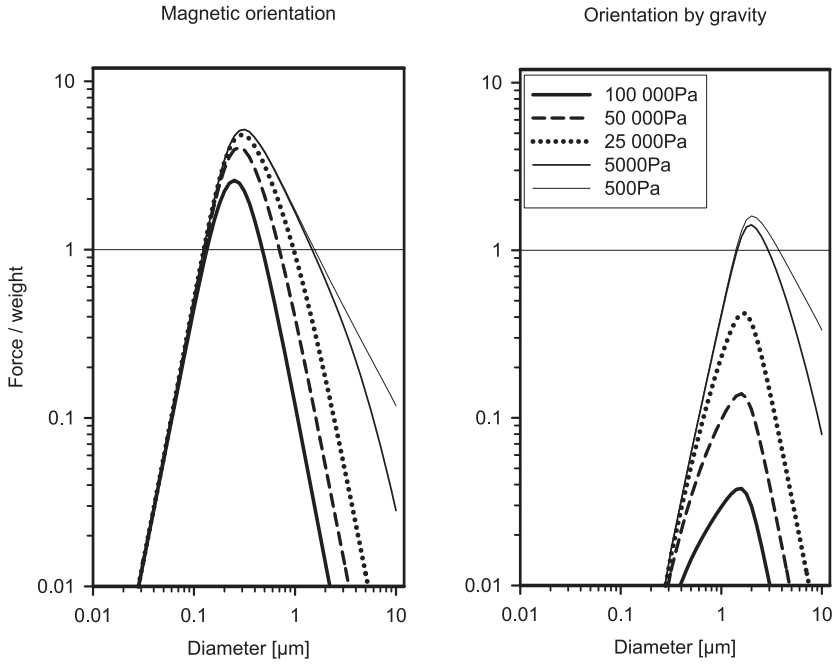

Fig. 10 Relative photophoretic $\Delta\alpha$ force: Left: Magnetic orientation of the particle. Right: Orientation by gravity. For conditions above the horizontal line, levitation in the atmosphere is possible.

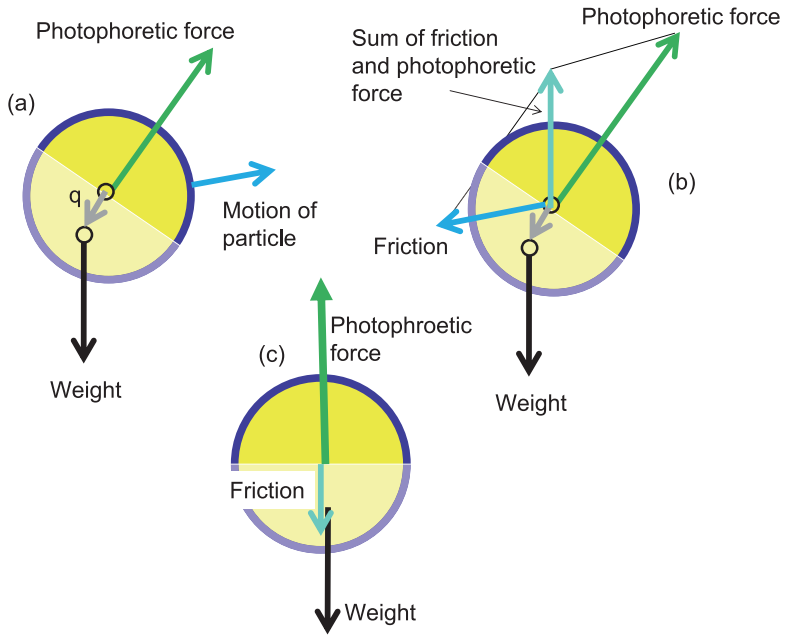

Fig. 11 Orientation of a particle by gravity: (**a**) The center of mass of the particles is displaced by a vector **q**. The photophoretic force (due to different accommodation coefficients) added to the weight of the particles causes a motion to the right. (**b**) The friction is a vector to the left (**b**), adding friction and photophoretic force yields a vertical vector. Since the two vertical vectors are anchored at different points, a torque on the particle forces it to rotate (**c**) until the two anchor points are above each other (**c**).

(c) Other types of photophoresis

In the two previous sections we have assumed the particle to be spherical and having a rather symmetric distribution of the accommodation coefficients on the surface. It is hard to imagine that particles formed by combustion, coagulation, condensation on existing surfaces, mechanical abrasion or interstellar dust particles fulfill these requirements. It can be assumed that particles illuminated by light have a temperature gradient on their surface (needed in ΔT force), but it is unrealistic for a particle to have the same temperature everywhere on an inhomogeneous surface, as

we assumed for the $\Delta\alpha$ force. Thus $\Delta\alpha$ and ΔT photophoresis will most likely occur simultaneously.

An inhomogeneous surface of the particles will also cause a photophoretic torque. The radiometer itself (**Fig. 2**) is an example. Two arrangements where a photophoretic torque will act are shown in **Fig. 12**. The shape **(a)** is the "Spitzenradiometer" (pointed radiometer) theoretically investigated by Hettner (1924). The pointed ends of the body will release more thermal energy, thus be colder. The photophoretic force is in the direction of the temperature gradient, resulting in a counterclockwise torque. The particle **(b)** with an inclusion on the surface having a different accommodation coefficient will have a clockwise torque, if the accommodation coefficient of the surface of the inclusion is smaller than for the remaining surface. Simultaneously, an upwards $\Delta\alpha$ force acts on this particle.

In addition to the torque and the $\Delta\alpha$-force, this particle with the inclusions (**Fig. 12b**) will also have a ΔT force. In the stationary state, the orientation of the photophoretic torque will be parallel to the direction of light, resulting in a helical motion around the direction of the illumination. The direction of the photophoretic $\Delta\alpha$ force need not agree with the direction of the photophoretic torque (both vectors are particle-fixed). Depending on their angle to each other, the resulting motion can be in the direction of the light or opposite (for theoretical details, see Preining, 1966, p. 130, for observations, see Lustig and Söllner, 1932).

For the $\Delta\alpha$ force, an inhomogeneous distribution of the accommodation coefficient on the surface is needed. In reality this will not be two homogeneous hemispheres, as assumed above, but a particle with a complicated surface structure. Therefore in addition to the $\Delta\alpha$ force, a photophoretic torque will make the particle rotate around a particle-fixed axis. This rotation has to be added to the linear motion caused by the $\Delta\alpha$ force. Therefore the simple picture of **Fig. 9** has to be replaced by a helical movement around the field line with a constant pitch, obviously with Brownian disturbances superimposed. The average velocity or the force in the direction of the magnetic field is not altered. The same is true for gravito-photophoresis.

In an inhomogeneous horizontal illumination, oscillations along a vertical axis are possible. Consider a particle performing gravito-photophoresis with an additional photophoretic torque. The particle will have a helical movement upwards and out of the horizontal beam of light. With lower illumination, both the gravito-photophoretic force and the torque decrease and after some time for temperature adjustment, the particle follows a helical downward movement with a different pitch and then resumes the upward motion, see **Fig. 1f**.

In two inhomogeneous light beams in the opposite direction, complicated closed loops in the horizontal direction are possible, in rotating magnetic fields the particles have even more impressive orbits, for details see Preining (1966).

Fig. 12 Examples for particle shapes which cause photophoretic torque. (**a**) The "Spitzenradiometer" (Hettner, 1924). The points dissipate more thermal energy and are thus colder. Due to the temperature difference, a counterclockwise torque arises. (**b**) A particle with an impurity on the surface having a different accommodation coefficient. Both a torque and a $\Delta\alpha$ force arise.

Advanced theories of photophoresis

The theories above have postulated a spherical particle with some inhomogeneities with respect to accommodation coefficient or density. Experimental evidence shows that non-spherical particles are better suited for photophoresis than spherical particles. For a full theory similar to a sphere, the following problems have to be solved: Heat sources in the particle, thermal conduction in the particle to obtain the temperature distribution on the surface, and information on the accommodation coefficients on the surface. This is already difficult for spherical particles; but for simple particle shapes and structures, solutions do exist: Spheroids (Ou and Keh, 2005), cylinders (Keh et al., 2001), convex particles with rotational symmetry (Zulehner and Rohatschek, 1990), and fractal structures, using the Berry-Percival method for light interaction and a Monte-Carlo method for molecular transfer to obtain ΔT and $\Delta\alpha$ forces (Cheremisin and Vasilyev, 2004). The Monte-Carlo method offers the advantage that for whatever shape and composition of the particle, a solution is possible with the constraint of sufficient supercomputer time and detailed information on the properties of the particle, which is not usually available. Nevertheless, the findings for the simple assumption of spherical particles agree quite well with experimental results for non-spherical particles.

Measurement of photophoretic forces I: Longitudinal photophoresis:

The following components for a successful measurement of photophoresis are needed: measuring chamber, radiation source, observation device, particle generator, pressure gauge as already described above. Since monodisperse particles could not be produced in the early days,

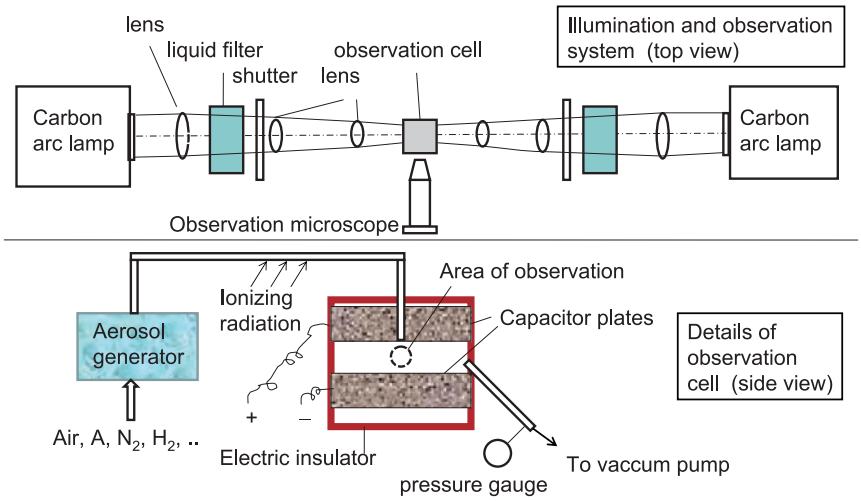

Fig. 13 Apparatus used by Ehrenhaft (1918) for the observation of photophoresis. Top: Light is concentrated by several lenses in the center of the observation cell. The observation is done through a microscope, perpendicular to the direction of illumination. The dark field illumination permits the observation of particles sizing down to tens of nanometers. The cell can be evacuated or pressurized and is made of an electrically insulating material. Bottom: Two metal plates serve as a capacitor to exert vertical forces on charged particles. The charging of the particles is done by ionizing radiation.

it was important to make as many measurements as possible with one particle. Electrostatic fields are used to bring the (charged) particles back to the initial state, being a very tedious job, especially if the pressure in the chamber was changed. So it required a lot of skill and patience to produce series of measurements which lead to the data points, e.g. shown in **Figs. 5** and **6**.

Ehrenhaft (1918) designed an observation cell and illumination system of maximum flexibility, a schematic can be seen in **Fig. 13**. The cell can be illuminated by the light of a carbon arc lamp, the infrared is filtered by a liquid filter, thus the illumination is polychromatic with wavelengths between 400 and 1200 nm. The light is concentrated by several lenses into the center of the observation cell. The flux density in the center can be up to 4000 times the solar constant. With a shutter, the illumination can be chosen to be from the right or the left side, or both. Particles in the cell are observed by a microscope, viewing perpendicular to the direction of illumination. The intense dark field illumination permits the recognition of particles down to less than 100 nm in diameter. The observation cell is made of the electrically isolating material ebonite, contains two metal plates forming a capacitor and has two glass windows for illumination and one to permit observation. Operation at low pressure is also possible. Particles are generated in various carrier gases, by processes such as electrical arc between various metal electrodes, evaporation in test tubes, or simply by using smoke, e.g. from the combustion of paper or cigarettes. The particles are charged by diffusion charging with ions produced by ionizing radiation.

To measure the photophoretic force, the particles are illuminated by light and the velocity of the horizontal motion is measured by stopping the time needed for a distance of 0.3 mm. Within this distance the light could be considered homogeneously. When the particle is close to the end of the field of view, the opposite illumination is used, bringing the particles back. When settling too far, a voltage is applied to the plates of the capacitor, lifting the charged particles up. In this way a series of measurements is possible with one and the same particle. When the particle is outside of the intense beam, the photophoretic force is negligible and the settling velocity and the velocity in the electric field can be measured. The diameter of the particle was measured by determining the settling velocity v and applying Stokes' Law: $d = \sqrt{\frac{18 \cdot \eta \cdot v}{\rho_p \cdot g \cdot C_s}}$ with ρ_p the density of the material forming the particle and C_s the slip correction. Using this technique, it was possible to determine the dependence of the photophoretic force on illumination, material, pressure, and with some modifications (see below), on external fields.

An impressive experiment demonstrating light absorption to be the reason for photophoresis has been performed by Déguillon (1950): A droplet of a dye solution is illuminated by a white light beam and shows positive photophoresis. The dye has a strong light absorption in a narrow band of wavelengths. If this wavelength range is filtered out of the beam by a slab of the same dye solution, the particle is still strongly illuminated, but shows no photophoresis.

The laser, CCD cameras and methods to produce monodisperse particles made observations simpler by far: An arrangement is shown in **Fig. 14** (Haisch et al., 2008). The

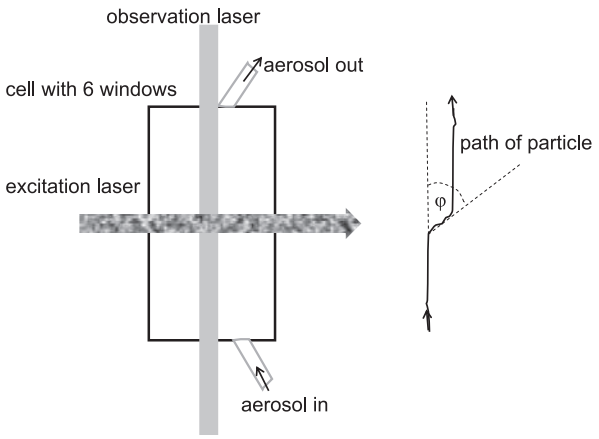

Fig. 14 Experimental determination of the photophoretic velocity: A continuous aerosol flow passes a small cell which is illuminated by a vertical laser beam. When illuminated by the horizontal laser beam, the particles move in the direction of the light. The motion of the particles is observed with a video camera. The path of the particles is shown on the right.

aerosol passes through a cell about 10 mm × 10 mm × 80 mm in size, having windows on all planes of the cuboid. The aerosol is illuminated by a green laser passing vertically through the cell. The excitation laser passes from the right to the left, the observation of the particles' path is performed with a CCD from the front (perpendicular to the drawing plane). The particles move vertically in the cell until passing through the excitation laser beam, which deflects particles with positive longitudinal photophoresis to the right. A schematic of the CCD picture is seen on the right side. Knowing the vertical velocity v_v of the particle, the photophoretic velocity v_{phot} can be obtained by the angle φ between the vertical and the direction in the laser beam by $v_{phot} = v_v \cdot \tan \varphi$. Monodisperse polystyrene latex spheres with no absorption for green light were used, so the observation laser does not cause photophoresis. With this set-up the dependence of the photophoretic velocity on the laser flux density and the particle size have been checked and agreement with theory has been found. The photophoretic velocity depends on the material of the particles; for substances such as $CuSO_4$, NaCl, $Cu(CH_3COO)_2$, $Ni(NO_3)_2$, $KMnO_4$, and others, and a size of 200 nm ± 50 nm, values between –0.48 and +0.03 mm/s have been found (Kykal, 2010, p. 100).

The force on a charged particles in the field of a capacitor offers the possibility to directly measure the photophoretic force. A capacitor having a homogeneous field does not allow a stable positioning of the particles perpendicular to the electric field. By using a capacitor with an insulated inner circular electrode at a higher voltage, a potential well can be created, keeping the particles horizontally stable in the center. Vertical stability is attained by observation of the particle's location with a position-sensitive detector and a feedback to the voltage of the central plate (Arnold et al., 1980, see **Fig. 15**).

The electrodynamic levitation (e.g. Wuerker et al., 1959, see also **Fig. 16**, many other configurations are in use, for a review see, e.g. Davis, 1997) offers the possibility of trapping the charged particles. The AC voltage 2 V_{ac} is applied between the ring electrode and the bottom and top electrode. Additionally, the DC voltage 2 V_{dc} is added. The non-uniform alternating field has a focusing effect and dynamically stabilizes the charged particle in the null point of the field. The additional DC field compensates the weight of the particle and brings it to the plane of symmetry of the electrodes. When illuminating the particle, e.g. by a vertical laser beam, the DC voltage V_g is adjusted to compensate the additional photophoretic force in order to keep the particle in position. The additional electric field multiplied by the particle charge equals the photophoretic force. For an application see, e.g. Wurm and Krauss (2008).

Measurement of photophoretic forces II: Field photophoresis

For measurement of field photophoresis, an orienting field is obviously needed. For magneto- or electro-photophoresis this field can be simply generated in the

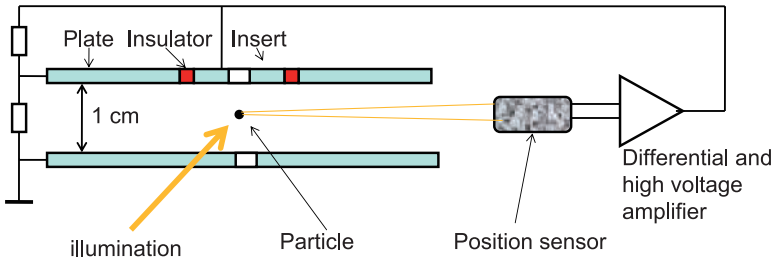

Fig. 15 Capacitor for measurement of the photophoretic force. The upper plate of the capacitor has a circular insert, which is kept at a higher voltage, stabilizing the particle horizontally in the center. The vertical stabilization is done with a position-sensitive photodetector.

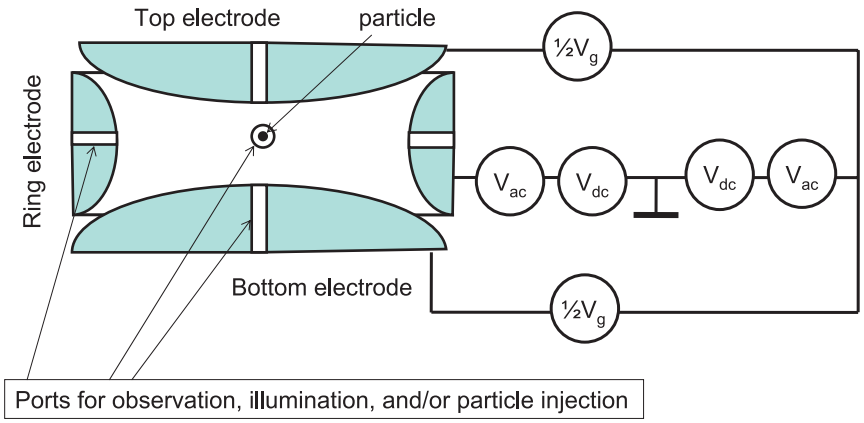

Fig. 16 Electrodynamic levitation of particles. An AC voltage is applied between the bottom and top electrode and the ring electrode in series with a DC voltage. By proper shaping of the electrodes, a rotational symmetric parabolic potential is created, trapping the charged particle in the center. When illuminated by a vertical beam, the position of the particle changes. By adjusting V_g, the particle is brought back into position and the force can be determined.

laboratory, whereas the gravitational field is omnipresent. Magneto-photophoresis has, e.g. been measured by Steipe (1952) and Preining (1953), using an arrangement similar to that in **Fig. 13**, with Helmholtz coils to produce the magnetic field, or to compensate the earth's magnetic field. The particles were generated by an arc discharge between iron electrodes, producing spherical particles of ferromagnetic iron oxides with a diameter around 400 nm and illuminated with flux densities comparable to the solar constant. The measured photophoretic velocities increased with increasing magnetic field strength due to better orientation. In the case of perfect orientation, the photophoretic velocities were between 50 and 300 µm/s, compared to the settling velocities between 6 and 30 µm/s. For a field strength equaling the earth's magnetic field, the photophoretic velocities were 50 to 80% of the maximum values, indicating that photophoretic levitation is possible in the atmosphere.

Since gravity cannot be switched on and off, the measurement of gravito-photophoresis is more elaborate (see, e.g. Jovanović, 2005, **Fig. 17**): An observation cell which can be evacuated has four windows. The illumination comprises a Xenon arc lamp (similar to daylight) and a lens system, producing a homogeneous illumination within the cell comparable to sunlight. A mirror opposite to the light entrance produces additional illumination, reducing longitudinal photophoresis. Observation is perpendicular to the illumination through a microscope lens and a CCD camera. The particle reservoir contains a powder of soot or graphite, etc. Tapping on the reservoir produces about 1000 particles which fall into the beam, a few of them show gravito-photophoresis, move upwards, and end their motion at the top of the illumination beam. The shutter is closed for a few seconds, the particles sediment and upon illumination move upwards again. In this way

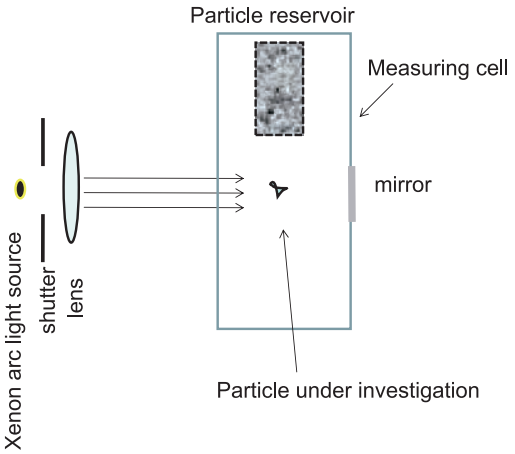

Fig. 17 Measurement of gravito-photophoresis. The cell is illuminated by light through one of the windows, and observation is perpendicular to this direction. Particles in the reservoir are released by knocking the cell slightly. Particles which show photophoresis are trapped at the top of the beam. Closing the shutter causes the particles to sediment, with open shutter the gravito-photophoretic velocity can be measured (Jovanović, 2005).

the velocity due to sedimentation and photophoresis can be measured. An electron microscope grid (normally shielded) can be positioned under the observation volume and the particles can be analyzed. **Fig. 18** gives the relation between the Feret diameter and the perimeter of the particles, the particles showing gravito-photophoresis have a larger perimeter, i.e. have a more irregular shape, as expected. Spherical black carbon particles (obtained by the atomization of India ink) do not show gravito-photophoresis.

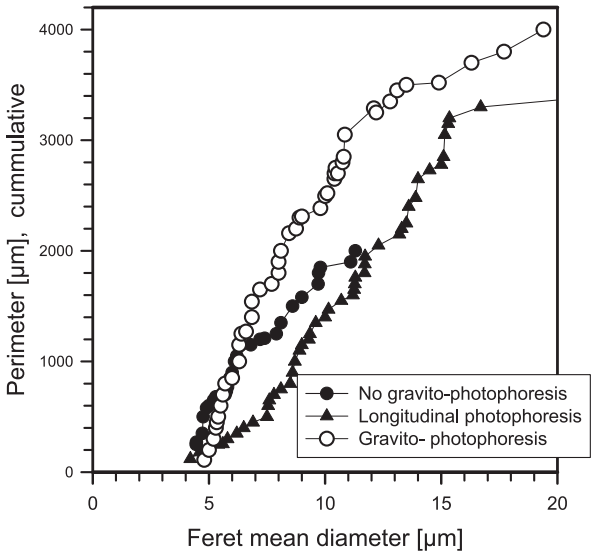

Fig. 18 Relation between the Feret diameter and perimeter of particles. The particles showing gravito-photophoresis have the largest perimeter, i.e. are the most irregular (Jovanović, 2005).

Application of photophoresis in various fields of aerosol science

Positive photophoresis can be used as a tool for the on-line separation of absorbing and non-absorbing particles. Particles are illuminated by an intense laser (808 nm), obtain a velocity in the direction of the light and perpendicular to the flow velocity due to the photophoretic force, and can be collected in a secondary flow (Haisch et al., 2008). Photophoretic particle trapping in a doughnut-shaped light intensity field and levitation is also possible (Desyatnikov et al., 2009).

Failures in electronic chip production are caused by particles which settle on the chip during production. Shielding the product from the unwanted contamination is traditionally achieved by thermophoretic or electrophoretic forces; but both interfere with the production process. Longitudinal photophoresis has been investigated as a possibility to push particles out of the sensitive range (Selvaraj, 1994; Periasamy et al., 1993). Since the only requirement for photophoresis is a light (laser) beam, interference with the production process is minimal. Furthermore, the photophoretic force increases with decreasing pressure for the particles of interest.

In the stratosphere and mesosphere, the air molecule's mean free path is between 1 and 100 µm due to the lower pressure, thus appreciable photophoresis can occur for all particles found there. Early laboratory investigations under stratospheric conditions revealed considerable upwards motion of NaCl particles by negative longitudinal photophoresis (Orr and Keng, 1964); on the other hand, Hidy and Brock (1967) estimate the effect of photophoresis on the settling velocity of the particles as negligible. Since an irregular particle or one with a magnetic or electric dipole moment has a preferred orientation in the gravitational, magnetic or electric field, gravito-magneto- or electro-photophoresis are important. This has been proven experimentally (Jovanović, 2005).

The existence of layers of particles in the stratosphere and mesosphere is a well-known fact (Junge et al., 1961; Bigg, 1964; Volz, 1971; Zuev et al., 1996, 2009; Berthet et al., 2002, Mateshvili et al., 1999; Gerding et al., 2003). Furthermore, soot particles are found at locations in the stratosphere with no evident sources (Pueschel et al., 2000). Soot particles absorb light, thus are hotter than the surrounding air, and they have a complex shape, which is important for gravito-photophoresis. So the movement of the particles upwards from the place where they are produced (Pueschel et al., 2000) can be explained. For the existence of particle layers in the atmospheres, it is necessary that (1) a lifting force on the particles compensates gravity and (2) that the particles return to their location after disturbance. Due to the complex structure of the stratosphere and mesosphere, locations can be found where these requirement are fulfilled (Cheremisin et al., 2005, 2011). The particles are illuminated by solar radiation amounting to 1360 W/m^2, thus light-absorbing particles consisting of black carbon or iron oxides can be levitated by gravito-, electro- or magneto- photophoresis. The outgoing terrestrial infrared radiation equals the solar constant, thus particles that are transparent in the visible but absorbing in the infrared are also candidates for photophoresis. For example, for ammonium sulfate, the imaginary part of the refractive index is $< 10^{-6}$ in the visible but increases to more than 1.0 at 10 µm, thus $(NH_3)_2SO_4$ is as absorbing in the infrared as black carbon in the visible (Bohren and Huffman, 1983, p. 438). In the Junge layer (Junge et al., 1961), sulfate particles have been found and Cheremisin et al. (2011) have shown that particles which strongly absorb in the infrared only and sized between 1 and 2 µm will be stable at ≈ 22 km. Particles formed from meteor smoke or debris of rockets can have a magnetic momentum and thus be oriented by the earth's magnetic field. The magnetic orientation is stronger than by gravity, see **Fig. 10**, so particles between 0.1 and 0.25 µm can form layers, e.g. at 76 to 82 km. Favorable conditions in the atmosphere for the formation of stable layers depend on time, latitude, longitude, and particle size. Particles with sizes between 0.1 and 5 µm can form layers between 18 and 90 km altitude at various times of the year, latitude and longitude. For details see Cheremisin et al. (2011). A comparison of the backscatter ratio of the Kamchatka LIDAR station 2007 to 2008 and the calculated stability zones shows an almost perfect agreement (Cheremisin et al., 2012).

Photophoresis can have an influence on coagulation:

After reflection from the surface of a particle heated by light absorption, the gas molecules have a higher velocity, they can repel adjacent particles by impaction and thus slow coagulation (Cheremisin and Kushnarenko, 2013). The magnitude of the force is considerable and comparable to electrostatic forces: e.g. two 50-nm particles separated by three radii, illuminated by 1360 W/m^2 at a pressure of 1000 Pa, the repelling force is 30 times the weight of the particles, for 250- and 500-nm particles the factors are 10 and 7. At night, the particles are colder than the surrounding air and thus have a small attractive force. This repelling force slows coagulation, the coagulation constant is reduced by a factor of up to 10.

During combustion, the high temperatures cause strong infrared and visible radiation, and light-absorbing particles are present. The main force on the particles is by thermophoresis powered by the temperature gradients, but the photophoretic forces cannot be neglected. They are responsible for the formation of stable soot shells around a fuel droplet (Pera et al., 1999), and amount to about 10% of the deposition force to cold surfaces (Castillo et al., 1990).

Photophoresis is an important force involved in planet formation. In a gas-rich, optically thin circumstellar disk, the motion of particles ranging from 1 μm to 10 cm will be dominated by photophoresis, moving the particles opposite to gravity to a distance from the star where the gas density reaches a value at which photophoresis equals all other forces at work. Thus the formation of ring-like structures of dust distribution around a star can be explained naturally (Krauss and Wurm, 2005), and the formation of protoplanets is significantly influenced by photophoresis (Wurm and Krauss, 2006; Krauss et al., 2007).

In the fight against global warming by geo-engineering, particles could be positioned in the stratosphere or mesosphere. They should reflect sunlight and remain suspended as long as possible. The photophoretic force can be very helpful, since a long residence time can be achieved this way. A particle optimized for this purpose could be a disk of 10 μm in diameter, having a layer of Al_2O_2 at the top, Al in the middle and $BaTiO_3$ at the bottom and a thickness of 10 nm. Orientation is caused by the electric field (Keith, 2010), i.e. electro-photophoresis prevents settling.

For completeness it is mentioned that the term photophoresis is also used for the motion of hydrocolloids illuminated by an intense laser beam. But for photophoresis, the thermal slip is needed. In that case, it is actually the radiation pressure, see Eqn. (1), that makes the particle migrate (Helmbrecht et al., 2007).

Acknowledgements

The author is thankful for the infrastructure made available by Professor Tohno, School of Energy Science of the University of Kyoto and the Zentralbiliothek für Physik Wien, which is an almost infinite source for hard-to-find literature. Most of this paper was presented as a plenary lecture during the European Aerosol Conference 2012 in Granada. I thank the organizers L. Alados and F.J Olmo Reyes for giving me the chance to investigate this interesting subject in depth.

List of symbols

Symbol	Name	Unit	Definition	Remark
A	Absorption cross-section	m^2	$A = \frac{1}{4} \cdot d^2 \cdot Q_a$	Fictitious surface through which the absorbed light passes
B	Magnetic flux density	T		
$\overline{c}$	Mean velocity of gas molecules	m·s^{-1}	$\sqrt{\overline{c^2}} = \sqrt{\frac{3RT}{M}}$	
C_s	Slip correction	none		
d	Diameter	m, μm, nm		
E_{emitt} E_{abs}	Emitted, absorbed IR flux	W		IR flux absorbed and emitted by a particle; must be balanced with absorbed visible flux and power transferred by accommodation to molecules
g	Gravity constant	m·s^{-2}	$g \approx 10$m·s^{-2}	Acceleration on earth due to gravity
H	Transferred energy flux	W		Energy flux transferred by the gas molecules from the particle surface
J_1	Asymmetry parameter for absorption	none	Yalamov et al., 1976	$\lvert J_1 \rvert = \frac{1}{2}$ for opaque particles

Symbol	Name	Unit	Definition	Remark
k	Boltzmann constant	$J \cdot K^{-1}$	$k = 1.38 \cdot 10^{-23}\ J \cdot K^{-1}$	
$k_g\ k_p$	Thermal conductivity	$W \cdot m^{-1} \cdot K^{-1}$		k_g conductivity of gas, k_p conductivity of particle's material
$L(x)$	Langevin function	none	$L(x) = \frac{1}{\tanh x} - \frac{1}{x}$	
M	Molecular mass	$kg \cdot kMol^{-1}$		
m	Magnetic moment	Am^2		Symbol m also used for mass
p	Pressure	Pa		
q	Displacement	m		Vector between center of gravity and center of photophoretic force
Q_e	Absorption efficiency	none		Absorbed radiation divided by the radiation incident on the particle
R	Gas constant		$R = 8314\ J\ kMol^{-1}\ K^{-1}$	
S	Flux density	$W \cdot m^{-2}$	$S = \frac{dP}{dA}$	Energy of radiation passing per time through a surface
T	Absolute temperature	K		
x		none	$x = \frac{m \cdot B}{kT}$ or $= \frac{m \cdot g \cdot q}{kT}$	Ratio of potential energy $E_p = m \cdot B$ or $E_p = m \cdot g \cdot q$ and thermal energy $E_{th} = k \cdot T$
α	Accommodation coefficient	none	$\alpha = \frac{T - T_0}{T_s - T_0}$	Probability for a gas molecule to diffusely reflect from the particle's surface with the temperature of the surface
γ		none	$\gamma = \frac{c_p}{c_v}$	Ratio of specific heat at constant pressure and specific heat at constant volume
η	Viscosity	Pa·s		
κ	Thermal creep coefficient	none		$\kappa = 1.14$ for 10% specular-reflected molecules
ρ	Density	$kg \cdot m^{-3}$		ρ_p density of material-forming particle
$\overline{\theta^2}$	Square of angular displacement	rad^2	$\overline{\theta^2} = \frac{2}{\pi} \cdot \frac{kT}{\eta d^3} \cdot t$	The mean square angle of rotation in time t

References

Akhtaruzzaman A.F.M., Lin S.P., Photophoresis of absorbing particles, Journal of Colloid and Interface Science, 61 (1977) 170–182.

Angelo R.L., Experimental determination of selected accommodation coefficients, Thesis, Aeronautical Engineer, California Institute of Technology, Pasadena, California, USA, 1951, 177 pp.

Arnold S., Amani Y., Orenstein A., Photophoretic spectrometer, Review of Scientific Instruments, 51 (1980) 1202–1204.

Arnold S., Lewittes M., Size dependence of the photophoretic force, Journal of Applied Physics, 53 (1982) 5314–5319.

Bakanov S.P., Thermophoresis in gases at small knudsen numbers, Soviet Physics Uspekhi, 35 (1992) 783.

Barber P.W., Hill S.C., Light scattering by particles: Computational methods, World Scientific, Singapore, 1990, 261 pp.

Berthet G., Renard J.B., Brogniez C., Robert C., Chartier M., Pirre M., Optical and physical properties of stratospheric aerosols from balloon measurements in the visible and near-infrared domains. I. Analysis of aerosol extinction spectra from the AMON and SALOMON balloonborne spectrometers, Applied Optics, 41 (2002) 7522–7539.

Bigg E.K., Atmospheric stratification revealed by twilight scattering, Tellus, 16 (1964) 76–83.

Bohren C.F., Huffman D.R., Absorption and scattering by small particles, John Wiley & Sons, New York, 1983, 530 pp.

Brand S., Dahmen H.D, Elektrodynamik, Springer, Berlin, 2005, 689 pp.

Castillo J.L., Mackowski D.W., Rosner D.E., Photophoretic modification of the transport of absorbing particles across combustion gas boundary layers, Progress in Energy and Combustion Science, 16 (1990) 253–260

Cheremisin A.A., Vasilyev Yu.V., Matheamtical model of the processes of particle levitation in the earth atmosphere under the force of Photophoresis, *The International conference on Computational Mathematics ICCM-2004* June 21–24, Novosibirsk, Russia, 2004.

Cheremisin A.A., Vassilyev Y.V., Horvath H., Gravito-photophoresis and aerosol stratification in the atmosphere, Journal of Aerosol Science, 36 (2005) 1277–1299.

Cheremisin A.A., Shnipov I.S., Horvath H., Rohatschek H., The

global picture of aerosol layers formation in the stratosphere and in the mesosphere under the influence of gravito-photophoretic and magneto-photophoretic forces, Journal of Geophysical Research: Atmospheres, 116 (2011) D19204.

Cheremisin A.A., Marichev V.N., Bychkov V.V., Shevtsov B.M., Novikov P.V., Shnipkov I.S., Observations of aerosol of different origin by Siberian -Far Eastern LIDAR network and photophoresis, European aerosol conference 2012, September 2-7, Granada, Spain, 2012.

Cheremisin A.A., Kushnarenko A.V., Photophoretic interaction of aerosol particles and its effect on coagulation in rarefied gas medium, Journal of Aerosol Science, 62 (2013) 26–39.

Chernyak V., Beresnev S., Photophoresis of aerosol particles, Journal of Aerosol Science, 24 (1993) 857–866.

Ciro W.D., Eddings E.G., Sarofim A.F., Experimental and numerical investigation of transient soot buildup on a cylindrical container immersed in a jet fuel pool fire, Combustion Science and Technology, 178 (2006) 2199–2218.

Davis E.J., A history of single aerosol particle levitation, Aerosol Science and Technology, 26 (1997) 212–254.

Déguillon F., Photophorese—La photophorese des suspensions dans l'air de solutions colorees et le coefficient d'absorption de celles-ci", C.R. Hebd. Scéanc. Acad. Sci, Paris, 231 (1950) 274–275.

Desyatnikov A.S., Shvedov V.G., Rode A.V., Krolikowski W.Z., Kivshar Y.S., Photophoretic manipulation of absorbing aerosol particles with vortex beams: theory versus experiment, Opt. Express, 17 (2009) 8201–8211.

Dusel P.W., Kerker M., Cooke D.D., Distribution of absorption centers within irradiated spheres, J. Opt. Soc. Am., 69 (1979) 55–59.

Ehrenhaft F., Über eine der Bown'schen Molekularbewegung in den Flüssigkeiten gleichartige Molekularbewegung in den Gasen und deren Molekularkinetischer Erklärungsversuch, Wiener Berichte, 116 (1907) 1139–1149.

Ehrenhaft F., Die photophorese, Annalen der Physik, 361 (1918) 81–132.

Fuchs N.A., The Mechanics of Aerosols, Pergamon, Oxford, 1964, 408 pp.

Gerding M., Baumgarten G., Blum U., Thayer J.P., Fricke K.H., Neuber R., Fiedler J., Observation of an unusual mid-stratospheric aerosol layer in the arctic: Possible sources and implications for polar vortex dynamics, Annales Geophysicae, 21 (1999) 1057–1069.

Haisch C., Kykal C., Niessner R., Photophoretic velocimetry for the characterization of aerosols, Analytical Chemistry, 80 (2008) 1546–1551.

Helmbrecht C., Niessner R., Haisch C., Photophoretic velocimetry for colloid characterization and separation in a cross-flow setup, Analytical Chemistry, 79 (2007) 7097–7103.

Hettner G., Zur theorie des radiometers, Zeitschrift für Physik, 27 (1924) 12–22.

Hettner G., Zur theorie der photophorese, Zeitschrift für Physik, 37 (1926) 179–192.

Hidy G.M., Brock J.R., Photophoresis and descent of particles into the lower stratosphere, Journal of Geophysical Research, 72 (1967) 455–460.

Hinds W.C., Aerosol Technology, Properties, Behavior, and Measurement of Airborne Particles, Wiley Interscience, 1982, 424 pp.

Jovanović O., Gravitophotophorese stark absorbierender Partikel für den stratosphärischen Druckbereich (Gravitophotophoresis of strong absorbing particles for the stratospheric pressure range), PhD. Dissertation, University of Vienna, 2005, 129 pp.

Junge C.E., Chagnon C.W., Manson J.E., Stratospheric aerosols, Journal of Meteorology, 18 (1961) 81–108.

Keh H.J., Tu H.J., Thermophoresis and photophoresis of cylindrical particles, Colloids and Surfaces A: Physicochemical and Engineering Aspects, 176 (2001) 213–223.

Keith D.W., Photophoretic levitation of engineered aerosols for geoengineering, Proceedings of the National Academy of Sciences, 107 (2010) 16428–16431.

Knudsen M., Eine Revision der Gleichgewichtsbedingung der Gase Thermische Molekularströmung, Ann. Phys., 31 (1910a) 205–229.

Knudsen M., Thermischer Molekulardruck der Gase in Röhren, Annalen der Physik, 33 (1910) 1435–1448.

Knudsen M. Die molekulare Wärmeleitfähigkeit der Gase und der Akkomodationskoeffizient, Ann. Phys., 34 (1911) 593–656.

Krauss O., Wurm G., Photophoresis and the pile-up of dust in young circumstellar disks, The Astrophysical Journal, 630 (2005) 1088–1092.

Krauss O., Wurm G., Mousis O., Petit J.-M., Horner J., Alibert Y., The photophoretic sweeping of dust in transient protoplanetary disks, Astron. Astrophys., 462 (2007) 977.

Kykal C., Einsatz der Photo-Thermophorese zur Aerosolcharkterisierung, PhD. Thesis, Technische Universität München, Munich, Germany, 2010.

Landau L.D., Lifschitz E.M., Lehrbuch der theortiechen Physik,vol 2, Klassische Fledtheorie, 480 pp, Akademische Verlagsgesellschaft, Berlin, 1988.

Lustig A., Söllner A., Über photophorese von silberpartikeln, Zeitschrift für Physik, 79 (1932) 823–842.

Mackowski D.W., Photophoresis of aerosol particles in the free molecular and slip-flow regimes, International Journal of Heat and Mass Transfer, 32 (1989) 843–854.

Mateshvili N., Mateshvili G., Mateshvili I., Gheondjian L., Avsajanishvili O., Vertical distribution of dust particles in the earth's atmosphere during the 1998 leonids, Meteoritics & Planetary Science, 34 (1999) 969–973.

Mattauch J., Versuche über die druckabhängigkeit der photophorese, Annalen der Physik, 390 (1928) 967–980.

Orr C., Keng E.Y.H., Photophoretic effects in the stratosphere, Journal of the Atmospheric Sciences, 21 (1964) 475–478.

Ou C.L., Keh H.J., Low-knudsen-number photophoresis of aerosol spheroids, Journal of Colloid and Interface Science, 282 (2005) 69–79.

Parankiewicz I., Über die lichtpositive und die lichtnegative photophorese.(Untersuchungen am Schwefel und Selen), Annalen der Physik, 362 (1918) 489–518.

Pedraza D.F., Klemens P.G., Effective conductivity of polycrystalline graphite, Carbon, 31 (1993) 951–956.

Pera A., Garcia-Ybarra P.L., Castillo J.L., Soot diffusive transport effects, affecting soot shell formation in droplet com-

bustion, Proc. Mediterranean Combust Symp., (1999) 275–285.
Periasamy R., Selvaraj J., Donovan R.P., Nemanich R.J., Photophoretic Deflection of Particles in Subatmospheric Pressure Chambers (extended abstract),TECHCON '93, Atlanta, GA, September 28–30, 1993.
Preining O., Untersuchungen über Photophorese an zerstäubten Silberstahl, Acta Physica Austriaca,7 (1953) 147–154.
Preining O., Photophoresis, Chapter V of *Aerosol Science*, C.N. Davies, Ed. Academic Press, London and New York, 1966, pp. 111–135.
Pueschel R.F., Verma S., Rohatschek H., Ferry G.V., Boiadjieva N., Howard S.D., Strawa A.W., Vertical transport of anthropogenic soot aerosol into the middle atmosphere, Journal of Geophysical Research: Atmospheres, 105 (2000) 3727–3736.
Reed L.D., Low knudsen number photophoresis, Journal of Aerosol Science, 8 (1977) 123–131.
Reiss M., Versuche über die Druckabhängigkeit der Photophorese bei hohen Gasdrücken, Phys Z., 36 (1935) 410–413.
Rohatschek H., Theorie der Photophorese—Ergebnisse und Probleme, Staub, 39 (1955) 45–64.
Rohatschek H., Semi-empirical model of photophoretic forces for the entire range of pressures, Journal of Aerosol Science, 26 (1995) 717–734.
Rubinowitz A., Radiometerkräfte und Ehrenhaftsche Photophorese (I and II), Ann. Phys., 62 (1920) 691–715; 716–737.
Schmitt K.H., Modellversuche zur Photophorese im Vakuum, Vakuum Technik, 10 (1961) 238–242.
Selvaraj J., Photophoretic deflection of particles in subatmospheric pressure chambers, Thesis, North Carolina State University, 1994
Steipe L. Untersuchungen über Magnetophotophorese, Acta Physica Austriaca, 6 (1952) 1–6.
Tauzin P., Lespagnol A., Relation entre la magnétophotophorèse et le ferromagnetism, Comptes rendues hebdomad, Séances Académie Sciences, Paris, 230 (1950) 1853–1855.
Thoré M., Le radiomètre d'absorption, Les Mondes, 42 (1877) 585–586.
Tipler P.A., *Physics for scientists and Engineers*, WH Freeman, 1991, Chapter 29 and problem 51.
Volz F.E., Stratospheric Aerosol Layers from Ballooonborne Horizon Photographs, Bull. Amer. Meteor. Soc., 52 (1971) 996–998.
Wuerker R.F., Shelton H., and Langmuir R.V., Electrodynamic containment of charged particles, Journal of Applied Physics, 30 (1959) 342–349.
Wurm G., Krauss O., Concentration and sorting of chondrules and CAIs in the late solar nebula, Icarus, 180 (2006) 487–495.
Wurm G., Krauss O., Experiments on negative photophoresis and application to the atmosphere, Atmospheric Environment, 42 (2008) 2682–2690.
Yalamov Yu.I., Kutukov V.B., Shchukin E.R., Theory of the photophoretic motion of the large-size volatile aerosol particle, Journal of Colloid and Interface Science, 57 (1976) 564–571.
Zuev V.V., Burlakov V.D., A.V. El'nikov, Results of long-term lidar observation of eruption aerosol formations in the stratosphere over tomsk after the mount pinatubo eruption, Proceedings of the Sixth Atmospheric Radiation Measurement (ARM) Science Team Meeting DOE CONF-9603149, March 1996 San Antonio, Texas, 1996, 383–387.
Zuev V.V., Balin Yu.S., Bukin O.A., Burlakov V.D., Dolgii S.I., Kabashnikov V.P., Nevzorov A.V., Osipenko F.P., Pavlov A.N., Penner I.E., Samoilova S.V., Stolyarchuk S.Yu., Chaikovskii A.P., Shmirko K.A., Results of joint observations of aerosol perturbations of the stratosphere at the cislinet network in 2008, Atmospheric and Oceanic Optics, 22 (2009) 295–301.
Zulehner W., Rohatschek H., Photophoresis of nonspherical bodies in the free molecule regime, Journal of Colloid and Interface Science, 138 (1990) 555–564.

Author's short biography

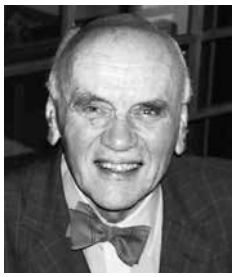

Helmuth Horvath

Helmuth Horvath, born 1941 in Vienna, studied experimental physics in Vienna, Ph.D. in 1966 under the guidance of O. Preining. Extended scientific visits with the universities of Washington, Colorado, Santiago de Chile, Kyoto and Granada. Professor of Experimental Physics in Vienna 1980 to 2006. Research interest in all aspects of the physics of aerosols, especially optics.

KONA Powder and Particle Journal No. 31 (2014) 200–213/Doi:10.14356/kona.2014011 Original Research Paper

Population Balance Model for Crushed Ore Agglomeration for Heap Leach Operations †

Nikhil Dhawan, Samira Rashidi and Raj K Rajamani *

[1] *Department of Metallurgical Engineering, University of Utah, USA*

Abstract

Agglomerate size distribution is a pretreatment step in low grade heap leach operations. The present work focuses on modeling the evolution of size distribution in batch agglomeration drum. Up to now there has been no successful work on modeling of crushed ore agglomeration although the framework for population balance modeling of pelletization and granulation is readily available. Different batch agglomeration drums were used to study the agglomeration kinetics of copper, gold and nickel ores. The agglomerate size distribution is inherently subject to random fluctuation due to the very nature of the process. Yet, with careful experimentation and size analysis the evolution of size distribution can be followed. The population balance model employing the random coalescence model with a constant rate kernel is shown to work well in a lab scale agglomerator experiments. It was observed that in a small drum agglomerates begin to break in a short time whereas the growth is uniform in the larger drum. The experimental agglomerate size distributions exhibit self-preserving size spectra which confirms the applicability of coalescence rate based model. The present work lays out the fundamentals for applying the population balance concept to batch agglomeration, specifically crushed ore agglomeration. The experimental difficulties and how to overcome them are described.

Keywords: Heap leaching, crushed ore agglomeration, agglomerate size and population balance model

1. Introduction

Heap leaching is one of the promising economic and green processes for the treatment of lean ores of copper, nickel, and gold. Acid or cyanide solution is percolated through a large heap of ore body and leached out metal is collected after several days.

During heap building i.e. the transport of ore material to the heap, severe segregation of material can occur which results in poor bulk permeability and ore percolation. Introduction of agglomeration step prior to heap building results in minimal segregation and solution flow through heap. It is well understood that percolation is highly dependent on the size distribution of the crushed ore, because fine particles tend to wash out and plug the pores in the heap. Therefore, it is important to bind fines to coarse particles to improve overall percolation.

Agglomeration pretreatment is required for ores which either contain excessive amounts of clay or an excessive quantity of fines generated during crushing. While agglomeration has become common pretreatment step in heap leach operations, the fundamental understanding of the agglomeration process for crushed ores is still lacking (Bouffard, 2005; Dhawan et al., 2013).

Crushed ore agglomerates can take two forms: fine particles adhering to coarse particles and fine particles adhering to each other. The former is similar to granulation whereas latter is referred as pelletization. For binder assisted agglomeration, adhesion and cohesion forces are dominant whereas surface tension and capillary forces prevail in non-binder/wet agglomeration (Kodali et al., 2011).

The residence time for agglomeration and the binding agents dominantly control the growth and mechanism of agglomeration. For hard to crush ores, the dominant mechanism of agglomeration growth is layering of fines on bigger particles, i.e., rim agglomerates whereas, newly nucleated agglomerates are expected to be more prevalent in high clay content ores such as nickel-laterite ores.

Generally, the agglomerated ore has a distinct particle size distribution (PSD) with a slight increase of the top size but a very large increase in the lower sizes. Typically, sizes are 60 mm to 2 mm with all of the minus 2 mm adhering to the coarser particles or between themselves (Miller, 2010). The author reviewed the crushed ore agglomeration process up to 2012 and did not come up on modeling studies on the topic (Dhawan, 2013; Dhawan et al., 2013). Some

† Accepted: July 16, 2013
[1] William Browning Bldg., 135 S 1460 E, Rm 412, Salt Lake City, UT 84112, USA
* Corresponding author:
E-mail: raj.rajamani@utah.edu
TEL: +1-801-581-3107 FAX: +1-801-581-4937

of the possible reasons can be the stochastic nature of process, experimental difficulties and lack of instrumentation for fundamental studies. Therefore, in this work the fundamentals for applying the population balance concept to batch agglomeration is laid out. Also, some other aspects of the evolution of agglomerate size distribution (ASD) are carefully studied using four different ores.

2. Literature review

Agglomeration results from direct interactions between discrete particles, and the agglomerate formation and growth can be mechanistically described with phenomenological models (Hogg, 1992). The basic mechanisms observed in agglomeration systems include coalescence, crushing and layering, snowballing and nucleation. These have been discussed in detail in the past (Kapur and Fuerstenau, 1969, Sastry, 1975; Kapur and Runkana, 2003; Liu et al., 2012).

Coalescence refers to the production of large-size agglomerates by clumping or fusing together of two or more particles. When agglomerates collide and stick or pack together in a geometric configuration favorable with respect to the rest of the moving charge, the conglomerate of agglomerates begins to roll and eventually deforms and forms the next larger agglomerate. The coalescence events cause discrete changes in the size of the agglomerates with an overall decrease in the agglomerate population without any change in their mass. Often coalescence is observed to be the most important mechanism responsible for growth in a batch system. Coalescence mechanism contributes wholly or partially to the growth of agglomerates made from materials of wide size distributions, whereas crushing and layering mechanism is the dominant mode in narrow sized particle populations (Kapur and Fuerstenau, 1969; Sastry, 1975; Kapur and Runkana, 2003). These authors reported that it holds strongly in the initial stages of agglomeration and almost throughout the batch agglomeration of materials with naturally comminuted and wider size distributions. Coalescence applies to wide distributions due to size independence, whereas crushing and layering applies to narrow size distributions due to size dependence. Unlike pelletization, the crushed ore agglomeration primarily contains wider feed size distribution of sizes up to 1.5 inch, employs retention times as low as 1-3 min and lacks stable acid-binder within the bed. Moreover, the coexistence of fines (minus 75 micron) micron and larger sizes makes the growth mechanism and particle-particle interaction cumbersome in agglomeration.

At present no definitive modeling studies have been reported on crushed ore agglomeration (Dhawan et al., 2013). Considering these facts, modeling studies of pelletization and granulation forms the starting point. In the past, pelletization and granulation have been studied in detail. The pelletization studies were carried out with very fine sizes in the 100 μm size range whereas granulation studies were also restricted to a maximum feed size of 10 mm. In these studies, it is important to mention that narrow feed size distribution, longer agglomeration times and stable binder conditions were the influencing factors. The size enlargement modeling has been done primarily with the concept of population balance model. Pelletization systems have utilized the coalescence model, whereas granulation studies used partition coefficient for an equilibrium model without considering agglomeration kinetics (Litster et al., 1986; Kapur and Runkana, 2003).

The population balance for a well-mixed batch system undergoing coalescence alone is described in the literature (Kapur and Fuerstenau, 1969; Kapur and Runkana, 2003) as Eq. (1).

$$\frac{\partial_{n(v,t)}}{\partial_t} = -\frac{1}{N_T^a}\int_0^\infty \lambda(u,v,t)n(u,t)n(v,t)\,du + \frac{1}{2N_T^a}\int_0^v \lambda(u,v-u,t)n(u,t)n(v-u,t)\,du \qquad (1)$$

In this equation, u and v refers to volume of agglomerate, $n(v,t)$ is the number density function, $\lambda(u,v,t)$ is coalescence kernel rate, N_T is the total number of particles at time t, and α is space system parameter. This is the time continuous and size continuous population balance model.

The total volume should be conserved in the system since agglomerates of volume v_i and v_j combine together to form an agglomerate of volume $v_i + v_j$ at all times as shown in **Fig. 1**.

In modeling, coalescence is the most difficult mechanism. However, it is needed to formulate the population balance in terms of number distribution by volume because granule volume is conserved in a coalescence event. An important parameter in population balance modeling (PBM) is the growth rate (coalescence kernel (λ)) that signifies the degree of agglomeration. The kernel dictates the overall rate of coalescence, as well as the effect of granule size on coalescence rate. The order of the kernel has a major effect on the shape and evolution of the granule size distribution. Most of the kernels are empirical or semi-empirical and must be fitted to plant or laboratory data. Modeling growth where deformation is significant is more difficult. It can be assumed that a critical cutoff size determines which combination of agglomerate sizes is

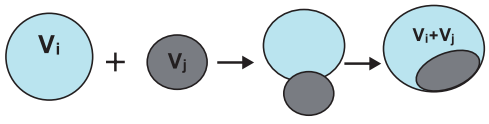

Fig. 1 Schematic of coalescence mechanism.

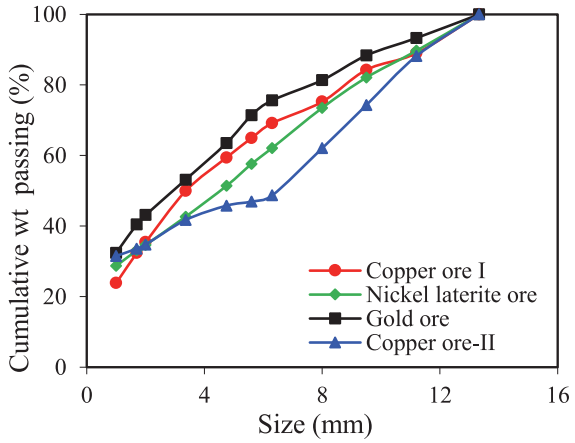

Fig. 2 Feed size distributions of different ores used.

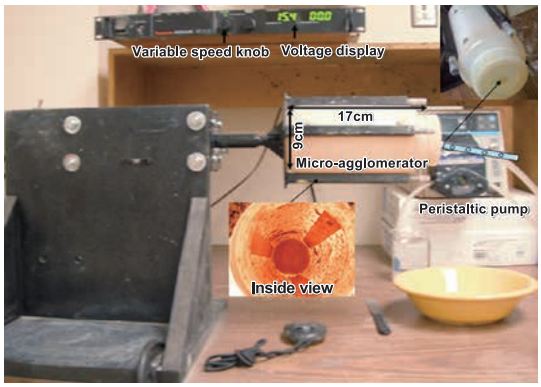

Fig. 3 Image of micro-agglomerator and ancillary equipment.

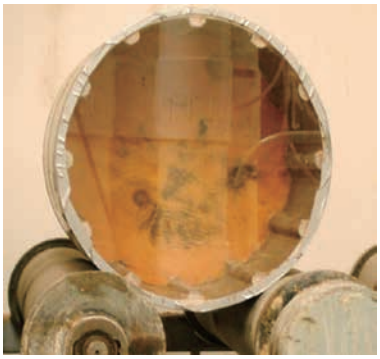

Fig. 4 Photograph of the agglomeration drum.

capable of coalescence. Coalescence of particles is mainly dictated by its inertia. As with chemical reactors, the degree of mixing within the agglomerator has an important effect on the final ASD because of its influence on the residence time distribution (Snow et al., 2009).

3. Materials and methods

Four ores provided by different mining companies were used in this study. The ores were screened into various size fractions and the size distribution of ores used in the experiments is shown in **Fig. 2**. The major difference between the ores is weight percentages of minus 200 mesh. Copper ore-II and nickel ore feeds are finer than gold ore and copper ore-I (minus 200 mesh% Cu-I: 7.4, Cu-II: 23.6, Au: 10.6, Ni: 14.9). The top size fed to the laboratory agglomerator was limited to 13 mm to insure that agglomerates were not too large for subsequent column leaching and secondly to accommodate the size and capacity of the drums used in this study. The bulk densities of copper-I, copper-II, nickel and gold ores are 1.42, 1.55, 1.17 and 1.67 g/cc, and the natural moisture content is 0.26, 2.6, 13.4 and 1.4%, respectively.

The preliminary experiments were conducted using a micro-agglomerator as shown in **Fig. 3**. The agglomeration drum was made using a 1 liter fluorinated polyethylene (FLPE) Nalgene bottle 9 cm in diameter by 17 cm in length. Three polytetrafluoroethylene (PTFE) lifters placed 120° apart were attached in the drum. Each lifter was 2 cm wide, 14.3 cm long and 6 mm thick. The small drum was mounted in a horizontal bracket and was driven with a 24 V D.C. motor and can run at variable speeds up to 76 rpm (Dhawan, 2013).

Based on several experiments, it was observed that in small drums the presence of large particles hindered the growth of other agglomerates. This caused incomplete agglomeration and thereby failing the objective of studying the behavior of each ore type. To avoid such behavior, lab-scale drum, shown in **Fig. 4**, was used in this study. This drum is a copy of the drum used in previous studies by Kapur and Fuerstenau (1969) and Sastry and Fuerstenau (1973) at the University of California Berkeley. The drum is a fully enclosed water-tight drum machined from an aluminum block, measuring 12 inches in diameter and 6.9 inches in length. Twelve lifters of 20 mm diameter were attached length wise uniformly around the inner periphery of the drum to prevent any sliding of the charge and imparted a rolling and cascading action to the agglomerates. The inner surface of the drum was lined consistently with silicone coated polyurethane gloss finish to eliminate ore charge sticking. The drum lining was refurbished whenever there was a change in ore type. The use of scraper was not considered to avoid any interference with the experiment. A transparent acrylic plastic cover on the drum enabled convenient withdrawal of product and observation of the charge motion.

In crushed ore agglomeration, volume loading is generally kept low, up to 8%. This low volume filling of the drum can be seen as a single layer of charge and thereby not enough capacity to carry on. In general, large particles migrate to the outer side of cascading charge, whereas smaller particles are at the lower or inner region. Under these conditions large particles can break intermediate

size agglomerates.

For PBM, number size distribution is a prerequisite. Therefore, batch experiments corresponding to different time intervals were conducted in the lab-scale drum. Following the experiment, number size distribution for each time step was also determined in an image analysis set up. A batch of known weight corresponding to 7% volume loading was introduced into the drum. Next, the drum was rotated for 5 min without any other additives. Then a premeasured amounts of sulfuric acid solution (Copper ore-I, II and nickel ore) or cyanide solution (gold ore) was added to the drum in a short time (less than 30 seconds). In other words, the ore was prewetted to minimize the incomplete wetting of the tumbling charge during solution delivery.

After that, the drum was closed with the lid and was placed on two horizontal rubber rollers. It was rotated at 24 rpm (30% critical speed) for a specified time. At a predetermined time interval, the rotation was stopped and the moist agglomerated ore was spread on a tarp. The material was further sampled by cone and quartering technique a representative sample of 450–500 grams was collected. The sample was air dried at room temperature for 24 hours. Then the dried sample was analyzed under image analysis set up for number size distribution. To avoid experimental error or concerns regarding effect of drying and sampling, for each time interval, a new batch experiment was conducted for the entire duration of 1, 2, 2.5, 3 or 4 min.

The standard cone and quartering technique was used in this work only because there are no other practical methods that will work with soggy ore agglomerates that have a wide size distribution. The material is piled in a heap so that the natural segregation in the heap is nearly symmetrical. The conical pile is then spread from the center to form a flattened disk of material. Then, the disk is divided into quarters using a flat wooden plank. A pair of opposite quarters is removed, and the other pair is used as the representative sample. Depending on the mass needed, the material can be coned and quartered again. Certainly, the procedure is tedious, time consuming and prone to human error. The representative agglomerate sample was air dried at room temperature before sieve size analysis.

The procedure for number size distribution of agglomerates involves primarily image analysis and shape factor to convert between mass and number distribution. A dry sample was placed on black paper under the image analysis setup. Individual agglomerates particles were moved apart from each other on the paper so that there was no overlap. The setup requires proper lighting conditions so that the particles do not reflect light. The pictures were taken by a camera (Fujifilm® FINEPIX® XP10). Next, the images were processed through ImageJ® software from which the number size distribution was obtained. Once the particles are captured in an image file, each particle area is known and its size is determined. In the image analysis, it is assumed that the particles are spherical in shape. This may be a very drastic assumption but very much necessary for modeling. In the modeling part the volumes of particles are added to generate agglomerate volume. Considering the different response of each ore type, the shape factors effect was not included in the population balance model. However, using shape factors, converting number size distribution (image analysis) to weight size distribution (sieve size) is possible.

4. Model Development

The time evolution of the PSD is commonly obtained from the solution of the general population balance model governing the dynamic behavior of a particulate process. Several numerical methods have been used for solving the steady-state or dynamic population balance equation. These include the full discretization method (Hounslow et al., 1988), method of moments, fixed and moving pivot discretized methods (Sastry and Gaschignard, 1981), high-order discretized methods (Ramkrishna and Mahoney, 2002). Based on the detailed literature review, the PBM equation used in this work was adapted from Kapur and Runkana (2003).

The rate of coalescence in restricted-in-space environment should be proportional to number of particles of size i and number fraction of particles of size j, or vice versa. Hence, specific rate constant or coalescence kernel λ by definition is independent of the size of the interacting agglomerates. Under these stipulations, the generalized PBM Eq. (1) reduces to Eq. (2) (Kapur and Fuerstenau, 1969; Sastry and Fuerstenau, 1973; Kapur 1978).

$$\frac{dn_i(t)}{dt} = -\lambda n_i(t) + \frac{\lambda}{2N(t)} \sum_{j=1}^{i-1} n_{i-j}(t) n_j(t) \tag{2}$$

The basic postulate of the model is that the particle mass is well mixed and the collision of frequency and the probability of coalescence are independent of size. The coalescence model also assumes that the nucleation of the moist feed has already been completed in the first few revolutions and hence, only the mechanism of coalescence is operative.

In this model, the size interval is discretized into a large number of intervals. Interval i represents a volume v_i of particles in that interval. Further, interval i is assumed to represent a volume $i \times v_1$ where v_1 is the smallest volume representing the first interval. Such a formulation allows a pair of size classes to coalesce and yet form a larger volume that is already defined as a size class. Thus, volume conservation is guaranteed. In the model Eq. (2), $n_i(t)$ is the number of particles of size i at time t in the agglomeration drum, λ is average random coalescence rate constant, $N(t)$ is total number of particles at time t. The derivative term in

the Eq. (2) gives the time rate of number of particles of size *i*. The second term depicts the disappearance of size *i* due to agglomeration of size *i* with all other sizes. The third term depicts that the formation of particles of size *i* due to coalescence (below size *i*) of size *i* with size *i-j*.

In this formulation, particle of size *i* disappear in proportion to the number fraction $n_j(t)/N(t)$ of particles of size *j* surrounding it. Likewise, particles of size *i* agglomerate with size *j* in proportion for the number fraction of size *i* surrounding it. Summing Eq. (2) over all sizes, it can be shown that the rate of depletion of the total number of agglomerates, $N(t)$, conforms to the first order decay kinetics as shown in Eq. (3). The solution of Eq. (3), which is the total number of agglomerates at any instant $N(t)$ is given by Eq. (4).

$$\frac{dN(t)}{dt} = -\frac{\lambda}{2}N(t) \tag{3}$$

$$N(t) = N(0)e^{-\frac{\lambda}{2}t} \tag{4}$$

However, the random coalescence model includes some assumptions. It involves pure agglomeration process; all agglomerates are spherical and equal probability of coalescence for all size classes. It can be argued that a single-parameter coalescence kernel is sufficient for short agglomeration time provided the total volume of the system is conserved. If necessary, the single coalescence kernel can be transformed into a matrix form. In other words, the coalescence between size class *i* with class *j* can be distinguished with a coalescence rate λ_{ij} instead of a single value of λ used for all size classes. Under this formulation, Eq. (2) is rewritten as Eq. (5). Therefore, the coalescence kernel becomes a set of m^2 values or m × m matrix, where m is the total number of intervals. The kernel matrix is symmetric because rate of coalescence is identical for size *i* with size *j* as it is for size *j* with size *i*.

The matrix enables the assignment of coalescence rate values as is needed between particles. However, this assignment is done from a primary value λ determined. For example, two large particles of sizes 20 and 24 mm cannot coalesce to form 44 mm agglomerate. Hence, their coalescence rate may be set to a small value, small as $\lambda/100$. The lambda matrix can predict size distribution more accurately if the precise interaction between sizes can be formulated.

$$\frac{dn_i}{dt} = -n_i(t)\sum_{j=1}^{m}\lambda_{ij}\frac{n_j(t)}{N(t)} + \sum_{j=1}^{i-1}\lambda_{i-j,j}n_{i-j}(t)\frac{n_j(t)}{N(t)} \tag{5}$$

The matrix formulation is shown in **Fig. 5**. The coalescence rate λ is determined graphically by plotting the total number of agglomerates remaining as a function of time. The analytical solution to the integro-differential equation

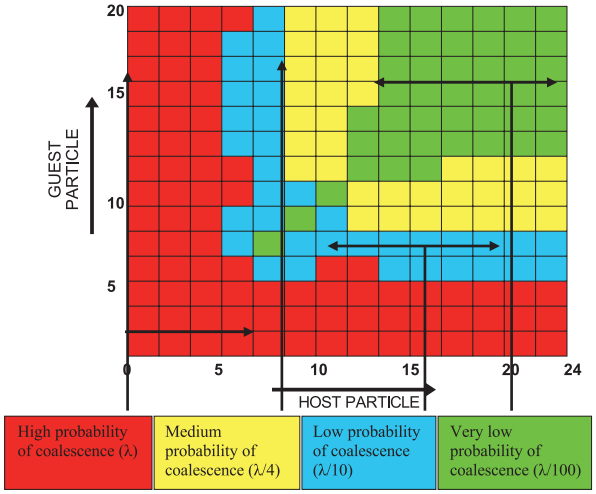

Fig. 5 Formulation of Lambda matrix for random coalescence model.

is only known for special forms of the coalescence kernel with an assumed initial number density distribution.

The lack of analytical solutions necessitates the use of numerical techniques. A popular method is method of size discretization (Kapur and Runkana, 2003) that involves discretizing the particle size domain into a relatively small number of size classes, and then monitoring the number and mass of particles in each size class so as to minimize if not eliminate the finite domain error. Volume is used as the size descriptor for the sake of convenience in handling death and birth terms. Often in the laboratory, the size distribution is measured with a set of sieves. Since a few sieves are used, only size fractions are measured in each size interval. In other words, the measured information is not sufficient to convert to the continuous density function. Therefore, the reverse course is followed: discretize the continuous size model, and get a discretized model with discrete solution.

As per model Eq. (2), the volume intervals and number of particles in each volume interval were specified. Assuming all agglomerates as perfect spheres and knowing their respective size fractions were the prerequisites for the model framework. Considering the maximum agglomerate size to be approximately 25 mm that covers a volume of 10,000 mm^3, 4,000 intervals each of volume 2.5 mm^3 were used to cover the entire volume range. For example, 1.7 mm agglomerate means agglomerate retained on 1.7 mm screen and passed through 2.5 mm screen.

Similarly, the number size distribution of particles at time zero or particle size distribution of the drum feed was also calculated. Based on the volume intervals, a set of 4,000 ordinary differential equations (ODE's) were solved simultaneously using Matlab software. After each experiment the number of agglomerates with their respective sizes was determined. A MATLAB™ code was written to count the number of agglomerates in each volume interval.

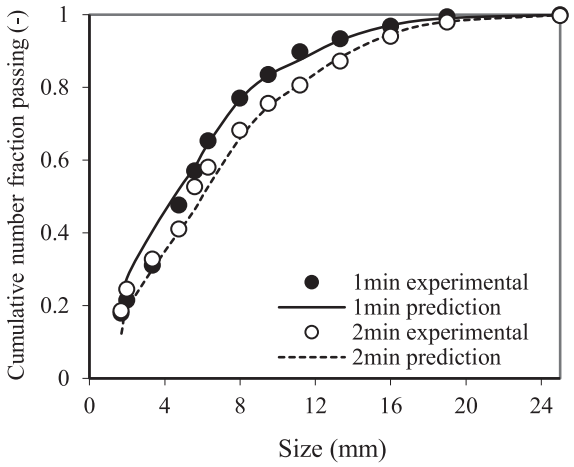

Fig. 6 Comparison of experimental number size distribution and model predictions for fine copper-I ore feed at different time.

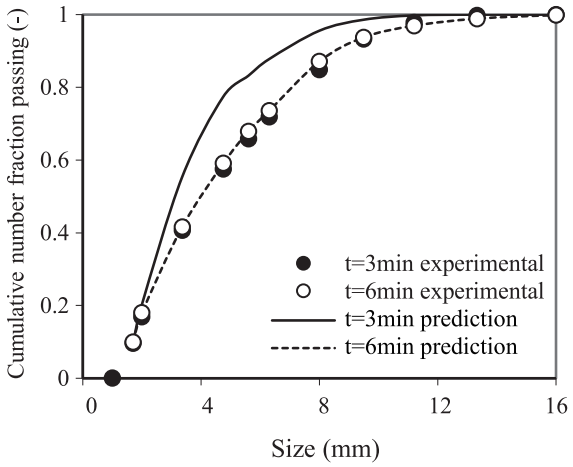

Fig. 7 Comparison of experimental number size distribution and model predictions for coarse copper-I ore at different time.

The population balance model was solved using discretization procedure at defined screen sizes. The numerical package used for solving the set of differential equations was the Matlab function "ode45 and ode15s", which is an ODE solver within the "Optimization" toolbox. Both of the functions were yielding very similar results. Since ode45 function was taking less time, it was selected for all the simulation work. The ode45 solver uses a variable step Runge-Kutta numerical algorithm. For all the simulations, a time step of 0.001 min was used.

5. Results and Discussion

The experiments were determined based on the numerous preliminary experiments done in the lab-scale and micro-agglomerator drums. The results of these experiments were also used for determining optimum agglomeration conditions. However, for the sake of brevity only typical results are shown here. Preliminary experiments were conducted on copper ore using fine feed size distribution (minus 1 mm) to test the applicability of the population balance model. For modeling purposes, one expects a gradual and smooth coarsening of size distribution. The evolution of PSD with time should be smooth as it is in other size enlargement operations.

From image analysis methodology, it was observed that the number of agglomerates remaining in the drum is decreasing with increase in residence time. The coalescence rate was different for each experiment and also varies with the amount of solution added. The range of coalescence rate for all the experiments is 0.4–2.4 per minute. A typical model prediction as compared to experiment results is shown in **Fig. 6**. It is evident that model prediction and experimental results are in agreement.

Based on the success of PBM model predictions in fine feed experiments, scoping experiments were performed in the microagglomerator with wide feed size distribution. **Fig. 7** show typical copper ore model predicted and experimental agglomerate size distribution. It is evident from the figure that model prediction and experimental results are not satisfactory. Moreover, there is not a smooth transition of ASD with time as was expected. In fact, ASD corresponding to 3 and 6 min are same, which indicates saturation or equilibrium size distribution.

Based on many similar experiments, it was confirmed that longer retention times lead to restricted growth or finer ASD which indicates there is breakage of agglomerates. In particular, the majority of the experimental ASD showed breakage after 3 min. Since ASD curves collapse on each other it seems that after certain time there is an equilibrium size distribution. It can be argued that breakage and agglomeration occurs in the drum within 3 min. Therefore, in this study, larger retention time was not attempted because most plant scale agglomerators run at 2 or 3 min mean retention time. The expectation is that in the first 3 min growth is much larger than breakage.

In regular crushed agglomeration, however, the evolution of PSD with time is not as smooth as it is in other size enlargement operations such as pelletization. The sources of such behavior include, (1) irregular shape of agglomerates which makes it difficult to determine actual volume, (2) mixing of ore particles with acid solution seems to be never uniform within the agglomerator unless prewetted, (3) agglomerates break mainly due to weak adhesion between large and small particles, (4) due to lack of wetting of fine ore particles, the growth rates may vary in the small and intermediate sizes, (5) in general, small particles layer large particles, but if too much fines are present, they themselves, can agglomerate but they break up on collision. In the first few revolutions, the nucleation of the moist feed completes, but due to lack of uniform wetting

nucleation itself is random.

The modeling of agglomeration with PBM is approached with a view to make it reasonably simple so that it may become a tool in plant operations for the prediction of ASD. However, the inevitable irregularities in the experiments pose a severe challenge to the approach. Obviously, agglomerates are not perfectly spherical and wetting with acid solution is not uniform either. However, with these considerations, it is worthwhile to see how crushed ore agglomeration may be brought under control to study the underlying growth rates.

It was thought that the reason for some of the unfavorable model predictions is due to the use of single coalescence rate for all size classes. The logical next step is to try different coalescence rate for pairs of size classes, i.e., the coalescence rate constant is different pairs of coalescing size classes, as described in model eq. (5).

The cumulative number fraction passing using a single lambda value (scalar lambda), experimental data and a matrix of lambda values is compared in **Fig. 8**. It is quite clear that experimental data do not fit really well with different matrix lambda for most of the ASD. Rather, the model prediction fits well with the single value of lambda. However, with a better understanding of coalescence rate of different sizes, the matrix predictions can be improved. However, the matrix formulation requires more detailed micro-scale investigation of underlying mechanisms that was beyond the scope of this work.

Coalescence rate model worked well even with an approximated growth rate. The prediction for first few minutes was accurate however it fails at longer retention time because the size distribution does not conform to regular growth behavior for any ore. With these experimental and model analyses, it was realized that the experiments should be done in a larger drum. It was expected that due to more free space in a larger drum, better cascading action and regular growth will occur. Therefore, to study the agglomeration behavior of different ore types and to delineate the other relevant effects all modeling experiments were done in the lab-scale drum.

Although no rigorous statistical analysis of the experimental precision has been attempted, it is nevertheless important to consider in a qualitative sense the possible source of errors. The two main sources of error are the procedure adopted for measurement of the agglomerate size and the stochastic nature of the process. Firstly, the agglomerates are not geometrically perfect spheres and the measured agglomerate size is based on the estimate of circular diameter. Moreover, the image analysis system loses its precision at sizes less than 1 mm. The second error is due to stochastic fluctuations of size distribution about the average agglomerate size mean. Agglomeration dynamics is subject to probabilistic laws, and as such, two agglomeration experiments carried out under identical

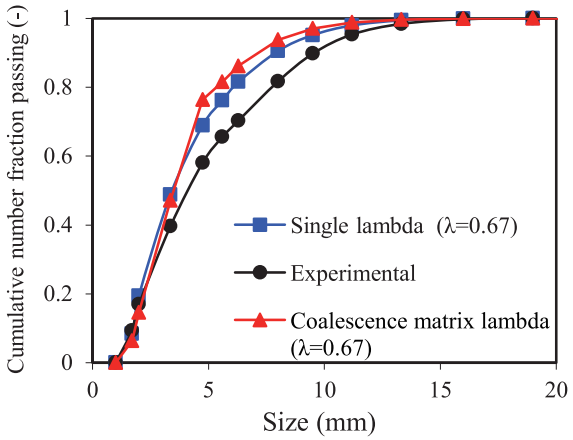

Fig. 8 Comparison of experiment and and model predictions at t= 3 min for copper-I ore using lambda matrix.

conditions have only a finite probability of showing the same ASD.

In the small agglomeration drum, however, the stochastic nature is magnified due to small number of agglomerates participating in each size class. In very large drums the stochastic nature will be smoothed out by the very large number of agglomerates present.

Based on preliminary experiments it was evident that higher retention time (i.e., more than 3-4 min) does not contribute to further agglomerate growth. Therefore, the maximum retention time in the drum was limited to 4 min. Since the coalescence rate plays a major role in the underlying model, its accuracy is vital. Hence, all experiments were done at four time intervals so that better approximation of slope can be obtained. To avoid experimental errors such as stopping the drum to collect the sample, each time step was done in different batches. Therefore, one complete experiment involves four batch experiments between 1-3 min. Each experiment was carried out at different moisture conditions and was part of the planned agglomeration growth range. Also, the drum volume filling (7%) and drum speed (30% N_c) were kept constant for all experiments.

The visual appearance of agglomerates is one of the first hand experiences regarding agglomeration behavior. Long duration agglomerates are generally characterized by smoother surface and shape. A typical screen shot of copper-II ore agglomerates under image analysis set up is shown in **Fig. 9**. It is evident from the figure that agglomerate shape becomes more regular (spherical) at a longer retention time.

A series of experiments were done with copper-I ore in the lab scale drum. A typical experiment results is shown here. **Fig. 10**, **11**, **12** show the photographs of the agglomerates, experimental ASD, semi-log plot of total number versus time, and model prediction overlaid on experimental data. It is difficult to recognize any appreciable growth pattern from agglomerate photographs. But the surface sheen

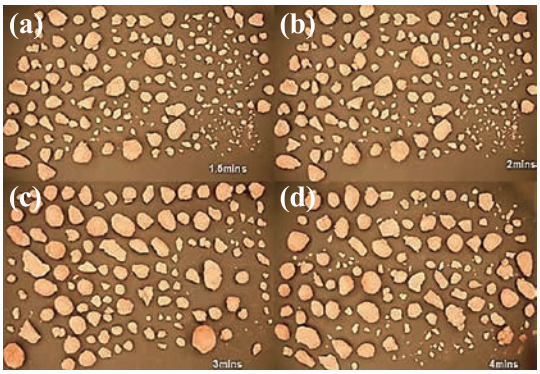

Fig. 9 Typical screenshot of copper-I ore agglomerate samples under image analysis set up at different time intervals (increasing left to right: **(a)** 1.5 min, **(b)** 2 min, **(c)** 3 min, **(d)** 4 min.

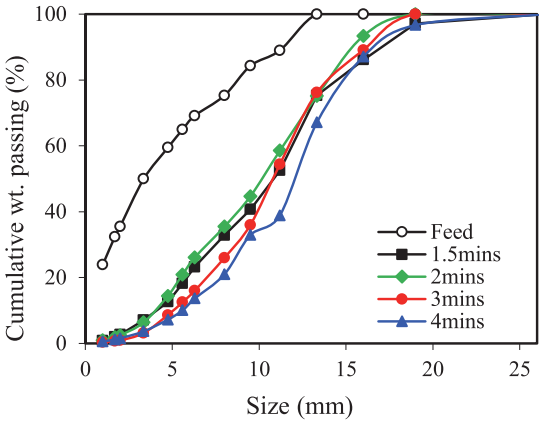

Fig. 11(a) Agglomerate size distribution for copper-I ore (weight percent).

Fig. 10 Photograph of copper-I ore agglomerate sample at different time intervals (increasing left to right: **(a)** 1.5 min, **(b)** 2 min, **(c)** 3 min, **(d)** 4 min.

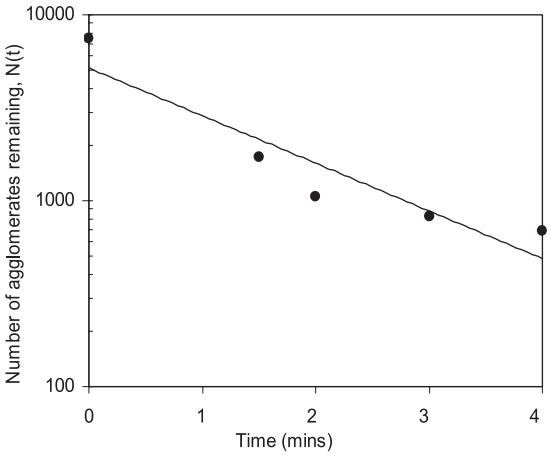

Fig. 11(b) Semi-log population plot for growth rate determination for copper-I ore.

increases at high moisture conditions as seen in **Fig. 10**.

In each of these experiments some overlap between successive ASD was noticed as in **Fig. 11(a).** The growth rate was not large enough to show sufficient advance in these intervals. The closeness or cluster between ASD curves possibly indicates that certain equilibrium size distribution is unique for agglomerates and it will not move further irrespective of retention time. In some experiments it is evident that the model prediction for initial time, i.e., 1 min does not fit well with experimental ASD. This is due to the slope approximation made from 0–4 min (**Fig. 11b**). It can be seen from the population plot that the number of agglomerates decreases at a faster rate during the initial 1 min period than other times. This is due to the presence of a large amount of fines present at start time. In other words, the decay or population of agglomerates is not progressing at exactly same rate as expected in the model. Even then, with average growth rate, the model predictions are still satisfactory as shown in **Fig. 12**. Similar results were obtained for different experiments involving different moisture content. Similarly, copper-I ore experiments were also conducted in the micro-agglomerator in order to study the variation in growth rates in different size of drums.

Fig. 13 compares the growth rate as a function of moisture between the microagglomerator and the lab-scale drum. The growth rate trend is the same in both the drums. However, the coalescence rate was slightly less in microagglomerator as compared to the lab-scale drum. Obviously, there is better cascading and tumbling action achieved in the lab scale drum and hence the higher growth rate. Moreover, the breakage problem arises at longer agglomeration times in the microagglomerator. Considering the similar behavior of agglomerates in these two drums, all experiments for nickel, gold and copper-II ores were only done in the lab-scale drum.

Similarly series of experiments were done with nickel laterite ore, copper-II and gold ore at different moisture levels in the lab scale drum. For the nickel ore, based on

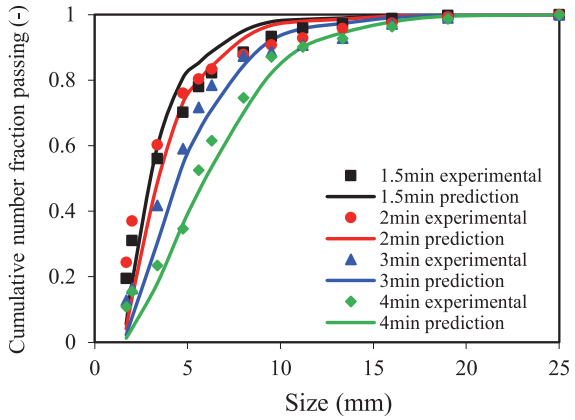

Fig. 12 Comparison of experimental number size distribution and model predictions for copper-I ore at different time intervals.

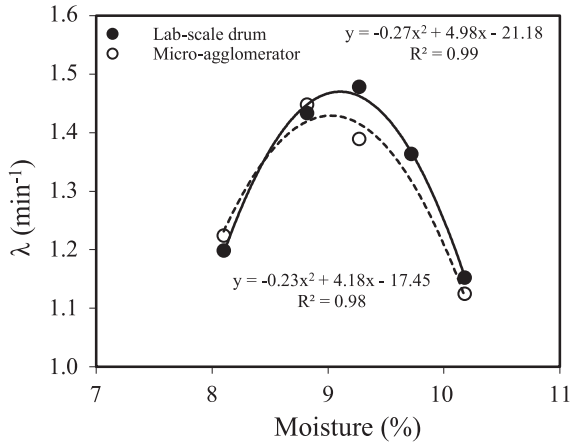

Fig. 13 Comparison of variation of coalescence rate with moisture for copper-I ore.

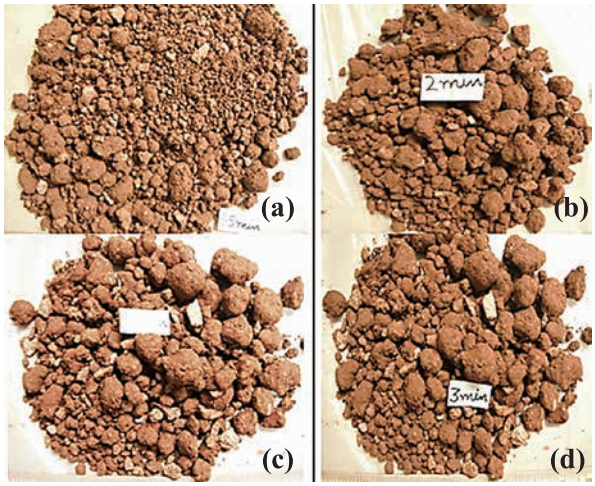

Fig. 14 Photograph of nickel ore agglomerate sample at different time intervals, increasing left to right: (**a**) 1.5 min, (**b**) 2 min, (**c**) 2.5 min, (**d**) 3 min.

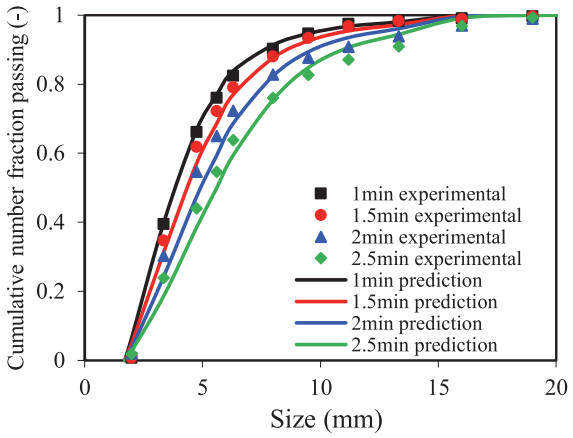

Fig. 15 Comparison of experimental number size distribution and model predictions for nickel ore at different time intervals.

the photos as shown in **Fig. 14**, there is a notable absence of surface sheen on the agglomerates even at high moisture content (36%). However, long duration agglomerates were possessing smoother surface and shape. It was observed that moist ore sticking was slightly higher at longer time for this ore; therefore, agglomeration time was limited only to 3 minutes.

The population decay or decrease in the number of agglomerates with time was more uniform. On drying, agglomerates became highly friable and hence released a significant amount of fines on contact. Hence, the size measurement was restricted up to 2 mm for the same reason. It is important to mention that the background color of image analysis setup was changed to light grey to gain contrast between agglomerates and background.

The gradual growth of agglomerate under specified conditions points to a good fit between experiments and model prediction. The ASD at different time intervals were plotted in accordance with the random coalescence model. A comparison of experimental and predicted ASD is shown in **Fig. 15**. It can be seen that there is a reasonable fit between experiment and the model prediction. The closeness between experimental data and the theoretical lines confirms the soundness of the model.

It can be observed from **Fig. 16** that moisture content certainly alters the coalescence or growth rate. However, for most of the experiments it is close to 1.1 min^{-1}, which is slightly less than that for copper-I ore. For practical purposes, an average value of coalescence rate 1.1 min^{-1} is reasonable for nickel ore.

For copper-II ore, there is slight difference in visual appearance among different experiments. The slight difference between appearances is the dark contrast at high moisture conditions. A surface sheen was never observed on this ore type even at high moisture content, because of high clay content. However, long duration agglomerates had a smoother surface and regular shape as shown in

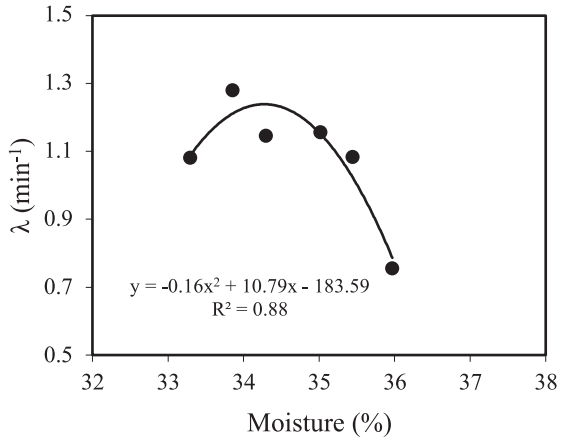

Fig. 16 Variation of coalescence rate (λ) with moisture content for nickel ore.

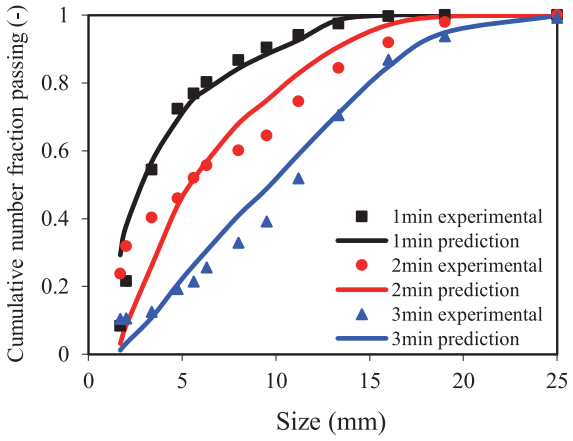

Fig. 18 Comparison of experimental number size distribution and model predictions for copper-II ore at different time intervals.

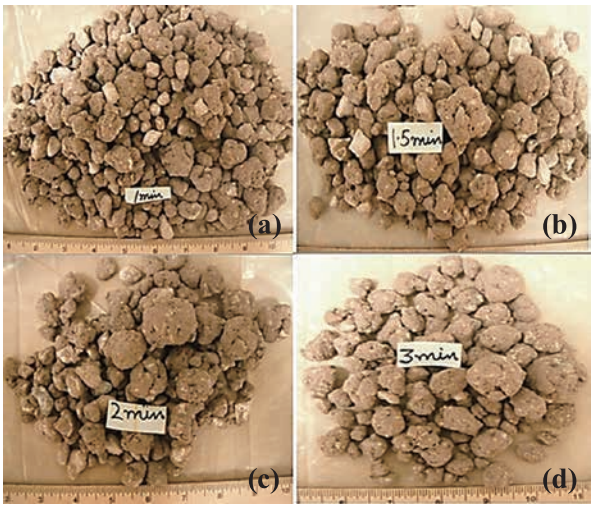

Fig. 17 Photograph of copper-II ore agglomerate sample at different time intervals, increasing left to right: (**a**) 1 min, (**b**) 1.5 min, (**c**) 2 min, (**d**) 3 min.

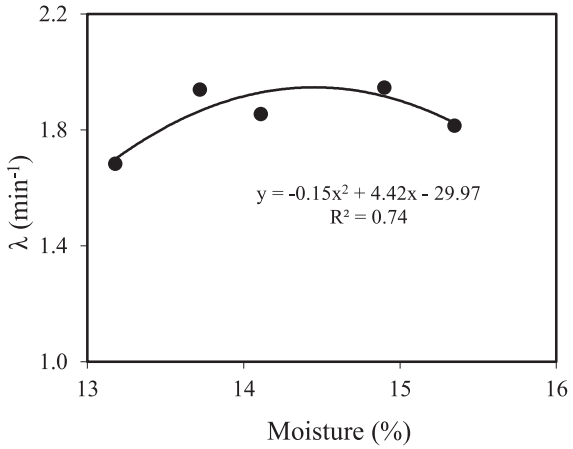

Fig. 19 Variation of coalescence rate with moisture for copper-II ore.

Fig. 17. Based on scoping experimental results, the agglomeration times were confined up to 3 min. It is important to mention that the population decay or decrease in the number of agglomerates with agglomeration time was steepest for copper-II ore as compared to copper-I ore and nickel laterite ore. The agglomerates were of different characteristics in terms of shape and partial wetting.

From experimental observations, it was seen that as soon as the liquid was added to the charge, lumps were formed. Therefore, some particles were found unwetted even after agglomeration. It was rare to observe any remaining fine particles for copper-II ore. Since there is appreciable agglomerate growth under specified conditions, it is reasonable to expect a good fit between experiments and model prediction. The ASD at different time intervals were plotted in accordance with the random coalescence model as shown in **Fig. 18**. There is some misfit between experimental and predicted ASD. This is because of steep slope change from 0–1 min as compared to other times. Also, the absence of intermediate size classes in this ore type leads to unusual agglomeration behavior.

The value of coalescence rate is almost twice as compared to copper-I and nickel laterite ore as shown in **Fig. 19**. In general, there seems to be a midpoint value close to 14% moisture where the rate is at its maximum value. However, for most of the experiments it is close to 1.9 min^{-1}, which is almost twice that for nickel ore. For practical purposes, an average value of 1.9 min^{-1} is useful.

Unlike other ores, the photographs of gold ore agglomerates at different time intervals and at different moisture conditions show a significant variation. With each time step, the transition to smoother surface and shape, appearance of coarser agglomerates at longer times are evident as

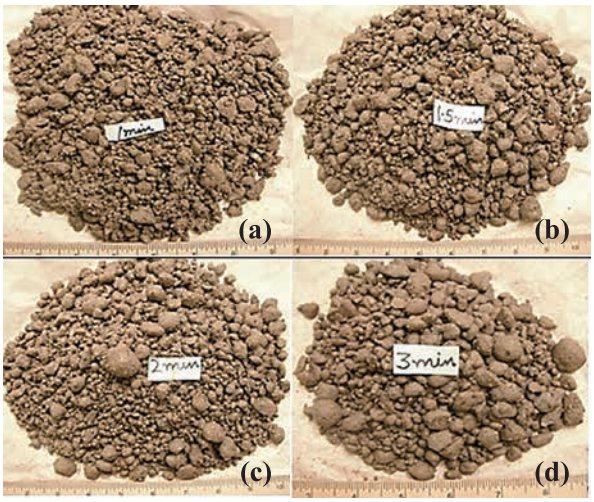

Fig. 20 Photograph of gold ore agglomerate sample at different time intervals (increasing left to right: **(a)** 1 min, **(b)** 1.5 min, **(c)** 2 min, **(d)** 3 min.

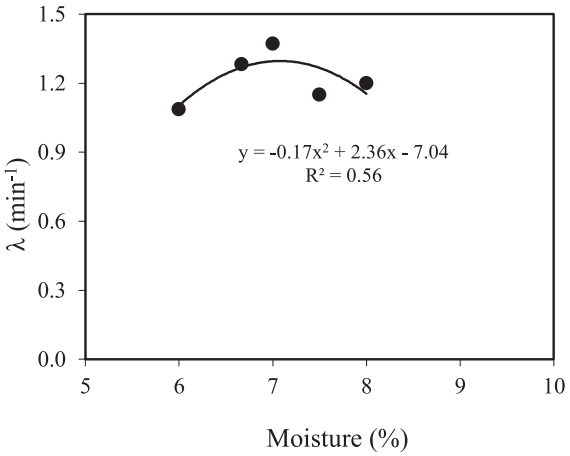

Fig. 22 Variation of coalescence rate (λ) with moisture for gold ore.

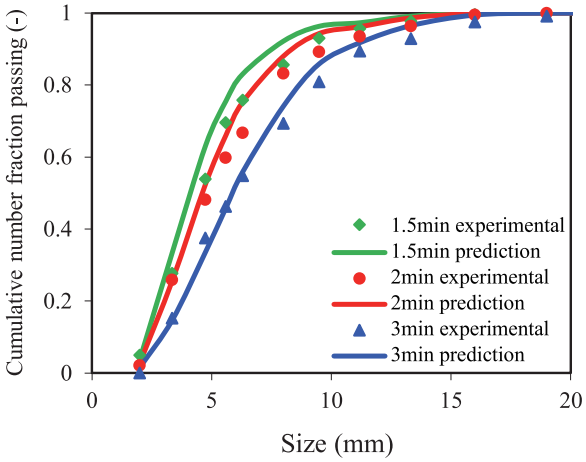

Fig. 21 Comparison of experimental number size distribution and model predictions of gold ore at different time intervals.

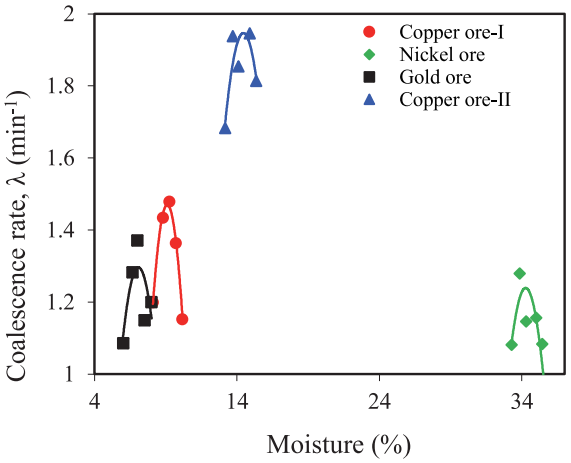

Fig. 23 Variation of coalescence rate for all ore types with moisture.

shown in **Fig. 20**. The appearance of surface sheen on the agglomerates indicates the range of optimum moisture content. Considering the regular agglomerate growth shown by agglomerates under specified conditions, it is reasonable to expect a regular fit between experiments and model prediction. A comparison of experimental and predicted ASD is shown in **Fig. 21**. It can be seen from these figures that there is reasonable fit experiment and model prediction. The closeness between experimental data and the theoretical lines confirms the soundness of the model.

The growth rate of gold ore under different moisture conditions is shown in **Fig. 22**. In general, there seems to be a midpoint value close to 7–8% moisture where the growth rate is maximum. However, for most of the experiments it is close to 1.2 min^{-1}, which is nearly the same as that of copper-I ore and nickel ore.

For comparison purposes, the variation of coalescence rate with moisture for all ore types is shown in **Fig. 23**. For each ore type, the moisture content certainly changes the growth rate. In general, there seems to be an optimum moisture value where maximum rate was observed. However, based on magnitude copper-II ore grows almost at a rate two times as that of nickel ore.

In general, it can be seen that the overall agreement is reasonably good between experimental size distributions and those predicted by the random coalescence model. Considerable deviation occurs, especially at the initial time step due to rapid coalescence of fines in the feed. In some experiments the number size distribution curves overlapped at two different times. This is expected in view of the fact that, firstly, the coalescence rate constant used in the development of this model was taken to be a constant for all agglomerate sizes, and secondly, any error in the measurement of the circular diameter of the

agglomerate is magnified on taking its cube when computing the agglomerate volume.

6. Theoretical validation

Sastry (1975) reported that agglomerate growth by coalescence is a sufficient condition for observing the self-preserving size spectra, which implies that there exists a unique ASD in a batch system which is independent of the material and processing conditions. The similarity distribution of the agglomerates is independent of the ore type and conditions of agglomeration, and is uniquely determined by the coalescence kernel.

It has been reported that the pellet growth by coalescence is a sufficient condition for observing the self-preserving size spectra and not necessarily the only one. Also, self-preserving size spectra of green pellets is a characteristic of the batch agglomeration. Mathematical analysis of the coalescence process indicated that there exists a self-preserving, pseudo-time- independent size distribution of agglomerates.

Based on mathematical transformations, it was argued if the coalescence kernel is a homogeneous function of its arguments, then the coalescence process has a self-preserving type of size distribution. However, it was emphasized that such a self-preserving distribution may be only a particular solution and may or may not be unique (Sastry, 1975). In other words, when experimental data exhibits self-preserving spectra then random coalescence is a valid approach to pursue. Therefore, the numerical solution of the population balance model with constant coalescence rate and experimental data for gold ore is plotted in **Fig. 24**.

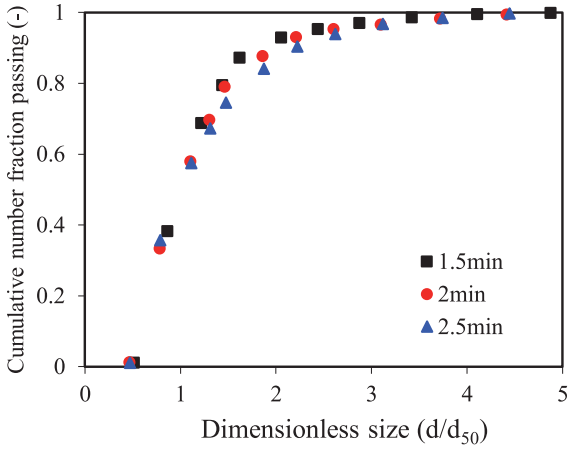

Fig. 24(a) Experimental self-preserving agglomerate number size distribution for gold ore.

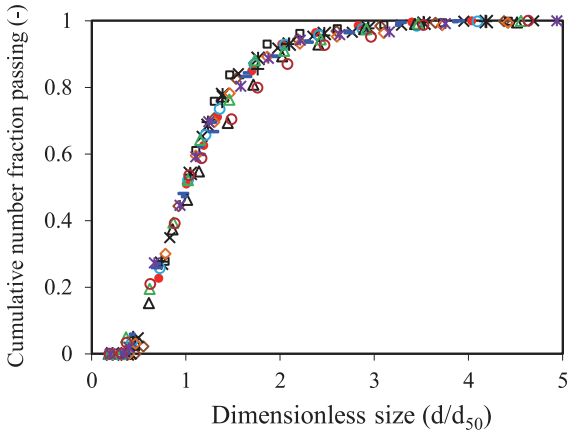

Fig. 24(b) Computed self-preserving agglomerate number size distribution for gold ore.

7. Conclusions

Population balance model for batch agglomeration has been developed. The model predicts the evolution of ASD in the batch agglomeration drum. The size distributions of the agglomerates in the specified time are adequately described by the random coalescence model. The model was verified for four ore types and different moisture level for each ore type. The kinetics of agglomeration designated by the coalescence rate is affected by the moisture content of the system. The copper-II ore exhibits the highest growth rate, whereas nickel laterite ore exhibits the slowest rate among the ores tested. A reasonable fit implies that the model accurately accounts for agglomerates growth due to coalescence taking place in the drum. The population balance model is more than adequate for application to batch agglomeration drums. The use of small drums leads to both agglomeration and breakage within a few minutes. The use of larger drums smooth out random fluctuations and minimizes breakage of agglomerates. Hence, for modeling purposes the use of as large drum as possible is recommended. Agglomerates are certainly irregular particles. However, the assumption of spherical agglomerates held pretty well in the population balance modeling effort. Experimental ASD exhibit self-preserving spectra and is found to be independent of operating conditions and is uniquely determined by the coalescence mechanism.

Acknowledgements

The authors would like to thank AMIRA International and the sponsors (related mining companies) for permission to publish the work. The authors also acknowledge the funding from AMIRA under P986 project. Any findings, opinions, and conclusions in this paper are those of the authors and not those of AMIRA International or its sponsors. Thanks are due to Professor Michael Moats, Michael

Free and JD Miller for active discussions throughout the work.

References

Bouffard S.C., Review of agglomeration practice and fundamentals in heap leaching, Mineral Processing & Extractive Metallurgy Review, 26 (2005) 233–294.

Dhawan N., Safarzadeh M., Miller J., Moats M., Rajamani R., Crushed ore agglomeration and its control for heap leach operations, Minerals Engineering, 41 (2013) 53–70.

Dhawan N., Modeling of crushed ore agglomeration for heap leach operations, PhD thesis, University of Utah, Publication No. 3561756, 2013.

Hogg R., Agglomeration models for process design and control, Powder Technology, 69 (1992) 69–76.

Hounslow M.J., A discretized population balance for nucleation, growth, and aggregation, AIChE Journal 34 (1988) 1821–1832.

Kapur P.C., Fuersteanu D., Coalescence model for granulation, Industrial & Engineering Chemistry Research, 8 (1969) 56–62.

Kapur P.C., Balling and Granulation, Chapter 10, Academic Press, 1978, pp. 55–123.

Kapur P.C., Runkana V., Balling and granulation kinetics revisited, International Journal of Mineral Processing, 72 (2003) 417–427.

Kodali P., Depci T., Dhawan N., Wang X., Lin C., Miller J.D., Evaluation of stucco binder for agglomeration in the heap leaching of copper ore, Minerals Engineering, 24 (2011) 886–893.

Litster J., Waters A., Nicol S., A model for predicting the size distribution of product from a granulating drums, Transactions of the Iron and Steel Institute of Japan, 26 (1986) 1036–1044.

Liu L., Robinson D., Addai-Mensah J., Population balance based modeling of nickel laterite agglomeration behavior, Powder Technology, 223 (2012) 92–97.

Miller G., "Agglomeration drum selection and design," *Proceedings of XXV International Mineral Processing Congress*, Brisbane, Australia, 2010, pp. 193-202.

Ramkrishna D., Mahoney A., Population balance modeling promise for the future, Chemical Engineering Science, 57 (2002) 595–606.

Sastry K., Fuerstenau D., Mechanisms of agglomerate growth in green pelletization. Powder Technology, 7 (1973) 97–105.

Sastry K., Similarity size distribution of agglomerates during their growth by coalescence in granulation or green pelletization, International Journal of Mineral Processing, 2 (1975) 187–203.

Sastry K., Gaschignard P., Discretization procedure for the coalescence equation of particulate process, Industrial & Engineering Chemistry Research 20 (1981) 355–361.

Snow R., Allen T., Ennis B., Litster J., Size reduction and size enlargement, in: Perry Chemical Engineers Handbook, McGraw-Hill, 2009.

Vethosodsakda, T., Evaluation of crushed ore agglomeration, liquid retention capacity, and column leaching, Master's thesis, Department of Metallurgical Engineering, University of Utah, 2012.

Author's short biography

Nikhil Dhawan

Nikhil Dhawan did his B.Tech in Metallurgical Engineering at Punjab Engineering College, India. Afterwards, he received his Ph.D. in Metallurgical Engineering at the University of Utah, USA under supervision of Prof. Raj Rajamani. His research interest includes comminution particularly HPGR technology and agglomeration practice. Presently he is working as a scientist at CSIR-IMMT Bhubaneswar, India.

Samira Rashidi

Samira Rashidi is a Ph.D. student in Metallurgical Engineering. She received her BSc and MSc degrees from AmirKabir University, Iran. Her Ph.D. thesis is mainly about studying energy-size relationships of different ores in lab-scale HPGR. Her background research focuses on modelling and simulation of comminution technology.

Raj Rajamani

Raj Rajamani is a professor of Metallurgical Engineering Department at the University of Utah. His research interests are: Modeling charge motion in ball, SAG and AG mills, fluid flow in pulp lifters, CFD modeling of hydrocyclones, modeling of high pressure grinding rolls and eddy current separation of electronic waste. He is recipient of Gaudin Award (2008) for his work in the application of DEM methods in the modeling of charge motion in grinding mills and for his contributions to the basic science of comminution and classification. He received his B.E. (Honours) degree from Annamalai University, India, M. Tech from Indian Institute of Technology, Kanpur, India and Ph.D. from the University of Utah.

KONA Powder and Particle Journal No. 31 (2014) 214–233/Doi:10.14356/kona.2014012 Original Research Paper

Morphology and Nanostructure of Granular Materials Built from Nanoparticles †

Jose L. Castillo *, Santiago Martin, Daniel Rodriguez-Perez, Alvaro Perea and Pedro L. Garcia-Ybarra

[1] *Departamento de Fisica Matematica y de Fluidos, Facultad de Ciencias, UNED, Spain*

Abstract

Nanopowders or nanoparticles can be used as building blocks for the preparation of new materials with a prescribed structure. Monte Carlo simulations have shown that the morphological properties (bulk porosity and surface roughness) of a granular deposit can be tailored by properly adjusting the velocity of the particles approaching the deposit. Based on these theoretical predictions, experiments have been conducted to prepare nanostructured materials from carbon nanoparticles. By electrohydrodynamic atomization of a liquid suspension (carbon nanoparticles dispersed in ethanol), an electrospray of small droplets is generated. The charged droplets are driven by the electric field with the ethanol evaporating along the droplet path, leaving dry nanoparticles that deposit on the collecting surface. The surface roughness of the resulting material has been characterized as a function of the voltage drop. Moreover, catalytic suspensions of platinum supported on carbon nanoparticles (Pt/C) in Nafion®-alcohol solutions have been electrosprayed over carbon paper to prepare electrodes for proton exchange membrane fuel cells (PEMFC). The fuel cell power density was measured as a function of the platinum loading and the range of parameters leading to optimal platinum utilization was obtained.

Keywords: nanopowders, powder deposits, granular materials, deposit morphology, electrospray, catalytic materials, fuel cell electrodes

1. Introduction

Powder technologies have increased their application field ranging from environmental issues of social concern (i.e. the filtration and elimination of unwanted powders and the reduction of particulate emissions from industrial activities, car engines or energy production) to the fabrication of new materials with specific properties. Thus to comply with the social needs and the environmental regulations, the control of particle emissions requires the development of clever filtration systems (Konstandopoulos and Papaioannou, 2008). On the other hand, the fabrication of advanced materials from aerosols promotes the development of new powder processing techniques (Milosevic et al., 2009; Naito et al., 2009; Yurteri et al., 2010). In all these cases, a proper knowledge of the dynamics of particle-laden gases is needed to control the particle motion (Garcia-Ybarra et al., 2006; Rosner et al., 1992) and the deposition of particles on the walls confining the gas stream (Castillo and Rosner, 1989; Castillo et al., 1990; Garcia-Ybarra and Castillo, 1997). This dynamic control allows either the delivery of the powdered material to specific locations (as it is required in filtration systems or in some pharmaceutical applications of aerosols) or to avoid the deposition of particles on some valuable surfaces (in applications ranging from large furnaces to the fabrication of microelectronic devices, for instance).

The distinctive large surface/volume (surface/mass) ratio of powders make them especially suitable for applications requiring a large active surface area which is the case for catalyst applications or pharmaceutical products, as well as for different solvent-based fabrication techniques. In this way, powders can be used as building blocks for the preparation of new materials (Luyten et al., 2010) which still retain this large surface/volume ratio as a distinctive feature. This is the central topic of this work: the fabrication of granular materials from powders (Section 3) emphasizing several ways to control the structure of the final product (based on the simulations described in Section 2) and showing in Section 4 a specific application of these granular materials (their performance as fuel cell electrodes).

Granular materials formed by the accumulation and adhesion of incoming aerosol particles acquire a morphological structure controlled by the form of the constitutive particles and by the way in which these particles arrive and

† Accepted: July 18, 2013
[1] Senda del Rey 9, 28040 Madrid, Spain
* Corresponding author:
E-mail: jcastillo@ccia.uned.es
TEL: +34-913-987-122 FAX: +34-913-986-697

attach to the forming material (Rodriguez-Perez et al., 2005, 2007). A proper control of the aerosol particle dynamics may lead to granular deposits with a well-prescribed bulk morphology and surface structure.

This paper joins together three complementary studies. First, in Section 2, a Monte Carlo simulation is used to relate the final structure of a granular material to the arrival dynamics of the constitutive particles. The knowledge gained with the simulations guides the preparation of materials with a given morphology and nanostructure. To achieve this goal, and as the key starting point, a simplified theoretical model is implemented to simulate the growth of a granular material from the deposition of aerosol particles. Monte Carlo simulations of particle deposition provide a correlation of the growing deposit morphology (bulk porosity and surface roughness) with the aerosol dynamics.

These theoretical predictions are then checked by performing some experiments conducted under controlled conditions. Thus, in Section 3, a liquid suspension containing carbon nanoparticles is electrosprayed at a constant flow rate to form a cloud of small liquid droplets. The electrically charged droplets are driven by an externally imposed electrical field and evaporate along their flight toward a collecting plate, leaving dry nanoparticles which deposit on the collector. The parameters controlling the electrospray dynamics are the physical properties of the liquid suspension (surface tension, electrical conductivity, ...), the flow rate and the voltages applied at the electrospray needle and at the collector plate. For a given liquid, there is a range of flow rates where a proper combination of needle voltage and collector voltage leads to an electric field at the needle that keeps the electrospray working in a stable cone-jet mode, Martin et al. (2012). These voltages also play a major role in controlling the electrical field at the collector (which affects the dynamics of the dry nanoparticles arriving to the forming deposit). The structure of the final granular deposit is analyzed as a function of some of these controlling parameters (applied voltages and liquid conductivity) and the results are compared with the Monte Carlo simulation predictions.

Finally, in Section 4, the use of these highly porous materials as fuel cell electrodes is analyzed by preparing cathodes made by this electrospraying and deposition technique starting with a liquid suspension with carbon nanoparticles doped with platinum. The performance of such a cathode as compared with the performance of a cathode prepared by a standard (impregnation) technique is studied in a test fuel cell with controlled gas feeding, cell working temperature and outlet pressure. The platinum utilization (maximum fuel cell power per gram of platinum in the cathode) obtained with the electrosprayed cathode is an order of magnitude larger than the platinum utilization achieved with standard cathodes.

The details of this research carried out at three complementary levels (*i*: theoretical simulations, *ii*: preparation of granular materials, and *iii*: demonstration of their performance as electrodes) are presented in the following **Sections 2–4**. In Section 5, the relations between these three research lines are discussed.

2. Monte Carlo simulations of granular deposit formation

2.1 Model description

The growth of a granular material from the deposition of nanopowders (aerosol particles in the surrounding gas phase) comprises several steps: particle arrival, particle attachment to the deposit and deposit re-structuring. Each step is governed by some distinctive mechanisms. Thus the particle arrival is affected by the particle dynamics above the deposit. Particle attachment depends on particle arrival velocity and on the intensity of the forces between the deposit and the impinging particle (see for instance Walton, 2008). Moreover, deposit restructuring linked to the coagulation, sintering and compaction of the deposit is controlled by particle coalescence dynamics which is strongly dependent on temperature and on the presence of vapors that may condense between the particles. One may try to model the formation of a granular material including all these phenomena, but it is clear that such a model would require the determination of a large number of parameters measuring the importance of the different physical mechanisms controlling these three steps. Instead of trying to model all these details, one may focus on the mechanisms which play a major role and disregard all the other effects.

Following this approach, a Monte Carlo (MC) method has been implemented to simulate the motion of particles above the deposit and the other two effects have been oversimplified by assuming a *complete passive deposit*. Thus in this model (Rodriguez-Perez et al., 2005, 2007; Tassopoulos et al., 1989) once a new particle reaches the deposit, this particle remains attached at the touching location and does not move anymore. This assumption (absence of rebounding and re-entrainment of particles in the gas) is valid when the kinetic energy of the impacting particle is low with respect to the potential energy of the interaction between two particles in contact or when a kind of glue coats the particles enhancing their sticking. Moreover, deposit restructuring is disregarded and the particles incorporated into the deposit keep their original shape. This *frozen deposit* assumption is valid when the working temperature is not elevated (i.e. is much lower than the fusion temperature) and the ambient pressure is not too high, in such a way that particle coalescence within the deposit is precluded.

Under these simplified assumptions, the only remaining

factor to control the deposit formation (i.e. the deposit evolution and the final structure of the resulting material) is the dynamics of particle arrival to the collecting surface.

In the MC simulations, time and space are discretized, depicting the particle motion at intervals of time τ and the particle position on a cubic lattice of size a (which coincides with the particle diameter). That is, τ is the characteristic time for a particle displacement equal to the particle diameter a. Therefore, time and space are measured in units of τ and a, respectively. A spatial domain with a square base $L \times L$ (i.e., $na \times na$) and periodic boundary condition on the lateral walls is used.

The concentration of particles in the gas phase is assumed to be small and thus the motion of each particle is not affected by the other aerosol particles. In this case, the deposit growth is due to the successive arrival of *uncorrelated* particles and can be modeled by a sequence of independent events, each due to a single particle. Thus one can introduce a particle at a random position over the topmost height of the deposit and follow its motion until either the particle moves far away from the deposit (escaping from capture and being carried by the gas) or it touches the deposit and attaches there. The MC model simulates the motion of one particle after another, depicting the evolution of the deposit growth evolution.

The motion of an aerosol particle in a gas is split into two distinct contributions:

- A deterministic motion that can be due to gas advection, inertia, sedimentation or any phoretic motion (thermophoresis, photophoresis, ...). This *convective motion* is characterized by a mean value of the particle velocity, υ. This mean (ensemble-averaged) velocity would be taken time- and space-independent and with the same value for all incoming particles.
- A random motion superimposed on the mean particle motion and due to a stochastic transport process (Brownian diffusion, eddy diffusion, random fields ...). Thus in a reference system moving with the mean velocity υ, each particle performs a random motion with the mean square displacement increasing linearly with time, $\Delta r^2 = 2n_d Dt$, Einstein (1905), where n_d stands for the space dimensions ($n_d = 2$ in a two-dimensional space, and, $n_d = 3$ in the three-dimensional case). The importance of this random motion is measured by the diffusion coefficient, D.

In this way, the assumption of independent aerosol particles (i.e. that the motion of each particle is not affected by the other aerosol particles) can be relaxed considering that the aerosol cloud generates a mean field (as in the case of electrically charged particles that will be considered in the following section) plus a random force (due to the incessant temporal and spatial changes on the distribution of particles inside the cloud). The mean field affects the deterministic motion of each individual particle (that is,

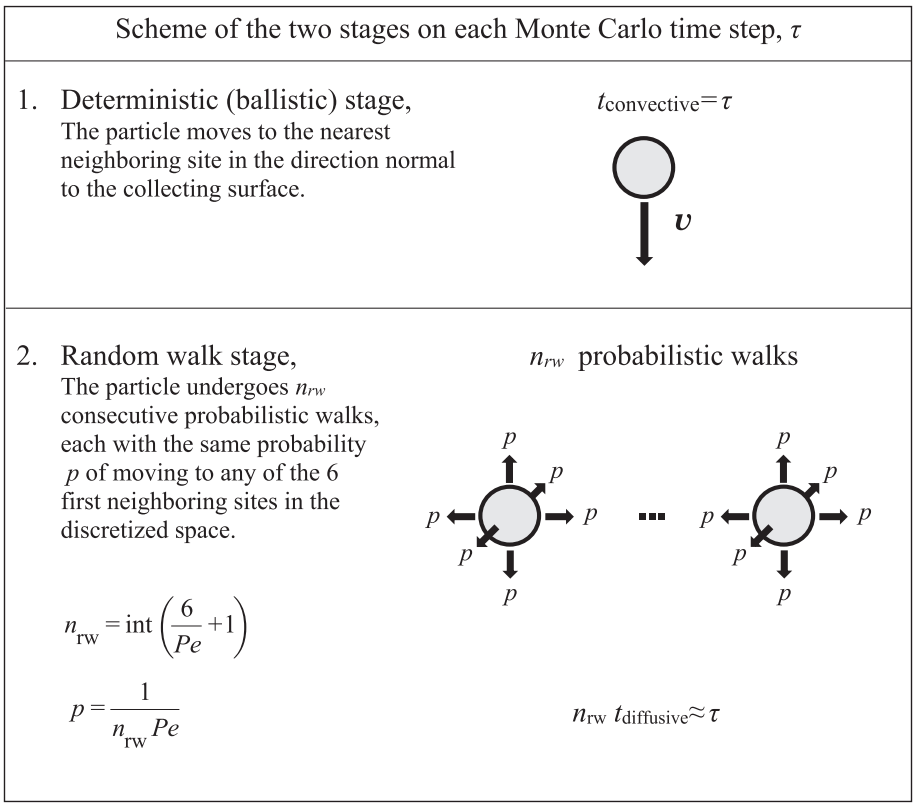

Fig. 1 Two-stage Monte Carlo simulation. Deterministic stage and random-walk stage (with n_{rw} consecutive probabilistic walks).

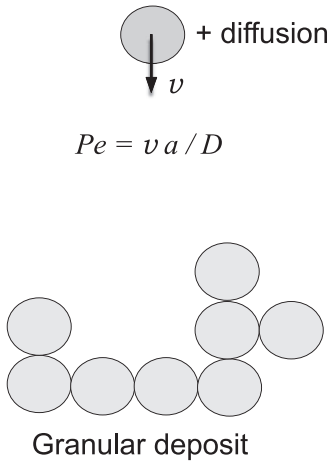

Fig. 2 Sketch of deposit growth on an attracting surface. Particle arrival by deterministic + diffusive transport.

the value of υ), whereas the random contribution adds to the particle Brownian motion (or even plays the major role in the random particle motion). These Monte Carlo simulations do not represent the motion of aerosol particles along the whole particle path but the arrival of the particle to form the granular deposit, in this sense υ stands for the (ensemble-averaged) arrival velocity which results from the gas-aerosol interactions and by the presence of other fields acting on the particle dynamics.

Therefore, the model incorporates three independent variables: a, υ, and D. Once the direction of the particle velocity is given (perpendicular to the collector in our simulations), the particle speed, υ, together with the characteristic length (the particle diameter, a) and the diffusion coefficient (D) can be combined to form the Peclet dimensionless number

$$Pe = \frac{\upsilon a}{D} \tag{1}$$

This Peclet number, Pe, measures the relative importance of the mean particle motion with respect to the random particle motion. The limit $Pe \to \infty$ corresponds to a ballistic behavior of the aerosol particles moving with constant speed υ and vanishing diffusion whereas the opposite case, $Pe = 0$, accounts for the pure diffusive limit ($\upsilon \to 0$). Indeed, the Peclet number can be written as the ratio of the characteristic times associated to the two contributions to the particle motion,

$$Pe = \frac{t_{\text{diffusive}}}{t_{\text{convective}}} \tag{2}$$

With the characteristic convective time given by $t_{\text{convective}} = a/\upsilon$, and the characteristic diffusive time by $t_{\text{diffusive}} = a^2/D$.

On this discretized space, the two contributions to the particle motion are simulated by two stages (**Fig. 1**):

- The deterministic (ballistic) stage. Each time step, the particle moves to the nearest neighboring site in the direction normal to the collecting surface. Therefore, τ is the characteristic convective time, $\tau = t_{\text{convective}} = a/\upsilon$.
- The random walk stage. The diffusive time $t_{\text{diffusive}}$ is of the order of Pe times the convective time τ. Each time step, the particle then undergoes n_{rw} consecutive probabilistic walks, each with the same probability p of moving to any of the 6 first neighboring sites in the discretized space (and a probability for remaining at its current site given by $q = 1 - 6p$), with

$$n_{\text{rw}} = \text{int}\left(\frac{6}{Pe} + 1\right) \tag{3}$$

The characteristic diffusion time is of the order of the characteristic time for each single random motion. As in this two-stage scheme, there are n_{rw} single random steps for each time step τ, it results $t_{\text{diffusive}} \approx \tau/n_{\text{rw}} \approx \tau Pe$. Thus the value of the probability p is chosen to provide the value of Pe; that is $p = 1/(n_{\text{rw}} Pe)$.

The MC simulation starts with a flat and clean collecting surface at the lower boundary of the computation domain. The simulation scheme based on these two stages is implemented to trace the motion of one aerosol particle until either it escapes from the computation domain or it touches the deposit (the collecting surface or another particle that has already being fixed to it). In the first case, the particle escapes and in the second case the particle becomes part of the deposit contributing to the deposit growth. After that, a new particle is introduced at a random location on a plane parallel to the collecting plate and located one site above the uppermost location of the deposit.

It can be shown (see for instance Tassopoulos et al., 1989 or Rodriguez-Perez et al., 2005) that this computation scheme corresponds to the discrete description of an ensemble of diluted aerosol particles whose number density (number concentration per volume), n_{p}, is governed by a convective diffusive equation (in dimensionless variables, measuring time in $t_{\text{convective}}$ units and distances in units of the characteristic length, a, and therefore, velocities in units of the mean particle velocity)

$$Pe\,\frac{\partial n_{\text{p}}}{\partial t} + Pe\,\upsilon \cdot \nabla n_{\text{p}} = \nabla^2 n_{\text{p}} \tag{4}$$

with Pe representing the ratio of characteristic times given by Eq. (2).

2.2 Structure of granular (powdery) deposits formed on attracting surfaces

For an attracting surface, the mean particle velocity υ is directed towards the collecting surface and the relative intensity of the surface attraction with respect to particle diffusion is given by the Peclet number Pe. The sequence of particles driven to the attracting surface forms a granular deposit on this surface (**Fig. 2**) whose main structural features were derived by Rodriguez-Perez et al. (2005,

2007) and Castillo et al. (2010). A computer drawing of the structure of the granular deposits is given by **Fig. 3a** showing the lateral view of a deposit for a low value of the Peclet number ($Pe = 0.1$) with the grey intensity decreasing with the depth of the field in the figure (for illustration purposes, only the upper half of the deposit is shown). On the other hand, **Fig. 3b** shows the upper view of the same deposit characterized by bunches of particles forming a rough surface on the scale of the particle size. Moreover, **Figs. 4a & b** depict the lateral and upper view, respectively, of a deposit formed by particles whose motion is characterized by $Pe = 1$. Lastly, **Figs. 5a & b** correspond to $Pe = 100$. In all these figures, the MC domain has a square base of 512 × 512 cells and the simulation is stopped when the same maximum deposit height ($h_{max} = 1024\ a$) is reached. It becomes clear that ballistic-dominated deposition (large Peclet numbers, **Figs. 5**) leads to compact deposits with a rough patched surface. However, diffusion-controlled deposits (low Peclet numbers, **Figs. 3**) are tree-like and fluffy, with a very porous bulk structure formed by open structures and a highly branched surface.

The deposit bulk structure can be analyzed by determining the *mean density* (the occupation number or relative number of space cells occupied by particles within the deposit) at different heights, $\rho(h)$. To achieve representative values, the density at each height is averaged over 10 deposit simulations performed with the same Peclet number. It turns out that the bulk of the granular deposit becomes layered in three different regions (**Fig. 6**):

- A bottom layer (*near-wall region*) whose structure is affected by the presence of the flat collecting surface. Here, the density decreases continuously from a high surface cover at the collecting plate down to the value at the next layer.
- A middle layer (*consolidated region*) characterized by a plateau with a constant mean density where new particles can no longer arrive from the surrounding gas.

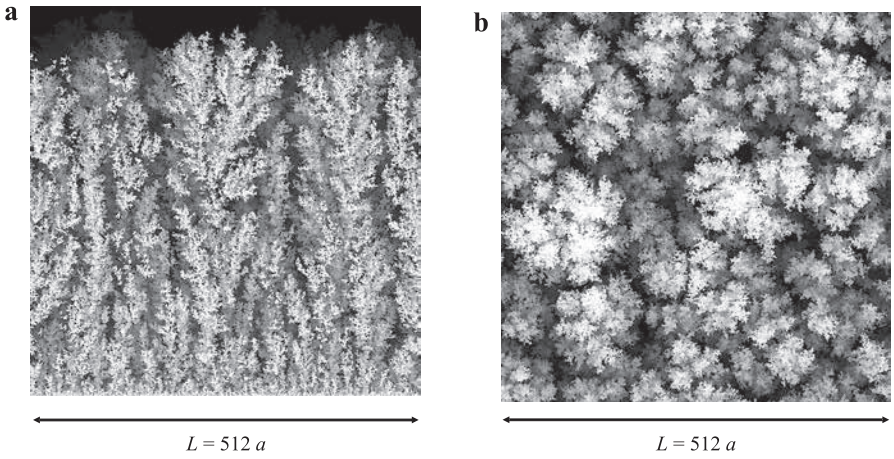

Fig. 3 **a**, Lateral view of the granular deposit with the grey intensity decreasing with the depth of the field. Here $Pe = 0.1$, $L = 512a$, $h_{max} = 1024a$. **b**, Upper view of the same deposit shown in **Fig. 3a**.

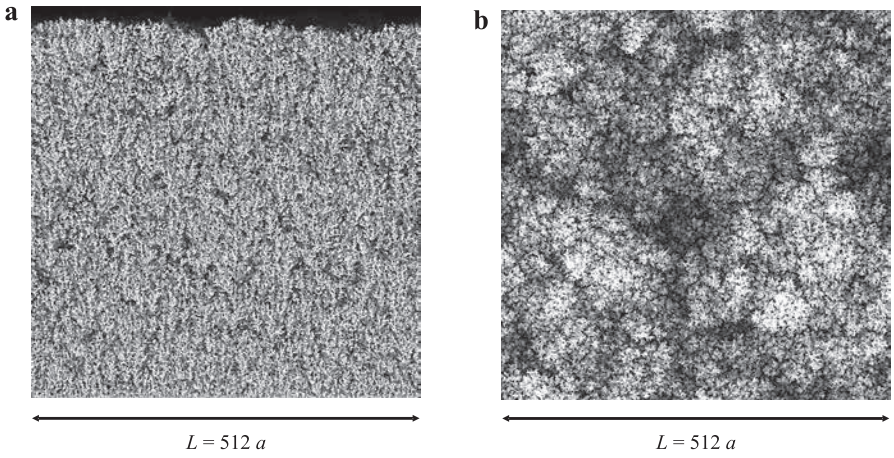

Fig. 4 **a**, Lateral view of the granular deposit with the grey intensity decreasing with the depth of the field. Here $Pe = 1$, $L = 512a$, $h_{max} = 1024a$. **b**, Upper view of the same deposit shown in **Fig. 4a**.

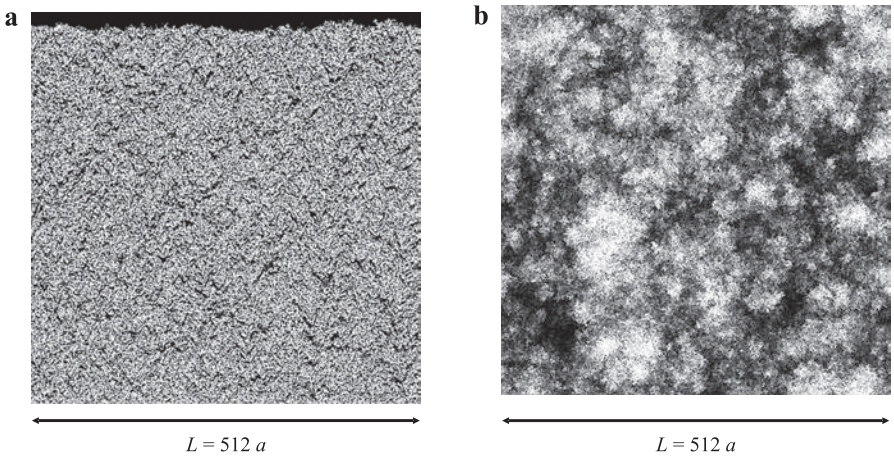

Fig. 5 **a**, Lateral view of the granular deposit with the grey intensity decreasing with the depth of the field. Here $Pe = 100$, $L = 512a$, $h_{max} = 1024a$. **b**, Upper view of the same deposit shown in **Fig. 5a**.

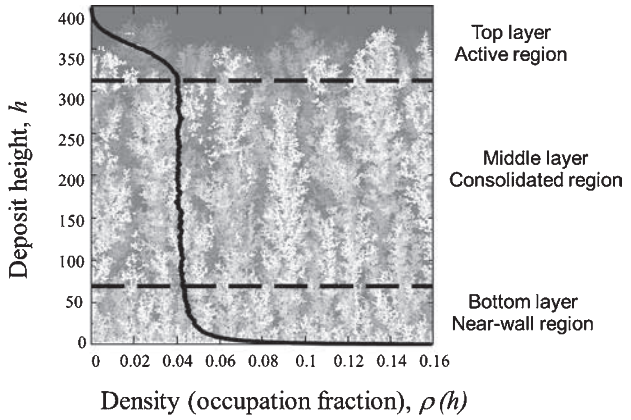

Fig. 6 Density profile (averaged over 10 deposit simulations performed with the same Peclet number) showing the three-layer structure of a deposit for $Pe = 0.1$, the deposit height h measured in units of cell size, a.

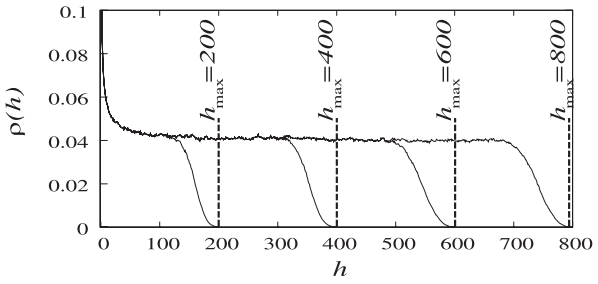

Fig. 7 Density profile (averaged over 10 deposit simulations) for $Pe = 0.1$ and different maximum heights h_{max} (measured in units of cell size, a). The arrival of new particles at the deposit (increasing h_{max}) enlarges the thickness of the consolidated region where the mean density is almost constant and time-independent.

- A top layer (*active region*) open to the ambient air and still active for new particle attachment.

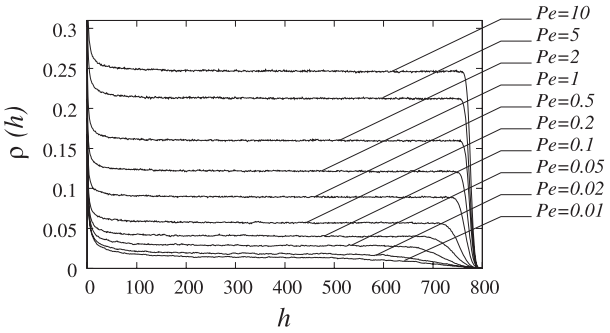

Fig. 8 Density profile for the same maximum height $h_{max} = 400$ (measured in units of cell size, a), and different Pe numbers.

The size of the bottom layer depends on the Peclet number, whereas the thickness of the active regions increases slightly with time. Some properties of these two extreme regions were provided by Rodriguez-Perez et al. (2005, 2007). Here we will focus on the features of the consolidated region. The thickness of this central consolidated region depends on the deposition time. In **Fig. 7**, the density profile (averaged over 10 deposits) for $Pe = 0.1$ is represented, depending on the maximum deposit height, h_{max} (measured in units of cell size, a). It becomes clear that the arrival of new particles to the deposit (increasing h_{max}) enlarges the thickness of the consolidated region where the mean density is almost constant and time-independent, as it was already obtained by Houi and Lenormand (1984).

In **Fig. 8** the mean density profile is depicted for deposits grown at different Peclet numbers up to the same maximum height, showing that the consolidated region becomes more porous (and the depth of the active region thickness increases) as Pe decreases. When the tendency of the particles to move toward the collecting surface is reduced, a more porous deposit with a larger active surface is obtained.

A detailed analysis of the granular deposits for different *Pe* numbers leads to correlation of the mean density of the consolidated region with the particle Peclet number, *Pe* (**Fig. 9**), resulting in

$$\bar{\rho}(Pe) = \rho_\infty \left(1 + \frac{Pe_0}{Pe}\right)^{-B} \tag{5}$$

where ρ_∞ stands for the maximum occupation fraction and Pe_0 is a normalizing Peclet number. In our simulations

$$\rho_\infty = 0.302;\ Pe_0 = 4.8;\ B = 0.52 \tag{6}$$

The fitting expression Eq. (5) has a general application whereas the numerical values of the fitting coefficients given in Eq. (6) indeed depend on the model features. Thus, for on-lattice models like the one used here, the limiting occupation fraction for ballistic deposition is $\rho_\infty = 0.302$. However, for off-lattice models (when the particle location is not restricted to the lattice cells but can be any point in the computational space), a packing density (normalized with respect to the maximum density of fully packed spheres) $\rho_\infty = 0.17$ is achieved (Jullien and Meakin, 1987). Moreover here, ρ_∞ accounts for the relative number of occupied cells, but for comparison with the mass density of actual deposits one has to take into account the fraction of the cell occupied by a particle, which in the case of a spherical particle in a cubic lattice corresponds to $\pi/6$. Moreover, the value of Pe_0 depends on other model features such as the space dimension or the angle between the mean velocity and the collecting surface (taken as perpendicular directions here).

Note that in the case of a material with fractal dimension D_F, when looking at a cubic volume V of side $2R$ built on any point inside the material, the mean occupation fraction would depend on R in the form

$$\bar{\rho}(Pe,R) = \frac{N_{\text{occupied}}(Pe,R)}{N(R)} \propto \frac{R^{D_F}}{R^3} \tag{7}$$

where N_{occupied} is the number of occupied cells, and N is the total number of cells in the volume V.

Based on Eq. (7), the fitting expression (5) defines a characteristic length

$$R_{Pe} = 1 + \frac{Pe_0}{Pe} \tag{8}$$

such that the granular deposit looks fractal at length scales smaller than R_{Pe}, (measured in units of the particle size, a) with the mean density depending on the volume as specified by (7). However, for larger volumes, the fractal structure becomes embedded in V, with the mean occupation fraction becoming independent of the size of V as indicated by Eq. (5). R_{Pe} is thus a *cut-off distance* for the fractal structure of the consolidated deposit. In the absence of particle diffusion (ballistic limit), the cut-off distance shrinks to the particle size whereas in the opposite (pure diffusion) limit, the whole deposit remains fractal at all the scales. The existence of a cut-off length for the fractal structure was also proposed by Nagatani (1989) in the context of particle aggregation.

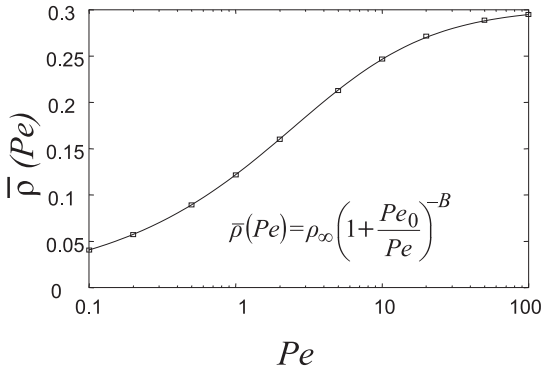

Fig. 9 Mean density in the consolidated region of the deposit as a function of *Pe*.

Thus diffusion dominates on the short distances being responsible for the fractal structure of the deposit on the small length scales up to R_{Pe}, whereas convection introduces the cut-off distance R_{Pe} (which increases as diffusion becomes more and more important) beyond which a constant mean density is achieved and the fractality is swept off.

Therefore, the numerical value of the exponent B in Eq. (5) is related to the fractal dimension induced by diffusion at the short scales. For diffusion-limited deposition, a deposit in the pure diffusive limit ($Pe = 0$) has a fractal dimension $D_{\text{DLD}} = 2.5$ (Tolman and Meakin, 1989), and it turns out that

$$B = 3 - D_F \approx 3 - D_{\text{DLD}} \tag{9}$$

Eq. (5) provides the density of a granular deposit as a function of the particle dynamics in the gas over the collecting surface, with the dynamics characterized by the Peclet number. On the base of these simulations, one can prepare materials with a prescribed bulk density or mean porosity and with a tailored structure by controlling the way the particles arrive at the attracting surface. Also, layered materials formed by the superposition of layers with a different mean density can be prepared by modifying the particle dynamics during different timed intervals.

This result has a broad application. For example, Elmøe et al. (2009) carried out a simulation of particle capture by filters and found out that the dusty layer growing over the filter has a mean density which is well fitted by Eq. (5).

Indeed, the MC simulation described here is free from any constraining hypothesis, and thus Eq. (5) is expected to be valid in any dusty layer created by accumulation of fine particles in the absence of erosion or deposit consolidation. The simulation opens doors for the design of controlled experiments dealing with material processing from

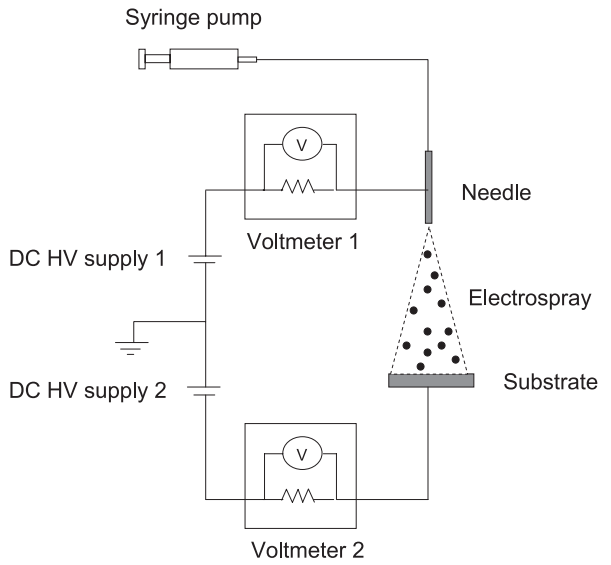

Fig. 10 Sketch of the experimental set-up. The liquid suspension in the syringe is pumped through the needle and a potential difference between the metallic needle and the collector substrate is maintained. Evaporation of the droplets formed in the electrospray leaves dry charged nanoparticles which are attracted by the substrate.

aerosols. One of these doors is explored in the following section.

3. Granular materials built from the deposition of an electrosprayed liquid suspension

3.1 Electrosprayed liquid suspensions

The simple model underlying the MC simulations described in the previous section shows the trends for controlling the deposit structure and indicates several ways to prepare granular materials from nanopowders with a tailored morphology depending on their final use. A step forward in nanomaterial research will consist of the performance of experimental studies that could confirm these theoretical predictions. To achieve this goal, an experimental set-up (sketched in **Fig. 10**) was implemented to generate nanoparticles in a gas that are later driven towards a collecting surface. In this study, a standard catalyst ink commonly used for preparing electrodes that are valuable for proton exchange membrane fuel cells (PEMFC) was used. The inks are constituted by a catalyst supported on carbon nanoparticles (Pt/C: 10 wt% Pt on Vulcan XC-72R) dispersed in a liquid solvent (ethanol 96% v/v, Aldrich) and an ionomer (Nafion® 5 wt% in lower aliphatic alcohols and water). The Nafion® loading was fixed to 30 wt% in the solid fraction (fraction of dry mass of Nafion® on the dry mixture of Nafion® and Pt/C). The electrical conductivity of the liquid suspension was

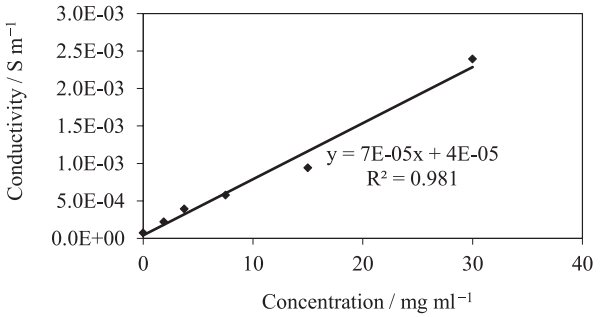

Fig. 11 Liquid electrical conductivity dependence on the concentration of carbon nanoparticles in the suspension.

measured as a function of the concentration of carbon nanoparticles (**Fig. 11**), showing that the electrical conductivity can be well fitted by a linear dependence on the concentration of carbon nanoparticles.

The electrospray technique (Barrero and Loscertales, 2007, Jaworeck and Sobczyk, 2008) is used to generate almost monodispersed sprays of small electrically charged droplets from this liquid suspension. The liquid suspension is ultrasonically dispersed for at least 2 hours before the electrospray deposition is started. Then, a syringe pump (KDS 100) drives the liquid suspension through a stainless steel needle (inside diameter of 0.75 mm) at a constant flow rate Q. Moreover, by means of two DC high-voltage power supplies (Bertan 225-30R and Spellman MM15P2.5W, respectively), a high voltage difference is applied between the metallic needle (kept at a constant voltage V_n) and the flat collecting plate (at a voltage V_p) respectively, with this plate located some distance away from the needle tip. The electric charge passing through the needle and the charge collected by the plate are measured by two ammeters (Isotech IDM67) inserted in the circuit lines of the needle and the substrate connections to their respective power supplies.

The electrically conducting liquid in the needle is affected by the electric field there (Fernandez de la Mora, 2007; Higuera, 2010), which leads to an accumulation of charges at the liquid surface formed at the needle exit. Under suitable conditions, the electrical stresses elongate this surface to form a Taylor cone with a very thin jet emerging from the cone tip (**Fig. 12**). In this cone-jet configuration, the jet is steady and adjusts to the fixed flow rate Q. At some distance away from the cone tip, the jet breaks up in a spray with droplets much smaller than the needle diameter forming a cloud of tiny droplets with a narrow distribution of droplet sizes (**Fig. 12**). The flow rate and liquid properties (conductivity, surface tension, density) determine the characteristic droplet size (Chen and Pui, 1997; Fernandez de la Mora and Loscertales, 1994; Gañan-Calvo et al., 1997; Yurteri et al., 2010). Due to the dependence of the electrical conductivity on the nanoparticle concentration (**Fig. 11**), a wide range of droplet sizes

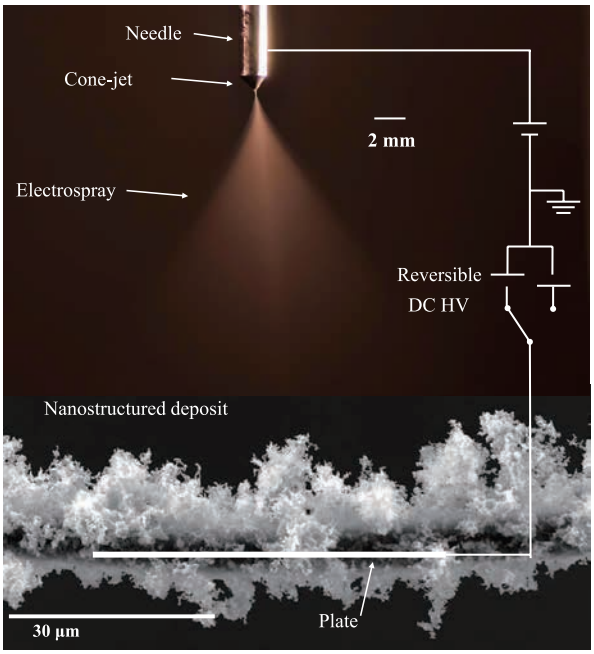

Fig. 12 Composed picture of the electrospray depicting the cone-jet and the electrosprayed cloud together with the resulting nanostructured deposit. For illustration purposes, the SEM image of the deposit is enlarged with a different length scale (given by the horizontal bar at the bottom).

can be analyzed. These charged droplets evaporate along their flight in the gas leaving dry charged nanoparticles which are driven by the electric field towards the collecting surface. The arriving nanoparticles accumulate on the collector plate and form a structured granular deposit. The Nafion® covering the nanoparticles facilitates their adhesion to the deposit and reduces particle surface diffusion after adhesion. **Fig. 12** is a composed picture representing the whole electrospraying process. The cone-jet at the needle exit forms the electrosprayed droplet cloud and the dry nanoparticles form a nanostructured deposit on the collector plate. For illustration purposes, the deposit image in **Fig. 12** is an enlarged SEM image superimposed on the needle-electrospray picture with the scale for the SEM image given by the scale bar at the bottom, whereas the 2-mm bar is the scale for the rest of the picture.

The cone-jet mode remains stable for a range of parameters (Cloupeau and Prunet-Foch, 1994; Li, 2007; Martin et al., 2012; Noymer and Garel, 2000; Ragucci et al., 2000; Tang and Gomez, 1996; Yurteri et al., 2010). Roughly, when the electrical field at the needle tip is weak, the surface accumulation of charges is low and the electrical stresses are not able to comply with the flow rate Q. Then, the cone-jet cannot be maintained in a steady way and the system works in a dripping mode with a sparse sequence of large droplets being formed at the needle tip. The droplet grows by the continuous arrival of liquid pushed by the syringe pump until the meniscus cannot support the

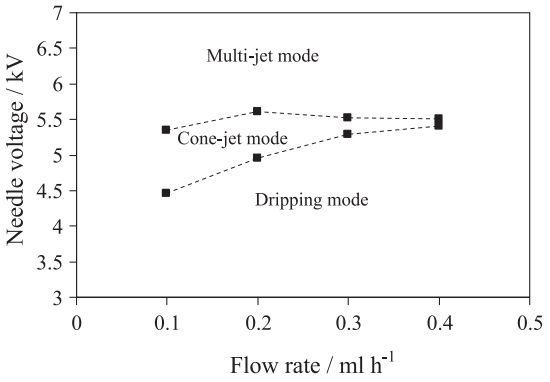

Fig. 13 Stability domain for electrospraying a catalytic ink in the cone-jet regime when a voltage is applied to the needle but the substrate is connected to ground. The electrical conductivity of the catalytic ink was 5.77×10^{-4} S m^{-1} and the needle-substrate distance was fixed at 3.5 cm.

attached droplet (as large as the needle diameter) which detaches from the needle and a new dripping cycle starts. Moreover, for high enough voltage differences, the electric field at the Taylor cone is quite large, the cone-jet becomes unstable and the electrospray evolves to a more complex configuration (Gu et al., 2010; Kim et al., 2011): oscillatory mode, multiple-jet mode or electrical discharges in the surrounding gas, among others.

The parameter space where the electrospray works in the steady cone-jet mode is one of the issues that must be investigated in advance for determining the range of flow rates and the corresponding applied voltages for which the liquid suspension can be electrosprayed in a regular and continuous manner (Martin et al., 2012). **Fig. 13** shows the steady cone-jet domain of a catalyst ink (whose electrical conductivity was 5.77×10^{-4} S m^{-1} and for a needle-substrate distance fixed to 3.5 cm) when a positive voltage is applied to the needle while the collector plate is connected to ground. In this cone-jet mode the electrospray induces primary droplets and smaller satellite droplets with most of the electrosprayed liquid mass contained in the primary droplets. To obtain the cone-jet mode domain given in **Fig. 13**, the different electrospraying regimes have been identified by observing the liquid meniscus at the needle tip. The liquid shape at the needle exit was visualized using a CCD camera (Panasonic AW-E600E) coupled with an optical zoom (Optem 70XL). Due to the known hysteresis phenomena linked to the cone-jet stability, the voltage range leading to a stable cone-jet was determined, starting always with a formed cone-jet. Therefore, the resulting range of voltages for a stable cone-jet corresponds to the widest possible range. Starting with a stable cone-jet within the stability island, the applied voltages were either decreased or increased until the cone-jet became unstable, giving rise to the dripping mode or the multijet mode, respectively.

In a recent work (Martin et al., 2012), the stable cone-jet domain was extended by keeping the collector under a negative voltage (and the surroundings to ground). Larger flow rates can be achieved with this double polarization configuration and the electrospray remaining in a stable cone-jet mode.

Outside of this cone-jet domain, the nanoparticles arriving at the deposit would have a broader distribution of sizes (due to the uneven atomization process and the subsequent coagulation of the nanoparticles within the original liquid droplets when drying), and each nanoparticle will have a different dynamics when approaching the collector (due to the dependence of the electrical mobility on size and charge of the particle). Therefore, to compare the morphology of the nanostructured deposits with the results obtained with the MC simulations described in Section 2, the electrospray should work in the steady cone-jet mode.

The main objective of the electrospraying process is to collect all the charged nanoparticles emitted by the needle on the substrate and to form, after the solvent evaporation, a porous deposit consisting of the catalyst particles. The efficiency in the capture of the electrosprayed particles may be substantially improved if an opposite voltage with respect to the needle voltage is applied to the collector substrate. In the double polarization scheme depicted in **Fig. 10**, the charged particles are forced by the electric field to deposit preferentially over the substrate, thus reducing the leakage of flying nanoparticles and improving the performance of the deposition process. Moreover, the electrospray cone-jet domain may be substantially enlarged by proper selection of the voltage at the collecting plate, and a noticeable increase in the flow rate range for electrospraying in the cone-jet mode can be achieved (Martin et al., 2012). Thus, in summary, the double polarization can be used to control the electric field at the needle tip (which indeed is the key factor for achieving a stable cone-jet electrospray) as well as the electric field at the collecting plate (which determines the particle motion over the deposited material and thus the corresponding particle Peclet number). The Peclet given by Eq. (1) becomes

$$Pe = \frac{va}{D} = \frac{qE_p\, a\, b}{kT\, b} = \frac{qE_p\, a}{kT} \tag{10}$$

where b is the particle mobility, q the particle charge, E_p the electric field at the collecting plate, k the Boltzmann constant and T the gas temperature. Eq. (10) indicates that Pe is the ratio of the particle electrical drift to the intensity of the particle thermal motion, being proportional to the electrical field over the collecting plate.

3.2 Morphology of the electrosprayed catalytic layers

As expected from Eq. (10) and from the results of the MC simulations given in Section 2.2, the nanostructure of the granular deposit depends on the suspension properties, on the mass flow rate Q, and on the voltages (V_n and V_p) applied.

In all the cases presented in this section, the electrosprayed deposits were carried out at a needle-substrate distance of 3.5 cm and a voltage drop of 7 kV between the needle and the collector plate (+5.5 kV voltage applied at the needle with the collector kept at –1.5 kV). This double polarization configuration has two main advantages:

- It reduces the particles losses by setting the collector plate to a negative voltage with respect to ground, then favoring the deposition of the catalyst particles on the electrode instead of on the surroundings which are to ground potential.
- Larger flow rates can be achieved (beyond those indicated in **Fig. 13**) with the electrospray remaining in a stable cone-jet mode (Martin et al., 2012).

Fig. 14 provides some SEM images of the deposited catalyst layers with the same deposit accumulative mass (same final ultra-low Pt loading, 0.01 $mg_{Pt}cm^{-2}$) obtained for several flow rates and different electrical conductivities of the catalyst ink (note that the liquid electrical conductivity increases with the concentration of nanoparticles in the original liquid suspension as shown in **Fig. 11**). The micron bar in **Figs. 14a–d** and **f** is 20 μm in length, whereas in **Fig. 14e**, it corresponds to 500 nm. Moreover, **Fig. 15** shows a diagram of the flow rates and conductivities of the catalyst ink that give rise to the different morphologies depicted in **Fig. 14**.

Each SEM image in **Fig. 14** is representative of a type of deposit. The morphology of the catalyst layer can be classified as a fractal-like structure (a), accumulation of patched clusters (b), compact deposits based on a fractal structure (c) and compact deposits formed from patched clusters (d).

Thus **Fig. 14a** shows a fractal-like deposit characteristic of low Peclet numbers which are obtained for low-conductivity suspensions electrosprayed at moderate flow rates (♦ points in **Fig. 15**). Moreover, **Fig. 14e** shows a closer view of the same deposit.

The fractality of the granular deposit is better seen in the general views a) to d) than in the closer views such as e). In **Fig. 14a** there is no evidence of any dominant macroscopic length because the corresponding characteristic length R_{Pe} (see Eq. 8) is larger than the picture size (compare with the simulation shown in **Fig. 3b**, corresponding to $Pe = 0.1$, which leads to $R_{Pe} \cong 50$). **Figs. 14b to 14d** show large and rather homogeneous clusters where fractality is confined to much smaller sizes (see **Figs. 4b** and **5b**, corresponding to $Pe = 1$ and $Pe = 100$, respectively, leading to $R_{Pe} \cong 5$ and $R_{Pe} \cong 1$, respectively).

These fractal-like structures **(Figs. 14a** and **e)** are composed of clusters (of a few catalyst particles each) with a characteristic size of approximately 100 nm and arranged in a dendritic way. This is the most appropriate type of

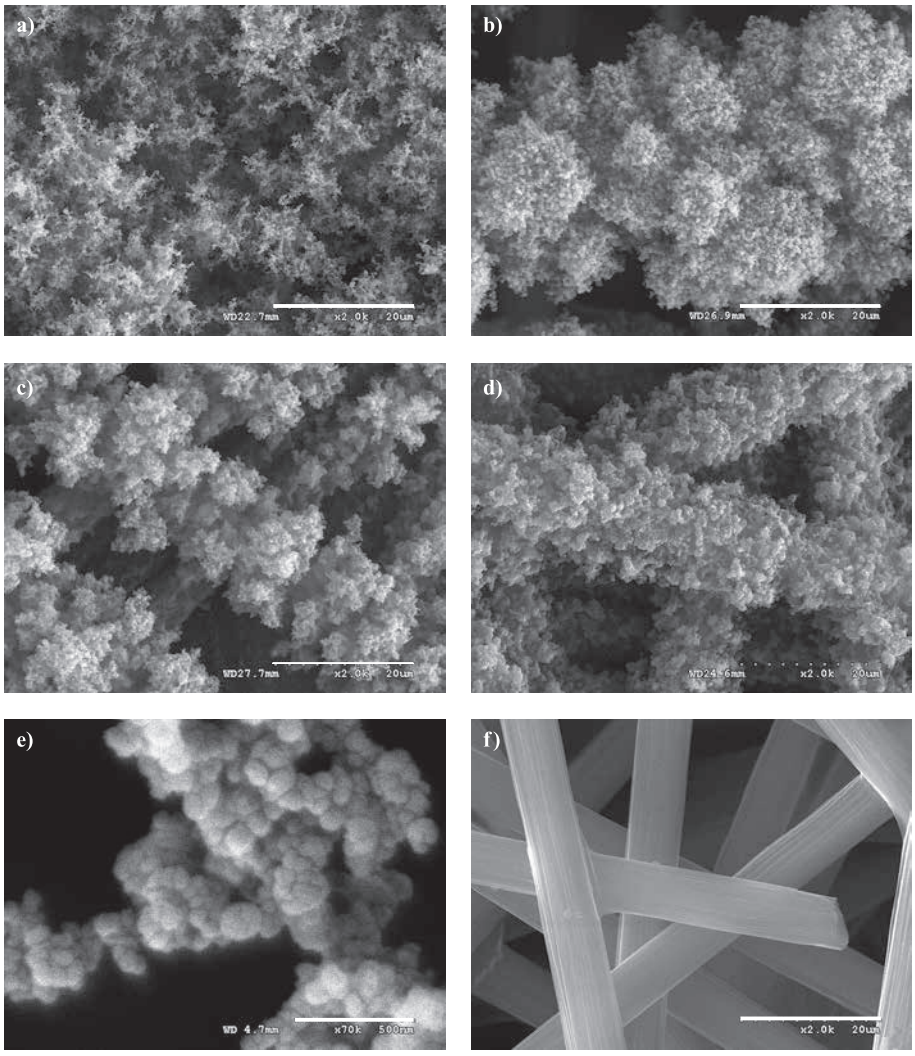

Fig. 14 SEM micrographs of the morphologies of the electrosprayed deposits classified as: **a**) fractal-like, **b**) patched clusters, **c**) and **d**) compact structures. Moreover, **e**) shows a closer view of the building blocks forming the fractal-like deposits, whereas **f**) shows the carbon paper substrate used as deposition substrate. All the electrosprayed deposits were carried out at a needle-substrate distance of 3.5 cm, a voltage drop of 7 kV (+5.5 kV voltage applied at the needle and the collector kept at –1.5 kV) and the Pt loading was 0.01 $mg_{Pt}cm^{-2}$. The micron bar in figures **a**)–**d**) and **f**) is 20 μm in length, in **e**) the bar corresponds to 500 nm.

catalytic deposit for PEMFC electrode preparation (due to the large active surface area). The small size of the catalyst clusters causes most of the catalyst to be exposed to the surface and available for the reactant gas. Besides this, the dendritic arrangement of the catalyst clusters results in a highly porous deposit with an enhanced permeability and increased active surface. One can expect that all these morphological properties of the granular material lead to high catalyst utilization when used as a catalyst layer.

On the other hand, **Fig. 14b** shows a deposit formed by patched clusters of thousands of single particles (◇ points in **Fig. 15**). These patched clustered deposits (composed of large aggregates of catalyst clusters with sizes in the micrometer range) appear for moderate Peclet numbers (larger flow rates than those for fractals deposits). Here, the granular material is more compact, leaving void spaces between the substrate fibers which diminish the effective surface of the catalytic layer. There is a significant amount of the catalytic material located in the inner regions of these large clusters that may lead to poorer catalyst utilization. Furthermore, **Fig. 14c & d** are compact deposits (with the arriving particles compacting on the initial carbon paper which is shown in **Fig. 14f**) representative of large Peclet numbers (achieved when the flow rate is large enough, see □ and △ points in **Fig. 15**). These compact deposits result from an incomplete evolution of the droplets during their flight toward the substrate. The droplets do not have enough time to evaporate and Coulomb fissions (Maxwell explosions due to the accumulation of electrical charges on the liquid droplet whose repulsion

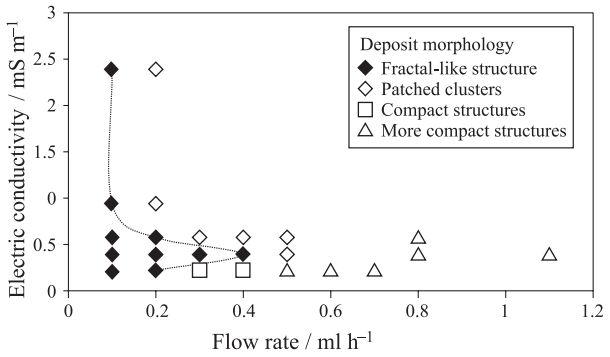

Fig. 15 Two-parameter diagram with the different types of deposit structures shown in **Fig.14**, depending on the electrical conductivity of the catalytic ink and the flow rate. Symbol ♦ corresponds to type **a**) fractal-like, ◇ is for **b**), □ for **c**) and △ for type **d**) deposits.

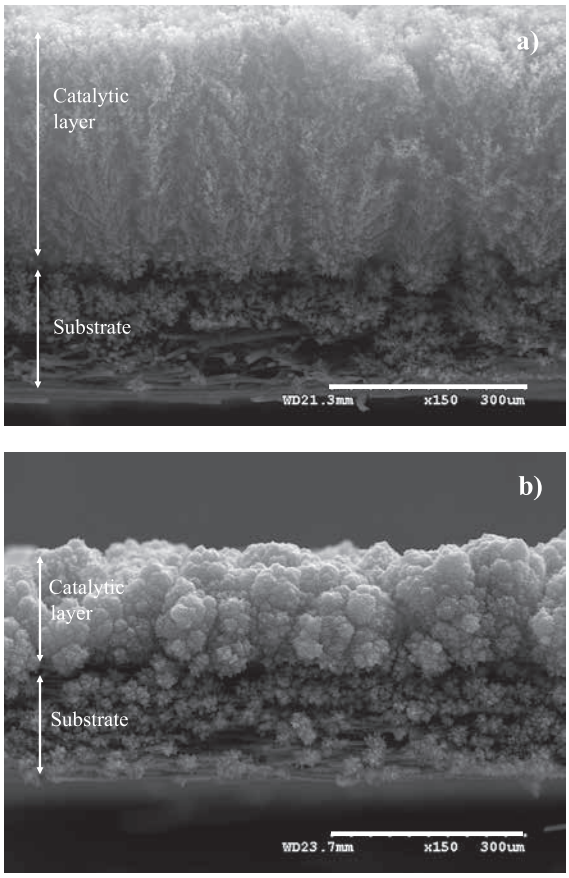

Fig. 16 Cross-sectional SEM micrographs of catalytic deposits electrosprayed over a carbon paper substrate (**a**) fractal-like structures for a flow rate $Q = 0.2$ ml h^{-1} and (**b**) patched clustered deposit obtained for $Q = 0.5$ ml h^{-1}. Same platinum loading (0.1 mg$_{Pt}$cm^{-2}) and same micron bar (300 μm) in both images.

overcomes the surface tension) are not in effect to reduce the droplet size. Therefore, the deposit is formed from wet suspensions with the ethanol evaporating later on. Note that the Monte Carlo simulation described in Section 2 considers that any particle reaching the deposit attaches to the touching position. This condition is not fulfilled in the case of collected droplets carrying a dry residue. Therefore, the results derived from these simulations cannot be directly used when complete drying does not occur during the droplet flight but the droplet evaporates after arrival.

When the Peclet number associated to the arriving droplets corresponds to a fractal-like deposit, the resulting dry compact deposit is as the one depicted in **Fig. 14c**, with fractal patches formed on the original fibers. Lastly, when the droplet Peclet number corresponds to a clustered deposit, the structure of the dry deposit is depicted by **Fig. 14d**, with denser deposits on the fibers leaving larger voids between them.

The diagram depicted in **Fig. 15** represents the region of the parameter space (electrical conductivity versus flow rate, for a constant voltage drop and a fixed needle-plate distance) leading to fractal-like structures (with the limits of this fractal-like region depicted by the dashed line). The deposit structure is different on each side of the dashed line. For a given electrical conductivity of the catalytic suspension (see **Fig. 11**), there is a threshold flow rate below which fractal-like structures are formed. Flow rates higher than this threshold value give rise to patched cluster structures or compact structures. The diagram shows that the range of flow rates leading to fractal-like structures expands as the electrical conductivity of the suspension decreases until a critical electrical conductivity is reached. For even lower electrical conductivities, the range of fractal-like deposits is substantially reduced. Moreover, beyond the fractal thresholds and above the critical electrical conductivity, the deposit structure is based on patched clusters. Finally, for electrical conductivities lower that the critical value, the fractal deposit becomes first compact based on fractals and later on compact based on patched clusters as the flow rate increases.

When the needle-substrate distance is increased sufficiently, the ethanol has enough time to evaporate along the droplet flight and only dried base deposits (type a or b) are achieved. Work to obtain a complete diagram of the deposit microstructure depending on several controlling parameters is currently underway.

On the base of the knowledge gained with these experiments, the suspension with an electrical conductivity of 5.77×10^{-4} S m^{-1} was electrosprayed under the same conditions (3.5 cm distance between needle and collector, and a voltage drop of 7 kV) for longer time periods on a carbon paper collector with two different flow rates: a flow rate $Q = 0.2$ ml h^{-1} lying in the range of fractal deposits, and a larger flow rate $Q = 0.5$ ml h^{-1} beyond that domain and leading to patched cluster deposits (see **Fig. 15**). A square carbon paper with a dimension of 5 cm^2 was used as a substrate. The mass of deposited nanoparticles was the same in both cases (leading to the same Pt loading of

0.1 $mg_{Pt}cm^{-2}$ in the catalytic layer). **Fig. 16** shows SEM lateral views of the respective catalytic layers deposited over the carbon paper substrate.

The SEM image of the deposit made at a flow rate of 0.2 ml h^{-1} (**Fig. 16a**) reveals its fractal character as it is formed by dendritic trees approximately 300 μm in height, and resembling very much the MC simulated deposits for low Peclet numbers (see **Fig. 3a**). However, the deposit made at the higher flow rate of 0.5 ml h^{-1} (beyond the fractal threshold in **Fig. 15**) exhibits a more compact structure as it is based on the growth of patched clusters that lead to globular structures after a long deposition time (**Fig. 16b**). The same amount of material was deposited in both cases (Figs. 16a and b). Therefore, at the higher flow rate (**Fig. 16b**) and as consequence of the compactness, the thickness of the deposit was reduced to about one-half with respect to the deposit shown in **Fig. 16a**.

The porosity for these deposits has been estimated as the proportion of the void volume to the total volume of the catalytic layer (Baturina and Wnek, 2005; Gasteiger et al., 2003). Despite the difference in the thickness of the catalyst layer, the porosity is very similar in both cases. For the fractal deposit made at the lower flow rate (Q = 0.2 ml h^{-1}, **Fig. 16a**), a porosity of 98% was measured, whereas the more compact deposit (Q = 0.5 ml h^{-1}, **Fig. 16b**) has a 95% porosity (thus, the occupation fraction or mean density was doubled in the second deposit as it becomes clear from the reduction in the deposit height). In any case given their high porosity, both types of deposits will present similar mass transport resistances in the gas phase although, as was indicated before, the catalyst utilization will be lower in the compact deposit because a significant amount of the catalyst is incrusted inside the patched cluster and is thus unavailable for the reactants in the gas.

It should be mentioned that these values of material porosity are significantly higher than those reported in the literature for catalyst layers prepared by other conventional techniques. Thus, for the decal method (Gasteiger et al., 2003) and the air-brush spray technique (Ihonen et al., 2002), porosity values in the range of 60% and 30%, respectively, have been obtained for catalyst layers with loadings close to 0.1 $mg_{Pt}cm^{-2}$. Using the electrospray technique, Baturina and Wnek (2005) reported a porosity of 84% for a similar catalyst loading (0.09 $mg_{Pt}cm^{-2}$).

To complete the analysis, the surface distribution of the catalyst and the ionomer was determined by energy-dispersive X-ray spectrometry (EDX) for the fractal-like catalytic layer presented in **Fig. 16a**. **Fig. 17** shows the EDX spectrum with the elements detected in the sample surface corresponding to the catalyst (Pt/C) and the Nafion® ionomer (sulfonated tetrafluoroethylene). **Table 1** provides the results from a local quantitative analysis of the catalytic layer shown in **Fig. 16a**, measured at different locations on the top surface of the material. No appreciable composition differences on the surface of the catalytic layer were observed, indicating that the electrospray process occurs in a spatially uniform manner (same radial distribution). This means that in the electrospray phase, the constituents of the catalyst ink are homogenously distributed and there is no accumulation of a component in any particular region within the electrospray. Therefore, the atomization-deposition process maintains the homogeneous distribution

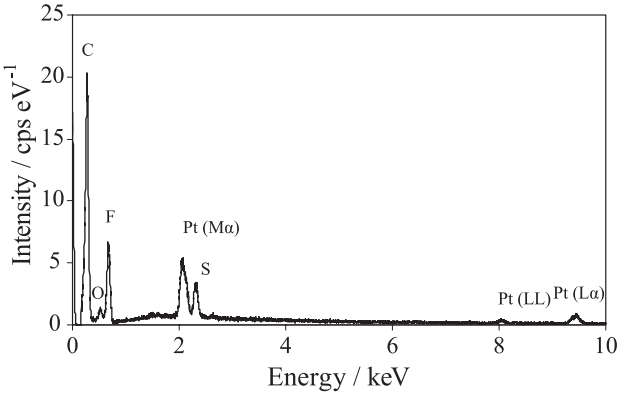

Fig. 17 EDX spectrum of the fractal-like deposit shown in **Fig. 16a**.

Table 1 Quantitative analysis of the elemental composition corresponding to the EDX spectra taken at different surface locations of the catalyst layer of **Fig. 16a**

	EDX Location								
Element composition (wt. %)									
C	19.70	19.87	19.46	19.76	18.68	18.12	19.60	19.54	19.40
Pt	5.24	4.93	4.81	5.64	5.50	4.76	4.91	5.14	5.41
F	63.93	64.23	64.70	63.60	64.67	66.16	64.22	64.06	63.90
S	1.61	1.64	1.68	1.70	1.80	1.85	1.79	1.76	1.72
O	9.51	9.33	9.34	9.51	9.33	9.11	9.47	9.50	9.57

of the original liquid suspension. Note that the double polarization with the collector at an opposite voltage with respect to the needle is used to focus the charged particles to the collecting area. Moreover, the main contribution to the deposit comes from the larger primary droplets as the tiny satellite droplets carry a small fraction of the nanoparticles in the liquid suspension.

The morphological properties of the deposits discussed in this section confirm the MC simulations results of Section 2.2. Fractal and open deposits are obtained when diffusion dominates the deposition process (low Peclet number corresponding to a weak electrical field at the collecting surface in the case of electrosprayed suspensions), whereas the deposit porosity decreases as the relative importance of diffusion decreases (the Peclet number increases). These results provide a way to prepare materials from powders that have a given consolidated structure. The main features of this analysis are not restricted to any deposition mechanism (the electrical drift of charged particles in the experiments shown here) but have a broader application. Indeed, it applies to any other particle-dominated transport combined with particle diffusion.

Given the morphology of the materials formed by this technique (high porosity and large effective surface area), they can be used as catalytic layers with wide applications. Their use as electrodes for PEM fuel cells is discussed in the next section.

4. Applications. Electrodes for fuel cells

The morphological properties (structural stability, large porosity, low weight and high active surface) of granular material growth from nanopowders as those shown in **Fig. 16** make them suitable for use as catalytic materials. A small amount of catalyst on the nanopowders composing the material will be enough to achieve a high catalytic performance, as the catalyzers on the original powders will still remain mostly at the active surface of the generated material. These days, the proper manufacture of fuel cell electrodes is one of the areas requiring a high utilization of catalyzers, as Pt requirements strongly affect the development of these technologies. Indeed, DOE 2007 pointed out that one of the main challenges that has to be overcome for introducing fuel cells as competitive power supply devices is to reduce the catalyst loading at the electrodes without compromising the fuel cell performance by means of increasing the catalyst utilization (maximum power output per gram of Pt at the electrodes).

In a Proton Exchange Membrane Fuel Cell (PEMFC) working with hydrogen and oxygen as reactants, both gases (in some cases the oxygen diluted in an inert gas such as nitrogen) enter through different inlet ports (**Fig. 18**) and are distributed by the gas diffusion layers (carbon

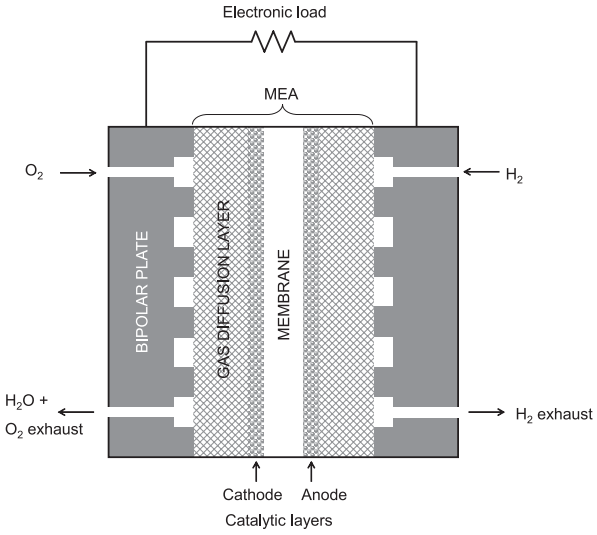

Fig. 18 Schematic of a hydrogen-oxygen PEM fuel cell.

fiber paper or carbon fiber cloth). These gas currents are kept separate by a Membrane Electrode Assembly (MEA). The MEA is formed by two porous catalytic materials (acting as electrodes) with a thin membrane (the polymeric electrolyte) between them. Hydrogen is dissociated by adsorption on the Pt at the surface of the anode; the electron in the hydrogen atom generates the fuel cell electrical current, whereas the proton diffuses through the anode and the electrolyte to reach the cathode surface. On the cathode side, oxygen molecules are also adsorbed on the platinum dots and the oxygen atoms react with the incoming protons (receiving an electron from the electrode) to form water. Water management is quite important in these fuel cells as a certain degree of humidity in the MEA is required to favor the proton transport, whereas flooding of the cathode would inhibit the adsorption of oxygen and stop the reactive process. To achieve an effective process, the electrodes should be:

- Porous materials to facilitate the penetration of the gases.
- Good electrical conductors to allow for the electron and proton transfer.
- Catalytically active. Thus, a catalyst must be evenly distributed on the material surface with a very large effective area available for catalytic reaction.

The materials described in the previous section which were generated by electrospraying a liquid suspension containing Pt-doped carbon nanoparticles fulfill all these requirements. They have over a 90% porosity (see **Fig. 16**) and are good electrical conductors due to the combination of the carbon nanoparticles (electron conductors) with Nafion® (proton conductor). Moreover, the Pt dots on the carbon nanoparticles form a large catalytically active area not just restricted to the topmost region of the material but well distributed on the entire surface inside the material

pores. Based on these properties, we used them as the cathode in an MEA and tested their efficiency in a fuel cell monitored in our laboratory (Martin et al., 2010a, 2010b).

In these MEAs, the electrolyte was a Nafion® 212 membrane compressed between the two electrodes. The ensemble was bonded by hot pressing at a pressure of 5 MPa and a constant temperature of 120°C applied for 2 min. The electrochemical performance of these MEAs was tested in a commercial fuel cell hardware accommodating a 5-cm^2 single cell geometry (FC05-01SP Electrochem, Inc.) connected to an external electronic load (Hocher & Hackl ZS-506). The fuel cell hardware employs machined graphite flow field plates with serpentine flow patterns and copper gold-plated current collectors. The feed gases were dry oxygen and dry hydrogen supplied by mass flow controllers (Bronkhorst Hi-Tec). Thus the fuel worked in a self-humidifying regime.

A reference MEA was prepared with the two electrodes made using a standard impregnation method with a Pt loading of 0.3 $mg_{Pt}cm^{-2}$ at the cathode and 1 $mg_{Pt}cm^{-2}$ at the anode. In a second MEA with the same electrode at the anode, the cathode was prepared by the described electrospray method with an ultra-low Pt loading of only 0.012 $mg_{Pt}cm^{-2}$; that is, a reduction of 1/25 in the amount of Pt with respect to the reference cathode. The electrosprayed electrode was prepared under the conditions to obtain the fractal material corresponding to the SEM image shown in **Fig. 16a** (i.e. a flow rate $Q = 0.2$ ml h^{-1}, a catalytic suspension with an electrical conductivity of 5.77×10^{-4} S m^{-1}, a needle-to-collector-plate distance of 3.5 cm, and a voltage drop of 7 kV).

The performance of both MEAs are compared in **Fig. 19**. **Fig. 19a** shows the fuel cell characteristic polarization curve, voltage provided by the device (left vertical axis) and the resulting power density (right vertical axis) versus the current density (Martin et al., 2010a, 2010b). Solid triangles correspond to the reference MEA whereas squares are for the MEA with the electrosprayed cathode. Although the reference MEA seems to offer a higher performance, it should be emphasized that the Pt content is 25 times larger in the reference cathode. Therefore, the electrosprayed MEA is able to attain 59% of the maximum power density supplied by the reference MEA but with only 4% of the catalyst loading on the cathode.

The potential benefits of the electrosprayed catalytic layer become evident when the catalyst utilization is evaluated. The specific power (fuel cell power per gram of Pt in the cathode) is represented in **Fig. 19b**. The maximum catalyst utilization (referred to the cathode) attained for the MEA with the electrosprayed cathode was 11.5 kW g^{-1}, whereas a significantly lower value of 0.78 kW g^{-1} was obtained by the MEA with electrodes prepared by a conventional impregnation method. Thus, the MEA with the electrosprayed cathode achieved a maximum catalyst

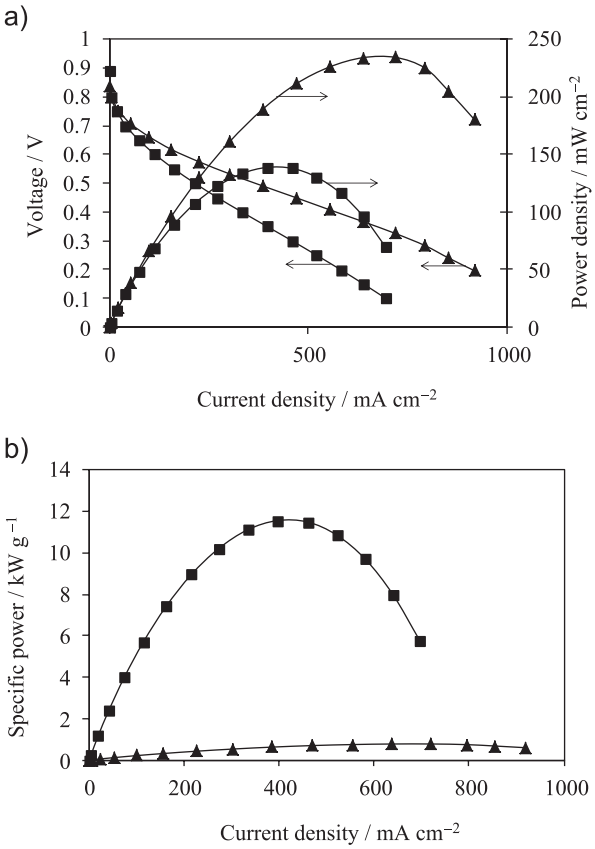

Fig. 19 **a**) Polarization curve (left axis) and power density (right axis), and **b**) specific power curve. (▲) reference MEA with a cathode prepared by an impregnation technique and a Pt loading of 0.3 $mg_{Pt}cm^{-2}$, (■) MEA with an electrosprayed cathode and a Pt loading of 0.012 $mg_{Pt}cm^{-2}$. All measurements were carried out with dry (non-humidified) H_2/O_2 at a cell temperature of 70°C and atmospheric pressure on cathode and anode exits.

utilization almost 15 times larger than the utilization reached by the reference MEA under the same working conditions. This factor of 15 is quite promising for future applications.

Note that the catalyst utilization of the electrosprayed MEA may even be increased if more suitable operating conditions of the cell are selected. Thus **Fig. 20** shows the increase of the cell performance when the back-pressure at the cathode and the anode exit lines is increased from atmospheric pressure up to 1.7 bar overpressure. For the electrosprayed MEA, a maximum cathode specific power of 19.1 kW g^{-1} was attained (although not shown in this figure, the performance of the reference MEA also increases with the fuel cell working pressure, but this improvement is rather moderate with respect to the electrosprayed MEA). The resulting platinum utilization is comparable to that achieved by cathodes prepared by sputtering, a well-established method for depositing ultra-low Pt loadings. Using these sputtered electrodes, specific power values between 14 kW g^{-1} and 20 kW g^{-1} have been

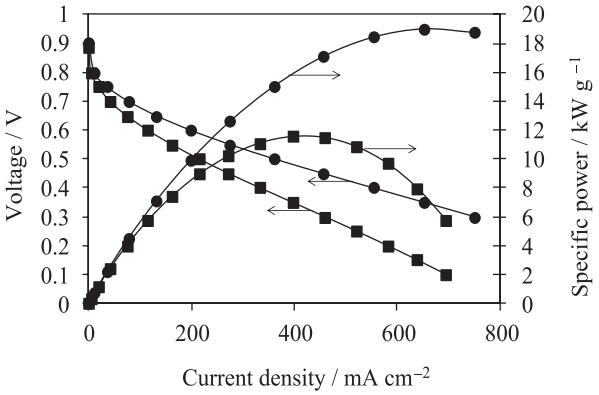

Fig. 20 Polarization and specific power curves for the MEA with the electrosprayed cathode when the back-pressure on the cathode and the anode exits is increased from atmospheric (■) up to 1.7 bar (●). All measurements were carried out with dry (non-humidified) H_2/O_2 at a cell temperature of 70°C.

reported (Caillard et al., 2008; Cavarroc et al., 2009; Gruber et al., 2005). However, the sputtering technique requires a strict atmospheric control and vacuum conditions that make it quite expensive and difficult to scale-up. In contrast, the electrospraying method described in this paper is carried out with a simple and inexpensive experimental set-up (only a pump-needle system and two high-voltage power supplies), the technique has no vacuum requirements and can be easily scaled-up, making it an attractive option for the mass-production of electrodes for the fuel cell industry.

5. Discussion of results and conclusions

The results presented here open a new line of research for the preparation of granular materials from nanopowders. Nanopowders or nanoparticles can be used as building blocks for making new materials with a prescribed structure. For deposits formed by monodisperse particles, a way of controlling the final deposit morphology by adjusting the dynamical behavior of the particles when approaching the collecting surface has been shown.

Thus a simple model of particle motion has been used to simulate the deposit evolution, considering two contributions to the particle motion: A mean (ensemble-average) determinist arrival velocity v normal to the collecting surface plus a superimposed random motion characterized by a diffusion coefficient D. The resulting control parameter is the Peclet number, $Pe = va/D$, where a is the particle diameter. This Peclet number measures the relative importance of the deterministic motion to the random contribution. Thus, the limit of infinite Peclet numbers corresponds to ballistic deposition when particles follow straight trajectories normal to the collector. Whereas the opposite limit of vanishing Peclet number accounts for a pure Brownian motion. A Monte Carlo simulation has been performed to track the particle motion and their attachment to the evolving deposit. These simulations have shown that deposits formed by particles with a large value of the Peclet number (near the ballistic limit) are more compact (see **Fig. 5a**) but have quite a rough surface (**Fig. 5b**). However, for low Peclet numbers, the deposit presents a tree-like structure with large voids (**Fig. 3a**) and its surface is quite rough with large pores entering deep into the deposit bulk (**Fig. 3b**). In any case, an analysis of the deposit mean density allows definition of three different regions in the deposit (**Fig. 6**). Thus there is a denser region close to the initially flat collecting surface where the density changes rapidly from a maximum value at the deposit bottom until reaching a middle plateau region where the mean deposit density remains constant and independent of the deposit height. These two regions form the frozen or consolidated deposit where new particles can no longer be attached. On top of the plateau regions, there is an active region where the density decreases from the constant plateau value down to a vanishing value at the uppermost layer of the deposit. On this active region, new particles may be incorporated to consolidate the deposit. A detailed analysis of the plateau region shows that the mean density there depends only on the Peclet number associated with the motion of the particles which arrive to form the deposit. This mean bulk density is given by Eq. (5). This simple relation is one of the main results of the Monte Carlo simulations because (when the features of the particle motion are given) it allows the deposit densityt to be known in advance. In summary, these Monte Carlo simulations have shown that the morphological properties (bulk porosity and surface roughness) of a granular deposit can be tuned by properly adjusting the velocity of the particles approaching the deposit.

On the basis of these theoretical predictions, experiments have been conducted to prepare nanostructured materials from carbon nanoparticles. These nanoparticles enter the gas from the atomization of a liquid suspension using the electrospraying technique (**Fig. 10**). Thus the liquid suspension is pumped at a fixed flow rate through a syringe where a high voltage is applied. The charges accumulate on the liquid surface and a stable cone-jet can be achieved (**Fig. 12**) by proper selection of the applied voltage and liquid flow rate (see **Fig. 12**). When the electrospray works in a steady cone-jet mode, the jet breaks up forming small liquid droplets. These droplets are charged and become affected by the externally imposed electrical field that drifts them towards a collector plate located in front of the ejecting needle and perpendicular to it. The evaporation of the liquid along the droplet path leaves dry nanoparticles which deposit on the collector. The intensity of the electrical field over this collector determines the

mean particle velocity there, and then the corresponding Peclet number. Using this technique, nanostructured deposits with a tree-like structure have been grown. The scanning electron microscope (SEM) images of the deposits are quite similar to the images of the deposits formed by Monte Carlo simulations (compare the SEM image of the real deposits shown in **Fig. 16** with the simulated deposit represented in **Fig. 3**). In general terms, the experiments confirm the theoretical predictions that denser deposits (or more porous deposits depending on the requirements) can be made when the control parameters are properly adjusted.

The accordance of the theoretical predictions with the experimental results facilitates the preparation of porous granular materials made from powders. These materials have a rough surface with large pores that penetrate into the bulk resulting in a bulk structure of highly interconnected pores. This open structure is especially suitable for applications requiring a large active surface area as in the case of catalysis or any surface-activated heterogeneous reaction. To check the validity of these materials for these kinds of applications, a granular deposit prepared by the indicated electrospraying technique was used as a cathode in a PEM fuel cell. The resulting material surface can be tailored to render a high-quality catalytic electrode for use in a proton exchange membrane fuel cell (PEMFC). Catalytic suspensions of platinum supported on carbon nanoparticles (Pt/C) in Nafion®-alcohol solutions electrosprayed over carbon paper were used in an experimental fuel cell set-up. In previous works, the fuel cell power density was measured as a function of the platinum loading and the range of parameters was obtained, leading to optimal platinum utilization for a given fuel cell efficiency (Martin et al., 2010a, 2010b). The tests on a controlled fuel cell have shown that the electrosprayed deposits were able to reach a fuel cell performance which overcomes the maximum catalyst utilization achieved with cathodes prepared by state-of-the-art techniques (Martin et al., 2013).

The results for the fuel cell cathode show the validity of the method in a particular case. But the same methodology can be used for other applications. The structure of the material can be tailored according to the application needs to have a given porosity and surface composition. Moreover, layered or composed materials (with a different porosity or different composition on each layer) can be prepared by adequate changes in the control parameters (liquid flow rate and applied voltages in the electrospraying technique) which determine the dynamics of the particles approaching the deposit.

Acknowledgements

This work was supported by research funding agencies in Spain: Ministerio de Ciencia e Innovación (grant ENE2008-06683-C03-01, and program Consolider-Ingenio 2010 grant CSD2010-00011), and also by Comunidad de Madrid (project HYSYCOMB, S2009ENE-1597). A collaborative agreement with YFLOW Company (Malaga, Spain) is also acknowledged. The advice from YFLOW team, Prof. Ignacio G. Loscertales (University of Malaga) and Prof. Antonio Barrero† (University of Seville) was essential for the electrospray set-up and operation. Moreover, Jose L. Castillo and Pedro L. Garcia-Ybarra thanks Prof. Daniel E. Rosner (Yale University, New Haven, CT, USA) and Dr. Athanasios G. Konstandopoulos (CERTH/CPERI, Thessaloniki, Greece) for many years of fruitful discussions on these topics and Prof. Sotiris E. Pratsinis (ETH Zurich) for encouraging us to write this paper.

References

Barrero A., Loscertales I.G., Micro- and nanoparticles via capillary flows, Annual Review of Fluid Mechanics, 39 (2007) 89–106.

Baturina O.A., Wnek G.E., Characterization of Proton Exchange Membrane Fuel Cells with Catalyst Layers Obtained by Electrospraying, Electrochemical Solid-State Letters, 8 (2005) A267–A269.

Caillard A., Charles C., Boswell R., Brault P., Improvement of the sputtered platinum utilization in proton exchange membrane fuel cells using plasma-based carbon nanofibres, Journal of Physics D Applied Physics, 41 (2008) 185307.

Castillo J.L., Mackowski D., Rosner D.E., Photophoretic Modification of the Transport of Absorbing Particles Across Combustion Gas Boundary Layers, Progress in Energy and Combustion Science, 16 (1990) 253–260.

Castillo J.L., Rodriguez-Perez D., Martin S., Perea A., Garcia-Ybarra P.L., Structure of Granular Deposits Formed by Aerosol Particles Conveyed by Fluid Streams, in: Fitt, A.D.; Norbury, J.; Ockendon, H.; Wilson, E. (Eds.), Mathematics in Industry, vol 15: Progress in Industrial Mathematics at ECMI 2008, Springer-Verlag, 2010, pp. 455–461.

Castillo J.L., Rosner D.E., Theory of Surface Deposition from a Unary Dilute Vapor-Containing Stream, Allowing for Condensation within the Laminar Boundary Layer, Chemical Engineering Science, 44 (1989) 925–937.

Cavarroc M., Ennadjaoui A., Mougenot M., Brault P., Escalier R., Tessier Y., Durand J., Roualdès S., Sauvage T., Coutanceau C., Performance of plasma sputtered fuel cell electrodes with ultra-low Pt loadings, Electrochemistry Communications, 11 (2009) 859–861.

Chen D.-R., Pui D.Y.H., Experimental investigation of scaling laws for electrospraying: dielectric constant effects, Aerosol Science and Technology, 27 (1997) 367–380.

Cloupeau M., Prunet-Foch B., Electrohydrodynamic spraying functioning modes: a critical review, Journal of Aerosol Science, 25 (1994) 1021–1026.

DOE, Hydrogen, Fuel Cell and Infrastructure Technologies Program Multi-Year research, Development and

Demonstration Plan, DOE Editor, Department of Energy, US, 2007.

Einstein A., Über die von der molekularkinetischen theorie der wärme geforderte bewegung von in ruhenden flüssigkeiten suspendierten teilchen, Annalen der Physik, 322 (1905) 549–560. See Einstein A., Investigations on the Theory of Brownian Movement, Dover, New York, 1956, p. 17 and successive.

Elmøe T.D., Tricoli A., Grunwaldt J.-D., Pratsinis S.E., Filtration of nanoparticles: Evolution of cake structure and pressure-drop, Journal of Aerosol Science, 40 (2009) 965–981.

Fernandez de la Mora J., The fluid dynamics of Taylor cones. Annual Review of Fluid Mechanics, 39 (2007) 217–243.

Fernandez de la Mora J., Loscertales I.G., The current emitted by highly conducting Taylor cones, Journal of Fluid Mechanics, 260 (1994) 155–184.

Gañan-Calvo A., Davila J., Barrero A., Current and drop size in the electrospraying of liquids. Scaling laws, Journal of Aerosol Science, 28 (1997) 249–275.

Garcia-Ybarra P.L., Castillo J.L., Mass Transfer Dominated by Thermal Diffusion in Laminar Boundary Layers, Journal of Fluid Mechanics, 336 (1997) 379–409.

Garcia-Ybarra P.L., Castillo J.L., Rosner D.E., Drag on a Porous Sphere with Self-Similar Structure: An Asymptotic Analysis, Journal of Aerosol Science, 37, (2006) 413–428.

Gasteiger H.A., Gu W., Makharia R., Mathias M.F., Sompalli B., Beginning-of-life MEA performance-Efficiency loss contributions, in: Vielstich W., Lamm A., Gasteiger H.A. (Eds.), Handbook of Fuel Cells: Fundamentals. Technology and Applications, vol. 3, John Wiley & Sons, 2003, pp. 593–610.

Gruber D., Ponath N., Müller J., Lindstaedt F., Sputter-deposited ultra-low catalyst loadings for PEM fuel cells, Journal of Power Sources, 150 (2005) 67–72.

Gu W., Heil P.E., Choi H., Kim K., Generation of stable multi-jets by flow-limited field-injection electrostatic spraying and their control via I-V characteristics, Journal of Physics D: Applied Physics, 43 (2010) 492001.

Higuera F.J., Numerical computation of the domain of operation of an electrospray of a very viscous liquid, Journal of Fluid Mechanics, 648 (2010) 35–52.

Houi D., Lenormand R., Particle deposition on a filter medium, in: Family F., Landau D.P. (Eds.), Kinetics of aggregation and gelation, Elsevier Science Publishers, 1984, pp. 173–176.

Ihonen J., Jaouen F., Lindbergh G., Lundblad A., Sundholm G., Investigation of Mass-Transport Limitations in the Solid Polymer Fuel Cell Cathode II. Experimental, Journal of the Electrochemical Society, 149-4 (2002) A448–A452.

Jaworek A., Sobczyk A.T., Electrospraying route to nanotechnology: An overview, Journal of Electrostatics, 66 (2008) 197–219.

Jullien R., Meakin P., Simple Three-Dimensional Models for Ballistic Deposition with Restructuring, Europhysics Letters, 4 (1987) 1385–1390.

Kim H.-H., Kim J.-H., Ogata A., Time-resolved high-speed camera observation of electrospray, Journal of Aerosol Science, 42 (2011) 249–263.

Konstandopoulos A.G., Papaioannou E., Update on The Science and Technology of Diesel Particulate Filters, KONA Powder and Particle Journal, 26 (2008) 36–65.

Li J., On the stability of electrohydrodynamic spraying in the cone-jet mode, Journal of Electrostatics, 65 (2007) 251–255.

Luyten J., Mullens S., Thijs I., Designing With Pores—Synthesis and Applications, KONA Powder and Particle Journal, 28 (2010) 131–142.

Martin S., Garcia-Ybarra P.L., Castillo J.L., Electrospray Deposition of Catalyst Layers with ultra-low Pt Loadings for PEM Fuel Cells Cathodes, Journal of Power Sources, 195 (2010a) 2443–2449.

Martin S., Garcia-Ybarra P.L., Castillo J.L., High Platinum Utilization in ultra-low Pt Loaded PEM Fuel Cell Cathodes Prepared by Electrospraying, International Journal of Hydrogen Energy, 35 (2010b) 10446–10451.

Martin S., Perea A., Garcia-Ybarra P.L., Castillo J.L., Effect of the collector voltage on the stability of the cone-jet mode in electrohydrodynamic spraying, Journal of Aerosol Science, 46 (2012) 53–65.

Martin S., Martinez-Vazquez B., Garcia-Ybarra P.L., Castillo J.L., Peak utilization of catalyst with ultra-low Pt loaded PEM fuel cell electrodes prepared by the electrospray method, Journal of Power Sources, 229 (2013) 179–184.

Milosevic O., Mancic L., Rabanal M.E., Gomez L. S., Marinkovic K., Aerosol Route in Processing of Nanostructured Functional Materials, KONA Powder and Particle Journal, 27 (2009) 84–106.

Nagatani T., Growth model with phase transition: drift-diffusion-limited aggregation, Physical Review A, 39 (1989) 438–451.

Naito M., Abe H., Kondo A., Yokoyama T., Huang C.C., Smart Powder Processing for Advanced Materials, KONA Powder and Particle Journal, 27 (2009) 130–143.

Noymer P.D., Garel M., Stability and atomization characteristics of electrohydrodynamic jets in the cone-jet and multi-jet modes, Journal of Aerosol Science, 31 (2000) 1165–1172.

Ragucci R., Fabiani F., Cavaliere A., Muscetta P., Noviello, C., Characterization of stability regimes of electrohydrodnamically enhanced atomization, Experimental Thermal and Fluid Science, 21 (2000) 156–161.

Rodriguez-Perez D., Castillo J.L., Antoranz J.C., Relationship between Particle Deposit Characteristics and the Mechanism of Particle Arrival, Physical Review E, 72 (2005) 021403.

Rodriguez-Perez D., Castillo J.L., Antoranz J.C., Density Scaling Laws for the Structure of Granular Deposits, Physical Review E, 76 (2007) 011407.

Rosner D.E., Mackowski D.W., Tassopoulos M., Castillo J., Garcia-Ybarra P.L., Effects of Heat Transfer on the Dynamics and Transport of Small Particles Suspended in Gases, Industrial and Engineering Chemistry Research, 31 (1992) 760–769.

Tang K., Gomez A., Monodisperse electrosprays of low electric conductivity liquids in the cone-jet mode, Journal of Colloid and Interface Science, 184 (1996) 500–511.

Tassopoulos M, O'Brien, J.A., Rosner D.E., Simulation of Microstructure Mechanism Relationship in Particle

Deposition, AICHE Journal, 35 (1989) 967–980.
Tolman S., Meakin P., Off-lattice and hypercubic-lattice models for diffusion-limited aggregation in dimensionalities 2–8, Phys. Rev. A, 40 (1989) 428–437.
Walton O.R., Review of Adhesion Fundamentals for Micron-Scale Particles, KONA Powder and Particle Journal, 26 (2008) 129–141.
Yurteri C.U., Hartman R.P.A., Marijnissen J.C.M., Producing Pharmaceutical Particles via Electrospraying with an Emphasis on Nano and Nano Structured Particles—A Review, KONA Powder and Particle Journal, 28 (2010) 91–115.

Author's short biography

Jose L. Castillo

Jose L. Castillo received an M.Sc. in Physics from Universidad Autonoma de Madrid and a Ph.D. in Physics from UNED. He has been an associate research scientist at Yale University (Chemical Engineering Department), collaborator at Los Alamos National Laboratory (Center for Nonlinear Studies, Los Alamos, NM) and sabbatical visitor at University of Miami (Department of Physics). He is a professor at UNED, member of the editorial board of the Journal of Aerosol Science, and representative of the Spanish Aerosol Society at the European Aerosol Assembly. He was president of the Experimental Science Committee for the assessment of non-tenure university positions at ANECA (National Agency for Quality Evaluation and Accreditation, Spain), and is now an ANECA deputy director for academic staff evaluation.

Santiago Martin

Santiago Martin received a B.Sc. in physics and an M.Sc. in applied physics (fuel cell research) from UNED. He received his Ph.D. thesis at UNED in the applications of electrohydrodynamic spraying for the generation of nanostructured catalyst layers for PEM fuel cell use.

Daniel Rodríguez-Perez

Daniel Rodríguez-Perez received an M.Sc. and a Ph.D. in physics from UNED. He is a senior lecturer at UNED working, among other areas, in discrete Monte Carlo computer simulation of growing structures.

Author's short biography

Alvaro Perea

Alvaro Perea received an M.Sc. in physics from Universidad Complutense de Madrid and a Ph.D. in physics from UNED. He is a senior lecturer at UNED, working in the area of particle transport phenomena.

Pedro L. Garcia-Ybarra

Pedro L. Garcia-Ybarra received an M.Sc. in physics from Universidad Autonoma de Madrid and a Ph.D. in physics from UNED, after a predoctoral stay at Université de Provence (Aix-Marseille I, France). He has been a Chercheur Associé at Université de Rouen (France), visiting research scientist at Yale University (Chemical Engineering Department), Universidad Nacional Autonoma de Mexico (UNAM) and University of California at San Diego (Center for Energy and Combustion Research). He is currently a professor at UNED, after being head of the Fossil Fuels Department at CIEMAT (Madrid). He is the secretary of the Spanish Section of the Combustion Institute.

KONA Powder and Particle Journal No. 31 (2014) 234–246/Doi:10.14356/kona.2014013 Original Research Paper

Scalable Production of Nanostructured Particles using Atomic Layer Deposition †

Aristeidis Goulas and J. Ruud van Ommen *

[1] *Department of Chemical Engineering, Delft University of Technology, the Netherlands*

Abstract

Core-shell nanoparticles and other nanostructured particles have high potential in applications such as heterogeneous catalysis and energy conversion and storage. However, a hurdle in their utilization is that typically, large amounts of such nanostructured materials are required. Gas-phase coating using atomic layer deposition (ALD, a variant of chemical vapour deposition) can be used to provide the surface of a particle with either an ultrathin continuous coating or a decoration of nanoclusters. When carried out in a fluidized bed, ALD is an attractive way of producing nanostructured particles with excellent scale-up potential.

We demonstrate the fabrication of catalysts by deposition of the active phase (Pt) on fluidized nanoparticles (TiO_2 P25) at atmospheric pressure. We show that ALD is a technique that 1) guarantees efficient use of the precursor; 2) allows precise control of the size and loading; 3) can be used for low and medium loading of catalysts by adjusting the number of repeated cycles; 4) leads to high-quality (low impurities level) end-products.

Keywords: atomic layer deposition, nanostructured particles, clusters, platinum, titania, catalyst

1. Introduction

In recent years, researchers have proposed a wide range of novel nanostructured materials for applications such as catalysis (Canlas et al., 2012; Li and Somorjai, 2010) and photovoltaic devices (Jancar et al., 2010; Kamat, 2008). Often, such materials use nanostructured particles as building blocks. In this paper, we will use the term nanostructured particles for particles of at least two materials, typically a host particle (not necessarily < 100 nm) onto which a second material is present in some structured way, e.g. as a film or set of clusters with dimensions < 100 nm. For most applications in catalysis and energy conversion and storage, large amounts of such materials are required. Most of the current synthesis routes for nanostructured particles, however, do not take into account the scalability of the process. It is not considered whether the synthesis of small amounts of materials in stirred flasks could be taken to some large-scale reactor to produce commercial amounts of materials. Moreover, the amount of waste produced in small-scale synthesis typically receives little or no attention.

While for research purposes it is not a problem to produce 100 g of waste to obtain 1 mg of a desired product, such a ratio is unacceptable at industrial scale. Sheldon (1992) proposed quantifying the efficiency of chemical processes by the *E*-factor: the mass ratio of waste to desired product. **Table 1** gives the *E*-factor for some industry segments. It is clear that nanomaterial production has the poorest performance by far. If nanomaterials are going to be widely applied in medicine, energy conversion and storage, their product throughput will increase to approximately the levels of pharmaceuticals and fine chemicals, respectively, which will give unacceptable amounts of waste. If we do not improve the manufacturing routes for nanomaterials drastically, it will lead to a low public acceptance and fewer market introductions of products based on such materials.

One of the reasons why the current synthesis of nanostructured particles is so polluting is that a combination of solvents and surfactants is often used, and the produced concentration of nanoparticles is very low; this yields very high *E*-factors. Moving to the gas phase eliminates the use of solvents, and is therefore intrinsically cleaner. Moreover, gas-phase processes are typically easier to scale up when nanostructured materials (Wegener et al., 2011) are concerned, although there are exceptions. For example, graphene can be more easily synthesized in large amounts in the liquid phase than in the gas phase (Coleman, 2012). When producing nanostructured particles in the gas phase, two basic approaches are possible:

(1) Directly synthesizing the nanostructured particles from precursors.

† Accepted: July 29, 2013

[1] 2628 BL Delft, the Netherlands

* Corresponding author:
E-mail: j.r.vanommen@tudelft.nl
TEL: +31-15-278-2133 FAX: +31-15-278-5006

Table 1 Annual product throughput for a typical plant and *E*-factor comparison for different material classes (based on Sheldon (2007) and Eckelman et al. (2008)).

Industry segment	Annual product throughput (log kg)	*E*-factor	Typical amount of waste (log kg)
Oil refining	9–11	~0.1	9
Bulk chemicals	7–9	< 1–5	8
Fine chemicals	5–7	5–50	7
Pharmaceuticals	3–6	25–100	6
Nanomaterials	2–3	100–100,000	6

(2) First producing the host or core particles, and then depositing the second material on them.

The first approach has the advantage of minimizing the number of steps in the production process; it can be considered as an example of process intensification. Several illustrative examples of this approach can be found in literature (Knijnenburg et al., 2013; Minnermann et al., 2013; Stepuk et al., 2012). However, it is not always straightforward to control the obtained morphology, and tuning of parameters might be needed when moving to a new combination of materials. The second approach—separating particle production and particle decoration—gives more degrees of freedom. Moreover, it has the advantage that commercially available particles can be used. It will depend on the individual application which of the two approaches is preferred. In this paper, we will focus on the second approach, and especially on its second step: depositing nanostructured material on already available particles.

For the well-controlled deposition of material at the nanoscale, a number of approaches are available. Some of them are line-of-sight methods, and are therefore not easily applicable to particles; examples are e-beam deposition (Laukaitis et al., 2006) and sputtering (Ferguson et al., 2008). Other methods can be applied to particles, but are not so easy to scale-up. An example is electrospraying deposition of nanoparticles (Ellis et al., 2010; Yurteri et al., 2010), which might be useful for pharmaceutics production, but could be cumbersome for applications that require large amounts of materials. Chemical vapour deposition (CVD) and similar techniques can be applied to particles and have a good scale-up potential, but have difficulty in reaching nanoscale precision. Atomic layer deposition (ALD) is a modified version of CVD that can achieve such precision. We will discuss it in more detail in the next section.

This paper will discuss ALD as a method of producing nanostructured particles that is scalable and has a limited production of waste. We will use the deposition of platinum nanoclusters on titania nanoparticles as an example.

2. Atomic layer deposition for the production of nanostructured particles

2.1 Atomic layer deposition

Atomic layer deposition (ALD) is a technique that relies on the distinct, consecutive binding of two (or more) compounds in a combined structure under a self-limiting chemisorption/reaction scheme. ALD presents basic self-assembly characteristics (Kim et al., 2009). However, one can argue whether it fully matches the definition of self-assembly as given by Gates et al. (2005): the spontaneous organization of two (or more) components to form larger aggregates by means of covalent and/or non-covalent bonds. Nevertheless, ALD is an inherently rational technique relying on a layer-by-layer (or cluster-by-cluster) assembly of the deposited materials. Similar to the production of layered composite natural or biomimetic materials such as nacre (Finnemore et al., 2012), ALD can be considered as a bio-inspired approach for the fabrication of tailored nanomaterials. ALD proceeds through a sequence of self-terminated gas-solid reactions (R_1 and R_2) that can be expressed as (King et al., 2007):

$$R_1\text{: } [S]\text{:}(OH)_y^* + x(MLn) \rightarrow [S]\text{:}(OH)_yM_x(L)_{n-y}^* + y(HL)$$

$$R_2\text{: } [S]\text{:}(O)_yM_x(L)_{n-y}^* + yH_2O$$

$$\rightarrow [S]\text{:}(M_xO_y)\text{:}(OH)_y^* + (n-y)(HL)$$

where S represents the surface of the support particle, y is the number of active sites, x is the number of metal-ligand molecules involved in the reaction, n specifies the number of ligands in the metal-ligand (M, L) precursor complex and * indicates the location of the relevant active species in the surface.

Unlike traditional wet-phase or gas-phase deposition (e.g. CVD) schemes, ALD offers digital control of the process since the growth of the materials relies on the number of repeated cycles rather than on the exposure

time or concentration of precursors. Moreover, the sub-nm precision (induced by the use of molecular-sized building blocks) enables the exact translation of the material design to an accurately fabricated structure.

2.2 Particle nanostructuring

Despite the foundation of ALD as a technique to grow thin, uniform layers of materials (hence its alternative name atomic layer epitaxy), the technique has also been used in the deposition of particle clusters during the initial growth stage (Haukka and Suntola, 1997). This observed deviation from the ideal character of the technique gave rise to an interest in applications that essentially rely on the utilization of a support material of particulate matter for the deposition of an active material. There are several factors affecting growth during the initial stages of ALD. These factors can be divided into three groups as depicted in **Fig. 1**. We will briefly discuss them with respect to the deposition of a (noble) metal on an oxide-terminated surface:

(1) Looking at the surface properties of the particulate support material, surface-termination-related growth limitations can be the result of the surface density of the reactive adsorption sites (usually in the range of 1–10 OH groups per nm^2 for oxide supports (Elam et al., 2007)) and of the preferential interaction of the precursor molecules with certain types of reactive sites. Additionally, surface roughness can also affect the growth (Lu and Stair, 2010).

(2) The binding process of the precursor is also important with a number of key factors such as the steric hindrance of the ligand, poisoning of reactive adsorption sites by contaminants or fragments of the precursor, and the chemisorption kinetics affecting the deposition (Elam et al., 2007; Haukka and Suntola, 1997).

(3) Considering the activation step (usually referring to the second ALD half-cycle, where the activation of the surface via the removal of the remaining ligand and the repopulation of the surface with reactive sites takes place), the interaction of the deposited phase and the support is mainly responsible for a series of events that eventually result in the formation of bigger clusters. Some of the important parameters are the temperature in the deposition chamber, the duration of the dosage times (Feng et al., 2010; Liang et al., 2012), the tendency of metals to minimize their surface energy through the formation of stable metal-metal bonds, and the dewetting of the oxide-metal surface due to the significance of lattice mismatch (Lu et al., 2012). Finally, the redistribution of active species during the oxidation-reduction treatment can be considered as an overall affecting condition (Xie et al., 2012).

ALD line-of-sight independency for the precursor delivery enables the deposition in high-aspect-ratio, complex topologies, and high-surface-area substrates. The limiting condition is the presence of a certain surface functionality

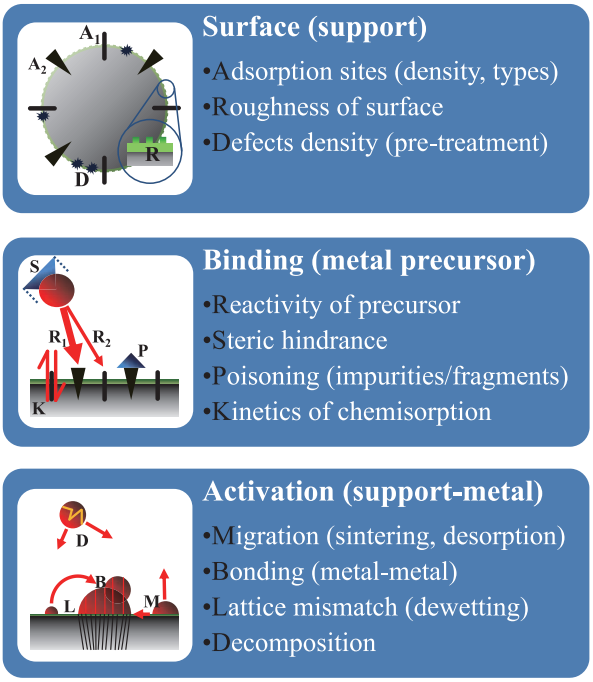

Fig. 1 Island growth dependence on surface-, binding- and activation-related parameters during the ALD of noble metals.

to promote material growth by ALD. Ultrathin seeding layers deposited by ALD (usually 0.2–1.1 nm thick) can further enhance the growth in support surfaces that show slow/inhibited growth behaviour.

So far, ALD has been used in the modification of oxide supports via the growth of thin layers of oxides, resulting in the fabrication of particulate support materials that can retain some inherited structural properties of the parent material (e.g. external surface area) while modifying others (e.g. acidity, pore size for mesopores, blocking of micropores, surface functionality, etc.). ALD coverage—especially in the initial growth regime—is just a fraction of a true monolayer value. An effort to study the monolayer coverage of various oxides on oxide powders shows that the coverage increases in the order of $SiO_2/TiO_2 < TiO_2/SiO_2 < Al_2O_3/SiO_2$ or TiO_2 (average values of 10%, 19% and 30–57% as shown in **Table 2**.

Looking at the different structuring possibilities, ALD can be used for particle nanostructuring, either to induce or inhibit certain composition and structure functionalities. Depending on the growth type of the deposited material, core/shell or core/seed particles (inactive core/active shell or seeds) can be fabricated in an activation scheme. Noble metals (Pt, Pd, Ru, Ir) have been deposited as core/seed active structures so far, while core/shell particles are usually functionalized with the deposition of transition metal oxide shells (e.g. TiO_2 and ZnO). ALD has proven its potential to unlock new application areas for core/seed nanoparticles, since it can reach extremely small sizes

Table 2 Growth per cycle (GPC) of ALD-deposited common oxides (TiO_2, SiO_2, Al_2O_3) on oxide powders (supports).

		Support			References
		SiO_2	TiO_2	Al_2O_3	
GPC (Å cycle^{-1})	SiO_2	–	0.3	–	(Kim et al., 2009)
	TiO_2	0.6	–	–	(Lei et al., 2012; Mahurin et al., 2006; Sereda et al., 2012; Williams et al., 2012)
	Al_2O_3	1.1	2.0	1.2	(Cronauer et al., 2011; Feng et al., 2010; Feng et al., 2011; Hakim et al., 2005; Hakim et al., 2006; King et al., 2007; Lei et al., 2012; Sereda et al., 2012)

(about 1 nm) of deposited particles (clusters) compared to conventional (wet-chemistry-based) techniques. ALD can deposit a variety of different materials (or combinations of them); a comprehensive review of the compounds that can be deposited by ALD was recently presented (Miikkulainen et al., 2013).

In certain applications, it can be desirable to modify—or even fully suppress—the activity of particles; a passivation scheme can yield core/shell particles of a reversed composition (active core/inactive shell). In the case of core/seed particles, this technique was developed as a protection scheme, applicable on the seed-nanoparticles. The most commonly used passivation materials are oxides such as Al_2O_3 and SiO_2, with the required thickness ranging from values as low as 0.5 nm up to 50-nm films, depending on the application. Special treatment can tailor the nature of the protective layer to induce a certain accessibility (Canlas et al., 2012; Lu et al., 2012). Moreover, supported active multi-component materials (e.g. multimetallic catalysts) can also be prepared via ALD either in a consecutive deposition scheme (He et al., 2010; He et al., 2012; Molenbroek et al., 1998) or—recently—a mixed-metal ALD process (Christensen et al., 2010; Lei et al., 2012). A schematic depiction of the different possibilities for ALD modifications of different functionalities is shown in **Fig. 2**.

Thus, ALD offers a 3-stage rational design approach for the synthesis of nanostructured particles. In the first stage, the active phase can be deposited with high precision, either in the form of thin films or nanoparticles. Protection of the active phase can be achieved either by full overcoats (passivation) or partial coverage (preferential growth on the support). Finally, selectivity is induced by manipulating the accessibility of the active phase (in a passive, e.g. thermal treatment, or active, e.g. blocking agent grafting way).

2.3 Reactor technology

Materials of a particulate nature often pose challenges during their treatment with ALD due to the high total surface area that needs to be coated and the—often present—requirement of coating high-aspect-ratio structures

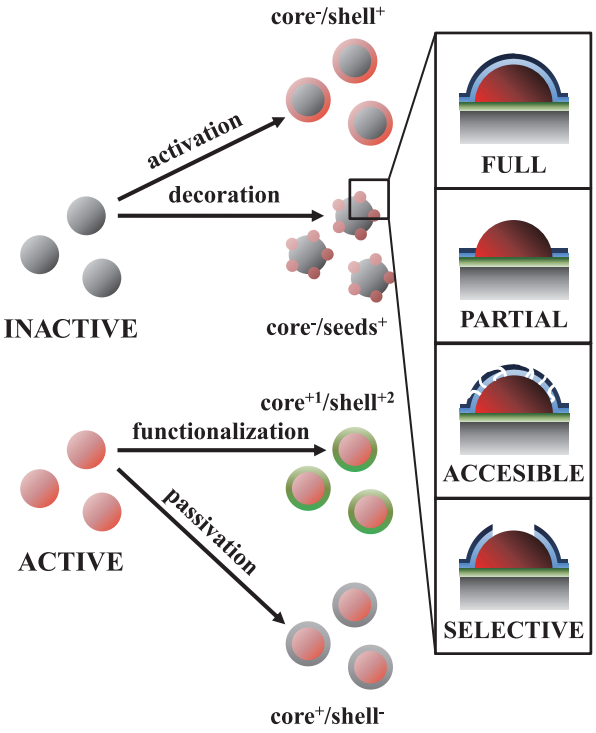

Fig. 2 Functionalization possibilities for active and inactive particles by film or cluster deposition via ALD.

such as micropores. Flow-type reactors for ALD introduced by Microchemistry Ltd. (primarily designed for the treatment of flat substrates) have been also used for the treatment of powders; the MC-120/F-120 being one of the most commonly used reactor type. In the reaction chamber, the reactant, introduced from the top of the fixed powder bed (up to 10 g), is allowed to chemisorb and react for a sufficient time to reach saturation (Lakomaa et al., 1992). This reactor configuration yielded consistent saturation coverage (±0.2 atoms nm^{-2}) but required reasonably high pulsing times (on the hour-scale) due to the relatively high operating pressure of 1–10 kPa. Recently, a modification of the reactor cell to a semi-fluidized powder cell was reported for particle ALD (Rauwel et al., 2011).

A viscous-flow ALD reactor (Elam et al., 2002) operating at reduced pressure (120–270 Pa) has also been used by researchers in Argonne National Laboratory for ALD

treatment of powders. High-surface-area supports (up to 930 m^2g^{-1}) have been effectively coated, at faster saturation exposure times (on the min-scale). Only small batches (up to 1 g) of materials have been processed in this viscous-flow reactor type.

Additionally, modifications of conventional ALD reactors aiming at the minimization of gradients (concentration, temperature) during the deposition introduced the use of fluidized bed reactors (Hirva et al., 1994). A fluidized bed ALD reactor operating at low pressure (133–1066 Pa) introduced by Wank et al. (2004) has been extensively used. Large batches of powders (up to 75 g) have been effectively coated in this reactor type, successfully proving the scale-up potential. Since many of the powders used as substrates exhibit cohesive behaviour, fluidization assistance methods such as stirring or vibration are typically required. van Ommen et al. (2012) give an overview of the various assistance methods to fluidize nanopowders. Although it may sound counterintuitive, nanopowders can indeed be fluidized. In contrast to particles of say 200 µm, however, nanoparticles are not fluidized individually but as agglomerates: very dilute structures of around 200 µm consisting of ~10^{10} primary particles (van Ommen et al., 2012).

Despite the fact that the fluidized bed reactor provided a good scalability potential in terms of the batch handling capabilities, the high total surface area of the powders—and the subsequent need for large amounts of precursor dosing (due to the residence time of the gaseous precursor in the fluidized bed)—called for research focussed on more efficient utilization of the precursor. The use of a rotary reactor operated at very low pressures (less than 133 Pa) was suggested (McCormick et al., 2007), in an effort to obtain a static exposure scheme and proper mixing during deposition. In this reactor, fluidization and agitation of the particles is achieved by rotation, and therefore a constant gas flow is not required. However, it was not demonstrated that this reactor was more efficient than a fluidized bed in terms of precursor utilization. Until today, this reactor has been used to coat batches of up to 2 g. A different rotary reactor configuration was recently proposed (Longrie et al., 2012). They operate this reactor at a very low pressure (< 2 Pa). Their system is capable of applying both thermal and plasma-enhanced ALD.

Recently, the atmospheric pressure operation of a fluidized bed ALD reactor was demonstrated for the growth of thin films (Beetstra et al., 2009) and the deposition of highly-dispersed nanoparticles (Goulas and van Ommen, 2013). Although the pulsing times required are longer than the equivalent in low-pressure operation, the process was proven to be efficient in terms of precursor utilization while excluding the need for expensive vacuum equipment. Fluidization at atmospheric pressure is also more attractive from the perspective of the scale-up potential. To our knowledge, the 120 g-batch of $LiMnO_4$ particles

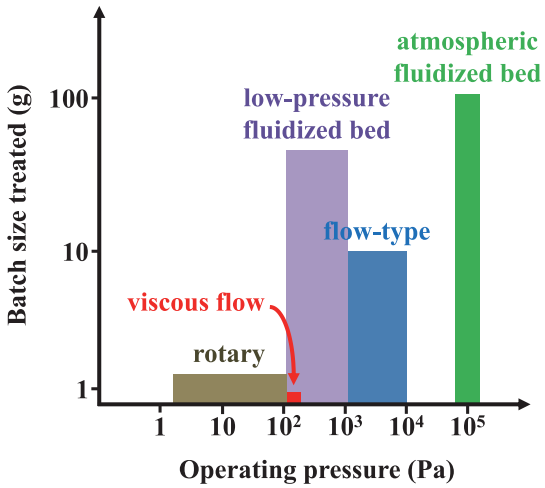

Fig. 3 Categorization of the main research ALD reactors used for particle nanostructuring based on the operating pressure range and maximum batch size reported (logarithmic scales).

coated via ALD in this fluidized batch is the largest amount reported in open literature. The next step is to move from batch to continuous production, e.g. via the pneumatic transport of particles (van Ommen, 2010); research on such reactors is currently being carried out in our group. A summary of the main types of reactors used is given in **Fig. 3**.

Moreover, certain commercial reactors such as the Beneq P400 (Nevalainen et al., 2012), Ultratech/Cambridge NanoTech Savannah 100 (Sun et al., 2013), Picosun SUNALE R-200B (Williams et al., 2012) and a shower-head reactor from Korean Vacuum Tech. Ltd. (Yoon et al., 2011) have been already used for ALD on particles.

2.4 Example: deposition of platinum nanoclusters by ALD

The ability to precisely tailor the structure of particles on a nanoscale gives us a tool to greatly improve metal-supported catalysts, enhancing atom efficiency while minimizing the cost of the expensive and scarce metal of the active phase. Currently, Pt, Ir, Rh are all priced above $32,000 per kg. In an effort to establish well-defined structure-reactivity correlations and unravel the role of size in nanocatalysis, materials with well-controlled dimensions in the size of (sub) nanometres have to be delivered. Apart from achieving better material utilization—a high surface-to-volume ratio yields a high amount of active sites per active material mass—different functionalities can also be assessed, due to the changed local reactivity characteristics of nanoparticles (more corners, edges, kinks) compared to their bulkier counterparts. Considering that in the *fcc* structure of Pt (atomic diameter of 0.278 nm), 12 shell atoms can cover 1 metal atom to form the single full-shell cluster (n = 1) (Schmid, 1990), the structure has

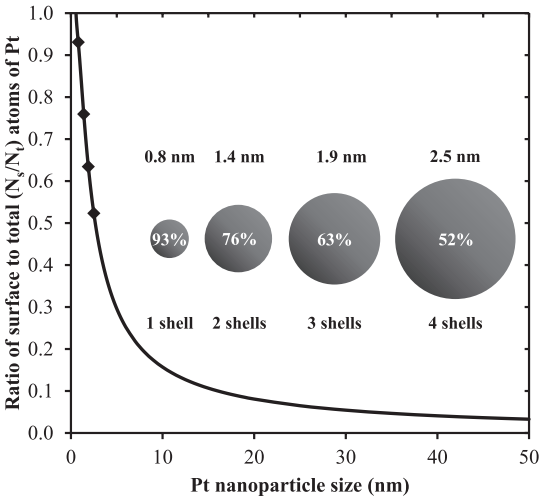

Fig. 4 Ratio of surface to total (N_s/N_t) atoms as a function of the Pt nanoparticle size (inline graphic indicates the size and percentage of Pt nanoparticles for 1 to 4 shells in the *fcc* cluster).

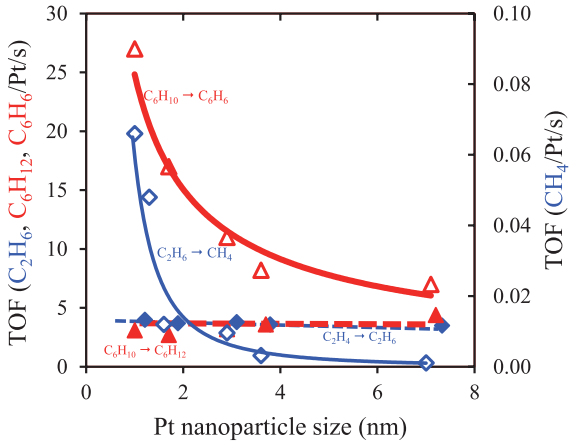

Fig. 5 TOF values for structure-insensitive Pt-catalysed reactions, marks indicate experimentally determined data-points (C_2H_4 hydrogenation: blue dotted line and ◆, C_6H_{10} hydrogenation: red dotted line and ▲) and structure-sensitive reactions (C_6H_{10} dehydrogenation: red solid line and △, C_2H_6 hydrogenolysis: blue solid line and ◇; plotted on secondary vertical axis) (based on Somorjai and Park (2008)).

93% of its atoms on the outer surface (**Fig. 4**). The N_s/N_t is inversely proportional to the number of shells (n^{-1}), this decrease can be seen in a 2.5 nm nanoparticle, where only 52% of its atoms are directly accessible and thus highlighting the reactivity potential of smaller clusters.

The activity of catalytically promoted reactions is often expressed as the turnover frequency (TOF) which describes the amount of moles converted per mole of the exposed catalyst material. The particle structure (size and shape) can affect the TOF if the reaction is intrinsically dependent on size/shape or is structure-sensitive, while some other reactions are not affected by the size (intrinsically size/shape-independent or structure-insensitive). For structure-sensitive reactions, a positive size effect marks an inversely proportional relationship between particle size and TOF, while a negative size effect shows a proportional interaction (antipathetic particle size-TOF dependence). For structure-insensitive reactions, the main objective during deposition is the maximization of dispersion to achieve optimal use of the catalytic material. Typical Pt-catalysed structure-insensitive reactions are ethylene and cyclohexane hydrogenation, while an example of positively size-dependent reactions are the hydrogenolysis of ethane and the dehydrogenation of cyclohexane (Somorjai and Park, 2008). As seen from **Fig. 5**, small Pt nanoparticles (≤ 3 nm) can greatly improve the TOF of structure-sensitive reactions. Additionally, the catalyst selectivity can also be improved by controlling the particle size distribution over a narrow range, as demonstrated for hydrogenation reactions (Somorjai and Park, 2008).

The first report of a supported Pt catalyst fabricated by ALD was the Pt/Al_2O_3 and Pt/SiO_2 hydrogenation catalysts prepared by Lashdaf et al. (2004). The cyclopentadienyl precursor (trimethyl) methylcyclopentadienyl-platinum (IV) ($MeCpPtMe_3$) was used as a source of Pt and air was used for the removal of the organic ligand at 350°C. For a single exposure of the precursor, larger islands were observed in SiO_2 (3.1 nm) as compared to the Al_2O_3 support (1.2 nm) in consistency with the available number of active OH groups (proportional to the available surface area and surface density). Additionally, an acetylacetonate Pt precursor ($Pt(acac)_2$) was utilized at lower deposition temperatures of 180–200°C, which had as a drawback the inclusion of carbon-based impurities of a high concentration (~3.5 wt.%) in the catalyst (Plomp et al., 2008; Vuori et al., 2006).

The importance of Pt as a catalytic material has driven efforts for deposition on strontium titanate, titania, zirconia and alumina high-surface-area supports in the temperature window of 150–300°C (Christensen et al., 2009; Enterkin et al., 2011; Lobo et al., 2012; Setthapun et al., 2010; Xie et al., 2012). Moreover, the technique has also been used for the doping of Co-based Fischer-Tropsch catalysts with small amounts of Pt (0.1 wt.%) that acts as a promoter (Cronauer et al., 2011). Recognizing the technique's potential for creating the high dispersion characteristics necessary in fuel cell applications, ALD has been used for the decoration of relevant carbon-based supports such as carbon aerogel, tungsten-carbide, multi-walled carbon nanotubes, graphene nanosheets and carbon nanotube/graphene oxide hybrid materials (Hsieh et al., 2012; Hsu et al., 2012; Hsueh et al., 2012; King et al., 2008; Sun et al., 2013). Additionally, bimetallic Ru-Pt and Pt-Pd catalysts have also been fabricated (Christensen et al., 2010; Lei et al., 2012). All the aforementioned efforts were carried out in fixed bed reactors that treated small batches of the

powders (< 1 g).

Zhou et al. (2010) reported the deposition of Pt islands on TiO_2 nanoparticles in a fluidized bed reactor operating at reduced pressure. Additionally, highly dispersed Pt clusters have been deposited effectively on micron-sized SiO_2 (Li et al., 2010), resulting in an extremely low loading of $3.1 \cdot 10^{-6}$ mg cm^{-2} ($3.1 \cdot 10^{-8}$ kg m^{-2}) for 3 ALD cycles. According to a recent publication, thermal decomposition of the Pt precursor along with Pt nanoparticle sintering at a deposition temperature of 320°C are responsible for the disruption of the self-limiting ALD feature (Liang et al., 2011).

3. Experimental

Atomic layer deposition in a fluidized bed reactor operating at atmospheric pressure conditions was used for the decoration of TiO_2 nanoparticles with Pt nanoclusters. The deposition scheme involves the sequential exposure of the support material to $MeCpPtMe_3$ and ozone (Goulas and van Ommen, 2013) at 250°C. The ALD reaction proceeds via a mechanism proposed by Kessels et al. (2009) adapted to the following generic scheme:

$$R_1{:}[Ti]{:}(O)_3^* + 2(CH_3C_5H_4)Pt(CH_3)_3$$

$$\rightarrow [Ti]{:}2(CH_3C_5H_4)Pt(CH_3)_2^* + CH_4 + CO_2 + H_2O$$

$$R_2{:}[Ti]{:}2(CH_3C_5H_4)Pt(CH_3)_2^* + 24O_2$$

$$\rightarrow [Ti]{:}[2Pt]{:}(O)_3^* + 16CO_2 + 13H_2O$$

The custom-built fluidized bed ALD reactor consists of a vertical reaction chamber with an inner diameter of 10 mm that was loaded with ~0.25 g of nanoparticles, supported on a porous metallic gas distributor. The TiO_2 nanoparticles used (Aeroxide P25 from Degussa, ≥ 99.5% purity) were sieved prior to deposition. Their surface area was ~50 m^{2}g^{-1} and their average primary particle size was 21 nm with a crystal structure of about 85% anatase and 15% rutile. During fluidization, these particles formed agglomerates of around 200 μm.

The precursor (trimethyl) methylcyclopentadienyl-platinum (IV) (Strem Chemicals, 99% purity) was utilized as a Pt source. The precursor was transported in the reaction zone by means of a dry nitrogen carrier gas (N_2, 99.999 vol.%) that was diverted through the precursor bubbler (50°C). A dry air stream enriched with ozone (around 1.5 wt.%) was used as an oxidizer agent for the removal of the precursor ligands and repopulation of the support surface with active sites. Ozone was obtained by feeding the dry air flow (0.20 L min^{-1}) through an ozone generator (OAS Topzone). No significant decomposition of ozone was observed during the transportation of the stream to the reactor zone via the reactor distributor. Nitrogen was also used for the intermediate purging pulses that were implemented to evacuate the reactor from the excess of the precursor and the reaction by-products during the ALD half-cycles. During operation, the TiO_2 powder was suspended in an N_2 flow of 0.20 L min^{-1} (corresponding superficial gas velocity of 4.2 cm s^{-1}), ensuring that the particles were sufficiently mixed. Fluidization was assisted using a dual vibromotor. The reaction temperature of 250°C was maintained by means of an IR-heater with feedback control. A more elaborate description of the set-up is given by Beetstra et al. (2009). The loaded TiO_2 nanoparticles were pretreated (heating under inert atmosphere) to ensure a constant initial number of active OH-groups in the surface. The typical pulsing sequence for Pt-N_2-O_3-N_2 consisted of exposure times of 3–12 min for $MeCpPtMe_3$, and 10 min for ozone separated by N_2 purging pulses of 10 min.

Optical emission spectrometry (ICP-OES) using a Perkin Elmer Optima 3000 DV spectrometer was used to determine the amount of Pt deposited. The level of carbon impurities in the samples was monitored by IR absorption spectroscopy in a C/S determinator (LECO CS-225). The structure of the deposited islands was determined from TEM images using a FEI Tecnai TF20 microscope equipped with an EDX detector (Oxford Instruments). XRD measurements were carried out with a Bruker D8 Advance diffractometer. The BET surface area of the coated and uncoated samples was determined via N_2 adsorption with a Quantachrome Autosorb-6B surface area analyser.

4. Results and Discussion

Two of the important intrinsic properties of ALD are the self-saturating character of the growth for a single cycle and the linear increase of the amount of material deposited by increasing the amount of cycles. Coating powder batches of increased surface area (up to 14 m^2 per sample batch) requires much longer precursor exposure, oxidation and purging times. It has been shown that during the prolonged exposure times, the reactor temperature should be properly controlled to avoid thermal decomposition of the precursor (Liang et al., 2011). When utilizing a lower deposition temperature (250°C instead of 320°C), an indication of the self-saturating ALD characteristic was seen (as shown in **Fig. 6**) with the Pt loading stabilizing at ~1.6 wt.% after 12 min of precursor exposure.

The average Pt particle size from TEM image processing was estimated to be about 1.5 nm for a Pt pulse of 3 min and appeared to be stabilized for exposures up to 12 min. Uniform decoration of the support material with Pt nano-

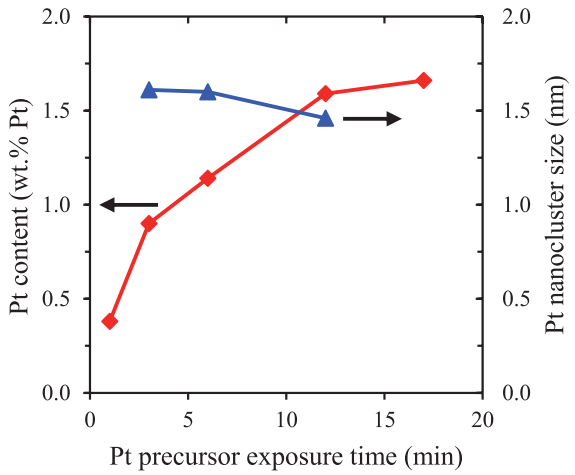

Fig. 6 Estimated Pt content (red line and ◆) and nanocluster size (blue line and ▲; on secondary vertical axis) for varied Pt precursor exposure times and 1 ALD cycle.

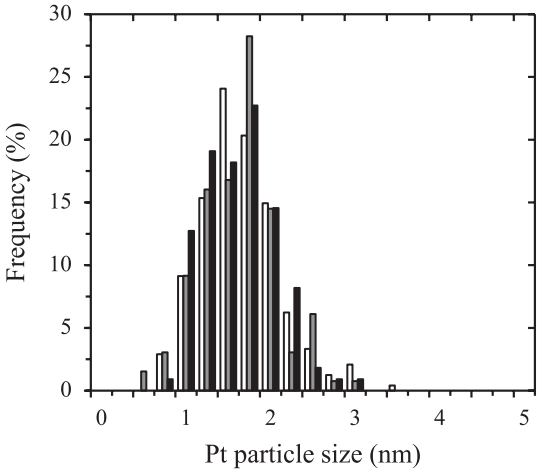

Fig. 8 Pt particle size distributions derived from TEM image processing for samples obtained after 3 min (white bars), 6 min (grey bars) and 12 min (black bars).

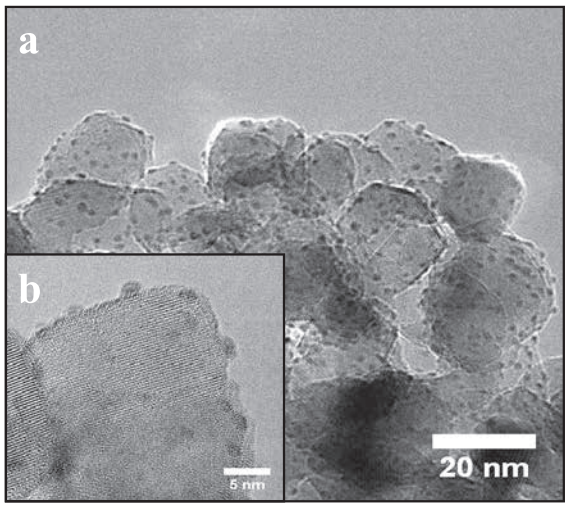

Fig. 7 TEM image of the Pt nanoparticles decorating the surface of the TiO_2 support after 1 ALD cycle of 3 min Pt precursor exposure. The inline image depicts the decoration at the edge of the TiO_2 crystal.

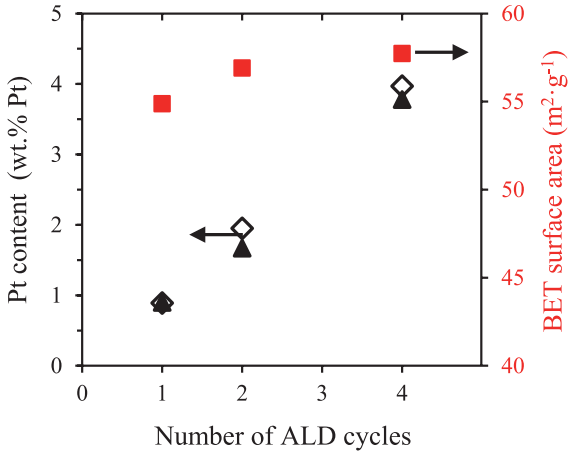

Fig. 9 Pt content measured by ICP (▲) and predicted loading value for ideal ALD (◇) along with specific surface area (■) for 1–4 ALD cycles (Pt content values corrected for changes in surface area after deposition).

clusters was obtained as shown in **Fig 7**. The particle size distributions presented in **Fig. 8** verify that the process was well controlled and resulted in very similar, narrowly distributed particles. Moreover, the TEM pictures indicated that the Pt nanoclusters were nicely distributed over the titania particles. This can be explained by the very open structure of the agglomerates, as well as by their dynamic nature: they constantly break-up and reform into new agglomerates (van Ommen et al., 2012).

Precursor utilization for exposure times in the saturation regime was relatively low: only ~50% of the Pt precursor provided was eventually loaded in the support. Using ALD for the fabrication of ultra-low loading catalysts, sub-saturated pulses can be implemented to achieve maximum utilization of the precursor. An exposure time of ¼ the saturation time resulted in a deposition amount of about half of the equivalent amount deposited for operation in the saturation regime. The corresponding precursor utilization was estimated to be 95% in that case. An estimation of the *E*-factor value was made, considering Pt/TiO_2 as the final product (~10–20% of the loaded TiO_2 is lost as waste during handling). The outlet waste stream contains the gas products of the organic ligand decomposition and the excess amounts of oxidizer gas used (O_3/O_2, without taking into account N_2). The equivalent calculated *E*-factor of the deposition process is ~6–7, fitting in the range of 5–50 that describes processes of the fine chemicals industry (Sheldon, 2007).

Additionally, the loading of the catalyst can be precisely controlled by the number of ALD cycles performed. **Fig. 9**

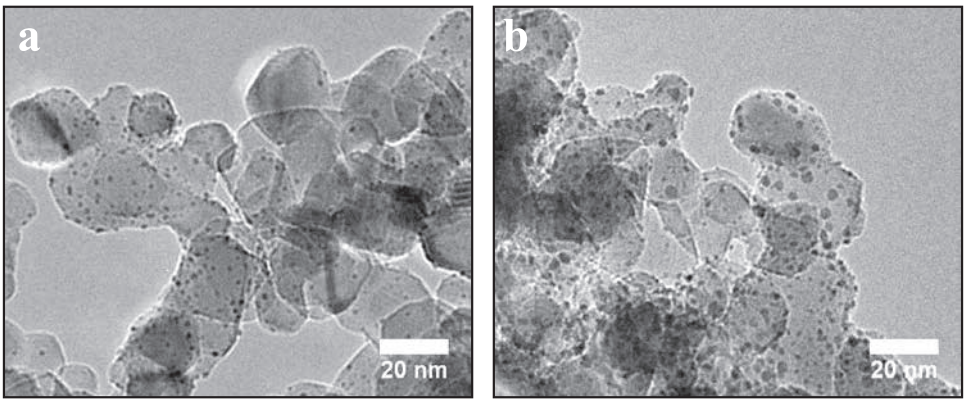

Fig. 10 Overview TEM images of Pt nanoclusters deposited on the TiO_2 support for 1 ALD cycle (**a**) and 5 ALD cycles (**b**).

presents the measured content of Pt (wt.% of Pt) along with the theoretically predicted value for ideal ALD growth, together with the change in value of the specific surface area of the support. Increasing the number of cycles from 1 to 4 shows a monotonic increase of the Pt loading, verifying the proportional relation between the deposited amount and the number of ALD cycles. The surface area showed a small increase of 5%, in agreement with deposition of small Pt nanoclusters on non-porous supports. The loadings of the catalysts obtained here are higher than the ones obtained in a fluidized bed reactor operating at reduced pressures (Zhou et al., 2010). The use of ozone—a more powerful oxidizer—is one possible cause, but the effect of pressure should also be carefully considered in future studies.

The use of ozone allowed the process temperature to be lowered during the oxidizing step. This can have a beneficial effect on the dispersion of the noble metal nanoparticles, as it prevents their sintering to a certain extent. To further probe the dispersion of the Pt nanoclusters, we examined several TEM images, applying image analysis (ImageJ). A sample of 1 ALD cycle deposited for 12 min exposure time (1.6 wt.%) and 5 ALD cycles deposited for 5 min exposure time (5.8 wt.%) are shown in **Fig. 10**. As the number of cycles increases, the particle nanoclusters increase in size. All the particle size distributions were calculated based on the processing of 100–200 Pt nanoparticles from different images. The presence of Pt (small clusters of darker contrast on the lighter crystalline support material) was further verified by qualitative EDX analysis. As discussed above, the average particle size increased from 1.5 nm to about 2.3 nm while the particle size distribution was—for both cases—very narrow (**Fig. 11**). The possibility of ALD to deposit small nanoparticles, even for high loadings of noble metals, makes it a promising fabrication technique for low-and medium-loading noble metal catalysts.

ALD offers a simple way to control the particle size of

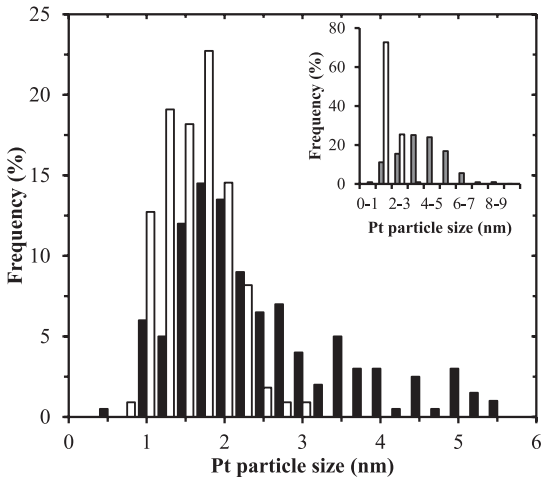

Fig. 11 Particle size distribution derived from TEM image processing for Pt nanoclusters deposited onto the TiO_2 support after 1 ALD cycle (white bars) and 5 ALD cycles (black bars). The inline graph shows the particle size distribution of the 1 ALD cycle Pt/TiO_2 (1.6 wt.%, white bars) and of a Pt/TiO_2 catalyst prepared via photodeposition (1.5 wt.%, grey bars) (Colón et al., 2010).

Pt, which is illustrated in the inline graph of **Fig. 11**. The ALD catalyst is compared to a Pt/TiO_2 catalyst of similar loading (1.5 wt.%) prepared via the photodeposition technique (Colón et al., 2010). The low average particle size obtained by ALD (1.5 nm versus 3.9 nm) ensures a higher utilization of the expensive active material. The increase in the noble metal specific surface area (186 m^2g^{-1} versus 72 m^2g^{-1}) is expected to contribute positively to the performance of similar catalytic systems. This thus demonstrates that atomic layer deposition using a fluidized bed reactor at atmospheric pressure is an attractive method that combines scalability and high precision for the fabrication of catalysts and other nanostructured materials.

5. Conclusions and outlook

In the past decades, ALD has firmly established its position as a high-precision thin-film manufacturing technique for the microelectronics industry. Realizing the potential of ALD as an integral nanofabrication toolbox for the design, fabrication and modification of advanced materials is opening a new range of possibilities. The application of ALD to particles enables the production of a whole range of novel nanostructured particles for, among others, catalysis, energy conversion and storage, and medical applications.

In this paper, we focused on the fabrication of catalysts by deposition of the active phase (Pt) on a particulate substrate (TiO_2 P25 nanoparticles). We demonstrated that ALD is a technique that 1) guarantees efficient use of the precursor; 2) allows precise control of the size and loading; 3) can be used for low and medium loading of catalysts by adjusting the number of repeated cycles; 4) leads to high-quality (low impurities level) end products.

The future demands for the high-volume production of tailored nanostructured materials require innovation in reactor design for ALD processes. Currently, fluidized bed reactors are the first choice for particle ALD, enabling tonne-scale production in the near future. Operating these reactors at low pressures favours the removal of gaseous compounds in the purging steps; however, operation at atmospheric conditions is beneficial for the scale-up potential.

Compared to liquid-based synthesis routes, ALD improves the fabrication compliance with the principles of Green Chemistry: absence of solvents/residues, minimization and easy handling of the reaction by-products (waste) and overall simplification of the production route (all process steps rely on robust gas-solid-based unit operations). The low value of the *E*-factor (comparable to the fine chemicals industry) clearly shows the way to more sustainable production schemes. The high degree of deposition control (size, composition, distribution) highlights the potential for high-end-value products such as noble metal-supported catalysts. Mild temperature and pressure conditions make the technique compatible with temperature-sensitive materials.

As ALD matures further, certain research challenges will have to be overcome: gaps such as the need for research on novel precursors (e.g. for silver and gold) and the requirement of clear understanding of process parameters (effect of pressure, growth mechanisms, and overexposure role on the deviation from ideal behaviour). Many challenging areas related to materials properties and nanostructuring can be addressed in a scalable production scheme offered by ALD. Bringing fundamental science and engineering principles together, ALD is effectively driving surface chemistry at an atomic resolution, while enabling industrial-scale production.

Acknowledgements

Financial support from the European Research Council (AggloNanoCoat and CONiA projects) is gratefully acknowledged. The authors would like to thank Ms. Andrea Fabre for her careful proofreading of the manuscript.

References

Beetstra R., Lafont U., Nijenhuis J., Kelder E.M., van Ommen J.R., Atmospheric Pressure Process for Coating Particles Using Atomic Layer Deposition, Chemical Vapor Deposition, 15 (2009) 227–233.

Canlas C.P., Lu J., Ray N.A., Grosso-Giordano N.A., Lee S., Elam J.W., Winans R.E., Van Duyne R.P., Stair P.C., Notestein J.M., Shape-selective sieving layers on an oxide catalyst surface, Nature Chemistry, 4 (2012) 1030–1036.

Christensen S.T., Elam J.W., Rabuffetti F.A., Ma Q., Weigand S.J., Lee B., Seifert S., Stair P.C., Poeppelmeier K.R., Hersam M.C., Bedzyk M.J., Controlled Growth of Platinum Nanoparticles on Strontium Titanate Nanocubes by Atomic Layer Deposition, Small, 5 (2009) 750–757.

Christensen S.T., Feng H., Libera J.L., Guo N., Miller J.T., Stair P.C., Elam, J.W., Supported Ru−Pt Bimetallic Nanoparticle Catalysts Prepared by Atomic Layer Deposition, Nano Letters, 10 (2010) 3047–3051.

Coleman J.N., Liquid Exfoliation of Defect-Free Graphene, Accounts of Chemical Research, 46 (2012) 14–22.

Colón G., Maicu M., Hidalgo M.C., Navío J.A., Kubacka A., Fernández-García M., Gas phase photocatalytic oxidation of toluene using highly active Pt doped TiO_2, Journal of Molecular Catalysis A: Chemical, 320 (2010) 14–18.

Cronauer D.C., Jacobs G., Linganiso L., Kropf A.J., Elam J.W., Christensen S.T., Marshall C.L., Davis B.H., CO Hydrogenation: Exploring Iridium as a Promoter for Supported Cobalt Catalysts by TPR-EXAFS/XANES and Reaction Testing, Catalysis Letters, 141 (2011) 968–976.

Eckelman M.J., Zimmerman J.B., Anastas P.T., Toward Green Nano, Journal of Industrial Ecology, 12 (2008) 316–328.

Elam J.W., Groner M.D., George S.M., Viscous flow reactor with quartz crystal microbalance for thin film growth by atomic layer deposition, Review of Scientific Instruments, 73 (2002) 2981–2987.

Elam J.W., Zinovev A.V., Pellin M.J., Comstock D.J., Hersam M.C., Nucleation and Growth of Noble Metals on Oxide Surfaces Using Atomic Layer Deposition, ECS Transactions, 3 (2007) 271–278.

Ellis N., Yurteri C.U., van Ommen J.R., Development of a continuous nanoparticle coating with electrospraying, in Kim S. D., Kan Y., Lee J. K., Seo Y. C. (Eds.), Fluidization XIII-New paradigm in fluidization engineering, New York: Engineering Conferences International (2010).

Enterkin J.A., Setthapun W., Elam J.W., Christensen S.T., Rabuffetti F.A., Marks L.D., Stair P.C., Poeppelmeier K.R., Marshall C.L., Propane Oxidation over $Pt/SrTiO_3$ Nanocuboids, ACS Catalysis, 1 (2011) 629–635.

Feng H., Elam J.W., Libera J.A., Setthapun W., Stair P.C., Palladium Catalysts Synthesized by Atomic Layer Deposition for Methanol Decomposition, Chemistry of Materials, 22 (2010) 3133–3142.

Feng H., Lu J., Stair P.C., Elam J.W., Alumina over-coating on Pd nanoparticle catalysts by atomic layer deposition: Enhanced stability and reactivity, Catalysis Letters, 141 (2011) 512–517.

Ferguson P.P., Todd A.D.W., Dahn J.R., Comparison of mechanically alloyed and sputtered tin–cobalt–carbon as an anode material for lithium-ion batteries, Electrochemistry Communications, 10 (2008) 25–31.

Finnemore A., Cunha P., Shean T., Vignolini S., Guldin S., Oyen M., Steiner U., Biomimetic layer-by-layer assembly of artificial nacre, Nature Communications, 3 (2012) 966:1–6.

Gates B.D., Xu Q., Stewart M., Ryan D., Willson C.G., Whitesides G.M., New Approaches to Nanofabrication: Molding, Printing, and Other Techniques, Chemical Reviews, 105 (2005) 1171–1196.

Goulas A., van Ommen R.J., Atomic layer deposition of platinum clusters on titania nanoparticles at atmospheric pressure, Journal of Materials Chemistry A, 1 (2013) 4647–4650.

Hakim L.F., Blackson J., George S.M., Weimer A.W., Nanocoating Individual Silica Nanoparticles by Atomic Layer Deposition in a Fluidized Bed Reactor, Chemical Vapor Deposition, 11 (2005) 420–425.

Hakim L.F., McCormick J.A., Zhan G.-D., Weimer A.W., Li P., George S.M., Surface Modification of Titania Nanoparticles Using Ultrathin Ceramic Films, Journal of the American Ceramic Society, 89 (2006) 3070–3075.

Haukka S., Suntola T., Advanced Materials Processing by Adsorption Control, Interface Science, 5 (1997) 119–128.

He M., Chernov A.I., Fedotov P.V., Obraztsova E.D., Sainio J., Rikkinen E., Jiang H., Zhu Z., Tian Y., Kauppinen E.I., Niemelä M., Krause A.O.I., Predominant (6,5) Single-Walled Carbon Nanotube Growth on a Copper-Promoted Iron Catalyst, Journal of the American Chemical Society, 132 (2010) 13994–13996.

He M., Liu B., Chernov A.I., Obraztsova E.D., Kauppi I., Jiang H., Anoshkin I., Cavalca F., Hansen T.W., Wagner J.B., Nasibulin A.G., Kauppinen E.I., Linnekoski J., Niemelä M., Lehtonen J., Growth Mechanism of Single-Walled Carbon Nanotubes on Iron–Copper Catalyst and Chirality Studies by Electron Diffraction, Chemistry of Materials, 24 (2012) 1796–1801.

Hirva P., Venäläinen T., Pakkanen T.A., Controlled Deposition from the Gas Phase of Surface Species on Amorphous Supports: Preparation of Ruthenium-Bipyridine Catalysts for 1-Hexene Hydroformylation and Water-Gas Shift Reaction, Journal of Catalysis, 148 (1994) 722–728.

Hsieh C.-T., Liu Y.-Y., Tzou D.-Y., Chen W.-Y., Atomic Layer Deposition of Platinum Nanocatalysts onto Three-Dimensional Carbon Nanotube/Graphene Hybrid, The Journal of Physical Chemistry C, 116 (2012) 26735–26743.

Hsu I.J., Kimmel Y.C., Jiang X., Willis B.G., Chen J.G., Atomic layer deposition synthesis of platinum-tungsten carbide core-shell catalysts for the hydrogen evolution reaction, Chemical Communications, 48 (2012) 1063–1065.

Hsueh Y.-C., Wang C.-C., Kei C.-C., Lin Y.-H., Liu C., Perng T.-P., Fabrication of catalyst by atomic layer deposition for high specific power density proton exchange membrane fuel cells, Journal of Catalysis, 294 (2012) 63–68.

Jancar J., Douglas J.F., Starr F.W., Kumar S.K., Cassagnau P., Lesser A.J., Sternstein S.S., Buehler M.J., Current issues in research on structure–property relationships in polymer nanocomposites, Polymer, 51 (2010) 3321–3343.

Kamat P.V., Quantum Dot Solar Cells. Semiconductor Nanocrystals as Light Harvesters, The Journal of Physical Chemistry C, 112 (2008) 18737–18753.

Kessels W.M.M., Knoops H.C.M., Dielissen S.A.F., Mackus A.J.M., van de Sanden M.C.M., Surface reactions during atomic layer deposition of Pt derived from gas phase infrared spectroscopy, Applied Physics Letters, 95 (2009) 013114:1–3.

Kim H., Lee H.-B.-R., Maeng W.-J., Applications of atomic layer deposition to nanofabrication and emerging nanodevices, Thin Solid Films, 517 (2009) 2563–2580.

King D.M., Spencer II J.A., Liang X., Hakim L.F., Weimer A.W., Atomic layer deposition on particles using a fluidized bed reactor with in situ mass spectrometry, Surface and Coatings Technology, 201 (2007) 9163–9171.

King J.S., Wittstock A., Biener J., Kucheyev S.O., Wang Y.M., Baumann T.F., Giri S.K., Hamza A.V., Baeumer M., Bent S.F., Ultralow Loading Pt Nanocatalysts Prepared by Atomic Layer Deposition on Carbon Aerogels, Nano Letters, 8 (2008) 2405–2409.

Knijnenburg J.T.N., Hilty F.M., Krumeich F., Zimmermann M.B., Pratsinis S.E., Multimineral nutritional supplements in a nano-CaO matrix, Journal of Materials Research, 28 (2013) 1129–1138.

Lakomaa E.-L., Haukka S., Suntola T., Atomic layer growth of TiO_2 on silica, Applied Surface Science, 60–61 (1992) 742–748.

Lashdaf M., Lahtinen J., Lindblad M., Venäläinen T., Krause, A.O.I., Platinum catalysts on alumina and silica prepared by gas- and liquid- phase deposition in cinnamaldehyde hydrogenation, Applied Catalysis A: General, 276 (2004) 129–137.

Laukaitis G., Dudonis J., Milcius D., YSZ thin films deposited by e-beam technique, Thin Solid Films, 515 (2006) 678–682.

Lei Y., Liu B., Lu J., Lobo-Lapidus R.J., Wu T., Feng H., Xia X., Mane A.U., Libera J.A., Greeley J.P., Miller J.T., Elam J.W., Synthesis of Pt–Pd Core–Shell Nanostructures by Atomic Layer Deposition: Application in Propane Oxidative Dehydrogenation to Propylene, Chemistry of Materials, 24 (2012) 3525–3533.

Li J., Liang X., King D.M., Jiang Y.-B., Weimer A.W., Highly dispersed Pt nanoparticle catalyst prepared by atomic layer deposition, Applied Catalysis B: Environmental, 97 (2010) 220–226.

Li Y., Somorjai G.A., Nanoscale Advances in Catalysis and Energy Applications, Nano Letters, 10 (2010) 2289–2295.

Liang X., Zhou Y., Li J., Weimer A., Reaction mechanism studies for platinum nanoparticle growth by atomic layer deposition, Journal of Nanoparticle Research, 13 (2011) 3781–3788.

Liang X., Lyon L., Jiang Y.-B., Weimer A., Scalable synthesis of palladium nanoparticle catalysts by atomic layer deposition,

Journal of Nanoparticle Research, 14 (2012) 1–12.

Lobo R., Marshall C.L., Dietrich P.J., Ribeiro F.H., Akatay C., Stach E.A., Mane A., Lei Y., Elam J., Miller J.T., Understanding the Chemistry of H_2 Production for 1-Propanol Reforming: Pathway and Support Modification Effects, ACS Catalysis, 2 (2012) 2316–2326.

Longrie D., Deduytsche D., Haemers J., Driesen K., Detavernier C., A rotary reactor for thermal and plasma-enhanced atomic layer deposition on powders and small objects, Surface and Coatings Technology 213 (2012) 183–191.

Lu J., Stair P.C., Low-Temperature ABC-Type Atomic Layer Deposition: Synthesis of Highly Uniform Ultrafine Supported Metal Nanoparticles, Angewandte Chemie International Edition, 49 (2010) 2547–2551.

Lu J., Fu B., Kung M.C., Xiao G., Elam J.W., Kung H.H., Stair P.C., Coking- and Sintering-Resistant Palladium Catalysts Achieved Through Atomic Layer Deposition, Science, 335 (2012) 1205–1208.

Mahurin S., Bao L., Yan W., Liang C., Dai S., Atomic layer deposition of TiO_2 on mesoporous silica, Journal of Non-Crystalline Solids, 352 (2006) 3280–3284.

McCormick J.A., Cloutier B.L., Weimer A.W., George S.M., Rotary reactor for atomic layer deposition on large quantities of nanoparticles, Journal of Vacuum Science & Technology A: Vacuum, Surfaces, and Films, 25 (2007) 67–74.

Miikkulainen V., Leskelä M., Ritala M., Puurunen R.L., Crystallinity of inorganic films grown by atomic layer deposition: Overview and general trends, Journal of Applied Physics, 113 (2013) 021301:1–101.

Minnermann M., Grossmann H.K., Pokhrel S., Thiel K., Hagelin-Weaver H., Bäumer M., Mädler L., Double flame spray pyrolysis as a novel technique to synthesize alumina-supported cobalt fischer–tropsch catalysts, Catalysis Today, 214 (2013) 90–99.

Molenbroek A.M., Haukka S., Clausen B.S., Alloying in Cu/Pd Nanoparticle Catalysts, The Journal of Physical Chemistry B, 102 (1998) 10680–10689.

Nevalainen K., Isomäki N., Honkanen M., Suihkonen R., McNally T., Harkin-Jones E., Syrjälä S., Vuorinen J., Järvelä P., Melt-compounded nanocomposites of titanium dioxide atomic-layer-deposition-coated polyamide and polystyrene powders, Polymers for Advanced Technologies, 23 (2012) 357–366.

Plomp A.J., Vuori H., Krause A.O.I., de Jong K.P., Bitter J.H., Particle size effects for carbon nanofiber supported platinum and ruthenium catalysts for the selective hydrogenation of cinnamaldehyde, Applied Catalysis A: General, 351 (2008) 9–15.

Rauwel E., Galeckas A., Rauwel P., Nilsen O., Walmsley J., Rytter E., Fjellvaåg H., ALD Applied to Conformal Coating of Nanoporous γ-Alumina: Spinel Formation and Luminescence Induced by Europium Doping, ECS Transactions, 41 (2011) 123–130.

Schmid G., Clusters and colloids: bridges between molecular and condensed material, Endeavour, 14 (1990) 172–178.

Sereda G., Marshall C., Libera J.A., Dreessen J., Grady A., Turner M., Effect of Atomic Layer Deposition Support Thickness on Structural Properties and Oxidative Dehydrogenation of Propane on Alumina- and Titania-Supported Vanadia, Catalysis Letters, 142 (2012) 399–407.

Setthapun W., Williams W.D., Kim S.M., Feng H., Elam J.W., Rabuffetti F.A., Poeppelmeier K.R., Stair P.C., Stach E.A., Ribeiro F.H., Miller J.T., Marshall C.L., Genesis and Evolution of Surface Species during Pt Atomic Layer Deposition on Oxide Supports Characterized by in Situ XAFS Analysis and Water−Gas Shift Reaction, The Journal of Physical Chemistry C, 114 (2010) 9758–9771.

Sheldon R.A., Organic synthesis. Past, present and future, Chemistry and Industry (London), 23 (1992) 903–906.

Sheldon R.A., The E Factor: fifteen years on, Green Chemistry, 9 (2007) 1273–1283.

Somorjai G.A., Park J.Y., Colloid Science of Metal Nanoparticle Catalysts in 2D and 3D Structures. Challenges of Nucleation, Growth, Composition, Particle Shape, Size Control and Their Influence on Activity and Selectivity, Topics in Catalysis, 49 (2008) 126–135.

Stepuk A., Krämer K.W., Stark W.J., Flame synthesis of complex fluoride-based nanoparticles as upconversion phosphors, KONA Powder and Particle Journal, 30 (2012) 267–275.

Sun S., Zhang G., Gauquelin N., Chen N., Zhou J., Yang S., Chen W., Meng X., Geng D., Banis M.N., Li R., Ye S., Knights S., Botton G.A., Sham T.-K., Sun X., Single-atom Catalysis Using Pt/Graphene Achieved through Atomic Layer Deposition, Scientific Reports, 3 (2013) 1775:1–9.

van Ommen J.R., (2010): WO Patent Application, 2010/100235 A1.

van Ommen J.R., Valverde J., Pfeffer R., Fluidization of nanopowders: a review, Journal of Nanoparticle Research, 14 (2012) 1–29.

Vuori H., Lindblad M., Outi A., Krause I., Preparation of noble metal catalysts by atomic layer deposition: FTIR studies, in Gaigneuax E.M., Devillers M., De Vos D.E., Hermans S., Jacobs P.A., Ruiz P., (Eds.), Studies in Surface Science and Catalysis, Louvain-la-Neuve: Elsevier , 2006.

Wank J.R., George S.M., Weimer A.W., Coating Fine Nickel Particles with Al_2O_3 Utilizing an Atomic Layer Deposition-Fluidized Bed Reactor (ALD–FBR), Journal of the American Ceramic Society, 87 (2004) 762–765.

Wegener S.L., Marks T.J., Stair P.C., Design Strategies for the Molecular Level Synthesis of Supported Catalysts, Accounts of Chemical Research, 45 (2011) 206–214.

Williams P.A., Ireland C.P., King P.J., Chater P.A., Boldrin P., Palgrave R.G., Claridge J.B., Darwent J.R., Chalker P.R., Rosseinsky M.J., Atomic layer deposition of anatase TiO_2 coating on silica particles: growth, characterization and evaluation as photocatalysts for methyl orange degradation and hydrogen production, Journal of Materials Chemistry, 22 (2012) 20203–20209.

Xie H., Lu J., Shekhar M., Elam J.W., Delgass W.N., Ribeiro F.H., Weitz E., Poeppelmeier K.R., Synthesis of Na-Stabilized Nonporous t-ZrO_2 Supports and Pt/t-ZrO_2 Catalysts and Application to Water-Gas-Shift Reaction, ACS Catalysis, 3 (2012) 61–73.

Yoon J.-H., Jung S.-C., Kim J.-S., Photocatalytic effects for the TiO_2-coated phosphor materials, Materials Chemistry and Physics, 125 (2011) 342–346.

Yurteri C.U., Hartman R.P.A., Marijnissen J.C.M., Producing Pharmaceutical particles via Electrospraying with an emphasis on nano and nano structured particles—A review, KONA Powder and Particle Journal, 28 (2010) 91–115.

Zhou Y., King D.M., Liang X., Li J., Weimer A.W., Optimal preparation of Pt/TiO_2 photocatalysts using atomic layer deposition, Applied Catalysis B: Environmental, 101 (2010) 54–60.

Author's short biography

Aristeidis Goulas

Aristeidis Goulas received his Dipl. Eng. in chemical engineering from Aristotle University of Thessaloniki in 2008 and his MSc degree in sustainable energy technology from Delft University of Technology in 2011. He then joined the Product and Process Engineering group (Delft University of Technology) as a researcher. His work focuses on gas-phase nanostructuring techniques for the fabrication of novel nanostructured materials.

J. Ruud van Ommen

J. Ruud van Ommen received his MSc degree in chemical engineering in 1997, followed by a Ph.D. in 2001, both from Delft University of Technology (the Netherlands). He has been a faculty member at Delft since, with stints at Chalmers University of Technology (Sweden, 2004/2005) and the University of Colorado Boulder (USA, 2009). In 2011, he received an ERC starting grant to investigate the interplay between the agglomeration and coating of nanoparticles in the gas phase. Currently, he is an associate professor at Delft University, leading a research team with the focus on scalable processes to make nanostructured materials.

KONA Powder and Particle Journal No. 31 (2014) 247–264/Doi:10.14356/kona.2014016 Original Research Paper

Recycling-Oriented Investigation of Local Porosity Changes in Microwave Heated-Concrete†

Nicholas R. Lippiatt and Florent S. Bourgeois*

[1] *Laboratoire de Génie Chimique UMR CNRS 5503, Université de Toulouse, France*

Abstract

Large quantities of concrete waste are being produced continuously throughout the world, of which only a fraction are downcycled as construction backfill or as road-base. Seeking total concrete recyclability, this work concerns the development of microwave-based solutions for the separation of individual constituents of concrete. By focusing on the interaction between microwaves and concrete at the microscopic level, the paper makes important connections between local changes in the microwave-heated concrete texture and macroscopic changes in mechanical properties. Through analysis of the concrete texture using SEM imaging, it is found that the microwave heating of concrete causes fracture porosity. The size and shape of fracture porosity can be correlated with recycling performance indicators; namely aggregate liberation, concrete strength and product fineness. In particular, the work finds that only a short exposure to microwaves promotes the formation of a primary fracture network responsible for selective liberation of aggregates. Longer exposure to microwave heating creates a secondary network of smaller fractures that spreads throughout the cement phase, which is directly associated with the changes in mechanical strength of concrete and product fineness.

The work introduces the concept of textural versus physical liberation, and shows that while microwave heating creates a high selective textural liberation of aggregate particles, the comminution of microwave-heated concrete may not necessarily yield high physical liberation. The work concludes that the key to designing a microwave-based process for concrete recycling resides in finding comminution and separation technologies that can best harvest the benefits of the textural and mechanical changes produced by microwave heating.

Keywords: concrete, recycling, microwave heating, fracture porosity

1. Introduction

Concrete is the most-used manufactured product on the planet, as a consequence it also constitutes a large fraction of urban waste. Many countries already make use of concrete waste as backfill and road base. Countries such as the Netherlands and Denmark manage to recycle over 80% of the construction and demolition (C&D) waste they generate (Fischer and Davidsen, 2011; Symonds, 1999). Nonetheless, a large fraction of concrete waste is not used and the concrete that is recycled is invariably downcycled, as can be seen by the ratio of virgin aggregate to recycled aggregate used in concrete production (Klee, 2009). Using crushed concrete as a replacement for coarse aggregate reduces the mechanical performance of the final product in proportion with the fraction of crushed concrete used. This effect is significantly greater when crushed concrete is used as a replacement for fine aggregates, which is why concrete waste is almost never used in this way. The reason crushed concrete reduces the performance of concrete compared to virgin aggregate appears to be due to adhered cement paste and how it reacts to new cement as it cures (Tam et al., 2007). The first step to complete concrete recyclability therefore is finding an effective technique to decrease the volume of adhered cement on recycled aggregates.

Microwave heating is especially applicable to processing multiphase materials as it uses the differences in thermal and dielectric properties between distinct phases to generate fractures and weaken the material. A simple version of this scenario is a strongly dielectric material embedded in a continuous microwave transparent material. In fact, this basic scenario closely resembles what is found for mineral ores, for which microwave heating as a companion treatment step before crushing and milling has been considered for some time and has been shown to weaken the ore and increase mineral liberation, hence mineral yield (Kingman et al., 2004a). The ever-present question is whether the benefit of the increased yield

† Accepted: August 20, 2013
[1] CNRS-Laboratoire de Génie Chimique UMR 5503, 4 Allée Emile Monso BP 84234, 31432 Toulouse Cedex 4, France
* Corresponding author:
E-mail: florent.bourgeois@inp-toulouse.fr
TEL: +33-534-323-633 FAX: +33-534-323-700

exceeds the energy required for the process. As the price of minerals and metalliferous ores and the efficiency of microwave processing technology increase, one might predict that this will soon be the case.

In the case of concrete waste, one could argue that the development of a microwave-based recycling process has perhaps even more potential than with mineral beneficiation. Some arguments to this effect include:

- Recycling concrete has the potential of eliminating a waste stream altogether by recycling all its constituents. Being a high-value man-made material with significant energy and material footprint, the recycling of concrete is a priority.
- Recycled cement can re-enter the clinker-making process (Costes et al., 2010) and thereby contribute to reducing the CO_2 emissions of clinker production by direct substitution with natural carbonates. Reusing cement will also contribute to preserving natural carbonate reserves. Also, the presence of already decarbonated and crystallised phases in recycled cement may also have a positive effect on the energy balance for making clinker, through a possibly reduced heat requirement due to the reduced initial mass and lower required temperatures.
- Recycled aggregate can re-enter the concrete-making process and contribute to preserving natural aggregate resources, which is becoming a scarce resource in developed countries, particularly when dealing with aggregates of alluvionary origin.
- The proximity of concrete waste to consumption areas may contribute to reducing transport associated with the concrete-making industry.

The sensitivity of concrete to microwaves has been known for some time. Using a 5-kW multimode microwave oven and exposure times up to 30 minutes, the possibility of liberating aggregates from hardened cement for concrete analysis purposes was tested over 30 years ago by Figg (Figg, 1974). His pioneering work with 100-mm cubes brought convincing evidence that microwaves could indeed induce boundary fracture at the aggregate-cement interface. At high power inputs, concrete has also been shown to respond explosively, with commercial applications in drilling (Jerby at al., 2002) and controlled spalling (White et al., 1995).

The application of microwave-heating to the issue of concrete recycling is a relatively new endeavour, but one that has already been shown to be effective. Akbarnezhad and co-workers (Akbarnezhad et al., 2011), using a 10-kW generator, showed microwave heating prior to physical comminution to improve recycled aggregate properties, and that this effect is superior to comparable techniques using purely mechanical means or a combination of mechanical means and conventional (external) heating. About the same time, the authors (Lippiatt and Bourgeois, 2012) showed that microwave heating of concrete increases the liberation of aggregate and cement, while decreasing the strength of concrete.

Eventually, impact breakage of these microwave-heated particles of concrete was carried out using a short Hopkinson bar (Bourgeois and Banini, 2002). Liberation was measured using a dissolution technique based on the work of Kiss and Schönert (Kiss and Shönert, 1980).

The results of this previous work validated the hypothesis that the microwave heating of concrete, followed by impact breakage, improves aggregate liberation, thereby opening avenues for recycling concrete. Moreover, the degree of liberation was found to increase non-linearly with exposure time, hence input microwave energy. The short and medium exposures did lead to a similar level of aggregate liberation, which exhibited a significant increase after the long exposure.

Cement liberation was not measured directly but by the mass lost during dissolution. Cement distributions were nearly the same for samples that had undergone short and medium microwave exposures, and cement fines increased dramatically with the longest treatment. It is noted that the sharp increase of cement liberation with the long exposure to microwaves, followed by impact breakage, mirrors the increase in liberation of aggregates by the same process.

Analysis of Hopkinson bar impact tests revealed both a reduction in impact fracture force with increasing exposure, and a progressive loss of elasticity of the concrete with the mechanical behaviour of the most damaged samples resembling that of a loose-packed bed.

These quantitative observations are conclusive indicators of the value of microwave heating for recycling concrete. In summary, when followed by impact breakage, the microwave heating of concrete increases aggregate liberation, increases cement fines and reduces concrete strength.

However, the macroscopic nature of these observations, which result from the combined effect of microwave heating and impact breakage, does not permit understanding what is actually happening inside concrete during microwave heating. The authors argue that some understanding about the microstructural changes that occur at the local scale inside concrete during microwave heating is essential for defining the scope and place of microwave heating in a concrete recycling process. The ultimate goal that this paper aims to move towards is to precisely unravel the elements of reconciliation between variations at the microscopic and macroscopic scales, so as to provide guidelines for the development of an efficient concrete recycling process.

2. Materials and methods

Our ability to relate observations between both scales requires that we quantify the textural changes that take

place inside concrete during microwave heating, especially near the aggregate-cement interface and inside the cement matrix itself. In the process of developing a satisfactory texture analysis protocol, several experiments were performed. This preliminary work led to some appreciation of what had to be quantified for the sake of understanding the link between changes in the microstructure and macroscopic behaviour of concrete. It was concluded that microstructure quantification would have to focus on the properties of cracks, whose patterns were found to change most significantly during microwave heating. Mineralogical changes, as measured by X-ray diffractometry, did not reveal significant changes in comparison. Having decided that the formation of cracks should be the focal point, efforts were allocated during this work to establishing an experimental protocol that would not alter the fractures caused by microwave heating. A non-destructive observation protocol using the scanning electron microscope for texture image acquisition was designed for this very purpose, avoiding altogether any requirement for crack impregnation, cutting or polishing after microwave treatment of the concrete samples.

2.1 Concrete sample preparation

The concrete used in this work was made with cement-enriched mixture (CEM) 1 52.5 Portland cement. Samples were mixed in five different ratios (See **Table 1**) with siliceous aggregate 2–2.5 mm in size. The sample preparation protocol is schematised in **Fig. 1**. Samples were cast in 20-mm cylinders, which after curing, would weigh about 10 g each. After setting in the mould for 24 hours they were removed and allowed to cure in water at room temperature for a minimum of 90 days.

The samples were then removed from soak and separated into lots of 12 units. One sample was reserved for mercury porosimetry analysis, ten for Hopkinson bar impact testing, and one was cut using a water-lubricated diamond saw to give an exposed cross-section. The purpose of this operation was to create a flat surface that could be readily observed after microwave treatment, without requiring any post-treatment cutting or polishing that could potentially alter the fractures induced by the heating process. An alternative would have been to impregnate uncut samples after microwave treatment with a polymer resin or Wood's metal, and then cut and polish to expose an observable flat surface. However, this approach was rejected outright for it had the potential to damage the fractured microstructure. One downside of the protocol that was adopted here over the alternative was that it made the observation of fractures possibly more difficult due to the lack of contrast of the fractures against

Table 1 Properties of concrete samples

Concrete samples	Water/Cement mass ratio	Aggregate/ Cement mass ratio
S1	0.4	0.6
S2	0.4	0.85
S3	0.4	1.6
S4	0.5	1.6
S5	0.6	1.6

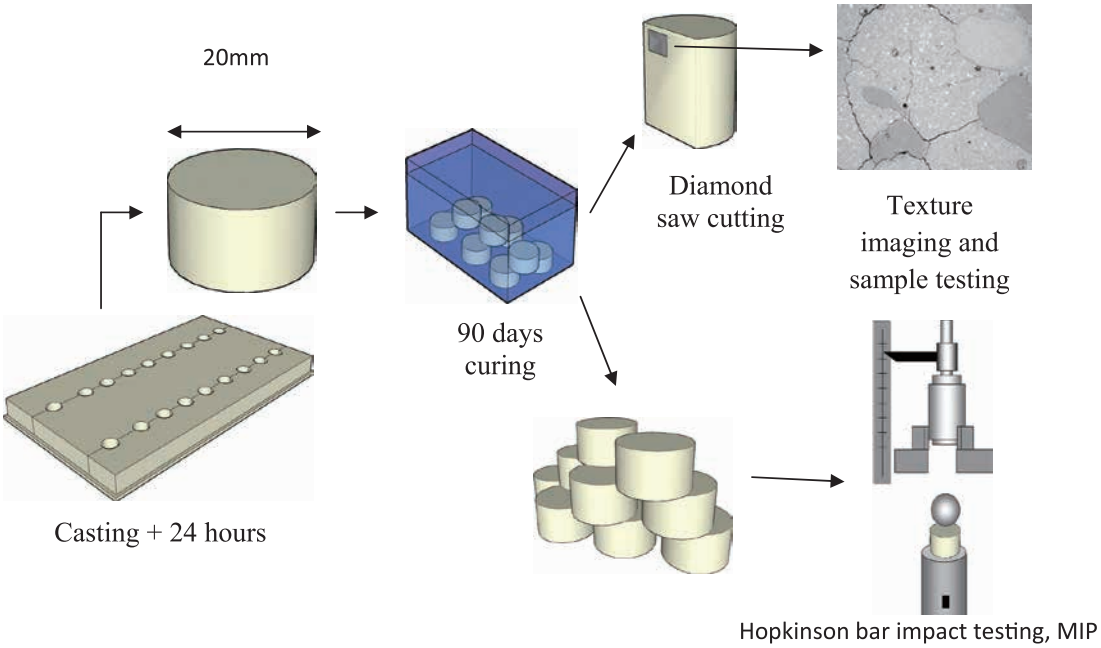

Fig. 1 Illustration of the concrete sample preparation protocol.

the solid phases. This was found to be a problem particularly with untreated samples. The measurement is based on a subjective judgement of contrast and shape. Untreated images showed even less contrast than treated samples.

Some might consider ten samples an insufficient number of samples for mechanical tests of this type. At this stage, the goal is merely to seek patterns so that more extensive testing and results distribution analysis is unnecessary. All results are presented with the mean and full range of measured values.

Prior to testing, samples were systematically dried at 50°C for 24 hours before any microwave treatment or analysis began so that all samples would be equally dry before testing. This was validated by measuring the sample mass changes with drying. After 24 hours at 50°C, the samples stopped losing mass at room temperature.

2.2 Microwave testing and sample post-treatment

Higher power densities are more effective in embrittling multiphase materials (Ali, 2010) and the highest power densities are produced in single-mode cavities (Kingman et al., 2004b). The samples were heat-treated in a 2-kW/2.45-GHz single-mode horizontal waveguide applicator designed by SAIREM. The samples were heated in the microwave system individually; the sample moulds were designed so as to make use of the 30-mm microwave transparent, cylindrical, silica sample holders. The position for the iris and the short circuit for minimum reflected energy were found manually. The iris position was kept constant for all tests. If the initial reflected energy was higher than expected, the short circuit was moved to accommodate. This change in position was never more than a few millimetres.

The samples were treated for 3 characteristic times and the power absorption signal was recorded. These times are seen in **Fig. 2**, and correspond to 15, 30 and 50 seconds called 'short', 'medium' and 'long' treatment, respectively. Short, medium and long microwave exposures are annotated as 'S', 'M' and 'L' so that S1-0, S1-S, S1-M and S1-L represent untreated, short, medium and long treatment times of concrete sample S1, respectively.

They were chosen as they were found to represent three distinctly different stages in the microwave heating cycle for the cast concrete samples under the conditions of the test. The 'short' time comes just after the initial absorption peak, during which 50 to 70% of the sample mass loss occurs, as water evaporates readily. The 'long' time occurs before the absorption starts to peak again, and the 'medium' time corresponds to an intermediate time between these two events. The formation of this microwave absorption peak usually occurred after approximately 50 seconds but was not totally predictable. It is assumed to occur after the formation of local thermal runway and consequently the formation of a plasma. Although the reflected power was measured in real time, the microwave cavity is an open system that can lose mass and energy by convection and evaporation, so the measured energy and power absorbed by each sample is only a guide, and cannot be used as absolute energy absorption by the samples.

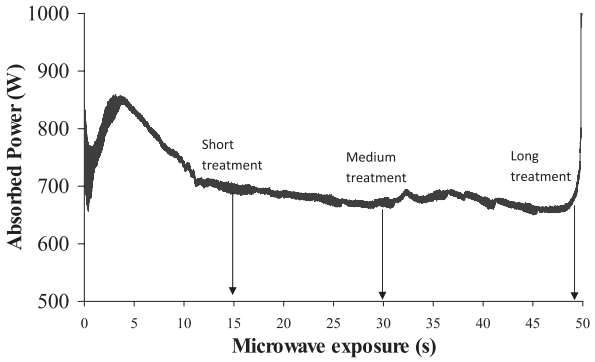

Fig. 2 Typical microwave power absorption record for a 20-mm cylindrical concrete sample (S1).

After cutting the power at the end of the test, an estimate of the average temperature reached by a sample was obtained using a Jules Richards Instruments Flashpoint FX400 infrared thermometer pointed at the sample surface. The temperature was measured on each of the sample's three surfaces. The mean of the highest recorded temperatures of each sample was recorded as the temperature achieved after treatment. Due to conduction with the experimental surface between measurements, the highest temperature measured was usually the first temperature measured. The maximum temperature was chosen as the representative temperature because of the temperatures measured, it exhibited the least variation. The four surfaces of cut samples were also measured but these values were not used in the temperature calculation due to the difference in sample mass. The samples were weighed individually prior to and after microwave treatment, in order to record the mass loss associated with the heating process. Initially, they all weighed about 10 g.

Eventually, a number of tests were systematically performed on the samples. These measurements included:

– Total porosity and pore size distribution by mercury intrusion porosimetry. This was performed using standard 400 MPa intrusion with a Micromeritics Autopore IV.
– Impact breakage testing using a vertical Hopkinson bar. The cylindrical steel bar used was 40 mm in diameter and 1.5 m long. The impactor was a 60-mm diameter, 825-g steel ball bearing dropped from a height of 163 mm and 200 mm. In previous work, a drop height of 163 mm was found to be the minimum required to break an untreated 20-mm concrete cylinder so it was used again for consistency. The 200-mm drop was used

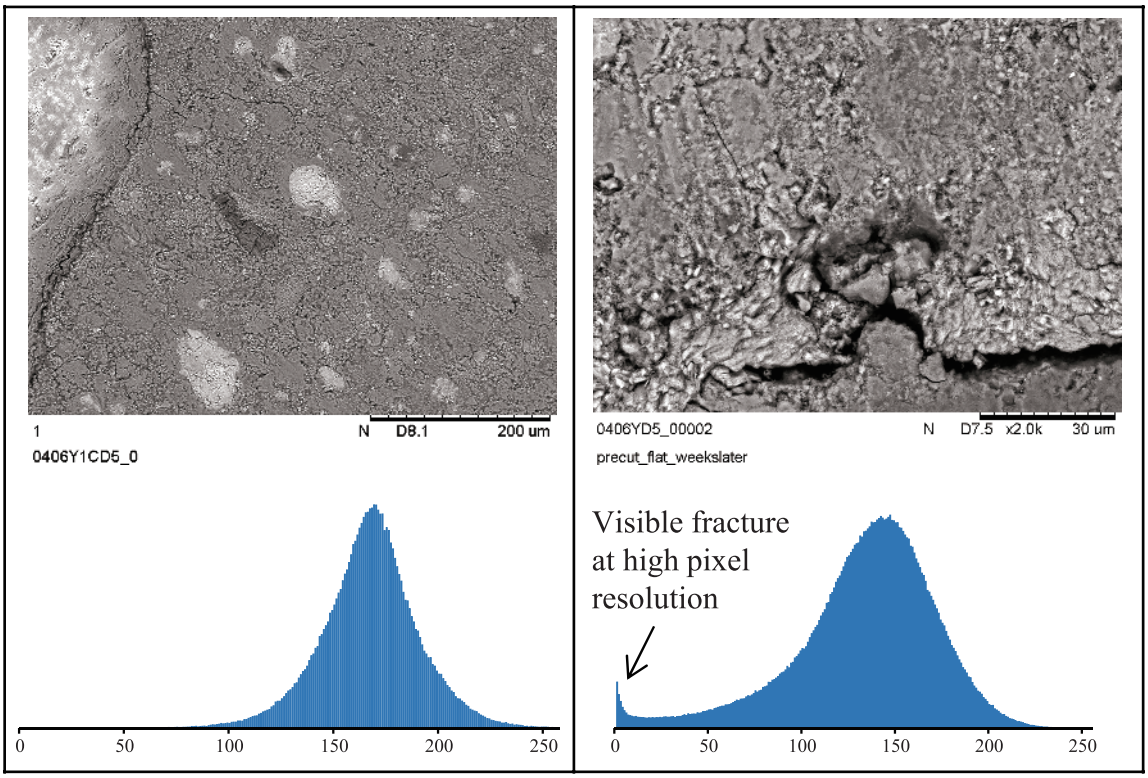

Fig. 3 Standard intensity histogram for SEM images of S1-0 sample. Left: 400× magnification = 0.9 μm/pixel, right 2000× magnification = 0.2 μm/pixel.

to decrease the number of unbroken samples. This does not affect the measure of force required to fracture a sample unless a sample is sufficiently damaged that it no longer displays brittle elastic fracture properties.

– Capture of flat surface images using a Hitachi TM3000 Tabletop Microscope SEM, at different resolutions. The following section is dedicated to this specific part of the sample analysis protocol, which deals with measuring the local effect of microwave heating on the concrete texture.

2.3 Acquisition and analysis of concrete texture images

As indicated previously, the flat surface of the concrete samples, whether treated or untreated, was observed as is by SEM, i.e. without any post-treatment tampering. The SEM images were obtained in this work using a Hitachi TM3000 set to an acceleration voltage of 15 kV. Image analysis of electron microscope images have already been used with success in concrete and cement analysis (Ben Haha et al., 2007; Igarashi et al., 2004; Wong et al., 2006). For the sake of analysing the fractures transecting the flat surface of the concrete samples, the use of SEM images proved to be rather challenging. Indeed the grey-scale intensity of SEM images shows significant overlap between the fractures and the solid phases. **Fig. 3** shows that almost every phase present is included in the same grey level peak.

Given the significant overlap in grey-scale intensity, the binarisation of images is difficult to automate. By careful preparation and observation of samples under sufficiently high magnification, as per the image on the right of **Fig. 3**, the intensity histogram can be separated sufficiently into different peaks so that automated image analysis can be performed on SEM images of concrete and other cement-based materials (Brough and Atkinson, 2000; Yang and Buenfeld, 2001). Examining larger objects such as aggregate particles and the fracture growth that occurs around them requires a lower magnification, meaning greater sample surface area in an image, for reasons of representativity. This lower zoom level has the side effect of condensing the grey-level histogram, making automated image analysis more difficult. Even when highlighted manually, there is the fear that fractures are mislabelled due to low contrast. By repeating the liberation measurement on 40× (9 μm per pixel) images, the uncertainty in the liberation measure was estimated to be no greater than 5% total interface length.

The fractures observed in this work are spaced at distances such that if images were taken at high magnification, say 2000×, then it was very easy to take an image that showed no fracture, even when the sample was highly fractured. When using a low magnification, say 50×, although the high area covered by an image meant the

image was more representative of the sample, it also meant that smaller cracks that were visible at higher magnifications would not be included in the analysis. The minimum zoom possible on the SEM equipment used is 40×, which corresponds to a pixel resolution of 9 μm per pixel. For this work, two zoom levels were chosen, 40× and 200×. Images taken at 40× zoom were chosen to measure the liberation of aggregates as, after cursory examination, a large apparent variation was observed between aggregate particles and this zoom level allowed the largest possible fraction of a sample to be investigated. Another set of images was taken at a zoom level of 200× so that crack networks not visible at a larger scale could be investigated. The number of images was chosen in such a way as to yield a satisfactory compromise between representativity (giving a stable average of textural properties) and keeping the number of images to a minimum, given the strain of the manual digitisation work involved. A scaled comparison of the size of images taken at different SEM magnification levels is shown in **Fig. 4**.

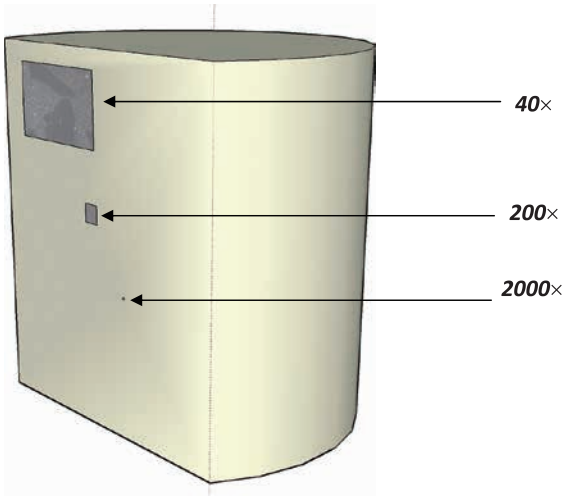

Fig. 4 Comparison of area covered at different zoom levels on sample cut surface.

To overcome the lack of contrast, sample images were highlighted manually. This technique, despite its tediousness, presents a satisfactory way to deal with the aggregate/cement contrast overlap simultaneously with the porosity/fracture contrast overlap. Although the technique has been rightfully identified as imperfect, it has also been used to justify the accuracy of automated image analysis methods (Brough and Atkinson, 2000). In this case, if one of the techniques is accurate, then both must be. **Fig. 5** shows an SEM image before and after highlighting. Aggregates and fractures are easily recognisable. The meaning of the colour-coding of the highlighted image fractures is explained later.

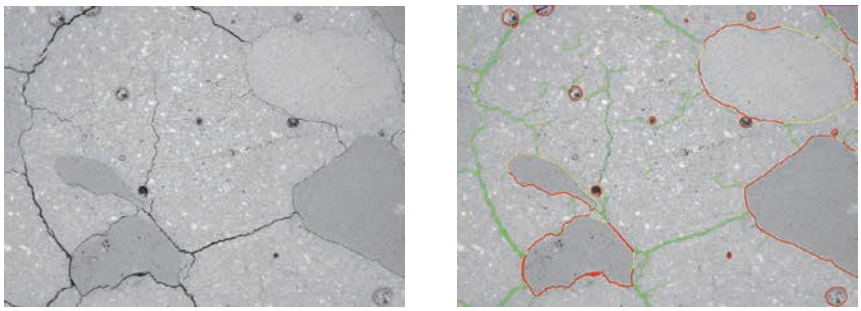

Fig. 5 Example of original and highlighted images taken at 40× zoom for an S1-M sample.

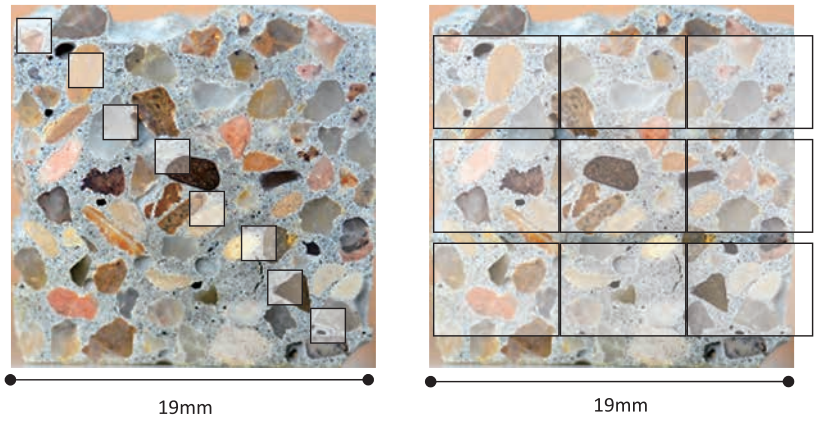

Fig. 6 Illustration of the concrete SEM imaging scheme. Left: images sampled at 200× magnification, Right: images sampled at 40× magnification.

Quantification of fractures being the focal point of the analysis of concrete microstructure after microwave heating, a number of properties were used to quantify fracture porosity.

Straightforward variables that can be measured are the length of, number of and width of cracks present in a given sample area. For the purpose of quantitative image analysis, it was decided to capture 10 SEM images for every sample, 480 pixels by 640 pixels in size, at 9 μm per pixel (40× magnification) and at 1.8 μm per pixel (200× magnification). **Fig. 6** shows the scale and positions of the 10 non-overlapping images for both resolution settings, relative to the 20 mm concrete sample.

Fractures were highlighted manually using a Wacom DTU-2231 interactive pen display. One advantage of this manual image analysis scheme is that it permitted careful hand delineation of different components present in the images, thereby differentiating different classes of fractures. The key highlighted components were:

- Aggregate/cement interface with fracture
- Aggregate/cement interface without fracture
- Fractures within the cement bulk
- Fractures within aggregate particles

As illustrated in **Fig. 7**, every component of interest to the work was highlighted using a distinct colour, which could eventually be used for counting purposes. Six colours, easily distinguished in RGB format, were used (pure green, pure blue, pure red, pure green/red-yellow, pure blue/red-magenta, pure green/blue-cyan), seven including the areas not highlighted (the entire grey-scale from black to white).

Having highlighted different components of interest with distinct colours, a number of insightful quantitative properties, which will be eventually tied to macroscopic variations in concrete properties and operating conditions, could be easily post-treated. They included the properties of fracture per se, as well as the properties that were deemed directly relevant to processing performance.

Starting with the former, the total crack length was measured from skeletonised highlighted images, whereas the total area of cracks, both in the cement bulk and between aggregate and cement paste, and average crack width were measured directly from the highlighted images.

In some images, it is sometimes difficult to tell the difference between a large pore that has formed from an air pocket and one that is the result of an aggregate that is no longer present. Both have a similar shape and appeared to have a similar effect on fracture growth. For initial analysis, all such objects were marked as liberated aggregate. This decision was made to reduce the subjectivity in the analysis process. A side effect of this decision is that all textural liberation values are overestimated. Re-analysis of the S1-0 samples places this variation no greater than 10% of the total aggregate interface length. As all samples were made in the same manner, it can be assumed that the quantity of such large pores is common between samples. Such a systematic error can be ignored in that its biasing the actual values does not change the comparative analyses and conclusions drawn.

Looking now at properties that relate directly to processing performance, the textural liberation of aggregates

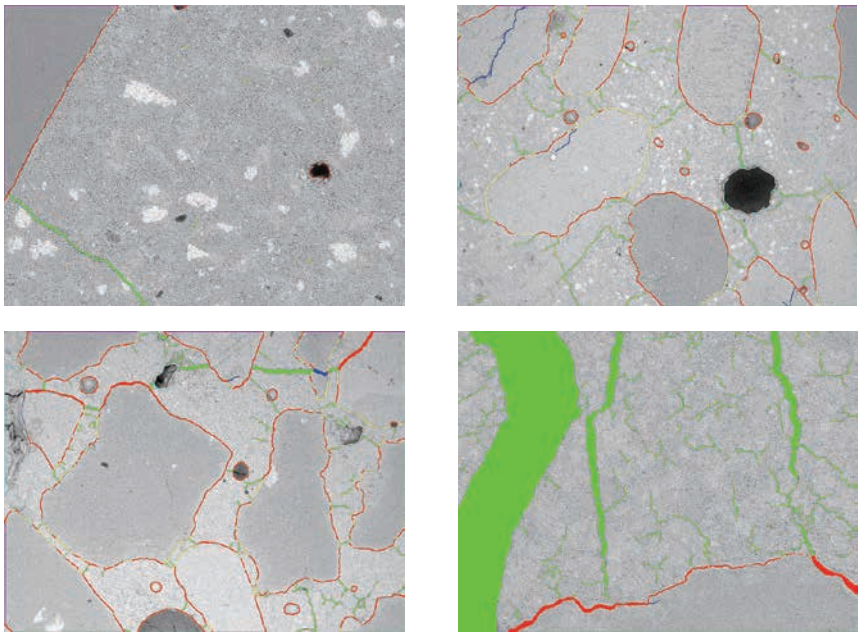

Fig. 7 Examples of highlighted SEM images. Clockwise from top left: S1-0 at 200× zoom, S1-S at 40× zoom, S3-L at 200× zoom, S4-M at 40× zoom.

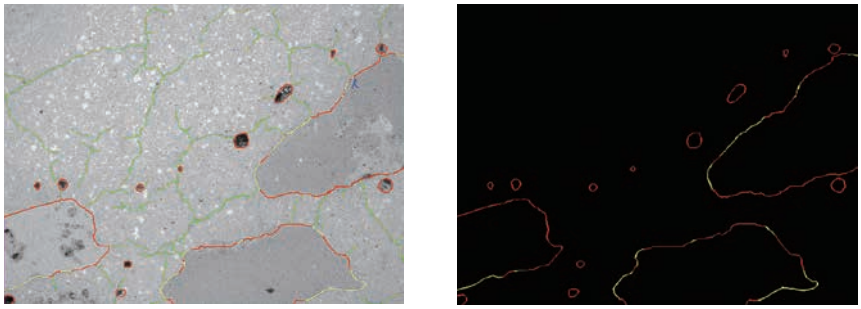

Fig. 8 Example of aggregate textural liberation measurement, S1-M at 40× zoom.

was defined as the ratio between the fractured and total aggregate boundary lengths. **Fig. 8** shows an image with a textural liberation value of 76%.

Aggregate liberation was measured using the 40× zoom (9 μm per pixel) images for the sake of representativeness. The cracks in the cement paste, however, were significantly finer, and were observed using 200× zoom (1.8 μm per pixel) images. During analyses it was found that there appeared to be two different types of fractures forming within the microwave-treated concrete samples. The first group formed the 'primary network', and included all the fractures at the interface of an aggregate particle and the cement paste and all fractures that branched from this interface. This network was visually identified as being made of a few large fractures which ran from aggregate to aggregate throughout the sample. The second group formed the 'secondary network', and included a large number of smaller fractures that spread throughout the cement phase. **Fig. 10** illustrates the 2 families of fractures, which were assigned different colours for quantification purposes. Aggregate fractures occurred also, especially in long-treated samples. However, aggregate fractures occurred to a far lesser extent than cement and grain boundary fractures so were not accounted for in the analysis, which allowed one of the nine colours to be re-assigned so as to permit differentiation between primary- and secondary-network cement paste fractures. In **Fig. 9** and **Fig. 10**, primary network fractures are displayed in yellow.

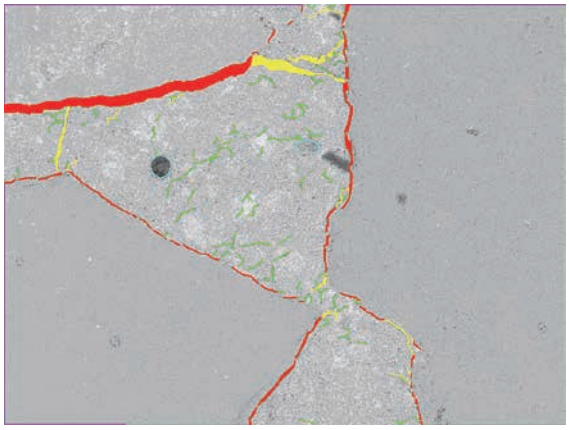

Fig. 9 Example of primary and secondary fracture network highlighting.

Once the images were skeletonised and fractures sorted into primary and secondary networks, the nodes and ends of fracture branches were then counted automatically. A branch is defined as a length of fracture between nodes and/or fracture ends.

Because the post-treatment of highlighted images is

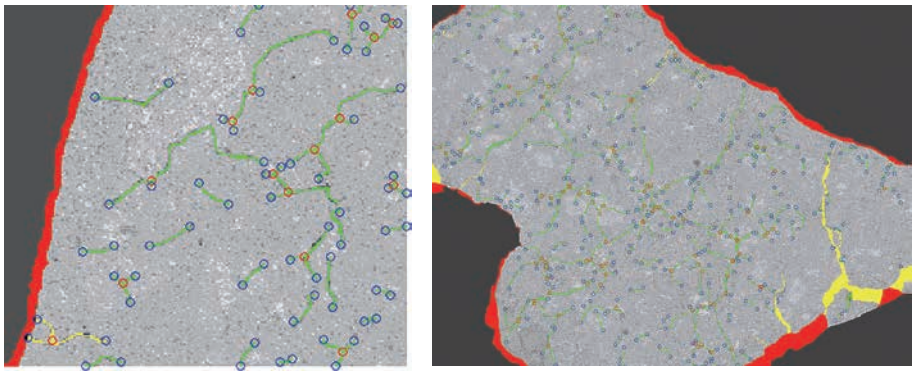

Fig. 10 Example of identification of branches and nodes in the secondary network of fractures. Yellow: primary-network-cement paste fracture, green: secondary-network fracture, red: aggregate/cement interface fracture-primary network, red circle: node, blue circle: branch end.

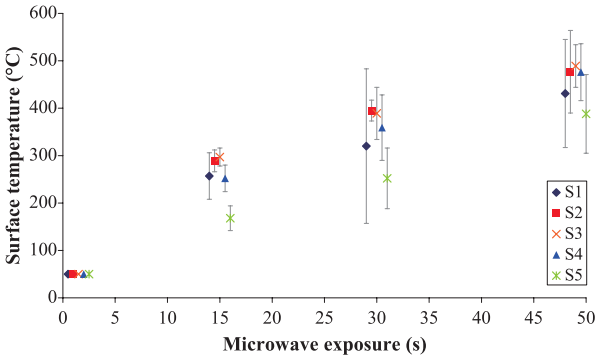

Fig. 11 Measurement of surface temperature as a function of test duration (exposure time offset for clarity).

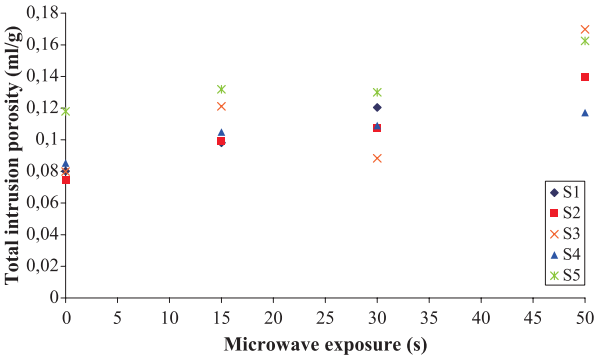

Fig. 13 MIP measurement of total sample porosity for S1 to S5 concrete samples.

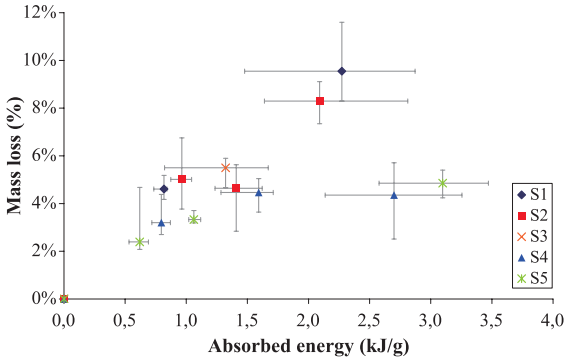

Fig. 12 Correlation between mass loss and energy absorption.

automated, some fractures will necessarily be misclassified, as for example some primary fractures will be connected to aggregates that are not contained in the image, or a primary fracture will branch into two almost identical branches. However, such occurrences are rather rare and do not change the value of the results obtained considering the large number of fractures.

3. Effect of microwave heating on concrete: macroscopic level results and analysis

This section presents the results of measurements made on concrete samples at a macro scale. It shows the temperature, mass loss, fracture strength and the MIP (mercury intrusion porosimetry) porosity changes associated with microwave treatment in different concrete samples. This macroscopic level analysis is used to justify the necessity for local, textural analysis of the effect of microwave heating on concrete.

Microwave treatment increases the temperature of concrete samples, albeit in a different way to that of conventional heating as external heating conducts from the sample surface, whereas microwave heating occurs within the sample. Nevertheless, the longer the application of microwave power, as shown in **Fig. 11**, the greater the temperature measured at the surface of the concrete samples. Despite the S5 sample exhibiting a slightly different trend, it is fair to say that the elevation of temperature, as measured at the samples' surface, is comparable for all concrete sample types tested with short, medium and long treatments.

With the samples tested, it can be concluded that the average temperature reached by the samples does not depend significantly on the variations in concrete properties, at least within the variable range represented in samples S1 to S5 (See **Table 1**). As can be seen in **Fig. 11**, the amount of energy absorbed by each sample is nearly proportional to time once the initial water absorption peak is over. The power input was set to the same 2 kW nominal value for each test. This implies that the differences in thermal properties, dielectric properties and mass compensate for each other and/or they are insignificant in the range tested. As will be seen later, differences in textural properties within the samples are also marginal, suggesting that microwave heating of concrete exhibits a low sensitivity to concrete properties. This is a valuable result from a recycling standpoint as it suggests a concrete recycling process will be insensitive to input properties and no special expense or effort is necessary to accommodate varying concrete waste streams.

The energy absorption by the concrete samples is strongly correlated with the mass loss, as shown in **Fig. 12**, which is itself caused by water loss during heating. It is possible that mass other than water can be lost, however, this effect is deemed insignificant and so all mass changes can be safely assumed to be due to the loss of water. It is also noted that X-ray diffraction spectra did not show any noticeable mineralogical changes between treated and untreated samples, confirming that decomposition of crystallised phases such as portlandite and calcite are marginal at best at such temperatures (Piasta et al., 1984).

By means of MIP, the changes in porosity were characterized with all 5 samples under their untreated and

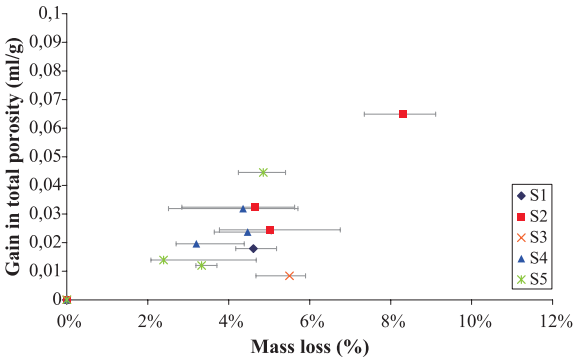

Fig. 14 MIP measurement of total sample porosity as a function of mass loss.

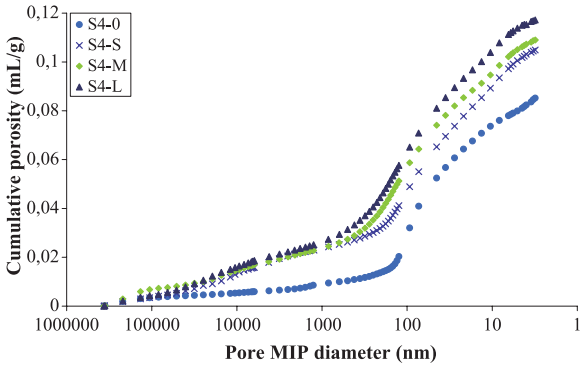

Fig. 15 Measurement of pore size distribution using MIP for sample S4.

microwave-heated states. **Fig. 13** shows the total intrusion porosity, a measure of the total volume of pores in the samples. The data is given on a sample mass basis. There is a consistent increase in total porosity with increased energy input into the concrete samples, for all concrete samples tested.

Although water loss plays a significant role in the porosity gain, as would naturally be expected, **Fig. 14** shows that there is no clear trend between the measured increase in sample porosity and the actual mass loss.

Assuming MIP accurately measures the total porosity, converting the mass loss from **Fig. 14** into the equivalent volume of liquid water shows that bulk water loss could not explain more than 60% of the pore volume that is created. Water loss must come from sources other than free water, such as the decomposition of portlandite and hydrated calcium-silicate (CSH).

This simple calculation indicates that more than 40% of the total porosity created and measured by MIP is associated with mechanisms other than bulk water loss during the exposure of concrete to microwave heating. This trivial analysis illustrates further the intrinsic complexity of porosity changes during the microwave heating of concrete, making a compelling argument for investigation of porosity changes at the local scale, by direct observation of concrete texture.

Fig. 14 seems also to indicate that the higher the water to cement ratio (w/c), the lower the contribution of water loss to the increase in total porosity. This observation indicates that whatever phenomenon other than bulk water loss is causing an increase in microwave-heated concrete porosity, it is associated with the w/c ratio and its effect on concrete microstructure, i.e. porosity. A more porous concrete sample is more prone to evaporation during microwave heating. If we assume the samples made with a higher w/c ratio had less water in their pores (relative to saturation) before treatment, then it makes sense that the evaporation of this type of water contributed less to pore formation. It is also logical that these concretes were more susceptible to other crack formation mechanisms related to drying as they would dry faster and thus be affected by these mechanisms sooner. The results also suggest that there is no significant pore growth due to excessive pore pressure as this would presumably occur more in the lower w/c ratio samples due to their smaller pore volumes. This does not mean that this phenomenon does not contribute significantly to mechanical changes or aggregate liberation. The explosive spalling of some low a/c samples in the first 5 seconds or so of microwave treatment (~100°C) might suggest this is an important phenomenon in terms of concrete recycling, but it does not appear to be an important phenomenon in increasing sample pore volume.

Despite its limitations, the pore size distribution measured by MIP can give some appreciation of the evolution of porosity within concrete samples with microwave heating. One example is given in **Fig. 15** for concrete sample S4. Bearing in mind the limitations of MIP measurement, namely its sensitivity to the ink-bottle effect (Diamond, 2000), what the measurements confirm is that a connected network of large pores, measured to be in the 1–100-μm range, exists in all microwave-treated samples. MIP does not measure this network in the untreated samples. This behaviour was consistently found with all concrete samples tested. One possible explanation is that the connected pores created by a short exposure are becoming larger as a result of heat-induced shrinkage of the cement phase. An interesting observation is that MIP does not appear to see noticeable changes below the 1-μm range between short and long exposure.

Along with changes in porosity, concrete performance is altered in a dramatic way by microwave heating. As reviewed earlier in the paper, the liberation of aggregate and cement was found to increase with exposure to microwaves. Analysis of microwave-heated samples using the Hopkinson bar also revealed strong changes in mechanical properties. **Fig. 16** shows the change in fracture force for the 5 samples considered in this paper, as an illustration of the embrittlement caused by microwave heating. Fracture

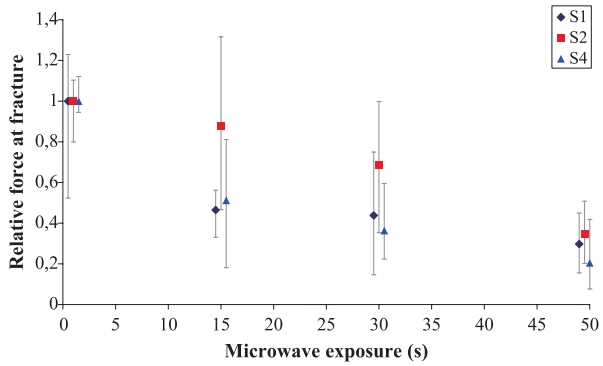

Fig. 16 Hopkinson bar measurements of impact fracture force on microwave-heated concrete samples (exposure time offset for clarity).

force is normalized by the fracture force for the untreated sample, which takes value 100%. This allows a simple assessment of the relative change in fracture force as a function of microwave exposure.

It is consistently found that the relative fracture force decreases continuously with increased exposure to microwaves, possibly with the largest loss in mechanical properties occurring after the short exposure. These are interesting observations, particularly in light of the knowledge that aggregate and cement liberation increases most significantly after a long exposure to microwaves, as seen earlier in **Figs. 1** and **2**. These observations suggest that there is some embrittlement phenomenon that is not effectively observed when using macro-scale measurement techniques, and there is not a direct link between changes in mechanical behaviour and physical liberation.

Overall, the macroscopic analysis has provided us with interesting insights about the changes that occur inside concrete during microwave heating, causing a change in mechanical behaviour, with a loss of resistance to impact fracture that varies continuously with increased exposure, and an increase in liberation of both aggregate and cement phases, albeit significant for the long exposure only. The main change related to concrete microstructure is associated with porosity, which increases continuously with exposure, as seen from both total porosity and pore size distribution measured by MIP. The changes in mechanical behaviour seem to vary as per the changes in total porosity, and a link between porosity and physical liberation of aggregates can be inferred.

The disparity between the evolution of physical liberation and mechanical properties with microwave exposure illustrates the need to further understand the microwave-heating concrete-embrittlement mechanisms with a local technique. For this work, image analysis of SEM images was chosen.

4. Effect of microwave heating on concrete: local level results and analysis

As discussed in the preceding section, the changes in porosity that occur during microwave heating of concrete are possibly numerous and complex, making the observation of porosity at the textural scale a compelling step towards unravelling the mechanisms by which microwave heating alters concrete. As will be shown here, textural analysis of the structure of fracture porosity provides an insightful angle on the mechanisms that take place inside concrete as it is being heated by microwaves, with views on recycling its elementary constituents.

Fig. 17 shows a superimposition of some highlighted images of sample S1. It is noted that the same general pattern applies to all the concrete samples tested in this work, with differences in the magnitude of the observed changes. Looking at the obvious changes in fracture porosity between the images, **Fig. 17** also validates the authors' selection of the 4 characteristic times along the heating process for the sake of quantifying the effect of microwave heating on concrete texture.

- Untreated concrete samples exhibit only few fractures, at both 40× and 200× magnification. Fractures are essentially found around the aggregates, in the region known as the interfacial transition zone (ITZ).
- After the short treatment, the sample having been heated for 15 seconds, a large-scale network of fractures appears, visible with the 40× magnification. These fractures seem to form a network connecting aggregate particles and also appear to run around them, going through the entire sample texture. This network is referred to as the "primary fracture network". As it is associated with aggregate grain boundaries, the formation of this network is directly associated with the liberation of aggregates.
- When the concrete sample is further heated to the medium condition (30 seconds), fractures from the primary network widen. Another network of smaller fractures develops that invades the cement paste. Because it appears to be nested within, and is of a smaller scale than the primary network of fractures, it is referred to as the "secondary fracture network".
- At the long exposure (50 seconds), while the primary network keeps widening, the quantity and length of the secondary network fractures increases significantly.

These generic observations are visible with every tested sample to a varying extent. From a range of observations that were repeatedly made during this study, it was ascertained that a strong correlation exists between the properties associated with the primary network and the loss of mechanical strength and liberation of aggregate particles. The properties of the secondary network further explain the mechanical changes but more importantly provide the

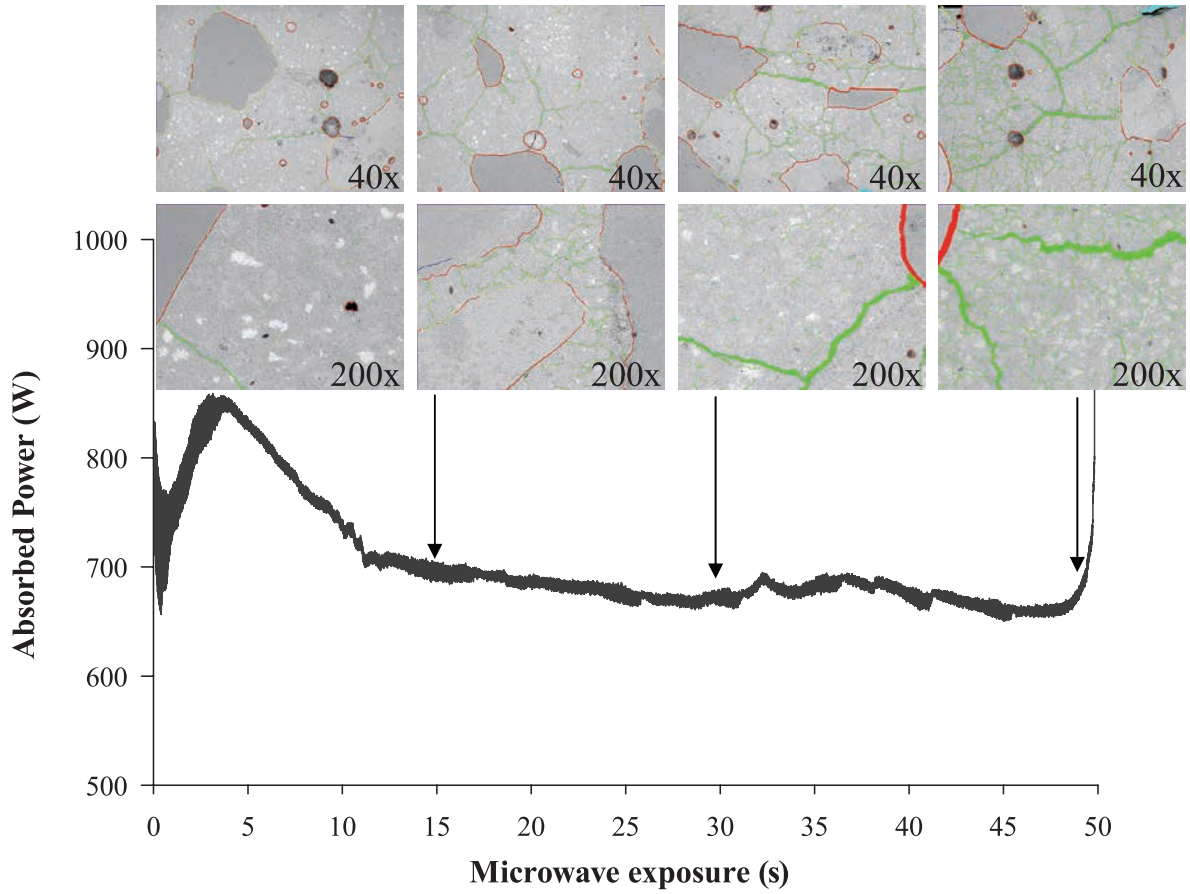

Fig. 17 Local observation of porosity changes with microwave treatment of S1.

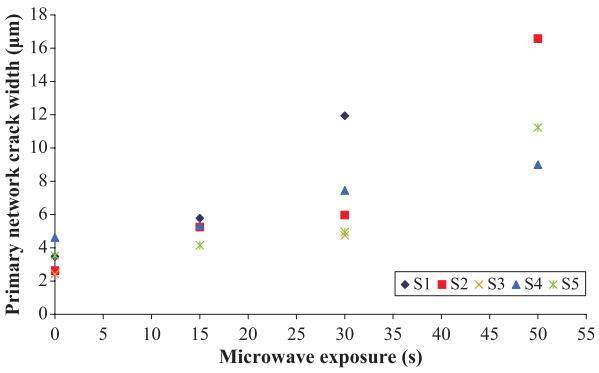

Fig. 18 Variations in primary network fracture width with microwave treatment time.

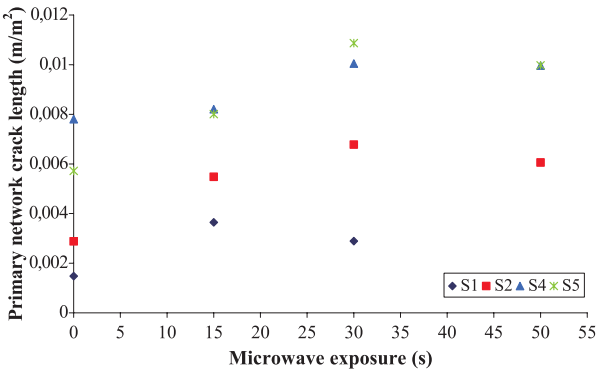

Fig. 19 Variations in primary network length with microwave treatment time.

link between textural liberation and physical liberation, as measured by impact testing, specifically the fineness of the cement paste fragments after impact testing.

Because these networks correlate directly with the macroscopic properties of microwave-heated concrete samples discussed in the previous section, their formation and growth are thought to hold the key to concrete recycling. The following section is concerned with quantification of both primary and secondary fracture networks.

4.1 The primary fracture network

The primary network may be quantified in a number of ways. Accessible properties from two-dimensional images include average properties such as total length, surface area and crack branch number, and statistical properties such as crack branch length and size distributions. As seen in **Fig. 18**, the width of primary network cracks increases very rapidly with microwave exposure. Conversely, as seen in **Fig. 19**, once the network is formed after a short

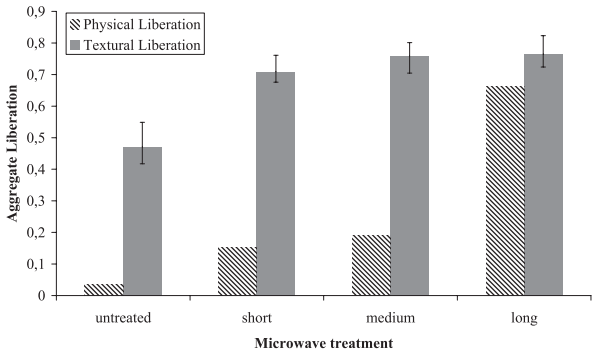

Fig. 20 Comparison between physical liberation (Lippiatt and Bourgeois, 2012) and textural liberation of aggregate particles.

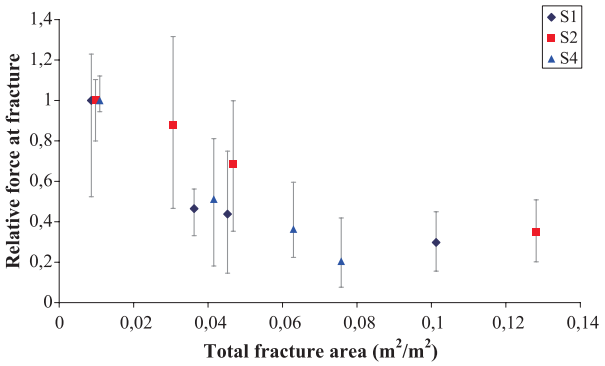

Fig. 21 Relative change in concrete strength, as measured by the relative force at fracture as a function of the combined area of primary and secondary networks relative to the cement paste area.

exposure, the length of the primary network is relatively unchanged. What this indicates is that the fractures that form this network widen with increased exposure, but do not propagate significantly beyond the extent reached after a short exposure to microwaves. The mechanisms associated with the change in thickness of primary-network fractures are deemed to be associated with drying shrinkage of the cement matrix. Because of the specific properties of the ITZ with its high porosity, micro-fracturing and water content (Roy and Idorn, 1993), a strong local reaction to microwave heating is bound to occur around the ITZ during microwave heating, and the formation and growth of the primary fracture network is expected.

By definition, the primary network is associated with what was earlier defined as the textural liberation, which accounts for the fraction of the aggregate perimeter that is liberated in the 2D analysis. **Fig. 20** compares physical liberation, as measured by acid dissolution, with textural liberation. Because the work presented here spans a long period of time, these measurements were not made on the same samples, hence changes in sample properties may contribute marginally to the observed differences. The error bars represent the range of textural liberation values from all the tested samples, the height of the bar representing the average value. The physical liberation values were measured on 10 mm cubes (Lippiatt and Bourgeois, 2012).

Textural liberation is already significant with the untreated sample. The high porosity of the ITZ, often with extensive micro-fracturing, is well documented (Roy and Idorn, 1993). Using MIP, Roy and Idorn estimated values of porosity in the ITZ as high as 37%. Mehta and Monteiro (Mehta and Monteiro, 2005) predict a high level of aggregate boundary fracturing from drying shrinkage during concrete heating, hence the observation of the primary network formation during microwave heating is expected.

Fig. 20 shows that textural liberation reaches a very high value after the shortest of the three measured microwave exposures, and it does not increase significantly after that. Aggregates are highly liberated inside the concrete texture after a short exposure to microwaves only. This is an important piece of information from a processing standpoint, as an increased duration of microwave heating becomes directly an increase in energy consumption. Nevertheless, upon impact breakage testing, the aggregate particles remain trapped inside the cement matrix. Indeed, the 2D analysis finds 70% of the aggregate boundaries being liberated in the concrete sample for the short exposure, when only 15% of the aggregate is physically liberated after single-particle impact breakage of a short-treated sample. It is fair to conclude that single-particle impact breakage cannot harvest the liberation induced by microwave heating. In other words, an alternate form of comminution is required to take advantage of the textural liberation of aggregate particles.

Eventually, for the long exposure setting, the physical and textural liberation of aggregates converge towards the same value. This is explained by the secondary network invading the cement phase, as intense fracturing of the cement phase is necessary for single-particle impact breakage to yield liberated aggregates.

It was shown above that the strength of concrete decreased with microwave exposure, the same can be said of concrete stiffness. Textural image analysis showed an increase in the total crack length, total crack area and average crack width. This increase in crack width was significantly more pronounced in the primary network and specifically the aggregate/cement paste interface fractures. It is impossible to separate the effects of total fracture area and aggregate interface crack width on the mechanical properties as these two values increase together during microwave heating, but it has been noted that concrete stiffness is largely dependent on the ITZ (Mehta and Monteiro, 2005). In this work stiffness is measured with Hopkinson bar impact testing as defined by Tavares and King (Tavares and King, 1998). **Fig. 22** shows that as expected, the stiffness of the samples decreases rapidly with the increase in

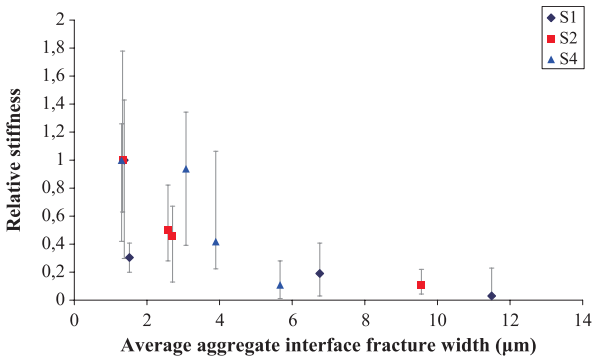

Fig. 22 Change in concrete stiffness with aggregate interface crack width.

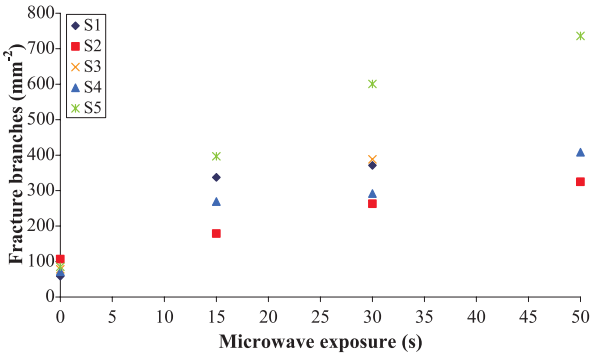

Fig. 24 Number of branches per cement area in secondary network.

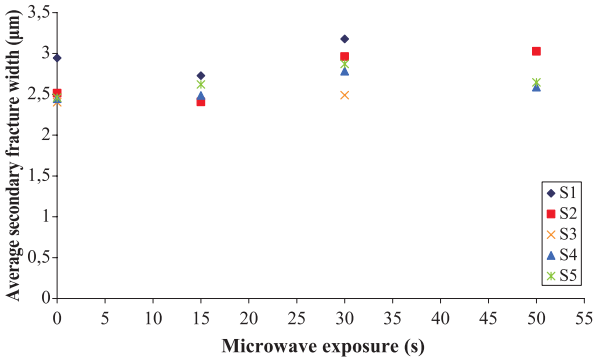

Fig. 23 Variations in secondary-network properties with microwave treatment time.

aggregate interface fracture width. The rate of change slows at higher temperatures, presumably as once aggregate and cement paste is separated the stiffness becomes dependent on the cement phase only, and increasing the size of this separation has no further effect. Similarly, concrete strength has been linked with porosity, the textural measure most analogous with porosity is the total crack area which increases steadily with microwave exposure and shows a strong correlation with loss of concrete strength and can be seen in **Fig. 21**. When compared with **Fig. 19**, it can be seen that the growth of the primary network can not be responsible for the strength loss in samples that have experienced a longer treatment, because while strength continues to decrease, the increase in primary-network fracture length slows with further microwave exposure.

Two-dimensional analysis of the fracture networks has a limited scope for understanding the way by which their properties correlate with operating conditions and with recycling performance indicators. Having clearly established that these fracture networks hold the key to concrete recyclability at the local scale, it appears that three-dimensional observation and analysis is the next logical step. Currently, X-ray tomography has a resolution that is fully compatible with that required to capture the primary network, at a resolution of say about 10 µm per voxel. The authors have started capturing tomographic images of 20-mm heated concrete samples, which confirm that the primary network is a highly connected network that percolates through heated concrete samples. On the other hand, capturing three-dimensional information about the secondary network is clearly more complex because the required resolution must be of the order of a micrometer or less. Nevertheless, the seemingly random occurrence of this network through the cement phase means that 3D properties of the secondary fracture network can possibly be inferred from 2D images using statistical means.

4.2 Analysis of the secondary network

The fracture network that forms during the microwave heating of concrete has been divided in two. The primary fracture network is associated with the aggregate grain boundary, and occurs with short exposure to microwaves, whereas the secondary network occurs randomly in the cement phase and spreads with increased exposure to microwave heating. Just as for the primary network, properties of interest of the secondary network include average properties such as total length, surface area and crack branch number, and statistical properties such as crack branch length, nodes, ends and width distributions. Contrary to the primary network fractures, **Figs. 23**, **24** shows that on average, cracks from the secondary network do not appear to grow wider with microwave treatment, but the total length and number of branches per unit area do increase with microwave heating time. The crack branch length distribution follows a log-normal distribution, as shown in **Fig. 25**, and does not change significantly between samples nor with increased heating duration. Put another way, the growth of individual fractures in the cement paste and the growth of the secondary fracture network as a whole occur together and in constant proportion. This is not unexpected as once the

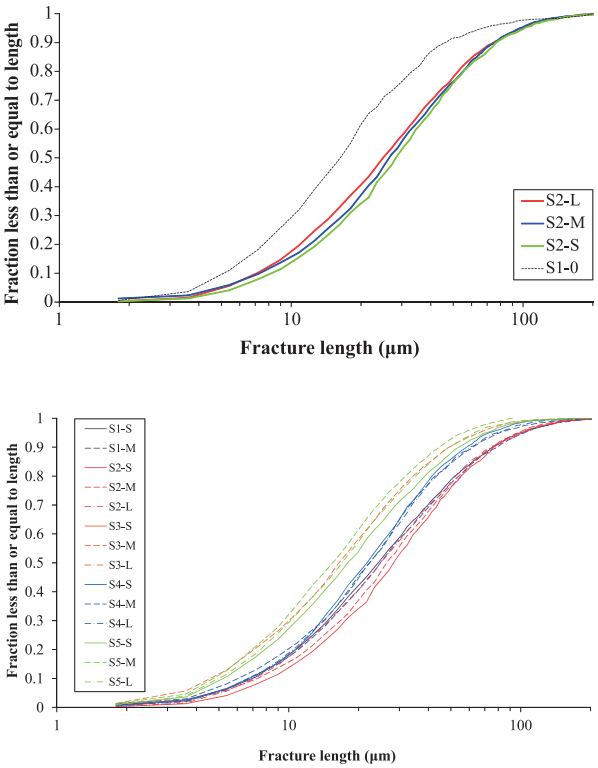

Fig. 25 Branch size distributions, secondary fracture network. Top: for sample S2. Bottom: for samples S1 to S5.

cement paste is disconnected from the aggregate, shrinkage is no longer constrained. This distribution is directly associated with the fineness of the fragments that form after comminution of the microwave-heated concrete samples. Additional research is required, however, in order to correlate the topological properties of the secondary network to the size distribution of the fragments obtained by comminution.

To finalise the discussion about the two fracture networks identified in this work, it was decided to take a look at their relative significance on properties of relevance to the recycling problem. As discussed earlier, the secondary crack length increases with microwave exposure time, i.e. with concrete energy absorption. **Fig. 26** shows the variation between total secondary network crack length relative to the total crack length and microwave exposure time. **Fig. 27** shows that while the total crack length increases steadily with increased microwave exposure, the rate of increase of the secondary-network crack length is faster, and is the key player in the loss of mechanical strength of microwave-heated concrete. As an illustration of this last point, **Fig. 28** shows the measured relationship between the secondary network total crack length relative to the total crack length and the strength of the concrete samples measured by HPB. The correlation is significant, with strength dropping almost in linear proportion to the increase in secondary network total crack length.

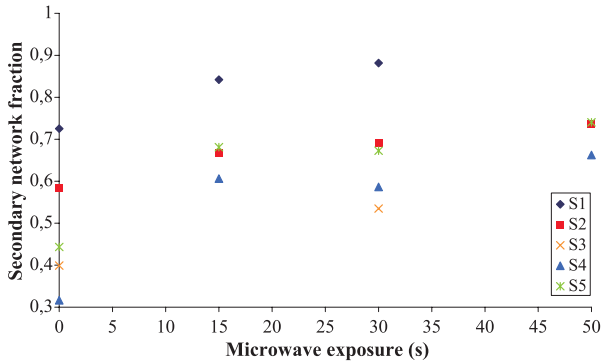

Fig. 26 Fraction of total crack length composed of secondary network.

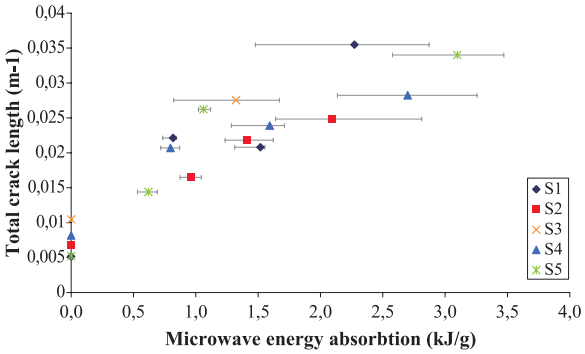

Fig. 27 Total combined crack length of primary and secondary network.

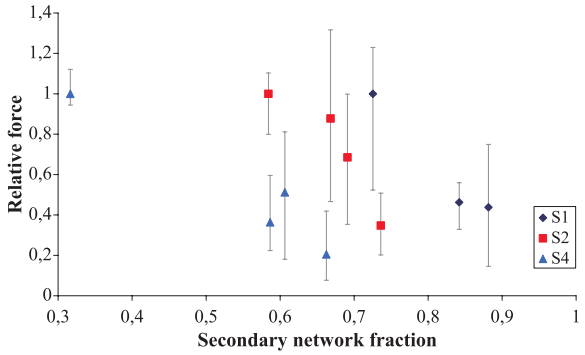

Fig. 28 Relative change in fracture force with fraction of total network length composed of secondary network.

5. Implications for development of a microwave -based concrete recycling process

This work, through local analysis of changes in the structure of porosity that occurs during the microwave heating of concrete, has added additional evidence to the body of existing knowledge about the potential value of microwave heating for the development of a concrete recycling process. The pattern of crack growth is evidence of drying shrinkage as it is the only crack formation mechanism to occur over the entire temperature range observed.

Importantly for concrete recycling, these results show that microwave heating causes fractures to occur at the aggregate/cement paste interface, and importantly for energy efficiency, these are the first microwave-induced fractures to form. Also of note is the observation that the properties of individual concretes are relatively unimportant. This will make the implementation of a microwave-based concrete recycling process easier as it will not require adaptation to different waste sources.

The analysis of fracture porosity has shown that microwave heating interacts strongly with the ITZ to generate a large-scale network of fractures at the aggregate/cement paste interface. Experimental results indicate that this primary network of fractures forms with a short exposure to microwaves. As previously stated, the most efficient microwave generators for embrittlement are those with the highest power output, however, this is based on the assumption that the key embrittlement mechanism is differential thermal expansion. It is still desired that the process is selective, and the higher the power of the microwave generator, the faster heating occurs, the less that conduction can play a role and the more selective the process is. Therefore a high-power generator is most likely still desirable but as dehydration appears to be the key mechanism in the microwave processing of concrete waste, one may expect the point at which increasing power output is no longer economical is lower than it would be for a similar application in mineral processing. In any case the technology needs to be perfected and the appropriate compromise found.

It was noted in a previous work (Lippiatt and Bourgeois, 2012) that the liberation of aggregate particles is seen only after extensive microwave treatment. This was measured using macro techniques, sample fracture then selective dissolution. Conversely, local techniques, i.e. SEM inspection of treated samples used in this work, show that fracture at the cement/aggregate interface occurs much earlier in the treatment process. What occurs later under extended microwave exposure is more extensive fracture growth throughout the cement paste. This extended cement crack growth greatly reduces the strength of the concrete sample and causes the sample to break into much smaller fragments when crushed under impact. It was due to this fragmentation in the cement paste that liberation was measured by impact fracture at such a high level for long-treated samples in this previous work, rather than any actual increase in the separation of the aggregate particles and cement paste.

The SEM results suggest that the aggregate and the cement were well separated, but unless an appropriate mechanical comminution technique is selected, the aggregate samples will remain encased within larger cement paste fragments. Development of an industrial solution would also require identification of an appropriate comminution process to exploit this primary network so as to close the gap between physical and textural liberation with minimum energy consumption.

The above discussion considers optimisation of the liberation of aggregates, and ignores other important dimensions of the process, towards which results from this work bring answers. Once comminution has taken place, a concrete's aggregate and cement paste would have to be separated. One possibility that can be inferred from this work's results would be to induce a dense secondary fracture network by microwave heating prior to comminution in order to generate cement fines, which could then easily be separated from liberated aggregates by dry screening. Moreover, reducing the cement paste to a fine powder would help facilitate the recycling of the cement paste. From these considerations, there is significant scope for development of a microwave-based recycling process, however, given that the microwave heating step is necessarily part of a processing chain that includes comminution, separation and transport, finding the right operating conditions is going to require additional research and development work.

6. Concluding remarks

The applicability of microwave heating to the recycling of concrete is an important issue, given the increase in demand for concrete, the scarcity of natural aggregate resources and the environmental footprint of clinker production. While a number of published works have shown the potential of developing a microwave-based recycling process based on macroscopic measurements relevant to concrete recycling performance, namely aggregate liberation, product fineness and mechanical embrittlement, this work establishes links between fracture porosity and observed macroscopic effects through local texture observation and analysis.

The work associates the formation of two fracture networks with specific recycling issues:

– The primary fracture network is constituted of large connected fractures that are associated with the aggregate grain boundaries, and occurs with short exposure to microwaves. This network, by essence, is responsible for the textural liberation of aggregates. The primary network appears to occur at the early stage of microwave heating.
– The secondary network is constituted of seemingly randomly occurring cracks which spread through the cement phase with increased exposure to microwave heating. This dense network of smaller fractures is strongly linked to the loss of mechanical strength of concrete, and the degree of actual physical liberation of aggregate particles obtained after impact fracture of microwave heated concrete samples.

Mechanisms responsible for the formation and growth of both primary and secondary fracture networks are undoubtedly complex, but the evidence from this work indicate that they are controlled by local drying shrinkage, which starts at the interfacial transition zone around aggregate particles and eventually spreads throughout the bulk of the cement matrix.

Capitalising on the high degree of textural liberation of aggregate particles obtained after a short microwave heating time only, meaning lower energy consumption, requires identification of a suitable comminution solution. The inefficiency of single-particle impact fracture to physically liberate aggregate particles that were texturally liberated suggests that impact-based comminution equipment is not the best option. It is thought that shear-inducing comminution technologies such as high-pressure grinding rolls should be investigated in conjunction with microwave heating.

The longer exposure to microwaves, however, yields extensive growth of secondary network fractures in the cement matrix and subsequent production of cement fines through comminution. Increased cement fines may be valuable for the separation of aggregates from cement and recycling of the cement itself as part of the overall recycling scheme.

In the end, it can be concluded that finding the best position and operating conditions for the microwave heating step in the concrete recycling chain is not a clear-cut situation. The setting of the microwave heating process to grow the primary and secondary fracture networks to a specific level depends on the subsequent process steps, including comminution, product separation and possibly transport.

Having looked at the local scale, one important conclusion from this work is that development of a microwave-based concrete recycling process must consider the processing chain in its entirety.

Acknowledgements

The authors acknowledge the financial support of the Agence Nationale de la Recherche (the French National Research Agency) through the COFRAGE project from the ECOTECH research programme. The authors want to acknowledge Dr. Emmanuel Cid, Senior Research Scientist with the Laboratoire de Génie Chimique, for his valuable contribution to the image analysis of the fracture patterns.

References

Akbarnezhad A., Ong K.C.G., Zhang M.H., Tam C.T., Foo T.W.J., Microwave-assisted beneficiation of recycled concrete aggregates, Construction and Building Materials, 25 (2011) 3469–3479.

Ali A.Y., Understanding the effects of mineralogy, ore texture and microwave power delivery on microwave treatment of ores, Ph.D. thesis, University of Stellenbosch, 2010.

Ben Haha M., Gallucci E., Guidom A.,Scrivener K.L., Relation of expansion due to alkali silica reaction to the degree of reaction measured by sem image analysis, Cement and Concrete Research, 37 (2007) 1206–1214.

Bourgeois F., Banini G., A portable load cell for in-situ ore impact breakage testing, International Journal of Mineral Processing, 6 (2002) 31–54.

Brough A.R., Atkinson A., Automated identification of the aggregate–paste interfacial transition zone in mortars of silica sand with portland or alkali-activated slag cement paste, Cement and Concrete Research, 30 (2000) 849–854.

Costes J.R., Majcherczyk C., Binkhorst I.P., Total recycling of concrete, Commissariat à l'Énergie Atomique, online publication, 2010.

Diamond S., Mercury porosimetry an inappropriate method for the measurement of pore size distributions in cement-based materials, Cement and Concrete Research, 30 (2000) 1517–1525.

Figg J., Microwave heating in concrete analysis, Journal of Applied Chemistry and Biotechnology, 24 (1974) 143–155.

Fischer C., Davidsen C., Europe as a recycling society, Report for the European Environment Agency, 2011.

Igarashi S., Kawamura M., Watanabe A. Analysis of cement pastes and mortars by a combination of backscatter-based SEM image analysis and calculations based on the powers model, Cement and Concrete Composites, 26 (2004) 977–985.

Jerby E., Dikhtyar V., Aktushev O., Grosglick U., The microwave drill, Science, 298 (2002) 587–589.

Kingman S.W., Jackson W., Bradshaw S.M., Rowson N.A., An investigation into the influence of microwave treatment on mineral ore comminution, Powder Technology, 146 (2004a) 176–184.

Kingman S.W., Jackson K., Cumbane A., Bradshaw S.M., Rowson N.A., Greenwood R., Recent developments in microwave assisted comminution, International Journal of Mineral Processing, 74 (2004b) 71–83.

Kiss L., Shönert K., Liberation of two component material by single particle compression and impact crushing, Aufbereit.-Tech, 30 (1980) 223–230.

Klee H., The cement sustainability initiative, Progress report for the World Business Council for Sustainable Development, Duesseldorf, Geneva, 4 June 2009.

Lippiatt N., Bourgeois F., Investigation of microwave-assisted concrete recycling using single-particle testing, Minerals Engineering, 31 (2012) 71–81.

Mehta P., Monteiro P., Concrete: microstructure, properties and materials, 3rd Revised edition, McGraw-Hill Professional, 2005.

Piasta J., Sawicz Z., Rudzinski L., Changes in the structure of hardened cement paste due to high temperature, Matériaux et Constructions, 17 (1984) 291–296.

Roy D.M., Idorn G.M., Concrete microstructure, Strategic Highway Research Program, National Research Council, Washington, DC, 1993.

Symonds Group, Construction and demolition waste

management practices and their economic impacts, Report for the European Commission in association with ARGUS, COWI and PRC Bouwcentrum, 1999.

Tam V.W.Y., Tam C.M., Wang Y., Optimization on proportion for recycled aggregate in concrete using two-stage mixing approach, Construction and Building Materials, 21 (2007) 1928–1939.

Tavares L.M., King R.P., Single-particle fracture under impact loading. International Journal of Mineral Processing, 54 (1998) 1–28.

White T.L., Foster D.J., Wilson C.T., Schaich R., Phase II microwave concrete decontamination results, Oak Ridge National Laboratory, 1995.

Wong H.S., Head M.K., Buenfeld N.R., Pore segmentation of cement-based materials from backscattered electron images, Cement and Concrete Research, 36 (2006) 1083–1090.

Yang R., Buenfeld N.R., Binary segmentation of aggregate in SEM image analysis of concrete, Cement and Concrete Research, 31 (2001) 437–441.

Author's short biography

Nicholas Lippiatt

Nicholas Lippiatt holds a masters in materials science (France) and completed his bachelor's degree in materials engineering at the University of Queensland in Brisbane, Australia. He is currently completing a Ph.D. in materials science (Laboratoire de Génie Chimique, Institut National Polytechnique de Toulouse) in France on the use of microwave heating technology for concrete recycling.

Florent Bourgeois

Prof. Bourgeois holds a B.Eng. in materials science (France) and a Ph.D. in extractive metallurgy (University of Utah). He worked as a research fellow for the CRC Mining (Australia) from 1994 to 1996, and as a lecturer in minerals processing with the University of Queensland from 1997 until 2000. Between 2001 and 2005, he worked as project leader for the French Geological Survey's processing department. He now holds a tenured position at the University of Toulouse. His field of expertise is particulate process design and modelling, with emphasis on comminution, liberation, texture modelling, sampling of minerals and wastes.

KONA Powder and Particle Journal No. 31 (2014) 265–270/Doi:10.14356/kona.2014017 Original Research Paper

Numerical Prediction of the Bulk Density of Granular Particles of Different Geometries†

Kasra Samiei*, Girma Berhe and Bernhard Peters

[1] *Research Group in Engineering Science, Faculty of Science, Technology and Communication, University of Luxembourg, Luxembourg*

Abstract

The Discrete Element Method (DEM) is increasingly used to simulate the motion of granular material in engineering devices. The most widely used shape to model granular particles is the sphere due to its simplicity which facilitates computations. However, with increasing advancement and popularity of the DEM approach, a more accurate representation of real granular shapes is becoming intensely important. This paper is an attempt to predict the bulk density of granular particles of cylindrical shape by DEM. The method used to model tube-like particles is the composite method where the tube-like particle is composed of a number of spherical sub-shapes. The results show that the DEM prediction of the bulk density of tube-like particles were accurate provided that a sufficient number of spherical sub-shapes was used to construct the particle. In addition, the bulk density of granular particles in the shape of 32-face polyhedrons was also investigated. It was shown that 32-face polyhedrons can be approximated as spheres provided that the rolling resistance of the shape is taken into consideration.

Keywords: bulk density, DEM, numerical analysis, granular matter, particle shape

1. Introduction

Granular materials are complex systems of a large number of particles of various sizes, shapes and materials. Under different circumstances they reveal different behavior such as solid-, liquid- or gas-state behavior. In fact, the science of granular flow is not yet as well understood and well developed as other classes of materials (Pöschel and Schwager, 2005; Campbell, 2006). In order to predict and optimize the behavior and motion of granular matter in engineering devices, numerical simulation tools are increasingly employed (Cleary, 2004). The continuous increase in computing power is now enabling researchers to implement numerical methods that deduce their global characteristics from analyzing the individual behavior of each grain. This forms the foundation of the Discrete Element Method (DEM) which is, to date, the leading approach to simulate the dynamics of granular media.

However, predicting the behavior of such a complex physical system by computer models has its own challenges. One of the main challenges of DEM is in modeling the complex shapes which the granular particles often exhibit in reality. The most widely used particle shape in DEM is the sphere due to its simplicity. With increasing advancement and popularity of the DEM approach, the expectations of its capabilities rise, too. More realistic modeling of granular particles of various geometries is becoming increasingly necessary.

Different methods already exist to model complex shapes in DEM which will be briefly noted here. More complete reviews of different methods in DEM to model non-spherical shapes are reported by Hogue (1998), Latham and Munjiza (2004), Haff (1993) and Ristow (1994).

One approach is to model the complex shape as a cluster of spherical sub-shapes. Different variations of the so-called composite method can be found in the literature. The sub-shapes can be connected to one another by damped springs (Buchholtz and Pöschel, 1994; Pöschel and Buchholtz, 1993; Maeno, 1996; Lu and McDowell, 2007), or else the aggregate shape can be considered as rigid (Gallas and Sokolowski, 1993; Nolan and Kavanagh, 1995; Mutze, 2006). The sub-shapes used to construct the complex shape might also overlap each other. The sub-shapes do not necessarily need to be spheres; for example, triangular sub-shapes have been developed which are useful to model shapes with sharp edges (Pöschel and Buchholtz, 1995), and arc sub-shapes can be used to construct oval shapes (Wang et al., 1999). Another approach to model non-spherical shapes is to address the shape as it is and develop analytical methods for the detection of contacts. Such analytical methods are already developed for some

† Accepted: August 22, 2013
[1] L-1359, Luxembourg
* Corresponding author:
E-mail: kasra.samiei@unileoben.ac.at
TEL:+43-3842-402-5821 FAX: +43-3842-402-5802

Table 1 Mechanical and contact properties used in the DEM analysis

mechanical property	unit	spherical particles	container	tubular particles	container	polyhedral particles	container
density	kg/m^3	1350	2520	1350	1350	1350	1350
Young's modulus	N/m^2	3.38×10^8	72×10^9	3.38×10^7	3.38×10^7	3.38×10^8	3.38×10^8
Poisson's ratio	–	0.41	0.22	0.41	0.41	0.41	0.41
contact property coefficient	unit	particles	particle/wall	particles	particle/wall	particles	particle/wall
restitution	–	0.8	0.85	0.8	0.8	0.8	0.8
sliding friction	–	0.5	0.5	0.5	0.5	0.5	0.5
rolling friction	–	0.001	0.001	0.001	0.001	0.0016	0.0016

shapes such as ellipsoids (Lin and Ng, 1995; Lin and Ng, 1997; Allen et al., 1989; Perram et al., 1984; Perram and Wertheim, 1985; Ouadfel and Rothenburg, 1999; Johnson et al, 2004) and polyhedrons (Cundall, 1988; Zhao et al., 2006). Superquadrics are also proposed (Barr, 1981) and used in DEM studies, e.g. superellipsoids (Wellmann et al., 2008; Cleary et al., 1997). A different method is the virtual space method where the space is divided into discrete voxels (Munjiza, 2004; Jia and Williams, 2001). Each particle takes up some space in the digitized space for which the corresponding voxels would be identified. Two particles are in contact if they both occupy the same voxel.

Each of these methods has its own advantages and disadvantages but a common challenge remains the computational costs and complexity of modeling complex shapes. The most widely accepted method, at least in commercial software, is the composite approach. However, according to Kruggel-Emden et al. (2008), the validity of the method has not been sufficiently tested and verified. This paper, therefore, is an attempt to further study the validity of the composite approach and to investigate its capabilities and limitations.

The application chosen to verify the method is the poured bulk density of granular particles. The dependency of the bulk density on the shape of the individual particles has long been recognized (Riley and Mann, 1972; Fonner et al., 1966; Ridgway and Rupp, 1969), which makes the case suitable for validating the composite method.

2. DEM study

Specific boundary conditions for the DEM study are presented for each case in **Table 1**. The friction and restitution coefficients are based on simple lab tests conducted on sample particles, and are verified by the available data in the literature (Engineers handbook; Engineering toolbox; Bennett and Meepagala, 2006; Beardmore, 2012). The time step was fixed at 10^{-5} and the end time of the simulation was set to 8 seconds when all particles come to rest and the kinetic energy tends to zero. Since the size of the container in all simulations and experiments was chosen to be identical, it suffices to compare the height of the packed bed. The height of the packed bed is calculated as the distance of the highest point of the packed bed after complete settlement to the bottom of the container. It is worth noting that the height of the packed bed in each experiment reported here is not comparable because in each case, a different number of particles and sometimes different size of container is used. The objective is therefore to compare the numerical results with the experiments in three independent cases presented in **Table 1**.

The rolling friction is included in order to account for the resistance of the spheres against rolling due to small deviations from the spherical shape. An assumption taken regarding the shape of the tube-like particles is that the hollowness of the tubes was neglected in the DEM study, i.e. the particles were assumed to be full. The explanation is that the hollowness of the tubes does not affect the packing of the particles for small hole diameters because other particles cannot penetrate through the inner hole or the penetration is negligible. Another simplifying assumption is made regarding the Young modulus of the moving particles, whereas the Young modulus is reduced one order of magnitude from the original value. Conducting a sensitivity analysis confirmed the findings of several other studies (Kawaguchi et al., 1997; Ketterhagen et al., 2007; Ketterhagen et al., 2005; Tuley et al., 2010; Hogue and Newland, 1994; Pérez, 2008; Silbert et al., 2001; Kruggel-Emden et al., 2007) that lowering the stiffness within a certain range does not affect the results of the DEM simulation. This is due to the fact that although changing the stiffness constant does affect the duration of a single collision, the velocity and trajectory of the particle after the collision is only dependent on the coefficient of restitution and the coefficients of friction. However, the particle's hardness should be large enough so that the maximum overlap does not exceed the particle's radius, in which case the particles pass through each

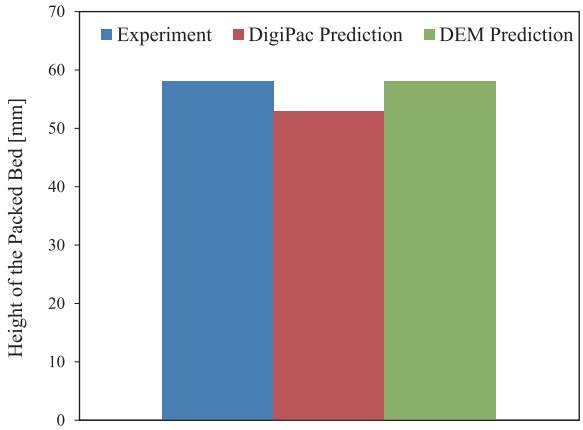

Fig. 1 Experimental and numerical results of the packing behavior of spherical particles.

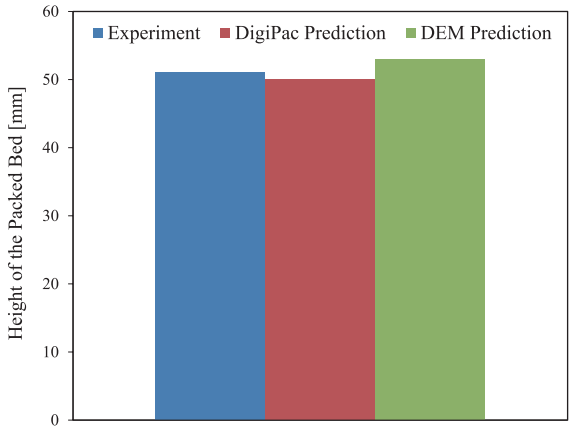

Fig. 2 Experimental and numerical results of the packing behavior of tubular particles.

other. Without this assumption, the time step should have been reduced to accurately resolve the impact of small sub-shapes used to construct the tubular particles. This assumption is therefore necessary to reduce the high computational costs of the simulation of tube-like particles. The tube-like particles are modeled by the composite method as an aggregate of spherical sub-shapes. In this case, each tube is represented by 20 spheres which cluster and form the cylindrical shape. The same coefficient of rolling friction as spheres is assigned to the cylinders when they roll around the principal axis of rotation.

The 32-face polyhedrons used in the experimental study (Gan et al., 2004; Jia et al., 2007) are quite similar in shape to spheres and are therefore represented by spheres in this work. The coefficient of rolling friction is raised slightly for the polyhedral particles because their divergence from perfect spheres is an intrinsic characteristic of the shape. The diameter of the representative sphere can be taken as either the outer or inner diameter of the polyhedron. Both assumptions are considered in this study. The outer diameter of the polyhedron is defined as the diameter of the smallest sphere which can be drawn that contains the whole polyhedron. Alternatively, the inner diameter of the polyhedron is defined as the diameter of the biggest sphere which can be drawn that will be fully contained inside the polyhedron. The outer diameter of the 32-face polyhedron used in this study is 8.2 mm and the inner diameter is 7.5 mm. Similar to the tube-like particles, the hollowness of the polyhedral particles is neglected and the spheres are assumed to be full.

3. Results

The results of the DEM study are presented in this section along with the corresponding experimental results to validate the numerical approach. Also for comparison, the results of the digital approach applied by Gan et al. (2004) and Jia et al. (2007) based on the method of virtual space are presented. In their method called DigiPac, a particle is just a coherent collection of digitized pixels which are stored as integers or bits. Although DigiPac is able to model particles of arbitrary shapes, consideration of particle interactions is limited to their geometric constraints.

As an initial validation case, the packing behavior of 660 spheres was predicted by DEM. Validation of the simple case of spheres is necessary before advancing to more complex particle geometries. The results, demonstrated in **Fig. 1**, show that DEM prediction of the bulk density of spherical particles is in agreement with the experimental results.

The results of the prediction of the bulk density of tubular particles are shown in **Fig. 2**. Despite the slight over-prediction of the height of the packed bed, the DEM prediction of the bulk behavior of the tube-like particles is quite acceptable. The small error can be explained by the approximation of the tube-like shape as a cluster of spheres in the DEM study.

Fig. 3 shows the prediction of the bulk behavior of polyhedral particles. It is evident that the inner diameter approximation is a good approximation and provides results in quite good agreement with the experimental results. On the other hand, the outer diameter approximation does not yield a good approximation of the polyhedral shape.

4. Conclusions

DEM modeling of granular grains of complex shapes is still a young research topic. This study is an attempt to verify the most commonly used method to model non-spherical shapes, i.e. the composite method. The composite method is used to predict the bulk density behavior of granular particles of cylindrical geometry. The numerical results are compared with a digital

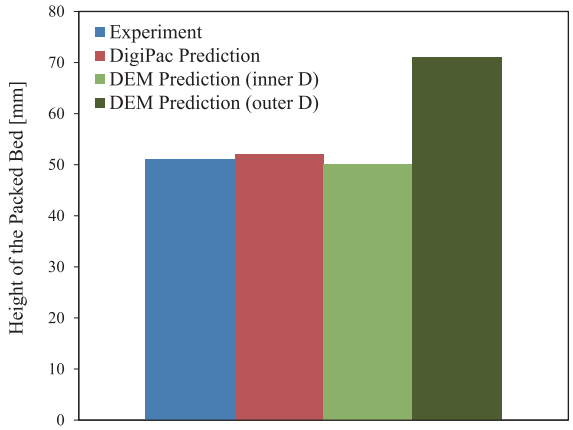

Fig. 3 Experimental and numerical results of the packing behavior of 32-face polyhedral particles approximated in a DEM study by spheres with either inner diameter or outer diameter of the polyhedron.

method called DigiPac applied by Gan et al. (2004) and Jia et al. (2007). The results of both methods are compared with the experimental results provided by the same authors. The comparison verifies the competence of the composite method in predicting the bulk density of cylindrical particles. The capabilities of the DigiPac method has already been discussed in the author's work and is not repeated here. In addition to cylinders, the bulk density of 32-face polyhedrons is also investigated and it is verified that a 32-face polyhedron can be approximated by a sphere with a diameter being the inner diameter of the polyhedrons. Future work should attempt to predict the bulk behavior of other geometries such as conical, cubic and ellipsoidal particles.

Acknowledgements

Experiments presented in this paper were carried out using the HPC facility of the University of Luxembourg.

References

Allen M.P., Frenkel D., Talbot J., Molecular dynamics simulation using hard particles, Computer Physics Reports, 9 (1989) 301–353.

Barr A.H., Superquadrics and angle-preserving transformations, IEEE Comput Graph Appl, 1 (1981) 11–23.

Beardmore R., Coefficients of Friction, 2012, <www.roymech.co.uk/Useful_Tables/Tribology/co_of_frict.htm> accessed: 27.08.2012.

Bennett J., Meepagala R., The Physics factbook, Coefficient of Restitution, 2006, <hypertextbook.com/facts/2006/restitution.shtml> accessed 27.08.2012.

Buchholtz V., Pöschel T., Numerical investigation of the evolution of sandpiles, Physica A (1994) 202–390.

Campbell C., Granular material flows-an overview, Powder Technology, 162 (2006) 208–229.

Cleary P.W., Large scale industrial DEM modelling, Engineering Computations, 21 (2004) 169–204.

Cleary P.W., Stokes N., Hurley J., Efficient collision detection for three dimensional super-ellipsoid particles, in: Proceedings of 8th international computational techniques and applications conference CTAC97, Adelaide, 1997.

Cundall P.A., Formulation of a 3-dimensional distinct element model. 1. a scheme to detect and represent contacts in a system composed of many polyhedral blocks, International Journal of Rock Mechanics and Mining Sciences & Geomechanics Abstracts, 25 (1988) 107–116.

Engineering Toolbox, <www.engineeringtoolbox.com> accessed 21.10.2012.

Fonner D.E., Banker G.S., Swarbrick J., Micromeritics of granular pharmaceutical solids i: Physical properties of particles prepared by five different granulation methods, Journal of Pharmaceutical Sciences, 55 (1966) 181–186.

Gallas J.A.C., Sokolowski S., Grain non-sphericity effects on the angle of repose of granular material, International Journal of Modern Physics B, 7 (1993) 2037–2046.

Gan M., Gopinathan N., Jia X., Williams R.A., Predicting packing characteristics of particles of arbitrary shapes, KONA Powder and Particle Journal, 22 (2004) 82–93.

Goldstein H., Poole Jr. C.P., Safko J.L., Classical Mechanics, 3rd edition, Addison Wesley Publishing company, Cambridge, MA, 2001.

Hogue C., Newland D., Efficient computer-simulation of moving granular particles, Powder Technology, 78 (1994) 51–66.

Hogue C., Shape representation and contact detection for discrete element simulations of arbitrary geometries, Engineering Computations 15 (1998) 374–390.

Jia X., Gan M., Williams R.A., Rhodes D., Validation of a digital packing algorithm in predicting powder packing densities, Powder Technology, 174 (2007) 10–13.

Jia X., Williams R.A., A packing algorithm for particles of arbitrary shapes, Powder Technology, 120 (2001) 175–186.

Johnson S., Williams J.R., Cook B., Contact resolution algorithm for an ellipsoid approximation for discrete element modelling, Engineering Computations, 21 (2004) 215–234.

Kawaguchi T., Tanaka T., Tsuji Y., Numerical simulation of two-dimensional fluidized beds using the discrete element method (comparison between the two- and three-dimensional models), Powder Technology, 96 (1997) 129–138.

Ketterhagen W.R., Curtis J.S., Wassgren C.R., Kong A., Narayan P.J., Hancock B.C., Granular segregation in discharging cylindrical hoppers: A discrete element and experimental study, Chemical Engineering Science, 62 (2007) 6423–6439.

Ketterhagen W.R., Curtis J.S. and Wassgren C.R., Stress results from two-dimensional granular shear flow simulations using various collision models, Physical Review E, 71 (2005) 061307.

Kruggel-Emden H., Rickelt S., Wirtz S., Scherer V., A study on the validity of the multi-sphere discrete element method, Powder Technology, 188 (2008) 153–165.

Kruggel-Emden H., Simsek E., Rickelt S., Wirtz S., Scherer V., Review and extension of normal force models for the discrete element method, Powder Technology, 171 (2007) 157–173.

Latham J., Munjiza A., The modelling of particle systems with real shapes, Philosophical Transactions of the Royal Society of London, Series A: Mathematical Physical and Engineering Sciences, 362 (2004) 1953–1972.

Lin X., Ng T.T., A three-dimensional discrete element model using arrays of ellipsoids, Geotechnique, 47 (1997) 319–329.

Lin X., Ng T.T., Contact detection algorithms for three-dimensional ellipsoids in discrete element modelling, International Journal for Numerical and Analytical Methods in Geomechanics, 19 (1995) 653–659.

Lu M., McDowell G., The importance of modelling ballast particle shape in the discrete element method, Granular Matter, 9 (2007) 69–80.

Maeno Y., Numerical investigation of surface level instability due to a tube in a vibrating bed of powder, Physica A, 232 (1996) 27–39.

Munjiza A., The Combined Finite-Discrete Element Method, Wiley, 2004.

Mutze U. Rigidly connected overlapping spherical particles: a versatile grain model, Granular Matter, 8 (2006) 185–194.

Nolan G.T., Kavanagh P., Random packing of nonspherical particles, Powder Technology, 84 (1995) 199–205.

Ouadfel H., Rothenburg L., An algorithm for detecting inter-ellipsoid contacts, Computers and Geotechnics, 24 (1999) 245–263.

Pérez G., Numerical simulations in granular matter: The discharge of a 2d silo, PRAMANA - journal of physics, 70 (2008) 989–1007.

Perram J.W., Wertheim M.S., Lebowitz J.L., Williams G.O., Monte Carlo simulations of hard spheroids, Chemical Physics Letters, 105 (1984) 277–280.

Perram J.W., Wertheim M.S., Statistical mechanics of hard spheroids. i. overlap algorithm and the contact function, Journal of Computational Physics, 58 (1985) 409–416.

Pöschel T. and Buchholtz V., Static friction phenomena in granular materials: Coulomb law versus particle geometry, Physical Review Letters, 71 (1993) 3963–3966.

Pöschel T., Buchholtz V., Molecular dynamics of arbitrarily shaped granular particles, J. Phys. I France, 5 (1995) 1431–1455.

Pöschel T., Schwager T., Computational Granular Dynamics, Springer, Berlin, 2005.

Ridgway K., Rupp R., The effect of particle shape on powder properties, Journal of Pharmacy and Pharmacology, 21 (1969) 30S–39S.

Riley G.S., Mann G.R., Effects of particle shape on angles of repose and bulk densities of a granular solid, Materials Research Bulletin, 7 (1972) 163–169.

Ristow G.H., Granular dynamics: A review of recent molecular dynamics simulations of granular materials, Annual Reviews of Computational Physics I, (1994) 275–308.

Silbert L.E., Ertas D., Grest G.S., Halsey T.C., Levine D., Plimpton S.J., Granular flow down an inclined plane: Bagnold scaling and rheology, Physical Review E, 64 (2001).

Tuley R., Danby M., Shrimpton J., Palmer M., On the optimal numerical time integration for lagrangian dem within implicit flow solvers, Computers and Chemical Engineering, 34 (2010) 886–899.

Wang C.Y., Wang C.F., Sheng J., A packing generation scheme for the granular assemblies with 3d ellipsoidal particles, Int. J. Numer. Anal. Meth. Geomech., 23 (1999) 815–828.

Wellmann C., Lillie C., Wriggers P., Homogenization of granular material modeled by a three-dimensional discrete element method, Computers and Geotechnics, 35 (2008) 394–405.

Zhao D.W., Nezami E.G., Hashash Y.M.A., Ghaboussi J., Three dimensional discrete element simulation for granular materials, Engineering Computations 23 (2006) 749–770.

Author's short biography

Kasra Samiei

Kasra Samiei graduated from Amirkabir University of Technology, Tehran, Iran as a mechanical engineer specialized in solids design. He later completed his master's degree at the University of Boras, Sweden in "waste management and resource recovery technology". He holds a Ph.D. in engineering science from the University of Luxembourg. His main research focus is on computational granular dynamics in conjunction with computational fluid dynamics. He is currently a post-doctoral researcher at the University of Leoben, Austria.

Girma Berhe

Girma Berhe received his bachelor's degree in computer science (1996), and master's degree in information science (2001), both from Addis Ababa University, Ethiopia, and a Ph.D. in computer science (2006) from INSA de Lyon, France. He worked as a post-doctoral researcher from December 2006 to November 2007 in Institut National Polytechnic de Toulouse, France. He also worked as a senior researcher in the Faculty of Science, Technology and Communication, University of Luxembourg, from January 2008 to February 2011. His current research interests include distributed and high-performance computing, autonomic computing and mobile computing. He has published several journal papers and peer-reviewed international conference papers.

Bernhard Peters

A graduate in mechanical engineering (Dipl.-Ing.) and with a Ph.D. from the Technical University of Aachen, Bernhard Peters is currently head of the thermo-/fluid dynamics section at the University of Luxembourg and an academic visitor to the Lithuanian Energy Institute. After being a post-doctoral research associate at the Imperial College of London, he established a research team dedicated to the thermal conversion of solid fuels at the Karlsruhe Institute of Technology (KIT), and worked thereafter in industry at AVL List GmbH, Austria. His research activities include thermo-/fluid dynamics, in particular multi-phase flow, reaction engineering, numerical modeling, high-performance computing and motion and conversion of particulate materials.

The 47th Symposium on Powder Technology and the Ceremony for the 20th Anniversary of Establishment of Hosokawa Powder Technology Foundation

The 47th Symposium on Powder Technology was held together with the Ceremony for the 20th Anniversary of Establishment of Hosokawa Powder Technology Foundation at the Imperial Hotel Osaka, Japan on Tuesday, September 3, 2013. They were organized by Hosokawa Powder Technology Foundation with the sponsorship of Hosokawa Micron Corporation and the latter as one of special events of the Foundation. Over 200 people from the industries and academic organizations attended these events and had many discussions.

The theme of this symposium had been directly related with nanoparticles and nanotechnology since 2001 till last year for more than ten years but this time it has widened the range to the powder technology supporting the pioneering technology as well as the fundamentals in the fields of pharmaceuticals, ceramics, coal powder and composite materials as well as from the aspects of advanced simulation and powder processing machines without restricting to only the nanoparticles.

In the Ceremony for the 20th Anniversary of Hosokawa Foundation after the Symposium on Powder Technology, the Hosokawa Powder Technology Fellowship Supporting Award was presented by the Foundation president, Mr.Yoshio Hosokawa to six brilliant younger researchers in the field of powder technology. Following this presentation, Dr.Komiyama, the Chairman of Mitsubishi Research Institute and president emeritus of University of Tokyo, gave the special lecture on the revitalization for Japan.

Part I The 47th Symposium on Powder Technology

Theme: Progress of powder technology supporting the pioneering technology to the fundamentals

Opening address	Prof. Hiroaki Masuda, Prof. emeritus of Kyoto Univ.

Session 1 Chaired by Prof. Ko Higashitani, Prof. emeritus of Kyoto Univ.

Lecture 1

“Studies on novel pharmaceutical preparations based on particulate design”	Prof. Hirofumi Takeuchi, Gifu Pharmaceutical University

Lecture 2

“Microstructure design of ceramics by controlling the dispersion of fine particles in a liquid, and the application of the design technique to fabricate novel materials”	Dr. Tetsuo Uchikoshi, National Institute for Materials Science

Lecture 3

“Particle composite and microstructure control process and their application”	Prof. Junichi Tatami, Yokohama National University

Session 2 Chaired by Prof. Makio Naito, Osaka Univ.

Lecture 4

“Progress of simulation for particles behavior and its application to powder processing”	Prof. Junya Kano, Tohoku University

Lecture 5	
Powder technology for the development of advanced coal utilization power plant contributing to the energy security and environmental protection”	Dr. Hisao Makino, Central Research Institute of Electric Power Industry
Lecture 6	
“The latest powder technology for enhancing the functional capability of fine particles”	Mr. Masahiro Inoki, Hosokawa Micron Corporation

Part II Ceremony for the 20th anniversary of establishment of Hosokawa Powder Technology Foundation

Speech of the president	Mr. Yoshio Hosokawa, President of Hosokawa Powder Technology Foundation
Presentation ceremony for the fellowship supporting award	
Special lecture “The Revitalization for Japan —Innovation to realize the Platinum Society”	Dr. Hiroshi Komiyama, Chairman of the Institute, Mitsubishi Research Institute, Inc., President emeritus, University of Tokyo
Closing address	Mr. Kiyomi Miyata, President of Hosokawa Micron Corporation

Symposium on Powder Technology with more than 200 participants

Presentation ceremony for the fellowship supporting award

The 20th KONA Award

Dr. Hirofumi Takeuchi, Professor of Gifu Pharmaceutical University (GPU), was selected as the winner of the 20th KONA Award, which is sponsored by Hosokawa Powder Technology Foundation and given to the scientist(s) or group(s) who have achieved distinguished research works in the field of particle science and technology.

He received his B.S. (1979), M.S. (1981) and Ph.D. (1984) in pharmaceutical sciences from Kyoto University. He joined GPU as a faculty member in 1984, and became Lecturer in 1988 and associate professor in 1991. He spent 1 year as a visiting scientist at Faculty of Pharmacy and Pharmaceutical Sciences, University of Alberta, in 1989–1990. He is now Professor of GPU (2005–present). He served as the director of department of pharmaceutical sciences (2008–2010) and the dean of graduate school in GPU (2010–2012), and now he is the dean of GPU responsible for all students (2012–present).

He is now keeping a board member in several scientific societies such as the vice president of The Society of Powder Technology, Japan, and a member of the board of directors of The Academy of Pharmaceutical Science and Technology, Japan, and so on. He was also a member of Board of Scientific Advisors in Controlled Release Society (CRS) (2010–2012).

Dr. Takeuchi has made a great scientific contribution in the field of pharmaceutical technology based on powder and particle technology. His works are concerned with preparing new dosage forms of drugs in several administration routes such as oral, parenteral, pulmonary and ophthalmic. The common research concept in his research for dosage form development is “particle design”, which means preparations of functional particles for highly effective drug delivery.

He has reported several types of surface modified liposomes having pharmaceutical functions for drug delivery. It has been demonstrated that mucoadhesive liposomes can facilitate absorption of peptide drugs in oral or pulmonary administration by prolonging the retention time of the device at the objective part in the body. Recently the liposomal systems with optimally designed were found to deliver drugs into the posterior part of the eye with a simple eye drop administration. The research for developing these drug carriers has been highly evaluated because they are promising tools to develop the non-invasive drug therapy as an alternative method to an invasive method, injection.

Particle design research is also applied to oral solid dosage form design and its preparation process. These investigations contributed to development of a novel preparation method of rapidly oral disintegration tablet, which is one of the most interesting patient oriented dosage forms, by controlling the particle size of binder or preparing composite particles of excipient with fine silica particle for the tablet formulation. To complete these technologies, several basic researches regarding to granulation, tabletting and grinding have been conducted.

So far, the number of published original papers in these research fields is 245 and that of reviewed papers, book chapters and related articles is totally 100.

On March 6th , 2013, Mr. Yoshio Hosokawa, President of the Foundation, handed the 20th KONA Award to Dr. Takeuchi at the presentation ceremony held at Hosokawa Micron Corporation in Hirakata.

General Information

History of the Journal

In the history of KONA Powder and Particle Journal, two organizations have been playing an important role. The one is the Council of Powder Technology, Japan (CPT) and the other is the Hosokawa Powder Technology Foundation (Hosokawa Foundation). The CPT was established in 1969 by Hosokawa Micron Corporation as a nonprofit organization to enhance the activities of research and development on powder science and technology. The Hosokawa Foundation was established in 1991 as a public-service corporation approved by the Ministry of Education, Culture, Sport, Science and Technology of Japan. The issues from No.1 (1983) to No.12 (1994) of KONA were published by CPT and the issues from No.13 (1995) by the Hosokawa Foundation.

The aim of KONA in the early days was to introduce excellent Japanese papers to the world and thus KONA consisted of papers recommended by some Japanese academic societies and translated from Japanese to English. From the issue of No.8, the CPT changed its editorial policy to internationalize the KONA and to incorporate papers by authors throughout the world in addition to translated papers. In response to this change, three editorial blocks have been organized in the world; Asian-Oceania, American and European. The policy and system have not changed even after the Hosokawa Foundation has taken over from the CPT. From the issue of No.27 (2009), publication of translated papers has been terminated and only original papers have been published. The CPT is active still today and collaborates with the Hosokawa Foundation.

Aims and Scope

KONA publishes papers in a broad field of powder science and technology, ranging from fundamental principles to practical applications. The papers describing technological experiences and critical reviews of existing knowledge in special areas are also welcome.

The submitted papers are published only when they are judged by the Editor to contribute to the progress of powder science and technology, and approved by any of the three Editorial Committees.

The paper submitted to the Editorial Secretariat should not have been previously published.

Category of Papers

- Invited articles
  Review papers and special articles invited by the KONA Editorial Committees.
- Contributed papers
  Original research and review papers submitted to the KONA Editorial Committees, and refereed by the Editors.

Submission of Papers

Papers should be sent to each KONA Editorial Secretariat.

- Asia/Oceania Editorial Secretariat
  Dr. T. Yokoyama and Dr. L. Cui
  Hosokawa Powder Technology Foundation
  Shodai-Tajika, 1-9, Hirakata, 573-1132 Japan
- Europe/Africa Editorial Secretariat
  Dr. S. Sander or Ms. N. Faerber
  Hosokawa Alpine AG
  Peter-Dörfler-Straße 13-25
  D - 86199 Augsburg, Germany
- Americas Editorial Secretariat
  Dr. C. C. Huang
  Hosokawa Micron Powder Systems
  10 Chatham Road, Summit NJ 07901 USA

Publication in KONA Powder and Particle Journal is free of charge.

Publication Schedule

KONA is published annually. The publication date is around January 10th.

Subscription

KONA Powder and Particle Journal is distributed free of charge to senior researchers at universities and laboratories as well as to institutions and libraries in the field throughout the world. The publisher is always glad to consider the addition of names of those, who want to obtain this journal regularly, to the mailing list. Distribution of KONA is made by each Secretariat.

Free electronic publication of KONA Powder and Particle Journal is available at http://www.kona.or.jp

Instructions to Authors

(1) Manuscript format

- Electric files should be submitted to the Editorial Secretariat by online. Authors' short biography with less than 100 words per person and photograph of all the authors should be attached to the final version.
- The structure of manuscripts should follow the following order; title, authors, affiliations, abstract, graphical abstract, keywords, main text, (acknowledgement), (appendix), (nomenclature), references. The items with parentheses are not mandatory.
- Full postal addresses must be given for all the authors. Indicate the corresponding author by the mark"*" after the name. Telephone and fax numbers and e-mail address should be provided for the corresponding author.
- Abstract should not exceed 200 words.
- Graphical abstract should be a concise, visual summary of the article which will be displayed in the contents list either online or print.
- The appropriate number of keywords is 5 or 6.
- The maximum pages printed in KONA are supposed to be: 10 for an original paper and 15 for a review paper.
- Symbols and units should be listed in alphabetical order with their definition and dimensions in SI units.
- The color figures will appear in color on the Web (http://www.kona.or.jp) but only partly in color in the paper version.
- Concerning references, the alphabetical system should be adopted. Please use reference management software such as Endnote to manage references as far as possible.
  List: References should be arranged first alphabetically and then further sorted chronologically if necessary. More than one reference from the same author(s) in the same year must be identified by the letters "a", "b", "c", etc., placed after the year of publication.
  Examples:
  - Reference to a book:
  Strunk Jr. W., White E.B., The Elements of Style, fourth ed., Longman, New York, 2000.
  - Reference to a chapter in an edited book:
  Mettam G.R., Adams L.B., How to prepare an electronic version of your article, in: Jones B.S., Smith R.Z. (Eds.), Introduction to the Electronic Age, E-Publishing Inc., New York, 2009, pp.281–304.
  - Reference to a journal publication:
  Tsuji Y., Tanaka T., Ishida T., Lagrangian numerical simulation of plug flow of cohesionless particles in a horizontal pipe, Powder Technology, 71 (1992) 239-250.
  Text: All citations in the text should refer to:
  1. Single author: the author's name (without initials, unless there is ambiguity) and the year of publication;
  2. Two authors: both authors' names and the year of publication;
  3. Three or more authors: first author's name followed by "et al." and the year of publication.
  Citations may be made directly (or parenthetically). Groups of references should be listed first alphabetically, then chronologically.
  Examples: "as demonstrated (Allan, 1996a, 1996b, 1999; Allan and Jones, 1995). Kramer et al. (2000) have recently shown ...."

(2) Copyright and permission

- The original paper to be submitted to KONA has not been published before in any language or in any journal or media; it is not submitted and not under consideration for publication in whole or in part elsewhere.
- Authors are responsible for obtaining permission from the copyright holders to reproduce any figures, tables and photos for which copyright exists.
- Original papers submitted for publication become immediately the property of the Hosokawa Powder Technology Foundation and remain so unless withdrawn by the author prior to acceptance for publication or unless released by the Editor.
- The original papers in KONA should not be reproduced nor published in any form without the written permission of the Hosokawa Foundation.

HOSOKAWA MICRON

New Product

Air classifier integrating machines

Pulverizers : Impact mill, Jet mill, Ball mill

Product size : Tens of micron to sub micron

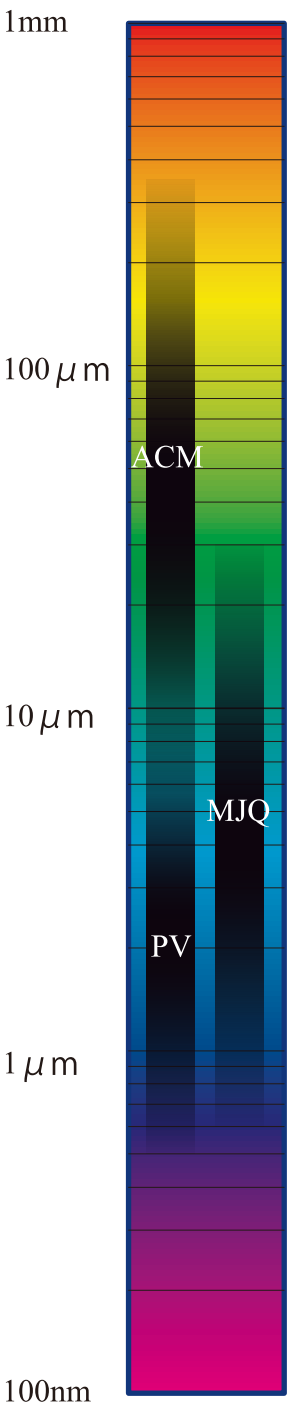

HOSOKAWA/MIKRO ACM Pulverizer ACM-HC

- ■Fine impact mill with a built in air classifier
- ■The latest model of ACM pulverizer
- ■High performance and energy saving
- ■No metal contamination
- ■Easy Disassembling and Cleaning
- ■Low noise operation
- ■Compact unit

HOSOKAWA/MICRON Micron Jet Type Q Air Classifying target jet mill MJQ

- ■Target jet mill with a built in air classifier
- ■High energy efficiency
- ■No material remaining in the mill
- ■Complete ceramics model interior
- ■Easy particle size control
- ■Easy to clean
- ■Designed for handling sticky material

HOSOKAWA/MICRON Pulvis Agitating Ball Mill PV

- ■Finest product by dry milling
- ■Compact design
- ■From Laboratory model to production machine
- ■Energy efficient
- ■Easy particle size control
- ■Easy access to inside of the mill
- ■Complete ceramics model interior

Contact to... http://www.hosokawamicron.com

Japan : Osaka +81-72-855-2224,Tokyo +81-3-5248-5700
(HOSOKAWA MICRON CORP. World Headquarters)

Our global network

Korea : +82-2-420-5691 (Hosokawa Micron (Korea) Ltd.)

China : +86-21-5306-8031 (Hosokawa Micron (Shanghai) Powder Machinery Co., Ltd.)

Germany : +49-821-59-06-0 (Hosokawa Alpine AG)
+49-7131-9070 (Hosokawa Bepex GmbH)

Netherlands : +31-314-373333 (Hosokawa Micron B.V.)

Russia : +7-812 3326200 (Hosokawa Micron Sankt Petersburg OOO)

U.K. : +44-1928-755-100 (Hosokawa Micron Ltd.)

U.S.A. : +1-908-277-9300 (Hosokawa Micron International Inc.)

HOSOKAWA MICRON GROUP

The Hosokawa Micron Group will always be the leading global company covering the mountain range of Powder Technologies. The Group has been a pioneer in the filed of powder and particle processing, blown film processing, and confectionary and bakery technologies. We provide R&D, engineering, manufacturing and services in various fields of the world's major industrial markets.

Global network

Process Technologies for Tomorrow

HOSOKAWA MICRON GROUP

Headquaters Location :
HOSOKAWA MICRON CORPORATION
http://www.hosokawamicron.co.jp